The supramolecular derivatisation of pharmaceutically relevant compounds *via* co-crystallization and cyclodextrin inclusion complexation

A thesis submitted to the University of Cape Town

In fulfilment of the requirements for the degree of

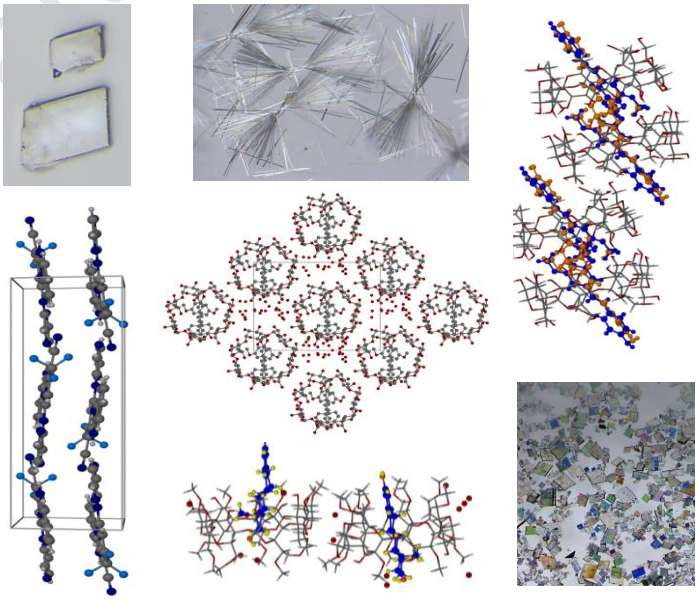
DOCTOR OF PHILOSOPHY

By: Alexios Ivan Vicatos

Supervisor: Professor Mino R. Caira

Department of Chemistry

June 2022



University of Cape Town

The copyright of this thesis vests in the author. No quotation from it or information derived from it is to be published without full acknowledgement of the source. The thesis is to be used for private study or non-commercial research purposes only.

Published by the University of Cape Town (UCT) in terms of the non-exclusive license granted to UCT by the author.

University of Cape Town

Declaration of Originality

I, Alexios Ivan Vicatos, hereby declare that the work on which this thesis is based is my original work (except where acknowledgements indicate otherwise) and that neither the whole work nor any part of it has been, is being, or is to be submitted for another degree in this or any other university. I authorise the University to reproduce for the purpose of research either the whole or any portion of the contents in any manner whatsoever.

Signed by candidate

Signature: Alexios Ivan Vicatos

Date: June 2022

Acknowledgements

1. I would like to dedicate this doctoral thesis to my supervisor, Professor Mino R. Caira. The support and knowledge that he gave me over the years of my doctoral degree have been invaluable. I am eternally thankful for his superb supervision, endless support, patience, generosity and mentorship.
2. My family and friends for their endless emotional and encouraging support, and especially my sister, Giselle, for her invaluable support.
3. The David and Elaine Potter Fellowship for providing financial support for my doctoral degree.
4. University of Cape Town for providing funding to cover fees.
5. Oppenheimer Memorial Trust for providing travel funding.
6. Dr. Godfrey Mayoka, for synthesizing the three pyrido[1,2-a]benzimidazole derivatives (GMP drug leads) at the Drug Discovery and Development Centre (H3D), under the directorship of Professor Kelly Chibale at the University of Cape Town. These compounds were the subject of an integral part of the investigation conducted during this doctoral study.
7. Professors Laura Catenacci, Milena Sorrenti, and Maria Cristina Bonferoni from the Department of Drug Sciences, University of Pavia, Italy, for supplying the active compound, pterostilbene. This compound was also the subject of an integral part of the investigation conducted during this doctoral study.
8. Dr Hong Su for single-crystal X-ray data-collection.
9. Dr Cesarina Edwards-Smith Simons and Christopher Thurling for their assistance with the high-performance liquid chromatography instrument and analysis.
10. The Supramolecular Chemistry Research Group for their generous support, assistance wherever necessary, and ideas.

Glossary

General

API	Active pharmaceutical ingredient
CD	Cyclodextrin
LAG	Liquid-assisted grinding
GRAS	Generally recognized as safe
Deriv	Derivative
H:G	Host:guest
S_0	Intrinsic aqueous solubility value
$S_{API(CD)}$	The aqueous solubility of the API in the form of a CD inclusion complex
S_{API}	The aqueous solubility of the API
K_c	Association constant

Experimental techniques

HPLC	High-performance liquid chromatography
FT-IR	Fourier transform infrared
DSC	Differential scanning calorimetry
TGA	Thermal gravimetric analysis
^{1}H NMR	Proton nuclear magnetic resonance
HSM	Hot stage microscopy

Chemical compounds

BES	β-estradiol
PRO	Progesterone
PTB	Pterostilbene
GMP	An internal codename for the pyrido[1,2-a]benzimidazole derivatives
α-CD	α-Cyclodextrin
β-CD	β-Cyclodextrin
γ-CD	γ-Cyclodextrin
DMB	Heptakis(2,6-di-*O*-methyl)-β-cyclodextrin
TMB	Heptakis(2,3,6-tri-*O*-methyl)-β-cyclodextrin
HPGCD	2-Hydroxypropyl γ-cyclodextrin
RAMEB	Randomly methylated β-cyclodextrin
HPBCD	2-Hydroxypropyl β-cyclodextrin

SBEBCD	Sulfobutyl ether β-cyclodextrin
HEBCD	Hydroxyethyl β-cyclodextrin
MBCD	Methylated β-cyclodextrin
PEG	Polyethylene glycol

GMP solvate crystal structures

GMP23·DMF	A solvate of GMP-23 and dimethylformamide
GMP31·DMF	A solvate of GMP-31 and dimethylformamide
GMP58·DMSO	A solvate of GMP-58 and dimethyl sulfoxide

GMP-coformer product code names and their components

GMP-23-MAL	GMP-23 and L-malic acid
GMP-23-NIC	GMP-23 and nicotinamide
GMP-31-MAL	GMP-31 and L-malic acid
GMP-31-NIC	GMP-31 and nicotinamide
GMP-58-MAL	GMP-58 and L-malic acid
GMP-58-NIC	GMP-58 and nicotinamide

Cyclodextrin complexes

β-CD·PTB	A hydrated β-CD – pterostilbene inclusion complex
β-CD·BES	A hydrated β-CD – β-estradiol inclusion complex
β-CD·PRO	A hydrated β-CD – progesterone inclusion complex
γ-CD·BES	A hydrated γ-CD – β-estradiol inclusion complex
γ-CD·PRO	A hydrated γ-CD – progesterone inclusion complex
DMB·BES	A hydrated DMB – β-estradiol inclusion complex
DMB·PRO	A hydrated DMB – progesterone inclusion complex

Crystallographic terms

ASU	Asymmetric unit
s.o.f.	Site-occupancy factor
U_{iso}	Isotropic thermal parameter
CSD	Cambridge Structural Database
PXRD	Powder X-ray diffraction
VTPXRD	Variable temperature powder X-ray diffraction
SCXRD	Single-crystal X-ray diffraction

RMSD	Root-mean-square deviation
$\Delta\rho$	Difference electron density

Solvents

DMSO-d_6	Deuterated dimethyl sulfoxide
DMSO	Dimethyl sulfoxide
DMF	Dimethylformamide
EtOH	Ethanol
THF	Tetrahydrofuran

Abstract

The supramolecular derivatisation of pharmaceutically relevant compounds *via* co-crystallization and cyclodextrin (CD) inclusion complexation was attempted in order to produce new solid forms of these compounds for potential pharmaceutical applications. The pharmaceutically relevant compounds investigated included (a) three drug leads, namely pyrido[1,2-a]benzimidazole derivatives [displaying activity against schistosomiasis (bilharzia)], (b) two steroidal compounds, namely β-estradiol (used for hormonal therapy and treatment of breast and prostate cancer), and progesterone (used for hormonal therapy), and (c) the potent antioxidant pterostilbene (displaying anti-cancer activity *inter alia*). Six new solid forms of the pyrido[1,2-a]benzimidazole derivatives resulted from their interaction with partner molecules L-malic acid and nicotinamide using 1:1 molar ratios of the starting materials. They were characterised by powder X-ray diffraction, thermal analysis and spectroscopic (FT-IR and ^{1}H NMR) techniques. Preliminary solubility studies indicated that for five of the forms, aqueous solubility increases for the drug leads in the range 2- to 20-fold were achieved. In addition, amorphous forms of the three pyrido[1,2-a]benzimidazole derivatives were prepared *via* grinding and also assessed for aqueous solubility improvement, with the result that only one of them indicated a 2-fold aqueous solubility increase.

In addition, nine new hydrated CD inclusion complexes with guests β-estradiol (BES), progesterone (PRO) and pterostilbene (PTB), were isolated using kneading and/or co-precipitation methods, and analysed using thermal analysis, powder X-ray diffraction and ^{1}H NMR analytical techniques. The CD inclusion complexes (with host-guest stoichiometries in parentheses) included β-CD·BES (2:1), γ-CD·BES (1:1), dimethylated β-CD·BES (1:1), β-CD·PRO (2:1), γ-CD·PRO (3:2), dimethylated β-CD·PRO (1:1), β-CD·PTB (1:1), γ-CD·PTB (1:1) and permethylated β-CD·PTB (1:1). The β-CD·BES, γ-CD·BES, β-CD·PRO and γ-CD·PRO inclusion complexes were assessed for their ability to improve the aqueous solubility of the respective steroids at 27 ^{o}C. The $S_{API(CD)}/S_{API}$ ratios for these CD complexes ($S_{API(CD)}$ indicating the solubility of each steroid in the form of the CD complex and S_{API} the solubility of the pure steroid), were 21.3 ± 0.1, 6.1 ± 0.3, 5.5 ± 0.1 and 19.9 ± 0.1 respectively, thus indicating that CD inclusion complexation increased the aqueous solubility of both steroids. Phase solubility studies of pterostilbene (PTB) with sulfobutylether β-CD (SBEBCD) and randomly methylated β-CD (RAMEB), indicated that the low aqueous solubility of PTB could be enhanced by factors of 1431

and 1356 respectively using 20 mM concentrations of SBEBCD and RAMEB at 25 ^{o}C. Single-crystal X-ray structures of six of the new CD inclusion complexes were elucidated, β-CD·BES, β-CD·PRO and γ-CD·PRO featuring severely disordered guest molecules, while analysis of β-CD·PTB, DMB·BES and DMB·PRO revealed the detailed modes of guest inclusion of the respective drugs unequivocally.

Table of contents

Chapter 1: Introduction

1.1) Overview....1
1.2) Cyclodextrins: A general overview and their structures....3
1.2.1) Overview of cyclodextrins (CDs)....3
1.2.2) The structures and resulting molecular properties of CDs....5
1.2.3) CD complex formation methodologies....7
1.2.4) The dynamic host-guest equilibrium....7
1.2.5) The formation of a CD inclusion complex....7
1.2.6) The toxicology of CDs....9
1.2.7) CD applications....9
1.2.8) The mechanism of API release from a CD molecule....10
1.2.9) The molecular geometry of a CD....13
1.2.10) Crystalline packing of the native CDs....15
1.3) Co-Crystals....19
1.3.1) Overview of co-crystals....19
1.3.2) Bonding in co-crystals....20
1.3.3) Co-crystal formation....21
1.3.4) Co-crystals in the pharmaceutical industry....22
1.3.5) Mechanism of API release from co-crystals....23
1.4) General aims and objectives....24
1.5) Pointwise summary of the aims and objectives....32
References....34

Chapter 2: Experimental methods

2.1) Materials....39
2.1.1) Pharmaceutically relevant compounds....39
2.1.2) Cyclodextrins (CDs)....39
2.1.3) Coformers....39
2.2) Co-crystal screening....40
2.2.1) Virtual co-crystal screening....40
2.2.2) Grinding experiments....40
2.2.3) Co-precipitation....40
2.3) Cyclodextrin inclusion....41
2.3.1) Kneading....41
2.3.2) Kneading a mixture of the molten API and the crystalline CD....42
2.3.3) Co-precipitation....42
2.3.3.1) Native cyclodextrins (CDs)....42
2.3.3.2) Methylated cyclodextrins (CDs)....42

2.4) Ambient temperature powder X-ray diffraction (PXRD).....43
2.5) Variable temperature powder X-ray diffraction (VTPXRD).....43
2.6) Single-crystal X-ray diffraction (SCXRD) analysis.....43
2.7) Proton nuclear magnetic resonance (^{1}H NMR) spectroscopy.....45
2.8) Fourier transform infrared (FT-IR) spectroscopy.....45
2.9) Thermal analysis.....45
2.9.1) Hot stage microscopy (HSM).....46
2.9.2) Thermal gravimetric analysis (TGA).....46
2.9.3) Differential scanning calorimetry (DSC).....46
2.10) Solubility analysis.....47
2.10.1) Solubility analysis *via* colour standard comparison for the GMP-coformer products.....47
2.10.2) Phase solubility analysis with CDs and pterostilbene.....48
2.10.3) Solubility analysis by gravimetric increments.....49
References.....50

Chapter 3: The supramolecular derivatisation of the pyrido[1,2-a]benzimidazole derivative series
3.1) Literature review.....51
3.2) Initial characterisation of GMP-23, GMP-31 and GMP-58.....52
3.2.1) Initial characterisation results for GMP-23.....54
3.2.1.1) Experimental powder X-ray diffraction (PXRD) characterisation of GMP-23.....54
3.2.1.2) Hot stage microscopy (HSM) analysis of GMP-23.....55
3.2.1.3) Thermal gravimetric analysis (TGA) of GMP-23.....56
3.2.1.4) Differential scanning calorimetry (DSC) analysis of GMP-23.....57
3.2.1.5) Single-crystal X-ray diffraction (SCXRD) analysis of the GMP23·DMF solvate.....59
3.2.1) The initial characterisation results for GMP-31.....67
3.2.2.1 Experimental powder X-ray diffraction (PXRD) characterisation of GMP-31.....67
3.2.2.2) Hot stage microscopy (HSM) analysis of GMP-31.....67
3.2.2.3) Thermal gravimetric analysis (TGA) of GMP-31.....68
3.2.2.4) Differential scanning calorimetry (DSC) analysis of GMP-31.....69
3.2.2.5) Single-crystal X-ray diffraction (SCXRD) analysis of the GMP31·DMF solvate.....70
3.2.3) The initial characterisation results for GMP-58.....80
3.2.3.1) Experimental powder X-ray diffraction (PXRD) characterisation of GMP-58.....80
3.2.3.2) Hot stage microscopy (HSM) analysis of GMP-58.....80
3.2.3.3) Thermal gravimetric analysis (TGA) of GMP-58.....81
3.2.3.4) Differential scanning calorimetry (DSC) analysis of GMP-58.....82
3.2.3.5) Single-crystal X-ray diffraction (SCXRD) analysis of GMP-58.....83
3.2.3.6) Single-crystal X-ray diffraction (SCXRD) analysis of the GMP58·DMSO solvate.....91
3.2.4) CD inclusion with GMP-23, GMP-31 and GMP-58.....98
3.2.5) Co-crystallization of GMP-23, GMP-31 and GMP-58.....98
3.2.5.1) Virtual co-crystal screening analysis.....98
3.2.5.2) Experimental co-crystal screening of GMP-23, GMP-31 and GMP-58.....110
3.2.5.3) Characterisation of GMP-23 form 2.....110
3.2.5.4) The crystalline morphology of GMP-23 form 2.....111
3.2.5.5) The PXRD analysis of GMP-23 form 2.....111

3.2.5.6) ^{1}H NMR analysis of GMP-23 form 2....113
3.2.5.7) Thermal gravimetric analysis (TGA) of GMP-23 form 2....114
3.2.5.8) Differential scanning calorimetry (DSC) of GMP-23 form 2....114
3.2.5.9) Further experimentation and discoveries....115
3.2.6.1) Products generated *via* interaction between GMP compounds and fused coformers....117
3.2.6.2) Fourier transform infrared (FT-IR) analysis of the GMP-coformer products....118
3.2.6.3) Confirmatory ^{1}H NMR analysis....119
3.2.6.4) Powder X-ray diffraction (PXRD) analysis....120
3.2.6.5) Hot stage microscopy (HSM) analysis....124
3.2.6.6) Thermal gravimetric analysis (TGA)....129
3.2.6.7) Differential scanning calorimetry (DSC) analysis....134
3.2.7) Solubility analysis *via* colour standard comparison....140
References....144

Chapter 4: Cyclodextrin inclusion of the antioxidant pterostilbene
4.1) Literature review....145
4.2) Overview of experimental results....147
4.2.1) The inclusion complex β-CD·PTB....147
4.2.1.1) SCXRD analysis of β-CD·PTB....147
4.2.1.2) Summary of results involving attempts to produce a pure bulk phase of β-CD·PTB for further characterisation....162
4.2.1.3) The initial isolation of β-CD·PTB *via* co-precipitation....163
4.2.1.4) ^{1}H NMR analysis of the harvested β-CD·PTB crystals....165
4.2.1.5) Attempts at forming β-CD·PTB *via* conventional kneading and a mechanochemical method involving guest melting....166
4.2.1.6) The discovery of a new polymorph of pterostilbene and the isolation of β-CD·PTB with a significantly higher purity....169
4.2.1.7) Hot stage microscopy (HSM) analysis....173
4.2.1.8) Thermal gravimetric analysis (TGA)....174
4.2.1.9) Differential scanning calorimetry (DSC) 175
4.2.2) The inclusion complex, γ-CD·PTB....177
4.2.2.1) Method of preparation *via* kneading and co-precipitation....177
4.2.2.2) ^{1}H NMR analysis of the γ-CD·PTB complex....178
4.2.2.3) Thermal analysis of γ-CD·PTB....179
4.2.2.3a) Hot stage microscopy (HSM) analysis....180
4.2.2.3b) Thermal gravimetric analysis (TGA)....181
4.2.2.3c) Differential scanning calorimetry (DSC)....182
4.2.3) The TMB·PTB inclusion complex....183
4.2.3.1) The initial isolation of TMB·PTB *via* co-precipitation....183
4.2.3.2) Crystal morphology....184
4.2.3.3) PXRD analysis....184
4.2.3.4) ^{1}H NMR analysis....185
4.2.3.5) Hot stage microscopy (HSM) analysis....186
4.2.3.6) Thermal gravimetric analysis (TGA)....187

4.2.3.7) Differential scanning calorimetry (DSC)....188
4.2.3.8) Variable temperature PXRD....189
4.2.4) Phase solubility investigation with randomly methylated β-CD (RAMEB) and sulfobutyl ether β-CD (SBEBCD) sodium salt....192
4.2.4.1) Overview and contextualisation of the investigation....192
4.2.4.2) Construction of the calibration curve....193
4.2.4.3) Phase solubility results with RAMEB and SBEBCD sodium salt....194
References....199

Chapter 5: Cyclodextrin inclusion complexation with β-estradiol and progesterone
5.1) Literature review....202
5.1.1) Literature review for CD inclusion complexes with β-estradiol....202
5.1.2) Literature review for CD inclusion complexes with progesterone....204
5.2) Overview of experimental results....208
5.2.1) The inclusion complexes: β-CD·BES and β-CD·PRO....209
5.2.1.1) Method of preparation....209
5.2.1.2) Crystal morphology of β-CD·BES and β-CD·PRO....209
5.2.1.3) ^{1}H NMR analysis of β-CD·BES and β-CD·PRO....210
5.2.1.4) PXRD analysis for β-CD·BES and β-CD·PRO....211
5.2.1.5) Hot stage microscopy (HSM) of β-CD·BES and β-CD·PRO....213
5.2.1.6) Thermal gravimetric analysis (TGA)....215
5.2.1.7) Differential scanning calorimetry (DSC) and variable temperature PXRD....217
5.2.1.8) Single-crystal X-ray diffraction (SCXRD) analysis of β-CD·BES and β-CD·PRO....224
5.2.2) The inclusion complexes γ-CD·BES and γ-CD·PRO....242
5.2.2.1) Method of preparation....242
5.2.2.2) Crystal morphologies of γ-CD·BES and γ-CD·PRO....242
5.2.2.3) ^{1}H NMR analysis of γ-CD·BES and γ-CD·PRO....243
5.2.2.4) PXRD analyses for γ-CD·BES and γ-CD·PRO....244
5.2.2.5) Hot stage microscopy (HSM) analysis of γ-CD·BES and γ-CD·PRO....246
5.2.2.6) Thermal gravimetric analysis (TGA)....248
5.2.2.7) Differential scanning calorimetry (DSC)....251
5.2.2.8) Single-crystal X-ray diffraction (SCXRD) analysis of γ-CD·PRO....253
5.2.3) Solubility analysis *via* gravimetric mass increments....261
5.2.4) The inclusion complexes DMB·BES and DMB·PRO....263
5.2.4.1) Method of preparation....263
5.2.4.2) Crystal morphologies of DMB·BES and DMB·PRO....263
5.2.4.3) ^{1}H NMR analysis of DMB·BES and DMB·PRO....264
5.2.4.4) PXRD analyses of DMB·BES and DMB·PRO....266
5.2.4.5) Hot stage microscopy (HSM) of DMB·BES and DMB·PRO....268
5.2.4.6) Thermal gravimetric analyses (TGA) of DMB·BES and DMB·PRO....271
5.2.4.7) Differential scanning calorimetry (DSC) of DMB·BES and DMB·PRO....273
5.2.4.8) Single-crystal X-ray diffraction (SCXRD) analysis....276
References....307

Chapter 6: Conclusions and future work

6.1) General conclusions.....311
6.1.1) Pyrido[1,2-a]benzimidazole derivatives (GMP-23, GMP-31 and GMP-58).....311
6.1.2) Pterostilbene.....313
6.1.3) β-estradiol and progesterone.....313
References.....315

Appendix

Section 1: General.....1
Section 2: The pyrido[1,2-a]benzimidazole derivatives (GMP-23, GMP-31 and GMP-58).....3
Section 3: Cyclodextrin inclusion with pterostilbene.....35
Section 4: Cyclodextrin inclusion with β-estradiol and progesterone.....43
References.....56

Chapter 1

Introduction

1.1) Overview

The supramolecular derivatisation of active pharmaceutical ingredients (APIs) has the potential to improve the physicochemical properties of these bioactive compounds. A significant number of APIs display potent bioactivity, with however, insufficient and unfavourable physicochemical properties. Examples of these shortcomings include inadequate aqueous solubility, low bioavailability, hygroscopicity and low dissolution rate, low thermal stability, high volatility, poor compressibility, degradation due to oxidation as well as ultraviolet light, visible light, heat and hydrolysis; in addition, adverse side effects include vile odours and tastes.[1,2] Supramolecular derivatisation involves modifying the solid form of the API, without compromising its chemical structure and it has the potential to improve the physicochemical properties of the API under investigation. These APIs can either be already approved and commercially available, or previously discarded during their development phase owing to inherently unfavourable physicochemical properties.

In recent years there has been growing concern that the output levels in the pharmaceutical industry, in terms of the number of new APIs reaching the market, have significantly declined over the past 70 years.[3–6] Many analysists have attempted to diagnose the causes of this declining trend, and even though there are extensive debates with regard to the severity of the decline, there is general consensus that the overall output of the research and development of APIs has declined, or at least remained stagnant,[7] despite an almost exponential increase in financial investment.[3,4,7,8] This could potentially result in pharmaceuticals becoming excessively expensive with fewer new entities reaching the market, and thus this issue needs to be addressed.[3] There are various debates around the cause of this decline, some of which include tighter regulation controls of APIs, shifts in investments (reducing the amount of available funds for research and development, while

expecting higher outputs) and the higher costs involved in utilising the new technological machinery employed in modern pharmaceutical industry.[3,5,9] Furthermore, two other reasons include arguments suggesting that the older screening methods were more productive despite technological advances,[3] and also that it is becoming increasingly more difficult to develop new APIs. Thus, there are speculations that generally all the APIs that were easier to develop have been exhausted.[3,8] The above-mentioned reasons are certainly contributors towards the declining trend in the pharmaceutical industry; however, many analysists believe that significant contributors are the market-related forces that have directed many investors to focus increasingly on "*blockbuster*" models.[3,4,9,10] Blockbuster products are pharmaceutical drugs that target very large patient populations, thus yielding exceptionally high profit returns for the pharmaceutical company when the new API is eventually developed. These blockbuster models are governed by remarkably high development costs and difficult targets with a low probability of success. Thus, this reflects the nature of the declining trend in new drug innovation in the pharmaceutical industry, coupled with the exponentially increasing financial investments.[3,10]

However, blockbuster models are limited to targeting a particular disease affecting very large patient populations and generally do not address the more specific needs of smaller patient population groups presenting multiple diseases.[10] The supramolecular derivatisation of commercially available APIs can address these needs by improving various physicochemical properties that were previously undesirable, thus making the modified APIs more efficient and effective for patients. The approval time for these modified APIs is also considerably reduced, since the unmodified API will have already been approved.

In addition, other critics argue that the declining trend in the pharmaceutical industry is not particularly concerning,[9,10] especially as APIs that have been modified by supramolecular derivatisation are not always accounted for in the statistical outputs of the pharmaceutical industry.[10] From the 1990s onwards, supramolecularly derivatised APIs have in fact contributed a significant fraction to the total number of approved pharmaceutical drugs.[10] Even though supramolecular derivatisation is generally not associated with considerably high financial returns (in comparison to the blockbuster model),[8,10] it has the potential to rectify this declining trend in the pharmaceutical industry, as well as improve a broad variety of APIs for multiple patient population groups with different medical needs.[10] Lastly, it also

has the potential to reduce the cost of a particular medicine should the supramolecular derivatisation of the API improve the solubility and bioavailability. Consequently, less of the API will be needed to perform the same effect in the patient, since the pharmacological effect is enhanced.[1] This is in contrast to the blockbuster model which is projected to make pharmaceuticals unaffordable given current trends.[3]

As mentioned previously, supramolecular derivatisation is also used to improve the physicochemical properties of potential APIs that have failed trials (either as a blockbuster model or smaller development model) and thus potentially allows the previously discarded API to become commercially available. As a result, supramolecular derivatisation of APIs is an important technique that warrants focus and investigation as it has the potential to rectify the declining trend in the pharmaceutical industry, reduce the cost of medicines, reduce the approval time of the pharmaceutical drugs, and target an extensive variety of diseases. There are various methods of supramolecular derivatisation, two of which include cyclodextrin (CD) inclusion complexation and co-crystallization. Both of these methods will be discussed in detail, as they were employed in the research conducted by the author of this doctoral thesis.

1.2) Cyclodextrins: A general overview and their structures

1.2.1) Overview of cyclodextrins (CDs)

The use of cyclodextrins (CDs) in supramolecular chemistry, particularly in the pharmaceutical industry, has gained increasing interest over the past century.[1,2,11–13] CDs are formed from the degradation of starch by a glucanotransferase enzyme causing an intramolecular transglycosylation reaction to occur,[1,11] and are produced annually on a thousand ton scale using environmentally friendly industrial processes.[11] Their ability to form host-guest complexes offers an extensive range for improving the physicochemical properties of countless guest molecules.[1,2,11–13] Their toxicity effects are minimal and can often be completely eliminated by selecting a particular delivery route, or by appropriate derivatisation of one of the native CDs. Consequently, their use for humans as host-guest supramolecular compounds is extensive.[1,2,11–14]

CDs are macrocyclic oligosaccharides which comprise a unique number of glucopyranose units linked by α-(1,4) bonds. The three most common native CDs (upon which many derivatives are based) are α-CD, β-CD and γ-CD which consist of 6, 7 and 8 glucopyranose units respectively (Figure 1.1).[1,2,11,12]

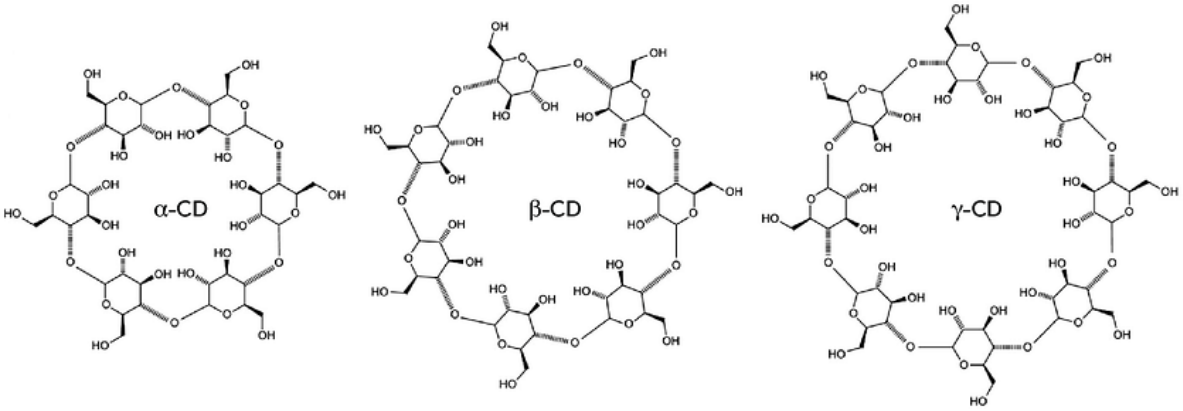


Figure 1.1: The three most common native CDs, namely α-CD, β-CD, γ-CD consisting of 6, 7 and 8 glucopyranose units respectively. Taken from Nikitenko *et al.*[15]

CDs were first discovered in 1891 by Villiers and it was only until the mid-20th century that these native CDs were isolated as well as characterised by X-ray crystallographic analyis.[1,11,14] The manufacture of these CDs is a multi-step process which incorporates an intramolecular transglycosylation reaction as a consequence of the degradation of starch by a CD glucanotransferase enzyme.[1,2,14] Further synthetic processes can be performed on these native CDs in order to form particular derivatives, which are specifically designed to further enhance the efficacy of the CD. This enhancement is not only due to the nature of the added substituent, but also due to the position of its attachment, as well as the number of substituents on the CD molecule.[2,14] Many of these derivatised CDs are also produced industrially in bulk, representative compounds being randomly methylated β-CD (RAMEB), hydroxypropyl β-CD (HPBCD), hydroxypropyl γ-CD (HPGCD) and sulfobutyl ether β-CD (SBEBCD). However, for a significant number of them the synthetic modification process is too costly and thus their commercial use is highly limited, despite their improved efficacy in particular applications.[11]

1.2.2) The structures and resulting molecular properties of CDs

The structural shape of CDs is that of a toroidal, tapered cone and the height of the native CD molecule is 7.9 ± 0.1 Å with an internal diameter whose ranges are 4.7 – 5.3 Å for α-CD, 6.0 – 6.5 Å for β-CD and 7.5 – 8.3 Å for γ-CD (Figure 1.2).[1,2,11,12,14]

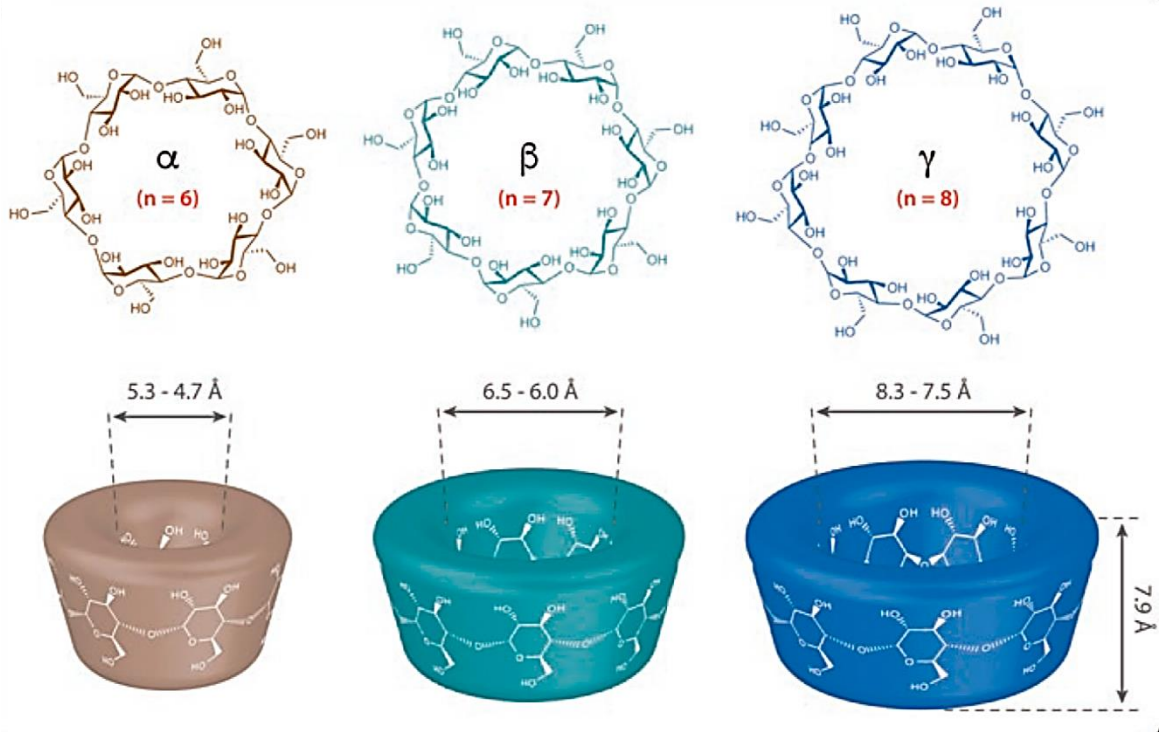


Figure 1.2: The molecular dimensions of α-CD, β-CD and γ-CD. The toroidal shape of the CD molecules is very evident in the series of images in the lower row. Taken from Lee *et al.*[16]

X-ray crystallographic studies have indicated that the primary hydroxyl groups (attached to C6 of each glucopyranose unit) are located on the narrower rim of the ring, while the secondary hydroxyl groups that are attached to C2 and C3 are located on the wider rim (Figure 1.3). This is a consequence of the $^4C_1$ chair conformation that all glucopyranose units generally adopt.[1,11,14] Furthermore, the O3 hydroxyl group of one glucopyranose unit can form a hydrogen bond with the O2 hydroxyl oxygen atom of an adjacent glucopyranose unit and thus a 'belt' of hydrogen bonds can form on the secondary rim.[11,14] This belt is complete for β-CD and it is believed that this specific type of intramolecular hydrogen bonding in β-

CD, as well as the relatively high crystal lattice energy, are the reasons for its lower aqueous solubility (18.4 ± 0.2 mg.cm^{-3} at 25 ^{o}C).[2,11] It would initially be expected that the aqueous solubility of the native CDs would increase with an increase in the number of hydroxyl groups, i.e. α-CD < β-CD < γ-CD. However, β-CD is anomalous owing to the formation of this 'belt' of hydrogen bonds on the secondary rim, and thus those hydroxyl groups involved in the 'belt' formation are not available for hydrogen bonding with water molecules. Consequently this results in β-CD having the lowest aqueous solubility of the three native CDs. The aqueous solubilities of α-CD and γ-CD are 129.5 ± 0.7 at 25 ^{o}C mg.cm^{-3} and 249.2 ± 0.2 mg.cm^{-3} at 25 ^{o}C respectively.[2]

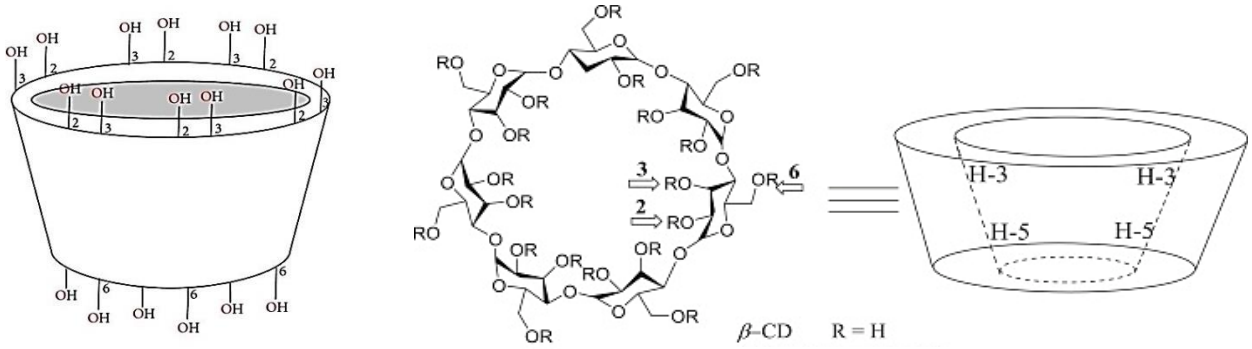


Figure 1.3: The O2 and O3 hydroxyl groups are positioned on the broader secondary rim, while the O6 hydroxyl groups are located on the narrower primary rim (left image). The glycosidic oxygen atoms are directed towards the interior of the CD cavity (central image). A schematic representation of β-CD illustrating that the H3 and H5 atoms are also directed towards the interior of the CD cavity. This diagram shows only two (of the seven) pairs of the H3 and H5 atoms. Adapted from Savjani *et al.* and Liu *et al.*[17,18]

The apolar hydrogen atoms attached to C3 and C5, as well as the ether-like, glycosidic oxygen atoms, are directed towards the internal cavity of the CD molecule (Figure 1.3).[1,2] This atomic arrangement results in the interior of the CD molecule being hydrophobic while the exterior is hydrophilic, due to the presence of peripheral hydroxyl groups.[1,2] Consequently, the most advantageous feature of CDs is that hydrophobic guest molecules of an appropriate shape or size can be accommodated in the hydrophobic cavity of the CD molecule to form a CD inclusion complex. This particular capability of CDs is of significant

interest to the pharmaceutical industry, where the hydrophobic guest molecule would be the API of interest.[1,2,12]

1.2.3) CD complex formation methodologies

There are numerous methods that can be used to form CD inclusion complexes, some of which include co-precipitation, slurry complexation, kneading, damp mixing and heating, extrusion, and dry mixing.[1] Co-precipitation is one of the most widely used techniques and depending on the experimental conditions it can result in the formation of single crystals, which may be sufficiently large and of adequate quality for single-crystal X-ray diffraction analysis. The other techniques mentioned above result in the formation of a very fine powder that is either compacted or loose.[1]

1.2.4) The dynamic host-guest equilibrium

It is important to note that in solution a dynamic equilibrium exists between the inclusion complex and the free host and free guest (CD·G ⇌ CD + G) and thus the guest molecule is not permanently situated in the cavity of the CD molecule in solution.[2,11,13] Therefore, the binding strength of the inclusion complex depends on (*inter alia*) the extent of the geometric fit between the host and guest molecules.[1] Furthermore, it is not a prerequisite that the entire hydrophobic guest molecule should fit inside the CD cavity; successful CD inclusion complexation can occur even if only a small hydrophobic residue of a larger guest molecule is included in the CD cavity.[1]

1.2.5) The formation of a CD inclusion complex

During the formation of a CD inclusion complex, no covalent bonds are broken or formed in either the host or guest molecules (Figure 1.4).[2] The ability for a CD inclusion complex to form is governed by two main factors, which include steric factors and the thermodynamics of the system. The steric factors are often noted as the initial requirement, since they depend on the relative size of the guest molecule (or the size of a particular hydrophobic residue of the guest molecule), and the cavity size of the CD molecule.[1,2] In other words, there should be a geometric or dimensional fit between the CD cavity and the guest molecule (Figure 1.4).

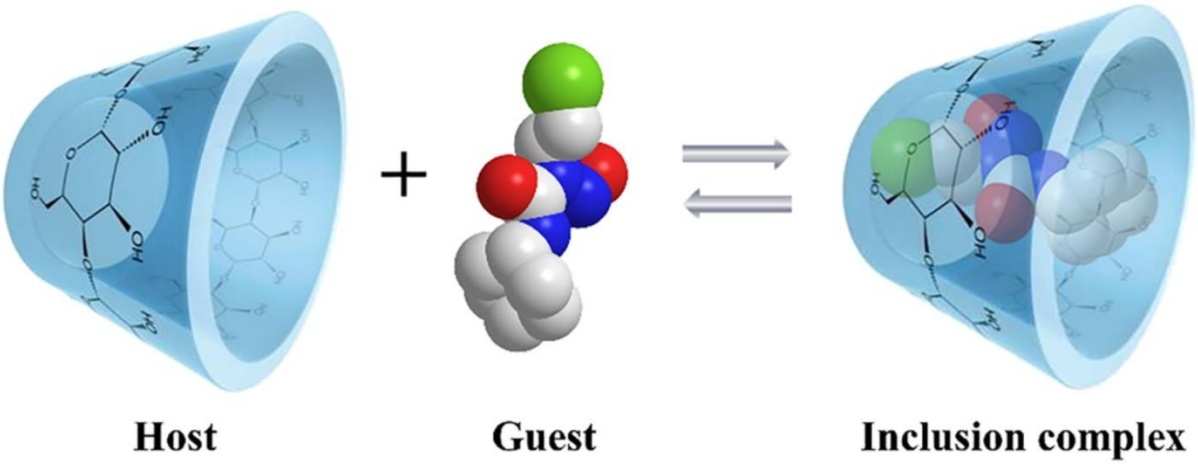


Figure 1.4: An illustration displaying the formation of a CD inclusion complex, where a guest molecule (an arbitrary molecule in this example) is accommodated in the cavity of the CD molecule. No covalent bonds are broken in either the host or guest molecule. Taken from Tian *et al*.[19]

For example, α-CD can accommodate small molecular weight guest molecules, or molecules with aliphatic side chains, while γ-CD can accommodate significantly larger guest molecules, such as steroids.[1] With regard to the thermodynamic aspects for complexation, there are four energetically favourable factors which contribute to this: (i) the enthalpy-rich polar water molecules are displaced from the apolar CD cavity (the most significant contributor), (ii) there is an increase in hydrogen bonding, as the displaced water molecules now interact with the hydrophilic exterior of the CD molecule, as well as with surrounding water molecules, (iii) there is an increase in hydrophobic interactions between the hydrophobic guest molecule and the hydrophobic CD cavity, and (iv) there is a decrease in repulsive interactions between the hydrophobic guest molecule and the aqueous environment, and between the polar water molecules and the hydrophobic CD cavity.[1,11] CD inclusion complexation involves a dual equilibrium process, where the initial complex formation is rapid and can often occur within seconds or minutes (depending on the reagents) and thereafter a significantly longer second equilibrium process takes place where the guest molecule makes fine conformational adjustments in order to exploit all the potential weak van der Waals bonding possibilities once inside the CD cavity.[1]

1.2.6) The toxicology of CDs

In general, all the CDs are considered practically non-toxic if they are administered orally, since their absorption in the gastrointestinal tract is minimal (generally less than 4%). However, an exception is RAMEB, as its oral bioavailability may be as high as 12% in rats, and consequently methylated CDs are not used for oral administration owing to their potential toxicity.[1,2] Furthermore, not all CDs can be administered parenterally (for example *via* intravenous injection or infusion), since CDs produce haemolytic effects on erythrocytes. A study conducted by Loftsson *et al*.[2] demonstrated this effect on human erythrocytes in a phosphate-buffered saline solution and they established the following serial order with respect to the severity of this haemolytic effect: methylated β-CD> β-CD> HPBCD> α-CD> γ-CD> HPGCD> SBEBCD. Thus, this series indicates the relative potential that these representative CDs have to disrupt cellular membranes and this series also correlates with the ability of CDs to extract or bind cholesterol from biological membranes.[2] This study indicated that the methylated β-CDs and β-CD cannot be administered parenterally, while the remaining CDs in the series can be delivered in this way. β-CD also cannot be administered parenterally owing to its lower aqueous solubility and at very high oral doses it can become toxic, thus caution is required in its administration.[2,14] Furthermore, other studies have also indicated that sulfated β-CD and maltosyl β-CD appear to be safe when administered parenterally.[1,11]

1.2.7) CD applications

CDs are extensively used in many industries, namely the pharmaceutical industry, food industry, textile industry, cosmetic industry and they are also used in bio-conservation and environmental protection.[1,11,14] This is owing to the fact that CD complexation generally has a considerable beneficial effect on the physicochemical properties of the included guest molecule while it is temporarily included in the CD cavity. From a pharmaceutical perspective, the benefits of CD inclusion of an API are extensive and some of these benefits are mentioned below. As previously stated, CDs can enhance the aqueous solubility (and hence the bioavailability) of an API that is either currently on the market or that has been previously discarded, and this can consequently often result in lower administered doses of the API to the patient.[1,11] Furthermore, liquid APIs or APIs that either sublime easily or are

volatile, can be transformed into a solid phase product formulation through CD complexation, and thus tabletting the improved formulation can be performed more easily than tabletting their individual former physical states.[1] CD complexation can also protect the included API from external factors, such as ultraviolet and visible light, oxidation and heat, as well as mask particular chemical residues of an API which can cause gastrointestinal irritation and thus potential adverse side effects.[1,11,14] CDs are also potential carrier compounds that can deliver a specific amount of an API to a targeted site over a controlled period of time.[13] Lastly, foul tastes or smells of particular APIs can also be masked by CD inclusion and this is particularly relevant for paediatric formulations.[1,11]

1.2.8) The mechanism of API release from a CD molecule

There are multiple mechanistic pathways whereby an API can be released from a CD inclusion complex and delivered to a biological membrane. The factors that determine which mechanistic pathway (or combination of pathways) will be followed, depend on the type of administration and the nature of the substituents.[20] It is important to state initially that the binding strength, and thus the relative kinetics of dissociation, of CD inclusion complexes is not a limiting factor for the release of the API to a particular biological membrane. As mentioned previously, a dynamic equilibrium exists between the CD and API molecules in solution,[2,11,13] and once this equilibrium is established the rate of association and dissociation of the complex is very rapid. The average time that the API molecule resides in the complex for both weak and strong binding CD inclusion complexes is between milli- to micro-seconds (or less) depending on the substituents.[20] Therefore, it is evident that the API is becoming freely available for absorption by a biological membrane; however, additional mechanisms must ensure that the API is preferably absorbed by the biological membrane rather than rapidly associating into a CD inclusion complex.[20] These mechanistic pathways that ensure CD inclusion complex dissociation, include dilution, competitive displacement, protein binding and API uptake into tissue.[2,20]

Dilution is the main driving force that causes complex dissociation for CD inclusion complexes displaying both weak and strong binding. In this context, complex dissociation implies the release of the API. This mechanism operates on the notion that the concentration of the CD inclusion complex becomes very low *in vivo*, and its dissociation can

occur easily, whereas association becomes challenging as the individual components become widely dispersed in the dilute solution *in vivo*.[20] Consequently, the biological membrane can then absorb the free API. It is important to note that the mechanism of dilution is dependent on the method of administration. For example, with oral administration, dilution occurs readily in the gastrointestinal tract; however, with ophthalmic delivery, negligible dilution occurs. In the case of weakly bound APIs, dilution alone is generally satisfactory and complementary mechanisms of API release from the CD complex are not necessary.[20] In a study by Stella *et al*.[20] a 1000-fold dilution (which is comparable to the level of dilution that will occur *in vivo*, this being both patient-mass and quantity-administered dependent) resulted in a reduction of the fraction of the drug bound to the CD from 98% to 5.7%.[20] Furthermore, the experiment was repeated but in the presence of a competing agent (competitive binding was added as a complementary mechanism of API release) and the drug bound to the CD was lowered to only 4.2%. However, in the case of a strongly binding CD inclusion complex, complementary mechanisms are necessary to release the API in sufficient amount.[20] Stella *et al.* also demonstrated in an example of a CD inclusion complex with strong binding that a 1000-fold dilution caused the fraction of drug bound to the CD to be reduced from 99.9% to only 47.5%. However, in the presence of a competing agent this value was further reduced to either 26.0% or 1.0% (depending on the concentration of the competing agent). Therefore, dilution does result in the release of the API from the CD inclusion complex; however, its level of effectiveness depends on the binding strength of the inclusion complex and thus complementary mechanisms are sometimes required.[20]

Competitive displacement is based on the principle that a co-administered substrate will have a greater affinity for the hydrophobic cavity of the CD than the API in the inclusion complex.[20] Thus, when the API dissociates from the CD inclusion complex during the rapid equilibrium process, association occurs preferably with the co-administered substrate and thus the API is displaced from the CD.[20,21] This mechanism is described in an example by Tokumura *et al*.[21] which revealed that despite the superior aqueous solubility displayed by the complex β-CD·cinnarizine relative to that of free cinnarizine, the *in vivo* bioavailability of cinnarizine was less than expected after oral administration.

However, when a displacing agent was added, namely phenylalanine, the bioavailability was improved, thus suggesting that cinnarizine was strongly bound to the CD inclusion complex.[20]

Protein binding is another mechanism by which an API can be released from a CD inclusion complex; however, proof that it actually occurs *in vivo* is not easily established.[20] The concept of this mechanism is that the proteins in a plasma solution will bind to the free API during the rapid dynamic equilibrium of the CD inclusion complex, thus hindering association of the API and CD molecules. This mechanism of API release is particularly relevant for parenteral administration.[20]

The mechanism which involves the API being taken up by the tissue, applies to those APIs that have physicochemical properties allowing them to rapidly diffuse through a biological membrane.[20] Alternatively, the membrane must possess a particular receptor or transporter for the API. Furthermore, the free CD and complex must not be absorbed by the biological membrane of interest. This mechanism is best illustrated in Figure 1.5 below, where the membrane (the tissue) absorbs the API, causing continual dissociation of the CD inclusion complex. This mechanism mostly applies to APIs that have strong binding affinities for the tissues, or in the case that the inclusion complex is administered where dilution will be negligible, for example, in ocular, sublingual, dermal, rectal, pulmonary and nasal administration.[20] Furthermore, this mechanism becomes particularly useful when a rapid uptake of the API is necessary, for example in ocular administration. If the absorption of the API is not sufficiently rapid, it would be removed by nasolacrimal duct drainage .[14,20]

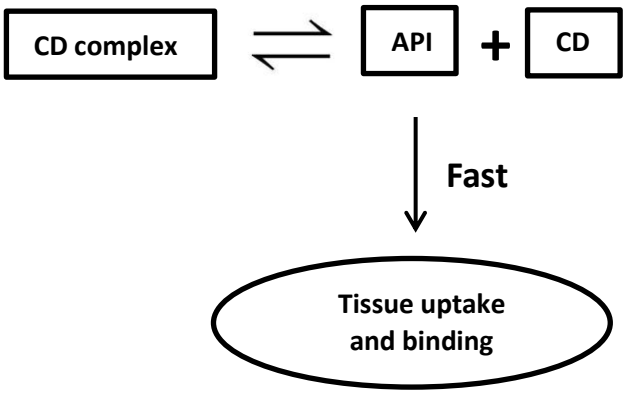


Figure 1.5: Schematic mechanism illustrating the dynamic equilibrium of CD inclusion complexes in solution with the API being taken up by tissues. Adapted from Stella *et al.*[22]

1.2.9) The molecular geometry of a CD

The molecular geometry of a CD molecule is distorted in its crystalline state and this is further exacerbated with complexation.[23] Consequently, these distortions can be quantified by hypothetically constructing an idealised O4-polygon (comprising the glycosidic oxygen atoms within the CD molecule) and defining specific geometrical parameters (Figure 1.6).[23,24] These comprise the parameter d that measures the torsion angles O4A(n)···O4A(n+1)···O4A(n+2)···O4A(n+3) of the O4-polygon, the parameter Φ that measures O4A(n-1)···O4A(n)···O4A(n+1) angles of the O4-polygon, the parameter *l* that measures the distance between each O4 atom and the centroid of the O4-polygon, and the parameter D that measures the consecutive O4···O4′ distances of the O4-polygon. Values of these geometrical parameters gleaned from X-ray diffraction studies of CD complexes can be compared with the ideal values to determine the extent of conformational distortion of the O4-polygon occurring upon guest inclusion.

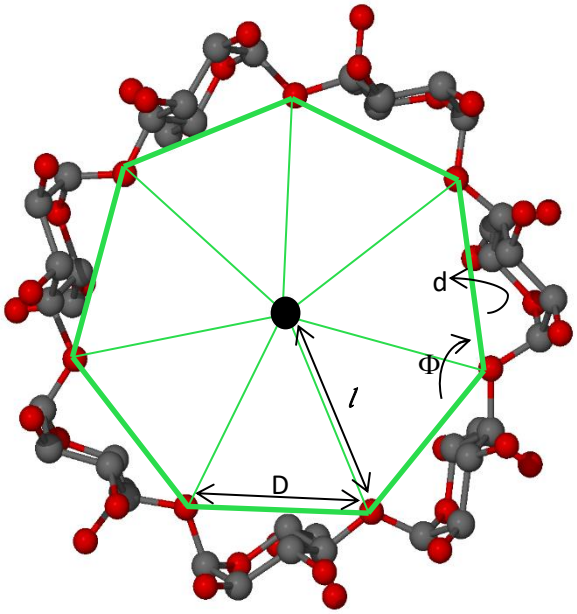


Figure 1.6: Principal parameters defining the geometry of the O4-polygon in β-CD.

Furthermore, there are three additional parameters, namely, D_3, α and τ_2 which also characterise the level of host molecule distortion; however, they are not related to the hypothetical O4-polygon. D_3 measures the O···O distances between adjacent glucose units of the O2(n)-H···O3(n-1) / O2(n)···H-O3(n-1) hydrogen bonds, and the parameter α measures the deviation from planarity of the O4 polygon. The latter is determined by measuring the deviation of each atom from the O4 mean plane (Figure 1.7a). Lastly, τ_2 measures the angle of inclination of each glucose unit relative to the O4 mean plane (Figure 1.7b). This is determined by measuring the acute angle between the O4 mean plane and a reference plane that passes through the atoms O4, C4, C1 and O4' (the 'backbone') of each glucose unit.

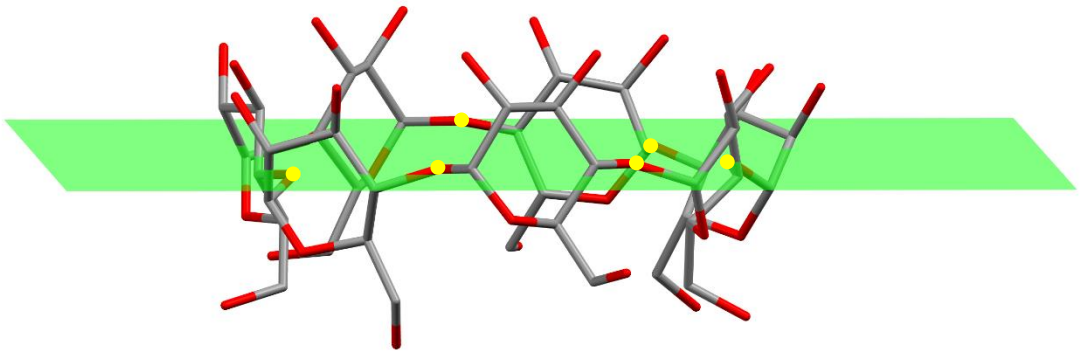


Figure 1.7a: The mean plane of the O4-heptagon in β-CD.

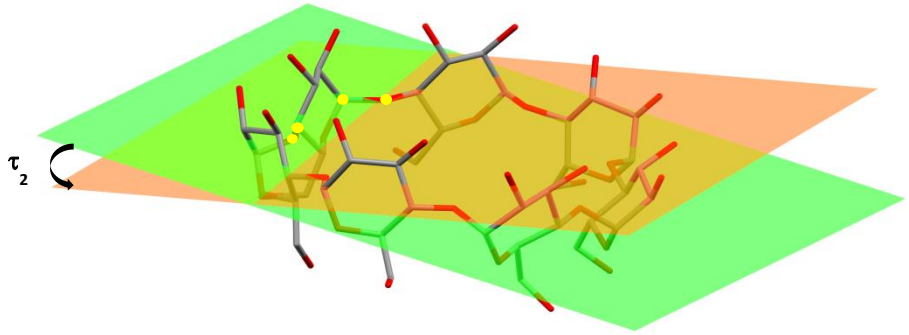


Figure 1.7b: The angle τ_2 is the acute angle between the O4 mean plane and a second plane that passes through the O4, C4, C1 and O4′ atoms of a glucose unit (highlighted in yellow).

1.2.10) Crystalline packing of the native CDs

CD inclusion complexes can crystallise in either channel- or cage-type packing arrangements, the specific type adopted by a complex depending on the cyclodextrin and the guest molecule, particularly the size of the latter.[25] With regard to the channel-type arrangement, the CD molecules stack one on top of the other forming an infinitely long channel. The CD molecules can arrange themselves in three different modes to form a channel.[25] These include a head-to-head arrangement (Figure 1.8, left), where the secondary rims of two CD molecules form a dimer through intermolecular O-H···O hydrogen bonds, and thereafter the -OH groups on the primary rims of each dimer form hydrogen bonds to other dimers to construct a channel. A head-to-tail (monomeric) arrangement is observed where hydrogen bonds exist between the secondary and primary rims of

consecutive CD molecules in a column (Figure 1.8, centre). Lastly, an alternating head-to-head and head-to-tail arrangement can also occur; however, this occurs in crystals of γ-CD inclusion complexes only (Figure 1.8, right).[25]

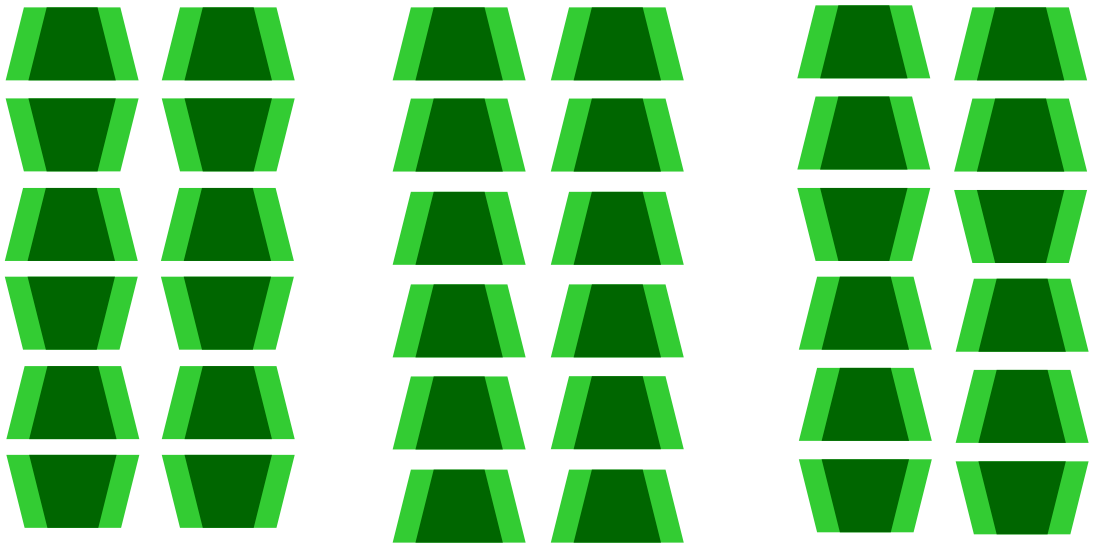


Figure 1.8: Examples of channel-type CD packing arrangements, namely head-to-head (left), head-to-tail (centre), and an alternating head-to-head and head-to-tail channel arrangement (right).

With regard to the cage-type packing arrangement, this is characterised by the fact that the primary rims of e.g., dimeric CD complexes are blocked by neighbouring dimers. Different packing patterns fall within the cage-type arrangements, including a brickwork pattern and a herringbone pattern (Figure 1.9).[25]

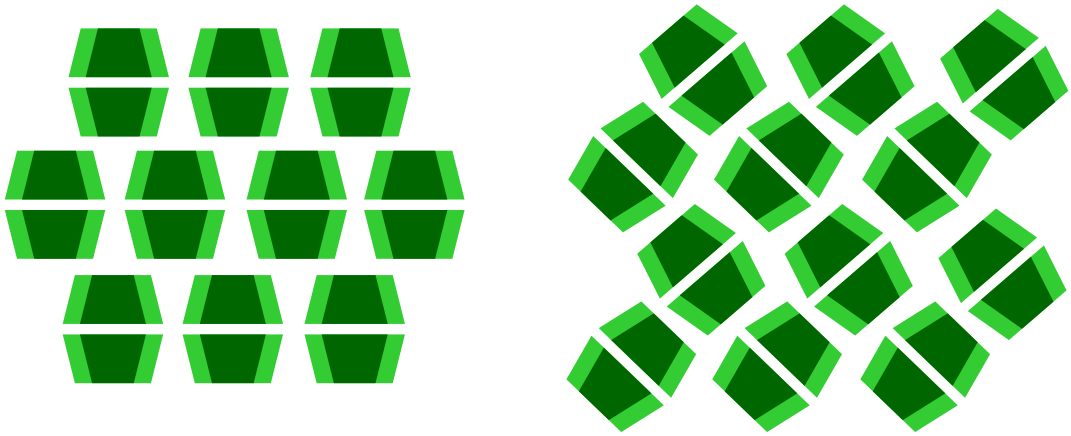


Figure 1.9: Examples of cage-type CD packing arrangements including, a brickwork pattern (left) and a herringbone pattern (right).

Analogous packing patterns can occur in monomeric complexes, as displayed in Figure 1.10.

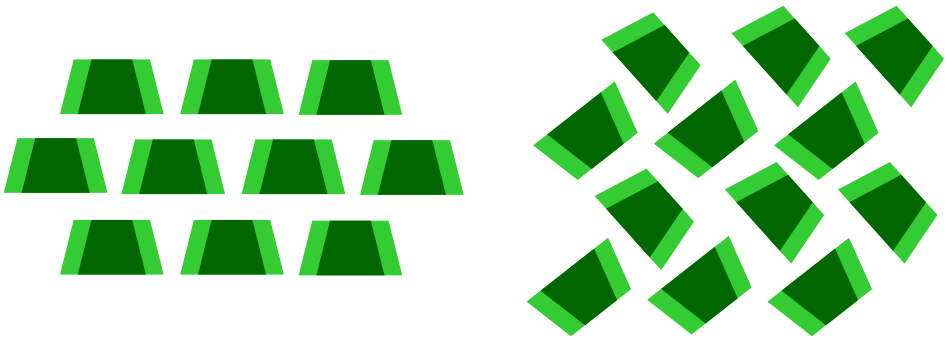


Figure 1.10: Monomeric brickwork (left) and herringbone (right) patterns.

The packing arrangements observed for α-CD inclusion complexes are mostly dependent on the size of the guest molecule.[25] If the guest molecule is small then a cage-type packing arrangement occurs, particularly the herringbone pattern, unless the guest molecule is a small aromatic, in which case the brickwork pattern is observed. On the other hand, for larger guest molecules that would protrude from either end of the CD molecules, a linear, channel-type packing arrangement is observed (for example with γ-CD which has a 4-fold rotation axis running parallel to the channel).[25]

In contrast, a different trend is observed for β-CD inclusion complexes where channel-type packing predominates with a head-to-head dimeric (or tetrameric) arrangement of the CD molecules and each CD dimer (or tetramer) is stacked on top of another with a small lateral displacement.[25] This results in a cage-type column stacking. The reason for this lateral shift is that there are seven glucose units in β-CD and, as a result, the presence of an axis of symmetry is not possible down the channel. Hence small displacements between the dimers (or tetramers) are observed. There are a few β-CD inclusion complex crystal structures with included water, ethanol and methanol that crystallize in the caged herringbone arrangement; however, it is suggested that the head-to-head motif predominates regardless of whether the size of a guest molecule is small enough to be included in one β-CD molecule.[25] The head-to-head dimeric arrangement is favoured because of strong hydrogen bonding between the two secondary faces of the CD molecules assisting in the stabilisation of the dimer. Hydrogen bonds also occur between primary faces of each dimer, which results in column-type stacking.[25]

Lastly, with regard to γ-CD inclusion complexes, two packing arrangements are observed which include the caged herringbone arrangement and the alternating head-to-head and head-to-tail channel arrangement.[25] However, the herringbone pattern occurs only when the 'guest' molecule is water, and the CD molecule is then often considered 'empty'. With any other included guest molecule a channel packing arrangement with the tetragonal space group $P4_12$ is observed and since γ-CD has eight glucose units, a linear channel stacking arrangement is observed with a 4-fold rotation axis along the channel. However, any included guest molecule is expected to be disordered unless it also has a 4-fold rotation axis that coincides with the rotation axis through the CD channel,[25] an example being 12-crown-4 (refcode DOCYID).[26] Furthermore, the γ-CD molecules are arranged uniquely in an alternating head-to-head and head-to-tail sequence and thus the channel is constructed from γ-CD trimers. This alternating sequence of γ-CD molecules cannot only occur from interactions along the channel axis and thus lateral interactions from trimers in adjacent columns, as well as interactions from water molecules between the channels, contribute to its stability.[25]

In summary, CD complexation presents a significantly apt method of supramolecular derivatisation of an API. Furthermore, as previously mentioned, co-crystallization is another highly effective and more recent method of supramolecular derivatisation of APIs, which is discussed in detail in the following section.

1.3) Co-Crystals

1.3.1) Overview of co-crystals

In addition to CD inclusion, the co-crystallization of a target compound with a so-called coformer (partner molecule) is another supramolecular approach to improving the physicochemical properties of the compound of interest.[27,28] The overall and broad definition of a co-crystal in the literature is that it is a multicomponent system incorporating two or more different molecules that are non-covalently bonded to each other.[29] As a result, multicomponent crystals such as clathrates, molecular salts, co-crystals, molecular adducts, and inclusion compounds are often also published in the literature under the same type of compound category.[30] Consequently, there are ongoing debates regarding the precise definition of a co-crystal and which particular multicomponent crystals should be included or excluded from the classification.[31,32] In a publication by Aakeröy *et al.*, the broad definition of a co-crystal with its variety of molecular associations was duly acknowledged; however, they proposed a set of rules where the purpose was to narrow the focus of the definition for their particular publication.[30] Therefore, they stated that a co-crystal can be defined as "a structurally homogeneous crystalline material that contains two or more neutral building blocks that are present in definite stoichiometric amounts."[30] Furthermore, the molecular components of the co-crystal must be neutral, which thus excludes all compounds that contain ions. Lastly, the molecular components must also be in a solid phase at ambient temperatures. This rule thus excludes all compounds that are solvates or hydrates, as well as inclusion compounds where the guest molecule is a gas. Therefore, the author of this doctoral thesis followed these same guidelines defining a co-crystal as presented in the publication by Aakeröy *et al*.[30]

Over the past few decades, co-crystallization has become increasingly important and widely practised in various fields, notably the pharmaceutical industry.[28,29,33] From a

pharmaceutical perspective, the co-crystal would contain the API of interest in its neutral form, and the other neutral molecular component(s) could either be another drug molecule (a different molecule from the API of interest), or co-crystal coformers.[27] These coformers are compounds that can form hydrogen bonding interactions with the molecule of interest, and in relation to the pharmaceutical industry, these would have to be "generally recognized as safe" (GRAS) classified compounds.[27] GRAS compounds are those which have been approved by the Food and Drug Administration (FDA) federal agency and considered safe to add to food substances and APIs. Examples of these GRAS compounds include nicotinamide, L-malic acid and succinic acid.[34]

1.3.2) Bonding in co-crystals

The bonding that occurs between the components in co-crystals consists of non-covalent interactions, which include hydrogen bonding, π-π stacking and van der Waals interactions; however, hydrogen bonding is the most prevalent.[35] Thus, in order to form co-crystals, the components must have hydrogen bonding functional groups that are complementary in order to form specific supramolecular synthons between the components. The term "supramolecular synthons" was derived by Desiraju as "*structural units within supermolecules which can be formed and/or assembled by known or conceivable synthetic operations involving intermolecular interactions*." Therefore, these synthons are structural units within supramolecules that are formed by known (or feasible) intermolecular interactions.[36] Consequently, the basis of co-crystal formation relies on site-specific intermolecular interactions that favour the formation of heteromeric interactions over self-assembly *via* homomeric interactions. Figure 1.11 displays examples of the different types of potential synthons, which include intramolecular hydrogen bonds, infinite chain assemblies, intermolecular ring formations, and discrete synthons for finite structures.[37]

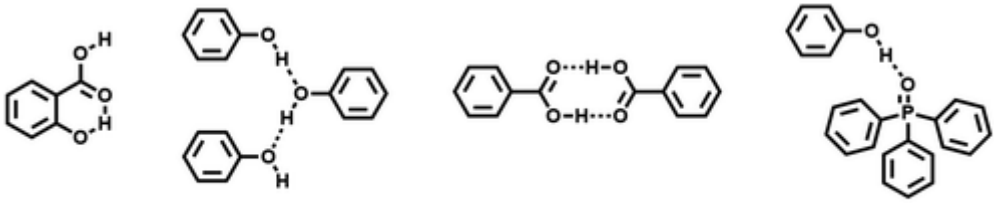


Figure 1.11: Examples of the different types of possible synthons, which include (a) intramolecular hydrogen bonds, (b) infinite chains, (c) intermolecular H-bonded rings and (d) discrete synthons for finite structures. Taken from Aakeröy *et al.*[37]

Figure 1.12 illustrates the molecular structure of a co-crystal of niflumic acid and caprolactam where hydrogen bond interactions occur in the form of eight membered ring synthons, as well as discrete and intramolecular synthons.[38]

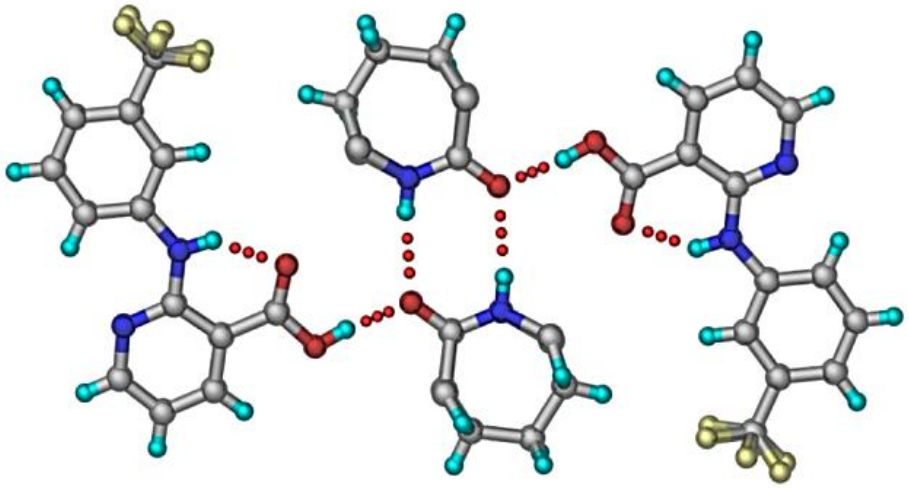


Figure 1.12: A co-crystal of niflumic acid (API) and caprolactam (coformer), displaying the hydrogen bond interactions in the form of eight membered ring synthons, as well as discrete and intramolecular synthons. Taken from Mittapalli *et al.*[38]

1.3.3) Co-crystal formation

There are many variables that impact the formation of co-crystals, some of which include the type of functional groups on the reagents, the solubility of these reagents in the solvent used, as well as a variety of experimental conditions, for example, the stoichiometric ratios

of the reagents, temperature, pH, stirring parameters, and the type of glassware used.[39] The overall mechanism for co-crystal formation is not well understood and thus controlling nucleation, crystallization and the resultant phase development of the co-crystal remains a scientific challenge.[39]

There are numerous preparative methodologies for the formation of co-crystals, some of which include grinding methods (dry solid-state grinding, or liquid-assisted grinding [LAG]), co-precipitation (either by solvent evaporation or slow-cooling methods), the slurry technique, hot melt extrusion, spray drying, freeze drying, supercritical fluid processing, and anti-solvent co-crystallization.[35,40] Co-precipitation is the only method that can result in the formation of single crystals of adequate size and quality for single-crystal X-ray diffraction, which provides invaluable solid-state structural information. From this perspective, co-precipitation is a widely used method, as the other techniques listed above all produce very fine crystallites in the form of a powder. Although the other preparative methods produce powders, they are generally simpler than co-precipitation, especially the grinding methods mentioned above. The utility of the grinding method, which can either be performed with a mortar and pestle or with an automated ball mill system, is also considered as a 'green chemistry' approach to co-crystal production and is very cost-effective, making it the most desirable method from an industrial perspective.[39,41]

1.3.4) Co-crystals in the pharmaceutical industry

The co-crystallization of APIs creates new variations of the API and often results in improving the physicochemical properties of the native drug. Some of the undesirable physicochemical properties of an API that can be addressed *via* co-crystallization include inadequate aqueous solubility, low dissolution rate, insufficient bioavailability, hygroscopicity, unsatisfactory compressibility (preventing tablet formation), high friability, and low thermal stability (resulting in a low melting point of the API).[28,29,32] In addition, co-crystallization allows the transformation of APIs that are either amorphous or difficult to crystallize into stable and easily handled solid crystalline substances.[32] Furthermore, APIs in a crystal form are also preferred from a production perspective as the crystallization process removes the impurities during formation.[33] Therefore, transforming amorphous APIs into co-crystals is also an advantage from these points of view.[32,33] Lastly, co-crystallization also

has the potential to significantly reduce the time it would normally take to develop a drug for commercial purposes (which averages ~13.5 years), by extending the patent life of already known pharmaceutical drugs.[42] Consequently, the financial implications of this aspect are highly valued by the pharmaceutical industry, and various treatments that are in demand can reach the commercial market at much earlier stages.[27,42]

1.3.5) Mechanism of API release from co-crystals

The solubility of a crystalline substance depends primarily on the crystal lattice energy, and thus, owing to the different lattice energy that would be possessed by a co-crystal of an API, the apparent solubility of the API would differ from those of the untreated API and coformer.[36,39] Consequently, in cases where the lattice energy of the co-crystal is small, its solubility profile can be explained by a concept known as the "spring and parachute" phenomenon (Figure 1.13).[36,39] When the co-crystal is in a solution (for example an aqueous medium), the API and coformer dissociate, resulting in the highly water soluble coformer dissolving and the hydrophobic API becoming supersaturated in the solution. This supersaturated metastable state of the hydrophobic API has a higher free energy than that of its solid crystalline state and this is referred to as the "spring" effect in Figure 1.13.[36] This high concentration of API rapidly leads to its precipitation, resulting in a major reduction in the concentration of dissolved API. It is therefore highly beneficial to maintain the supersaturated metastable state of the hydrophobic API for as long as possible in order to improve its overall solubility and bioavailability. This is referred to as the parachute effect (Figure 1.13).[36] Various crystal growth inhibitors such as polymers like polyvinylpyrrolidone, polyethylene glycol, and polyvinylpyrrolidone/vinyl acetate, can be incorporated into the solution to assist in maintaining the supersaturation of the API for an extended period of time.[36,39]

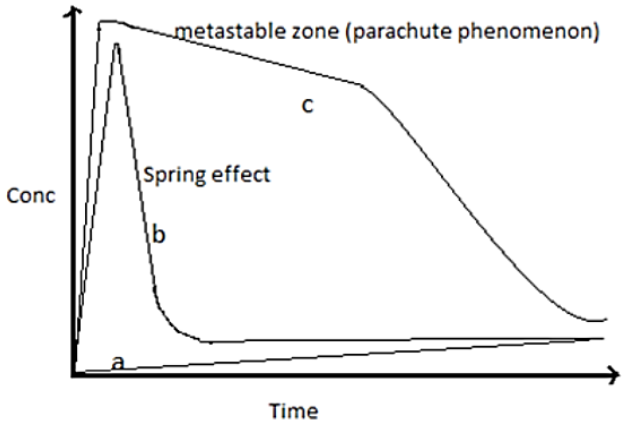


Figure 1.13: A depiction of the graphs which display certain solubility scenarios of hydrophobic drugs. a) The crystalline low soluble form of the drug. b) The rapid dissolution of the co-crystal resulting in a short-lived supersaturated state of the API (spring effect), which thereafter rapidly precipitates. This is a short-lived supersaturated metastable state of the hydrophobic drug, which readily falls to attain its crystalline state. c) The spring effect combined with the parachute effect (sustained API solubility) maintaining the metastable state of the API for an extended period of time. Taken from Mittapalli *et al* .[38]

It is also possible to tune the release rate of the API from the co-crystal with the careful selection of specific coformers. This offers a wide opportunity for controlled release forms of various pharmaceutical drugs.[39] As a result, co-crystals offer significant potential to improve the aqueous solubility (as well as other physicochemical properties that were mentioned above) of pharmaceutical drugs that are either available commercially, or still in their development phase.

1.4) General aims and objectives

The aim of this doctoral project was to synthesize supramolecular derivatives of selected pharmaceutically relevant compounds *via* co-crystallization and CD inclusion. During this study, such new supramolecular derivatives were isolated, characterised by a variety of physicochemical methods, and assessed for their ability to alter the aqueous solubility of the unmodified bioactive compounds.

The molecular structures of the pharmaceutically relevant compounds that were selected for this project are shown in Figures 1.14 and 1.15. They include three newly developed pyrido[1,2-a]benzimidazole derivatives (referred to as GMP-23, GMP-31 and GMP-58) which display activity against schistosomiasis (bilharzia). In addition, two prominent bioactive steroidal compounds were selected for study, namely 17β-estradiol [used in e.g., hormone

replacement therapy (HRT) and for the treatment of breast and prostate cancer] and progesterone (used in e.g., HRT and as a contraceptive).

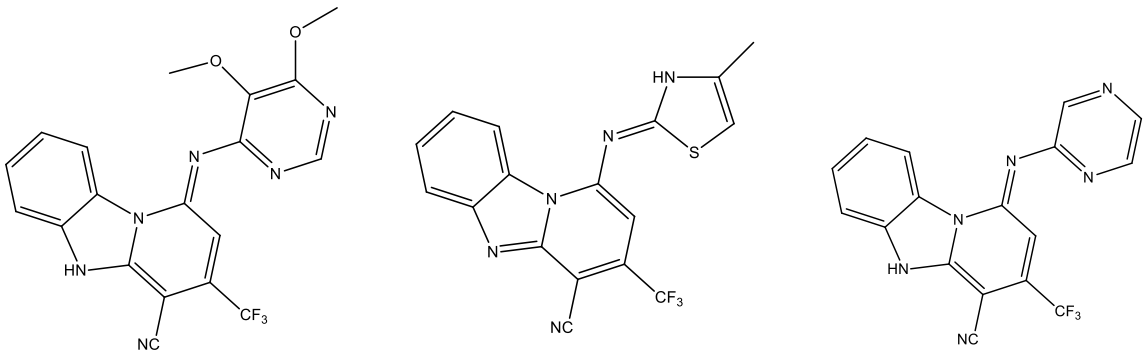


Figure 1.14: Molecular structures of one tautomer of GMP-23 (left), GMP-31 (centre) and GMP-58 (right).

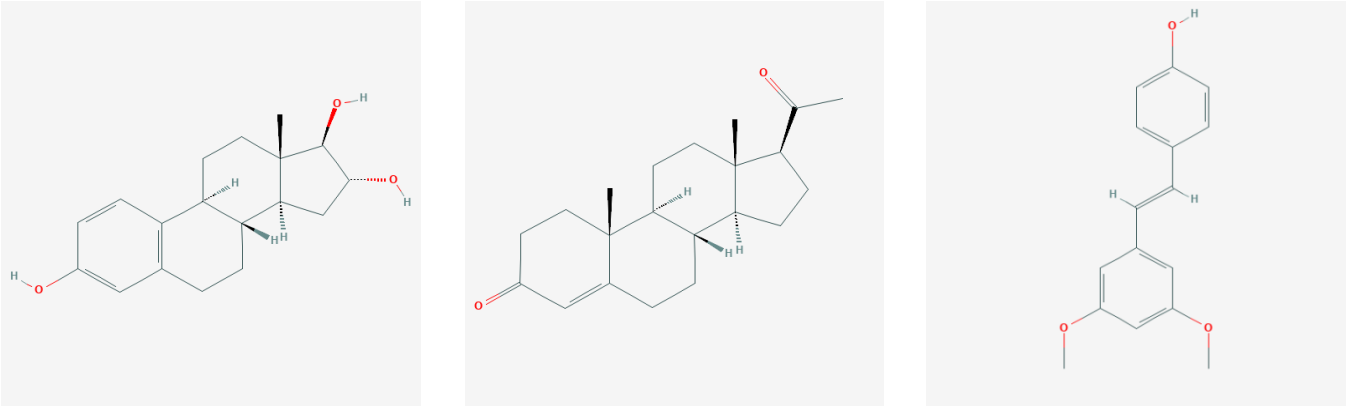


Figure 1.15: Molecular structures of 17β-estradiol (left), progesterone (centre) and pterostilbene (right). Taken from the National Center for Biotechnology Information .[43–45]

Finally, the naturally occurring compound pterostilbene which has been shown to display strong antioxidant activity with proven potential uses in the treatment of various types of cancers (including colon and prostate cancers), as well as atherosclerosis and Alzheimer's disease, was also earmarked for investigation in this study. All of these active compounds were primarily selected owing to their low aqueous solubility, which is a major shortcoming in terms of their bioavailability. Selected properties of the pharmaceutically relevant

compounds are provided in Table 1.1 and a detailed description of each is written thereafter.

Table 1.1: Selected properties of the pharmaceutically relevant compounds.[43–46]

Pharmaceutically relevant compound	Molecular formula	Molar mass ($g.mol^{-1}$)	Aqueous solubility ($mg.cm^{-3}$)	Melting point (^{o}C)
GMP-23	$C_{19}H_{13}N_6O_2F_3$	414.339	8×10^{-2} (at 23 ^{o}C)	241
GMP-31	$C_{17}H_{10}N_5F_3S$	373.354	$5 – 20 \times 10^{-3}$ (at 23 ^{o}C)	Decomposes at 225
GMP-58	$C_{17}H_9N_6F_3$	354.288	$5 – 20 \times 10^{-3}$ (at 23 ^{o}C)	Decomposes at 251
Pterostilbene	$C_{16}H_{16}O_3$	256.296	5.023×10^{-3} (at 25 ^{o}C)	89 – 92
β-Estradiol	$C_{18}H_{24}O_2$	272.382	3.6×10^{-3} (at 27 ^{o}C)	178 – 179
Progesterone	$C_{21}H_{30}O_2$	314.469	8.81×10^{-3} (at 25 ^{o}C)	121 - 122

It should be mentioned that the aqueous solubility of pterostilbene is contentious. Multiple publications refer to an aqueous solubility value of 2.1×10^{-2} $mg.cm^{-3}$ (temperature not specified) which originates from a manuscript in preparation from 2011.[47] The author of the present thesis prepared an aqueous solution of pure pterostilbene at 23 ^{o}C having one-half the concentration of the quoted solubility value, and despite vigorous stirring, undissolved material remained in suspension. In a publication by Silva *et al.*[48] the aqueous solubility of pterostilbene was quoted as 5.023×10^{-3} $mg.cm^{-3}$ (at 25 ^{o}C). In view of the above, the aqueous solubility value quoted by Silva *et al.*[48] has been used as a reference for our investigation, as the publication is more recent and the value was used to determine the stability constants for a wide variety of CD inclusion complexes in their publication.

The pyrido[1,2-a]benzimidazole derivative series: GMP-23, GMP-31 and GMP-58

A series of pyrido[1,2-a]benzimidazole derivative drug leads was recently developed by the Drug Discovery and Development Centre (H3D) by Dr. Godfrey Mayoka, under the supervision of the director of H3D, Professor Kelly Chibale at the University of Cape Town. The syntheses of these drug leads were published in 2017 and they were shown to have activity against schistosomiasis (also known as bilharzia).[49,50] Three of the drug leads from this series, namely GMP-23, GMP-31 and GMP-58 were investigated in this project in order

to improve their aqueous solubility, which is their major shortcoming for pharmaceutical applications (Table 1.1 above). Schistosomiasis is a parasitic infection which severely threatens populations in tropical and subtropical areas, with more than 200 million people infected and a further 700 million people in 74 countries at risk of being infected.[49,50] At present, praziquantel is the main therapeutic drug that is used to treat schistosomiasis; however, overuse and patient reliance have raised concern for drug resistance,[49] especially as there have been reports of a decrease in its clinical efficacy.[50] Consequently, the need for alternative therapeutic treatments is imperative and hence the discovery and synthesis of these pyrido[1,2-a]benzimidazole derivative drug leads in 2017 and 2018 represent a significant development.[49,50] The three selected drug leads from this series demonstrated >70% mortality of newly transformed schistosomula (NTS) *in vitro*, and for two of them (GMP-23 and GMP-58) a mortality rate of >90% was observed for NTS and adult worms.[49,50]

Many blood-dependent parasites, such as *Schistosoma mansoni*, have developed various mechanisms to protect themselves from the toxicity of free haem, for example by biocrystallizing the haem molecules into insoluble and inert hemozoin.[49] The crystallization of haem is a defence and survival mechanism for *Schistosoma mansoni,* and since the production of hemozoin is also not genome-encoded, hindering the crystallization of hemozoin is a therapeutic target for the treatment of schistosomiasis.[49]

Even though the exact mechanism of action of these novel pyrido[1,2-a]benzimidazole derivatives is unknown, it is believed that they can potentially prevent the production of hemozoin as a consequence of their common planar heterocyclic scaffold.[49] This structural architecture enables π-π interactions to take place between a drug and haem to form a haem-drug complex, which thus prevents hemozoin crystal growth.[49] As a result, the pyrido[1,2-a]benzimidazole derivative drug leads display significant potential as an alternative treatment for schistosomiasis.[49,50] Therefore, attempting to further characterise the three selected drug leads, namely, GMP-23, GMP-31 and GMP-58, and increase their extremely low aqueous solubilities is well justified.

Pterostilbene

Pterostilbene (systematic name trans-3,5-dimethoxy-4-hydroxystilbene, Table 1.1 above) is a member of the stilbene family of compounds which display biological activities such as anti-cancer, anti-inflammatory, anti-diabetic, anti-obesity, anti-atherosclerosis, anti-aging, neuro-protection and cardio-protection, owing to their antioxidant properties.[51–53] Pterostilbene is a naturally occurring phytoalexin that occurs in a variety of plant species in order to inhibit the growth of a parasite with which the plant has come into contact.[52] Pterostilbene is found predominantly in blueberries, as well as in certain varieties of grapes, and in wood (particularly Pterocarpus marsupium tree wood, also known as Indian Kino tree).[51,54] The molecular structure of pterostilbene is derived from the well-studied analogue, resveratrol, *via* methylation of two of the phenolic groups of one aromatic ring.[51] Studies have indicated that the lipophilicity, membrane permeability and thus biological potency are improved as a result of this chemical modification. Animal tests have shown that pterostilbene displays 80 - 95% bioavailability[54] in comparison to resveratrol, with only 20% bioavailability, thus rendering it the most bioavailable stilbene.[51–54] Furthermore, the half-life of pterostilbene is 105 minutes, which is 7.5 times longer than resveratrol (14 minutes) which makes it more effective as a pharmaceutical agent.[54]

Pterostilbene is currently undergoing clinical trials and there is significant interest in it as a treatment for cardiovascular disease, liver diseases, type 2 diabetes and particularly as a potent anti-cancer agent for many malignancies, as well as for resistant haematological malignancies.[51–54] *In vivo* studies on healthy, human subjects have indicated that doses of up to 250 mg per day of pterostilbene are safe for human consumption with no adverse side effects on the glucose marker, kidneys or livers of the volunteers. This study involved 80 volunteers that were administered pterostilbene for 6 – 8 weeks.[53]

Furthermore, treatments with blueberries also revealed complementary results in comparison with treatments with pure pterostilbene, which is what initially led to the idea that pterostilbene is the active ingredient responsible for the therapeutic effects in blueberries.[51] However, research in this area has not yet determined the correlation between the quantity of consumed blueberries (or pterostilbene in natural plant sources) and its therapeutic effects,[51] as the quantity of pterostilbene is not necessarily constant in

the plant sources. For example, it varies depending on the variety of blueberry (9.9 -15.1 $\mu g.kg^{-1}$ of fresh fruit),[52,54] and as a result, isolation of the active compound and its administration in a controlled manner is the preferred procedure for studying its efficacy.

The specific mechanism of action of pterostilbene depends on the disease system and further research is required from clinical trials to fully understand and finalise the details of each mechanism for each disease system.[51,53] However, in general, results have indicated that pterostilbene lowers oxidative stress and reduces the production of reactive oxygen species, such as superoxide anion (O_2^-) and hydrogen peroxide (H_2O_2), which are normally responsible for the initiation and development of multiple disease pathways.[51] When pterostilbene is administered, it scavenges reactive oxygen species (ROS) and thus prevents oxidative stress and ROS-induced damage to cells.[45] With regard to cancer treatment, pterostilbene induces apoptosis in tumour cells and prevents the initiation of multiple signalling pathways involved in carcinogenesis.[45] Pterostilbene also suppresses the expression of multiple genes that promote tumour formation, and simultaneously, it increases the expression of various tumour supressing genes.[45] Lastly, as an anti-inflammatory it lowers the expression of numerous inflammatory mediators, for example, tumour necrosis factor alpha, nuclear factor kappa B, interleukin 1beta, inducible nitric oxide synthase, and cyclooxygenases.[45]

Despite the promising therapeutic properties of pterostilbene, its major shortcoming is its relatively low aqueous solubility. Consequently, given the vast and highly relevant pharmaceutical benefits that pterostilbene displays, improving the aqueous solubility is of high importance.

β-estradiol

17β-estradiol (systematic name (17β)-Estra-1(10),2,4-triene-3,17-diol) is a naturally occurring steroid hormone that is produced predominantly in the ovaries of females during the lifespan of the reproductive system.[43,55–57] It circulates endogenously and is responsible for the maintenance of the reproductive tract and for secondary sexual characteristics (the features that occur during puberty) in females.[55,56] From a medical perspective β-estradiol is

also available commercially as a synthetic formulation in the form of an oral tablet, injection, vaginal gel, and as a topical patch, spray or cream.[56]

Pharmaceutically, β-estradiol is used to treat numerous diseases and disorders including breast cancer in women and men who have metastasis, androgen-dependent prostate cancer, and menopausal symptoms such as hot flushes, vaginal dryness, mood swings and sleep deprivation.[43,55,56,58] It is also used to prevent osteoporosis in menopausal women and it is used to treat women who have ovarian failure and consequent low oestrogen levels.[43,58] Lastly, it can also be used as a female contraceptive.[55]

The mechanism of action involves β-estradiol binding to intracellular target cell receptors, namely the α and β oestrogen receptors, that are inside the cytoplasm of the cell.[58,59] The receptor can move into the nucleus of the target cell once the β-estradiol is bound to its receptor ligand, and initiate the production of messenger RNA.[60] The messenger RNA can then interact with ribosomes to form particular proteins that apply the effects of β-estradiol on the cell.[60]

The low aqueous solubility of β-estradiol is its major disadvantage for oral use; however, a derivative, ethinyl estradiol, has been synthesized in order improve oral absorption and bioavailability.[58] A comparison between β-estradiol and ethinyl estradiol indicates that further improvements are still warranted, as the solubility enhancement has increased by approximately 3-fold only (3.6×10^{-3} mg.cm^{-3} vs 11.3×10^{-3} mg.cm^{-3} at 27 ^{o}C)[43,61] and the purchase prices of the medications are in a similar proportion (depending on the manufacturer and pharmaceutical dispenser). Consequently, CD inclusion complexation of β-estradiol has the potential to improve its aqueous solubility and bioavailability more significantly, which in turn could lower the retailing costs.

Progesterone

Progesterone is a naturally occurring steroid hormone that is produced by females and males; however, it is very pronounced in females during the reproductive cycle and pregnancy, as it is necessary for endometrial receptivity and embryo implantation which ensure that the pregnancy is properly established.[62,63]

The production of progesterone occurs primarily in the reproductive system of women, although it is also produced in the peripheral and central nervous systems by the gonads and adrenal cortex glands.[63] Synthetic therapeutic forms are commercially available to treat a variety of conditions, which in some cases can be linked to abnormally low levels of progesterone in females. Pharmaceutical progesterone is used to treat infertile women who already have a predisposition for low levels of progesterone; it is also used to treat secondary amenorrhea, abnormal uterine bleeding and to prevent endometrial hyperplasia as a result of hormone imbalances. Lastly, it can also be used as a female contraceptive.[44,62,63] In addition, further research is being conducted with progesterone as a therapy towards traumatic brain injury (for which there is currently no clinically proven treatment), as well as a new approach to treating patients with stimulant addictions for cocaine and nicotine.[63,64]

The mechanism of action involves progesterone receptors being activated by binding with progesterone. This causes dissociation of heat shock proteins (proteins that are formed by cells as a consequence of being exposed to stressful conditions), receptor phosphorylation, and transcription activation (which is performed by indirect or direct interaction with transcription factors).[44] These activated progesterone receptors reduce the number of oestrogen receptors (thus causing impeding effects on oestrogens), and increase their metabolism to inactive metabolites.[44] In addition, as a contraceptive, progesterone can prevent ovulation as well as thicken the consistency of the cervical mucus which makes it unfavourable for the penetration of sperm, thus preventing pregnancy.[62]

Commercially, progesterone is available in numerous formulations, including natural progesterone, synthetic progestins and micronized natural progesterone.[63] Synthetic progestins were initially designed to overcome the low bioavailability and absorption of natural progesterone; however, synthetic progestins are not chemically the same as natural progesterone and as a result, some of them can cause adverse side effects such as androgenic effects in the central nervous system, and changes in lipid levels, glucose levels, as well as vasomotility. In addition, they can also cause sedation and dizziness.[63] Consequently, synthetic progestins are no longer commonly used, especially since the development and approval of micronized natural progesterone in the 1980s. This product was formulated in reaction to the adverse side effects of synthetic progestins and it also

improved the bioavailability of progesterone exponentially, since the micronization of natural progesterone increases the surface area of the progesterone by significantly decreasing its average particle size, and thus absorption is facilitated.[63]

The administrative routes of progesterone include oral, nasal, vaginal, transdermal, rectal, intravenous, or intramuscular injection.[44,62,63] The low aqueous solubility of progesterone results in the oral route (which is often considered the most convenient one) being unfavourable; however, the micronized progesterone addressed this issue to a certain extent.[44,63] Finally, CD inclusion of progesterone has the potential to improve the efficacy of all the administrative routes as discussed above in section 1.2.8, pp. 10 – 13, and therefore attempts to make further improvements are warranted.

1.5) Pointwise summary of the aims and objectives

Investigation of the pyrido[1,2-a]benzimidazole derivatives (GMP-23, GMP-31 and GMP-58):

1) Co-crystal formation:

a) Perform a virtual co-crystal screening investigation in order to assess which are the most likely coformers to form co-crystals with the compounds.

b) Attempt the synthesis of co-crystals based on the findings from the virtual co-crystal screening analysis. This would include dry grinding experiments, liquid-assisted ('solvent drop') grinding experiments, and co-precipitation experiments. The co-precipitation experiments will be performed with the aim of forming single crystals.

2) CD inclusion complexation:

a) Select the appropriately sized CDs that could potentially allow the pharmaceutically relevant compounds to fit inside the CD cavity.

b) Attempt the synthesis of CD inclusion complexes using kneading and co-precipitation methods. The co-precipitation experiments will be performed with the intention of forming single crystals.

3) Characterise the products formed from the co-crystal and CD inclusion complexation experiments. This would include a variety of analytical techniques, for example, thermal techniques, X-ray diffraction and spectroscopic methods.

4) Investigate the change in the aqueous solubility of the potentially synthesized co-crystals and CD inclusion complexes, either by using gravimetric or spectroscopic techniques.

Investigation of the antioxidant compound pterostilbene and of the steroidal compounds β-estradiol and progesterone:

1) CD inclusion complexation:

a) Attempt to synthesize CD inclusion complexes using kneading and co-precipitation techniques. The CDs used will include the native CDs as well as selected methylated CDs.

2) Characterise the products formed during the CD synthesis. This characterisation would include various analytical techniques, such as X-ray diffraction, thermal techniques and spectroscopic methods.

3) Perform phase solubility studies (including association constant determination) on the antioxidant, pterostilbene, with selected CDs.

4) Determine the potential aqueous solubility enhancement of β-estradiol and progesterone in the form of selected CD complexes of these APIs.

References

(1) Del Valle, E. M. M. Cyclodextrins and Their Uses: A Review. *Process Biochem.* **2004**, *39* (9), 1033–1046. https://doi.org/10.1016/S0032-9592(03)00258-9.

(2) Loftsson, T.; Brewster, M. E. Pharmaceutical Applications of Cyclodextrins: Basic Science and Product Development. *J. Pharm. Pharmacol.* **2010**, *62* (11), 1607–1621. https://doi.org/10.1111/j.2042-7158.2010.01030.x.

(3) Scannell, J. W.; Blanckley, A.; Boldon, H.; Warrington, B. Diagnosing the Decline in Pharmaceutical R&D Efficiency. *Nat. Rev. Drug Discov.* **2012**, *11* (3), 191–200. https://doi.org/10.1038/nrd3681.

(4) Sams-Dodd, F. Is Poor Research the Cause of the Declining Productivity of the Pharmaceutical Industry? An Industry in Need of a Paradigm Shift. *Drug Discov. Today* **2013**, *18* (5–6), 211–217. https://doi.org/10.1016/j.drudis.2012.10.010.

(5) Ruffolo, R. R. Why Has R&D Productivity Declined in the Pharmaceutical Industry? *Expert Opin. Drug Discov.* **2006**, *1* (2), 99–102. https://doi.org/10.1517/17460441.1.2.99.

(6) Chandler, D. J. Something's Got to Give: Psychiatric Disease on the Rise and Novel Drug Development on the Decline. *Drug Discov. Today* **2013**, *18* (3–4), 202–206. https://doi.org/10.1016/j.drudis.2012.08.003.

(7) Munos, B. Lessons from 60 Years of Pharmaceutical Innovation. *Nat. Rev. Drug Discov.* **2009**, *8* (12), 959–968. https://doi.org/10.1038/nrd2961.

(8) Pammolli, F.; Magazzini, L.; Riccaboni, M. The Productivity Crisis in Pharmaceutical R&D. *Nat. Rev. Drug Discov.* **2011**, *10* (6), 428–438. https://doi.org/10.1038/nrd3405.

(9) Schmid, E. F.; Smith, D. A. Keynote Review: Is Declining Innovation in the Pharmaceutical Industry a Myth? *Drug Discov. Today* **2005**, *10* (15), 1031–1039. https://doi.org/10.1016/S1359-6446(05)03524-5.

(10) Cockburn, I. M. Is the Pharmaceutical Industry in a Productivity Crisis? *Innov. Policy Econ.* **2006**, *7*, 1–32.

(11) Szejtli, J. Introduction and General Overview of Cyclodextrin Chemistry. *Chem. Rev.* **1998**, *98* (5), 1743–1754. https://doi.org/10.1021/cr970022c.

(12) Zhang, J.; Ma, P. X. Cyclodextrin-Based Supramolecular Systems for Drug Delivery: Recent Progress and Future Perspective. *Adv. Drug Deliv. Rev.* **2013**, *65* (9), 1215–1233. https://doi.org/10.1016/j.addr.2013.05.001.

(13) Hirayama, F.; Uekama, K. Cyclodextrin-Based Controlled Drug Release System. *Adv. Drug Deliv. Rev.* **1999**, *36* (1), 125–141. https://doi.org/10.1016/S0169-409X(98)00058-1.

(14) Sá Couto, A.; Salústio, P.; Cabral-Marques, H. Cyclodextrins. *Polysaccharides* **2014**, 1–36. https://doi.org/10.1007/978-3-319-03751-6_22-1.

(15) Nikitenko, N. A.; Prassolov, V. S. Non-Viral Delivery and Therapeutic Application of Small Interfering RNAs. *Acta Naturae* **2013**, *5* (3), 35–53. https://doi.org/10.32607/20758251-2013-5-3-35-53.

(16) Lee, J.; Lee, S.-S.; Lee, S.; Oh, H. Bin. Noncovalent Complexes of Cyclodextrin with Small Organic Molecules: Applications and Insights into Host–Guest Interactions in the Gas Phase and Condensed Phase. *Molecules* **2020**, *25* (18), 4048. https://doi.org/10.3390/molecules25184048.

(17) Savjani, K. T.; Gajjar, A. K.; Savjani, J. K. Drug Solubility: Importance and Enhancement Techniques. *ISRN Pharm.* **2012**, *2012*, 1–10. https://doi.org/10.5402/2012/195727.

(18) Liu, L.; Xu, J.; Zheng, H.; Li, K.; Zhang, W.; Li, K.; Zhang, H. Inclusion Complexes of Laccaic Acid A with β -Cyclodextrin or Its Derivatives: Phase Solubility, Solubilization, Inclusion Mode, and Characterization. *Dye. Pigment.* **2017**, *139*, 737–746. https://doi.org/10.1016/j.dyepig.2017.01.001.

(19) Tian, B.; Xiao, D.; Hei, T.; Ping, R.; Hua, S.; Liu, J. The Application and Prospects of Cyclodextrin Inclusion Complexes and Polymers in the Food Industry: A Review. *Polym. Int.* **2020**, *69* (7), 597–603. https://doi.org/10.1002/pi.5992.

(20) Stella, V. J.; Rao, V. M.; Zannou, E. A.; Zia, V. Mechanisms of Drug Release from Cyclodextrin Complexes. *Adv. Drug Deliv. Rev.* **1999**, *36* (1), 3–16. https://doi.org/10.1016/S0169-409X(98)00052-0.

(21) Tokumura, T.; Nanbas, M.; Tsushima, Y.; Tatsuishi, K.; Kayano, M.; Machida, Y.; Nagai, T. Enhancement of Bioavailability of Cinnarizine from Its β-Cyclodextrin Complex on Oral Administration with Dl-Phenylalanine as a Competing Agent. *J. Pharm. Sci.* **1986**, *75* (4), 391–394. https://doi.org/10.1002/jps.2600750415.

(22) Stella, V. Mechanisms of Drug Release from Cyclodextrin Complexes. *Adv. Drug Deliv. Rev.* **1999**, *36* (1), 3–16. https://doi.org/10.1016/S0169-409X(98)00052-0.

(23) Harata, K. Structural Aspects of Stereodifferentiation in the Solid State. *Chem. Rev.* **1998**, *98* (5), 1803–1828. https://doi.org/10.1021/cr9700134.

(24) Saenger, W.; Jacob, J.; Gessler, K.; Steiner, T.; Hoffmann, D.; Sanbe, H.; Koizumi, K.; Smith, S. M.; Takaha, T. Structures of the Common Cyclodextrins and Their Larger AnaloguesBeyond the Doughnut. *Chem. Rev.* **1998**, *98* (5), 1787–1802. https://doi.org/10.1021/cr9700181.

(25) Saenger, W. Crystal Packing Patterns of Cyclodextrin Inclusion Complexes. *J. Incl. Phenom.* **1984**, *2* (3–4), 445–454. https://doi.org/10.1007/BF00662211.

(26) Kamitori, S.; Hirotsu, K.; Higuchi, T. Crystal and Molecular Structure of the γ-Cyclodextrin–12-Crown-4 1 : 1 Inclusion Complex. *J. Chem. Soc., Chem. Commun.* **1986**, No. 9, 690–691. https://doi.org/10.1039/C39860000690.

(27) Kumar, S.; Nanda, A. Pharmaceutical Cocrystals: An Overview. *Indian J. Pharm. Sci.* **2017**, *79* (6). https://doi.org/10.4172/pharmaceutical-sciences.1000302.

(28) Blagden, N.; Berry, D. J.; Parkin, A.; Javed, H.; Ibrahim, A.; Gavan, P. T.; De Matos, L. L.; Seaton, C. C. Current Directions in Co-Crystal Growth. *New J. Chem.* **2008**, *32* (10), 1659. https://doi.org/10.1039/b803866j.

(29) Vishweshwar, P.; McMahon, J. A.; Bis, J. A.; Zaworotko, M. J. Pharmaceutical Co-Crystals. *J. Pharm. Sci.* **2006**, *95* (3), 499–516. https://doi.org/10.1002/jps.20578.

(30) Aakeröy, C. B.; Salmon, D. J. Building Co-Crystals with Molecular Sense and Supramolecular Sensibility. *CrystEngComm* **2005**, *7* (72), 439. https://doi.org/10.1039/b505883j.

(31) Bond, A. D. What Is a Co-Crystal? *CrystEngComm* **2007**, *9* (9), 833. https://doi.org/10.1039/b708112j.

(32) Steed, J. W. The Role of Co-Crystals in Pharmaceutical Design. *Trends Pharmacol. Sci.* **2013**, *34* (3), 185–193. https://doi.org/10.1016/j.tips.2012.12.003.

(33) Almarsson, Ö.; Zaworotko, M. J. Crystal Engineering of the Composition of Pharmaceutical Phases. Do Pharmaceutical Co-Crystals Represent a New Path to Improved Medicines? *Chem. Commun.* **2004**, No. 17, 1889. https://doi.org/10.1039/b402150a.

(34) U.S. Food and Drug Administration https://www.cfsanappsexternal.fda.gov/scripts/fdcc/index.cfm?set=SCOGS&sort=Sortsubstance&order=ASC&showAll=true&type=basic&search= (accessed Jun 9, 2021).

(35) Raheem Thayyil, A.; Juturu, T.; Nayak, S.; Kamath, S. Pharmaceutical Co-Crystallization: Regulatory Aspects, Design, Characterization, and Applications. *Adv. Pharm. Bull.* **2020**, *10* (2), 203–212. https://doi.org/10.34172/apb.2020.024.

(36) Vemuri, V. D.; Lankalapalli, S. Insight into Concept and Progress on Pharmaceutical Co-Crystals: An Overview. *Indian J. Pharm. Educ. Res.* **2019**, *53* (4s), s522–s538. https://doi.org/10.5530/ijper.53.4s.147.

(37) Aakeröy, C. B.; Sinha, A. S. Chapter 1. Co-Crystals: Introduction and Scope; 2018; pp 1–32. https://doi.org/10.1039/9781788012874-00001.

(38) Mittapalli, S.; Mannava, M. K. C.; Sahoo, R.; Nangia, A. Cocrystals, Salts, and Supramolecular Gels of Nonsteroidal Anti-Inflammatory Drug Niflumic Acid. *Cryst. Growth Des.* **2019**, *19* (1), 219–230. https://doi.org/10.1021/acs.cgd.8b01298.

(39) Karimi-Jafari, M.; Padrela, L.; Walker, G. M.; Croker, D. M. Creating Cocrystals: A Review of Pharmaceutical Cocrystal Preparation Routes and Applications. *Cryst. Growth Des.* **2018**, *18* (10), 6370–6387. https://doi.org/10.1021/acs.cgd.8b00933.

(40) Ancheria, R. K.; Jain, S.; Kumar, D.; Soni, S. L.; Sharma, M. An Overview of Pharmaceutical Co-Crystal. *Asian J. Pharm. Res. Dev.* **2019**, *7* (2), 39–46. https://doi.org/10.22270/ajprd.v7i2.483.

(41) Sekhon, B. S. Pharmaceutical Co-Crystals - a Review. *ARS Pharm.* **2009**, *50* (3), 99–117.

(42) Paul, S. M.; Mytelka, D. S.; Dunwiddie, C. T.; Persinger, C. C.; Munos, B. H.; Lindborg, S. R.; Schacht, A. L. How to Improve R&D Productivity: The Pharmaceutical Industry's Grand Challenge. *Nat. Rev. Drug Discov.* **2010**, *9* (3), 203–214. https://doi.org/10.1038/nrd3078.

(43) National Center for Biotechnology Information (2020). PubChem Compound Summary for CID 5757, Estradiol. https://pubchem.ncbi.nlm.nih.gov/compound/Estradiol (accessed Jan 3, 2022).

(44) National Center for Biotechnology Information (2020). PubChem Compound Summary for CID 5994, Progesterone. https://pubchem.ncbi.nlm.nih.gov/compound/Progesterone (accessed Aug 9, 2020).

(45) National Center for Biotechnology Information (2020). PubChem Compound Summary for CID 5281727, Pterostilbene https://pubchem.ncbi.nlm.nih.gov/compound/Pterostilbene (accessed Aug 8, 2020).

(46) Yalkowsky, S.H., He, Y. *Handbook of Aqueous Solubility Data: An Extensive Compilation of Aqueous Solubility Data for Organic Compounds Extracted from the AQUASOL DATAbASE*; CRC Press LLC, Boca Raton, FL., 2003.

(47) Ivanisevic, I.; Andres, M. C.; Stephens, K.; Bethune, S.; Bower, M.; Wolfe, S.; Smit, J.; Gilkinson, A.; Roe, M. Manuscript in Preparation. **2011**.

(48) Silva, F.; Figueiras, A.; Gallardo, E.; Nerín, C.; Domingues, F. C. Strategies to Improve the Solubility and Stability of Stilbene Antioxidants: A Comparative Study between Cyclodextrins and Bile Acids. *Food Chem.* **2014**, *145*, 115–125. https://doi.org/10.1016/j.foodchem.2013.08.034.

(49) Okombo, J.; Singh, K.; Mayoka, G.; Ndubi, F.; Barnard, L.; Njogu, P. M.; Njoroge, M.; Gibhard, L.; Brunschwig, C.; Vargas, M.; Keiser, J.; Egan, T. J.; Chibale, K. Antischistosomal Activity of Pyrido[1,2- a]Benzimidazole Derivatives and Correlation with Inhibition of β-Hematin Formation. *ACS Infect. Dis.* **2017**, *3* (6), 411–420. https://doi.org/10.1021/acsinfecdis.6b00205.

(50) Mayoka, G.; Keiser, J.; Häberli, C.; Chibale, K. Structure–Activity Relationship and in Vitro Absorption, Distribution, Metabolism, Excretion, and Toxicity (ADMET) Studies of N -Aryl 3-Trifluoromethyl Pyrido[1,2- a]Benzimidazoles That Are Efficacious in a Mouse Model of Schistosomiasis. *ACS Infect. Dis.* **2019**, *5* (3), 418–429. https://doi.org/10.1021/acsinfecdis.8b00313.

(51) McCormack, D.; McFadden, D. A Review of Pterostilbene Antioxidant Activity and Disease Modification. *Oxid. Med. Cell. Longev.* **2013**, *2013*, 1–15. https://doi.org/10.1155/2013/575482.

(52) Estrela, J. M.; Ortega, A.; Mena, S.; Rodriguez, M. L.; Asensi, M. Pterostilbene: Biomedical Applications. *Crit. Rev. Clin. Lab. Sci.* **2013**, *50* (3), 65–78. https://doi.org/10.3109/10408363.2013.805182.

(53) Chan, E. W. C.; Wong, C. W.; Tan, Y. H.; Foo, J. P. Y.; Wong, S. K.; Chan, H. T. Resveratrol and Pterostilbene: A Comparative Overview of Their Chemistry, Biosynthesis, Plant Sources and Pharmacological Properties. *J. Appl. Pharm. Sci.* **2019**, *9* (7), 124–129. https://doi.org/10.7324/JAPS.2019.90717.

(54) McCormack, D.; McFadden, D. Pterostilbene and Cancer: Current Review. *J. Surg. Res.* **2012**, *173* (2), e53–e61. https://doi.org/10.1016/j.jss.2011.09.054.

(55) Roby, K. F. 17 Beta Estradiol. In *Reference Module in Biomedical Sciences*; Elsevier, 2019. https://doi.org/10.1016/B978-0-12-801238-3.98019-X.

(56) Drugs.com, Estradiol https://www.drugs.com/estradiol.html (accessed Aug 9, 2020).

(57) ChemSpider http://www.chemspider.com/Chemical-Structure.5554.html (accessed Aug 9, 2020).

(58) Drugbank, Estradiol https://www.drugbank.ca/drugs/DB00783 (accessed Aug 9, 2020).

(59) Hall, J. M.; Couse, J. F.; Korach, K. S. The Multifaceted Mechanisms of Estradiol and Estrogen Receptor Signaling. *J. Biol. Chem.* **2001**, *276* (40), 36869–36872. https://doi.org/10.1074/jbc.R100029200.

(60) Mandal, A. News-medical, Estradiol Mechanism https://www.news-medical.net/health/Estradiol-Mechanism.aspx#:~:text=Mechanism of action,the cytoplasm of the cell. (accessed Aug 9, 2020).

(61) National Center for Biotechnology Information (2020). PubChem Compound Summary for CID 5991, Ethinyl estradiol. https://pubchem.ncbi.nlm.nih.gov/compound/Ethinyl-estradiol (accessed Aug 9, 2020).

(62) Drugbank, Progesterone https://www.drugbank.ca/drugs/DB00396 (accessed Aug 12, 2020).

(63) Goletiani, N. V.; Keith, D. R.; Gorsky, S. J. Progesterone: Review of Safety for Clinical Studies. *Exp. Clin. Psychopharmacol.* **2007**, *15* (5), 427–444. https://doi.org/10.1037/1064-1297.15.5.427.

(64) Cooke, P. S.; Nanjappa, M. K.; Yang, Z.; Wang, K. K. W. Therapeutic Effects of Progesterone and Its Metabolites in Traumatic Brain Injury May Involve Non-Classical Signaling Mechanisms. *Front. Neurosci.* **2013**, *7*. https://doi.org/10.3389/fnins.2013.00108.

Chapter 2

Experimental methods

2.1) Materials

2.1.1) Pharmaceutically relevant compounds

β-estradiol ($C_{18}H_{24}O_2$) and progesterone ($C_{21}H_{30}O_2$) were purchased from Sigma-Aldrich Chemie GmbH (Steinheim, Germany). Pterostilbene ($C_{16}H_{16}O_3$) was purchased from Mega Resveratrol Candlewood Stars Inc. (Danbury, CT, USA). The three pyrido[1,2-a]benzimidazole derivative drug leads were synthesized and provided by the H3D laboratory at the University of Cape Town and will be referred to by their internal code names, *viz.* GMP-23, GMP-31 and GMP-58.

2.1.2) Cyclodextrins (CDs)

β-Cyclodextrin (β-CD; $C_{42}H_{70}O_{35}$), heptakis(2,6-di-*O*-methyl)-β-cyclodextrin (DMB; $C_{56}H_{96}O_{35}$), heptakis(2,3,6-tri-*O*-methyl)-β-cyclodextrin (TMB; $C_{63}H_{112}O_{35}$) and randomly methylated β-cyclodextrin [RAMEB; $(C_{42}H_{70-n}O_{35})(CH_3)_n$, n = 12] were purchased from Cyclolab (Budapest, Hungary). γ-Cyclodextrin (γ-CD; $C_{48}H_{80}O_{40}$) was purchased from Wacker, Biosolutions (Halle, Germany). Sulfobutyl ether β-cyclodextrin (SBEBCD) sodium salt $[(C_{42}H_{70-n}O_{35})(C_4H_8O_3SNa)_n$, n = 14] was purchased from Cyclolab (Budapest, Hungary).

2.1.3) Coformers

The coformers employed in co-crystallization experiments were purchased from Sigma-Aldrich Chemie GmbH (Steinheim, Germany) and Acros Organics (New Jersey, USA). A list of the coformers is provided in the Appendix under section 1, Table 1.1, p. 2.

2.2) Co-crystal screening

2.2.1) Virtual co-crystal screening

A virtual co-crystal screening exercise was conducted using the program Mercury.[1] This involved a molecular complementarity investigation in order to assess which compounds would be most suitable as potential coformers for co-crystallization with the GMP drug leads. The resulting list was significantly reduced, as only 'generally recognised as safe' (GRAS) coformers were selected from it. Thereafter, hydrogen bonding motif studies were also conducted in order to rank which of the selected coformers might have higher probability of forming co-crystals, based on the frequency of occurrence of certain hydrogen bonding synthons that have already been reported in the Cambridge Structural Database (CSD).[2]

2.2.2) Grinding experiments

The subsequent step in co-crystal screening involved grinding experiments. These were either performed as dry ('neat') co-grinding, or as liquid-assisted grinding (LAG) experiments. The dry co-grinding involved placing 1:1 stoichiometric quantities of the pharmaceutically relevant compound and pre-selected coformer into a mortar and grinding the mixture with a pestle for 15 minutes (unless otherwise stated). In contrast, the LAG experiments involved the same experimental procedure, except that a very small, measured volume of a pre-selected solvent was added during the grinding process in order to induce the reagent mixture to have a paste-like consistency. These experiments were performed in order to assess the possibility of synthesizing new crystalline phases.

2.2.3) Co-precipitation

The final step for the co-crystal screening experimentation involved co-precipitation. This involved the separate dissolution of the pharmaceutically relevant compound and the coformer (1:1 stoichiometric ratio) in a common organic solvent and stirring at a constant temperature (unless specified differently). The temperature that was used to dissolve the components in the organic solvent was specific to the solvent employed in the particular experiment. Once the individual components were fully dissolved, each solution was separately filtered into a common vial using a

nylon 0.45 µm microfilter. The resulting solution was exposed to differing conditions in order to allow co-precipitation to take place. These varying conditions are described below.

Slow evaporation: This method of co-precipitation permits the solvent to evaporate very slowly, which allows the dissolved product to eventually precipitate. Thus, after the two individual component solutions were separately filtered into the vial, the vial was sealed with parafilm and the latter was thereafter punctured with a few pin-sized holes. The vial was then left undisturbed on the laboratory bench in order to allow for evaporation over an extended period in a controlled manner by means of the punctured parafilm seal mentioned above.

Slow cooling: This process involved slow cooling of the heated, saturated solution containing the pharmaceutically relevant compound and the coformer without any evaporation occurring. After the separately heated component solutions were filtered into the vial, it was capped, tightly sealed and placed in a Dewar flask that had been filled with water and pre-heated to the same temperature as that of the solution. The Dewar flask was then covered and left undisturbed for three days while the water inside cooled to ambient temperature. This particular method is generally preferred as it often results in the precipitation of larger product crystals.

2.3) Cyclodextrin inclusion

2.3.1) Kneading

This process generally involved placing equimolar quantities of the API and the CD in a mortar with a small amount of Milli-Q® water.[3] In cases where the product stoichiometric ratio was known to be other than 1:1, the appropriate component masses were used. The mixture was then kneaded into a paste with a pestle for 40 minutes and where necessary, small increments of water were added. The purpose of adding water was to aid in the thermodynamic process of complex formation by providing the requisite complement of this solvent necessary for optimising the complex crystallinity, and thereafter to prevent the fully hydrated complex from degrading. The above procedure was performed when employing both native and methylated CDs, with the difference that, owing to the high aqueous solubility of the methylated CDs, only a miniscule amount of water was added during kneading, as opposed to a few drops when native CDs were used.

2.3.2) Kneading a mixture of the molten API and the crystalline CD

This involved inserting a known mass of the API into a glass vial which was then placed on a hotplate and heated to a temperature just above the melting point of the API. Once the API was completely melted, incremental amounts of the CD (to meet the required stoichiometric ratio) were added to the vial and kneaded with the API using a spatula. The duration of this process was 40 minutes.

2.3.3) Co-precipitation

Different preparative methods were employed for the native CDs (β-CD and γ-CD) and methylated CDs (DMB and TMB) and thus they are described separately below.

2.3.3.1) Native cyclodextrins (CDs): The methodology involved pre-dissolving the native CD in water that was heated to 70 ^{o}C and stirred at a continuous, rapid rate. The volume of water was dependent on the mass of CD used, as well as the type of CD, and consequently these specifications are stated for each experiment in subsequent sections. The API was then added very slowly to the aqueous CD solution in small increments and the resulting suspension was left to stir for a duration of 3 - 6 hours until all the reagents had dissolved. Thereafter, the solution was filtered into a clean, pre-warmed vial using a nylon 0.45 μm microfilter and prepared for either slow cooling or slow evaporation to allow the formation of complex crystals.

2.3.3.2) Methylated cyclodextrins (CDs): This process involved pre-dissolving the methylated CD in water at 23 ^{o}C while stirring at a constant, rapid rate. Similarly, the volume of water used was dependent on the mass and type of CD employed. The API was added in very small increments, each being required to dissolve before the subsequent increment was added. Where the dissolution of the API was challenging, temperature cycling was employed. This involved repetitively heating the stirring solution to 70 ^{o}C and then rapidly cooling it to 4 ^{o}C with the aim of promoting dissolution and CD inclusion of the API. Thereafter, the solution was filtered at 4 ^{o}C with a 0.45 μm nylon microfilter into a clean, pre-cooled vial which was then sealed and placed in the oven at 60 ^{o}C to allow the complex to crystallize.

2.4) Ambient temperature powder X-ray diffraction (PXRD)

Powder X-ray diffraction (PXRD) patterns were recorded at 23 ^{o}C for each reagent as well as the products formed from co-grinding, kneading and co-precipitation. The PXRD patterns of the various products were compared with those of the individual respective reactants in order to assess whether unique crystalline material had formed. PXRD analyses were performed on a Bruker D8 Advance powder diffractometer (Billerica, Massachusetts, U.S.A) using CuKα_1 radiation (λ = 1.5406 Å) with an X-ray generator set at 30 kV and 40 mA, as well as on a Bruker D2 Phaser desktop powder diffractometer (Billerica, Massachusetts, U.S.A) with CuKα_1 radiation (λ = 1.5406 Å) with the X-ray generator set at 30 kV and 10 mA. All samples were lightly ground (to minimise the effects of preferred orientation) and placed on a silicon zero-background sample holder. The scanning range was 4^{o} – 40^{o} 2θ with a step size of 0.0164^{o} and a primary beam path slit of 0.6 mm.

The sample holder was custom-made and consequently a shift of approximately +0.2^{o} occurred with the experimental PXRD patterns. This was evident when comparing the PXRD patterns of the experimental samples with the computed PXRD patterns.

2.5) Variable temperature powder X-ray diffraction (VTPXRD)

A series of consecutive PXRD patterns were recorded for a given crystalline product as a function of temperature in order to detect possible phase changes on heating. The PXRD patterns of the product recorded at the various selected temperatures were inspected to identify any changes in the angular positions of the peaks that might indicate a phase transition. This analysis was performed on a Bruker D8 Advance powder diffractometer (Billerica, Massachusetts, U.S.A) using CuKα_1 radiation (λ = 1.5406 Å), with a step size of 0.0164^{o} and a scanning range of 4^{o} – 40^{o} 2θ. The X-rays were generated at 30 kV and 40 mA. The sample preparation involved lightly grinding a large quantity of product to fill the metal sample holder evenly, and the sample was kept under vacuum throughout the duration of the experiment.

2.6) Single-crystal X-ray diffraction (SCXRD) analysis

A single-crystal four-circle X-ray diffractometer was used to determine the three-dimensional structures of crystals obtained from co-precipitation experiments. Once they were removed from their mother liquor, these crystals were immediately coated in Paratone N oil[4] (Exxon Chemical Co.,

TX, USA) in order to prevent a possible loss of included solvent molecules, and where necessary, the crystals were cut to a suitable size. A unit cell determination on these crystals was initially performed at room temperature to avoid possible transitions that might have arisen on rapid cooling. Before embarking on a full intensity data-collection, the measured unit cell parameters were compared with the entries in the Cambridge Crystallographic Database (CSD)[2] to establish whether they matched those of any deposited crystal structures. The unit cell determinations and data-collections were performed on a Bruker KAPPA APEX II DUO single-crystal X-ray diffractometer (Madison Wisconsin, U.S.A) and a Bruker D8 VENTURE SCXRD single-crystal X-ray diffractometer (Madison Wisconsin, U.S.A). The crystals were cooled to either 100(2) K or 173(2) K in a nitrogen vapour stream using an Oxford Cryostream cooler (Oxford Cryosystems Ltd, Oxford, U.K.). Subsequently, the collected intensity datasets were read into the program XPREP,[5] which determined the respective space groups (independently established by the author using the program LAYER implemented in the X-SEED[6] interface) and the structures were solved with the direct methods programs SHELXS-97 or SHELXT-97.[7] Thereafter, the structures were refined by full-matrix least-squares techniques with SHELXL-97,[7] implemented in the X-SEED[6] interface.

The technique of isomorphous replacement was used to solve several of the CD inclusion complex structures. This involved a CSD search for a CD complex crystallizing in the same space group and having very similar unit cell parameters. The atomic co-ordinates of the selected complex were placed in the .ins file of the new CD inclusion complex. Thereafter, all the water molecules, the guest atoms, as well as the freely-rotatable O6 atoms on the CD host molecule were deleted, leaving only the rigid skeleton of the CD molecule as the trial model. This model was thereafter refined isotropically and from subsequent difference Fourier maps the remaining atoms of the CD host of the new inclusion complex could be placed and refined anisotropically. Once the structure of the host molecule was settled, the difference electron density ($\Delta\rho$) peaks of the guest molecule were assigned, and refined initially isotropically and thereafter anisotropically.

Oxygen atoms of the water molecules in the CD inclusion complexes were identified by measuring the distances between the oxygen atoms on the CD molecule and unassigned $\Delta\rho$ peaks and evaluating whether they were in the range expected for O···O distances associated with O-H···O hydrogen bonds. The $\Delta\rho$ peaks with a height $\geq$ 2.0 e.Å^{-3} were subsequently assigned as water O atoms with full site-occupancy, as they displayed acceptable isotropic thermal parameters (U_{iso}) after refinement. However, the water O atoms that displayed abnormally large U_{iso} values after

refinement were deemed to represent 'partial' O atoms and were therefore constrained to have U_{iso} values equal to the average of those for the fully-occupied water oxygen atoms, and their individual site-occupancy factors (s.o.f.s) were treated as variables. In addition, several water oxygen atoms were disordered over two or three positions, such that the distance between the components was less than 2.5 Å. In the final cycles of refinement, the fully-occupied water oxygen atoms were treated anisotropically, while their disordered counterparts were refined isotropically.

2.7) Proton nuclear magnetic resonance (^{1}H NMR) spectroscopy

^{1}H NMR analyses were performed with the purpose of quantifying the stoichiometric ratios of the GMP solvates, GMP-coformer products and CD inclusion complexes. All the samples (with masses of 3 mg, unless stated otherwise) were dissolved in deuterated dimethyl sulfoxide (DMSO-d_6) at 23 ^{o}C in a clean, new vial. These experiments were performed on a Bruker Ultrashield 400 Plus Spectrometer (Billerica, Massachusetts, U.S.A) and the program MestReNova was used to analyse the resulting data.[8]

2.8) Fourier transform infrared (FT-IR) spectroscopy

FT-IR spectra were used exclusively to analyse the extent of the shifts in the carbonyl peaks of various coformers in order to assess whether hydrogen bonding interaction had occurred between a GMP compound and the respective coformer. The samples were pressed on sodium chloride windows and the spectra of the samples were recorded on a PerkinElmer Spectrum Two instrument, fitted with an attenuated total reflectance (ATR) attachment (Waltham, Massachusetts, US.A).

2.9) Thermal analysis

Thermal analysis was conducted in order to investigate the physical changes that the compounds might undergo during programmed heating. This analysis comprised three separate, but complementary techniques, namely hot stage microscopy (HSM), thermal gravimetric analysis (TGA) and differential scanning calorimetry (DSC).

2.9.1) Hot stage microscopy (HSM)

HSM was performed in order to visually monitor the behaviour of the sample as it was heated. The sample preparation involved placing the crystals on a glass slide and immediately immersing them in a small amount of silicone oil. The glass slide was subsequently placed on the platform of the thermocouple and the HSM unit was covered with a glass screw top cover. The crystals were generally heated at a constant rate of 10 $K.min^{-1}$ over the temperature range 23 – 400 ^{o}C, unless stated otherwise. The HSM experiment was viewed through a Nikon SMZ-10 stereoscopic microscope fitted with a Linkam THM600 hot stage and a Linkam TP92 temperature control unit. The images were captured by a real-time Sony Digital Hyper HAD colour video at selected temperatures. The captured images were viewed with the Soft Imaging Program AnalySIS.[9]

2.9.2) Thermal gravimetric analysis (TGA)

TGA was used to quantify the percentage mass loss of the compounds as a function of temperature. This analysis was used to quantify the number of water molecules present in the CD inclusion complexes, as well as the CD:API stoichiometric ratio in a few of the complexes whose guest molecules were released at higher temperatures. In addition, it was used to quantify the solvent content in certain solvated GMP products, and the coformer content in the GMP-coformer products. Furthermore, this technique gave insight into the thermal stability of the compounds. The sample preparation involved a rapid process of removing the crystals from their mother liquor in the vial and then lightly pressing them between a filter paper to dry their surfaces. It was imperative to start the experiment immediately after the mother liquor was removed in order to quantify the total amount of included water, especially for labile complexes. The masses that were used for the TGA analysis ranged between 0.7 mg and 2.0 mg. The experiments took place in open pans under dry nitrogen gas with a constant flow rate of 60 $cm^3.min^{-1}$. The samples were heated to a maximum temperature of 400 ^{o}C at a constant rate of 10 $K.min^{-1}$. These experiments were performed on the TA-Q500 (New Castle, Delaware, United States of America) with Universal Analysis 2000 software.

2.9.3) Differential scanning calorimetry (DSC)

DSC is a technique which measures the difference in the energy absorbed between a sample pan and reference pan when both are being heated simultaneously at a constant rate in a closed

furnace. DSC analysis was used to determine whether any exothermic or endothermic thermal events occurred within the sample upon heating. Thermal events, such as polymorphic transitions, recrystallization, dehydration, melting and decomposition are associated with exothermic or endothermic deviations from a baseline.

Sample preparation involved rapidly removing mother liquor from the crystal surfaces and placing the dry crystals in a crimped aluminium pan with two venting holes. The sample (mass range 1-2 mg) was heated at a constant rate of 10 $K.min^{-1}$ under dry N_2 purge gas with a flux of 60 $cm^3.min^{-1}$. The samples were generally heated to temperatures below their onset of decomposition. This terminating temperature was sample-specific and thus it is mentioned explicitly for each case. The samples could not be taken to decomposition temperatures owing to the sensitivity of the DSC instrument and consequently no comparisons were made between HSM and TGA results with regard to decomposition. These experiments were performed on a TA Discovery DSC 25 instrument (New Castle, Delaware, United States of America), and analysed with TRIOS software.[11]

2.10) Solubility analysis

2.10.1) Solubility analysis *via* colour standard comparison for the GMP-coformer products

This solubility investigation provided a fairly reliable indication of solubility enhancement of the GMP compounds in the form of the GMP-coformer products. It is acknowledged that this method is not ideal in terms of accurately quantifying a solubility value; however, more accurate analytical methods were unfortunately not available at the time. For example, high-performance liquid chromatography (HPLC) was unavailable as the instrument column had terminated at the time of this experiment, and regarding a gravimetric approach, the GMP-coformer products were too insoluble to utilise this method. Thus, as mentioned, this proposed method provided an approximate but fairly reliable indication of aqueous solubility modification.

This method involved partially dissolving an accurately weighed sample of approximately 1 mg of (a) each of the GMP-coformer products in 2 cm^3 of water and (b) each of the amorphous forms of the GMP compounds in 2 cm^3 of water. The resultant suspensions were stirred for one hour at 37 ^oC. In addition, reference solutions were simultaneously prepared under the same conditions by separately dissolving GMP-23, GMP-31 and GMP-58 in 2 cm^3 of water. Thereafter, the solutions

were filtered with a nylon 0.45 µm microfilter. The stirring apparatus used was a Radleys Standard stirring hotplate with a 2.5 cm high vial supporting stand attached to it. The vials were placed on the stand in a circle at a radius of 4 cm from the centre and stirred at a rate of 250 rpm for 72 hours.

A series of solutions with known concentrations was prepared for each of the GMP compounds, each series being used as a control to assess the extent of the dissolution of the products with reference to the respective colour changes. This preparation involved dissolving 0.1 mg of each GMP compound in 2 cm^3 of THF (a solvent that solubilises the GMP compounds very well) to form a stock solution for a particular GMP compound. Thereafter, eight vials were arranged with 0.01 cm^3 increments of the stock solution being added in a stepwise manner to these vials to make each successive vial more concentrated. The total volume of each vial was made up to 2 cm^3 with THF.

2.10.2) Phase solubility analysis with CDs and pterostilbene

Phase solubility experiments involving the antioxidant pterostilbene were performed with two cyclodextrins, namely SBEBCD sodium salt and RAMEB. Separate solutions of these CDs with increasing concentrations (4 mM, 8 mM, 12 mM, 16 mM and 20 mM) were prepared in a total volume of 4 cm^3 for each solution. Thereafter, an excess of pterostilbene was added to each vial and the suspension was stirred for 72 hours. This part of the experiment was performed on a 2.5 cm high vial supporting stand attached to a Radleys Standard stirring hotplate. The vials were placed on the stand in a circle and 2.0 cm from the centre of the stand. The stirring rate was set to 250 rpm at 23 ^oC, and the vials were protected from light. Thereafter, each solution was filtered with a nylon 0.2 µm microfilter and further diluted to 1:100 in order to be within a readable analytical range. The samples were subsequently analysed using HPLC, with a 60:40 acetonitrile:water mixture at 23 ^oC as the mobile phase.

A calibration curve for pterostilbene was also constructed, 5.20 mg of pterostilbene being dissolved in a 60:40 acetonitrile:water mixture in a 50 cm^3 volumetric flask at 23 ^oC. Thereafter, ten aliquots containing differing concentrations were analysed by HPLC at 23 ^oC. The instrument used was an Agilent 1220 Infinity LC system (Germany), with the separation being performed on an Agilent Poroshell 120 EC – C18 threaded column (4.6 mm × 50 mm), 2.7 µm particle size. The analytical data were recorded and analysed utilizing the software program Agilent ChemStation.[12]

2.10.3) Solubility analysis by gravimetric increments

This experiment was conducted for CD complexes of steroidal guest molecules, namely β-CD·BES, β-CD·PRO, γ-CD·BES and γ-CD·PRO, and the method involved the addition of small, accurately pre-weighed incremental amounts of a given CD inclusion complex (approximately 30 mg each) into a vial containing 3 cm^3 of water. A visual estimation of the solubility was established after the final suspension was stirred for 72 hours at 27 ^oC. This procedure ensured that a very narrow solubility range was spanned by the penultimate and final incremental CD inclusion complex additions, the final amount resulting in saturation of the solution.

The experiment was performed on the same equipment and utilized the same setup as previously described for the solubility analysis of the GMP products (section 2.10.1, pp. 47 – 48).

References

(1) Macrae, C. F.; Sovago, I.; Cottrell, S. J.; Galek, P. T. A.; McCabe, P.; Pidcock, E.; Platings, M.; Shields, G. P.; Stevens, J. S.; Towler, M.; Wood, P. A. Mercury 4.0 : From Visualization to Analysis, Design and Prediction. *J. Appl. Crystallogr.* **2020**, *53* (1), 226–235. https://doi.org/10.1107/S1600576719014092.

(2) Fábián, L. Cambridge Structural Database Analysis of Molecular Complementarity in Cocrystals. *Cryst. Growth Des.* **2009**, *9* (3), 1436–1443. https://doi.org/10.1021/cg800861m.

(3) Milli-Q Water, Millipore Corporation, Billerica, Massachusetts, USA.

(4) Paratone N Oil, Exxon Chemical Co., Texas, USA.

(5) XPREP, Data Preparation and Reciprocal Space Exploration. Version 2008/2, Bruker Analytical X-Ray Systems. 2008.

(6) Barbour, L. J. X-SEED, A Graphical Interface to SHELX. University of Missouri, Columbia, U.S.A, 1999.

(7) Sheldrick, G. M. A Short History of SHELX. *Acta Crystallogr. Sect. A Found. Crystallogr.* **2008**, *64* (1), 112–122.

(8) Chemistry Software Solutions, Mestrelab Research, S.L. MestReNova, Version: 6.0.2-5475. (Copyright, 2009).

(9) Soft Imaging System GmbH, Digital Solutions for Imaging and Microscopy, Version 3.1 for Windows (Copyright, 1987 – 2000).

(10) Universal Analysis 2000 (TA Instruments-Waters LLC), Version 4.5A for Windows 2000/XP/Vista (Copyright, 1998 – 2007).

(11) TA Instruments-Waters LLC. 159 Lukens Drive, New Castle, DE19720 2020.

(12) OpenLab CDS ChemStation Edition for LC & LC/MS Systems. Agilent Technologies. Version A.01.05. (Copyright 2001-2013).

Chapter 3

The supramolecular derivatisation of the pyrido[1,2-a]benzimidazole derivative series

3.1) Literature review

Three newly developed pyrido[1,2-a]benzimidazole derivatives display therapeutic activity towards schistosomiasis (bilharzia); however, their primary disadvantage is that they are extremely insoluble in aqueous media. These compounds include (E)-1-((5,6-dimethoxypyrimidin-4-yl)imino)-3-(trifluoromethyl)-1,5-dihydrobenzo[4,5]imidazo[1,2-a] pyridine-4-carbonitrile, (Z)-1-((4-methylthiazol-2(3H)-ylidene)amino)-3-(trifluoromethyl) benzo[4,5]imidazo[1,2-a]pyridine-4-carbonitrile and (E)-1-(pyrazine-2-ylimino)-3-(trifluoromethyl)-1,5-dihydrobenzo[4,5]imidazo[1,2-a]pyridine-4-carbonitrile (Figure 3.1.1). Hereafter, these three compounds will be referred to by their internal code names, *viz.* GMP-23, GMP-31 and GMP-58 respectively and their aqueous solubility data are provided in Table 3.1.1.

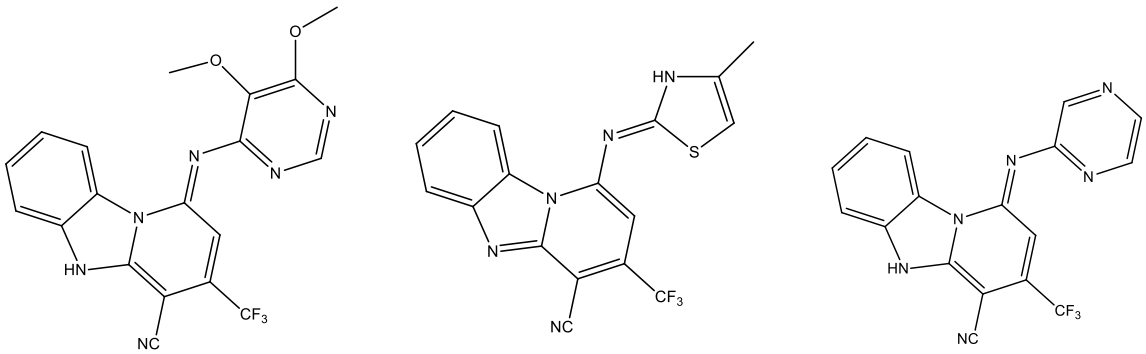


Figure 3.1.1: The molecular structures of a selected tautomer of GMP-23 (left), GMP-31 (centre) and GMP-58 (right).

Table 3.1.1: The aqueous solubility values for the three GMP compounds.

	Active compound	Aqueous solubility value (μM)
1	GMP-23	80 (at 23 ^{o}C)
2	GMP-31	5 – 20 (at 23 ^{o}C)
3	GMP-58	5 – 20 (at 23 ^{o}C)

The initial aim of this investigation was to characterise these three compounds using PXRD, SCXRD and thermal techniques (including TGA, DSC and HSM) and then assess their potential for supramolecular derivatisation with the intention of improving their respective aqueous solubility values to render them more favourable for eventual formulation. The ^{1}H NMR spectra of GMP-23, GMP-31 and GMP-58 were previously recorded in the laboratory in which they were synthesized. Scanned copies of these spectra have been placed in the Appendix under section 2.1, pp. 3 – 4 for reference purposes. The derivatisation methods that were attempted in this study included CD inclusion, co-crystallization, and finally a method that involved adding the active compounds to pre-selected molten coformers.

3.2) Initial characterisation of GMP-23, GMP-31 and GMP-58

In order to gain a comprehensive understanding of the structural features of the compounds in their solid state, SCXRD is one of the primary techniques that can provide such information. Thus, extensive experiments were conducted which involved recrystallizing the three GMP compounds in various solvents in an attempt to grow single crystals for SCXRD analysis. Four unique crystal structures were obtained from all the experiments conducted and these included a DMF solvate of GMP-23, a DMF solvate of GMP-31, a DMSO solvate of GMP-58 and the crystal structure of unsolvated GMP-58 (which could be recrystallized from either THF or DMF). These crystal structures will be described in detail in their respective sections below. In addition, during these recrystallization experiments, either a polymorph or a different tautomeric form of GMP-23, was also discovered, as described in detail later in this section. Tables 3.1.2, 3.1.3 and 3.1.4 provide the results for the various recrystallization experiments for the three GMP compounds. Approximately 2 mg of compound was used for each experiment. The shaded rows highlight the experiments that produced single crystals of adequate quality for SCXRD analysis.

Table 3.1.2: The recrystallization experiments for GMP-23.

Solvent	**Solvent volume (cm^3)**	**Temperature of dissolution (^oC)**	**Crystallization outcome**
Diethyl ether	5.0	25	No dissolution of sample.
Acetone	5.0	25	Extremely fine, yellow fibres.
EtOH	3.0	60	Extremely fine, yellow fibres.
Acetonitrile	3.0	60	Extremely fine, yellow fibres.
Ethyl acetate	4.0	25	Extremely fine, yellow fibres on the sides of vial.
DMSO	0.5	85	Clusters of extremely fine and long yellow needle fibres.
DMF	0.5	85	Large, light-yellow, irregularly shaped blocks growing as a conglomerate on a hair.
1,4 dioxane	1.0	85	Extremely long and fine yellow needle clusters.
Toluene	2.5	85	Extremely fine needles that crystallized in a conglomerate.
Cyrene	0.5	85	No precipitate after one year.
THF	0.5	60	Extremely fine, yellow crystal conglomerates.
EtOH:water	4.0	80	Extremely fine, yellow needle fibres that are thickly interwoven.
Water:THF	4.0	60	Long, yellow, thin needles.

Table 3.1.3: The recrystallization experiments for GMP-31.

Solvent	**Solvent volume (cm^3)**	**Temperature of dissolution (^oC)**	**Crystallization outcome**
Diethyl ether	5.0	25	No dissolution of sample.
Acetone	5.0	25	Extremely fine conglomerates of dark orange crystallites.
EtOH	3.0	60	Extremely fine conglomerates of dark orange crystallites.
Acetonitrile	3.0	60	Extremely fine conglomerates of dark orange crystallites.
Ethyl acetate	4.0	25	Extremely fine conglomerates of dark orange crystallites, located particularly on the sides of the vial.
DMSO	0.5	85	Initially, dark orange conglomerates of extremely fine crystallites resulted. A week later moderately sized, very light orange needles crystallized.
DMF	0.5	85	Dark orange conglomerates of extremely small crystal clusters along with significantly larger single crystals.
1,4 dioxane	1 .0	85	Dark orange conglomerates of very fine crystallites along with radial crystallizations of slightly larger needle clusters.
Toluene	5.0	85	No dissolution of sample.
Cyrene	0.5	85	No precipitate after one year.
THF	0.5	60	Clumps of extremely long and fine, hair-like, light orange crystals.
EtOH:water	4.0	80	Small very dark orange crystal clusters along with very dark orange dendritic crystals.
Water:THF	4.0	60	Dark orange needles with an abundance of superficial satellite crystallites. Satellite crystals appeared later presumably with loss of solvent.

Table 3.1.4: The recrystallization experiments for GMP-58.

Solvent	Solvent volume (cm^3)	Temperature of dissolution (^oC)	Crystallization outcome
Diethyl ether	5.0	25	No dissolution of sample.
Acetone	5.0	25	No dissolution of sample.
EtOH	5.0	60	No dissolution of sample.
Acetonitrile	5.0	60	No dissolution of sample.
Ethyl acetate	5.0	25	No dissolution of sample.
DMSO	0.5	85	Relatively large, light yellow-orange single needles (prepared by slow cooling).
DMF	0.5	85	Fine, long, light yellow single needles.
1,4 dioxane	1.0	85	Extremely fine and small needles that crystallize individually and in conglomerates at the bottom of the vial. Colour: yellow-orange.
Toluene	5.0	85	No dissolution of sample.
Cyrene	2.0	85	Very fine, yellow needles that crystallized in radial clusters in the shape of bow-ties and stars.
THF	1.0	60	Thin, yellow, single needles of medium thickness.
EtOH:water	4.0	80	No dissolution of sample.
Water:THF	4.0	60	Extremely long and very thin amber needles which had a tendency to crystallize with U-shaped morphology.

3.2.1) Initial characterisation results for GMP-23

3.2.1.1) Experimental powder X-ray diffraction (PXRD) characterisation of GMP-23

Figure 3.1.2 displays the experimental PXRD pattern of GMP-23 which was intended to be used as a reference to compare with the PXRD patterns of possible products that might ensue during the supramolecular derivatisation experiments involving GMP-23. In addition, further experimentation was performed to assess the result of dry grinding GMP-23 with a mortar and pestle for 15 minutes. The resulting pattern indicated that GMP-23 becomes amorphous with grinding, as there are no definitive peaks to indicate crystallinity throughout the angular range examined (Figure 3.1.2).

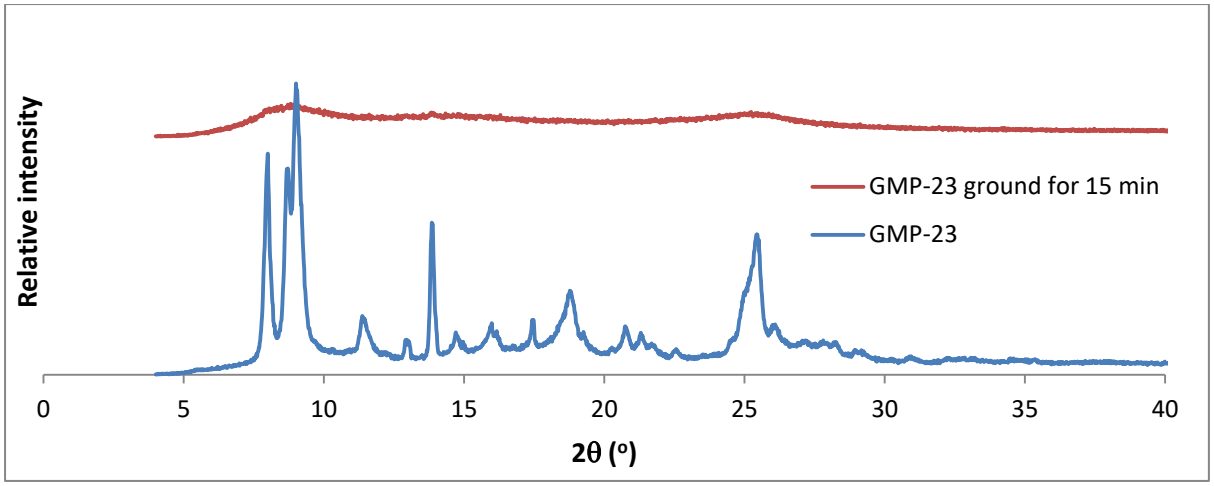


Figure 3.1.2: The PXRD patterns of GMP-23 before and after grinding for 15 minutes.

3.2.1.2) Hot stage microscopy (HSM) analysis of GMP-23

The HSM analysis displayed the thermal progression of GMP-23 at a heating rate of 10 $K.min^{-1}$ (Figure 3.1.3). Image A displays the appearance of GMP-23 prior to heating. At 78.6 ^{o}C the sample began to darken incrementally, which can be attributed to a very mild initial decomposition (image B). The very slow and steady darkening of the sample continued, as observed at 160.1 ^{o}C in image C, until the following event took place, namely the onset of a very slow melt at 194.6 ^{o}C (image D). As the melting rate increased, the darkening of the sample also increased (image E at 235.1 ^{o}C) until the sample was fully melted at 266.0 ^{o}C (image F). The onset of decomposition occurred thereafter, at 272.1 ^{o}C (image G).

Figure 3.1.3: A series of micrographs for the HSM analysis of GMP-23.



A: Initial temperature (26.4 °C).



B: Hardly discernible darkening of colour (78.6 °C).



C: Continuation of darkening of colour (160.1 °C).



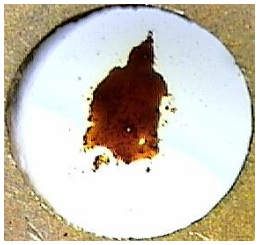
D: Onset of very slow melt (194.6 °C).



E: Melt suddenly becoming rapid (235.1 °C).



F: Fully melted (266.0 °C).



G: Onset of decomposition (272.1 °C).

3.2.1.3) Thermal gravimetric analysis (TGA) of GMP-23

The TGA analysis of GMP-23 (n=2) displayed two events, which included a minimal dehydration of the sample, as well as a decomposition at higher temperatures (Figure 3.1.4). This initial mass loss amounted to 0.7 ± 0.3% and was only noticed as a result of the fluctuations in the dTGA curve, which occurred between 19.0 ± 1.6 °C and 84.3 ± 0.9 °C. This mass loss can be attributed to the loss of water, as it appeared that the sample was slightly hygroscopic. When the original sample was produced it had been confirmed using ^{1}H NMR spectroscopy that there was no residual solvent remaining in the sample from the final recrystallization. Furthermore, the ^{1}H NMR spectrum displayed no solvent peaks other than the expected water peak at 3.33 ppm (due to the hygroscopic solvent DMSO-d_6) and the characteristic DMSO-d_6 solvent peak at 2.50 ppm. Consequently, the only possible substance to which the mass loss can be attributed, is water, and thus the sample was assumed to be slightly hygroscopic. Thereafter, GMP-23 remained thermally stable, as both the TGA and

dTGA curves displayed no thermal activity, until 222.1 ± 2.7 °C, when the main decomposition occurred.

The fact that the TGA and dTGA curves display almost no mass loss between the end of the dehydration and the onset of the decomposition confirms that the gradual darkening of the sample, as displayed in the HSM analysis, is a negligible level of decomposition. The negligible mass loss that occurred between the end of the dehydration (84.3 ± 0.9 °C) and the onset of decomposition (222.1 ± 2.7 °C) is 0.4 ± 0.1%. Consequently, it can be concluded that two types of decomposition occurred, namely an initial negligible amount over a broad temperature range, and then a significant main decomposition. Thus, despite the mild colour change during heating early on in the HSM analysis, it can still be claimed that the sample is thermally stable overall until the main decomposition.

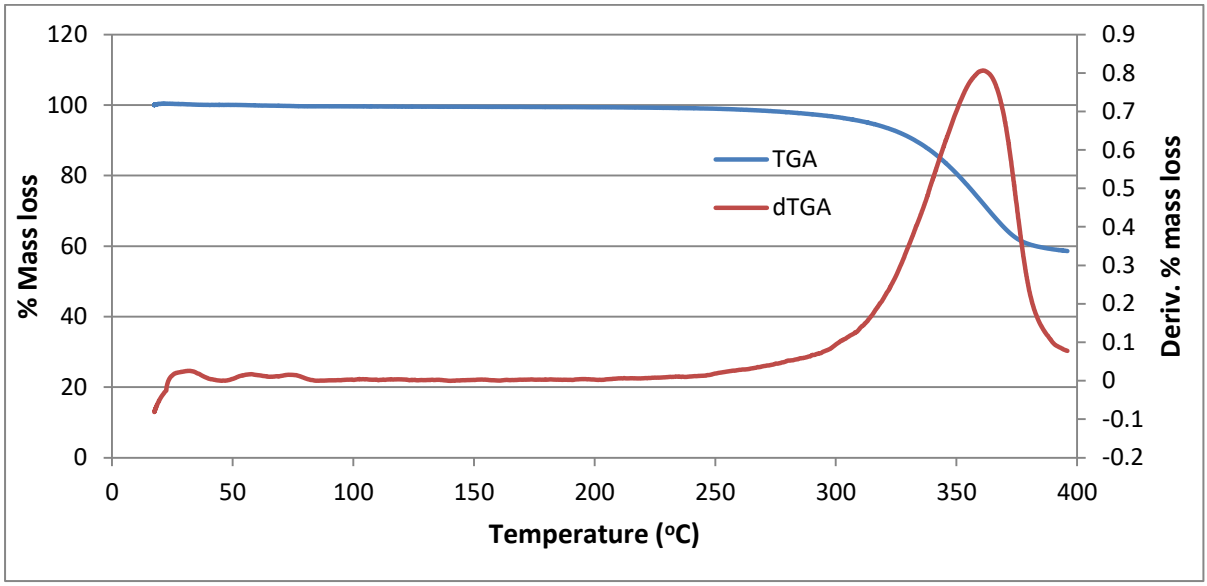


Figure 3.1.4: Representative TGA and dTGA curves for GMP-23.

3.2.1.4) Differential scanning calorimetry (DSC) analysis of GMP-23

The DSC curve of GMP-23 (n=2) displays one main endothermic event, namely the melt of the sample, along with minor exothermic and endothermic events throughout the experimental temperature range (Figure 3.1.5). No water loss was observed in the DSC

analysis owing to the fact that its presence was negligible, as seen in the overlaid TGA curve. The small endothermic and exothermic events that have peak temperatures of 85.3 ± 1.9 °C and 121.4 ± 0.1 °C respectively could be attributed to the very small amount of minimal decomposition that took place prior to the melt and the main decomposition event. In addition, the small exothermic peak at 215.2 ± 0.1 °C could be attributed to the slow and incremental decomposition that continued to occur until the melt. However, it could also signify a phase transition prior to the melt. Variable temperature PXRD would be required to confirm this, but owing to the fact that an extremely limited sample was available, it was not possible to perform this experiment. The onset of the melt occurred at 241.0 ± 0.1 °C with a peak temperature of 246.8 ± 0.1 °C and this event took place prior to simultaneous decomposition. The experiment was stopped at the start of the decomposition to prevent contamination of the DSC instrument cell.

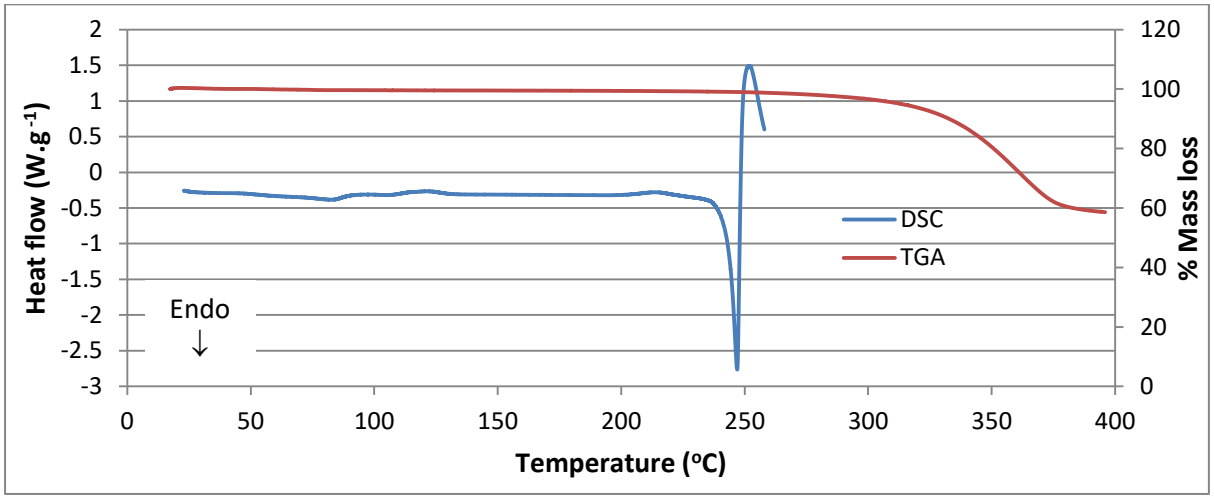


Figure 3.1.5: A representative DSC curve of GMP-23, with the respective TGA curve as a reference.

3.2.1.5) Single-crystal X-ray diffraction (SCXRD) analysis of the GMP23·DMF solvate

Data-collection and space group determination

Despite multiple failed attempts to crystallize an unsolvated form of GMP-23, the DMF solvate which was successfully isolated nevertheless provided insight into the type of hydrogen bonding and packing arrangement that can be expected to occur for GMP-23 and its derivatised analogues. The morphology of the GMP23·DMF solvate is depicted in Figure 3.1.6. This phase crystallized in the form of yellow, translucent and slightly irregular rectangular blocks. The intensity data were collected at 173(2) K since the crystallinity degraded at lower temperatures. The Laue symmetry was determined to be $\bar{1}$, indicating that the solvate crystallized in the triclinic crystal system. The only space groups in the triclinic crystal system are *P*1 and *P* $\bar{1}$, and since the value of $|E^2-1|$ was 0.993, indicating a centre of inversion, the space group *P* $\bar{1}$ was assigned.



Figure 3.1.6: The crystalline morphology of GMP23·DMF.

Structure solution and refinement

The crystal structure solution was achieved using SHELXT-97.[1] The electron density peaks of all the non-hydrogen atoms of the GMP-23 molecule and the DMF molecule were present

and most of the atom identities were already pre-assigned by the program. All the non-hydrogen atoms were appropriately numbered and initially refined isotropically and thereafter anisotropically. Hydrogen atoms were then placed in idealised positions according to the difference electron density ($\Delta\rho$) peak positions found in the difference Fourier map following structural refinement. These hydrogen atoms were placed using a riding model with isotropic temperature factors which ranged between 1.2 and 1.5 times the values of the U_{iso} parameters of their parent atoms.

Prior to X-ray analysis, a 1:1 host-guest stoichiometry for GMP23·DMF had been determined by ^{1}H NMR analysis, (where the 'host' refers to GMP-23 and the 'guest' refers to DMF). The results of this analysis can be viewed in the Appendix, section 2.2.1, pp. 5 – 6. This stoichiometry was further confirmed following application of the SQUEEZE procedure[2] conducted in PLATON,[3] as follows. The atoms of the DMF molecule were temporarily deleted and the difference electron density of the unit cell was indicated by the SQUEEZE procedure as corresponding to 78 electrons, which thus also indicated a 1:1 stoichiometric host-guest ratio.[a] The crystallographic data and details of the refinement for GMP23·DMF are presented in Table 3.1.5.

[a] The 78 electrons account for the guest molecule (DMF). Theoretically, the guest molecules contribute 80 electrons per unit cell, which is in excellent agreement, thus confirming the 1:1 host-guest stoichiometry determined by ^{1}H NMR.

Table 3.1.5: Crystal data and refinement parameters for GMP23·DMF.

Parameter	Value
Complex formula	$C_{19}H_{13}N_6O_2F_3 \cdot C_3H_7NO$
Formula weight ($g.mol^{-1}$)	487.45
Temperature (K)	173(2)
Wavelength (Å)	0.71073
Crystal system	Triclinic
Space group	$P\ \bar{1}$
a (Å)	7.3056(3)
b (Å)	12.7118(5)
c (Å)	13.2756(5)
α (°)	63.9425(11)
β (°)	82.9484(14)
γ (°)	83.8002(15)
Volume ($Å^3$)	1097.16(12)
Z	2
Calculated density ($g.cm^{-3}$)	1.4753
μ (mm^{-1})	0.119
F (000)	504
Crystal size (mm)	$0.14 \times 0.19 \times 0.27$
θ-Range scanned (°)	2.82 – 28.49
Index range	h:-9, 9; k:-17, 17; l:-17, 17
No. of reflections collected	59955
No. of unique reflections	5512
Data completeness (%)	99.1
Data/restraints/parameters	5512/0/320
S (Goodness-of-fit on F^2)	1.036
Final R indices R_1, wR_2, [I > 2σ(I)]	0.0371, 0.0868
R Indices, all data (R_1, wR_2)	0.0515, 0.0952
Largest diff. peak and hole ($e.Å^{-3}$)	0.36, -0.27

Molecular structure

The asymmetric unit (ASU) is displayed in Figure 3.1.7 and contains one GMP-23 molecule and one DMF molecule. No molecular disorder was evident and no constraints were required to restrain the bond lengths. The unit cell contains two ASUs that are related by a centre of inversion at ½, ½, ½, as illustrated in the unit cell diagram (Figure 3.1.8).

Calculation of the least-squares plane through the atoms of the tricyclic moiety of the GMP-23 molecule yielded atom deviations in the range -0.051(1) to 0.058(1) Å, confirming its planarity. In addition, the angle of intersection of the dimethoxypyrimidine substituent and the tricyclic moiety is 31.86(5)°.

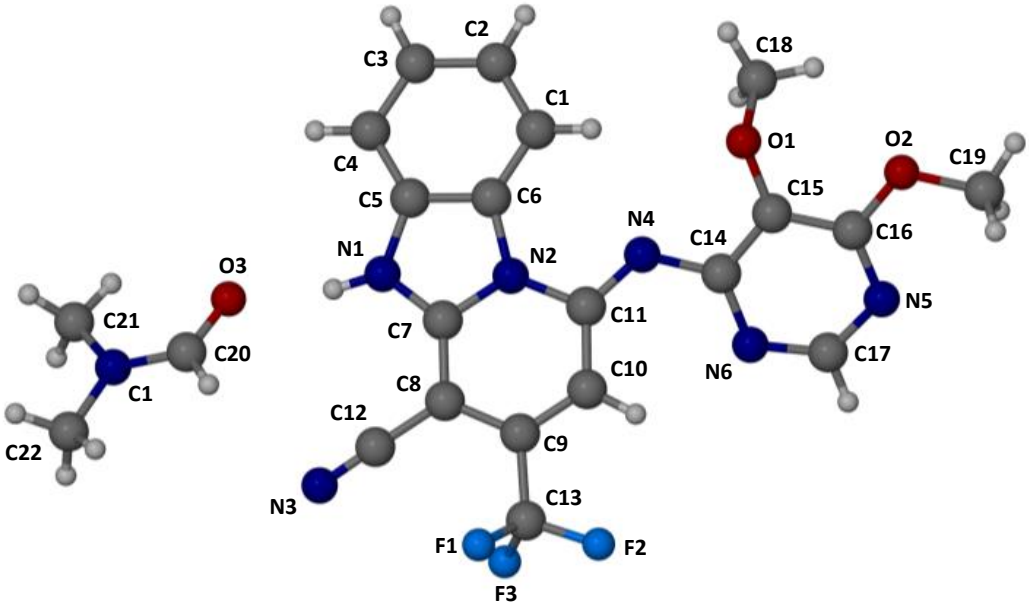


Figure 3.1.7: The ASU of GMP23·DMF.

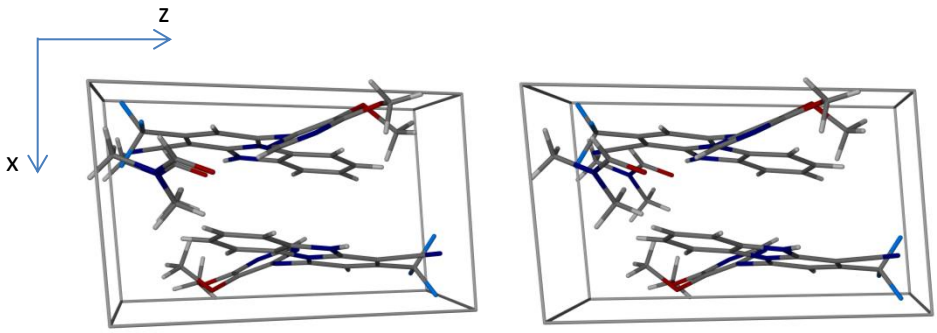


Figure 3.1.8: A perspective stereoscopic view of the unit cell of GMP23·DMF viewed down the b-axis, illustrating the two crystallographic units related by a centre of inversion at ½, ½, ½.

Hydrogen bonding

Both intramolecular and intermolecular hydrogen bonding were observed in the crystal structure and the parameters and details of these bonds can be seen in Table 3.1.6. The intramolecular hydrogen bonds include C1-H1···N4, C10-H10···N6 and C18-H18A···O2 (Figure 3.1.9).

Furthermore, the DMF molecule forms an intermolecular hydrogen bonded ring synthon [graph-set notation $R_2^2(9)$] with the substituents on the tricyclic ring system, as shown in

Figure 3.1.9. This synthon involves hydrogen bonds N1-H5···O3 and C20-H20···N3, which occur with adequate directionality, thus forming a stable hydrogen bonded ring formation to create the solvate. Lastly, C20-H20···O1' is a hydrogen bond which occurs between the ASU and a symmetry-generated molecule, effecting cohesion between consecutive layers of the crystal (Figure 3.1.10).

Table 3.1.6: The hydrogen bonding parameters for GMP23·DMF.

Interaction type	Hydrogen bond interaction	D-H (Å)	H···A (Å)	D···A (Å)	D-H···A (°)	Symmetry code
Intramolecular	C1-H1···N4	0.95	2.38	2.893(2)	113	x, y, z
Intramolecular	C10-H10···N6	0.95	2.40	2.926(2)	115	x, y, z
Intramolecular	C18-H18A···O2	0.98	2.53	3.073(2)	115	x, y, z
Intermolecular	C20-H20···N3	0.95	2.55	3.253(2)	131	x, y, z
Intermolecular	N1-H5···O3	0.88	1.86	2.718(2)	164	x, y, z
Intermolecular	C20-H20···O1	0.95	2.58	3.198(2)	123	-x, 1-y, 1-z

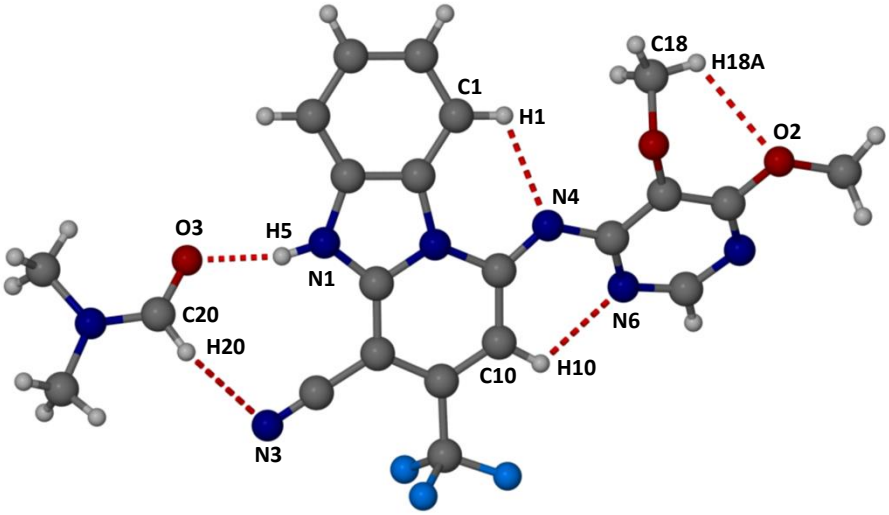


Figure 3.1.9: The intramolecular and intermolecular hydrogen bonding in the ASU.

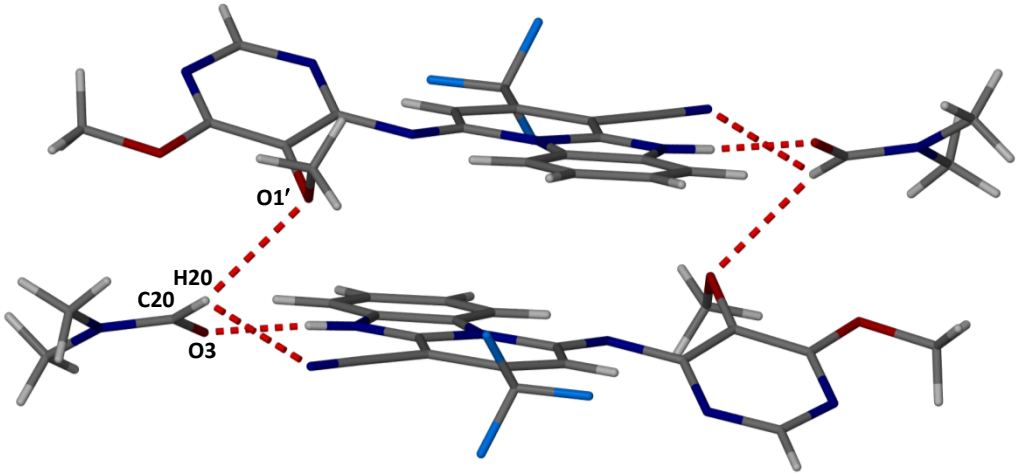


Figure 3.1.10: Host-guest H-bonds N1-H5···O3 and C20-H20···N3 and the intralayer H-bonds C20-H20···O1´.

Crystal packing

The molecules arrange themselves in brickwork-type layers with the DMF molecules fitting in between these layers (Figure 3.1.11).

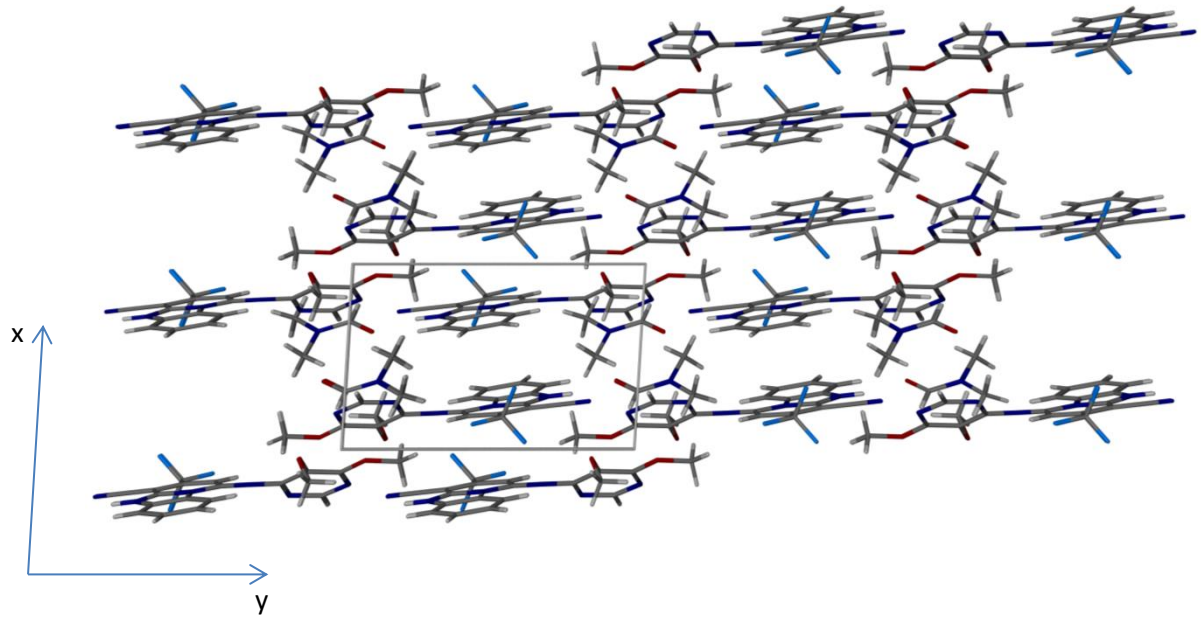


Figure 3.1.11: The brick-work packing arrangement viewed down the c-axis.

Furthermore, the successive layers of the GMP-23 molecules are not appropriately aligned with each other, and instead the molecules only align at every alternate layer. Consequently, this feature significantly reduces the extent of π-π stacking from occurring between the layers (Figure 3.1.12). Therefore, Table 3.1.7 displays the resultant π-π stacking interactions that were noted to occur between a particular ring fragment of the ASU (with reference to the ring-numbering scheme in Figure 3.1.12) and a specific ring fragment of a symmetry-generated molecule. The distances between the centres of gravity (Cg···Cg distances) of the two ring fragments, along with their respective ring slippage values are also quoted in Table 3.1.7.

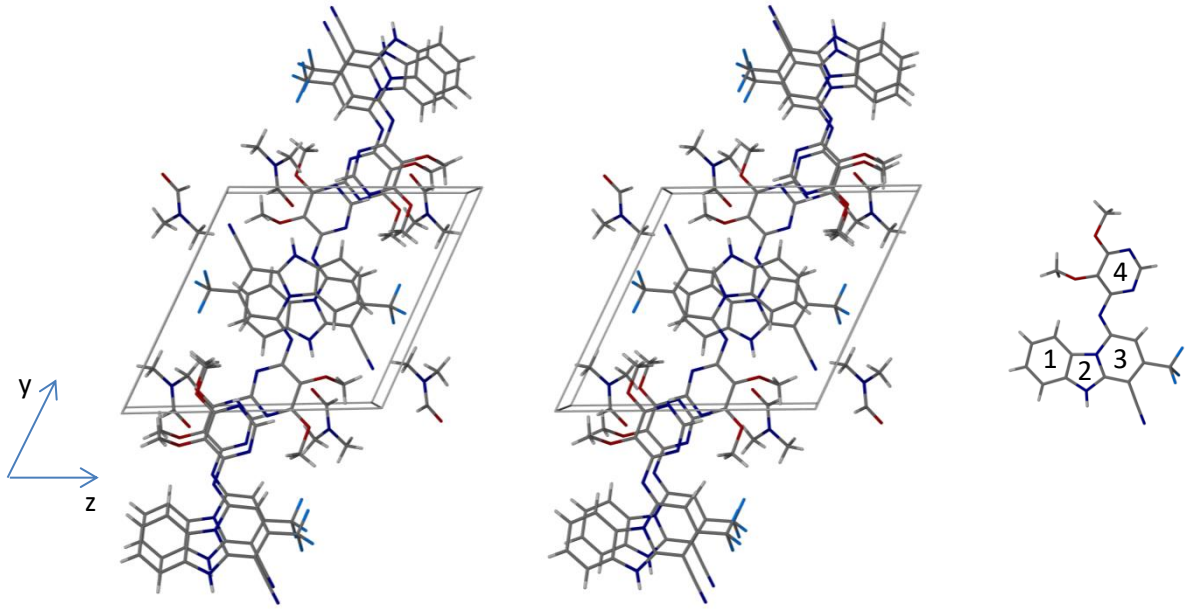


Figure 3.1.12: A stereoscopic view of the packing arrangement viewed down the a-axis displaying the alternating layered packing arrangement of the GMP-23 molecules, which significantly reduces π-π stacking from occurring between consecutive layers. The numbering scheme for the individual ring fragments of GMP-23 is supplied in the right-hand image.

Table 3.1.7: π-π stacking between specific ring fragments of the GMP-23 molecule.

Ring of the ASU	Ring of a symmetry-related molecule	Symmetry operator	Cg···Cg distance (Å)	Ring slippage (Å)
1	2	1-x, 1-y, 1-z	3.6691(8)	1.314
2	2	1-x, 1-y, 1-z	4.0291(8)	2.070
3	1	1-x, 1-y, 1-z	3.6012(7)	1.149

Calculated powder X-ray diffraction (PXRD) pattern

The calculated PXRD pattern based on the refined single-crystal X-ray structure of GMP23·DMF and the experimental PXRD pattern of GMP-23, are presented in Figure 3.1.13. It is expected that these two PXRD patterns will differ significantly in terms of both peak positions and intensities, as two different compounds are being compared. However, this does imply that the packing arrangement of GMP-23 is significantly different from that in the GMP23·DMF solvate crystal structure. Consequently, it is not possible to speculate what the packing arrangement in the crystal of GMP-23 itself might be; however, this SCXRD analysis of the DMF solvate has provided insight regarding the type of hydrogen bonding and packing arrangement that is possible when combining hydrogen bonding entities with GMP-23.

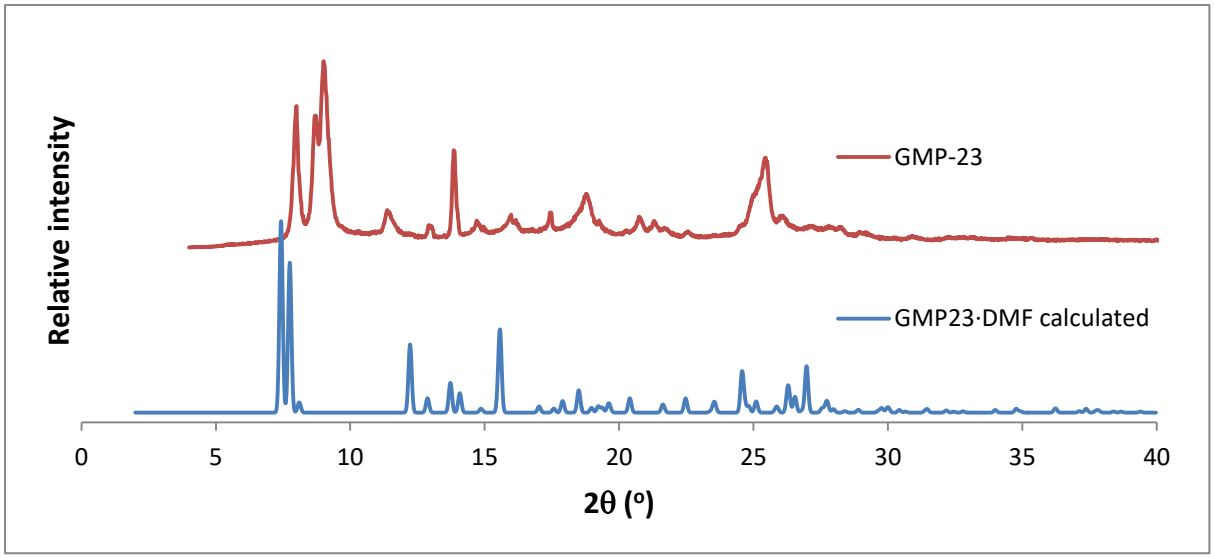


Figure 3.1.13: The calculated PXRD pattern based on the refined single-crystal X-ray structure of GMP23·DMF and the experimental PXRD pattern of GMP-23.

3.2.1) The initial characterisation results for GMP-31

3.2.2.1 Experimental powder X-ray diffraction (PXRD) characterisation of GMP-31

The experimental PXRD pattern of GMP-31 is shown in Figure 3.2.1, and as reported above for GMP-23, similar further experimentation was conducted in this case in order to assess the result after dry grinding GMP-31 for 15 minutes. The results indicated that this compound also became completely amorphous with grinding (Figure 3.2.1).

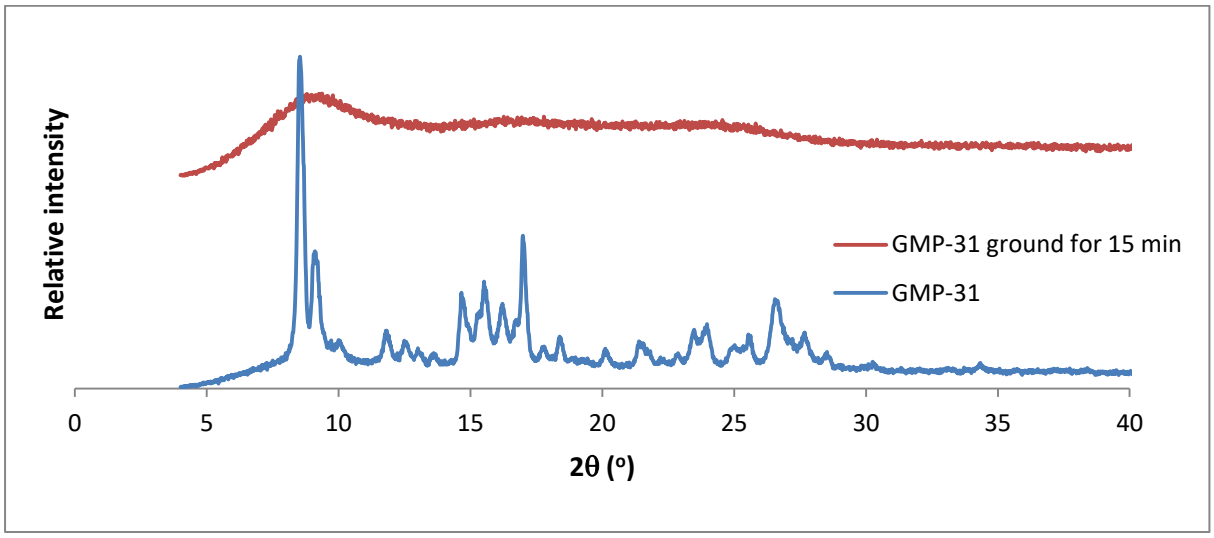


Figure 3.2.1: The PXRD patterns of GMP-31 before and after grinding for 15 minutes.

3.2.2.2) Hot stage microscopy (HSM) analysis of GMP-31

The HSM analysis of GMP-31 displayed the thermal progression of the sample over the heating range 30.6 ^{o}C – 357.8 ^{o}C at a rate of 10 K.min^{-1} (Figure 3.2.2). The initial appearance of the sample was recorded at 30.6 ^{o}C before heating commenced (image A), and at 120.1 ^{o}C the onset of a very slow decomposition commenced (image B). The slow decomposition continued beyond 171.0 ^{o}C and 198.7 ^{o}C at the same rate, yet became more pronounced (images C and D respectively). At 220.0 ^{o}C the rate of decomposition began to increase more

significantly (image E), until the onset of the melt and decomposition occurred at 265.5 ^{o}C (image F). Image G displays the onset of bubbling at 357.8 ^{o}C due to decomposition.

Figure 3.2.2: A series of micrographs for the HSM analysis of GMP-31



A: Initial temperature (30.6 ^{o}C).



B: Onset of very slow decomposition (120.1 ^{o}C).



C: Continuation of decomposition (171.0 ^{o}C).



D: Decomposition becoming more pronounced, yet still at a steady rate (198.7 ^{o}C).



E: Decomposition continuing at an increasing rate (220.0 ^{o}C).



F: Onset of decomposition melt (265.5 ^{o}C).



G: Onset of decomposition bubbles once melt has completed (357.8 ^{o}C).

3.2.2.3) Thermal gravimetric analysis (TGA) of GMP-31

The TGA curve of GMP-31 (n=2) displayed similar results to that of GMP-23 in the sense that there was an initial dehydration as a result of the compound also being slightly hygroscopic, and that the decomposition of the sample could also be identified over two stages (Figure 3.2.3). The dehydration of the sample was associated with the first mass loss which occurred between 21.7 ^{o}C and 85.4 ^{o}C and equated to 3.5 $\pm$ 1.4%. (The large standard deviation in this case signifies differences in hygroscopicity of the samples examined). One of the main differences between this TGA curve and that of GMP-23 is that the sample decomposed more readily after the end of the dehydration, which instead merged with the main decomposition event that occurred later at 225.1 $\pm$ 0.1 ^{o}C. Between the end of the

dehydration and the onset of the main decomposition (85.4 – 225.1 °C), the mass loss amounted to 1.7 ± 0.1% and consequently over this broad temperature range there was a small amount of decomposition occurring before it merged into the main decomposition event.

This result is reflected in the HSM analysis, where the sample darkened a lot more significantly earlier on at a very slow rate, and then at 220.0 °C the rate of the decomposition began to increase. As a result, this compound is not as thermally stable as GMP-23.

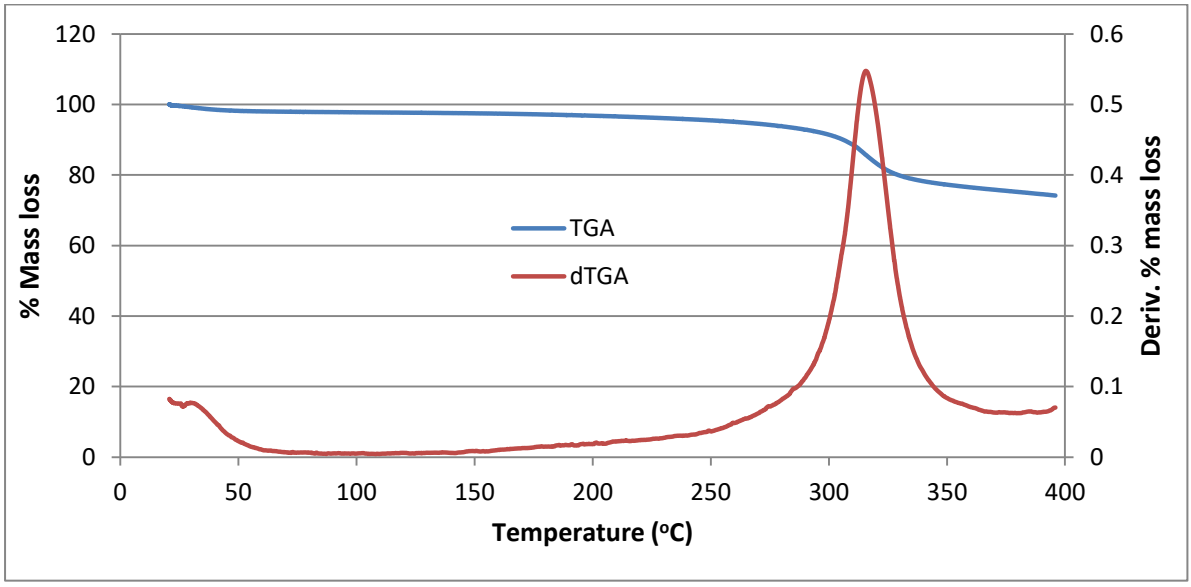


Figure 3.2.3: Representative TGA and dTGA curves for GMP-31.

3.2.2.4) Differential scanning calorimetry (DSC) analysis of GMP-31

The DSC curve of GMP-31 (n=2) displayed two endothermic events (Figure 3.2.4.). These can be attributed to the dehydration of the hygroscopic sample (peak temperature = 74.4 ± 3.2 °C), and the very broad initial decomposition of the sample (peak temperature = 216.6 ± 1.2 °C). This endothermic peak that represents the incremental initial decomposition of the sample is slightly pronounced, and thus it can be concluded that the sample was not completely thermally stable over this heating range before the main decomposition event.

These conclusions are complemented by the HSM and TGA results, both of which indicated a slight level of initial decomposition prior to the main decomposition event. The DSC experiment was terminated prior to decomposition in order to protect the cell from the resultant decomposition products of the sample.

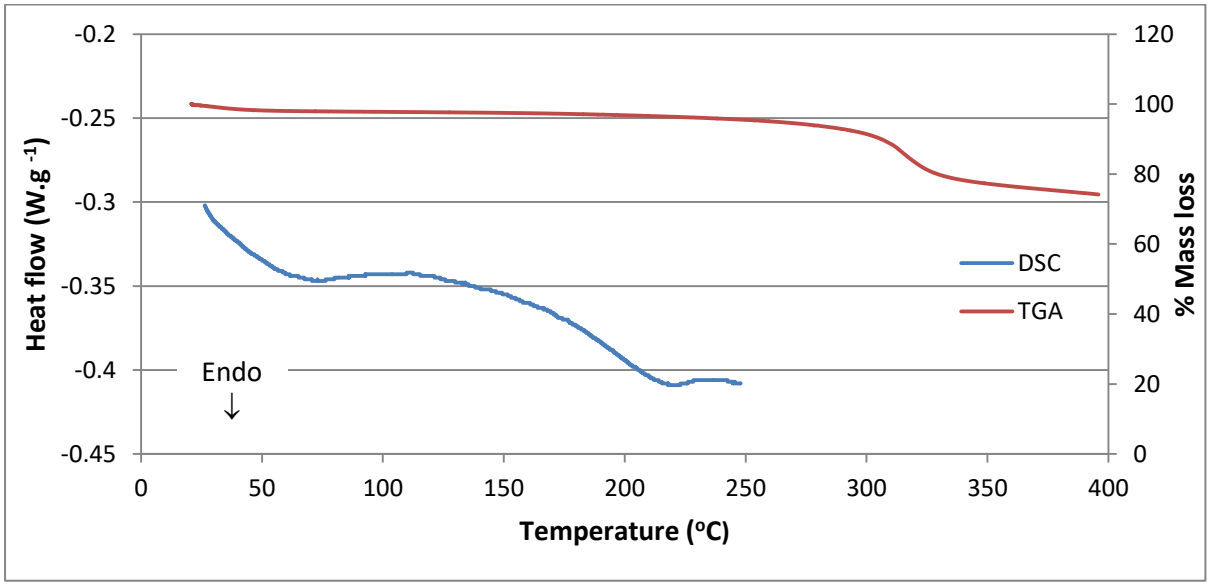


Figure 3.2.4: A representative DSC curve of GMP-31, with the respective TGA curve as a reference.

3.2.2.5) Single-crystal X-ray diffraction (SCXRD) analysis of the GMP31·DMF solvate

Morphological analysis

Although the crystal form of GMP-31 isolated for further study was solvated, the structural information obtained from the SCXRD analysis (see below) remained insightful in terms of the type of hydrogen bonding present and possible packing arrangement that can occur. Crystal preparation by the co-precipitation method presented two morphological forms as products (Figure 3.2.5). One form was an orange, translucent, rectangular-shaped crystal, which crystallized either as long, individual needles or in radial needle clusters. This was the morphological form that was used to collect the SCXRD data. The other crystal form was an extremely fine, dark orange, dendritic modification whose composition remains unknown.

Unfortunately, very little material was produced for this latter form and thus further characterisation analysis was not possible (or warranted given the scarcity of the starting material provided).

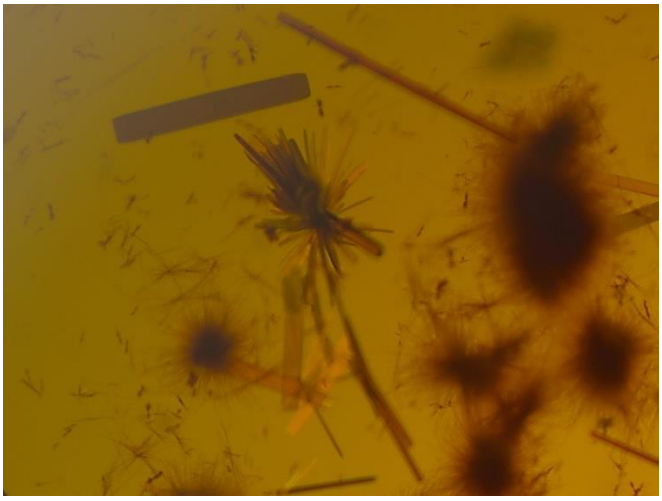


Figure 3.2.5: The different morphological forms of the product obtained when GMP-31 was recrystallized from DMF. The two forms consisted of rectangular, single crystals (either crystallising separately or as a radial cluster) and clusters of extremely fine dendritic fibres.

Data-collection and space group determination

A single, rectangular-shaped crystal was selected and the intensity data were collected at 173(2) K owing to the fact that, as with GMP23·DMF, GMP-31·DMF also degraded at temperatures below 173 K. The Laue group was *mmm* which indicated the orthorhombic system. The lattice type was determined to be primitive (condition 1 in Table 3.2.1) and from the remaining conditions limiting possible reflection, the space group *P*nma was deduced. [The alternative, non-centrosymmetric space group, *P*na2_1 was excluded as the value of $|E^2 - 1|$ for the intensity data was 0.945 (program XPREP[4]) indicating centrosymmetry].

Table 3.2.1: The conditions limiting possible reflections for the crystal of GMP31·DMF.

Number	Conditions limiting possible reflections	Deduction
1	hkl: none	Primitive lattice
2	0kl: k + l = 2n	n-Glide plane ⊥ to the a-axis
3	h0l: none	-
4	hk0: h = 2n	a-Glide plane ⊥ to the c-axis
5	[0k0: (k = 2n, redundant condition)]	-
6	[00l: (l = 2n, redundant condition)]	-
7	[h00: h = 2n, redundant condition)]	-

Structure solution and refinement

The crystal structure was solved using SHELXT-97,[1] and all the non-hydrogen atoms were assigned and initially refined isotropically and thereafter anisotropically. Following the location of hydrogen atoms in difference Fourier syntheses, they were included in idealised positions in a riding model with isotropic temperature factors ranging between 1.2 and 1.5 times the values of the U_{iso} parameters of their parent atoms.

The stoichiometry of the solvate was verified to be 1:1 with a TGA analysis of the solvated crystals, since the quantity of DMF lost during desolvation corresponded to a 1:1 host-guest ratio (GMP-31 termed as the 'host' molecule and DMF termed as the 'guest' molecule). The results of this TGA analysis can be viewed in the Appendix, section 2.2.2, p. 6. The stoichiometry was further verified by a SQUEEZE procedure[2] conducted in PLATON[3].[b] The crystal data and refinement parameters are presented in Table 3.2.2.

[b] The residual electron density in the unit cell (after the DMF molecules were omitted) corresponded to 158 electrons. Theoretically, the guest molecules contribute 160 electrons per unit cell, which is in excellent agreement, thus confirming the 1:1 host-guest stoichiometry determined by TGA.

Table 3.2.2: Crystal data and refinement parameters for the GMP31·DMF solvate.

Parameter	Value
Complex formula	$C_{17}H_{10}F_3N_5S \cdot C_3H_7NO$
Formula weight ($g.mol^{-1}$)	446.45
Temperature (K)	173(2)
Wavelength (Å)	0.71073
Crystal system	Orthorhombic
Space group	*P*nma
a (Å)	6.7262(8)
b (Å)	11.9164(12)
c (Å)	24.543(3)
α (°)	90
β (°)	90
γ (°)	90
Volume ($Å^3$)	1967.2(6)
Z	4
Calculated density ($g.cm^{-3}$)	1.507
μ (mm^{-1})	0.219
F (000)	920
Crystal size (mm)	0.09 x 0.12 x 0.21
θ-Range scanned (°)	1.90 – 28.35
Index range	h:-32, 32; k:-8, 8; l:-15, 15
No. of reflections collected	59280
No. of unique reflections	2647
Data completeness (%)	99.7
Data/restraints/parameters	2647/0/190
S (Goodness-of-fit on F^2)	1.030
Final R indices R_1, wR_2, [I > 2σ(I)]	0.0610, 0.1706
R Indices, all data (R_1, wR_2)	0.0796, 0.1880
Largest diff. peak and hole ($e.Å^{-3}$)	0.59, -0.96

Molecular structure

The asymmetric unit (ASU) of the GMP31·DMF solvate is displayed in Figure 3.2.6 and contains one GMP-31 molecule and one DMF molecule.

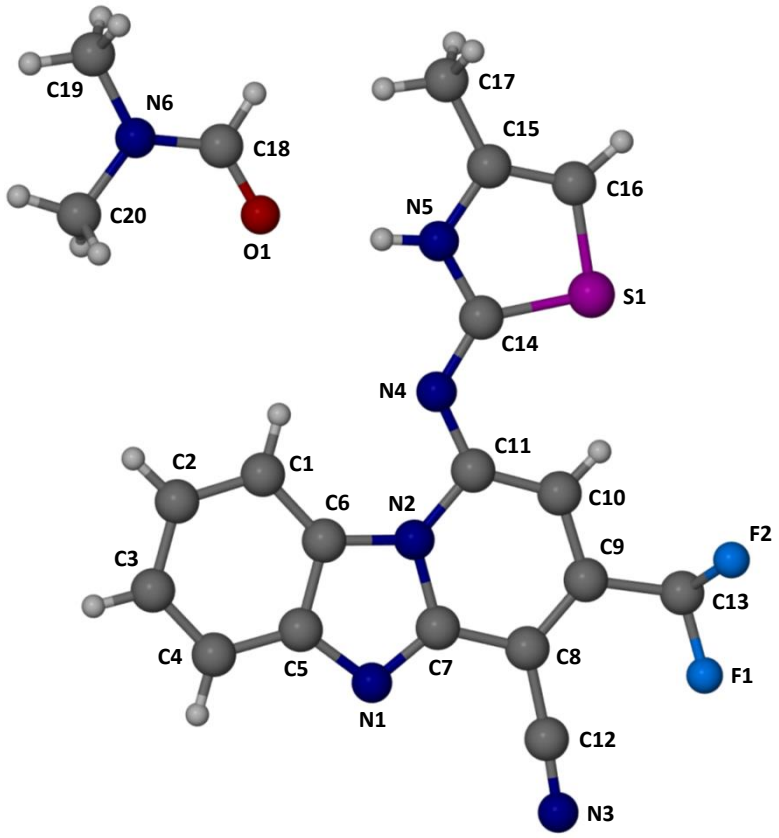


Figure 3.2.6: The ASU of GMP31·DMF.

The unit cell contains four crystallographic units that are related by an n-glide perpendicular to the a-axis and an a-glide perpendicular to the c-axis. In addition, there are mirror planes perpendicular to the b-axis positioned at 0.25 and 0.75 along the b-axis (Figure 3.2.7).

The two molecular components of the ASU (GMP-31 and DMF), are situated on the mirror plane, as shown in Figure 3.2.7, which also highlights the 'graphitic' stacking of successive molecular layers.

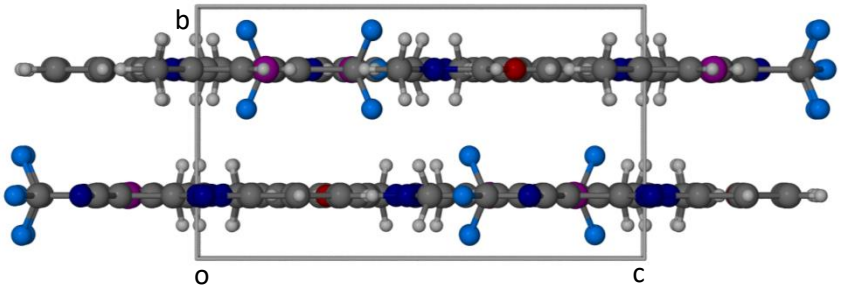


Figure 3.2.7: The unit cell of GMP31·DMF viewed down the a-axis displaying the stacking of two inversion-related layers.

Hydrogen bonding

Both intramolecular and intermolecular hydrogen bonding occur in the crystal. Two discrete intramolecular hydrogen bonds were observed, namely C1-H1···N4 and C10-H10···S1, which are responsible for retaining the planarity of the GMP-31 molecule (Figure 3.2.8). In addition, intermolecular hydrogen bonding occurs within the ASU, and with symmetry-related molecules. A single discrete classical hydrogen bond (N5-H5···O1) connects the DMF molecule to the GMP-31 molecule in the ASU. The hydrogen bonding parameters are provided in Table 3.2.3.

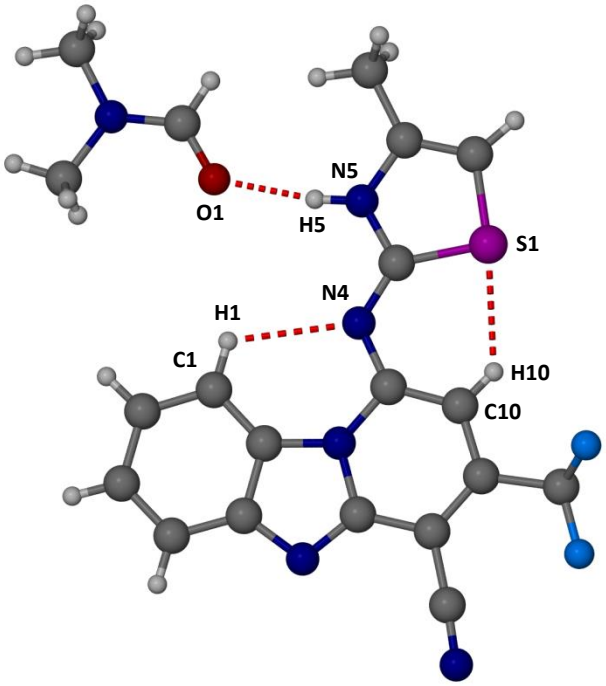


Figure 3.2.8: The intramolecular and intermolecular hydrogen bonding occurring in the ASU.

Table 3.2.3: Hydrogen bonding parameters for GMP31·DMF.

Interaction type	Hydrogen bond interaction	D-H (Å)	H···A (Å)	D···A (Å)	D-H···A (°)	Symmetry code
Intramolecular	C1-H1···N4	0.95	2.46	2.962(4)	113	x, y, z
Intramolecular	C10-H10···S1	0.95	2.37	3.082(3)	132	x, y, z
Intermolecular	N5-H5···O1	0.88	1.93	2.799(3)	171	x, y, z
Intermolecular	C16-H16···N3	0.95	2.33	3.275(5)	176	1/2+x, 1/2-y, 3/2-z
Intermolecular	C20-H20B···F2	0.98	2.30	3.253(3)	163	1-x, -1/2+y, 1-z
Intermolecular	C20-H20C···F2	0.98	2.30	3.253(3)	163	1-x, 1-y, 1-z

Furthermore, intermolecular hydrogen bonding takes place between consecutive planar molecular layers (Figure 3.2.9). Specifically, two of the methyl hydrogen atoms on the DMF molecule in the ASU were observed to form discrete hydrogen bonds to the fluorine atoms located in the planes above and below the DMF molecule. Lastly, atom C16 on the thiazole substituent forms a C-H···N hydrogen bond with N3 on the cyano substituent of a symmetry-generated molecule in the same plane. These intramolecular and intermolecular hydrogen bonds maintain the planar molecular arrangement, as well as providing crystal cohesion.

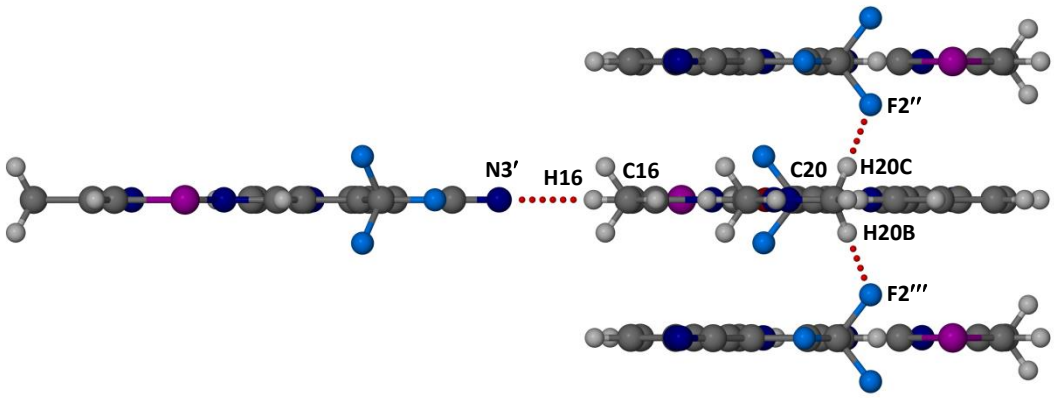


Figure 3.2.9: Intermolecular hydrogen bonding occurring between symmetry-generated GMP-31 molecules.

Crystal packing

Given that the solvate GMP31·DMF may also be regarded as an inclusion compound, with GMP31 as the 'host' and DMF as the 'guest', the description of the packing follows using these terms. The host and guest molecules pack in continuous, planar layers also forming a brickwork-type of layering with sequence AB, AB…, as observed in Figure 3.2.10.

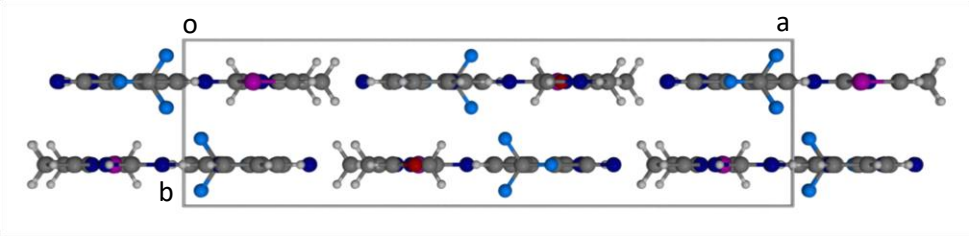


Figure 3.2.10: The planar brick-work type packing arrangement of GMP31·DMF viewed down the c-axis.

Figure 3.2.11 illustrates the view down the b-axis of the unit cell where it is possible to observe the two orientations of the GMP-31 molecules in the two consecutive layers shown. Consequently, with reference to the ring-numbering scheme in Figure 3.2.11, the resultant π-π stacking parameters are listed in Table 3.2.4.

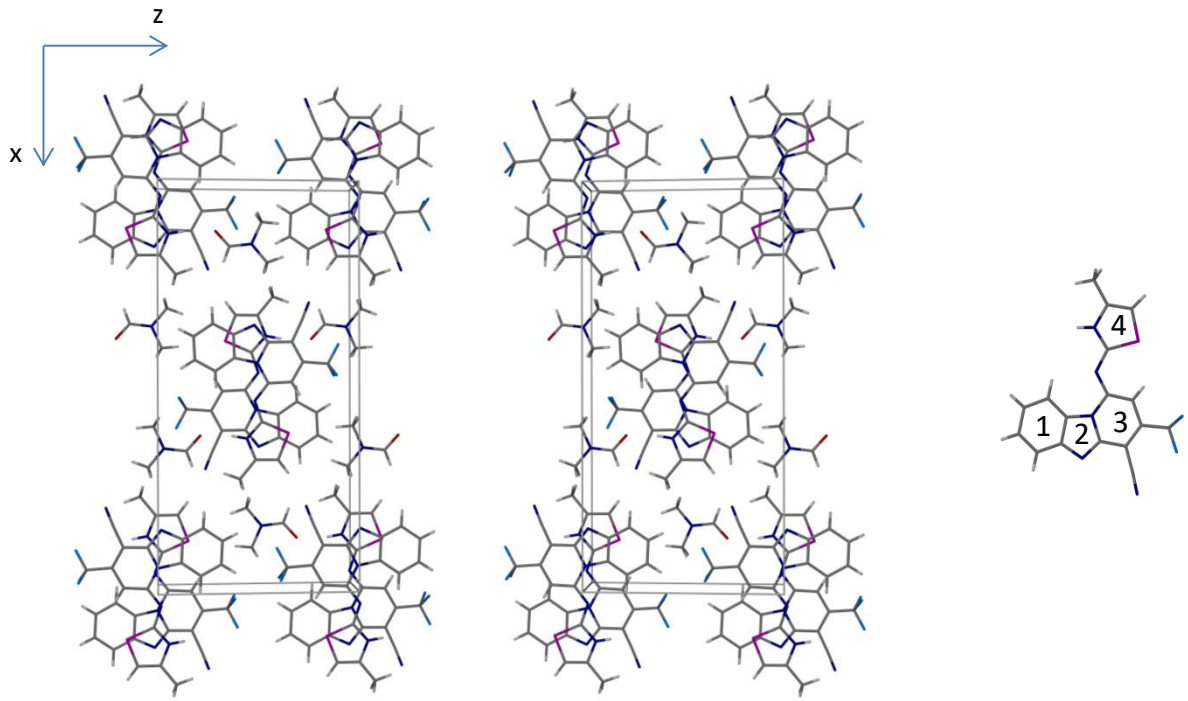


Figure 3.2.11: A stereoscopic view of the packing arrangement viewed down the b-axis displaying the alternating layered packing arrangement of the GMP-31 molecules, which significantly reduces π-π stacking from occurring between consecutive layers. The numbering scheme for the individual ring fragments of GMP-31 is supplied in the right-hand image.

Table 3.2.4: π-π stacking between specific ring fragments of the GMP-31 molecules.

Ring of the ASU	Ring of a symmetry-related molecule	Symmetry operator	Cg···Cg distance (Å)	Ring slippage (Å)
2	4	1-x, 1-y, 1-z	3.4652(6)	0.835
4	1	1-x, 1-y, 1-z	4.094(1)	2.334

Calculated powder X-ray diffraction (PXRD) pattern

Figure 3.2.12 shows the PXRD pattern that was calculated from the refined single-crystal X-ray structure of GMP31·DMF and the experimental PXRD pattern of GMP-31. Since they are two different compounds that are obviously not isostructural, it is not possible to speculate what the packing arrangement of the crystal of unsolvated GMP-31 might be. Nevertheless, the SCXRD analysis of GMP31·DMF provided valuable insight regarding the possible hydrogen bonding and packing arrangement that can occur when co-crystallizing GMP-31 with a partner molecule having H-bonding capacity.

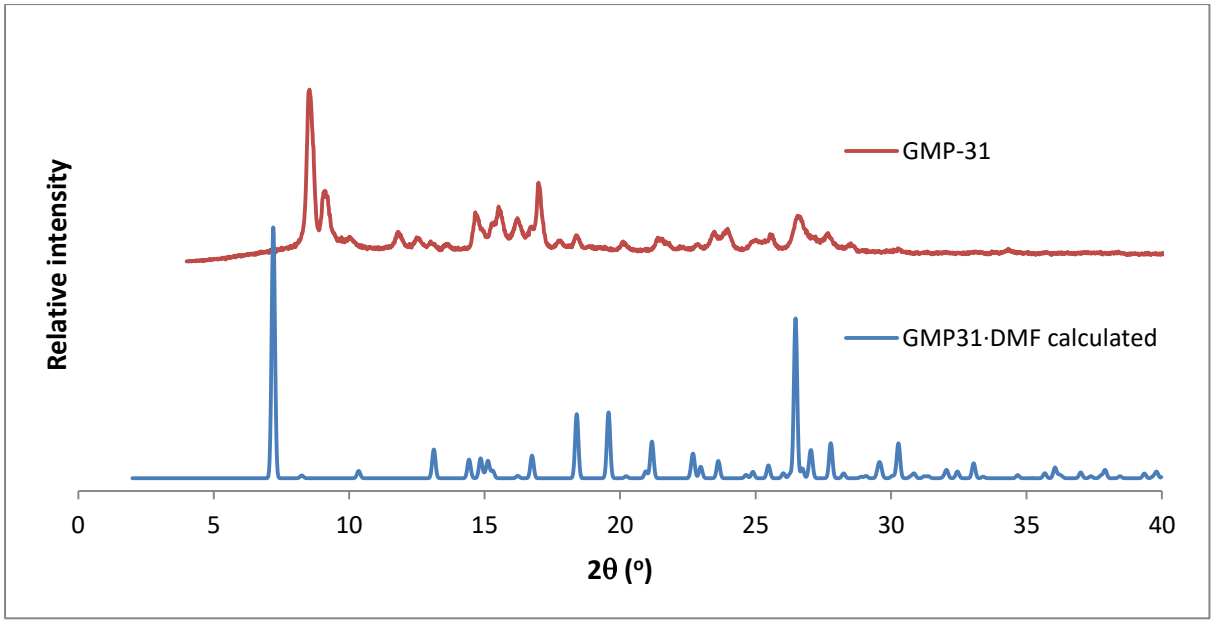


Figure 3.2.12: The PXRD pattern calculated from the single-crystal X-ray structure of GMP31·DMF and the experimental PXRD pattern of GMP-31.

3.2.3) The initial characterisation results for GMP-58

3.2.3.1) Experimental powder X-ray diffraction (PXRD) characterisation of GMP-58

Figure 3.3.1 displays the experimental PXRD pattern of GMP-58 along with that of the same material after dry grinding GMP-58 for 15 minutes. The results indicate that the crystallinity of GMP-58 is completely lost with grinding, as there are no distinct peaks throughout the angular range in the pattern of the ground product (Figure 3.3.1).

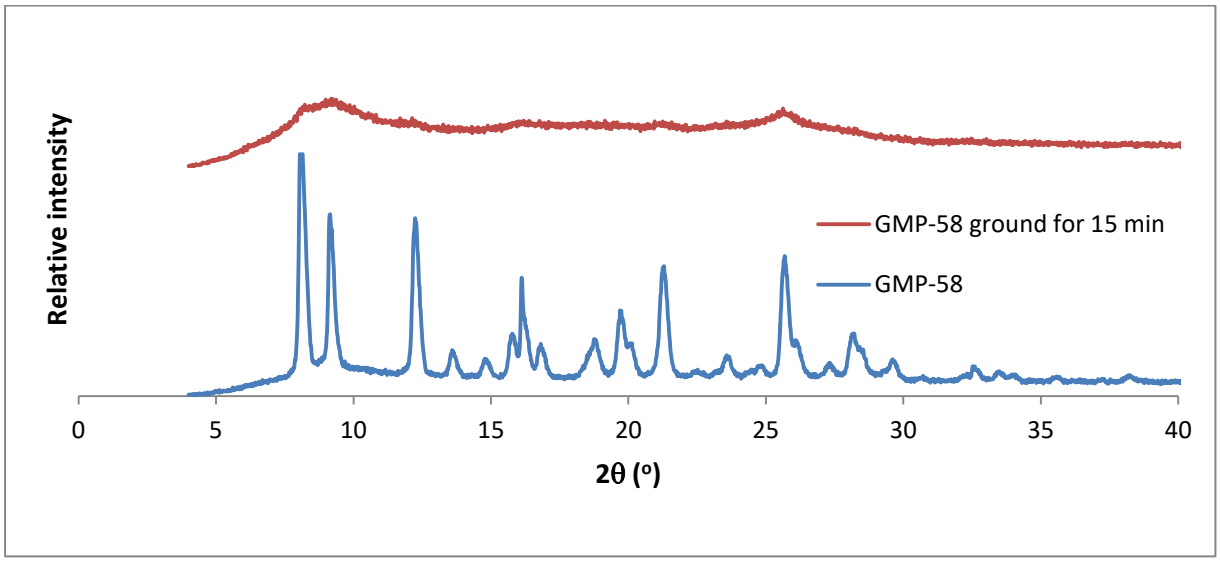


Figure 3.3.1: The PXRD patterns of GMP-58 before and after grinding for 15 minutes.

3.2.3.2) Hot stage microscopy (HSM) analysis of GMP-58

The HSM analysis for GMP-58 (Figure 3.3.2) displays the initial appearance of the compound at 30.9 ^{o}C before heating (image A). The first observed thermal event occurred at 150.2 ^{o}C where a very slow darkening of the compound took place (image B). This incremental darkening of the compound continued beyond 250.5 ^{o}C (image C), until a rapid decomposition commenced at 300.0 ^{o}C accompanied by a slow onset of a melt (image D). Image E displays the extent of the decomposition at 350.0 ^{o}C.

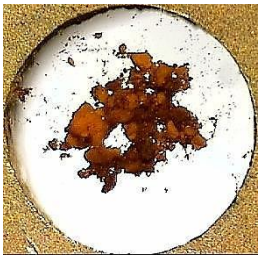
Figure 3.3.2: A series of micrographs for the HSM analysis of GMP-58.



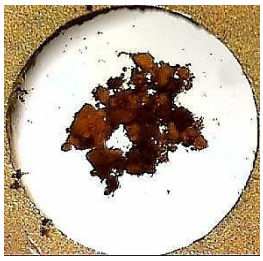
A: Initial temperature (30.9 °C).



B: Onset of a mild decomposition (150.2 °C).



C: Continuation of the incremental darkening of the compound (250.5 °C).



D: The start of a rapid decomposition and simultaneous melt (300.0 °C).



E: Very advanced decomposition (350.0 °C).

3.2.3.3) Thermal gravimetric analysis (TGA) of GMP-58

The TGA curve of GMP-58 (n=2) displayed the same thermal trends as those observed with GMP-23 and GMP-31 (Figure 3.3.3). This compound was the most hygroscopic of the three, as it displayed a mass loss of 4.8 ± 0.7% pertaining to the loss of water between the temperatures 20.9 ± 2.7 °C and 112.3 ± 0.9 °C. In addition, between 112.3 ± 0.9 °C and 251.4 ± 1.3 °C a percentage mass loss of 1.1 ± 0.1% occurred, representing a very slow and small decomposition over a broad temperature range. Since the percentage mass loss from this broad decomposition is relatively low, the compound can therefore be considered to be stable overall while being heated, until the onset of the main decomposition which occurred at 251.4 ± 1.3 °C.

The trends in the TGA results were reflected in the HSM analysis, where the compound darkened mildly (representing the slow, broad decomposition) over a wide temperature

range, until the temperature reached the point where a more rapid decomposition (and simultaneous melt) occurred at 300.0 ^{o}C.

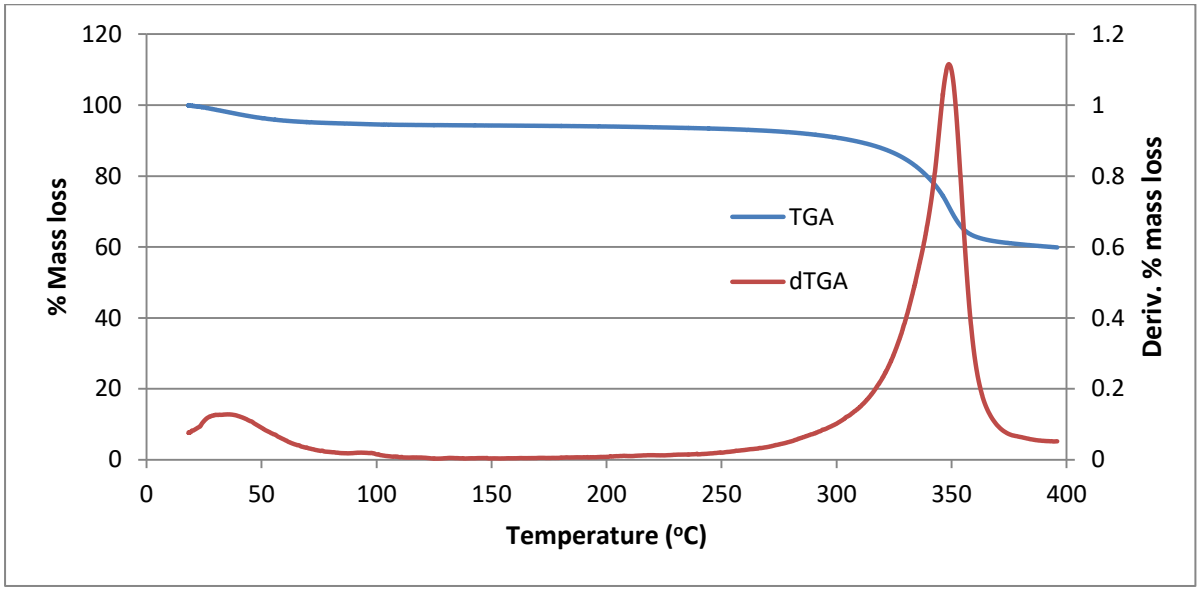


Figure 3.3.3: Representative TGA and dTGA curves for GMP-58.

3.2.3.4) Differential scanning calorimetry (DSC) analysis of GMP-58

The DSC curve of GMP-58 (n=2) displays only the dehydration of the hygroscopic compound as a single endothermic peak with a peak temperature of 98.5 $\pm$ 1.4 ^{o}C (Figure 3.3.4). It is very evident that this compound is the most hygroscopic of the GMP series, since it also has the largest dehydration peak in comparison with the other two GMP compounds. The DSC curve did not display any observable small exothermic or endothermic peaks that might have resulted from the broad and incremental initial decomposition that was revealed by the HSM and TGA experiments. Nonetheless, the broad and incremental decomposition displayed in the overlaid TGA curve is very negligible and thus it is still possible to confirm that the compound does have thermal stability before the main decomposition event. The DSC experiment was terminated at the start of the main decomposition in order to protect the cell of the instrument.

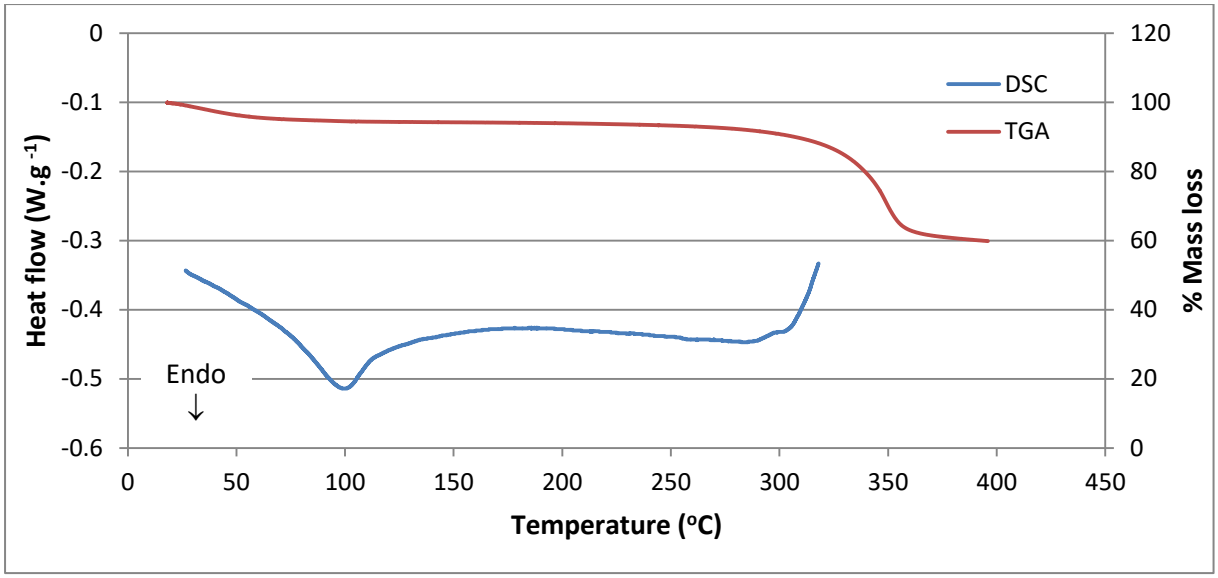


Figure 3.3.4: A representative DSC curve for GMP-58 (n=2) along with the respective TGA curve as a reference.

3.2.3.5) Single-crystal X-ray diffraction (SCXRD) analysis of GMP-58

Crystal morphology

The recrystallization experiments indicated that GMP-58 could be crystallized in a non-solvated form from either DMF or THF, and the single crystal that was selected for this SCXRD analysis was recrystallized from THF. The morphology of GMP-58 in the mother liquor is illustrated in Figure 3.3.5 below. It had a tendency to crystallize in the form of long, yellow needles.



Figure 3.3.5: The crystalline morphology of GMP-58 recrystallized from THF.

Data-collection and space group determination

The intensity data were obtained at 100(2) K from a single needle-shaped crystal that did not require cutting. The crystal system was found to be monoclinic, as the Laue symmetry was 2/*m*. A primitive lattice type was determined and along with the remaining conditions limiting possible reflections, the space group $P2_1/c$ was established (Table 3.3.1). This result was further confirmed by the program XPREP.[4]

Table 3.3.1: The conditions limiting possible reflections for the crystal of GMP-58.

Number	Conditions limiting possible reflections	Deduction
1	hkl: none	Primitive lattice
2	h0l: l = 2n	Glide plane ⊥ to b-axis with translation *c*/2
3	0k0: k = 2n	Two-fold screw axis parallel to b-axis

Structure solution and refinement

The structure was solved using SHELXS-97,[1] and the electron density peaks of the non-hydrogen atoms were all assigned to their corresponding atoms, which were initially refined isotropically and subsequently anisotropically. Inspection of the difference Fourier map revealed all of the hydrogen atoms, which were then included in idealised positions using a riding model with isotropic temperature factors between 1.2 and 1.5 times the values of the U_{iso} parameters of their parent atoms. The crystallographic data and details of the refinement are presented in Table 3.3.2.

Table 3.3.2: Crystal data and refinement parameters for GMP-58.

Parameter	Value
Molecular formula	$C_{17}H_9F_3N_6$
Formula weight ($g.mol^{-1}$)	354.30
Temperature (K)	100(2)
Wavelength (Å)	0.71073
Crystal system	Monoclinic
Space group	$P2_1/c$
a (Å)	6.8704(15)
b (Å)	19.363(4)
c (Å)	11.033(2)
α (°)	90
β (°)	97.779(7)
γ (°)	90
Volume ($Å^3$)	1454.2(9)
Z	4
Calculated density ($g.cm^{-3}$)	1.618
μ (mm^{-1})	0.130
F (000)	720
Crystal size (mm)	$0.02 \times 0.04 \times 0.15$
θ-Range scanned (°)	2.14 – 26.82
Index range	h:-18, 18; k:-40, 40; l:-28, 28
No. of reflections collected	20384
No. of unique reflections	3095
Data completeness (%)	99.2
Data/restraints/parameters	3095/0/235
S (Goodness-of-fit on F^2)	1.034
Final R indices R_1, wR_2, [$I > 2\sigma(I)$]	0.0593, 0.1122
R Indices, all data (R_1, wR_2)	0.1117, 0.1340
Largest diff. peak and hole ($e.Å^{-3}$)	0.26, -0.27

Molecular structure

The asymmetric unit (ASU) of GMP-58 is displayed in Figure 3.3.6 and this is the first crystallographic structural depiction of one of the three GMP compounds without any solvent component. A calculation of the least-squares plane through the tricyclic moiety yielded atom deviations in the range -0.022(3) Å to 0.032(3) Å, thus confirming its planarity. Furthermore, the angle of intersection of the pyrazine substituent and the tricyclic moiety is 10.0(1)^{o}.

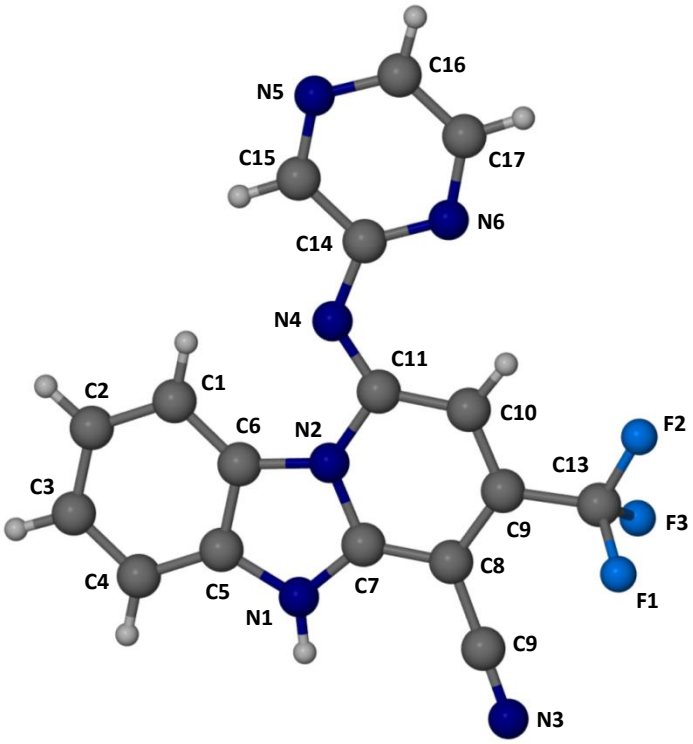


Figure 3.3.6: The ASU of GMP-58.

The unit cell of GMP-58 contains 4 molecules, as illustrated in the stereoscopic view in Figure 3.3.7, and it is evident that a centre of inversion exists at (½, ½, ½).

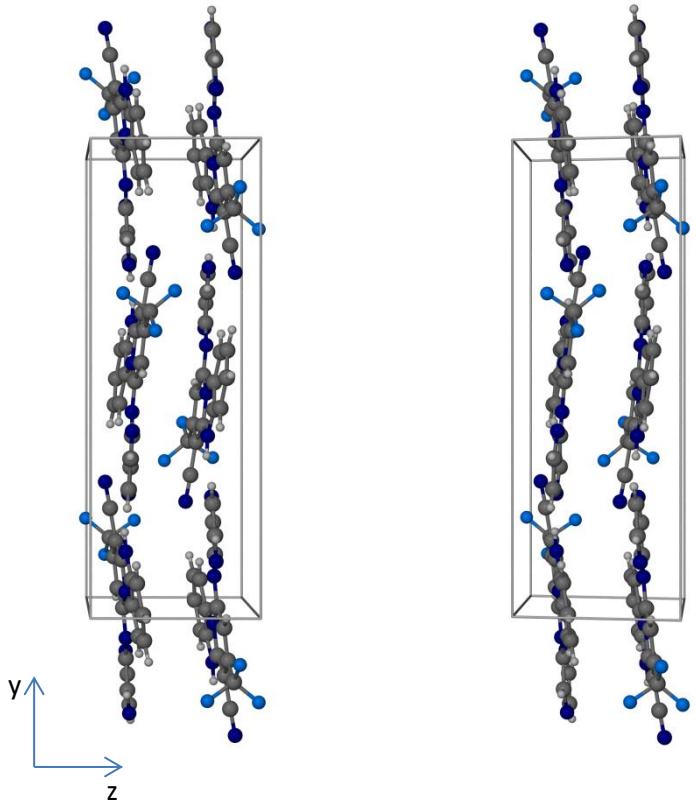


Figure 3.3.7: A stereoscopic perspective image of the unit cell content of GMP-58 viewed down the a-axis.

Hydrogen bonding

The intramolecular hydrogen bonding that occurs in the GMP-58 crystal structure primarily assists in retaining the particular molecular conformation observed (Figure 3.3.8). In addition, N-H···N and C-H···N intermolecular hydrogen bonding occur, as displayed in Figure 3.3.9. This results in forming a stable $R_2^2(9)$ ring synthon between the tricyclic fragment of one molecule and the pyrazine substituent of the other. The parameters for the intramolecular and intermolecular hydrogen bonds are provided in Table 3.3.3.

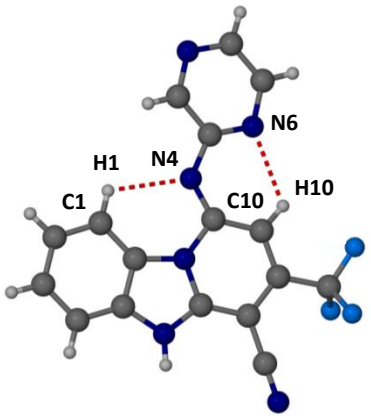


Figure 3.3.8: The intramolecular hydrogen bonding occurring in GMP-58.

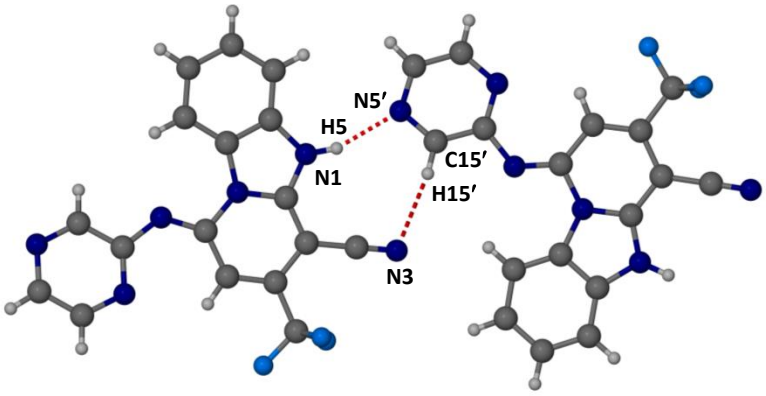


Figure 3.3.9: The intermolecular hydrogen bonding occurring between two GMP-58 molecules.

Table 3.3.3: Hydrogen bonding parameters for GMP-58.

Interaction type	Hydrogen bond interaction	D-H (Å)	H···A (Å)	D···A (Å)	D-H···A (°)	Symmetry code
Intermolecular	N1-H5···N5′	0.88	2.08	2.919(3)	160	x, y, z → 1-x, 1/2+y, 1/2-z
Intermolecular	C15′-H15′···N3	0.95	2.42	3.285(4)	151	1-x, -1/2+y, 1/2-z → x, y, z
Intramolecular	C1-H1···N4	0.95	2.38	2.887(4)	113	x, y, z
Intramolecular	C10-H10···N6	0.95	2.39	2.971(3)	119	x, y, z

Crystal packing

As illustrated in Figure 3.3.10, the overall packing arrangement involves stacking of undulating ribbons of H-bonded GMP-58 molecules. This Figure illustrates a projection down the b-axis, where it is possible to observe the two orientations of the GMP-58 molecules in consecutive layers, thus indicating that they are not superimposable. With reference to the ring-numbering in Figure 3.3.10, the resultant π-π stacking parameters for possible interactions noted to take place in the crystal structure are displayed in Table 3.3.4. The large slippage values indicate a negligible level of π-π stacking.

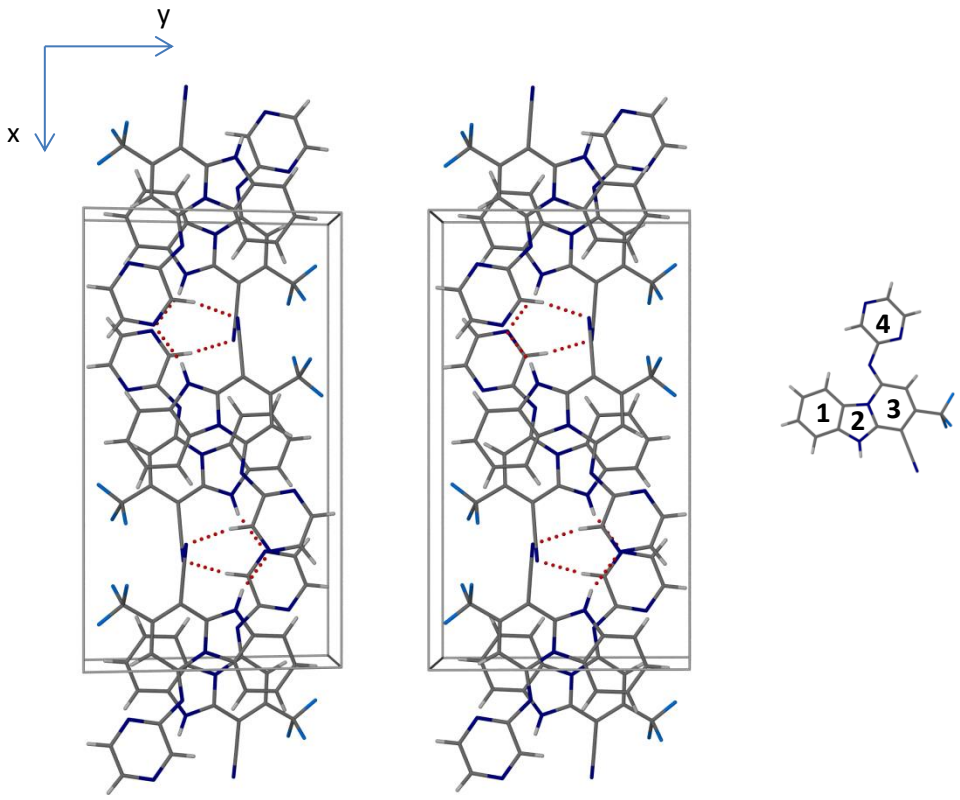


Figure 3.3.10: Stereoscopic perspective image of the packing arrangement viewed down the c-axis, displaying the alternating layered packing arrangement of the GMP-58 molecules, which significantly reduces π-π stacking from occurring between consecutive layers. The numbering scheme for the individual ring fragments of GMP-58 is provided in the right-hand image.

Table 3.3.4: π-π stacking between specific ring fragments of the GMP-58 molecules.

Ring of the ASU	Ring of a symmetry related molecule	Symmetry operator	Cg···Cg distance (Å)	Ring slippage (Å)
2	3	1-x, 1-y, 1-z	3.973(2)	2.240
3	1	1-x, 1-y, -z	3.7560(2)	1.772

Calculated powder X-ray diffraction (PXRD) pattern

The calculated PXRD pattern of this crystal structure correlates with the experimental PXRD pattern recorded for the starting material provided (Figure 3.3.11), which indicates that the crystal structure is representative of the bulk GMP-58 sample. Furthermore, it identifies the specific tautomeric form of the compound involved in all subsequent experiments conducted with GMP-58.

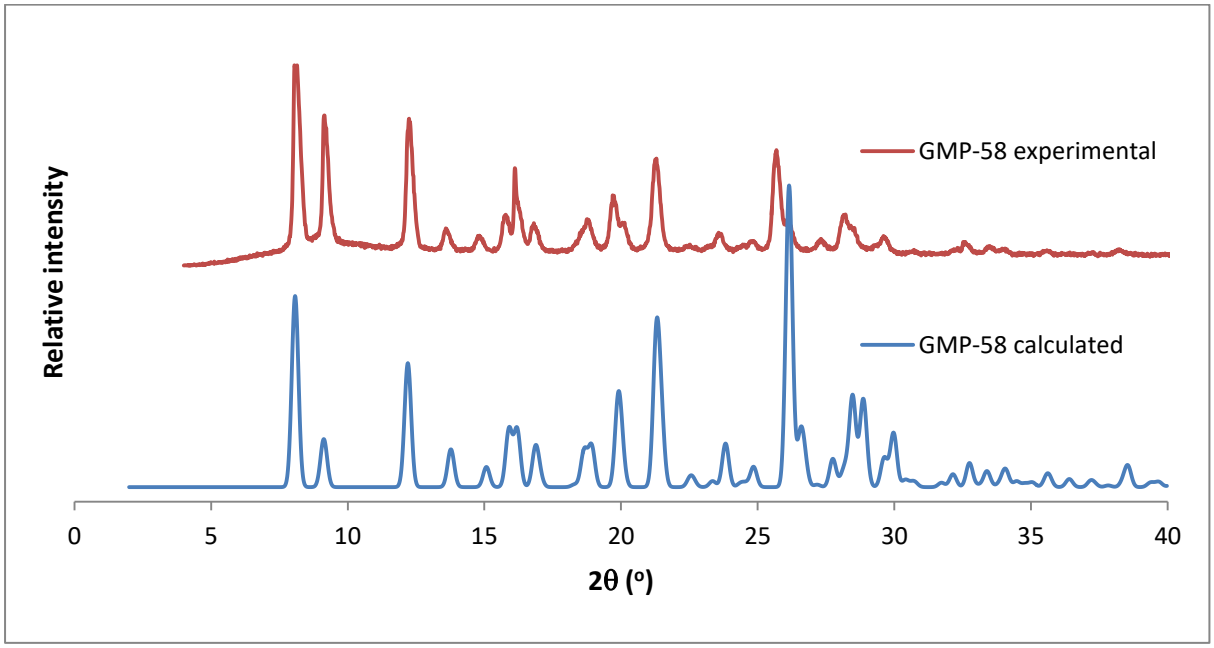


Figure 3.3.11: The PXRD pattern from the single-crystal X-ray structure of GMP-58 and the experimental PXRD pattern of GMP-58.

3.2.3.6) Single-crystal X-ray diffraction (SCXRD) analysis of the GMP58·DMSO solvate

Crystal morphology

In addition to the unsolvated form of GMP-58 described above, a DMSO solvate of GMP-58 was isolated and characterised using SCXRD. Figure 3.3.12 displays the morphology of GMP58·DMSO which crystallized only in the form of long, yellow needles.

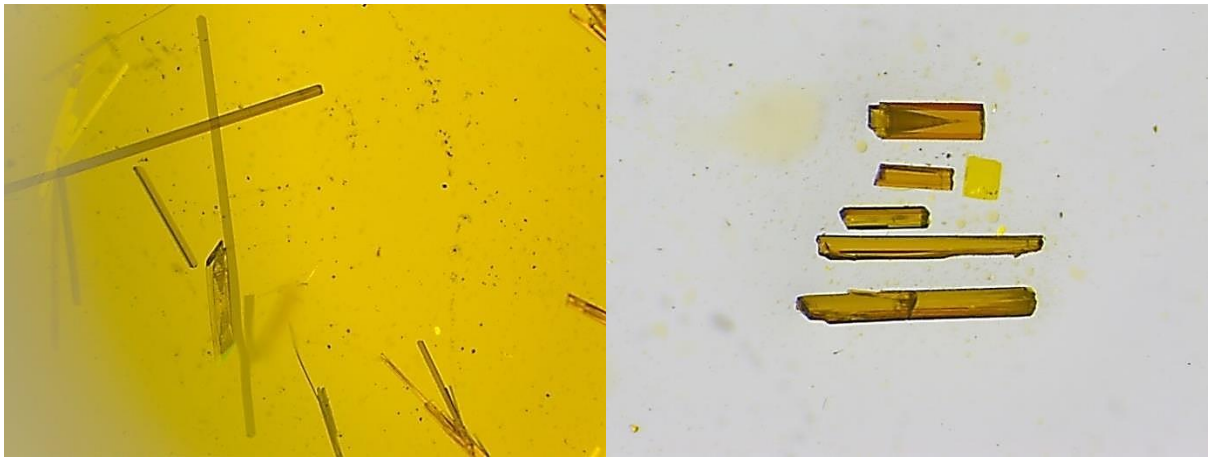


Figure 3.3.12: The crystalline morphology of GMP58·DMSO in a vial in the mother liquor (left) and the appearance of the crystals on a glass slide under Paratone oil (right).

Data-collection and space group determination

Intensity data-collection was performed at 100(2) K with a crystal specimen cut from a long needle. The crystal system was determined to be orthorhombic as three orthogonal mirror planes were observed in the intensity-weighted reciprocal lattice, thus indicating the Laue group *mmm*. A primitive lattice type was also determined and the space group *P*bca was assigned from the conditions limiting possible reflections (Table 3.3.5). This result was also confirmed by the program XPREP.[4]

Table 3.3.5: The conditions limiting possible reflections for the crystal of GMP58·DMSO.

Number	Conditions limiting possible reflections	Deduction
1	hkl: none	Primitive lattice
2	0kl: k = 2n	b-Glide plane ⊥ to the a-axis
3	h0l: l = 2n	c-Glide plane ⊥ to the b-axis
4	hk0: h = 2n	a-Glide plane ⊥ to the c-axis
5	[h00: (h = 2n, redundant condition)]	-
6	[0k0: (k = 2n, redundant condition)]	-
7	[00l: (l = 2n, redundant condition)]	-

Structure solution and refinement

The structure was solved using SHELXS-97,[1] and the same procedure as described for GMP-58 earlier in this section was used to refine this model. In addition, the stoichiometry of GMP-58·DMSO was determined by a TGA analysis which indicated a 1:1 host-guest stoichiometry (where GMP-58 is termed the 'host' and DMSO is termed the 'guest'). The results of this TGA analysis can be viewed in the Appendix, section 2.2.3, p. 7. In addition, a SQUEEZE procedure[2] conducted in PLATON[3] also indicated 1:1 stoichiometry.[a] The crystallographic data and details of the refinement are presented in Table 3.3.6.

[a] The residual electron density in the unit cell (after the omission of the DMSO molecules) corresponded to 372 electrons. Theoretically, the guest molecules contribute (8 × 42 =) 336 electrons per unit cell, which is in fair agreement, thus confirming the 1:1 host-guest stoichiometry which had been determined accurately by TGA.

Table 3.3.6: Crystal data and refinement parameters for the GMP58·DMSO solvate.

Parameter	Value
Complex formula	$C_{17}H_9F_3N_6 \cdot C_2H_6OS$
Formula weight ($g.mol^{-1}$)	432.43
Temperature (K)	100(2)
Wavelength (Å)	0.71073
Crystal system	Orthorhombic
Space group	*P*bca
a (Å)	23.2997(5)
b (Å)	6.6948(2)
c (Å)	24.7102(6)
α (°)	90
β (°)	90
γ (°)	90
Volume ($Å^3$)	3854.5(2)
Z	8
Calculated density ($g.cm^{-3}$)	1.490
μ (mm^{-1})	0.221
F (000)	1776
Crystal size (mm)	$0.19 \times 0.23 \times 0.31$
θ-Range scanned (°)	2.40 – 28.32
Index range	h:-31, 31; k:-8, 8; l:-32, 32
No. of reflections collected	85462
No. of unique reflections	4767
Data completeness (%)	99.4
Data/restraints/parameters	4767/0/273
S (Goodness-of-fit on F^2)	1.093
Final R indices R_1, wR_2, [I > 2σ(I)]	0.0360, 0.0900
R Indices, all data (R_1, wR_2)	0.0381, 0.0914
Largest diff. peak and hole ($e.Å^{-3}$)	0.41, -0.40

Molecular structure

The ASU of the GMP58·DMSO solvate is displayed in Figure 3.3.13 and comprises one GMP-58 molecule and one DMSO molecule. The particular tautomeric form of GMP-58 presented in this structure is the same as that determined for the non-solvated form of GMP-58, which could possibly indicate that this is the predominant crystallizing tautomeric form of GMP-58.

The tricyclic moiety of the GMP-58 molecule displayed planarity as a calculation of the least-squares plane through the atoms of this moiety yielded atom deviations in the range -0.040(1) Å to 0.047(1) Å. In addition, the angle of intersection of the pyrazine substituent and the tricyclic moiety is 6.07(5)°.

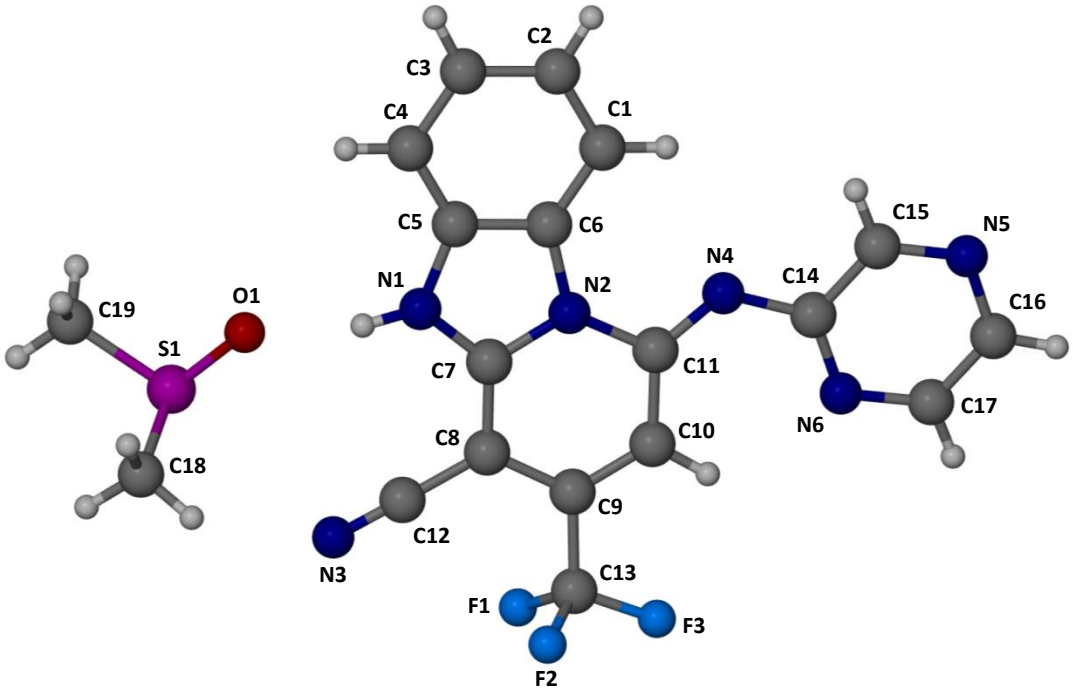


Figure 3.3.13: The ASU of GMP58·DMSO.

Hydrogen bonding

The GMP58·DMSO structure displays the same type of intramolecular C-H···N hydrogen bonding as previously mentioned for the GMP-58 structure, and these interactions are similarly responsible for the observed conformational arrangement (Figure 3.3.14). In addition, intermolecular hydrogen bonding predominantly takes place between GMP-58 and the DMSO solvent molecule in the ASU in the form of a discrete N-H···O hydrogen bond. However, there is a weak C-H···O′ intermolecular hydrogen bond that occurs between C16 on the pyrazine ring and the oxygen atom on a symmetry related DMSO molecule (Figure 3.3.15). The parameters of these hydrogen bonds are listed in Table 3.3.7.

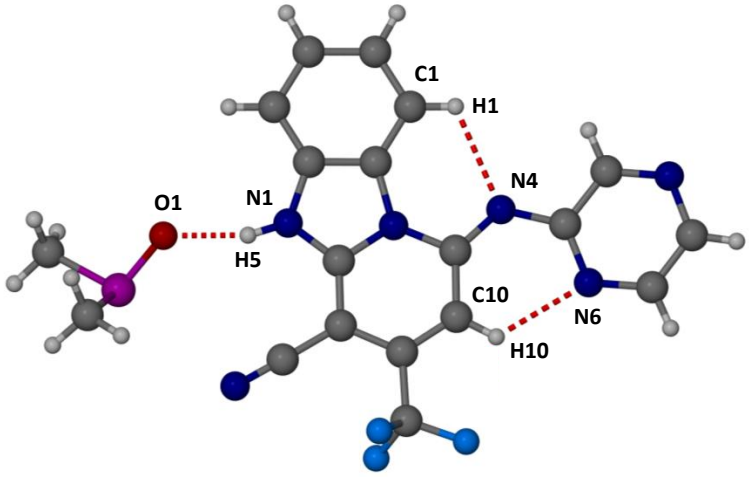


Figure 3.3.14: The intramolecular and intermolecular hydrogen bonding in the ASU of GMP58·DMSO.

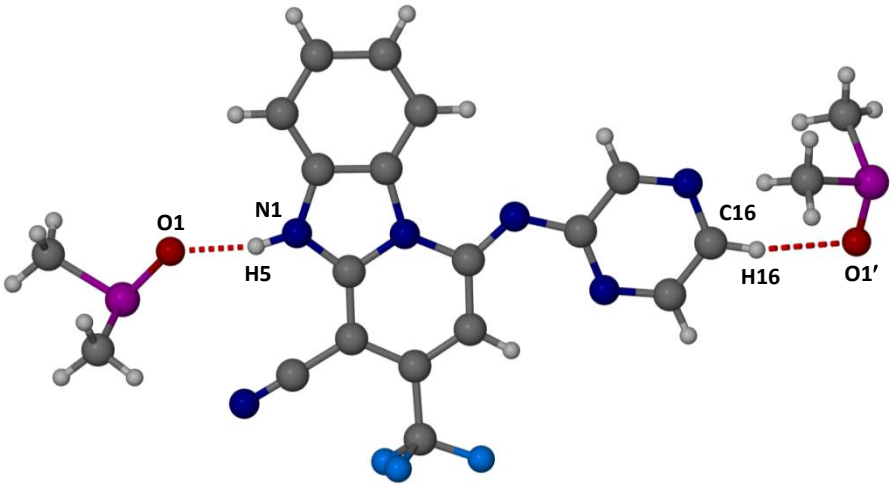


Figure 3.3.15: The intermolecular hydrogen bonding in GMP58·DMSO.

Table 3.3.7: Hydrogen bonding parameters for GMP58·DMSO.

Interaction type	Hydrogen bond interaction	D-H (Å)	H···A (Å)	D···A (Å)	D-H···A (°)	Symmetry code
Intramolecular	C1-H1···N4	0.95	2.43	2.9322(16)	113	x, y, z
Intramolecular	C10-H10···N6	0.95	2.28	2.8770(16)	120	x, y, z
Intermolecular	N1-H5···O1	0.88	1.79	2.6436(13)	163	x, y, z
Intermolecular	C16-H16···O1	0.95	2.45	3.2594(16)	143	3/2-x, 2-y, 1/2+z

Crystal packing

A significantly different packing arrangement occurs for GMP58·DMSO relative to the other three crystal structures involving the GMP compounds. Figure 3.3.16 displays a stereoscopic view of the packing arrangement projected down the a-axis, where the alternate rows of molecules are inclined to one another by approximately 30^{o}.

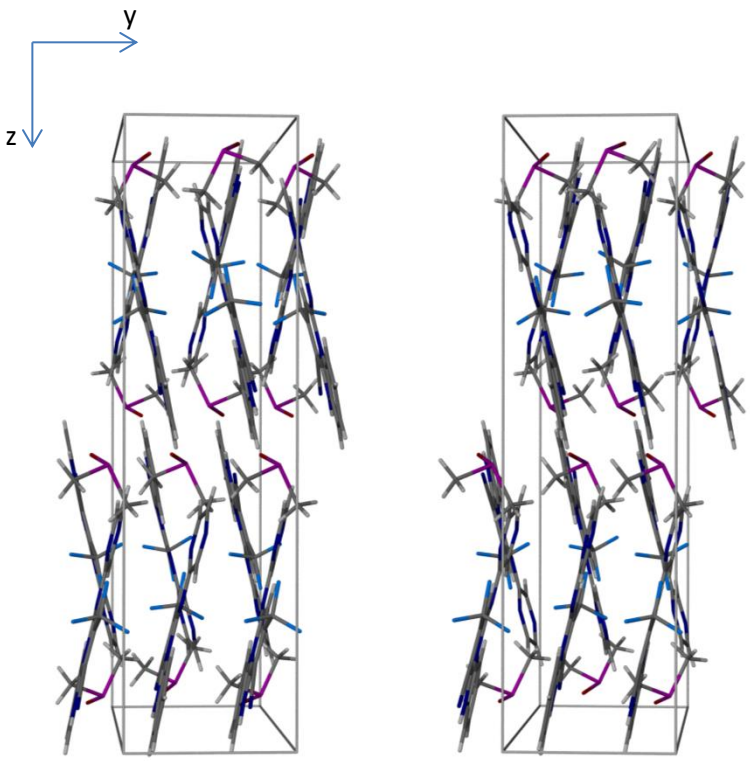


Figure 3.3.16: A perspective stereoscopic view of the packing arrangement along [100].

Furthermore, as observed in the other three crystal structures in the GMP series, the GMP-58 molecules in this crystal structure are not superimposable along consecutive layers, and instead are only superimposable every alternate layer. Consequently, this practically eliminates significant π-π stacking from occurring (Figure 3.3.17). Thus, with reference to the ring-numbering scheme in Figure 3.3.17, the negligible π-π stacking that was noted to take place is supplied in Table 3.3.8.

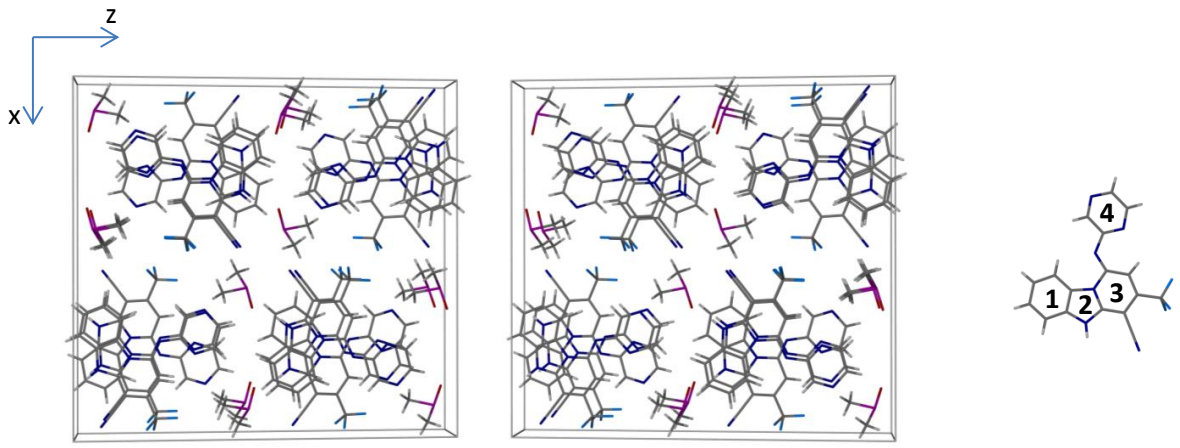


Figure 3.3.17: A perspective stereoscopic view of the packing arrangement viewed down the b-axis displaying the alternating layered packing arrangement of the GMP-58 molecules, which significantly reduces π-π stacking from occurring between consecutive layers. The numbering scheme for the individual ring fragments of GMP-58 is supplied in the right-hand image.

Table 3.3.8: π-π stacking between specific ring fragments of the GMP-58 molecule.

Ring of the ASU	Ring of a symmetry related molecule	Symmetry operator	Cg···Cg distance (Å)	Ring slippage (Å)
1	2	3/2-x, -1/2+y, z	3.3823(7)	0.779
2	2	3/2-x, -1/2+y, z	3.5779(7)	1.417
3	1	3/2-x, 1/2+y, z	3.7606(7)	1.732
4	4	3/2-x, 1/2+y, z	3.9519(7)	1.899

Calculated powder X-ray diffraction (PXRD) pattern

The calculated PXRD pattern from a single crystal of GMP58·DMSO is displayed in Figure 3.3.18 and is significantly different in all respects from the calculated PXRD pattern for GMP-58. Nonetheless, the crystal structure of GMP58·DMSO indicated an alternative hydrogen bonding scheme and packing arrangement that is possible with GMP-58 when crystallizing it with a different solvent capable of engaging in H-bonding.

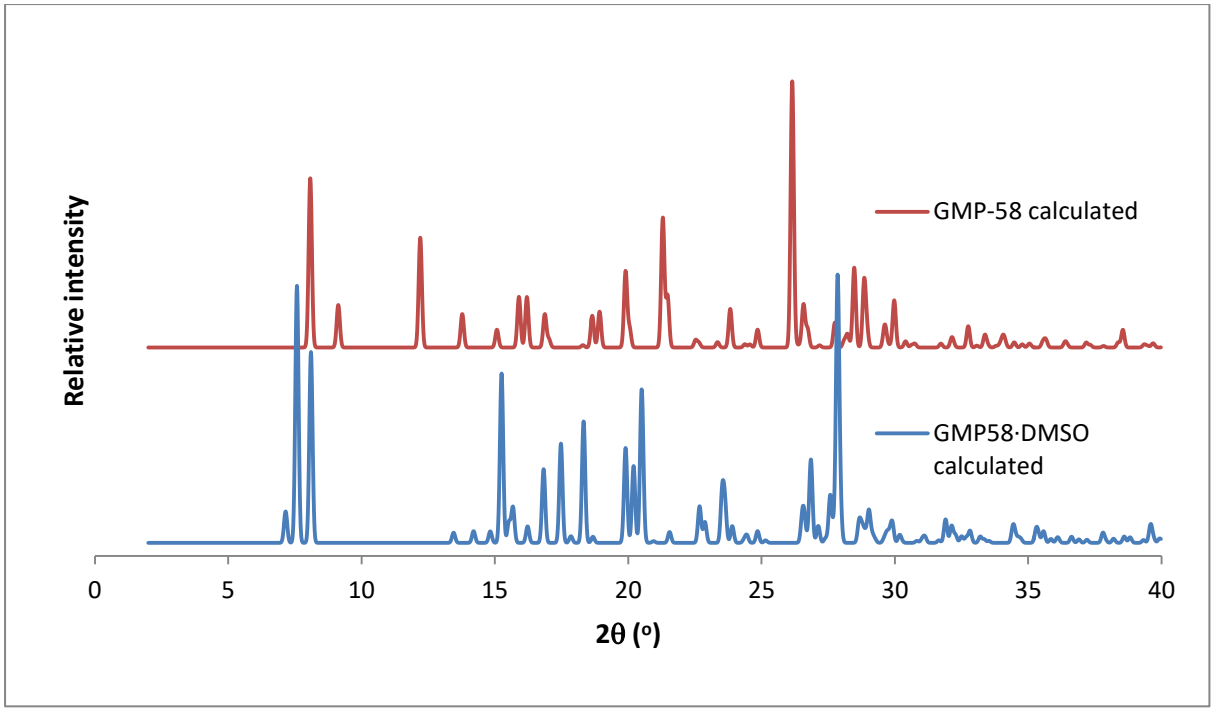


Figure 3.3.18: Calculated PXRD patterns of GMP and GMP·DMSO based on their respective refined X-ray structures.

3.2.4) CD inclusion with GMP-23, GMP-31 and GMP-58

Various experiments were performed in which the syntheses of inclusion complexes comprising either GMP-23, GMP-31 and GMP-58 with the native CDs (namely α-CD, β-CD and γ-CD) or with methylated CDs (namely DMB and TMB) were attempted *via* kneading and co-precipitation, as described in the Experimental methods, Chapter 2, section 2.3, pp. 41 – 42. All the attempted syntheses with each GMP and CD combination failed. Thus, it can be concluded that under the conditions employed, CD inclusion is not possible with GMP-23, GMP-31 or GMP-58.

3.2.5) Co-crystallization of GMP-23, GMP-31 and GMP-58

3.2.5.1) Virtual co-crystal screening analysis

Initially, a virtual co-crystal screening analysis was conducted using the Co-Crystal Design and Motif searching tools under CSD-Materials in the program Mercury,[5] in order to gain insight into which coformers might have greater propensity for forming co-crystals with the GMP compounds. Co-crystal screening is becoming an increasingly important study in

modern chemical practices that involve co-crystal production, as the knowledge-based approach that it provides saves both time and resources.[5] Therefore, this analysis is pertinent to this study, especially as a very limited amount of active compound had been available and thus only the most relevant experiments could be conducted.

There are multiple approaches to conducting co-crystal design; however, two prominent methods are screening by molecular complementarity, and screening by hydrogen (or halogen) bonding motifs.[5] Consequently, a two-step process was performed during this virtual co-crystal screening analysis. The first step (incorporating screening by molecular complementarity) involved compiling a list of coformers from the library of coformers in the CSD that are most likely to form co-crystals with the GMP compounds.[6] The second step (incorporating screening by hydrogen bonding motifs) involved ranking these coformers (provided from the first step) according to the most probable hydrogen-bonding candidates as co-crystal coformers.

The first step assesses the probability of co-crystal formation between an active ingredient and a coformer. For successful co-crystal formation there are five parameters for the individual co-crystal components that are considered, and the difference between the values of each parameter for the two co-crystal components must be small.[5,7] These five parameters include: the dipole moment, the proportion of oxygen and nitrogen atoms in each component intended for co-crystallization, and three shape descriptors that are based on a molecular bounding box: the short axis length, the ratio of the short and long axis, and the ratio of the medium and long axis.

The second step involves the chemist predicting which type of synthon arrangements can occur between the functional groups of a potential coformer and the active ingredient. These functional groups are thereafter investigated in the CSD to establish which synthons involving them occur most frequently, and thus based on that frequency it is possible to predict which coformers are more likely to form co-crystals.

The active compounds included three drug leads, namely GMP-23, GMP-31 and GMP-58, all of which have alternative tautomeric forms. The structures of these compounds (with possible tautomeric forms) are displayed below, each tautomeric form being referred to as a, b and c respectively (Figures 3.5.1 – 3.5.3).

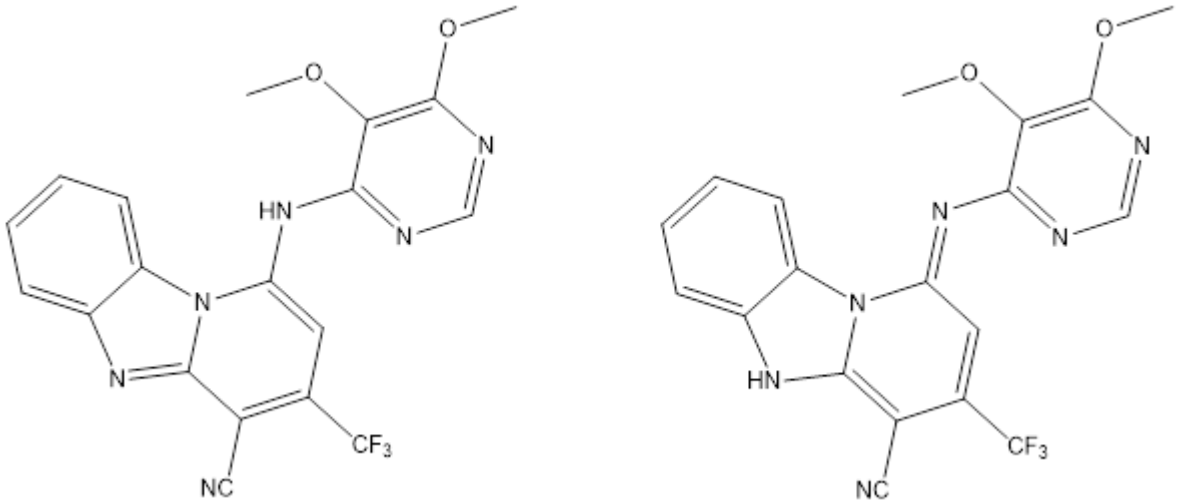


Figure 3.5.1: Two possible tautomeric forms of GMP-23: GMP-23a (left) and GMP-23b (right).

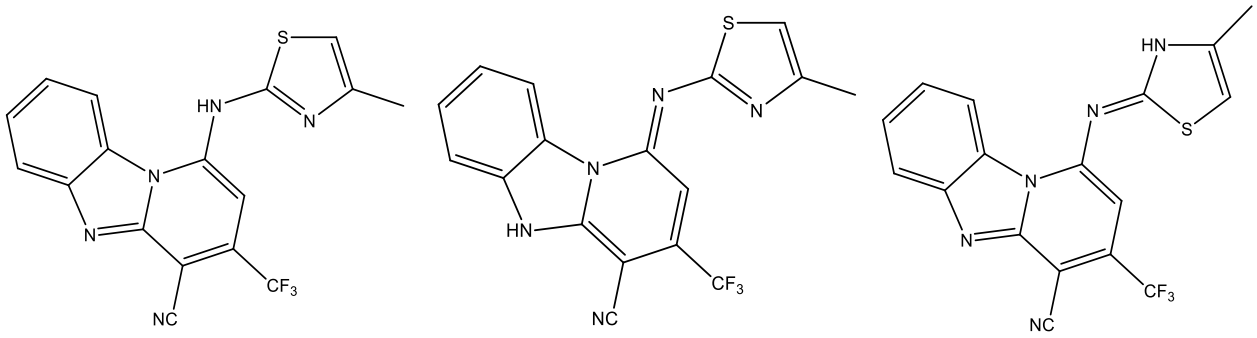


Figure 3.5.2: Three possible tautomeric forms of GMP-31: GMP-31a (left), GMP-31b (centre) and GMP-31c (right).

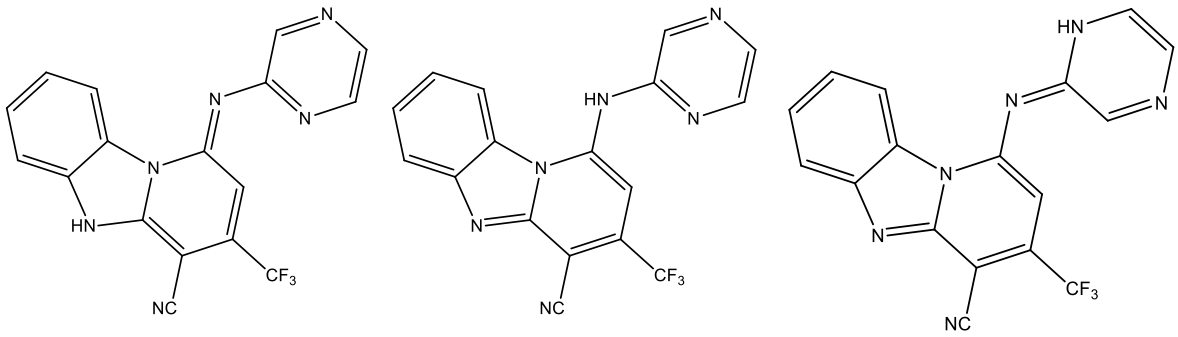


Figure 3.5.3: Three possible tautomeric forms of GMP-58: GMP-58a (left), GMP-58b (centre) and GMP-58c (right).

Each tautomeric form was selected as an input to the program during the first step of screening by molecular complementarity, and a list of potential coformers was generated for each. Despite the fairly extensive list of potential coformers generated for each

tautomeric search, only those that are generally recognized as safe ('GRAS') are reported in Tables 3.5.1 – 3.5.3.[8] (The full lists of potential coformers from this analysis are provided in the Appendix under section 2.3, pp. 8 – 10). Thereafter, these GRAS coformers were considered for the second step of the virtual screening analysis and ranked according to the most frequently occurring hydrogen bonding motifs.[8]

Table 3.5.1: The predicted GRAS coformers for GMP-23a and GMP-23b.

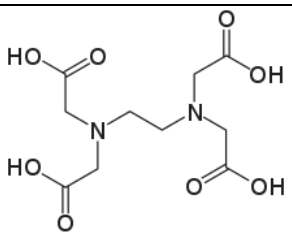
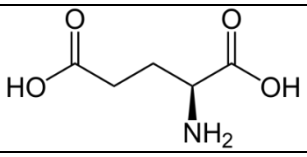
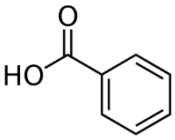
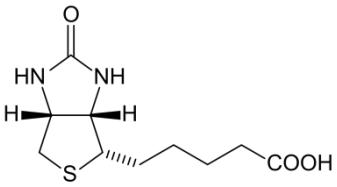
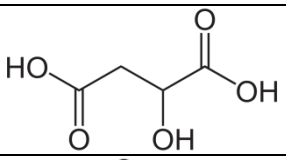
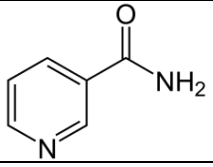
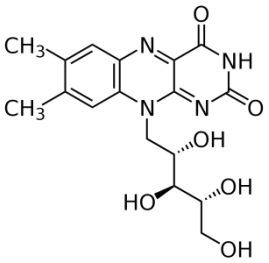
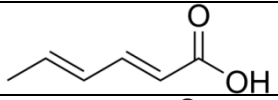
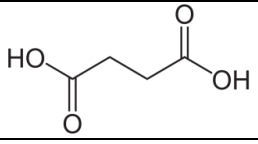
GMP-23a and GMP-23b GRAS coformers		
Number	**Coformer**	**Structure**
1	**EDTA** **(not available in the laboratory)**	
2	**L-glutamic acid**	
3	**Benzoic acid**	
4	**Biotin** **(not available in the laboratory)**	
5	**Malic acid**	
6	**Nicotinamide**	
7	**Riboflavin**	
8	**Sorbic acid**	
9	**Succinic acid**	

Table 3.5.2: The predicted GRAS coformers for GMP-31a, GMP-31b and GMP-31c.

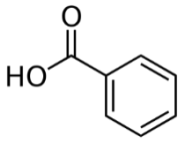
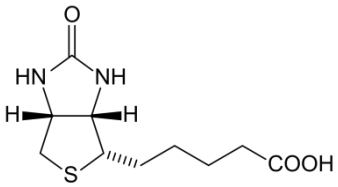
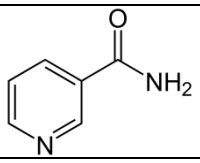
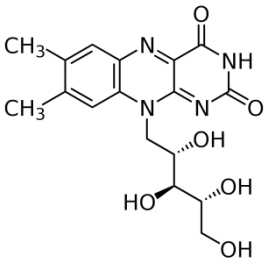
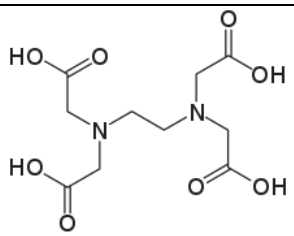
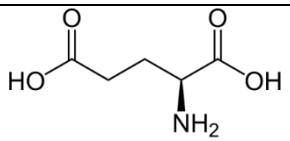
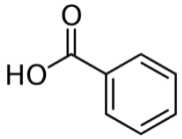
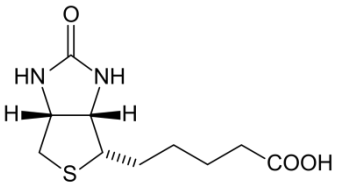
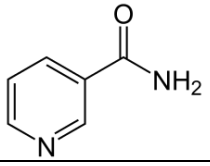
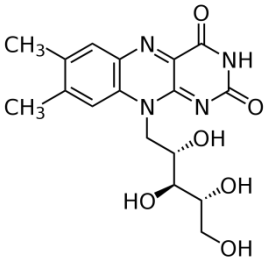
GMP-31a, GMP-31b and GMP-31c GRAS coformers		
Number	**Coformer**	**Structure**
1	**Benzoic acid**	
2	**Biotin** **(not available in the laboratory)**	
3	**Nicotinamide**	
4	**Riboflavin**	

Table 3.5.3: The predicted GRAS coformers for GMP-58a, GMP-58b and GMP-58c.

GMP-58a, GMP-58b and GMP-58c GRAS coformers		
Number	**Coformer**	**Structure**
1	**EDTA** **(not available in the laboratory)**	
2	**L-glutamic acid**	
3	**Benzoic acid**	
4	**Biotin** **(not available in the laboratory)**	
5	**Nicotinamide**	
6	**Riboflavin**	

In addition to the screening by molecular complementarity assessment, various hydrogen bonding motif analyses were conducted in an attempt to rank the selected coformers. Initally, potential hydrogen bonding sites that can form stable ring motifs were identified in each molecular tautomeric form (GMP-23a, GMP-23b, GMP-31a, GMP-31b, GMP-31c, GMP-58a, GMP-58b and GMP-58c), as indicated by the red circles in Figures 3.5.4 and 3.5.5. These

sites are also particularly relevant to the coformers that were identified from the screening by the molecular complementarity step.

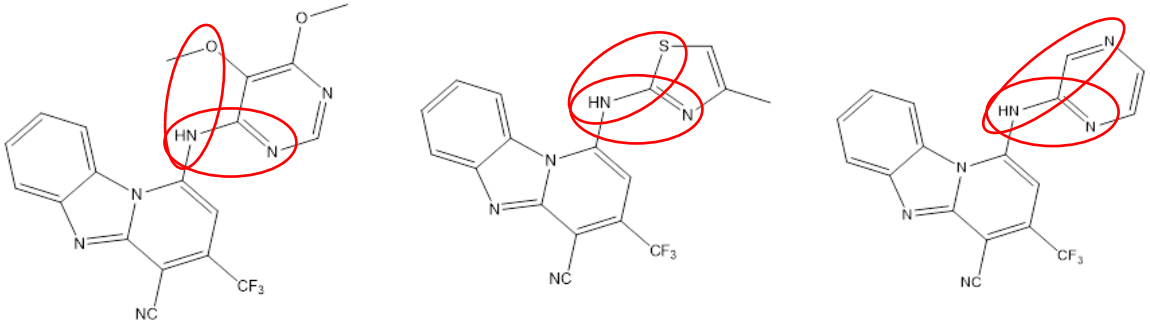


Figure 3.5.4: The hydrogen bonding sites (circled in red) that can potentially form stable ring motifs for the tautomeric forms of GMP-23a, GMP-31a and GMP-58a (left to right). The tautomeric forms of GMP-31c and GMP-58c would have the same potential hydrogen bonding sites as GMP-31a and GMP-58a.

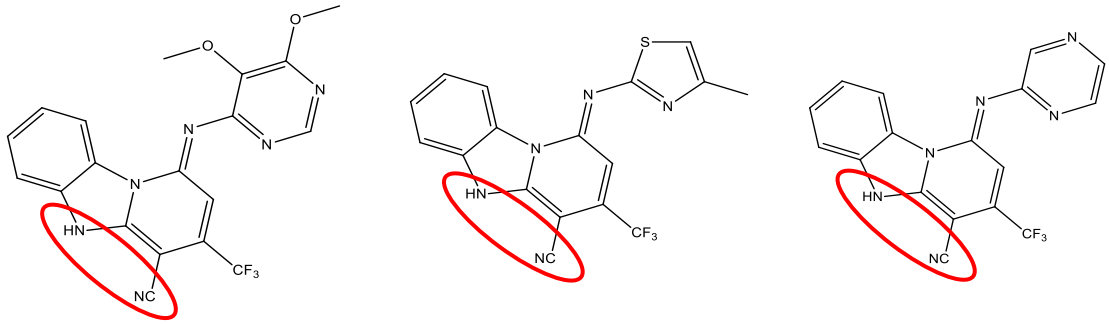


Figure 3.5.5: The potential hydrogen bonding sites (circled in red) that can form stable ring motifs for the tautomeric forms of GMP-23b, GMP-31b and GMP-58b (left to right).

Consequently, selected molecular fragments, along with their tautomeric forms, were drawn for each active compound (Figure 3.5.6). These molecular fragments were assessed for their frequency in forming hydrogen bonded ring motifs. This was performed with either the carboxylic acid functional group or the amide functional group, since these are the predominant ring-forming functional groups in the coformers obtained from the initial search (Table 3.5.4). With reference to these molecular fragments, the bond types which are displayed as dashed lines represent 'any' bond type. This is owing to the fact that the fragment is either part of a delocalised system within the active GMP compound, or that the fragment may be bonded to another molecular system with a different bonding structure. The analysis was conducted with the hypothetical hydrogen bonds between the molecular

fragments set to range within a distance ≤ to the sum of the van der Waals radii (+0.1 Å) of the relevant donor and acceptor atoms.

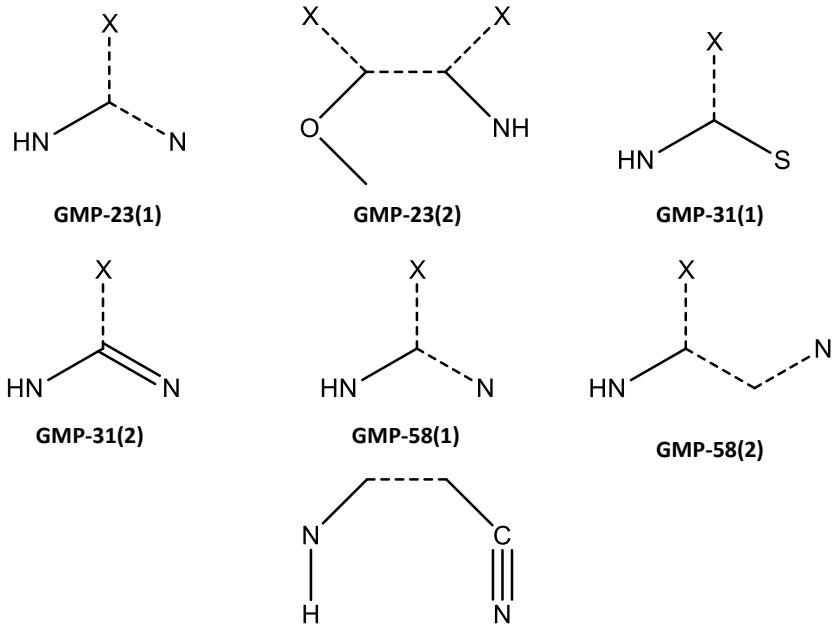


Figure 3.5.6: The molecular fragments of GMP-23(1), GMP-23(2), GMP-31(1), GMP-31(2), GMP-58(1), GMP-58(2) and the fragment that pertains to all three GMP compounds, namely GMP-23(3), GMP-31(3) and GMP-58(3). All molecular fragments are specific to particular tautomeric forms, allowing sensible hydrogen bonding ring formations with carboxylic and amide functional groups. The dashed bonds indicate any bond type and atom X indicates any atom.

Table 3.5.4: The frequencies of selected molecular fragments forming hydrogen bonded ring motifs.

Molecular fragment	**Number of structures with a carboxylic functionality as coformer**	**Number of structures with an amide functionality as coformer**
Molecular fragment GMP-23(1)	643	441
Molecular fragment GMP-23(2)	0	12
Molecular fragment GMP-31(1)	3	0
Molecular fragment GMP-31(2)	172	204
Molecular fragment GMP-58(1)	643	441
Molecular fragment GMP-58(2)	73	67
Molecular fragments GMP-23(3), GMP-31(3), and GMP-58(3)	0	16

Furthermore, additional hydrogen bonding motifs were also selected that focus on common discrete hydrogen bonding motifs, as well as ring-structured motifs that incorporate C-H···O or C-H···N hydrogen bonds. These additional hydrogen bonding motifs are also relevant to the three GMP active compounds (and account for their specific tautomeric forms), as well as the pre-selected coformers. These hydrogen bonding motifs are presented in Figure 3.5.7 and all of the motifs are relevant to GMP-23, GMP-31 and GMP-58, except for motifs a, b, i and j, which are only relevant to GMP-23 and GMP-58; similarly, k and l are relevant for GMP-31. As mentioned previously, atom X denotes any atom, the black dashed bond signifies any bond type, and the dashed red bond signifies a hydrogen bonding contact between a molecular fragment of the active compound and a molecular fragment of either an amide or carboxylic acid functional group from a coformer. Table 3.5.5 summarises the results of the number of structures listed in the CSD that have these types of hydrogen bonding motifs.

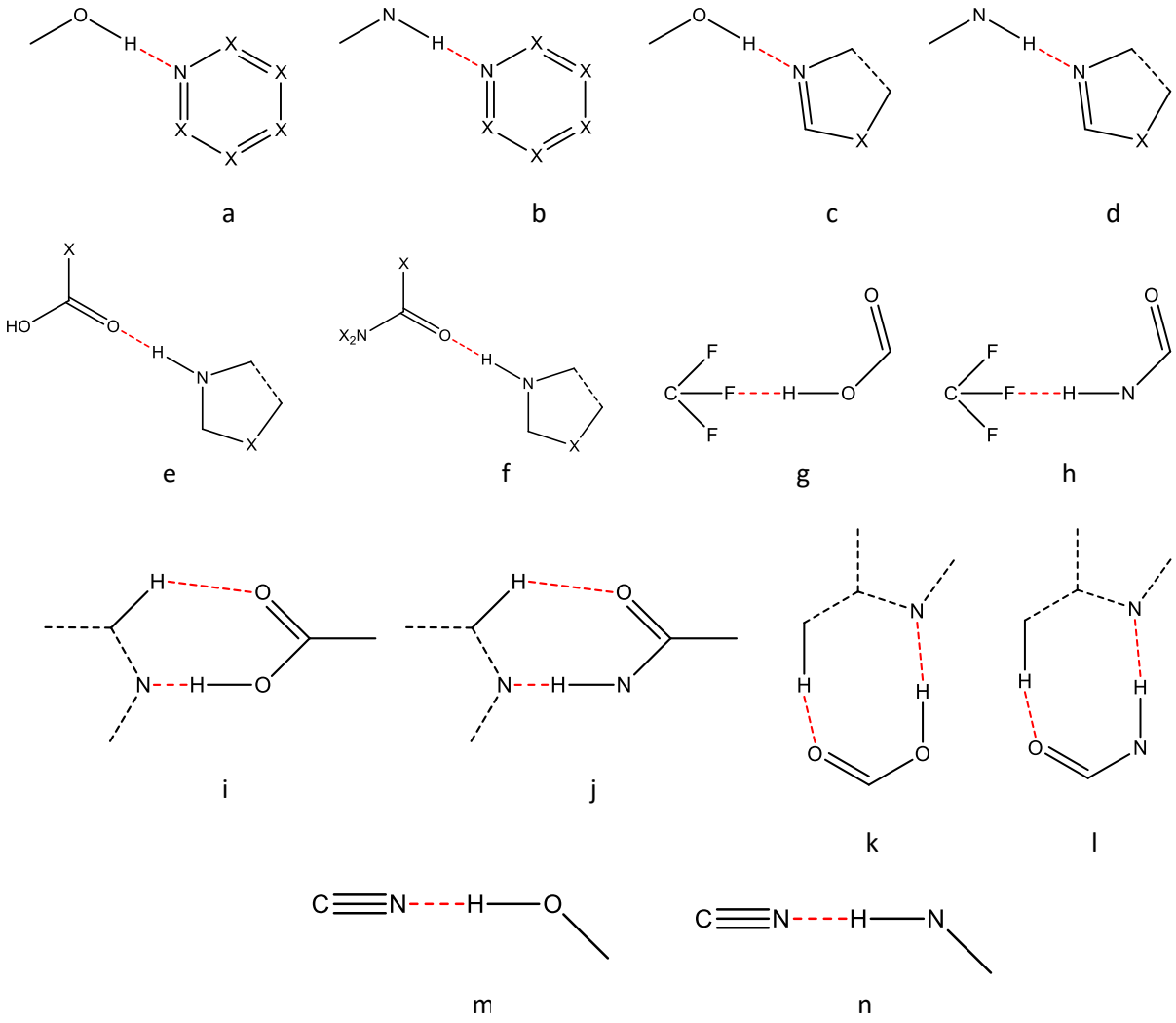


Figure 3.5.7: Hydrogen bonding motifs of molecular fragments that are relevant to the three GMP active compounds (and account for their tautomeric forms), as well as the pre-selected coformers.

Table 3.5.5: The number of reported structures in the CSD that contain the corresponding motif as displayed in Figure 3.5.7.

Hydrogen bonding motif	**Number of structures reported containing the respective motif**
a	6413
b	5765
c	2049
d	2948
e	192
f	144
g	219
h	135
i	1501
j	117
k	104
l	28
m	954
n	2904

In conclusion, the screening by molecular complementarity provided a valuable starting point for the pre-selection of a variety of coformers for co-crystal investigations. Furthermore, the screening by investigation of hydrogen bond motifs did not provide significant insight for ranking the list of pre-selected coformers, since all the pre-selected GRAS coformers could potentially form discrete and/or ring bonding motifs. In addition, since there are relatively few pre-selected GRAS coformers identified from the screening by molecular complementarity analysis, it was considered more reasonable to work with them all simultaneously.

However, once a co-crystal is obtained, it would be useful to take note of the type of hydrogen bonding motif(s) present in the crystal structure and compare that to the frequencies of the results from the "screening by hydrogen bond motifs" virtual investigation. This would enable one to compare the results and predictions obtained virtually with the experimental results.

3.2.5.2) Experimental co-crystal screening of GMP-23, GMP-31 and GMP-58

Multiple co-crystal screening experiments were performed with the pre-selected coformers, except for biotin and EDTA, which were not available in the laboratory. These experiments included dry grinding, liquid-assisted grinding (LAG), and co-precipitation experiments. Unfortunately, none of the experiments produced any confirmed co-crystalline phase that could be adequately isolated and further characterised. A few additional coformers (previously considered GRAS, and on the list from the "screening by molecular complementarity" virtual analysis) were also utilised, however, also with no success. These experiments are briefly described in the Appendix under section 2.4, pp. 11 – 13.

These co-crystal screening experiments did, however, produce either a serendipitous polymorph or a different tautomeric form of GMP-23 (referred to hereafter as GMP-23 form 2). This new form is discussed in more detail in the following section.

In a final attempt to form interactions between a GMP compound and a coformer, a different preparative technique was employed in which the coformer was pre-melted and the GMP compound was mixed into it to form a product. All the experiments that were conducted using this methodology displayed successful results and these products are further analysed and discussed later in this section.

3.2.5.3) Characterisation of GMP-23 form 2

The attempts at forming co-crystals with GMP-23 and a variety of coformers during co-precipitation experiments in EtOH, indicated that a serendipitous polymorph or tautomeric form of GMP-23 had been formed, as indicated by the PXRD results of the various products. The formation of this polymorph was not dependent on the presence of any coformer and required only the presence of a solvent (e.g., EtOH) to form. GMP-23 form 2 was characterised *via* PXRD, ^{1}H NMR spectroscopy, TGA and DSC.

3.2.5.4) The crystalline morphology of GMP-23 form 2

The morphology of GMP-23 form 2 has an extremely fine and dendritic characteristic to it (Figure 3.5.8) and thus it is evident that SCXRD analysis was not possible. Experiments were conducted with the intention of improving the morphology, and growing larger crystals of GMP-23 form 2 for SCXRD analysis. These experiments included extremely slow evaporation with an excess of solvent, as well as attempts to grow crystals in a capillary tube. However, all these experiments failed and the same thin and fibrous morphology resulted. Nevertheless, the remaining characterisation experiments were performed.

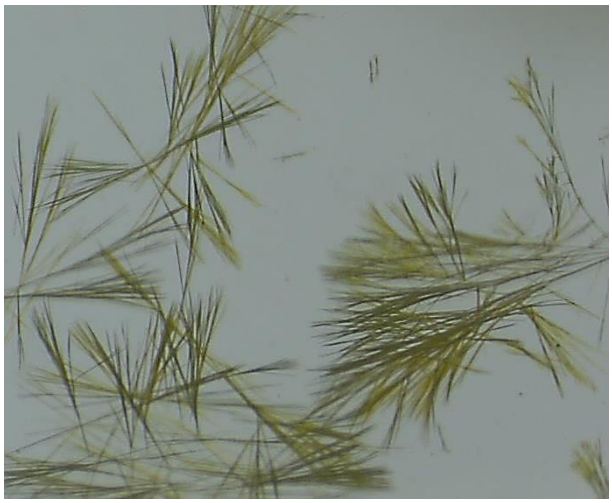


Figure 3.5.8: The extremely fine dendritic morphology of GMP-23 form 2.

3.2.5.5) The PXRD analysis of GMP-23 form 2

GMP-23 form 2 was initially identified *via* PXRD and Figure 3.5.9 displays its PXRD pattern and that of GMP-23, which clearly shows that they are distinct crystalline phases. Furthermore, Figure 3.5.10 displays a series of PXRD patterns of GMP-23 form 2 that was formed from co-precipitation experiments with various coformers using EtOH as the solvent. This PXRD comparative analysis confirms that the various coformers had no influence or effect on the formation of GMP-23 form 2. All the compared PXRD patterns are

identical in terms of their angular positions,[b] which correlated with the PXRD pattern of GMP-23 form 2 that was crystallized in the absence of a coformer.

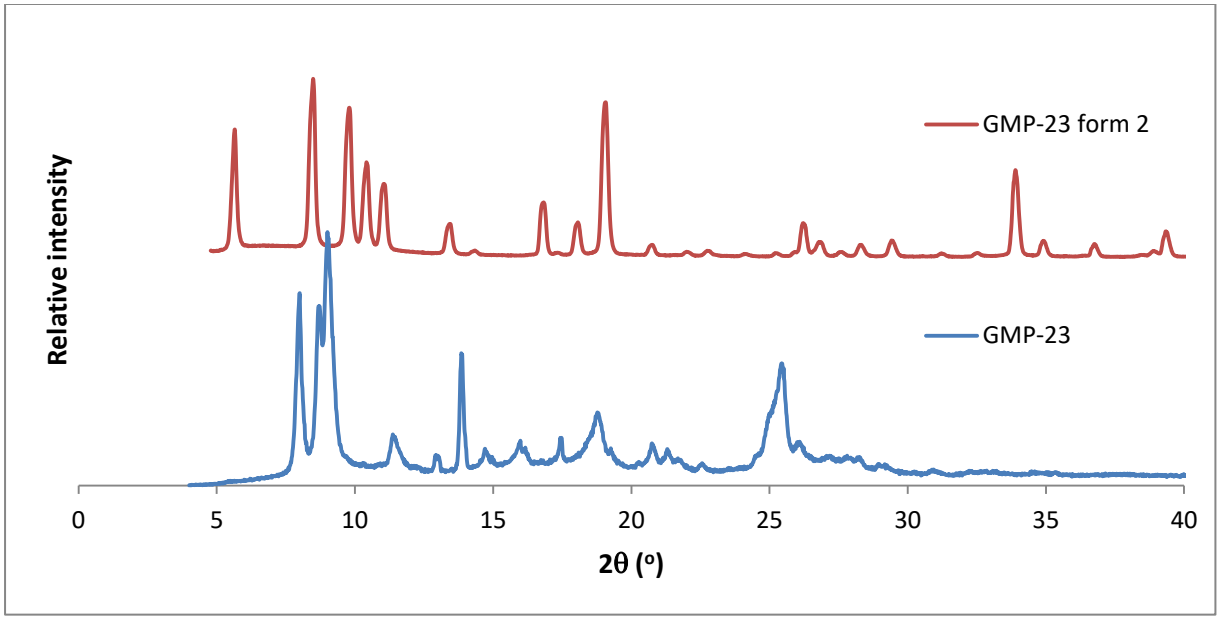


Figure 3.5.9: The PXRD patterns of GMP-23 as originally provided, and GMP-23 form 2 that was crystallized from EtOH.

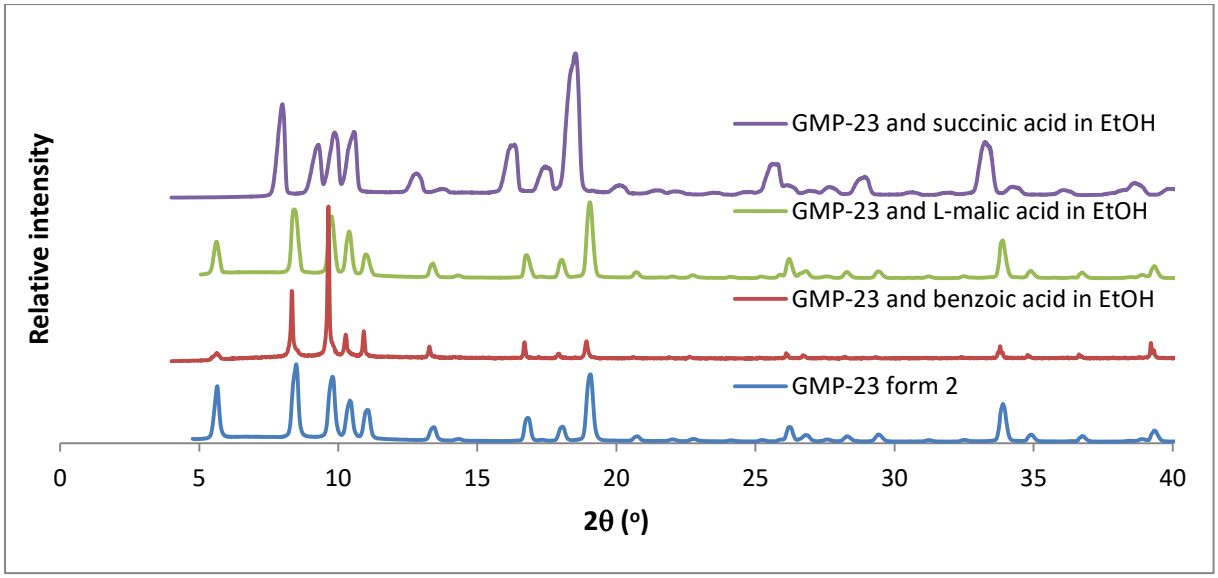


Figure 3.5.10: The PXRD patterns of GMP-23 form 2, as well as the products from a variety of co-precipitation experiments with GMP-23 using EtOH as the solvent.

[b] It is important to note that the angular peak positions of the PXRD pattern labelled "GMP-23 and succinic acid in EtOH" are slightly shifted to lower angular values and that the peak at 5.5° is absent. Its perceived absence could be a result of its having a zero intensity at that position for this particular sample. The overall shift was caused by a different sample holder being used, which caused the sample to be located at a different height in the instrument, thus causing a shift in the angular positions.

3.2.5.6) ^{1}H NMR analysis of GMP-23 form 2

The ^{1}H NMR analysis confirmed the purity of GMP-23 form 2, as the ^{1}H NMR spectrum contained only the peaks pertaining to GMP-23, with no peak contributions from EtOH (Figure 3.5.11). The ^{1}H NMR spectrum of GMP-23 in the Appendix under section 2.1.1, p. 3 can be used as a reference. The proton chemical shift peak values for EtOH are 1.06 ppm ($C\underline{H}_3$), 3.44 ppm ($C\underline{H}_2$) and 4.35 ppm ($O\underline{H}$) when analysed with DMSO-d_6 as solvent,[9] and not one of these peaks is present in this spectrum.[c] Consequently, any speculations of GMP-23 form 2 possibly being an EtOH solvate have been eliminated.

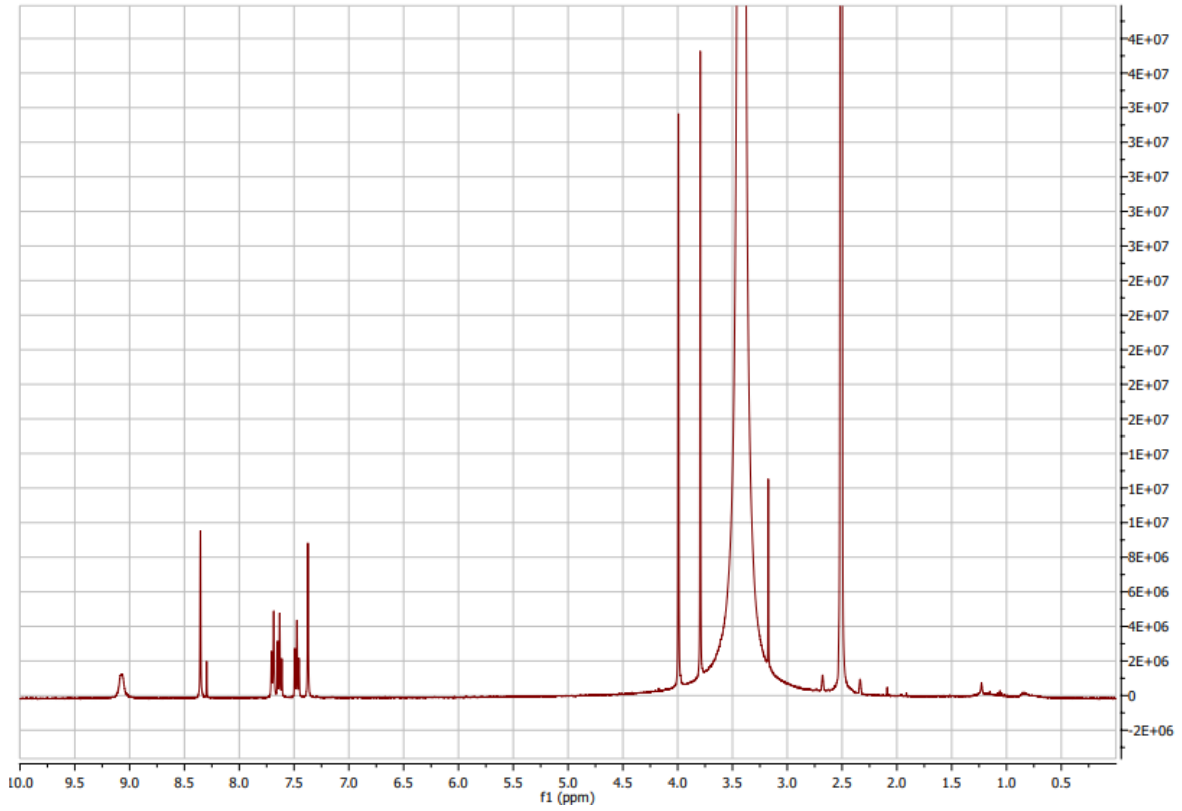


Figure 3.5.11: The ^{1}H NMR spectrum indicating the presence of GMP-23 without any contribution from EtOH.

[c] The large DMSO-d_6 peak at 3.30 ppm would overlap with one of the chemical shift signals (3.44 ppm) from EtOH. However, since the other two peaks from EtOH were not present, it is presumed that the third peak would also not be present.

3.2.5.7) Thermal gravimetric analysis (TGA) of GMP-23 form 2

The TGA curve of GMP-23 form 2 (n=2) was another technique confirming that no solvent was present, as the material was thermally stable until the onset of decomposition at 233.5 ± 2.3 ^{o}C (Figure 3.5.12). This was evident from the flat nature of the GMP-23 form 2 TGA curve until the onset of decomposition occurred. In addition, the TGA curves of GMP 23 form 2 and GMP-23 displayed the same overall thermal stability and onset of decomposition, the only difference being that the remaining mass after decomposition was slightly lower for GMP-23 (Figure 3.5.12).

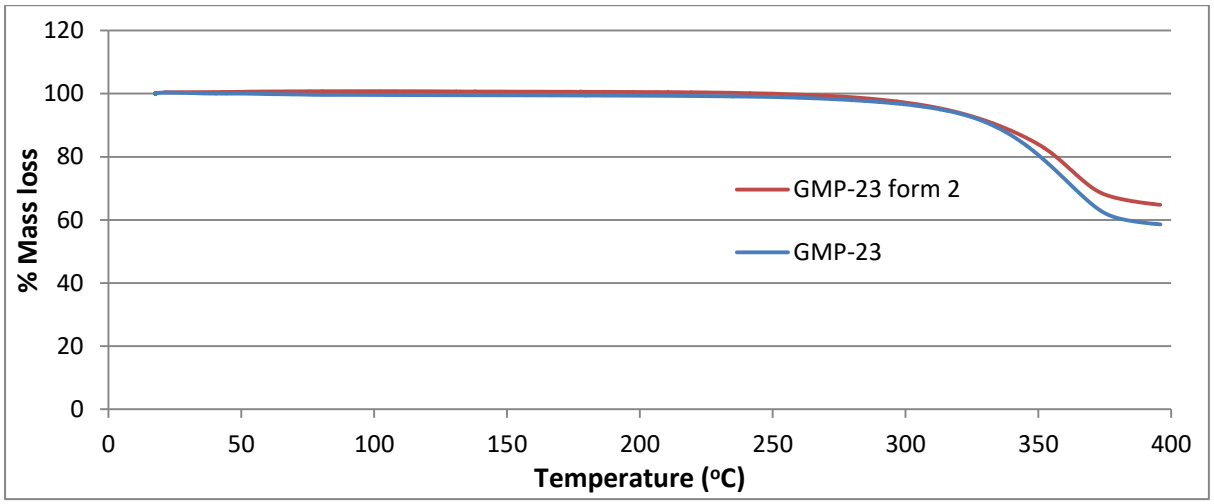


Figure 3.5.12: Representative TGA curves of GMP-23 form 2, and GMP-23.

3.2.5.8) Differential scanning calorimetry (DSC) of GMP-23 form 2

The results provided in the DSC curve of GMP-23 form 2 (n=2) (Figure 3.5.13) corresponded with the conclusions drawn from the TGA curve (described above), as the DSC curve of GMP-23 form 2 displayed no evidence of thermal activity until the expected melt before the simultaneous decomposition took place. Furthermore, it is evident that the peak temperature of the melt for GMP-23 form 2 (at 252.3 ± 0.1 ^{o}C) is slightly higher than the peak temperature of the melt for GMP-23 (at 246.8 ± 0.1 ^{o}C), thus confirming their different structural properties. Therefore, these results indicate that GMP-23 form 2 is not solvated

and it can be confidently stated that GMP-23 form 2 is indeed a polymorph or a crystal containing an alternative tautomeric form of GMP-23.

In addition, GMP-23 form 2 could be perceived to be more thermally stable than the original form of GMP-23, which displayed a very small amount of thermal activity prior to the main decomposition event. In contrast, GMP-23 form 2 displayed no initial decomposition or possible phase transitions occurring over a broad temperature range.

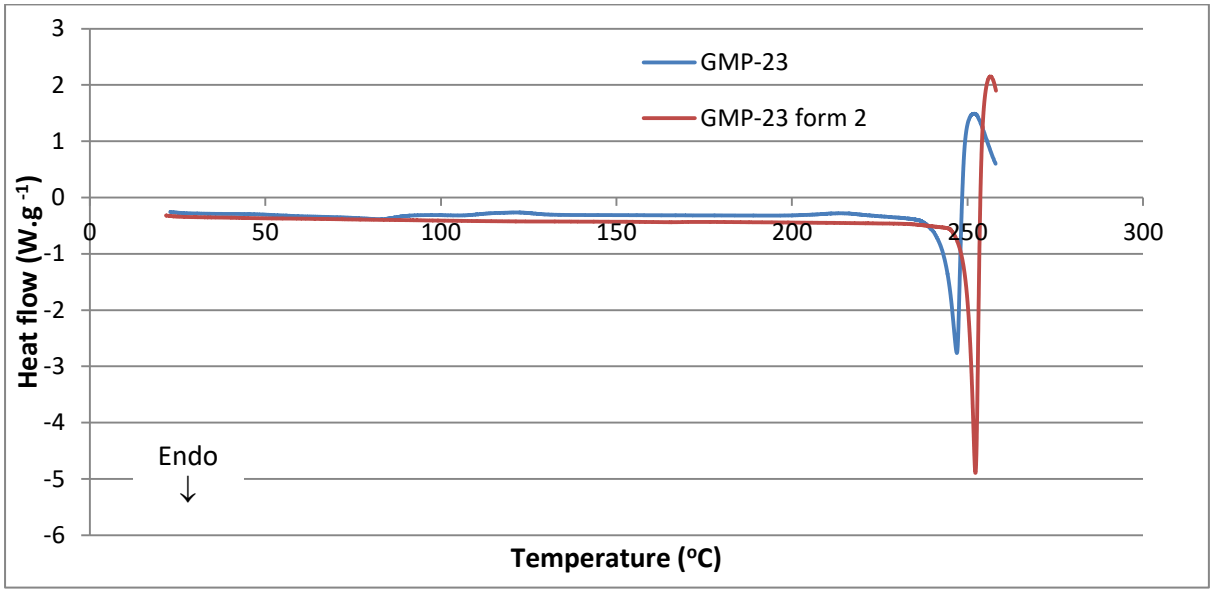


Figure 3.5.13: Representative DSC curves of GMP-23 and GMP-23 form 2.

3.2.5.9) Further experimentation and discoveries

Further experiments indicated that GMP-23 form 2 could also be produced by recrystallization from chloroform, chlorobenzene, 1,4 dioxane and THF. The comparative PXRD patterns displayed in Figure 3.5.14 indicate that the products formed have the same PXRD patterns. This signifies that the formation of GMP-23 form 2 is not restricted to EtOH only. These results also imply that there may be other solvents in addition to chloroform, chlorobenzene, 1,4 dioxane and THF that produce this particular polymorph or tautomeric form of GMP-23.

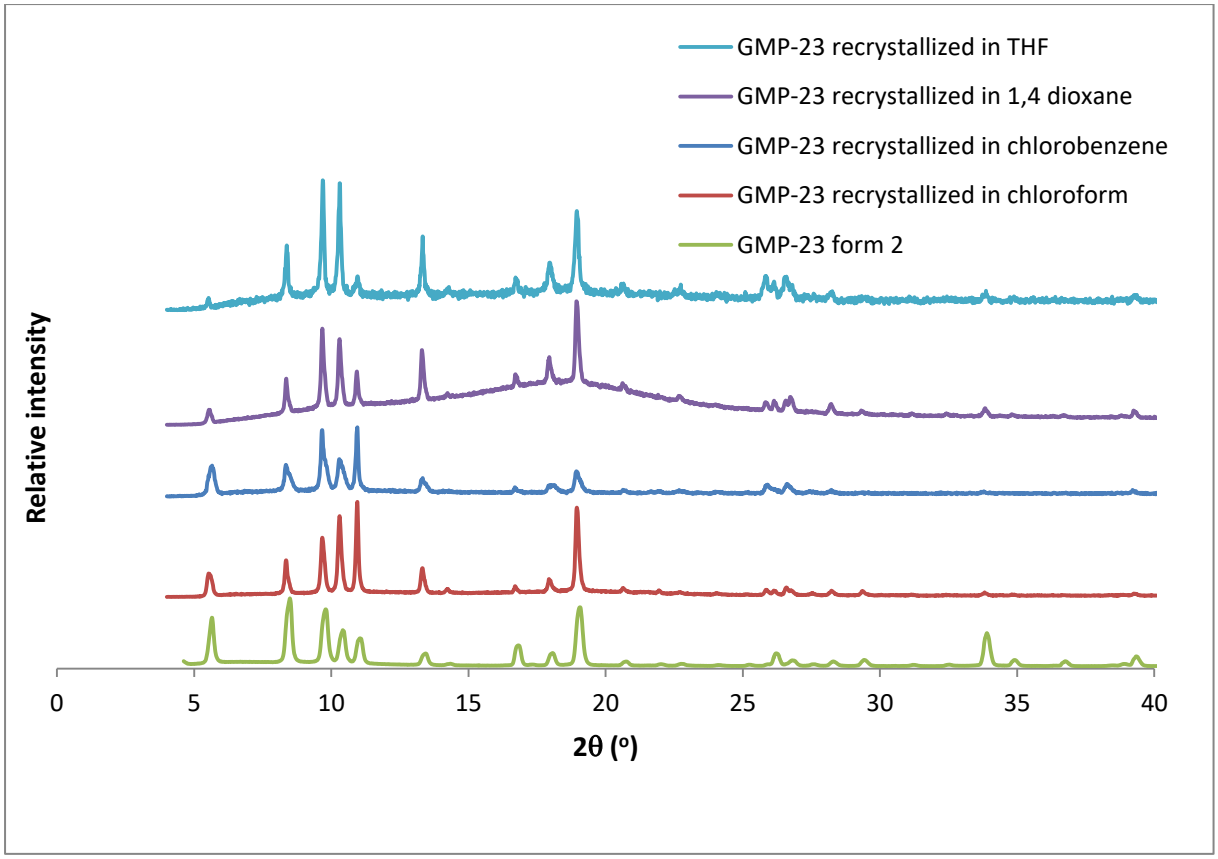


Figure 3.5.14: A series of PXRD patterns displaying GMP-23 form 2 and GMP-23, recrystallized from chloroform, chlorobenzene, 1,4 dioxane, and THF. All five patterns display the same phase.

3.2.6.1) Products generated *via* interaction between GMP compounds and fused coformers

As a final attempt to form products with the GMP active compounds and a respective coformer, a different preparative method was employed.

Masses of 10 mg for GMP-23 (0.0241 mmol), GMP-31 (0.0268 mmol) and GMP-58 (0.0282 mmol) were used, and the quantity of added coformer was calculated according to a 1:1 stoichiometric ratio between the respective GMP compound and respective coformer. The preparative method involved pre-melting the coformer in a vial on a hotplate at 140 ^{o}C and adding the respective GMP compound to this melt. Thereafter, the mixture was stirred with a sharp-tipped spatula on the hotplate for 3 minutes and left to cool thereafter.

Due to limitations regarding the available quantity of active GMP compounds, as well as the thermal properties of some coformers that sublime, only two coformers were selected (namely nicotinamide and L-malic acid). Columns two and three in Table 3.6.1 list the reagents of the six selected GMP-coformer combinations, and column four lists the code names of the final products of their interaction.

These GMP-coformer products were characterised using FT-IR and ^{1}H NMR spectroscopy, PXRD, HSM, TGA and DSC techniques. In addition, a solubility analysis was conducted in order to assess the influence that a respective coformer might have on the aqueous solubility of the GMP compounds.

Table 3.6.1: The six GMP-coformer combinations and code names of the products.

Number	Active compound	Coformer	Product code name
1	GMP-23	L-Malic acid	GMP-23-MAL
2	GMP-23	Nicotinamide	GMP-23-NIC
3	GMP-31	L-Malic acid	GMP-31-MAL
4	GMP-31	Nicotinamide	GMP-31-NIC
5	GMP-58	L-Malic acid	GMP-58-MAL
6	GMP-58	Nicotinamide	GMP-58-NIC

3.2.6.2) Fourier transform infrared (FT-IR) analysis of the GMP-coformer products

The FT-IR analysis provided the initial confirmation that interactions were taking place between the GMP active compounds and the corresponding coformers for the various GMP-coformer products. This was evident as the C=O stretching frequencies of the coformer in the GMP-coformer product were displaced to higher wavenumbers (Table 3.6.2).

An increase in the C=O stretching frequency of the GMP-coformer products indicates that the strength of the hydrogen bonding of the carbonyl group in the GMP-coformer product is less than that of the hydrogen bonding of this group in the pure coformer, thus indicating a change in molecular interactions.

With reference to Table 3.6.2, the GMP-coformer products containing L-malic acid (GMP-coformer product numbers 1, 3 and 5) all display large increases in the C=O stretching frequency, indicating a significantly lesser strength of carbonyl hydrogen bonding. In contrast, the GMP-coformer products containing nicotinamide (GMP-coformer product numbers 2, 4 and 6) display smaller shifts in the C=O stretching frequency.[a] The relevant full FT-IR spectra can be viewed in the Appendix under section 2.5, pp. 14 – 19, and an example (GMP-23-MAL) displaying a significant shift in the C=O stretching frequency is provided in Figure 3.6.1 below.

[a] It was necessary to conduct a baseline experiment for the coformers, which involved melting each coformer separately at 140 ^{o}C for 3 minutes and subsequently allowing it to cool rapidly without the presence of the GMP compound. The FT-IR spectra were recorded for these amorphous forms of L-malic acid and nicotinamide and the C=O stretching frequencies were 1691 and 1675 cm^{-1} respectively, indicating that no changes were observed in the C=O stretching frequencies of these coformers when they are exposed to this experimental method (the values are within the FT-IR instrumental error range). Thus, the C=O stretching frequency shifts of the coformers in the GMP-coformer products are solely due to the new environment created by the GMP molecules.

Table 3.6.2: The C=O stretching frequencies for the coformer and for the respective coformer in the GMP-coformer products.

Number	Active compound	Coformer	Coformer C=O stretching frequency (cm^{-1})	C=O stretching frequency of the coformer in the GMP-coformer products (cm^{-1})
1	GMP-23	L-Malic acid	1693	1711
2	GMP-23	Nicotinamide	1674	1680
3	GMP-31	L-Malic acid	1693	1727
4	GMP-31	Nicotinamide	1674	1680
5	GMP-58	L-Malic acid	1693	1718
6	GMP-58	Nicotinamide	1674	1680

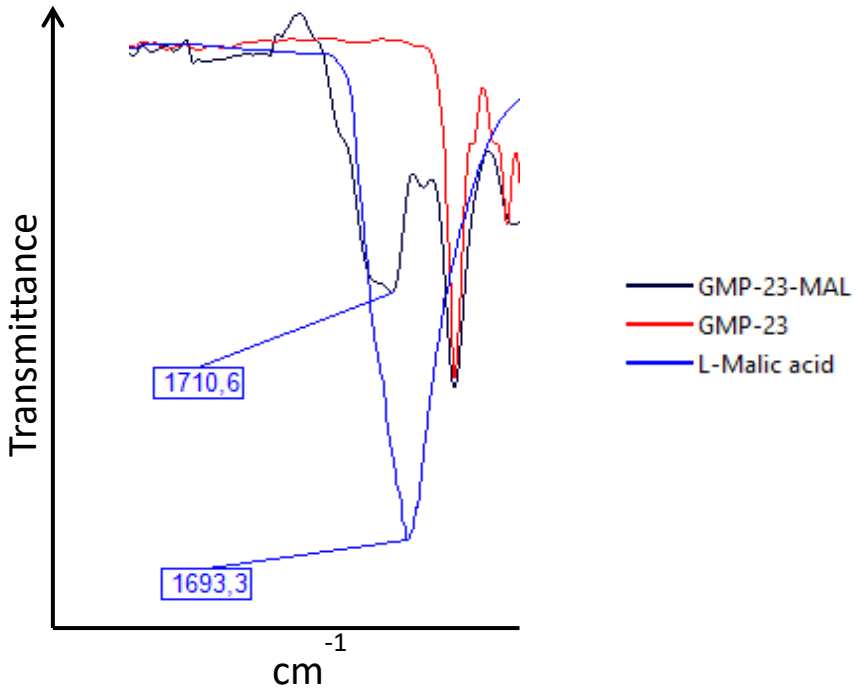


Figure 3.6.1 : FT-IR spectra of GMP-23-MAL, GMP-23 and L-malic acid.

3.2.6.3) Confirmatory ^{1}H NMR analysis

^{1}H NMR analyses were conducted to confirm that the components of the GMP-coformer products remained in a 1:1 stoichiometric ratio after the preparation at 140 ^{o}C. The results indicated that this was the case for each GMP-coformer product and that no coformer contribution had been lost after 3 minutes of preparation on the hotplate. The ^{1}H NMR spectra and assignments are available in the Appendix, section 2.6, pp. 20 – 28.

3.2.6.4) Powder X-ray diffraction (PXRD) analysis

The PXRD patterns of two of the GMP-coformer products (namely GMP-23-MAL and GMP-23-NIC) displayed new product phases, while the remaining four (namely GMP-31-MAL, GMP-31-NIC, GMP-58-MAL, and GMP-58-NIC) displayed only one component, namely the respective GMP compound.

Regarding the PXRD patterns of GMP-23-MAL and GMP-23-NIC, new product phases were evident, as they were different from the PXRD patterns of their respective starting materials (Figures 3.6.2 and 3.6.3).

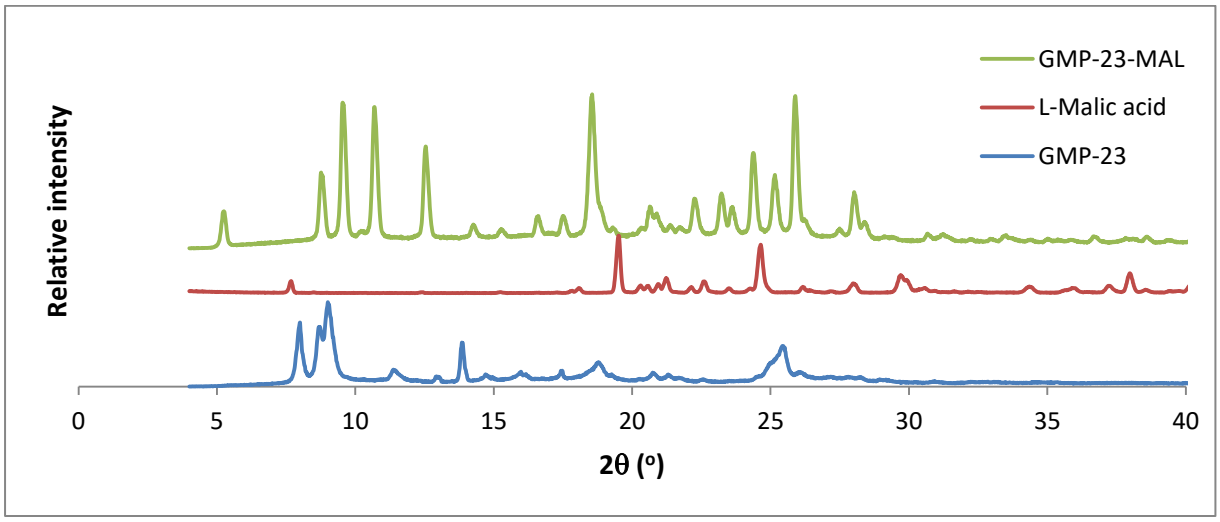


Figure 3.6.2: PXRD patterns of GMP-23, L-malic acid and GMP-23-MAL.

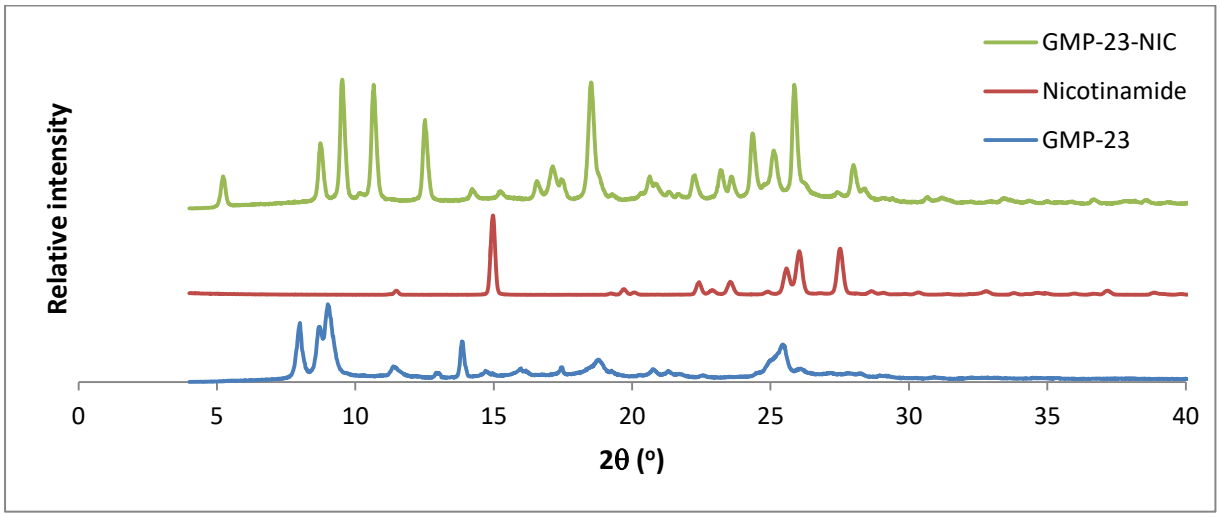


Figure 3.6.3: PXRD patterns of GMP-23, nicotinamide and GMP-23-NIC.

However, the PXRD patterns of GMP-23-MAL and GMP-23-NIC were practically identical, yet different from the PXRD pattern of GMP-23 form 2 (Figure 3.6.4). Therefore, these new product PXRD patterns could either be displaying another tautomeric form or polymorph of GMP-23 (with the coformers becoming amorphous, as observed in the other four experiments, which will be discussed below), or the formation of isostructural co-crystals. However, it is unlikely that GMP-23-MAL and GMP-23-NIC are isostructural co-crystals, as the respective coformers are structurally significantly different. Thus, the former possibility of their being present in another tautomeric form or as a polymorph of GMP-23 (with the respective coformers becoming amorphous, and thus not being observed in the PXRD pattern) is more likely.

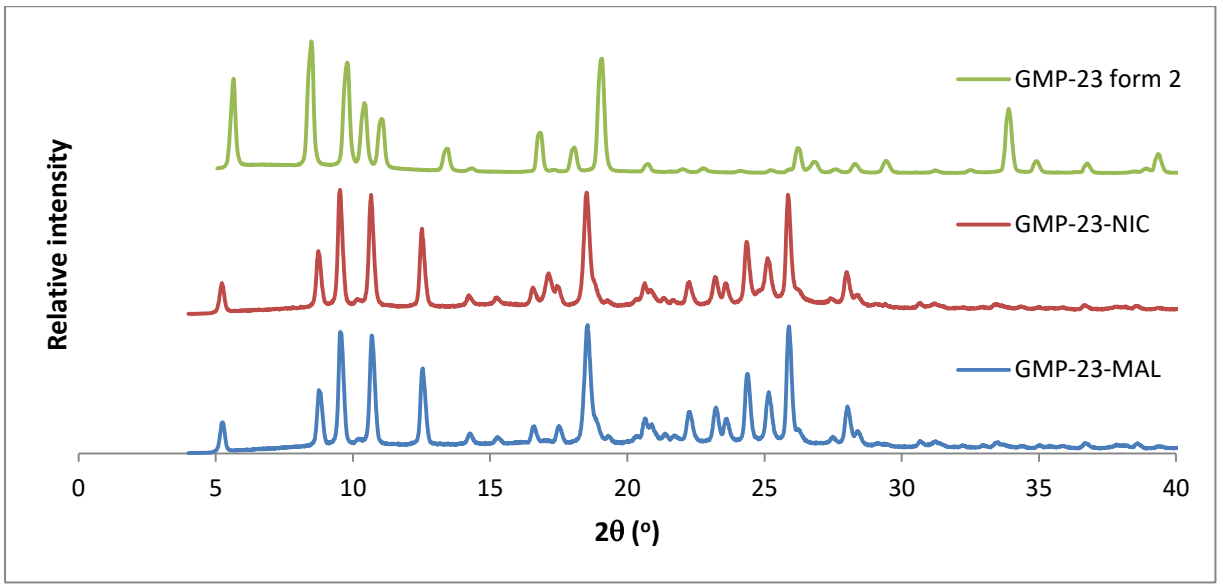


Figure 3.6.4: PXRD patterns of GMP-23-MAL, GMP-23-NIC, and GMP-23 form 2.

An additional experiment was conducted to assess whether GMP-23 can transform into another tautomeric form or polymorph when heated to 140 ^{o}C without the presence of the coformer; however, no change was observed. Therefore, the resulting tautomeric form or polymorph of GMP-23, is caused by the influence of the respective coformers and heating to 140 ^{o}C. Unfortunately, it was not possible to recrystallize GMP-23-MAL and GMP-23-NIC and replicate the PXRD patterns of these GMP-coformer products, as the components separated.

Regarding the PXRD patterns of the remaining four GMP-coformer products (namely GMP-31-MAL, GMP-31-NIC, GMP-58-MAL, and GMP-58-NIC), they displayed only one component of the two starting materials, namely the respective GMP compound. This is illustrated in the product PXRD patterns where the active GMP compound remained crystalline and the corresponding coformer became amorphous, and was thus not observed in the PXRD pattern of the respective GMP-coformer product (Figures 3.6.5 to 3.6.8). Therefore, this confirms that these GMP-coformer products are not polymorphs, co-crystals or salt products, as otherwise the product PXRD pattern would have peaks at different angular positions.

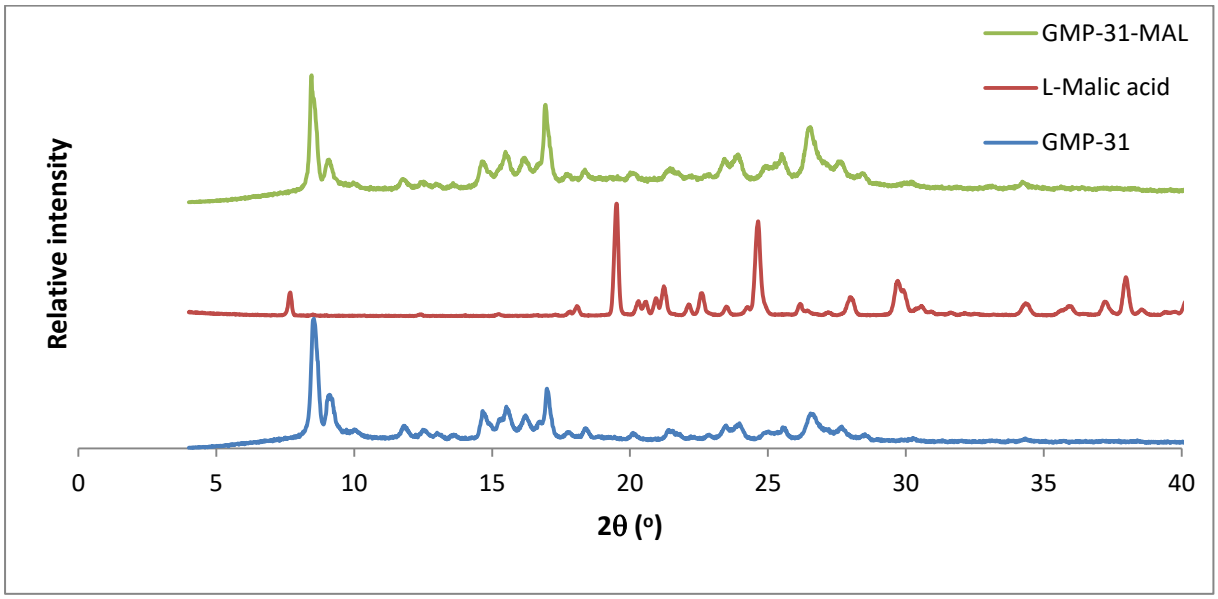


Figure 3.6.5: PXRD patterns of GMP-31, L-malic acid and GMP-31-MAL.

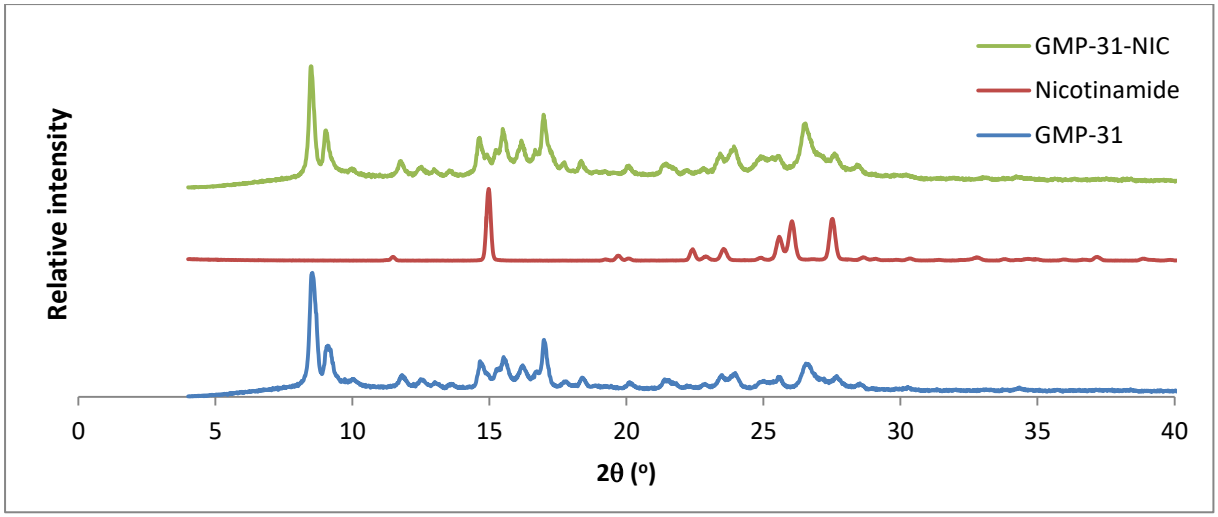


Figure 3.6.6: PXRD patterns of GMP-31, nicotinamide and GMP-31-NIC.

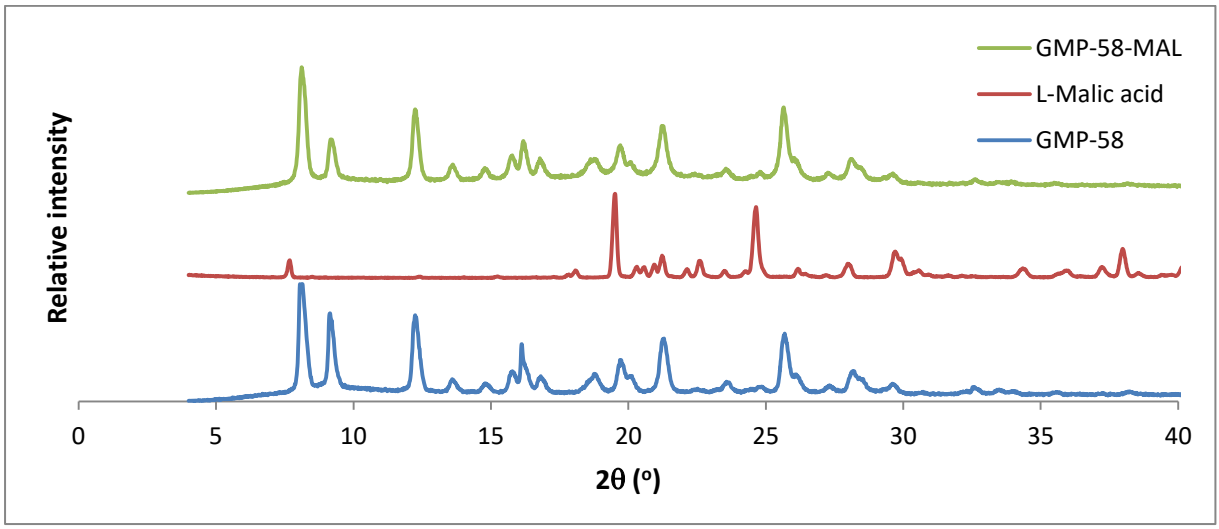


Figure 3.6.7: PXRD patterns of GMP-58, L-malic acid and GMP-58-MAL.

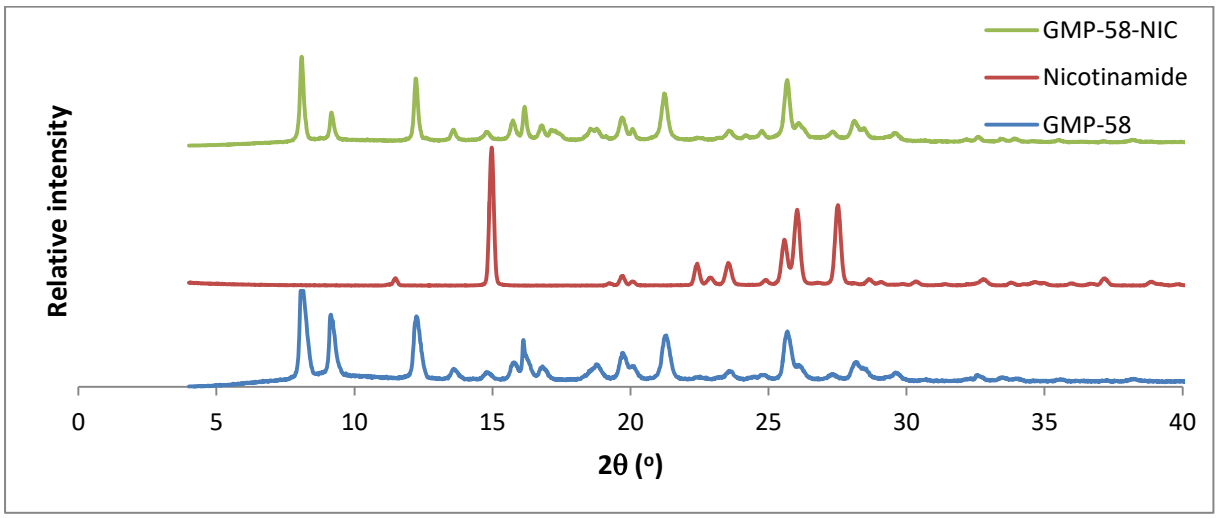


Figure 3.6.8: PXRD patterns of GMP-58, nicotinamide and GMP-58-NIC.

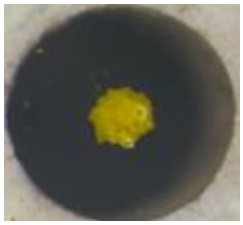
3.2.6.5) Hot stage microscopy (HSM) analysis

HSM analyses were conducted for all 6 GMP-coformer products and the observed visual thermal trends were very similar for all of them. The figures and results pertaining to these experiments are provided in the Figures 3.6.9 – 3.6.14 below, each figure representing an HSM experiment containing a series of micrographs for a particular GMP-coformer product. Each figure displays a series of micrographs which track the thermal progression of the particular GMP-coformer product and the captions below each micrograph describe the type of thermal event taking place.

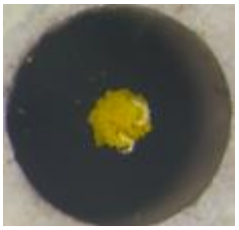
In general, all the GMP-coformer products displayed a gradual darkening in colour similar to what was described earlier in the characterisation of each pure GMP compound. This is possibly a very gradual and broad decomposition occurring slowly over a long time period while heating, and thus, it does not significantly impact on the stability of the GMP-coformer product. This is later confirmed by the TGA analyses. In addition, the HSM experiments also displayed bubbling, which was attributed to the loss of the coformer from the respective GMP-coformer products. However, two GMP-coformer products, namely GMP-23-NIC and GMP-58-NIC, did not display any bubbling activity. For these two GMP-coformer products it was presumed that the coformer was lost without bubbling, as it is later confirmed in the TGA analysis that the coformer was still removed.

Lastly, the GMP-coformer products displayed the onset of decomposition or sublimation (depending on the experiment), after the coformer had been removed (as also confirmed later by the TGA analysis). GMP-23-MAL and GMP-58-MAL both indicated that when the bubbling stopped (i.e., once the coformer had been fully removed), the onset of decomposition occurred, as the sample yellowed and browned significantly. However, with regard to GMP-31-MAL and GMP-31-NIC the onset of the decomposition bubbling merged with the end of the coformer loss. This was apparent by observing the rate of bubbling with the corresponding temperature, as well as assessing the progression of discoloration for these samples. The precise details and temperatures of these thermal events for each GMP-coformer product are provided in Figures 3.6.9 – 3.6.14 below.

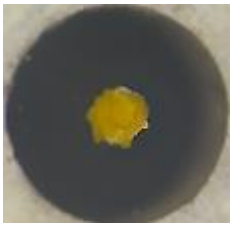
Figure 3.6.9: HSM for GMP-23-MAL.



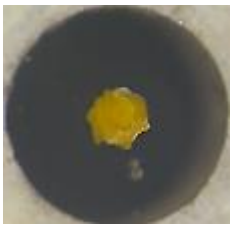
A: The initial appearance of GMP-23-MAL (25.0 °C).



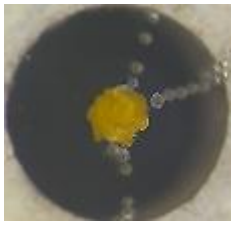
B: The onset of a very slow and broad decomposition (75.3 °C).



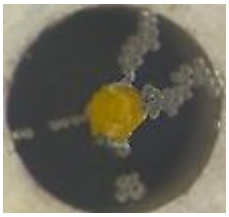
C: The continuation of the very slow and broad decomposition (185.3 °C).



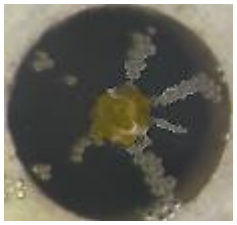
D: The onset of bubbling attributed to the loss of the coformer (186.4 °C).



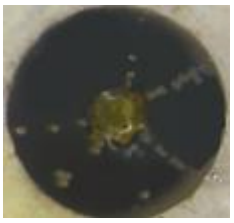
E: The bubbling increased at 194.4 °C.



F: The bubbling rate plateaued at 200.0 °C.

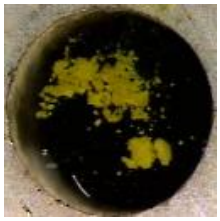


G: The bubbling rate decreased and the onset of the melt occurred (217.2 °C).

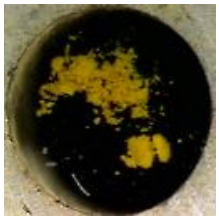


H: The bubbling stopped and the onset of decomposition occurred (233.2 °C).

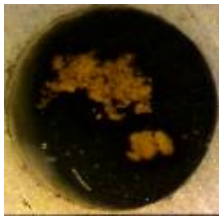
Figure 3.6.10: HSM for GMP-23-NIC.



A: The initial appearance of GMP-23-NIC (20.2 °C).



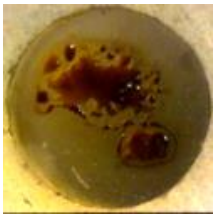
B: The onset of a very slow and broad decomposition. The sample slowly darkened in colour (150.1 °C).



C: The onset of the melt with a simultaneous decomposition thereafter (219.4 °C).

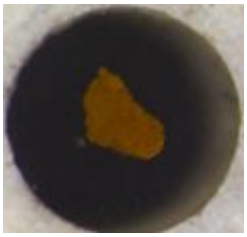


D: The sample was completely melted. Decomposition continued (247.4 °C).

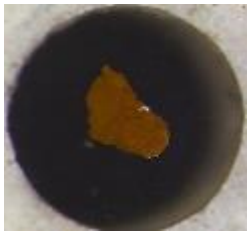


E: Significant decomposition of the melt (252.6 °C).

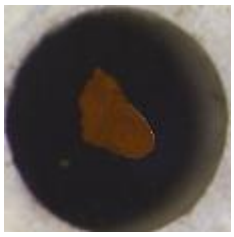
Figure 3.6.11: HSM for GMP-31-MAL.



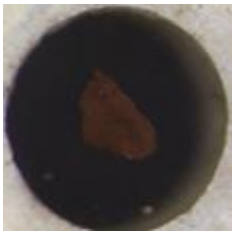
A: The initial appearance of GMP-31-MAL (35.0 °C).



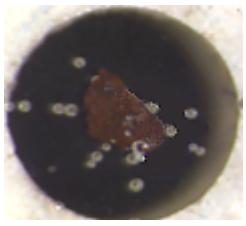
B: The onset of a very slow and broad decomposition (85.1 °C).



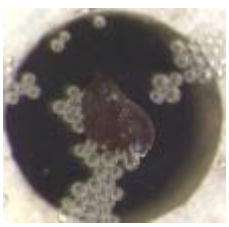
C: The continuation of the very slow and broad decomposition (115.2 °C).



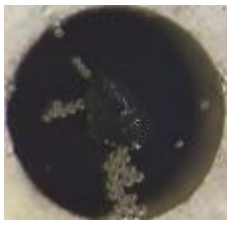
D: The onset of coformer loss. The bubbling began at 157.1 °C.



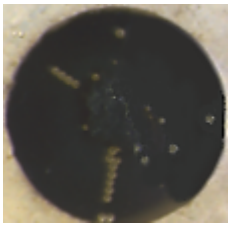
E: The bubbling increased slightly at 180.4 °C.



F: The bubbling rate became vigorous at 200.0 °C.

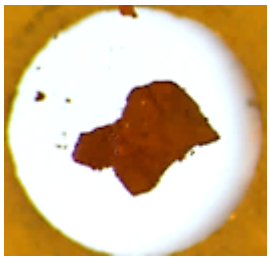


G: The bubbling rate decreased and a more significant decomposition along with sublimation was apparent (245.2 °C).

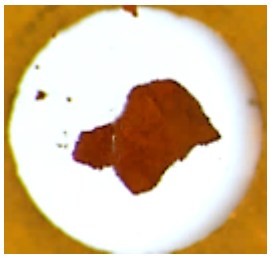


H: The bubbling ceased (294.2 °C).

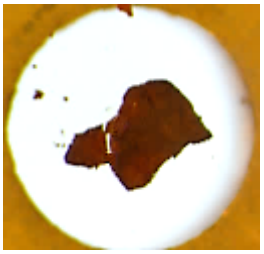
Figure 3.6.12: HSM for GMP-31-NIC.



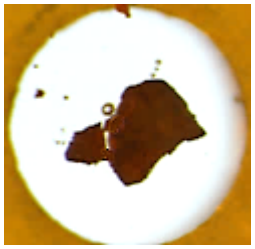
A: The Initial appearance of GMP-31-NIC (31.1 °C).



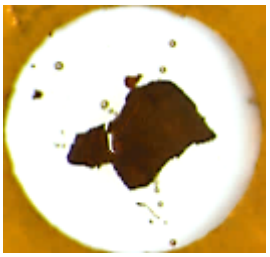
B: The onset of a very slow and broad decomposition. Hardly discernible darkening of the sample (105.0 °C).



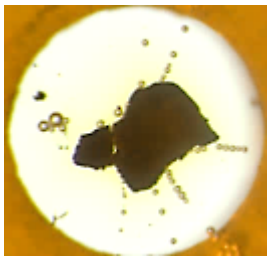
C: The continuation of the slow and broad decomposition (185.3 °C).



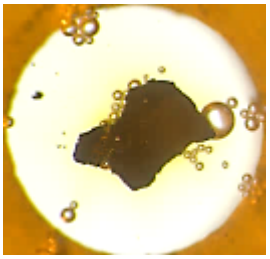
D: The onset of bubbling, as well as the very slow onset of sublimation. Both are possibly attributed to the loss of the coformer (193.4 °C).



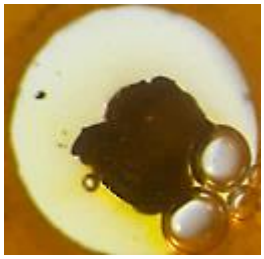
E: The bubbling rate increased along with further sublimation (235.7 °C).



F: The bubbling maintained a fast rate. (283.3 °C).

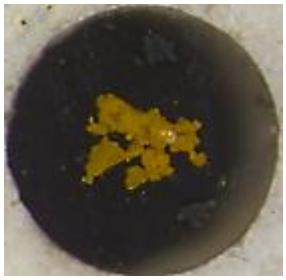


G: The onset of the decomposition melt, with the production of large decomposition bubbles (311.0 °C).

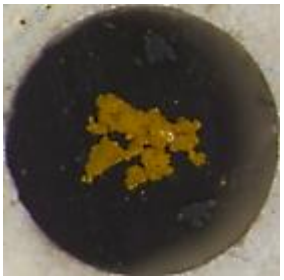


H: The continuation of the decomposition melt (321.4 °C).

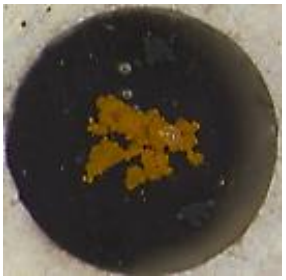
Figure 3.6.13: HSM for GMP-58-MAL.



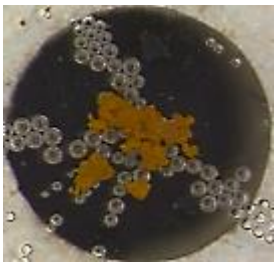
A: The initial appearance of GMP-58-MAL (30.1 °C).



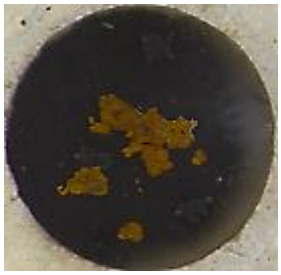
B: The onset of a very slow and broad decomposition. Hardly discernible darkening of the sample (90.0 °C).



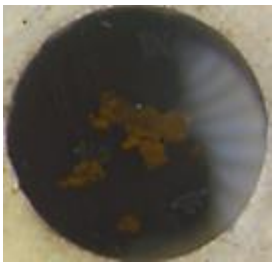
C: The onset of coformer loss (attributed to the bubbling at 184.2 °C).



D: The bubbling rate increased until it reached a peak at 209.4 °C.



E: The bubbling ceased and the onset of sublimation and decomposition began (253.2 °C).

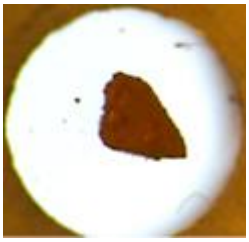


F: The continuation of the decomposition and sublimation, accompanied by the onset of a partial melt (305.2 °C).

Figure 3.6.14: HSM for GMP-58-NIC.



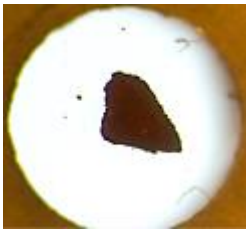
A: The initial appearance of GMP-58-NIC (35.0 °C).



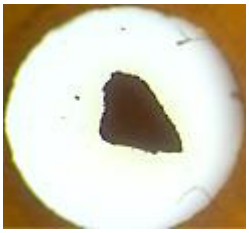
B: The onset of a very slow and broad decomposition. (sample began darkening at 105.3 °C).



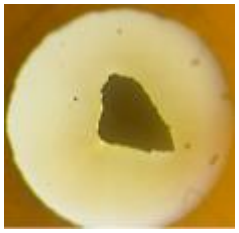
C: The continuation of the slow and broad decomposition (155.1 °C).



D: The onset of more significant decomposition and very subtle sublimation (255.2 °C).



E: The continuation of the decomposition and sublimation (275.0 °C).



F: The decomposition and sublimation continued (369.2 °C).

3.2.6.6) Thermal gravimetric analysis (TGA)

In general, the TGA curves of the six GMP-coformer products (n=2 for each sample), all displayed very similar thermal trends. These trends included a small amount of initial mass loss (owing to the fact that the GMP-coformer products appeared to be hygroscopic), the loss of the coformer, and the subsequent decomposition and sublimation (depending on the experiment). In addition, with reference to the HSM experiments, the TGA curves do not indicate any significant impact in the thermal stability of the GMP-coformer products as a result of the very gradual and broad decomposition occurring over a long time period. Any mass loss contributions from this thermal event observed in all the HSM experiments is seemingly negligible and thus not evident in the TGA curves. A more specific account for each GMP-coformer product is provided below.

Regarding the TGA curves for the GMP-coformer products GMP-23-MAL and GMP-23-NIC (Figures 3.6.15 and 3.6.16), both displayed a certain amount of dehydration at the start of the TGA curves amounting to 4.1 ± 0.1% and 1.0 ± 0.5% for GMP-23-MAL and GMP-23-NIC respectively. This was as a consequence of the GMP-coformer products possibly being hygroscopic. The onset of the loss of the coformers occurred at 106.2 ± 0.6 °C for GMP-23-MAL and amounted to 23.5 ± 0.4%, while for GMP-23-NIC, it occurred at 118.1 ± 1.9 °C with a mass loss of 22.1 ± 0.6%. These percentage mass losses corresponded to the theoretical values for 1:1 stoichiometric component contributions, namely 24.4% and 22.8% respectively.

The decomposition occurred after the full contribution of the coformer had been removed from both GMP-coformer products, and took place as a pseudo two-step process (as indicated in the dTGA curves). An initial slow decomposition occurred at 234.4 ± 0.2 °C for GMP-23-MAL and 236.5 ± 0.4 °C for GMP-23-NIC (both of which correlated within reasonable agreement of their respective HSM analyses). These initial decompositions were short-lived and were superseded by a more significant decomposition which occurred at 297.6 ± 0.6 °C for GMP-23-MAL and at 284.9 ± 1.1 °C for GMP-23-NIC.

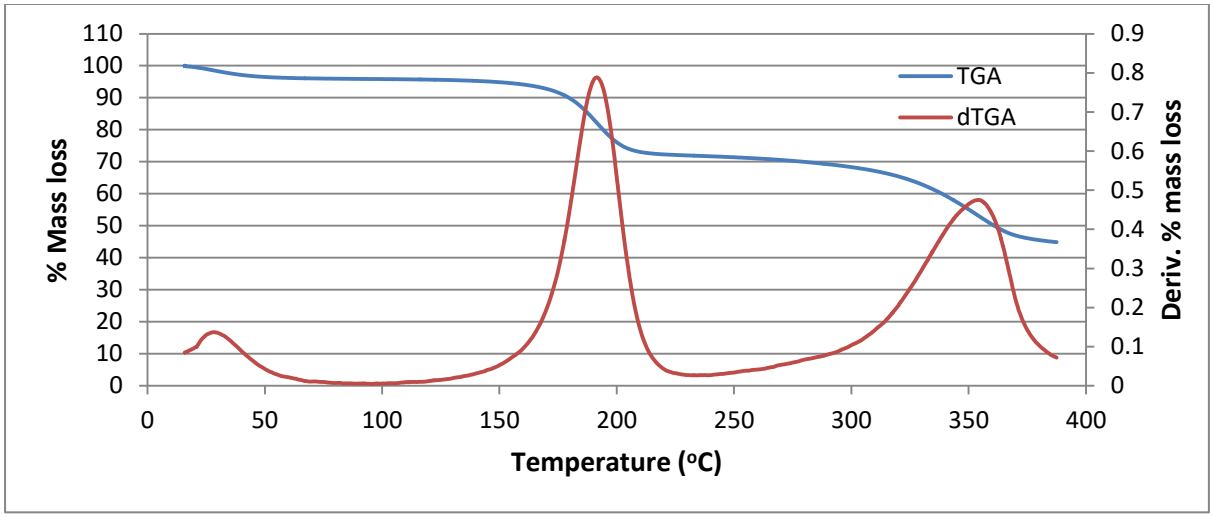


Figure 3.6.15: Representative TGA and dTGA curves for GMP-23-MAL.

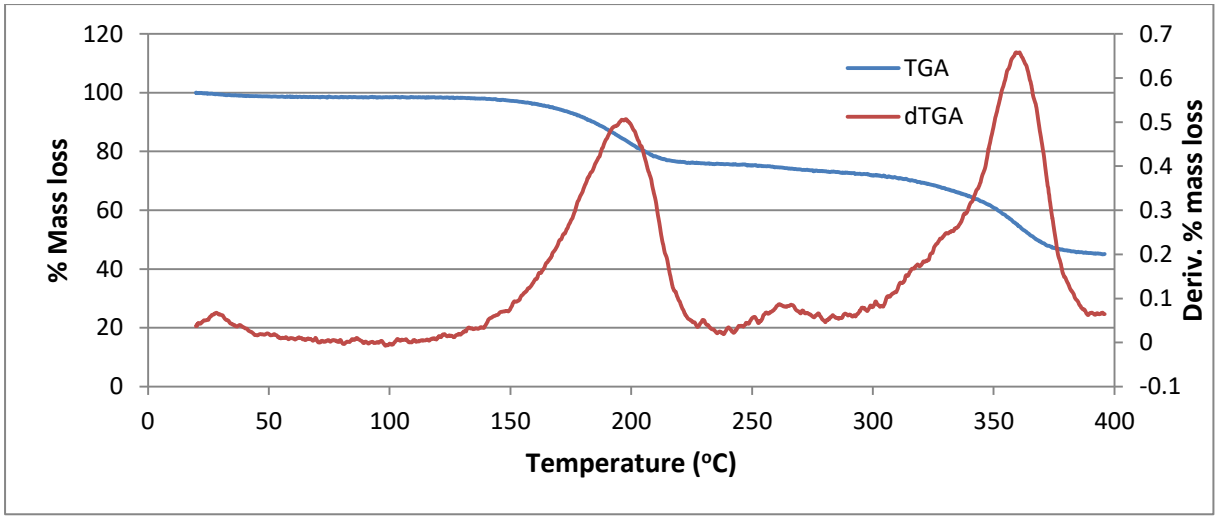


Figure 3.6.16: Representative TGA and dTGA curves for GMP-23-NIC.

The TGA curves of GMP-31-MAL and GMP-31-NIC, as represented in Figures 3.6.17 and 3.6.18, both displayed complementary thermal trends and were very similar to the TGA results obtained for GMP-23-MAL and GMP-23-NIC. The only exception was that the decompositions were a single-step process for GMP-31-MAL and GMP-31-NIC, as observed in their respective dTGA curves.

The percentage mass loss for the dehydration that occurred at the beginning of the two TGA curves was 5.3 ± 0.9% for GMP-31-MAL, and 1.4 ± 0.1% for GMP-31-NIC. The onset of the loss of the coformer took place at 105.4 ± 1.0 °C and amounted to 22.4 ± 0.7% for GMP-31-MAL, and for GMP-31-NIC the onset was at 119.3 ± 0.8 °C and amounted to 23.2 ± 0.5%. These percentage mass loss values of the respective coformers corresponded fairly reasonably to the theoretical values for a 1:1 stoichiometric loss of L-malic acid (26.4%) and nicotinamide (24.6%) from these GMP-coformer products. The onsets of decomposition (and simultaneous sublimation) occurred after the coformer was removed in single-step processes at temperatures of 252.8 ± 0.4 °C and 244.62 ± 7.8 °C for GMP-31-MAL and GMP-31-NIC respectively.

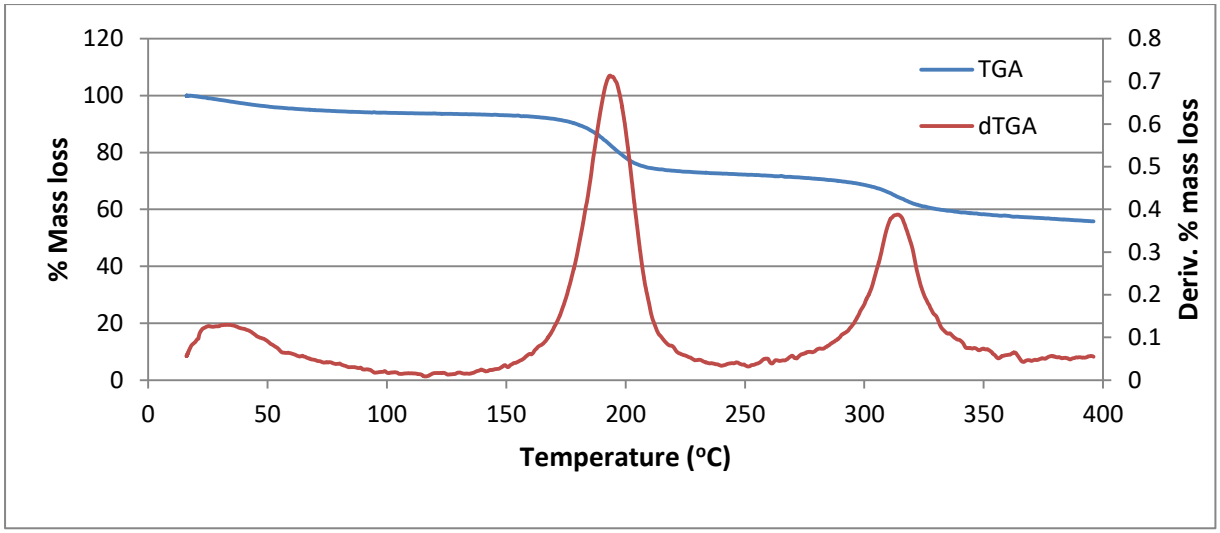


Figure 3.6.17: Representative TGA and dTGA curves for GMP-31-MAL.

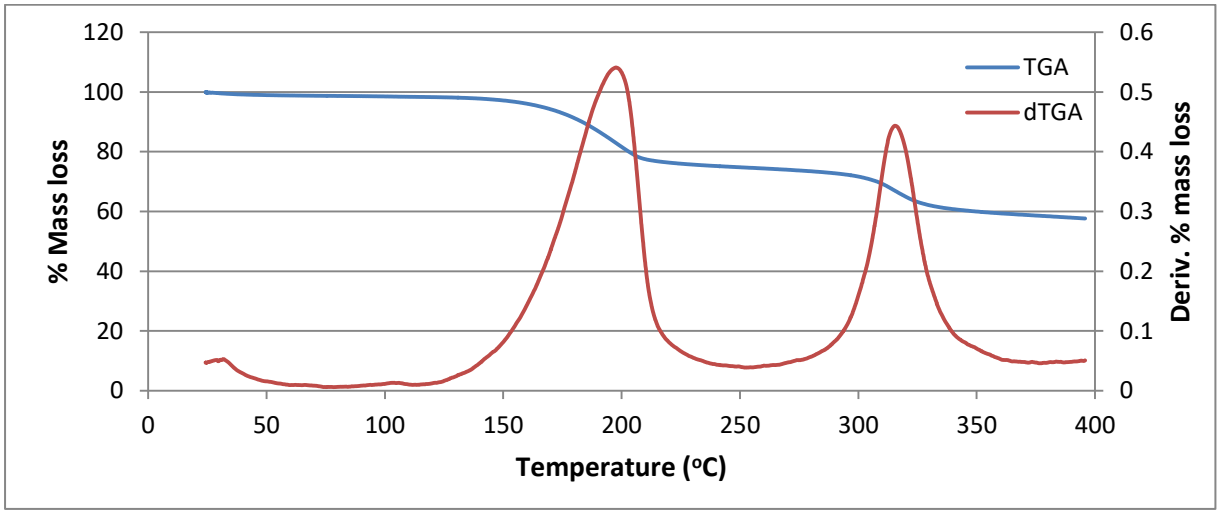


Figure 3.6.18: Representative TGA and dTGA curves for GMP-31-NIC.

In addition, the TGA results of GMP-58-MAL and GMP-58-NIC, as depicted in Figures 3.6.19 and 3.6.20, mirrored the thermal trends of GMP-31-MAL and GMP-31-NIC. Consequently, the specific values for the thermal trends of GMP-58-MAL and GMP-58-NIC are as follows: the dehydration occurred at the start of the TGA curves with a mass loss of 4.7 $\pm$ 0.6% for GMP-58-MAL, and 2.3 $\pm$ 0.7% for GMP-58-NIC; the onset of the coformer loss took place at 112.0 $\pm$ 0.7 ^{o}C (with a mass loss of 25.4 $\pm$ 0.1%) for GMP-58-MAL; and at 108.2 $\pm$ 0.2 ^{o}C (with a mass loss of 23.5 $\pm$ 0.2%) for GMP-58-NIC. The percentage mass losses of the coformers in GMP-58-MAL and GMP-58-NIC corresponded within reason to the theoretical mass losses

for 1:1 stoichiometric samples, namely 27.5% for L-malic acid and 25.6% for nicotinamide. Lastly, the onset of decomposition (and simultaneous sublimation) occurred as a single-step process at 262.2 ± 1.5 °C for GMP-58-MAL, and 262.4 ± 4.4 °C for GMP-58-NIC.

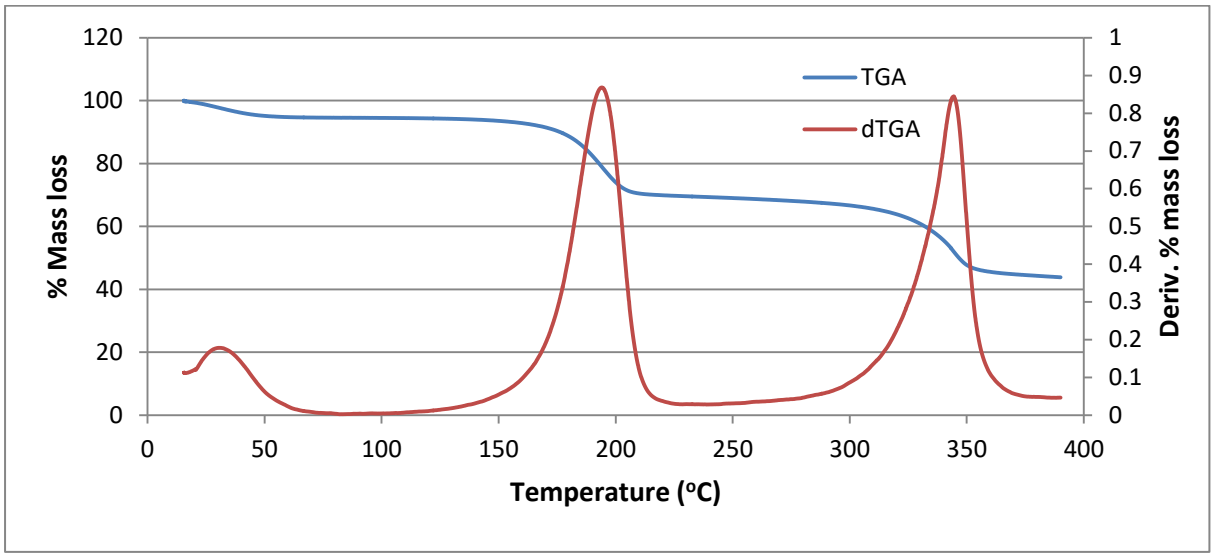


Figure 3.6.19: Representative TGA and dTGA curves for GMP-58-MAL.

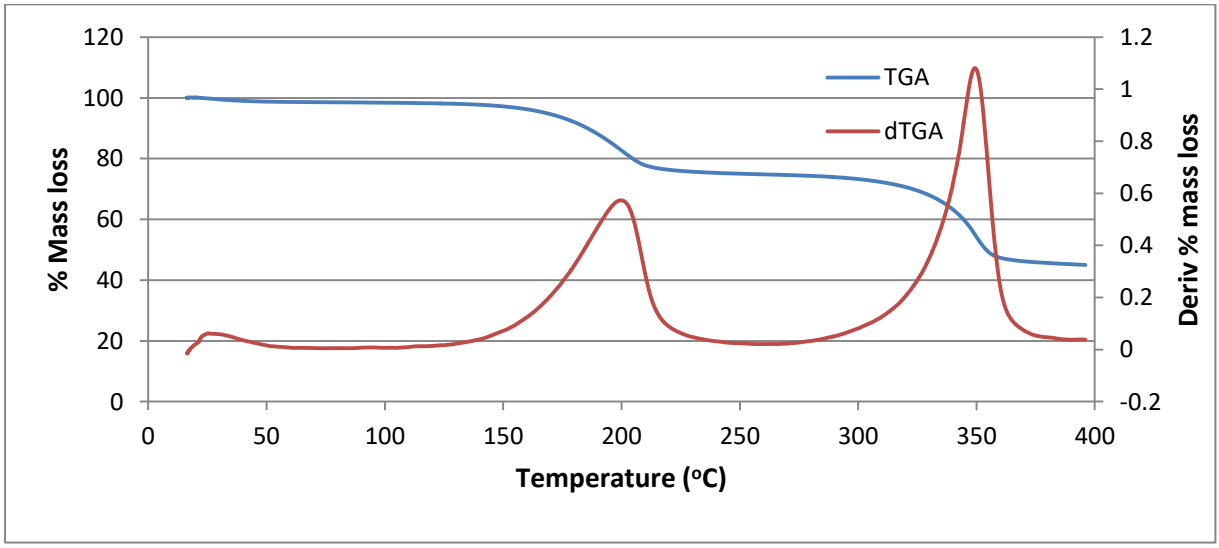


Figure 3.6.20: Representative TGA and dTGA curves for GMP-58-NIC.

3.2.6.7) Differential scanning calorimetry (DSC) analysis

The results of the DSC analyses of the six GMP-coformer products complemented the thermal trends observed in both the TGA and HSM experiments in terms of an initial dehydration taking place and the coformer being removed prior to the main decomposition or sublimation taking place (depending on the experiment). In addition, other thermal characteristics were also observed, which were previously not seen in either the HSM or TGA results. Figures 3.6.21 – 3.6.26 display the respective DSC curves and a brief description for each is provided below.

For all the experiments, the decomposition thermal event is not captured in the DSC curves, as the instrument was stopped prior to (or at) the start of the decomposition of the GMP-coformer product. This was done to protect the instrument from the gases caused by the decomposition of the GMP-coformer products.

The DSC curve of GMP-23-MAL (n=2) initially displayed two very small endothermic peaks with peak temperatures of 69.4 $\pm$ 0.3 ^{o}C and 91.2 $\pm$ 0.2 ^{o}C (Figure 3.6.21). These endothermic peaks could be attributed to the dehydration of the GMP-coformer product, as well as from a small amount of negligible decomposition of GMP-23 (as previously described during the characterisation of GMP-23). In addition, a slightly larger endothermic peak with an onset temperature of 114.6 $\pm$ 0.7 ^{o}C (peak at 122.8 $\pm$ 0.6 ^{o}C), occurred just before a very broad endothermic event (onset = 162.1 $\pm$ 0.5 ^{o}C, peak = 216.6 $\pm$ 0.1 ^{o}C).

It could be speculated that the endothermic peak at 114.6 $\pm$ 0.7 ^{o}C is a phase transition, which would require verification with variable temperature PXRD. However, owing to paucity of starting material, it was not possible to conduct this experiment. Thereafter the coformer is lost as represented by the broad endothermic peak described above, and complemented by the overlaid TGA curve. Lastly, the onset of decomposition occurred immediately after the coformer was lost.

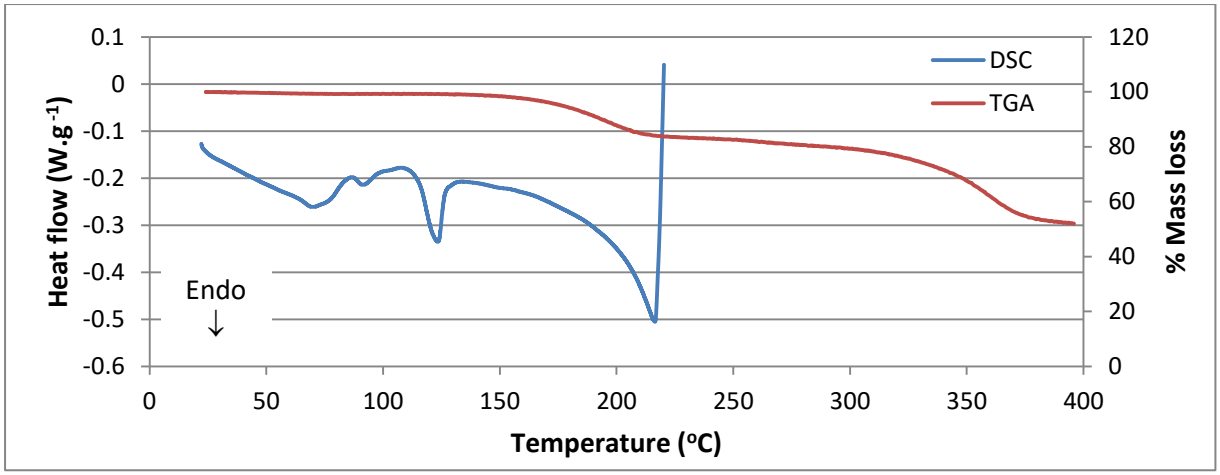


Figure 3.6.21: A representative DSC curve for GMP-23-MAL, with the respective TGA curve as a reference.

The DSC curve of GMP-23-NIC (n=2) in Figure 3.6.22 also displayed the slight dehydration (endothermic peak temperature at 65.8 ± 0.5 °C); however, thereafter a sharp endothermic peak occurred, followed by an exothermic peak and another endothermic peak consecutively, with peak temperatures of 108.6 ± 0.1 °C, 112.7 ± 0.3 °C and 127.8 ± 0.1 °C respectively. These consecutive thermal events represented the melt of nicotinamide form 3, which was immediately followed by a recrystallization to form 1, and thereafter the melt of form 1 occurred.[10] The nicotinamide in GMP-23-NIC at ambient temperatures was amorphous (as confirmed in the PXRD analysis in Figure 3.6.3) and thus it is expected that a glass transition would have occurred when the sample was heated, which transformed amorphous nicotinamide into polymorph 3. This glass transition appeared to be masked by the slight dehydration of the sample and thus was not observed in the DSC curve. The endothermic peaks that corresponded to the melting temperatures of the polymorphic forms 1 and 3 of nicotinamide were confirmed by the literature values, which are 128.8 – 129.3 °C and 108.9 °C respectively.[10] Immediately after the melt of polymorph 1, the loss of the coformer occurred (as also reflected in the TGA curve) with an onset temperature of 146.2 ± 0.6 °C and an endothermic peak temperature of 210.1 ± 0.3 °C, after which the decomposition commenced (not recorded in the DSC curve).

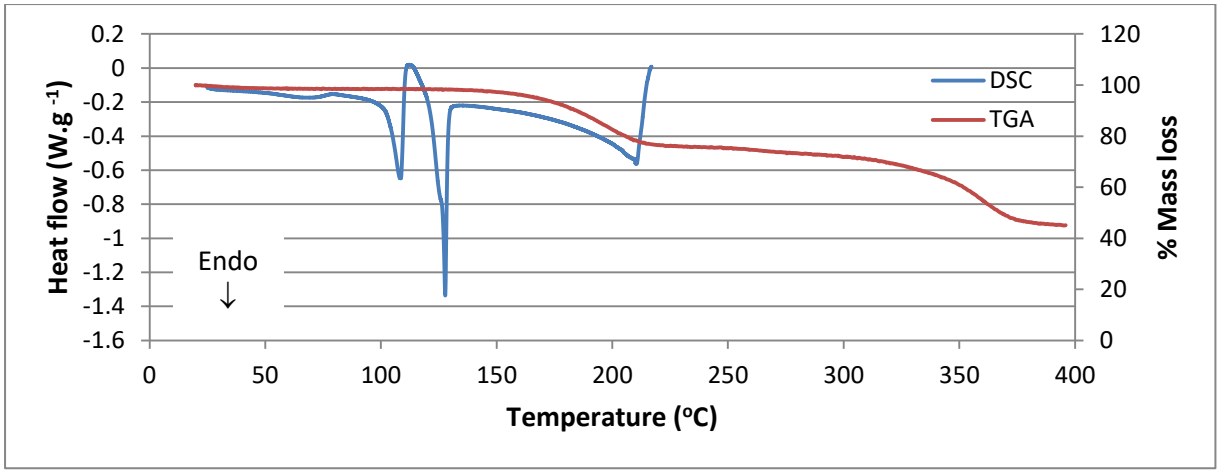


Figure 3.6.22: A representative DSC curve for GMP-23-NIC, with the respective TGA curve as a reference.

The DSC curve of GMP-31-MAL (n=2) displayed three endothermic thermal events (Figure 3.6.23). The first broad endothermic event had a peak temperature of 70.2 ± 1.0 and represented the dehydration of the hygroscopic GMP-coformer product. Thereafter, with an onset temperature of 102.9 ± 1.7 °C, an additional broad composite endothermic peak occurred, which could possibly represent a very small amount of initial decomposition taking place. Directly afterwards, and at an onset temperature of 174.3 ± 0.4 °C and peak temperature of 192.2 ± 1.0 °C, the loss of the coformer occurred, as represented by the large endothermic peak. This is also reflected in the overlaid TGA curve. The DSC curve also suggested that the decomposition took place a while after the coformer had been removed and not directly afterwards, as represented by the relatively flat baseline after the large endothermic event.

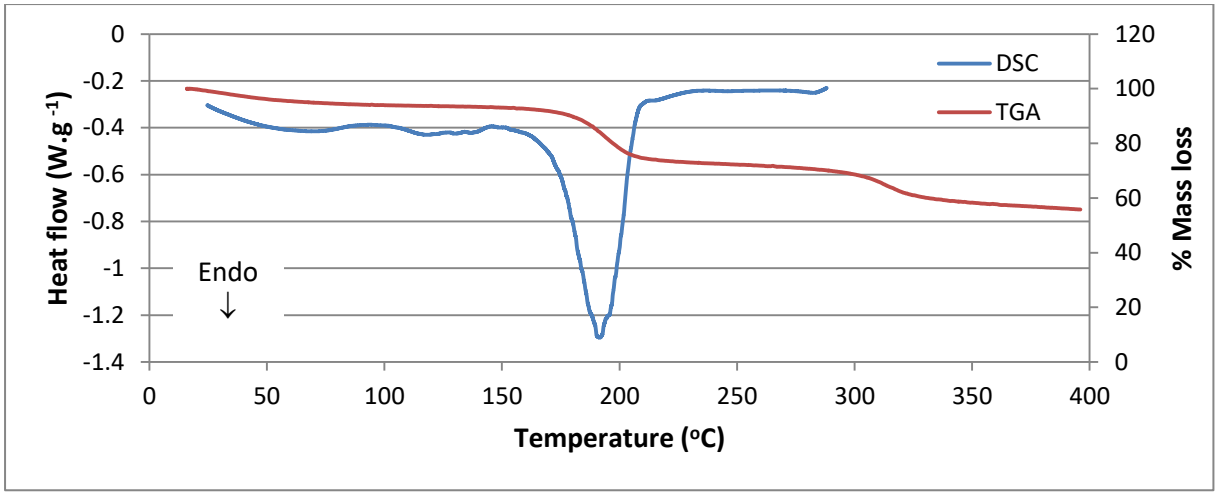


Figure 3.6.23: A representative DSC curve for GMP-31-MAL, with the respective TGA curve as a reference.

The DSC curve of GMP-31-NIC (n=2), as represented in Figure 3.6.24, displayed a very similar thermal trend to the DSC curve of GMP-23-NIC (Figure 3.6.22). Similarly, the small endothermic peak with a peak temperature of 60.5 ± 1.0 °C represented the dehydration of the hygroscopic GMP-coformer product. Thereafter, a similar pattern of consecutive endothermic, exothermic and endothermic peaks, with peaks at 106.1 ± 0.1 °C, 110.0 ± 0.2 °C, and 126.4 ± 0.1 °C, represented the melt of nicotinamide form 3, its recrystallization to form 1, and the subsequent melt of nicotinamide form 1. The successive broad endothermic peak signified the loss of nicotinamide with an onset temperature of 163.3 ± 2.3 °C and peak temperature of 237.0 ± 2.1 °C. Furthermore, this DSC curve indicated that the decomposition did not commence directly after the loss of the coformer, representing the main difference between this DSC curve and that of GMP-23-NIC.

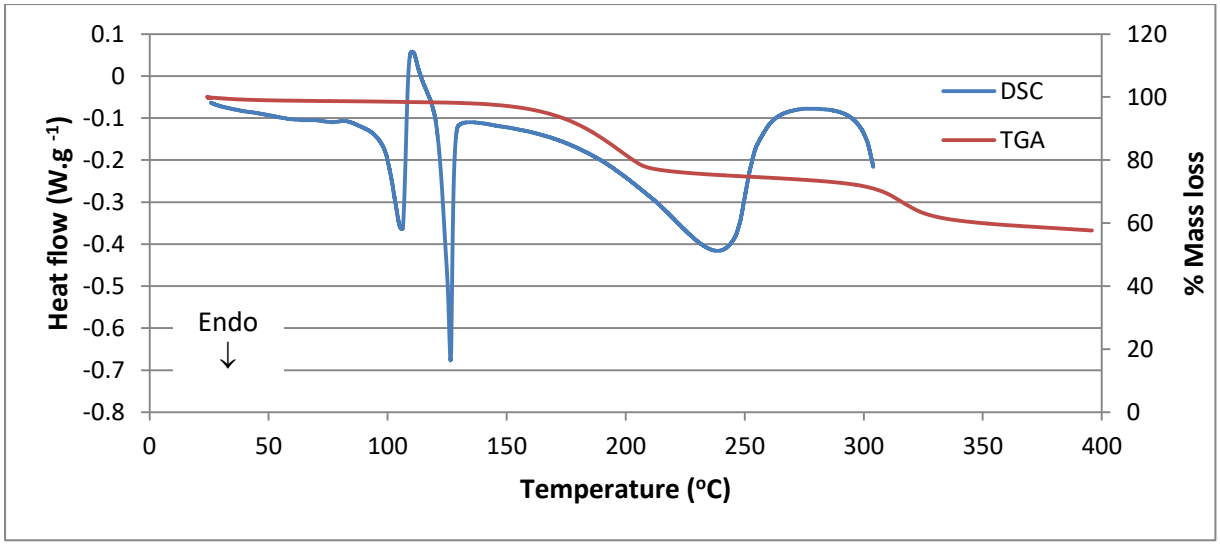


Figure 3.6.24: A representative DSC curve for GMP-31-NIC, along with the respective TGA curve as a reference.

The DSC curve of GMP-58-MAL (n=2) illustrated only two endothermic thermal events (Figure 3.6.25), representing the dehydration of the GMP-coformer product and the loss of the coformer. The dehydration endothermic peak occurred at 59.4 ± 0.7 °C and is the largest of these GMP-coformer products, thus suggesting that GMP-58-MAL is the most hygroscopic. This is also evident from the overlaid TGA curve. Lastly, the loss of the coformer had an onset temperature of 176.6 ± 0.7 °C and peak temperature of 198.9 ± 0.2 °C, correlating with the overlaid TGA curve.

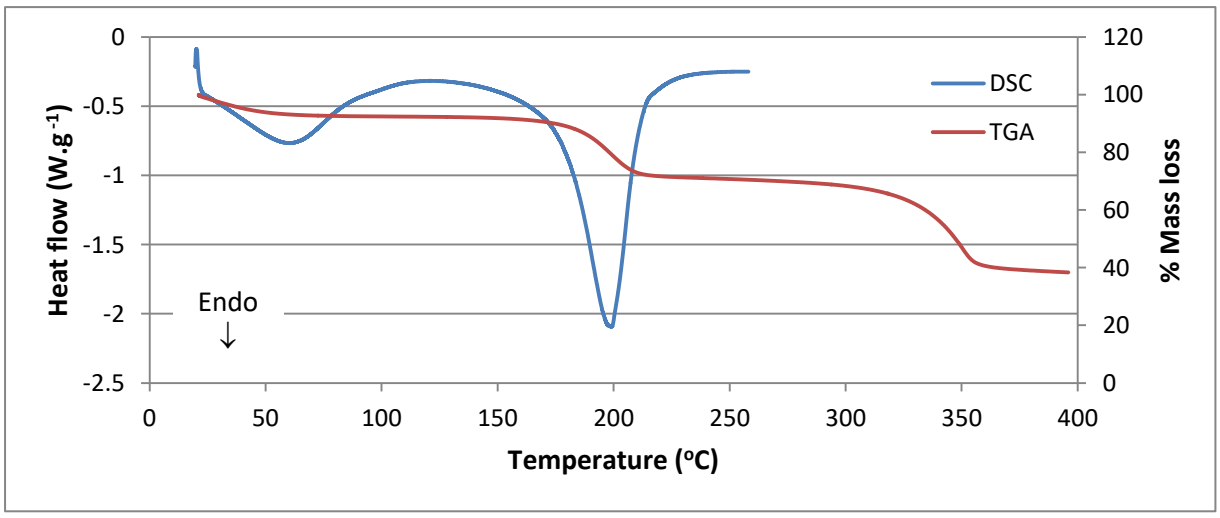


Figure 3.6.25: A representative DSC curve for GMP-58-MAL, with the respective TGA curve as a reference.

The DSC curve of GMP-58-NIC (n=2) as depicted in Figure 3.6.26, displayed different thermal trends to GMP-23-NIC and GMP-31-NIC. Initially, a small amount of dehydration was observed at an endothermic peak temperature of 67.5 ± 3.9 °C. Thereafter, nicotinamide melted as form 1 with a sharp endothermic peak temperature of 122.5 ± 1.4 °C. In contrast to the behaviour of GMP-23-NIC and GMP-31-NIC, heating of GMP-58-NIC did not result in nicotinamide transforming to form 3, and instead it transformed from amorphous nicotinamide to form 1 in this GMP-coformer product. However, the melt of nicotinamide form 1 was induced slightly earlier (literature value: 128.8 – 129.3 °C, experimental value: 122.5 ± 1.4 °C), possibly due to the presence of the GMP component. Lastly, nicotinamide was thereafter lost, as represented by the broad endothermic peak (onset temperature = 167.8 ± 1.4 °C, peak temperature = 239.8 ± 2.0 °C).

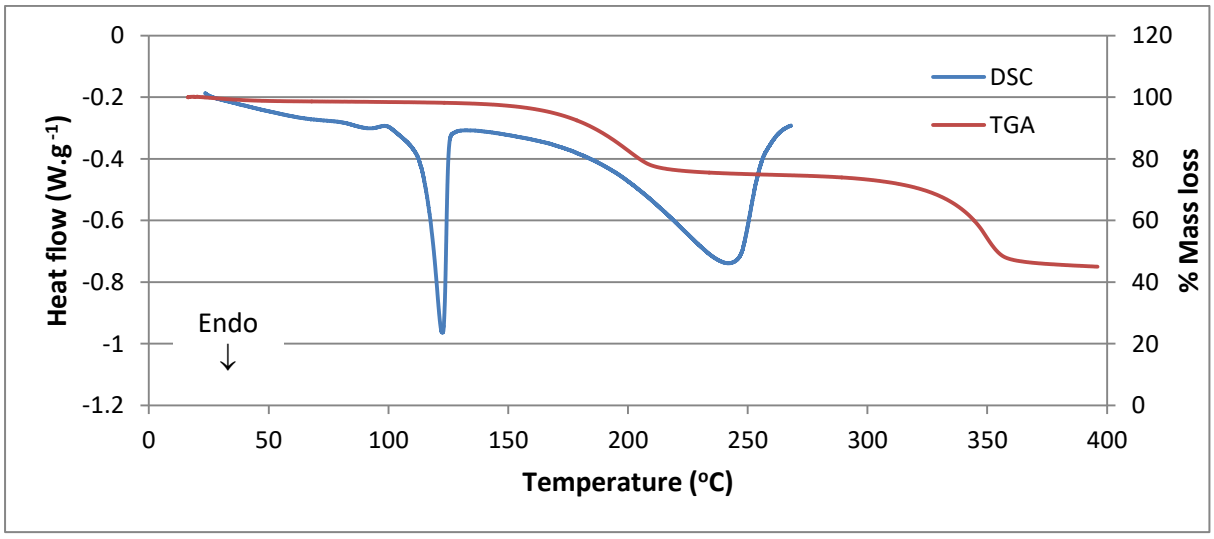


Figure 3.6.26: A representative DSC curve for GMP-58-NIC, with the respective TGA curve as a reference.

The DSC results confirmed that these GMP-coformer products were not eutectics as the melting points deduced from the endothermic peaks did not correspond to a lowered melting point of both components in a particular GMP-coformer product, and the coformer was also removed during heating.[11,12] Therefore, it can be concluded that the GMP-coformer products appear to fall into the category of solid dispersions, more specifically a

two-phase system containing the crystalline GMP compound in an amorphous coformer matrix.[11]

3.2.7) Solubility analysis *via* colour standard comparison

A solubility investigation was conducted on the six GMP-coformer products (GMP-23-MAL, GMP-23-NIC, GMP-31-MAL, GMP-31-NIC, GMP-58-MAL and GMP-58-NIC), as well as on the amorphous products resulting from dry-grinding each of GMP-23, GMP-31 and GMP-58 for 15 minutes. This solubility investigation was performed for the purpose of obtaining an indication of possible solubility enhancement of the GMP compounds in the form of these solid products of interest. It is acknowledged that the method described below is not ideal in terms of accurately quantifying a solubility change. Unfortunately, more accurate analytical methods were not possible; for example, a gravimetric approach (GMP-coformer products were too insoluble to utilise this method), and HPLC (unfortunately the instrument column had terminated). Thus, as mentioned, the proposed method provided a possible indication for aqueous solubility modification.

The full method for this experiment is available in the Experimental methods in Chapter 2, under section 2.10.1, pp. 47 – 48. In summary, it involved dissolving approximately 1 mg of each of the compounds of interest in 2 cm^3 of water in separate vials and stirring them for one hour at 37 ^oC. In addition, reference solutions were simultaneously prepared under the same conditions by separately dissolving GMP-23, GMP-31 and GMP-58 in 2 cm^3 of water. Thereafter, the solutions were filtered with nylon 0.45 µm microfilter filters.

Furthermore, a series of solutions with known concentrations was prepared for each of the GMP compounds, each series being used as a control to assess the extent of the dissolution of the products with reference to the respective colour changes. Examples of these results (featuring samples displaying no solubility increase, a moderate solubility increase, and a large solubility increase) are presented in Figures 3.7.1 – 3.7.5. The samples shown in the representative figures include GMP-31 ground, GMP-31-MAL and GMP-31-NIC. Table 3.7.1 below provides a summary of these results from this solubility study, which indicated that for most of the products there was a solubility enhancement. A full presentation of these results can be found in the Appendix, section 2.7, pp. 29 – 34.

Solubility results for products formed with GMP-31:

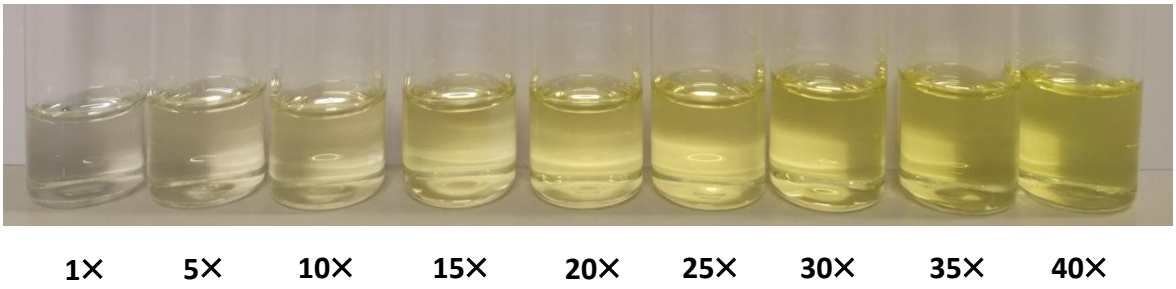


Figure 3.7.1: A series of reference concentrations of GMP-31, indicating how much more concentrated a particular vial is in comparison to the initial vial on the far left (labelled 1×).

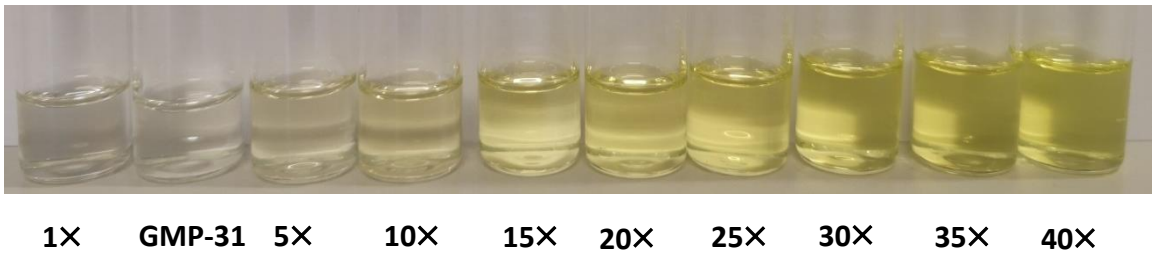


Figure 3.7.2: The solution containing the dissolved quantity of GMP-31 at 37 °C (labelled GMP-31). It is evident that the closest concentration is the reference solution labelled 1×.

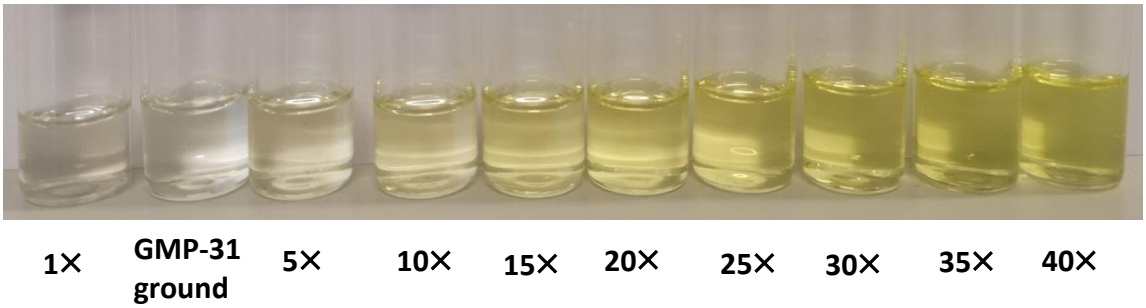


Figure 3.7.3: The solution containing the dissolved quantity of amorphous GMP-31 (GMP-31 ground for 15 minutes) at 37 °C. It is also evident that the closest concentration is the reference solution labelled 1× and thus no solubility increase was observed for the amorphous GMP-31 sample.

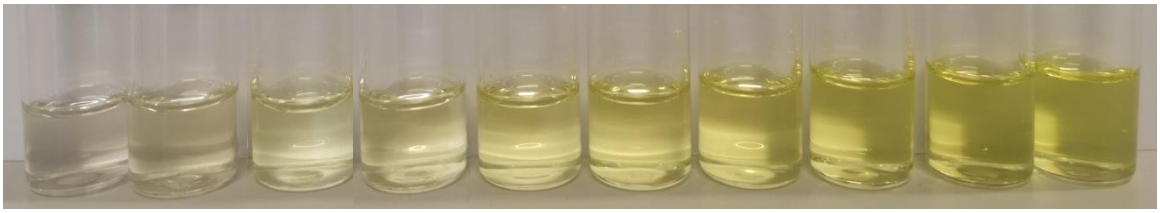


Figure 3.7.4: The solution containing the dissolved quantity of the product GMP-31-MAL at 37 °C. It is apparent that the closest concentration is that labelled 10× and thus an approximate 10-fold solubility increase was observed for GMP-31-MAL.

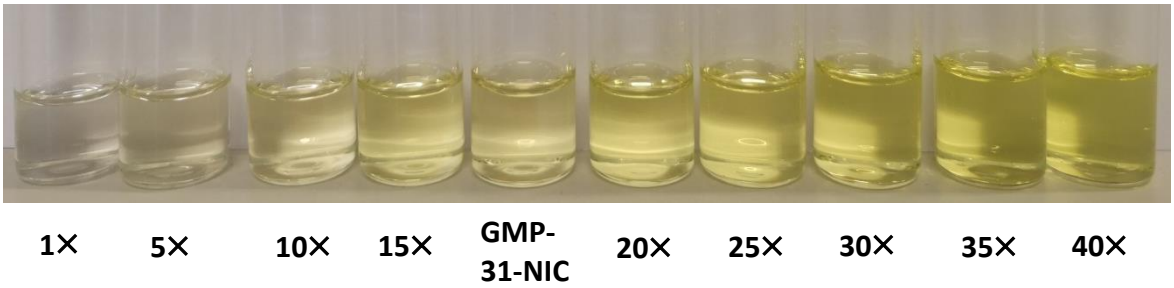


Figure 3.7.5: The solution containing the dissolved quantity of GMP-31-NIC at 37 °C. It is apparent that the closest concentration is between 15× and 20×, thus indicating an approximate solubility increase between 15-fold and 20-fold for GMP-31-NIC.

Table 3.7.1: The solubility enhancement factors for the products of interest.

Product	Solubility enhancement		Product	Solubility enhancement		Product	Solubility enhancement
GMP-23 ground	None		GP-31 ground	None		GMP-58 ground	2-fold
GMP-23-MAL	4-fold		GMP-31-MAL	10-fold		GMP-58-MAL	None
GMP-23-NIC	2-fold		GMP-31-NIC	(15 – 20)-fold		GMP-58-NIC	6-fold

In summary, with regard to the three pyrido[1,2-a]benzimidazole derivatives, single-crystal X-ray diffraction studies revealed definitive structural information pertaining to GMP-58, as well as three solvated forms of the three GMP compounds, namely GMP-23·DMF, GMP-31·DMF and GMP-58·DMSO. These structural analyses provided valuable evidence for the tautomeric forms present, as well as the conformation of the molecules, which enabled possible hydrogen bonding synthons to be assessed for potential co-crystal formation. Furthermore, the six GMP-coformer products were confirmed to be 1:1 two-phase solid

dispersions containing the crystalline GMP compound in an amorphous coformer matrix,[11] and for most of them a sizable solubility increase was achieved for their respective GMP component. Thus, it is also important to note that the possibility of GMP-23, GMP-31 and GMP-58 forming interactions with various coformers is not limited to L-malic acid and nicotinamide, and consequently there could be potential for generating many more products by the method employed to obtain the GMP-coformer products described in this study.

References

(1) Sheldrick, G. M. A Short History of SHELX. *Acta Crystallogr. Sect. A Found. Crystallogr.* **2008**, *64* (1), 112–122.

(2) Spek, A. L. PLATON SQUEEZE: A Tool for the Calculation of the Disordered Solvent Contribution to the Calculated Structure Factors. *Acta Crystallogr. Sect. C Struct. Chem.* **2015**, *71* (1), 9–18. https://doi.org/10.1107/S2053229614024929.

(3) Spek, A. L. PLATON. *Acta Crystallogr.* **2009**, *D65*, 148–155.

(4) XPREP, Data Preparation and Reciprocal Space Exploration. Version 2008/2, Bruker Analytical X-Ray Systems. 2008.

(5) Macrae, C. F.; Sovago, I.; Cottrell, S. J.; Galek, P. T. A.; McCabe, P.; Pidcock, E.; Platings, M.; Shields, G. P.; Stevens, J. S.; Towler, M.; Wood, P. A. Mercury 4.0 : From Visualization to Analysis, Design and Prediction. *J. Appl. Crystallogr.* **2020**, *53* (1), 226–235. https://doi.org/10.1107/S1600576719014092.

(6) Groom, C. R.; Bruno, I. J.; Lightfoot, M. P.; Ward, S. C. The Cambridge Structural Database. *Acta Crystallogr. Sect. B Struct. Sci. Cryst. Eng. Mater.* **2016**, *72* (2), 171–179. https://doi.org/10.1107/S2052520616003954.

(7) Fábián, L. Cambridge Structural Database Analysis of Molecular Complementarity in Cocrystals. *Cryst. Growth Des.* **2009**, *9* (3), 1436–1443. https://doi.org/10.1021/cg800861m.

(8) U.S. Food and Drug Administration https://www.cfsanappsexternal.fda.gov/scripts/fdcc/index.cfm?set=SCOGS&sort=Sortsubstance&order=ASC&showAll=true&type=basic&search= (accessed Jun 9, 2021).

(9) Babij, N. R.; McCusker, E. O.; Whiteker, G. T.; Canturk, B.; Choy, N.; Creemer, L. C.; Amicis, C. V. De; Hewlett, N. M.; Johnson, P. L.; Knobelsdorf, J. A.; Li, F.; Lorsbach, B. A.; Nugent, B. M.; Ryan, S. J.; Smith, M. R.; Yang, Q. NMR Chemical Shifts of Trace Impurities: Industrially Preferred Solvents Used in Process and Green Chemistry. *Org. Process Res. Dev.* **2016**, *20* (3), 661–667. https://doi.org/10.1021/acs.oprd.5b00417.

(10) Hino, T.; Ford, J. L.; Powell, M. W. Assessment of Nicotinamide Polymorphs by Differential Scanning Calorimetry. *Thermochim. Acta* **2001**, *374* (1), 85–92. https://doi.org/10.1016/S0040-6031(01)00491-9.

(11) Allawadi, D.; Singh, N.; Singh, S.; Arora, S. Solid Dispersions: A Review on Drug Delivery System and Solubility Enhancement. *Int. J. Pharm. Sci. Res.* **2013**, *4* (6), 2094–2105. https://doi.org/10.13040/IJPSR.0975-8232.4(6).2094-05.

(12) Dhande, L. B.; Deshmukh, M. T.; Khopade, A. N.; Shete, R. V.; Kunjir, V. V. A Review on Solubility Enhancement by Solid Dispersion Method. *J. Drug Deliv. Ther.* **2021**, *11* (1), 182–187. https://doi.org/10.22270/jddt.v11i1.4489.

Chapter 4

Cyclodextrin inclusion of the antioxidant pterostilbene

4.1) Literature review

Over the past decade, numerous published articles documenting studies of the inclusion complex formation between cyclodextrins (CDs) and pterostilbene (PTB) have aroused interest in this topic. The aim of these studies has primarily been to increase the aqueous solubility of PTB and hence its bioavailability.[1,2,11,12,3–10] The majority of these publications have investigated forming inclusion complexes for various applications (for example in the pharmaceutical and food industries) with the amorphous CDs, namely hydroxypropyl-β-CD (HPBCD) and hydroxypropyl-γ-CD (HPGCD).[1,2,12,3–6,8–11] However, the use of additional CDs has also been reported in other publications and these include α-CD, β-CD, γ-CD, methylated-β-CD and ethylated-β-CD.[2,4,5,7] The publications containing the research outlined above are described below.

The antimicrobial and anti-inflammatory effects of pterostilbene have been studied with HPBCD employed as a solubilizer.[1] The inclusion complex was prepared by dissolving pterostilbene in 15 mM HPBCD at a concentration of 1.25 $mg.cm^{-3}$.[1] A patent described an extraction and purification method for isolating pterostilbene from botanical sources and also mentioned the use of suitable carriers to solubilise pterostilbene in water and make it more bioavailable. These solubilizers included the native CDs with a preference for β-CD.[7] In addition, pharmacokinetic profiles of pterostilbene complexed with HPBCD were studied using Sprague-Dawley rats, and these experiments indicated a substantially improved bioavailability.[12] The complex solution was prepared by dissolving pterostilbene in HPBCD (up to a maximum concentration of 0.3 M) for the phase solubility study, as well as for the dosing formulations.[12]

Furthermore, Lacerda *et al.* have published four papers describing the therapeutic effects of

pterostilbene complexed with HPBCD.[6,9–11] The purpose of the complexation was to improve the solubility of pterostilbene, and the complex was prepared by adding an excess of pterostilbene to a 0.3 M solution of HPBCD, which was subsequently filtered and freeze dried.[6] These investigations were conducted *in vivo* with male Wistar adult rats (250-300 g), the therapeutic potential of pterostilbene being assessed for pulmonary hypertension,[6] as well as for acute myocardial infarction,[11] right heart failure,[10] and for reducing oxidative damage and modulating redox-sensitive proteins.[9]

Other publications involved investigating the development of an active food packaging, pterostilbene being complexed with HPBCD and HPGCD in equimolar ratios in order to improve its aqueous solubility.[5] Their results revealed that the hydroxypropyl-CDs had the ability to increase the aqueous solubility of pterostilbene by more than 700,000-fold. Furthermore, the same research group utilized HPBCD and HPGCD to form inclusion complexes with pterostilbene in equimolar ratios as antimicrobial agents against campylobacter, particularly in food packaging.[4]

An investigation was also conducted to assess the possibility of CD-pterostilbene complexation with the three native CDs (α-CD, β-CD and γ-CD), as well as three derivatised CDs (HPBCD, methyl-β-CD and ethyl-β-CD), and all resulting complexes were determined to have 1:1 host-guest ratios, as calculated from Benesi-Hildebrand plots.[2] The investigation established that the complexation constants (K_c) were significantly higher for the derivatised CDs, complexation with HPBCD displaying the highest value, and that the K_c value depends on factors including the type of CD, pH, temperature and the type of guest molecule.[2]

Lastly, an *in vitro* study was undertaken to assess the therapeutic potential of pterostilbene (PTB) for cardiac oxidative stress.[8] HPBCD was again used as a solubilizer and the HPBCD·PTB complex was prepared according to the methodology that Lacerda *et al.* used, as described above.[6,8]

Therefore, the significant ongoing research interest in forming CD inclusion complexes with pterostilbene warrants the need for further research to be conducted. Consequently, this study investigated the possibility of forming pterostilbene inclusion complexes with selected native and methylated CDs, with the primary aim of collecting structural information from SCXRD analysis, especially as this had not been previously achieved. In addition, the study

also investigated the possibility of PTB solubility improvement and determination of complex formation (or 'association') constants using phase solubility analysis with amorphous CDs, namely, RAMEB and SBEBCD sodium salt.

4.2) Overview of experimental results

Three crystalline CD inclusion complexes with pterostilbene having 1:1 host-guest stoichiometry have been isolated and characterised; they include β-CD·PTB, γ-CD·PTB and permethylated β-CD·PTB (TMB·PTB). The method of preparation and isolation for all these inclusion complexes required the implementation of some non-routine methods which will be explained in detail in this chapter. In addition, attempts were made to form an inclusion complex with 2,6-dimethylated-β-CD (DMB); however, in this case an oil was produced and no further characterisation was performed on this sample.

4.2.1) The inclusion complex β-CD·PTB

The β-CD·PTB inclusion complex was discovered once single crystals had formed after a co-precipitation experiment, details of which appear in Chapter 4, section 4.2.1.3, pp. 163 – 165. It was initially identified by measurement of the unit cell parameters of a crystal specimen, these data being different from those of either β-CD or pterostilbene. Consequently, an intensity data-collection was performed and the crystal structure was solved, confirming its identity as an inclusion complex. The X-ray structure of this new complex has recently been published,[13] and a detailed account of the crystal structure follows directly below. (The author's contribution to this paper included the X-ray structure determination of the β-CD·PTB complex and its comprehensive characterisation). Details of scale-up of this phase and its further characterisation are provided in Chapter 4, section 4.2.1.2, pp. 162 – 176.

4.2.1.1) SCXRD analysis of β-CD·PTB

Data-collection and space group determination

Single crystals of β-CD·PTB were carefully selected, especially as a mixture of β-CD and β-CD·PTB was present in the crystallization vial. A small, transparent crystal with a

rhombohedral habit was used for SCXRD analysis. The Laue symmetry was determined to be 2/*m*, indicating the monoclinic crystal system. In addition, a *C*-centred lattice was determined (condition 1, Table 4.1.1.). The listed reflection conditions indicate three possible space groups, namely *C*2, *Cm* and *C*2/*m*. However, *C*2 was the only suitable space group, since CD molecules are chiral. The lattice type and space group were confirmed by the program XPREP,[14] which also indicated a non-centric space group ($|E^2 - 1| = 0.770$). The numbering scheme for the molecular structures of pterostilbene and β-CD are provided in Figure 4.1.1 below.

Table 4.1.1: The conditions limiting possible reflections for β-CD·PTB.

Number	Conditions limiting possible reflections	Deduction
1	hkl: h+k = 2n	*C*-centred lattice
2	[h0l: (h = 2n, redundant condition)]	-
3	[0k0: (k = 2n, redundant condition)]	-

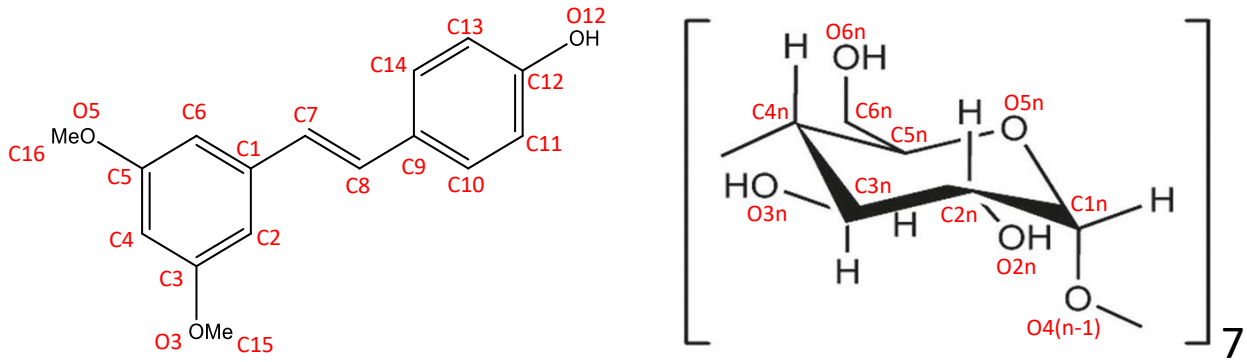


Figure 4.1.1: The atomic numbering scheme for the molecular structures of pterostilbene (left) and β-CD (right), where n represents one of the seven glucose units of the molecule.

Structure solution and refinement of β-CD·PTB

The hydrated β-CD·PTB inclusion complex structure was solved *via* isomorphous replacement, as outlined in the Experimental methods (Chapter 2, section 2.6, p. 44). A template structure, with the refcode TEZZUV,[15] was imported from the CSD,[16] and the non-hydrogen atoms of the host molecule were used as a trial model for that of β-CD·PTB.

Initially, the non-hydrogen atoms of the host molecule were refined isotropically and thereafter anisotropically (except where disorder was evident). The host atoms at the positions C6A1 and O6A1 displayed disorder over two positions in the resultant difference electron density ($\Delta\rho$) map. They were thus modelled by assigning site-occupancy values of *x* and 1-*x* to the major and minor disorder components, with *x* set as a free variable during the refinement. The site-occupancy factor (s.o.f.) of the atoms of the major component refined to 0.65(2). DFIX restraints were also applied to the C5-C6 bond lengths of the disordered pair in order to maintain them at reasonable values of 1.50 Å (σ = 0.01 Å). Furthermore, the hydroxyl oxygen atoms, O6A5 and O6A6 displayed abnormally high thermal motion and were thus refined isotropically. The hydrogen atoms were placed in idealised positions on the host molecule, using a riding model and isotropic temperature factors with values 1.2 times those of the U_{iso} parameters of their parent atoms.

Once the modelling of the host molecule was completed, the difference electron density peaks pertaining to the guest molecule were assigned. The entire guest molecule was disordered over two positions within the CD cavity and this was treated by assigning the disordered atom pairs s.o.f. values of 10.5 (where 10 fixes the corresponding s.o.f. value at 0.5), as well as corresponding PART numbers. Given the guest disorder, anisotropic refinement of the guest atoms was not warranted and in the final least-squares refinement their individual isotropic thermal parameters were optimised. In addition, several C-C and C-O bond lengths were also restrained with DFIX commands to maintain reasonable geometry. Lastly, hydrogen atoms of the two components of guest disorder were placed also using a riding model, as with the host molecule.

Thereafter, the oxygen atoms of the water molecules were assigned according to the procedure outlined in the Experimental methods, Chapter 2, section 2.6, pp. 44 – 45, and those with a full site-occupancy were refined anisotropically. The remaining water oxygen atoms were only partially occupied and thus were refined isotropically, their s.o.f. values being allowed to vary, whereas both components of the water molecules that were disordered over two positions were constrained to have equal U_{iso} thermal parameters. The hydrogen atoms of these water oxygen atoms were not apparent in $\Delta\rho$ maps and thus it was not possible to place hydrogen atoms on them. Finally, the SQUEEZE procedure[17] implemented in program PLATON[18] was performed in order to establish the host-guest

stoichiometry. The atoms of the disordered guest components were temporarily deleted and the resultant electron count indicated by the SQUEEZE procedure was 656 electrons,[a] which indicated a 1:1 host-guest stoichiometry.

The crystallographic data and details of the refinement are summarised in Table 4.1.2.

Table 4.1.2: Crystal data and refinement parameters for β-CD·PTB.

Parameter	**Value**
Complex formula	$2(C_{42}H_{70}O_{35})\cdot 2(C_{16}H_{16}O_3)\cdot 23.2(H_2O)$
Formula weight ($g.mol^{-1}$)	3200.49
Temperature (K)	100(2)
Wavelength (Å)	0.71073
Crystal system	Monoclinic
Space group	*C*2
a (Å)	19.484(3)
b (Å)	24.244(4)
c (Å)	16.674(3)
α (°)	90
β (°)	103.044(3)
γ (°)	90
Volume ($Å^3$)	7673(2)
Z	2
Calculated density ($g.cm^{-3}$)	1.3851
μ (mm^{-1})	0.122
F (000)	3416
Crystal size (mm)	$0.21 \times 0.18 \times 0.10$
θ-Range scanned (°)	1.68 – 25.70
Index range	h: -23, 23; k: -28, 28; l: -20, 20
No. of reflections collected	40393
No. of unique reflections	14322
Data completeness (%)	99.3
Data/restraints/parameters	14322/22/871
S (Goodness-of-fit on F^2)	1.034
Final R indices R_1, wR_2, [$I > 2\sigma(I)$]	0.0986, 0.2538
R Indices, all data (R_1, wR_2)	0.1382, 0.2880
Largest diff. peak and hole ($e.Å^{-3}$)	1.1, -0.72

[a] The 656 electrons account for the guest molecule as well as the water hydrogen atoms that were not modelled. Theoretically, the guest molecules contribute 544 electrons per unit cell, and the hydrogen atoms of the water molecules contribute 92.8 electrons per unit cell. Therefore, in order to obtain the guest electron density contribution from the SQUEEZE procedure, the water hydrogen atom count must be subtracted from the calculated total of 656 electrons per unit cell. This yields 563 electrons, which is in excellent agreement with the theoretical value of 544, thus confirming the 1:1 host-guest stoichiometry.

Molecular Structure

The asymmetric unit (ASU) of the inclusion complex is displayed in Figure 4.1.2 as a stereoscopic view. The disorder of the host molecule was relatively minor, only one of the seven hydroxyl methyl groups being disordered over two positions. However, the guest molecule was completely disordered and thus occupied two positions, with each disordered counterpart having a site-occupancy of 0.5 based on their relative difference electron density distributions. The mode of inclusion of pterostilbene is displayed in a space-filling model (Figure 4.1.3a). The phenolic rings of pterostilbene protrude from the primary side of the CD molecule, while the 3,5-dimethoxyphenyl rings are positioned in the cavity towards the secondary rim of the CD molecule. Figure 4.1.3b displays a cut-away view, and it is possible to observe the pseudo mirror relationship between the two components of guest molecule disorder.

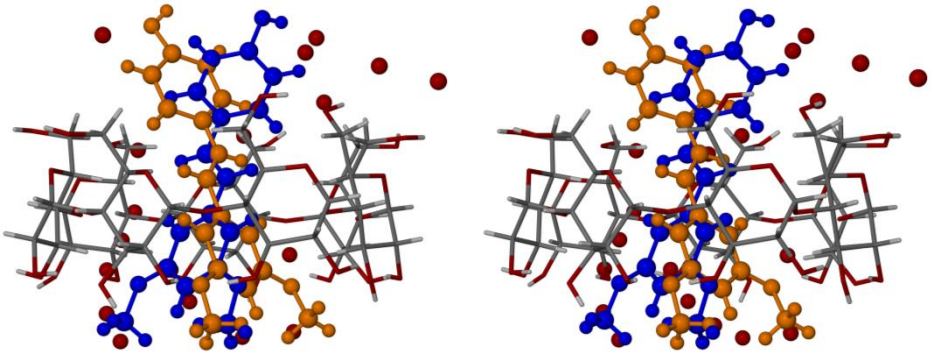


Figure 4.1.2: A stereoscopic view of the ASU of β-CD·PTB. The two components of the disordered pterostilbene guest molecule are displayed in orange and blue. The water molecules are represented by the individual oxygen atoms (red spheres).

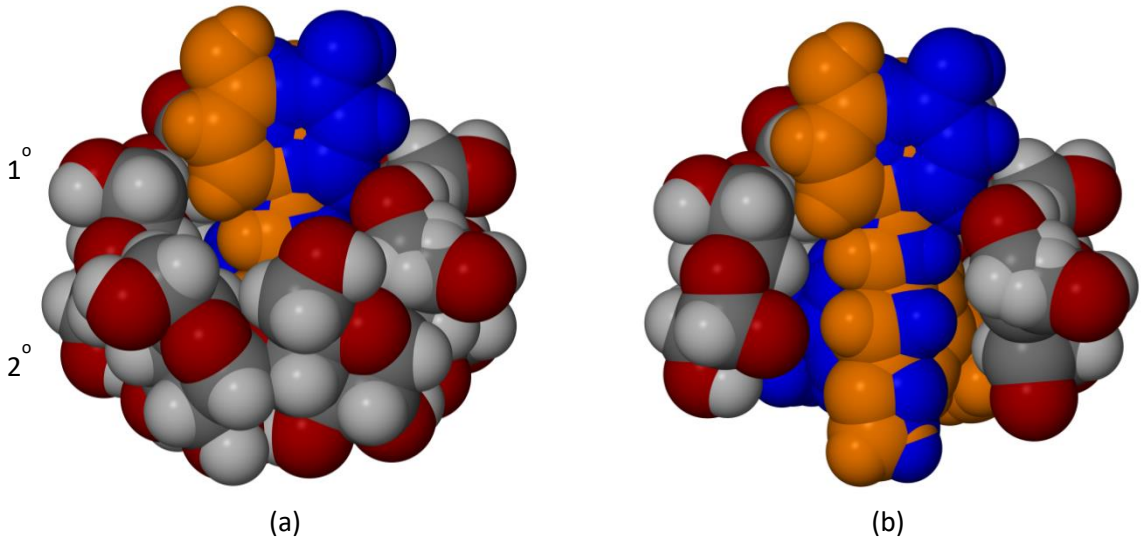


Figure 4.1.3: A space-filling representation displaying the mode of inclusion of the components of the guest molecule disorder in orange and blue (a), and the cut-away representation (b) displaying the pseudo mirror symmetry relationship of the two components. The primary (narrower) and secondary (wider) rims of the CD molecule are represented by the symbols 1° and 2° in figure (a). The water molecules are omitted for clarity.

The water molecules of the ASU were distributed over 20 sites, the sum of their s.o.f.s corresponding to 11.3 water oxygen atoms per monomeric CD, which was in good agreement with the TGA estimate of 11.6 ± 0.4 water molecules that will be described later in this chapter. Furthermore, the PLATON SQUEEZE routine[17] calculated 11.0 water molecules per monomeric CD. This procedure entailed temporarily removing only the water oxygen atoms in order to calculate the electron count in the void space of the crystal. This void space amounted to 1216 $Å^3$ totalling 439 electrons. This value corresponded to 43.9 water molecules per unit cell, and since there are four CD molecules per unit cell, the value corresponded to 11.0 water molecules per CD molecule. Thus, the consistency of these results strongly confirms that the stoichiometric formula of the hydrated inclusion complex is 2(β-CD)·2(PTB)·23.2H_2O. For simplicity, the complex will be (and has already been) referred to as β-CD·PTB. Finally, the refined values for the s.o.f.s and U_{iso} parameters of the water oxygen atoms are displayed in Table 4.1.3.

Table 4.1.3: The total number of water oxygen sites that were identified, with their respective s.o.f.s and U_{iso} values for β-CD·PTB.

Atom	s.o.f.	U_{iso} (Å^2)	Atom	s.o.f.	U_{iso} (Å^2)	Atom	s.o.f.	U_{iso} (Å^2)
OW1	1.00	0.043(2)	OW8	0.31(3)	0.06(1)	OW15	0.478(4)	0.079(6)
OW2	1.00	0.078(3)	OW9	0.69(3)	0.119(9)	OW16	0.66(3)	0.079(4)
OW3	10.50*	0.092(7)	OW10	0.69(2)	0.066(5)	OW17	0.68(2)	0.064(2)
OW4	0.74(2)	0.064(2)	OW11	0.373(2)	0.064(6)	OW18	0.27(2)	0.064(2)
OW5	1.00	0.098(4)	OW12	0.71(2)	0.064(2)	OW19	0.27(2)	0.064(2)
OW6	0.54(3)	0.095(8)	OW13	0.37(2)	0.079(4)	OW20	0.32(2)	0.064(2)
OW7	0.46(3)	0.049(6)	OW14	0.63(2)	0.079(4)			

*10.50 indicates a *constant* assigned value of 0.50.

Crystal Packing

Two of the ASUs illustrated above form a head-to-head dimer (Figure 4.1.4) with two-fold rotational symmetry (the C_2-axis lying parallel to the crystal b-axis and running through the centre of the dimeric unit). The packing arrangement consists of these stacked dimeric units that arrange themselves in columns parallel to the c-axis, with a significant lateral shift of each dimeric unit (Figure 4.1.4). This lateral shift allows part of the guest molecule to be accommodated in the void space between the columns. Thus, the crystal packing of β-CD·PTB differs somewhat from the more general packing arrangements that occur in β-CD complexes that crystallize in the space group *C*2. This more general packing arrangement has a smaller lateral shift of the stacked dimeric units. This is due to either the guest molecule fitting more appropriately within the column, or the guest molecules not being observed, since, due to their disorder their electron density is diluted throughout the length of the column.

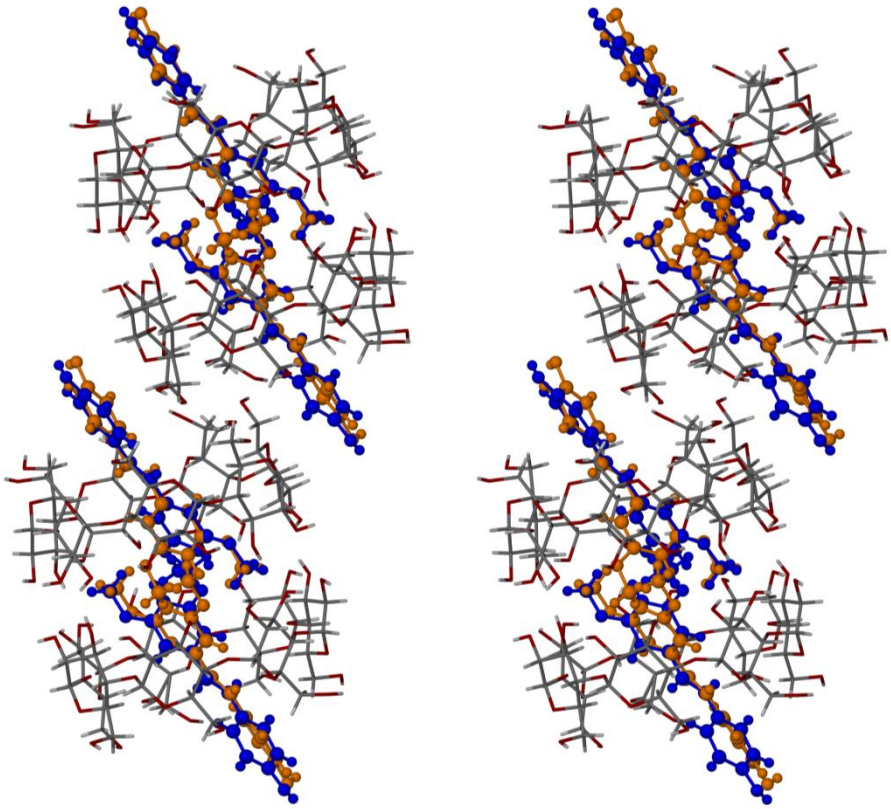


Figure 4.1.4: A stereoscopic view of a representative portion of the column packing arrangement consisting of two dimeric units, which shows the lateral shift of the stacked dimers to accommodate the protruding guest residues. The water molecules were omitted for clarity.

The unit cell dimensions for the β-CD·PTB complex are very similar to those of the β-CD complex of 4,7-dimethylcoumarin (CSD refcode MASBAJ) which also crystallizes in the space group *C*2. This is evident from the close match between the peak angular positions in the PXRD patterns based on their respective host molecule packing arrangements (Figure 4.1.5). However, their common PXRD pattern is quite distinct from that based on the packing arrangements of most β-CD complexes crystallizing in *C*2, that of AJUVEG (containing methylparaben as guest) being a representative case. Thus, we note that at least two distinct isostructural series of β-CD complexes with the common space group *C*2 exist. This finding, based on searches of the CSD, is relevant in the context of identifying new CD complexes *via* PXRD-matching using reference patterns for each known isostructural series.[13,19]

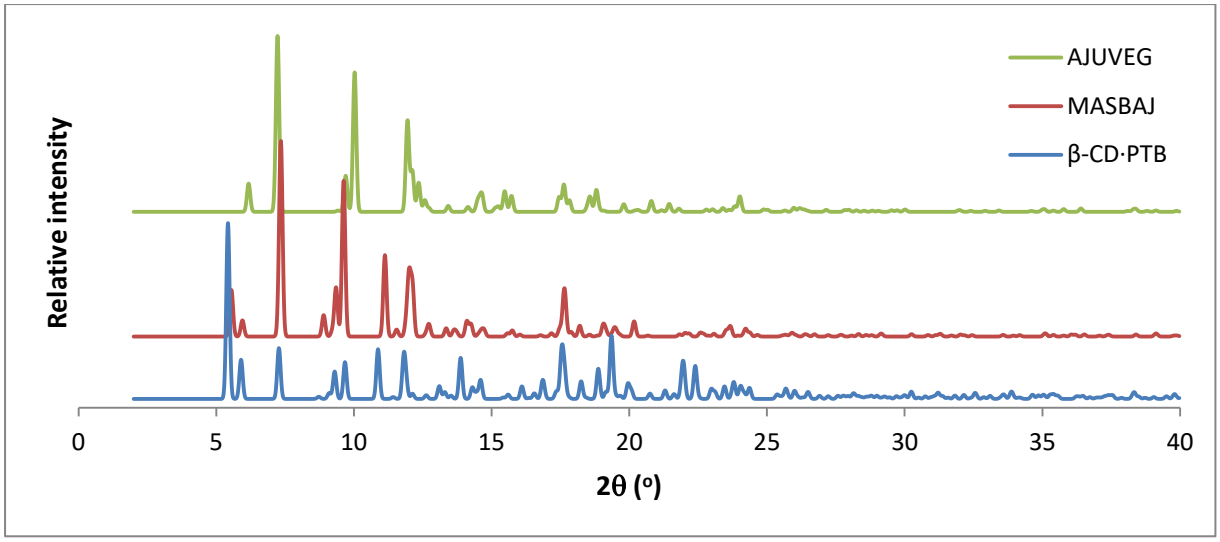


Figure 4.1.5: Calculated PXRD patterns generated using the atomic coordinates of the host molecules for AJUVEG, MASBAJ and β-CD·PTB. It is evident that MASBAJ and β-CD·PTB are isostructural.

Lastly, water molecules are positioned in the interstitial spaces between the columns, resulting in a complex system of OH···O hydrogen bonds consisting of water-water, water-host and water-guest hydrogen bonding interactions (Figure 4.1.6). These water molecules are essential for maintaining the crystallinity of the complex structure.

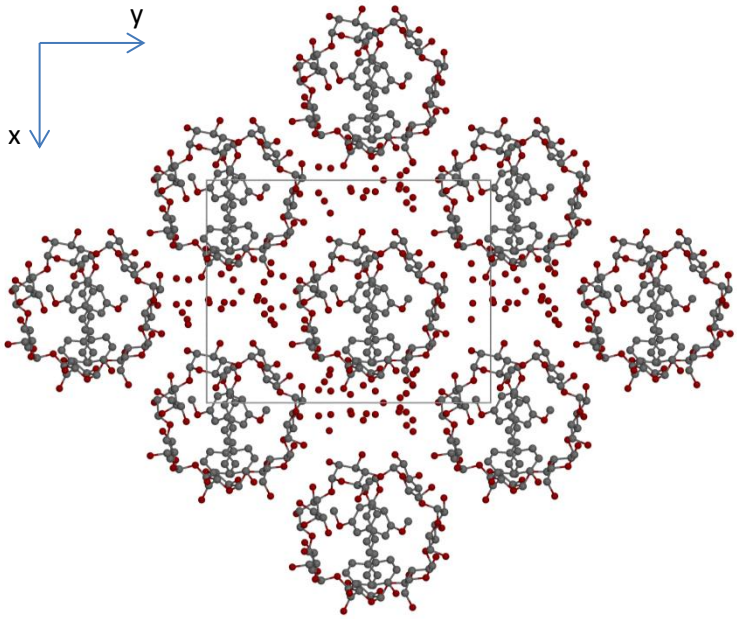


Figure 4.1.6: The packing arrangement of the inclusion complex viewed down the c-axis. The water molecules (represented by red spheres) fill the interstitial spaces between the columns of CD complex units. The *C*-centring of the inclusion complex is also evident. Hydrogen atoms were omitted for clarity.

Hydrogen bonding

Multiple intramolecular host hydrogen bonding of the type O-H···O occurred between the hydroxyl groups that are located on the secondary rims. These particular hydrogen bonds reinforce and stabilize the heptagonal geometry of the β-CD molecule (Figure 4.1.7).

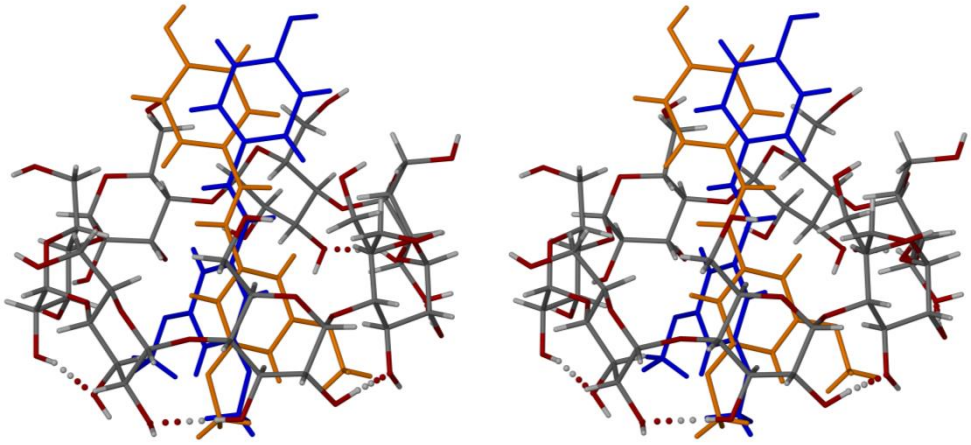


Figure 4.1.7: A stereoscopic view of the intramolecular hydrogen bonding on the secondary rim of the CD molecule. Water molecules are omitted for clarity.

In addition, intermolecular hydrogen bonding occurs between the O3-H hydroxyl groups from one of the CD molecules, and the O2-H or O3-H hydroxyl groups of the other CD completing the dimeric unit (Figure 4.1.8). The intramolecular and intermolecular hydrogen bonding parameters for the β-CD·PTB complex are displayed in Table 4.1.4.

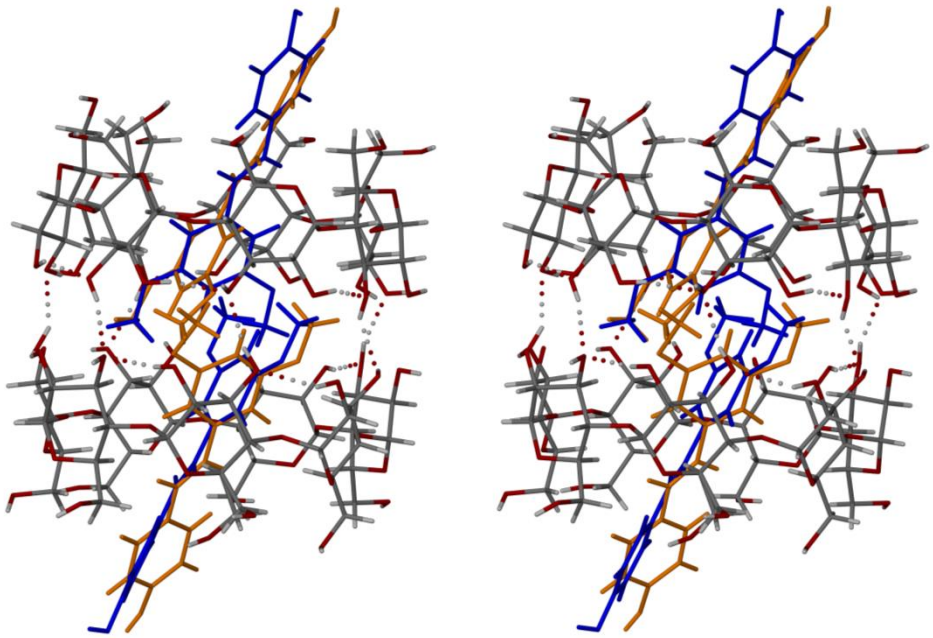


Figure 4.1.8: A stereoscopic view of the β-CD·PTB dimer showing the intramolecular and intermolecular host-host hydrogen bonding.

Table 4.1.4: Parameters for the hydrogen bond interactions in β-CD·PTB.

Interaction type	Hydrogen bond	D-H (Å)	H···A (Å)	D···A (Å)	D-H···A (°)	Symmetry code
O2-H···O3′ and O2-H···O2 Hydrogen bonds						
Intramolecular	O2A1-H2A2···O3A7	0.84	2.01	2.83(1)	165	x, y, z
Intramolecular	O2A2-H2A3···O3A1	0.84	2.11	2.82(1)	142	x, y, z
Intramolecular	O2A3-H2A4···O3A2	0.84	2.54	2.84(1)	102	x, y, z
Intramolecular	O2A4-H2A5···O3A4	0.84	2.07	2.89(1)	166	x, y, z
Intermolecular	O2A5-H2A5···O2A7	0.84	1.87	2.70(1)	171	1/2-x, 1/2+y, 1-z
Intramolecular	O2A6-H2A8···O3A5	0.84	2.56	2.88(1)	104	x, y, z
Intramolecular	O2A7-H2A7···O3A6	0.84	2.05	2.80(1)	148	x, y, z
O3-H···O2′ and O3-H···O3 Hydrogen bonds						
Intramolecular	O3A1-H3A2···O2A1	0.84	2.46	2.84(1)	108	x, y, z
Intermolecular	O3A1-H3A1···O3A7	0.84	2.01	2.83(1)	165	1-x, y, 1-z
Intramolecular	O3A2-H3A3···O2A3	0.84	2.03	2.82(1)	156	x, y, z
Intramolecular	O3A3-H3A3···O2A3	0.84	2.54	2.84(1)	102	x, y, z
Intermolecular	O3A6-H3A6···O3A2	0.84	2.23	2.971(9)	148	1-x, y, 1-z
O6-H···O5 and O6-H···O6 Hydrogen bonds						
Intermolecular	O6A2-H1···O6A1	0.84	1.91	2.72(1)	160	1-x, y, -z
Intramolecular	O6A2-H1···O5A2	0.84	2.47	2.80(1)	104	x, y, z
Intermolecular	O6A7-H6A7···O6A3	0.84	1.93	2.76(1)	170	-1/2+x, -1/2+y, z
C-H···O Hydrogen bonds						
Intermolecular	C1A7-H1A7···O2A4	1.00	2.46	3.31(1)	143	-1/2+x, -1/2+y, z
Intermolecular	C2A5-H2AX···O3A1	1.00	2.40	3.36(1)	160	-1/2+x, -1/2+y, z
Intermolecular	C2A7-H2AZ···O3A3	1.00	2.37	3.34(1)	163	-1/2+x, -1/2+y, z
Intramolecular	C6A1-H6A2···O5A2	0.99	2.58	3.46(2)	148	x, y, z
Intramolecular	C6A3-H9···O5A4	0.99	2.60	3.44(1)	143	x, y, z
Intramolecular	C6A1-H6A3···O7A1	0.99	1.57	2.38(2)	135	x, y, z
Intermolecular	C3A2-H3AY···O5A	1.00	2.24	3.18(2)	156	x, y, z
Intermolecular	C3A3-H3A8···O5B	1.00	2.22	3.14(2)	153	x, y, z
Intermolecular	C3A4-H3A9···O3A	1.00	2.59	3.33(2)	130	x, y, z
Intermolecular	C3A5-H3AA···O3A	1.00	2.49	3.31(1)	159	x, y, z
Intermolecular	C3A7-H3AZ···O3B	1.00	2.38	3.19(2)	137	x, y, z
Intermolecular	C11A-H11A···O12B	0.95	1.66	2.44(5)	137	x, y, z
Intermolecular	C4B-H4B···O3B	0.95	2.04	2.76(2)	131	1-x, y, 1-z

In addition, water-host, water-guest and water-water hydrogen bonding was inferred based on geometrical considerations, the water molecules acting as either hydrogen bond acceptors or donors. The water-host and water-guest interactions are summarized in Table 4.1.5.

Table 4.1.5: Parameters for the intermolecular interactions in β-CD·PTB involving water molecules.

Hydrogen bond interaction	D-H (Å)	H···A (Å)	D···A (Å)	D-H···A (°)	Symmetry code
O6A6-H3···O5W	0.84	1.91	2.749(18)	172	x, y, z
O6A5-H5···O17W	0.84	2.03	2.777(19)	147	x, y, z
O6A1-H6A1···O10W	0.84	2.07	2.833(17)	151	x, y, z
O6A3-H8···O5W	0.84	1.94	2.756(15)	165	1/2+x, 1/2+y, z
O12A-H12A···O9W	0.84	1.72	2.55(3)	170	x, y, z
O12A-H12A···O8W	0.84	1.41	2.06(3)	131	x, y, z
O2A3-H2A3···O12W	0.84	2.21	2.807(15)	128	1-x, y, 1-z
O3A4-H3A4···O2W	0.84	2.01	2.842(12)	173	1/2-x, 1/2+y, 1-z
O6A4-H6A4···O9W	0.84	1.89	2.72(3)	173	1/2-x, 1/2+y, 1-z
O6A4-H6A4···O8W	0.84	2.01	2.71(3)	141	1/2-x, 1/2+y, 1-z
O3A5-H3A5···O4W	0.84	2.22	2.934(14)	143	x, y, z
O3A5-H3A5···O11W	0.84	2.30	2.86(3)	125	x, y, z
O2A6-H2A6···O4W	0.84	2.30	3.136(14)	171	x, y, z
O2A6-H2A6···O18W	0.84	2.35	3.13(4)	156	x, y, z
O3A7-H3A7···O4W	0.84	2.59	3.184(14)	129	1/2-x, -1/2+y, 1-z
O3A7-H3A7···O11W	0.84	2.09	2.91(3)	167	1/2-x, -1/2+y, 1-z
C1A6-H4···O18W	1.00	2.32	3.18(4)	144	x, y, z
C1A6-H4···O19W	1.00	2.46	3.41(4)	158	x, y, z
O5A6···O7W*	-	-	3.01(2)	-	1/2-x, 1/2+y, -z
O5A6···O7W*	-	-	2.98(2)	-	x, y, z

*The water oxygen atom is the hydrogen bond donor

Host molecular geometry

The geometrical parameters describing the conformation of the O4-heptagon of the β-CD host molecule in β-CD·PTB are listed in Table 4.1.6 with reference to Figure 4.1.9.

Table 4.1.6: Geometrical parameters of the host molecule in the complex β-CD·PTB.

Residue	*l* (Å)	D (Å)	Φ (°)	d (°)	α[a] (Å)	D_3 (Å)	τ_2 (°)[b]
A1	4.987	4.409	130.3	-0.1	-0.047	2.83(1)	12.5
A2	5.137	4.330	126.4	3.4	0.031	2.82(1)	13.9
A3	5.062	4.408	128.9	-3.9	0.028	2.84(1)	3.1
A4	4.990	4.377	129.7	2.4	-0.060	2.89(1)	12.5
A5	5.053	4.409	128.4	-1.8	0.032	2.72(1)	9.6
A6	5.112	4.323	127.8	2.8	0.002	2.88(1)	12.2
A7	5.056	4.463	128.3	-2.7	0.014	2.80(1)	7.8

[a] mean esd: 0.005 Å; [b] mean esd: 0.3°

Key to symbols
l: the distance between each O4 atom and the centroid of the O4-polygon;
D: the consecutive glycosidic O4···O4′ distances;
Φ: the O4···O4′···O4′′ angle;
d: the O4···O4′···O4′′···O4′′′ torsion angle;
α, the deviation of each O4 atom from the mean O4-plane;
D_3: the O2···O3′ intra-ring distance;
τ_2: the tilt angle: the angle between the mean O4-plane and the plane containing O4, C4, C1 and O4′ of a given glucose ring.

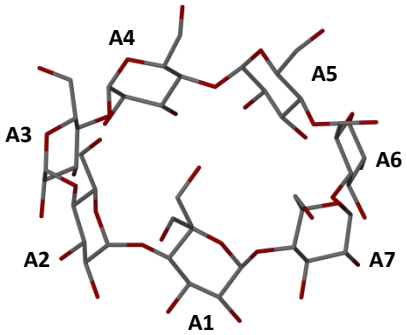


Figure 4.1.9: The numbering scheme of the β-CD·PTB glucose units.

In a regular heptagon, the seven angles are equal and the seven sides are equal; however, during crystallization of the CD molecules, the geometry of the O4-heptagon becomes distorted, since variations in the values of *l*, D and Φ occur, as host and guest molecules undergo complexation *via* mutual-induced fit. Regarding β-CD·PTB, the variation in the torsion angles (d) and the deviations (α) are relatively small, indicating that the extent of planarity of the O4-heptagon is high. Furthermore, the range of the D_3 values is between 2.72(1) Å and 2.89(1) Å, which is the typical range for O···O distances for O-H···O hydrogen bonds. The values of the tilt angles for the glucose residues range from 3.1° to 13.9°, and thus this range is smaller than that for uncomplexed hydrated β-CD (4.5° – 27.0°).[20] Consequently, it appears that distortion of the host molecules did appear as a result of a

mutual-induced fit that occurred between the host and guest molecules during complexation, in order to accommodate the guest molecules optimally. Further characterisation of β-CD·PTB will be discussed in the following section.

4.2.1.2) Summary of results involving attempts to produce a pure bulk phase of β-CD·PTB for further characterisation

More extensive experimentation was performed in order to further characterise β-CD·PTB. However, the isolation of the β-CD·PTB complex was exceedingly difficult and the crystallization of a completely pure bulk sample was not fully achieved. This was further complicated by reproducibility issues where, instead of forming the complex, different phases of pterostilbene were unexpectedly produced instead.

For simplicity, a brief summary of the results of the β-CD·PTB complex is provided below, with a more detailed analysis of the results being discussed later in this section. In summary, the β-CD·PTB complex was first discovered through co-precipitation experimentation, and a SCXRD analysis was performed. However, the product crystals in the vial were impure as β-CD significantly contaminated the sample containing the inclusion complex, complicating further experimentation. At this point traditional kneading experiments were conducted with no success. These experiments, at large, involved grinding the two components for 40 minutes in an equimolar ratio with the addition of water to achieve a paste-like consistency. Small variations to these kneading experiments were also attempted, as seen in the following six examples: kneading for 1 hour; kneading for 1.5 hours; placing the sample in an automated ball-mill and kneading it for three hours; kneading using different stoichiometric ratios; kneading the components for 40 minutes with a few drops of ethanol along with the water; and pre-dissolving the pterostilbene in ethanol and adding that solution dropwise to an aqueous paste-like consistency of β-CD and kneading for 40 minutes. Unfortunately, all of these variations failed to produce the desired complex phase in pure form.

Subsequently, an alternative kneading method (involving guest melting) was attempted and the PXRD pattern of the product displayed evidence of a different phase from that of the original components. The experiment involved pre-melting pterostilbene at 110 ^{o}C and adding β-CD in increments over a period of five minutes while kneading the mixture for 30 minutes. The product obtained was then recrystallized from water at 70 ^{o}C but the crystals that precipitated consisted of a mixture of β-CD and the inclusion complex β-CD·PTB. However, in another set of co-precipitation and recrystallization experiments, the temperatures of the aqueous solutions were increased to between 80 and 85 ^{o}C (which is

closer to the melting point of pterostilbene *viz.* 95 – 98 °C)[21] and another polymorph of pterostilbene was obtained instead, as confirmed by PXRD. After an additional two perfectly reproducible experiments aimed at isolating this polymorph, further attempts unexpectedly reproduced the β-CD·PTB inclusion complex at a significantly higher level of purity.

Consequently, the various attempts to isolate β-CD·PTB were challenging, with the various methods producing very different results. The PXRD patterns that represent β-CD·PTB produced *via* kneading with molten coformer and co-precipitation, as well as a calculated PXRD pattern from a single-crystal X-ray structure, all differed to a large extent (Figure 4.1.9). Nevertheless, the individual experiments are elaborated on further in this chapter, where the results that were obtained are carefully analysed.

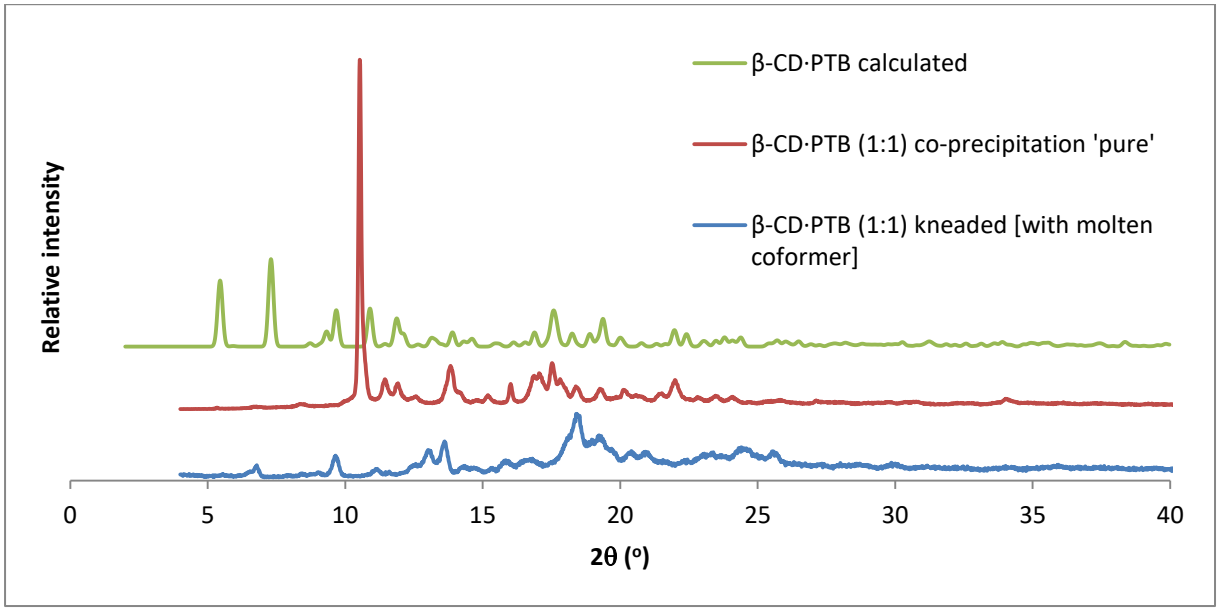


Figure 4.1.9: The PXRD patterns of β-CD·PTB formed *via* kneading [with molten coformer] (1:1), co-precipitation (1:1) and the PXRD pattern calculated from a single crystal.

4.2.1.3) The initial isolation of β-CD·PTB *via* co-precipitation

This method of preparation involved dissolving β-CD (22.14 mg, 0.020 mmol) in 2.5 ml of milli-Q water at 70 °C and adding pterostilbene (5 mg, 0.020 mmol) to the CD solution

slowly, which resulted in a suspension.[a] This suspension was stirred vigorously and it was necessary to add an excess of β-CD in order to dissolve the remaining pterostilbene. The solution was stirred for 3 days at 70 ^{o}C in order to fully attain the complexation equilibrium in solution. During these 3 days, the vial had to be tightly sealed in order to prevent any evaporation from taking place. This involved loosely covering the vial with parafilm and then pushing the plastic cork into the parafilm cover to form a seal. Furthermore, the cork was externally wrapped with parafilm to prevent the vapour pressure from lifting the cork, and the vial was protected from light.

The complex solution was subsequently filtered with a nylon 0.45 μm microfilter and left in a dark room to allow slow evaporation to take place. After 3 days, β-CD crystals precipitated and the complex crystals only appeared when the volume of the mother liquor was evaporated by a further 50%. The morphologies of the β-CD crystals and the complex crystals are significantly different: the former appear as large tablets with a chamfered corner, while the morphology of the complex crystals is that of very small rhombohedrons (Figure 4.1.10). Consequently, differentiating the two compounds from their crystalline morphology was possible. Thus, it was theoretically feasible to isolate the β-CD·PTB crystals by individually harvesting them from the vial. However, in practice this was significantly more challenging owing to their small size and the possibility of contamination from the mother liquor.

[a] The pterostilbene was added in miniscule increments into the β-CD solution, where it was necessary to wait until the solution became completely transparent (which is when all the pterostilbene had been dissolved) before adding the subsequent increment of pterostilbene.

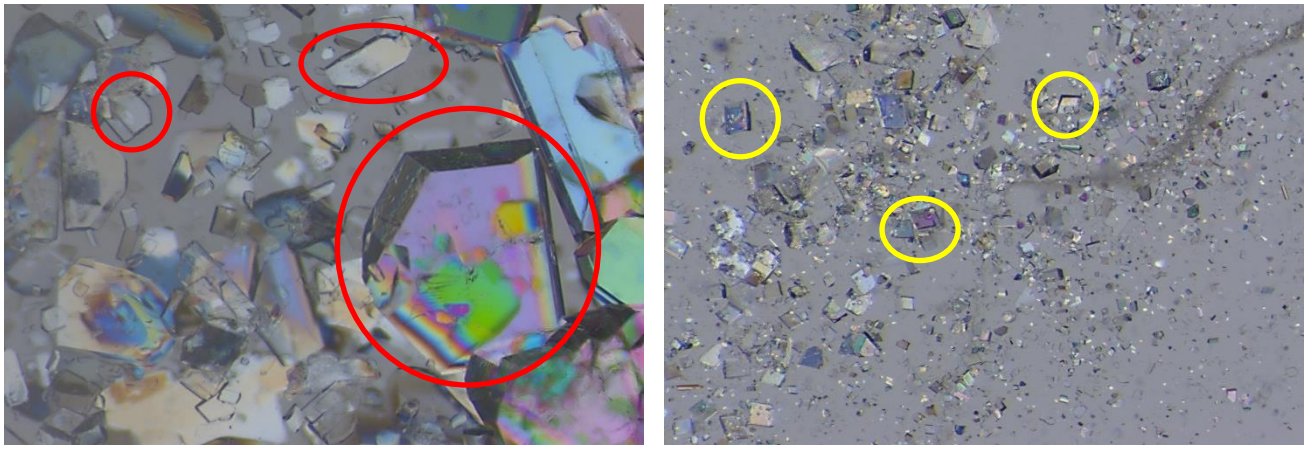


Figure 4.1.10: The typical morphology of β-CD where the chamfered corner of the tablet (circled in red) is evident. The rhombohedral morphology of the β-CD·PTB complex is circled in yellow.

4.2.1.4) ^{1}H NMR analysis of the harvested β-CD·PTB crystals

The method of individually harvesting complex crystals enabled 2 mg to be collected from four separate co-precipitation experiments for ^{1}H NMR analysis. However, the ^{1}H NMR results suggested that the harvested sample was contaminated with β-CD, as an approximate 1.4:1 host-guest stoichiometry was ascertained from this analysis (Figure 4.1.11 and Table 4.1.7). The stoichiometric ratio was established as 1:1 using the PLATON SQUEEZE procedure[17] as previously described in the SCXRD analysis. Even though great care was taken when harvesting the crystals for this experiment, a very small mass was used and this can often result in discrepancies in determining an accurate molar ratio, as the signal-to-noise ratio is very high. Generally, 10 mg of sample is required to obtain accurate ^{1}H NMR results for CD inclusion complexes, which was not possible in this case. In addition, the small crystals could have also been contaminated with residual β-CD in the mother liquor, which could have contributed towards the higher level of β-CD present in the ^{1}H NMR integration. The ^{1}H NMR spectrum can be viewed in the Appendix under section 3.1.1, p. 35.

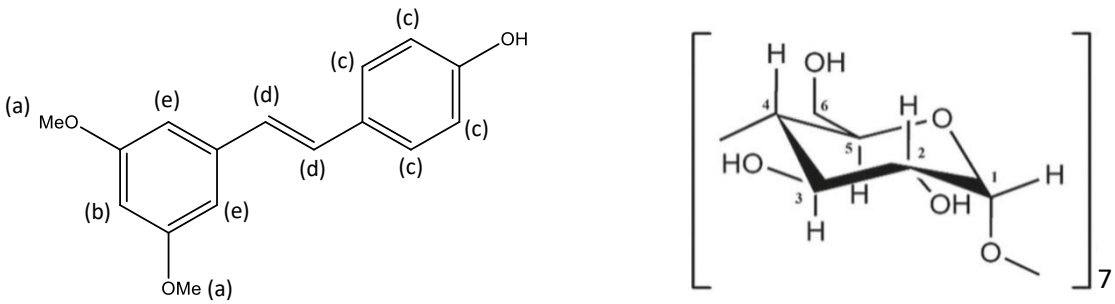


Figure 4.1.11: Molecular structures of pterostilbene (left) and β-CD (right). Specific atoms have been labelled for reference in the ^{1}H NMR analysis. Adapted from Guedes *et al.*[27]

Table 4.1.7: The ^{1}H NMR spectral analysis of an impure sample of β-CD·PTB.

Assignment	δ (ppm)	Integration	Multiplicity	Proton representation (per molecule)	Proton count (host:guest)
2X OC$\underline{H}_3$ (a) (PTB)	3.778	0.7195	singlet	6H	0.84
O$\underline{H}$-6 (β-CD)	4.388 – 4.415	1.0000*	triplet	7H	1.00
C$\underline{H}$-1 (β-CD)	4.836 – 4.845	0.9933	doublet	7H	0.99
O$\underline{H}$-3 and O$\underline{H}$-2 (β-CD)	5.653 – 5.696	2.0053	two separate doublets	14H	1.00
C$\underline{H}$ (b) aromatic (PTB)	6.373 – 6.383	0.0975	triplet (long range coupling)	1H	0.68
4X C$\underline{H}$ (c) aromatic (PTB)	6.715 – 6.785	0.4146	doublet of doublets	4H	0.73
C$\underline{H}$ (d) vinylic (PTB)	6.920 – 6.961	0.0997	doublet	1H	0.70
C$\underline{H}$ (d) vinylic (PTB)	7.133 – 7.174	0.0989	doublet	1H	0.69
2X C$\underline{H}$ (e) aromatic (PTB)	7.408 – 7.429	0.2079	doublet of triplets	2H	0.73

*reference integral

4.2.1.5) Attempts at forming β-CD·PTB *via* conventional kneading and an alternative 'kneading' method involving guest melting

As mentioned in the summary at the beginning of this section, multiple kneading experiments that involved grinding the combined reagents with a mortar and pestle into an aqueous, paste-like consistency produced a physical mixture instead of the inclusion complex (Table 4.1.8). Figure 4.1.12 illustrates a representative example of the outcome of one of these unsuccessful experiments, all of which displayed similar results. The PXRD patterns of the product resembled the PXRD pattern of β-CD with an additional peak at the

angular position of 8.5° 2θ, which is attributed to the polymorphic form of pterostilbene employed in this study.

Table 4.1.8: Various kneading experiments employed in attempts to form β-CD·PTB.

Number	Time (minutes)	Molar ratio employed (CD:PTB)	Solvent	Method of grinding	Results
1	40	1:1	Water	Kneading	Physical mixture
2	60	1:1	Water	Kneading	Physical mixture
3	90	1:1	Water	Kneading	Physical mixture
4	180	1:1	Water	Ball mill	Physical mixture
5	40	2:1	Water	Kneading	Physical mixture
6	40	1:1	Water with a few drops of ethanol	Kneading	Physical mixture
7	40	1:1	PTB pre-dissolved in EtOH and added dropwise to β-CD aqueous paste	Kneading	Physical mixture

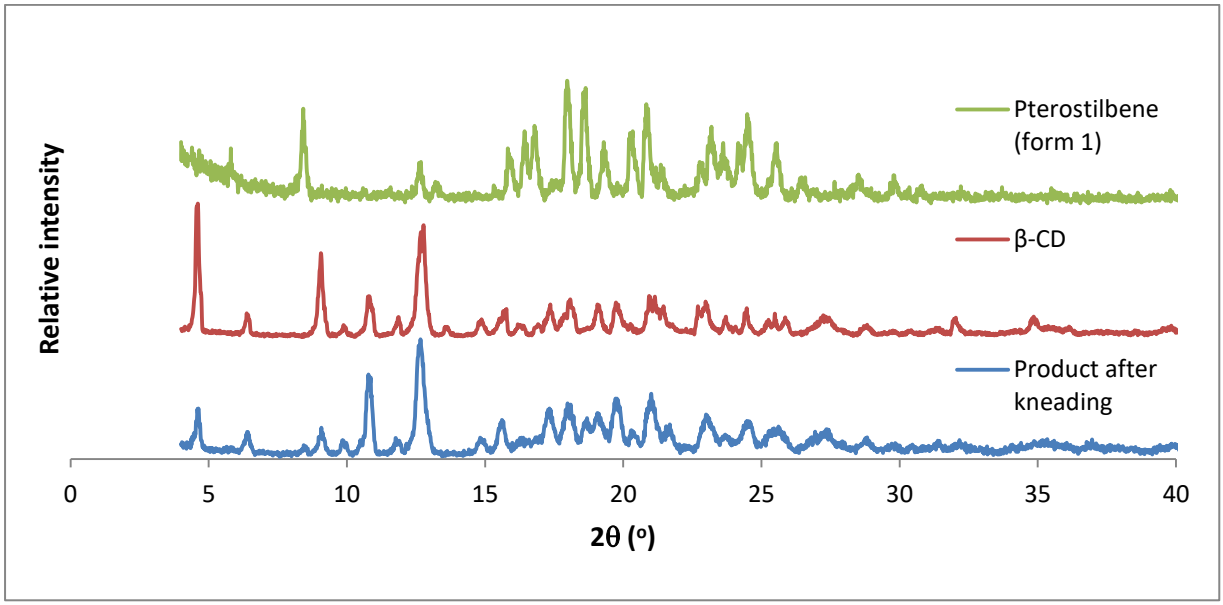


Figure 4.1.12: PXRD patterns of pterostilbene, β-CD, and the product after kneading β-CD and pterostilbene for 90 minutes. The latter PXRD pattern resembles that of β-CD with a peak from pterostilbene (form 1) at an angular position of 8.5° 2θ.

An alternative 'kneading' method was attempted with the API in a molten state and it successfully produced a new phase that was observed in the PXRD pattern of this product. This method involved pre-melting pterostilbene (10 mg, 0.040 mmol) at 110 ^{o}C in a glass vial and subsequently slowly adding the equimolar quantity of β-CD over a period of about 5 minutes to the melt, while 'kneading' the mixture with a spatula for a total of 30 minutes. Initially, the sample mixture had a crumb-like consistency; however, after approximately 20 minutes the mixture began to conglomerate into a pale, cream-coloured ball. The PXRD pattern of this product material is presented in Figure 4.1.13 with the PXRD patterns of the reagents.

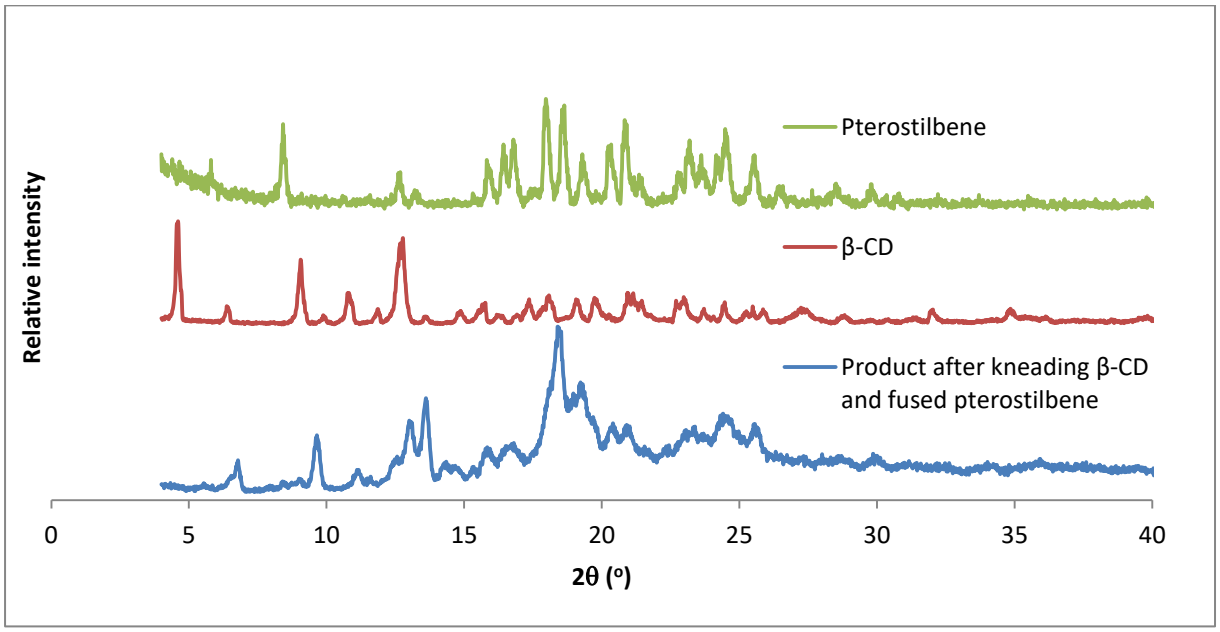


Figure 4.1.13: PXRD patterns of pterostilbene, β-CD and the product resulting from kneading β-CD and fused pterostilbene for 30 minutes.

It is evident that the product phase is not a physical mixture of the reagents; however, as displayed in Figure 4.1.9 in the summary at the beginning of this section, it did not correlate with either the PXRD pattern calculated from a single crystal of β-CD·PTB, or with a PXRD pattern of the product prepared *via* co-precipitation, or with any isostructural complex. As a result, it is not possible to produce the same complex phase established by single-crystal X-ray diffraction *via* kneading methods.

4.2.1.6) The discovery of a new polymorph of pterostilbene and the isolation of β-CD·PTB with a significantly higher purity

Attempts to isolate a purer batch of β-CD·PTB were performed by adding 3 ml of water to the product formed *via* the kneading process with molten coformer as described above and the mixture was heated between 80 and 85 ^{o}C until the product dissolved. After one hour of stirring the solution, it was filtered into clean, preheated vials and prepared for slow cooling in a Dewar flask. Instead of the complex forming, a very fine and thickly dendritic, white precipitate crystallized after two days (Figure 4.1.14), and was determined to be another polymorph of pterostilbene. This was based on a recent comparison of the data collated for this form with recently published data for six known polymorphs of pterostilbene.[22]

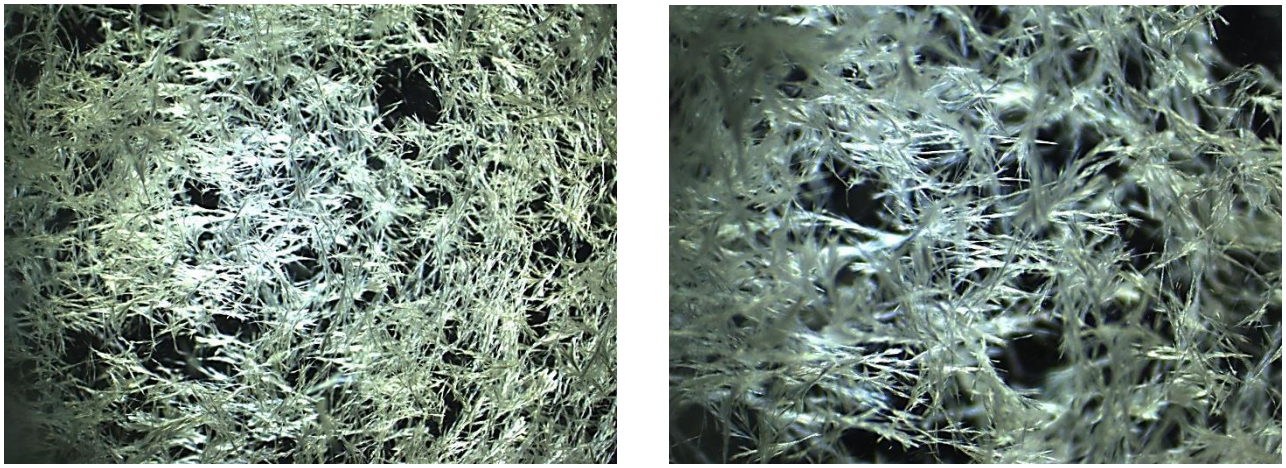


Figure 4.1.14: The dense dendritic morphology of a new polymorph of pterostilbene. The image on the right is a close-up of the image on the left.

The presence of this new polymorph was confirmed by ^{1}H NMR spectroscopy and by PXRD. The ^{1}H NMR spectrum (Appendix, section 3.1.2, p. 36) displayed that of pure pterostilbene without the presence of β-CD, thus proving that it was neither a complex nor a physical mixture. Figure 4.1.15 shows the PXRD pattern of this new polymorph with the PXRD patterns of the other six published forms of pterostilbene. It is evident from a comparison of the patterns that this new polymorph is a different phase, as many of its angular peak positions are unique.

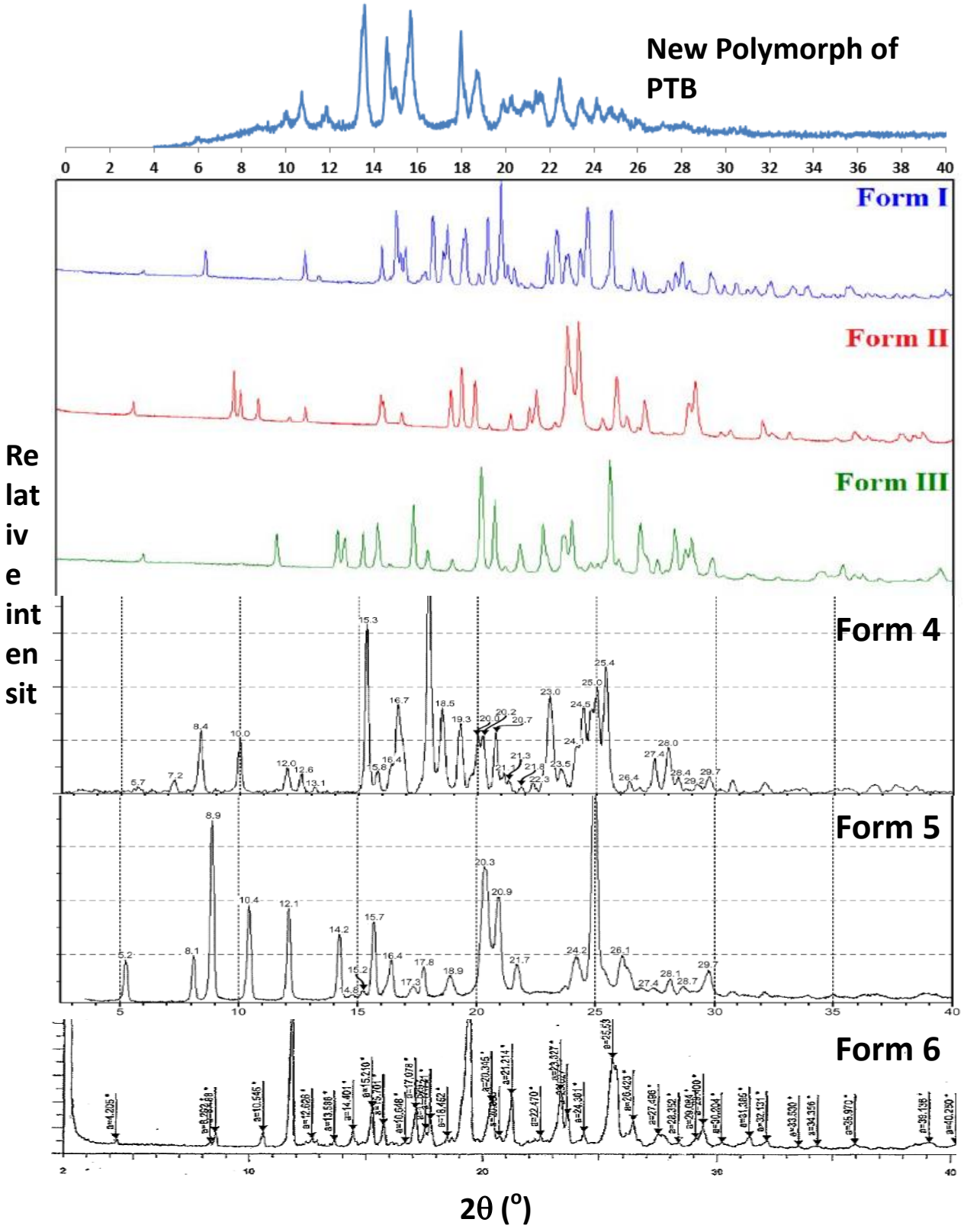


Figure 4.1.15: PXRD pattern of a new polymorph of pterostilbene and the PXRD patterns of the six published polymorphs of pterostilbene. Patterns for forms 1-6 have been taken directly from published papers, since these were the only sources available, and consequently their clarity is thereby limited.[23–25]

The method of producing this new polymorph was reproducible for a further four experiments (with the exception that the volume of the water had to be increased for a few of them, as the solute would instantaneously precipitate after filtering). However, this new polymorphic form seemed to be unstable, as it appeared to transform into form 1 readily. This was experienced with two subsequent experiments, from which slightly different PXRD patterns were obtained, despite the same methodology being used (Figure 4.1.16). These PXRD patterns shared some similarities with the initial PXRD pattern of this polymorph; however, there are significant differences with a few of the angular peak positions. Thus, it remains unknown as to which PXRD pattern is representative of the 'pure' form of this new polymorph and which are rather PXRD patterns of the phase undergoing transition. This experiment was repeated for the third time, except that the dendritic crystals were analysed only three days after their appearance and it was confirmed *via* PXRD that polymorph 1 was present for both samples. As a result, it can either be concluded that a new polymorph of pterostilbene initially crystallized and transformed into the more stable polymorph (form 1) within the three days, or that only pterostilbene form 1 initially crystallized.

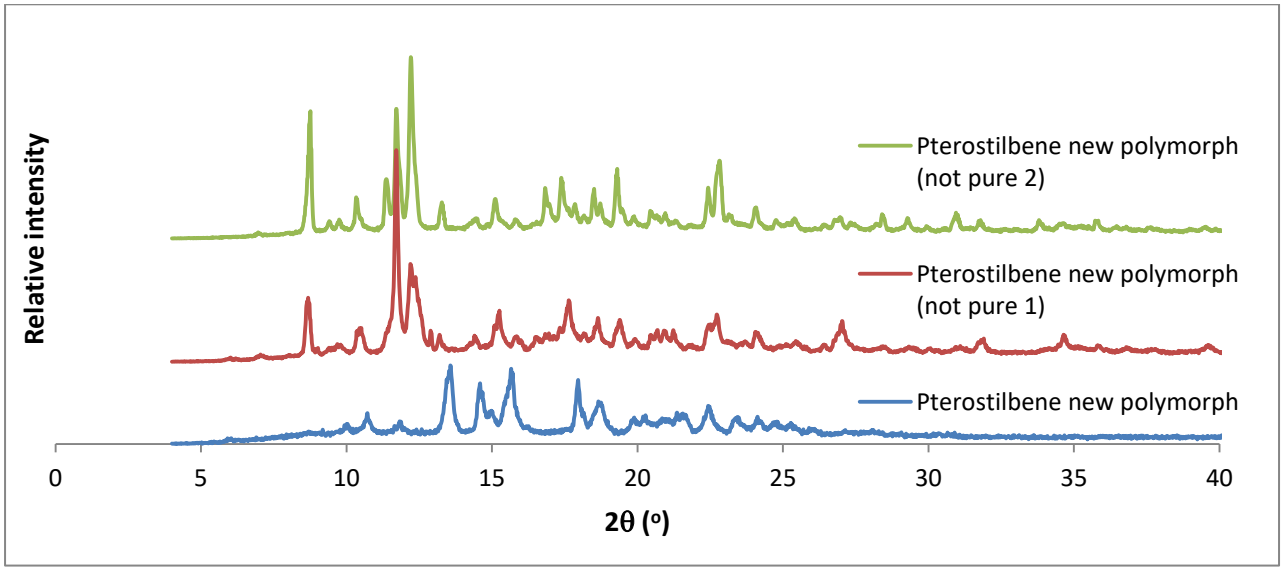


Figure 4.1.16: The PXRD pattern of a new polymorph of pterostilbene, and the two PXRD patterns of pterostilbene during a phase transition.

A final attempt was made to reproduce this new polymorph of pterostilbene in four simultaneous experiments, two of which involved recrystallizing the product formed from the kneading experiment with molten coformer, and another two which employed the initial co-precipitation methodology (with the exception that the solutions were heated to 85 ^{o}C and that slow cooling was used instead of slow evaporation). However, the results of all four simultaneous experiments unexpectedly produced seemingly pure batches of β-CD·PTB crystals based on the observed uniform morphology present (Figure 4.1.17).

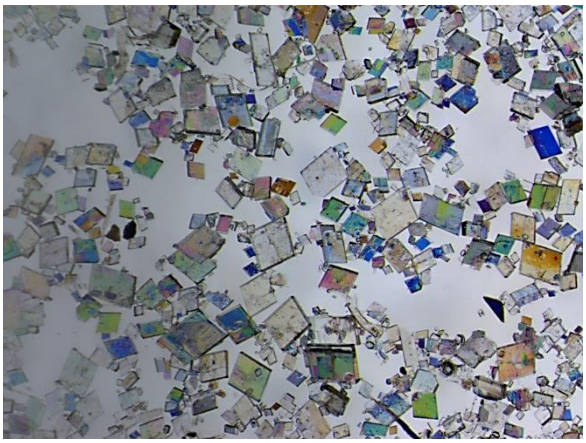


Figure 4.1.17: A sample of crystals displaying a significantly higher purity of β-CD·PTB. The general morphology is that of rhombohedrons (pertaining to β-CD·PTB) and very few crystals with chamfered edges (β-CD) are present.

In addition, extensive testing *via* measurement of their unit cell parameters was performed on many of these crystals and all displayed the same values of the cell parameters of the β-CD·PTB complex as identified in the SCXRD analysis. However, the PXRD pattern of the bulk sample of these crystals did not correlate with either the PXRD pattern calculated from a single crystal of β-CD·PTB, or with that of the product formed *via* the kneading process with molten coformer, nor does it resemble a mixture containing the PXRD pattern of β-CD and pterostilbene.

It remains unknown why β-CD·PTB suddenly formed using the methodology that previously produced the new polymorph of pterostilbene. However, the fact that the same nylon filter was being re-used from these previous experiments could have had an influence on preventing the polymorph of pterostilbene from forming. A possible explanation is that when the hot solution (containing β-CD and pterostilbene) was in the syringe, the solution

began to cool, which may have caused it to become supersaturated with pterostilbene. Thus, when the solution made contact with the membrane of the filter, the excess pterostilbene may have rapidly precipitated inside the filter as it came into contact with previous deposits of pterostilbene on the membrane of the filter.

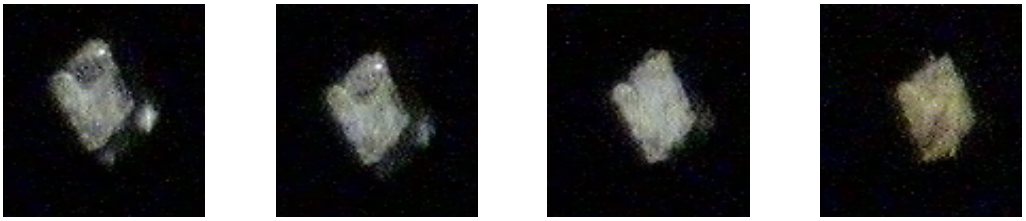
^{1}H NMR analysis was conducted on the bulk sample of these crystals in order to obtain a more accurate molar ratio, and even though a slightly higher mass was used (4 mg), the spectrum indicated a similar result to that previously obtained for β-CD·PTB, as described earlier (section 4.2.1.4, pp. 165 – 166), and with the internal integrations for the PTB molecule not adding correctly. This suggests (as mentioned previously) that in order to obtain an accurate spectrum, higher masses are required for the analyses. However, since it was not possible to reproduce these seemingly pure batches of the complex, additional sample could not be obtained for further experimentation.

Nevertheless, these four sets of experiments have thus far produced what seem to be the purest batches of β-CD·PTB based on a morphological appearance, and thus a full thermal analysis was conducted on this sample with the aim of quantifying the water content and recording the general thermal profile.

4.2.1.7) Hot stage microscopy (HSM) analysis

The HSM analysis provided visual evidence for the thermal events when a single crystal of β-CD·PTB (produced *via* co-precipitation) was heated at a constant rate of 10 K.min^{-1} (Figure 4.1.18). The results from the experiment were used to complement the thermal results observed later in the thermogravimetric analysis (TGA) and differential scanning calorimetry (DSC) experiment. Image A displays the initial appearance of β-CD·PTB prior to heating (23.3 ^{o}C). The dehydration of the crystal occurred at 39.1 ^{o}C, as represented by the onset of opacity in the top section of the crystal (image B). Full opacity was attained at 95.8 ^{o}C, which suggests that the dehydration of β-CD·PTB terminated at this temperature (image C). The loss of pterostilbene from the complex was not observed in this experiment (as it is later observed and discussed in the TGA and DSC results below). The onset of decomposition occurred at 306.9 ^{o}C (image D).

Figure 4.1.18: A series of micrographs from the HSM analysis of β-CD·PTB.



A: Initial appearance (23.3 °C). **B: Onset of opacity (39.1 °C).** **C: Maximum opacity achieved (95.8 °C).** **D: Onset of decomposition (306.9 °C).**

4.2.1.8) Thermal gravimetric analysis (TGA)

The preparation of β-CD·PTB for the TGA analysis (n=3) involved extracting the crystals from mother liquor in the vial, and repeatedly pressing them between a folded filter paper in order to ensure that all the surface water was removed.

The TGA curve indicated three thermal events taking place over the recorded temperature range (Figure 4.1.19). The first event is indicative of dehydration and occurred between 20.9 ± 1.9 °C and 100.3 ± 1.3 °C in a distinct two-step process (as indicated by the dTGA curve) and represents a water loss of 13.1 ± 0.4% which corresponds to 11.6 ± 0.4 water molecules per β-CD molecule assuming a 1:1 host-guest stoichiometric ratio.

The latter two thermal events, which included partial loss of the guest molecules and the decomposition of the host, overlapped to a small extent, which limited the accuracy of determining their individual characteristics. The onset of the partial loss of the guest molecules occurred at 227.7 ± 3.7 °C, which soon merged with the onset of decomposition which occurred at 286.7 ± 2.3 °C. The calculation for the water content can be viewed in the Appendix under section 3.1.3, p. 36.

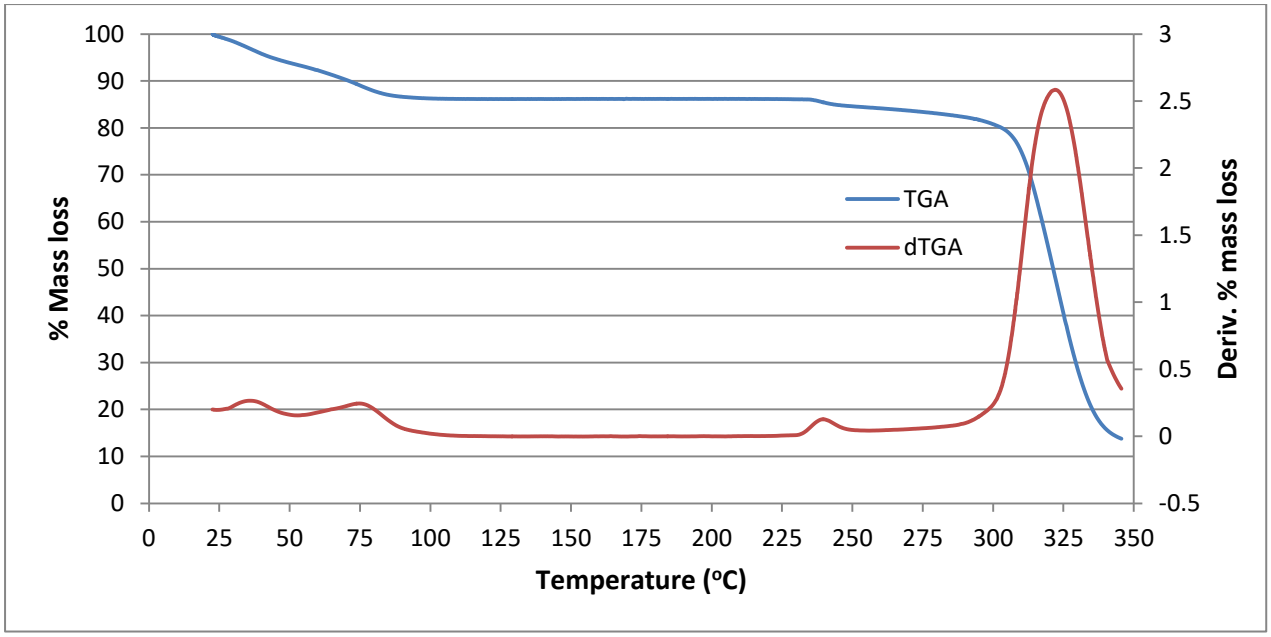


Figure 4.1.19: Representative TGA and dTGA curves for β-CD·PTB.

4.2.1.9) Differential scanning calorimetry (DSC)

The DSC curve of β-CD·PTB (n=3, Figure 4.1.20) displayed two thermal events over the recorded temperature range, which correlated with the results of the TGA analysis. The first event consisted of two overlapping, broad endotherms. The onset and peak temperatures for the first peak were 40.0 ± 2.7 °C and 66.1 ± 2.3 °C respectively, and for the second peak they were 82.7 °C ± 2.21 and 98.4 ± 1.6 °C respectively. These peaks represented a two-step dehydration of the complex, which correlated with the results displayed in the overlaid TGA curve, which was discussed above. The second thermal event is a composite set, which is initially characterised by a small sharp endothermic peak (onset temperature = 223.0 ± 0.2 °C; peak temperature = 225.0 ± 0.3 °C). This event is further accompanied by a very small consecutive endothermic and exothermic pair, occurring at peak temperatures 237.9 ± 1.6 °C and 242.6 ± 3.5 °C respectively. This composite event represents the partial loss of pterostilbene from the dehydrated inclusion complex, which correlates with the results displayed in the overlaid TGA curve. However, it is unknown whether a phase transition is occurring simultaneously, especially as a result of the presence of the endothermic and exothermic peak pair, which is often a general characteristic of a phase transition. Due to the limited sample mass, it was not possible to perform a variable temperature PXRD

experiment in order to verify this properly. However, these minor events occurring close to thermal decomposition at high temperatures are not significant in the context of this study.

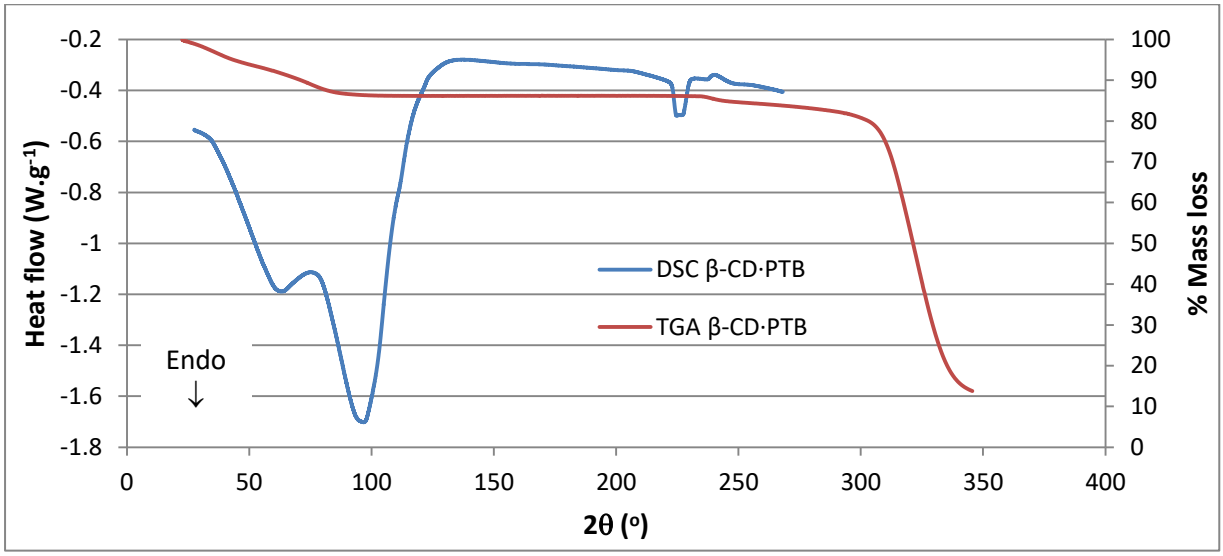


Figure 4.1.20: Representative DSC curve of β-CD·PTB, along with the respective TGA curve as a reference.

4.2.2) The inclusion complex, γ-CD·PTB

4.2.2.1) Method of preparation *via* kneading and co-precipitation

The hydrated γ-CD·PTB inclusion complex was initially prepared by kneading γ-CD (25.31 mg, 0.020 mmol) and PTB (5 mg, 0.020 mmol) in an equimolar ratio, and the PXRD pattern of the product after kneading was recorded. The angular positions of the peaks in the PXRD pattern of the product correlated with those of an isostructural γ-CD inclusion complex (refcode: DOCYID, containing the guest 12-crown-4)[26] that crystallizes in the tetragonal space group $P42_12$ (Figure 4.2.1). Thus, this confirmed the formation of a γ-CD·PTB complex *via* kneading.

It was also possible to isolate γ-CD·PTB *via* co-precipitation, either by creating a suspension with the kneaded sample at 60 ^{o}C in 10 ml of water while stirring, or by adding pterostilbene (5 mg, 0.0195 mmol) in a 1:1 stoichiometric ratio to a 10 ml aqueous solution of γ-CD at 70 ^{o}C. It is important to note that the complex is the insoluble species (the suspension) and it has an exceptionally fine particle size in the solution. In order to ensure complex purity, a slight excess of γ-CD was added to the solution to ensure that all the insoluble pterostilbene had reacted. Thereafter, the solution with the suspension was slowly filtered with a nylon 0.45 μm microfilter and the solid phase was subsequently washed with water (at 23 ^{o}C) by slowly injecting 1 ml of water into the filter with a syringe. This ensured that all the excess γ-CD was thereby removed. The γ-CD·PTB complex was harvested by clamping the nylon filter horizontally, cutting it open with a sharp knife and leaving it to dry overnight. The product (which is white in colour), could then be carefully scraped off the membrane of the filter. The PXRD pattern of γ-CD·PTB produced *via* co-precipitation also correlated with the PXRD pattern of the complex prepared by kneading (Figure 4.2.1).

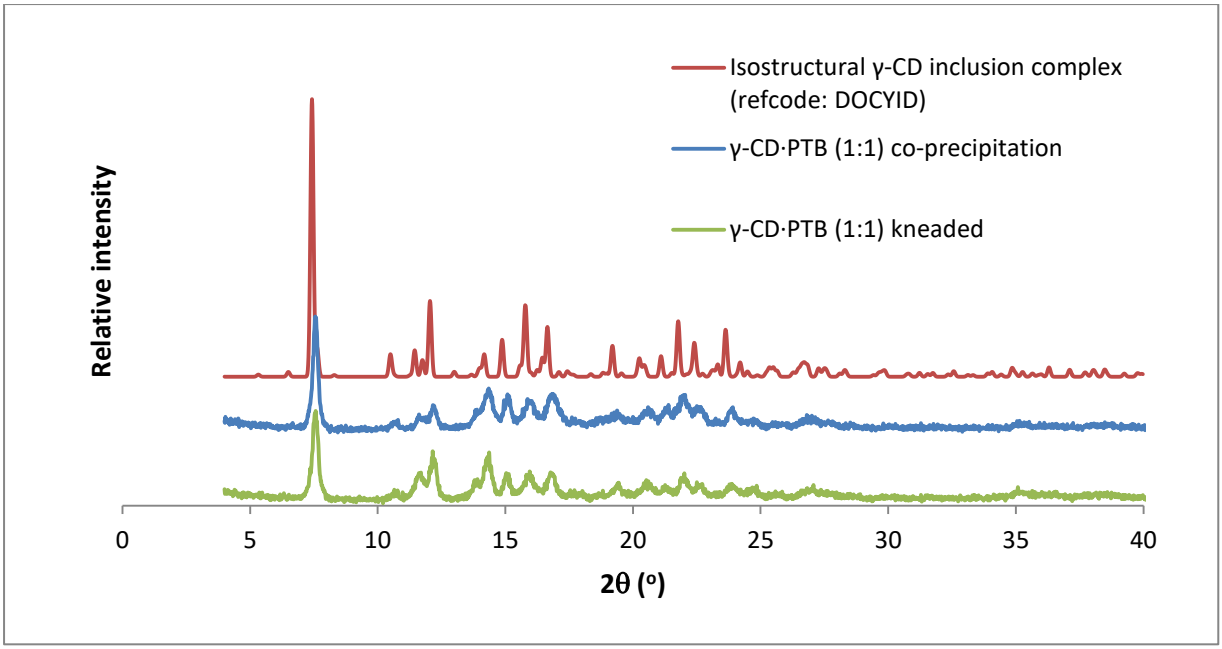


Figure 4.2.1: The PXRD patterns of γ-CD·PTB produced *via* kneading (1:1) and co-precipitation, as well as a PXRD pattern of an isostructural γ-CD inclusion complex (refcode: DOCYID).[26]

4.2.2.2) ^{1}H NMR analysis of the γ-CD·PTB complex

In order to isolate the pure complex and simultaneously confirm that the collected solid phase was a 1:1 inclusion complex, specific co-precipitation experiments were performed in duplicate (and referred to as "experiment 1" and "experiment 2"). The experiments involved kneading the reagents for 40 minutes with a large excess of γ-CD. The products were subsequently added to separate vials each containing 10 ml of water heated to 60 ^{o}C while stirring vigorously. The complexes were harvested as described above, and were thereafter dissolved in DMSO-d_6 for the ^{1}H NMR analysis. The results from both experiments indicated a 1:1 host-guest stoichiometry. Table 4.2.1 and Figure 4.2.2 display the results from experiment 2 as representative. Thus, this proved that despite the large excess of γ-CD added to the system, it was subsequently removed when the sample was washed with water in preparation for the ^{1}H NMR analysis, which consequently yielded a 1:1 complex stoichiometry. The ^{1}H NMR spectra for experiment 1 and experiment 2, as well as the tabulated results for experiment 1, can be viewed in the Appendix under sections 3.2.1 and 3.2.2, pp. 37 – 39.

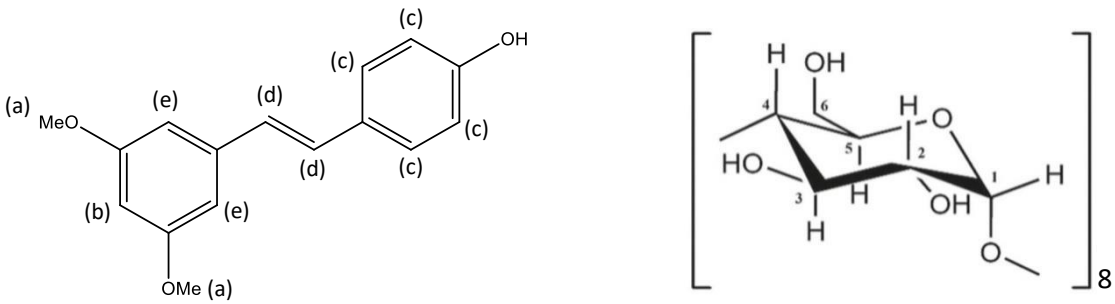


Figure 4.2.2: Molecular structures of pterostilbene (left) and γ-CD (right). Specific atoms have been labelled for the ^{1}H NMR analysis. Adapted from Guedes *et al.*[27]

Table 4.2.1: The ^{1}H NMR spectral analysis of γ-CD·PTB (experiment 2).

Assignment	δ (ppm)	Integration	Multiplicity	Proton representation (per molecule)	Stoichiometric ratio	Stoichiometric ratio (integer)
2X OC<u>H</u>$_3$ (a) (PTB)	3.777	0.7330	singlet	6H	0.98	1
O<u>H</u>-6 (γ-CD)	4.460 – 4.487	1.0000*	triplet	8H	1.00	1
C<u>H</u>-1 (γ-CD)	4.893 – 4.902	0.9788	doublet	8H	0.98	1
O<u>H</u>-3 and O<u>H</u>-2 (γ-CD)	5.686 – 5.730	1.9959	two separate doublets	16H	1.00	1
C<u>H</u> (b) aromatic (PTB)	6.371 – 6.382	0.1086	triplet (long range coupling)	1H	0.87	1
4X C<u>H</u> (c) aromatic (PTB)	6.714 – 6.785	0.4647	doublet of doublets	4H	0.93	1
C<u>H</u> (d) vinylic (PTB)	6.918 – 6.959	0.1151	doublet	1H	0.92	1
C<u>H</u> (d) vinylic (PTB)	7.131 – 7.172	0.1118	doublet	1H	0.89	1
2X C<u>H</u> (e) aromatic (PTB)	7.407 – 7.428	0.2272	doublet of triplets	2H	0.91	1

*reference integral

4.2.2.3) Thermal analysis of γ-CD·PTB

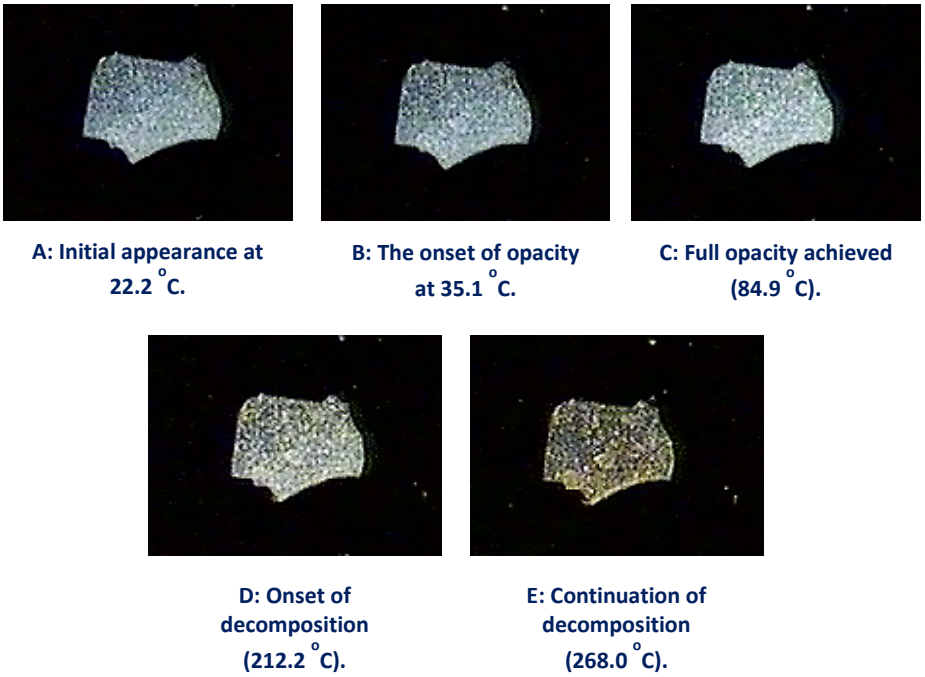
Three thermal analysis techniques were performed on the inclusion complex in order to characterise the water content and the onset of decomposition. For all thermal experiments, it is imperative to remove the surface water from the sample; however, this was challenging for γ-CD·PTB as the fine product particles formed a concentrated suspension on the membrane of the microfilter, unless left to dry. Therefore, the product was dried over a period of one day at 23 ^{o}C. The dried γ-CD·PTB complex was then placed in an open vial, which was inserted into a sealed larger vial with water at the bottom. The

complex was thus exposed to a closed atmosphere of water at 23 ^{o}C in order to hydrate itself under these conditions. Consequently, the thermal results provided an accurate estimate of the water content for the γ-CD·PTB complex in a hydrated environment at 23 ^{o}C.

4.2.2.3a) Hot stage microscopy (HSM) analysis

The HSM analysis displayed the visual representation of the dehydration and onset of decomposition of γ-CD·PTB over the temperature range from 22.2 ^{o}C until 268.0 ^{o}C (Figure 4.2.3). The initial appearance of γ-CD·PTB is displayed in image A at 22.2 ^{o}C; it consisted of a small fragment of a compacted fine precipitate. The barely discernible onset of opacity occurred at 35.1 ^{o}C and represented the onset of dehydration of the inclusion complex (image B). The complex was fully dehydrated once the maximum opacity was achieved for γ-CD·PTB, which occurred at 84.9 ^{o}C (image C). The subsequent thermal event was the onset of decomposition, which took place at 212.2 ^{o}C (image D) and continued until the decomposition became very apparent at 268.0 ^{o}C (image E).

Figure 4.2.3: A series of micrographs for the HSM analysis of γ-CD·PTB.



A: Initial appearance at 22.2 ^{o}C.

B: The onset of opacity at 35.1 ^{o}C.

C: Full opacity achieved (84.9 ^{o}C).

D: Onset of decomposition (212.2 ^{o}C).

E: Continuation of decomposition (268.0 ^{o}C).

4.2.2.3b) Thermal gravimetric analysis (TGA)

The TGA curve of γ-CD·PTB (n=3) displays two thermal events over the temperature range between 23 °C and 350 °C (Figure 4.2.4). The first event represents the loss of water as a single-step process between 18.7 ± 0.9 °C and 133.7 ± 5.1 °C.

The mass loss of 12.8 ± 0.4% corresponds to 12.7 ± 0.4 water molecules per complex unit. This calculation can be viewed in the Appendix under section 3.2.3, p. 39. The second thermal event is associated with the decomposition of γ-CD·PTB which took place at 275.2 °C.

In comparison with the HSM analysis, analogous thermal events were identified by TGA; however, their respective temperatures did not correlate, but this is often expected when comparing results performed on different instruments.

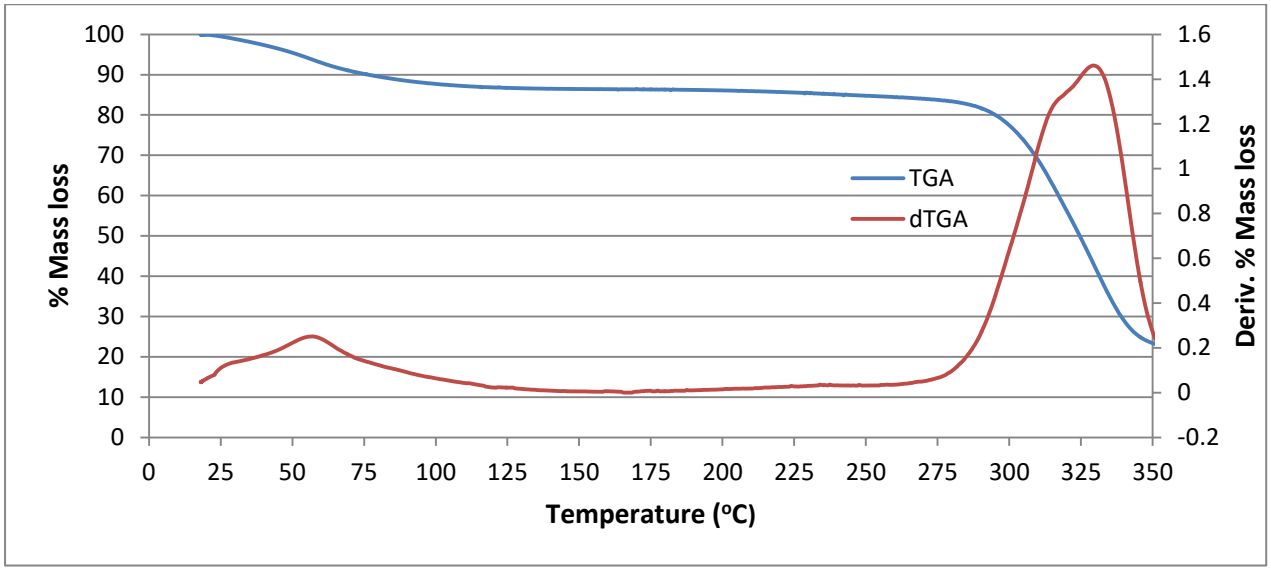


Figure 4.2.4: Representative TGA and dTGA curves for γ-CD·PTB.

4.2.2.3c) Differential scanning calorimetry (DSC)

The DSC curve (n=3) displayed one endothermic event as a single-step process, interpreted as complex dehydration (Figure 4.2.5). The DSC curve displays a single, broad, endothermic peak with onset temperature at 54.3 ± 1.2 °C (with the peak occurring at 90.1 ± 3.6 °C). The DSC curve also confirmed that the rate of water loss is uniform owing to the constant gradient and symmetry of the endothermic peak. The thermal trends of the events from the DSC and TGA experiments corresponded, indicating a suitable correlation, despite the dehydration onset temperatures not appearing to relate well. As mentioned, this disagreement of results is often caused by the measurement being performed on different instruments, and thus expected.

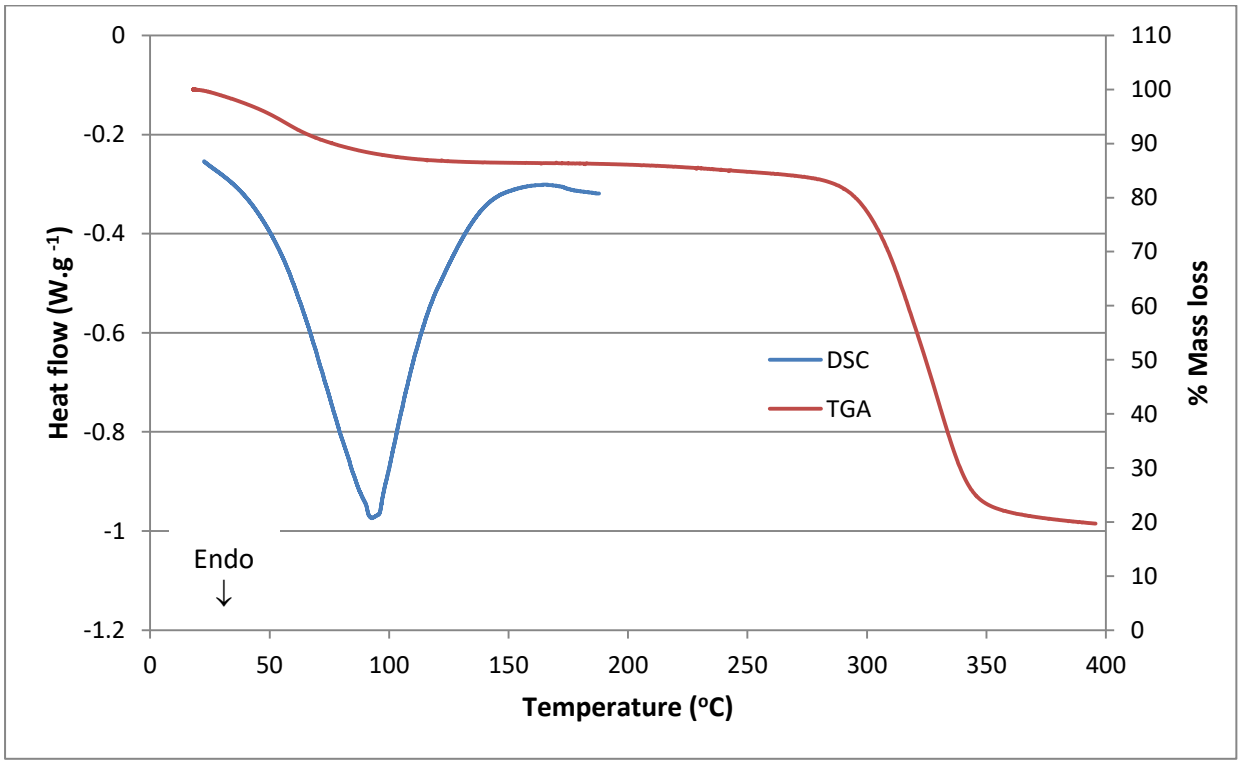


Figure 4.2.5: Representative DSC curve of γ-CD·PTB, with the respective TGA curve as a reference.

4.2.3) The TMB·PTB inclusion complex

4.2.3.1) The initial isolation of TMB·PTB *via* co-precipitation

The 1:1 inclusion complex formed between permethylated β-CD (TMB, for 'tri-methyl β-CD') and pterostilbene was initially isolated *via* co-precipitation, which required an excess of CD in order to form the complex in solution. The preparation involved dissolving TMB (78.05 mg, 0.0546 mmol) in 3 ml of Milli-Q water at 25 ^{o}C while stirring vigorously. PTB (7 mg, 0.0273 mmol) was subsequently added very slowly to the TMB solution and temperature cycling was used in order to promote solution complexation between each successive addition of pterostilbene. The pterostilbene had the tendency to aggregate in the form of an adhesive solid on the magnetic stirrer bar before it had complexed with the TMB. Thus, this adhesive solid was dried, crushed and re-added to the solution. (This type of aggregation occurred only in the solution containing TMB, and not with β-CD or γ-CD). The solution was left to stir for 3 – 4 days with the aid of temperature cycling and was subsequently filtered at 4 ^{o}C into a clean vial and placed in the oven at 60 ^{o}C to encourage the growth of crystals, which appeared as fine needles after one day.

Replication of this methodology to produce the crystals was somewhat challenging, as subsequent preparative methods required additional tailoring in order to obtain adequate crystals. The volume of water initially used to form the complex prior to filtering had to be increased constantly for successive experiments (sometimes to over 10 ml), to prevent immediate precipitation of the complex after being placed in the oven at 60 ^{o}C. The filtered complex solution that was placed in the oven was left for 2 days before the sealed vial was opened to promote small, periodic levels of evaporation. The remaining volume of solution had to be lowered very slowly over a five-week period to approximately 3 ml before crystals of better quality would start to form.

4.2.3.2) Crystal morphology

The morphology of the complex crystals is that of long, transparent 'whiskers' that radiate in the shape of a bow-tie (Figure 4.3.1). Attempts to collect SCXRD data for this complex were performed, where fragments of the largest needles were cut. However, the crystals diffracted very weakly and appeared to be severely twinned.

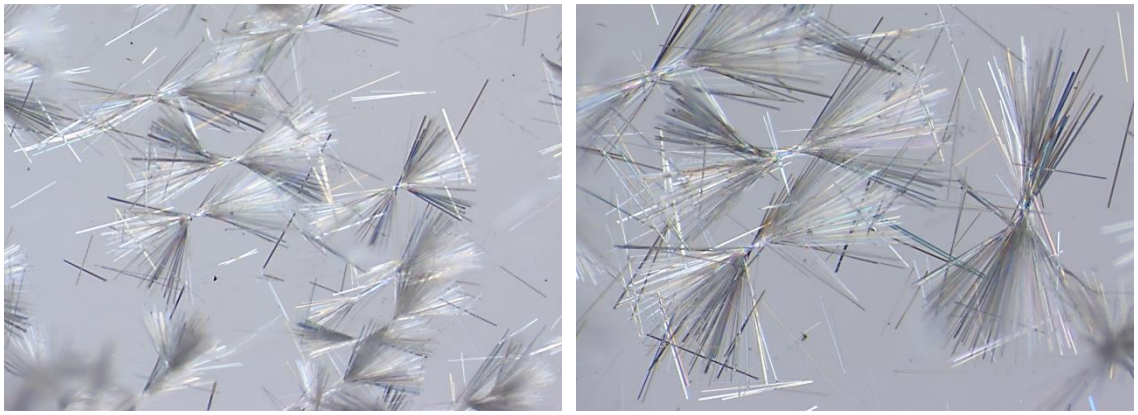


Figure 4.3.1: The acicular morphology of the TMB·PTB complex, which crystallized in the shape of bowties.

4.2.3.3) PXRD analysis

The TMB·PTB complex could also be formed *via* kneading of an equimolar mixture of the components, with water as the medium for 40 minutes, as the PXRD pattern of this product correlated with that of TMB·PTB produced *via* co-precipitation (Figure 4.3.2). The unit cell determination indicated that TMB·PTB crystallized in the orthorhombic crystal system with the following unit cell parameters: a = 14.737(3) Å, b = 30.886(7) Å, c = 58.77(2) Å, V = 26750(20) $Å^3$. TMB·PTB was not isostructural with any other TMB complex, and this was further confirmed by the fact that the PXRD pattern of TMB·PTB did not correlate with any of the PXRD patterns of other published TMB inclusion complexes.

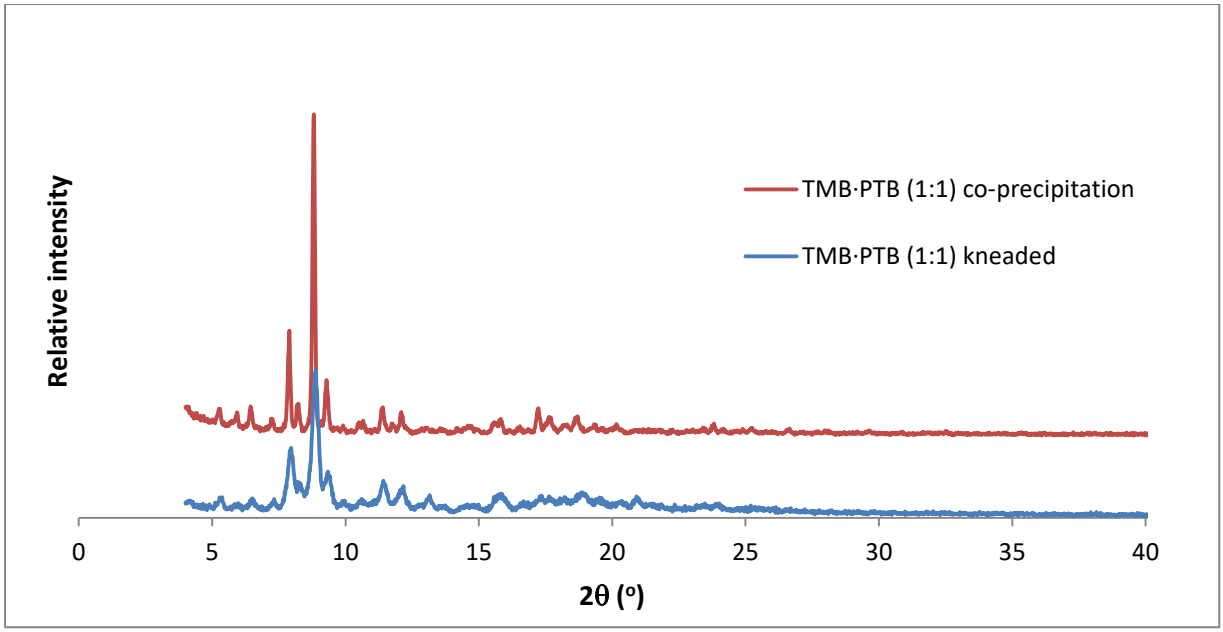


Figure 4.3.2: The PXRD patterns of the TMB·PTB inclusion complex produced *via* kneading and co-precipitation.

4.2.3.4) ^{1}H NMR analysis

The ^{1}H NMR analysis indicated a 1:1 molar ratio for the TMB·PTB complex that was produced *via* co-precipitation. The assignments of the spectral results are listed in Table 4.3.1 with reference to Figure 4.3.3 for atomic assignments. The ^{1}H NMR spectra can be viewed in the Appendix under section 3.3.1, p. 40.

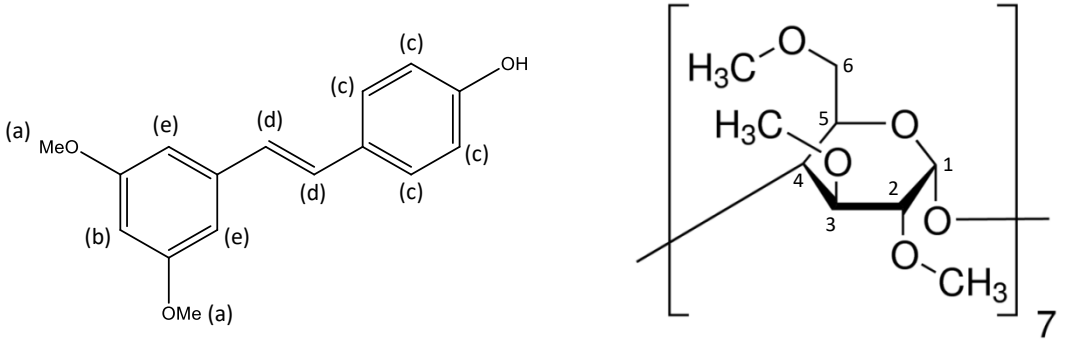


Figure 4.3.3: Molecular structures of pterostilbene (left) and TMB (right). Specific atoms have been labelled for the ^{1}H NMR analysis. Adapted from Sigma-Aldrich.[28]

Table 4.3.1: The ^{1}H NMR spectral analysis of TMB·PTB.

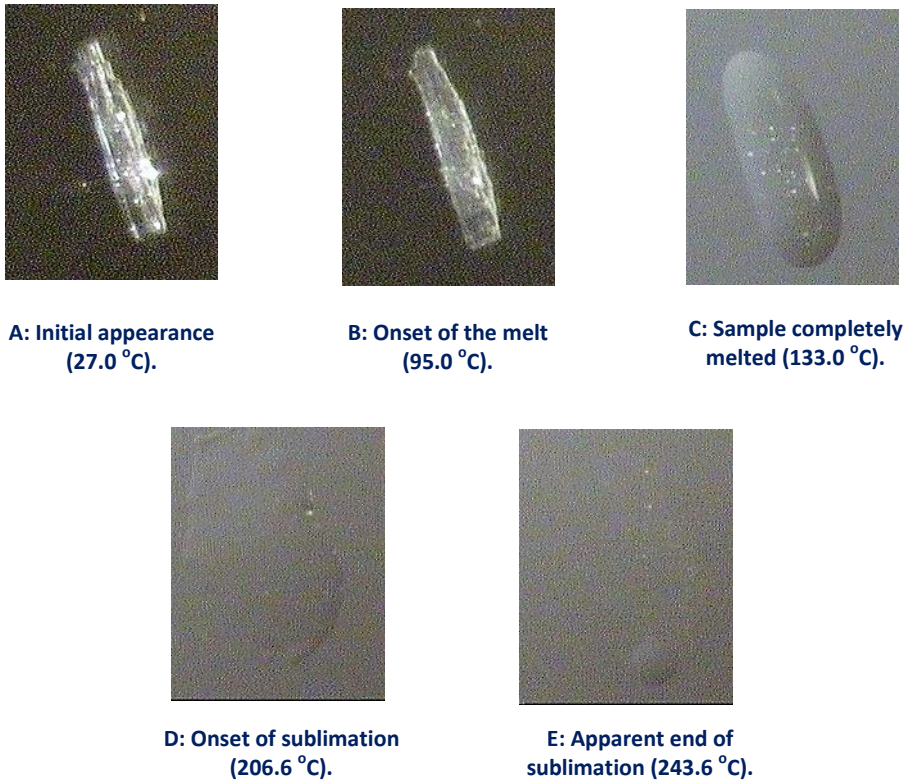
Assignment	δ (ppm)	Integration	Multiplicity	Proton representation (per molecule)	Stoichiometric ratio	Stoichiometric ratio (integer)
OC$\underline{H}_3$ (6) methoxy (TMB)	3.252	1.0762	singlet	21	1.08	1
OC$\underline{H}_3$ (3) methoxy (TMB)	3.400	1.0000*	singlet	21	1.00	1
OC$\underline{H}_3$ (2) methoxy (TMB)	3.507	1.0890	singlet	21	1.09	1
2X OC$\underline{H}_3$ (a) (PTB)	3.777	0.3035	singlet	6H	1.06	1
C$\underline{H}$ (b) aromatic (PTB)	6.371 – 6.382	0.0390	triplet (long range coupling)	1H	0.82	1
4X C$\underline{H}$ (c) aromatic (PTB)	6.715 – 6.784	0.1717	doublet of doublets	4H	0.90	1
C$\underline{H}$ (d) vinylic (PTB)	6.920 – 6.960	0.0391	doublet	1H	0.82	1
C$\underline{H}$ (d) vinylic (PTB)	7.132 – 7.174	0.0380	doublet	1H	0.80	1
2X C$\underline{H}$ (e) aromatic (PTB)	7.407 – 7.428	0.0856	doublet of triplets	2H	0.90	1

*reference integral

4.2.3.5) Hot stage microscopy (HSM) analysis

The micrographs from the HSM analysis are displayed in Figure 4.3.4 and represent the thermal progress of the complex over a temperature range of 27.0 – 243.6 ^{o}C. The initial appearance of TMB·PTB is displayed in image A at 27.0 ^{o}C and the first observable thermal event occurred at 95.0 ^{o}C, which represented the fairly sharp onset of a melt (image B). Thereafter, the crystal was completely melted at 133.0 ^{o}C, as displayed in image C. Furthermore, sublimation was observed at 206.6 ^{o}C (image D), as the melt began to slowly disappear by losing its convex nature and thus became flatter until it was no longer possible to make any further accurate visual observations beyond 243.6 ^{o}C (image E). It was thus concluded that the melt had apparently fully sublimed by this temperature.

Figure 4.3.4: A series of micrographs for the HSM analysis of TMB·PTB.



A: Initial appearance (27.0 °C).

B: Onset of the melt (95.0 °C).

C: Sample completely melted (133.0 °C).

D: Onset of sublimation (206.6 °C).

E: Apparent end of sublimation (243.6 °C).

4.2.3.6) Thermal gravimetric analysis (TGA)

The TGA curve displayed three separate thermal events (namely the dehydration, the loss of the guest molecules and sublimation) that occurred over the recorded temperature range (Figure 4.3.5). The first thermal event took place between 21.5 ± 2.7 °C and 36.6 ± 0.6 °C and represented a 0.6 ± 0.2% mass loss, which corresponded to 0.6 ± 0.1 water molecules per complex unit. The second thermal event corresponded to the loss of the guest molecules, pterostilbene, which occurred at 166.1 ± 7.2 °C. In contrast to the TGA curve of β-CD·PTB, this loss of the guest molecules and the onset of sublimation are distinctly separate events. This was confirmed since a mass loss percentage of 14.9 ± 1.4% indicated an equimolar H:G ratio, as it corresponded to the expected theoretical value of 15.2% for the dehydrated 1:1 TMB·PTB inclusion complex. This result is consistent with the ^{1}H NMR data which also indicated a 1:1 composition for this inclusion complex. The calculations for the dehydration and loss of the guest molecules can be viewed in the Appendix under

sections 3.3.2 and 3.3.3, p. 41. Lastly, the onset of the sublimation occurred once the guest molecules were removed, which was at 296.9 ± 15.2 °C.

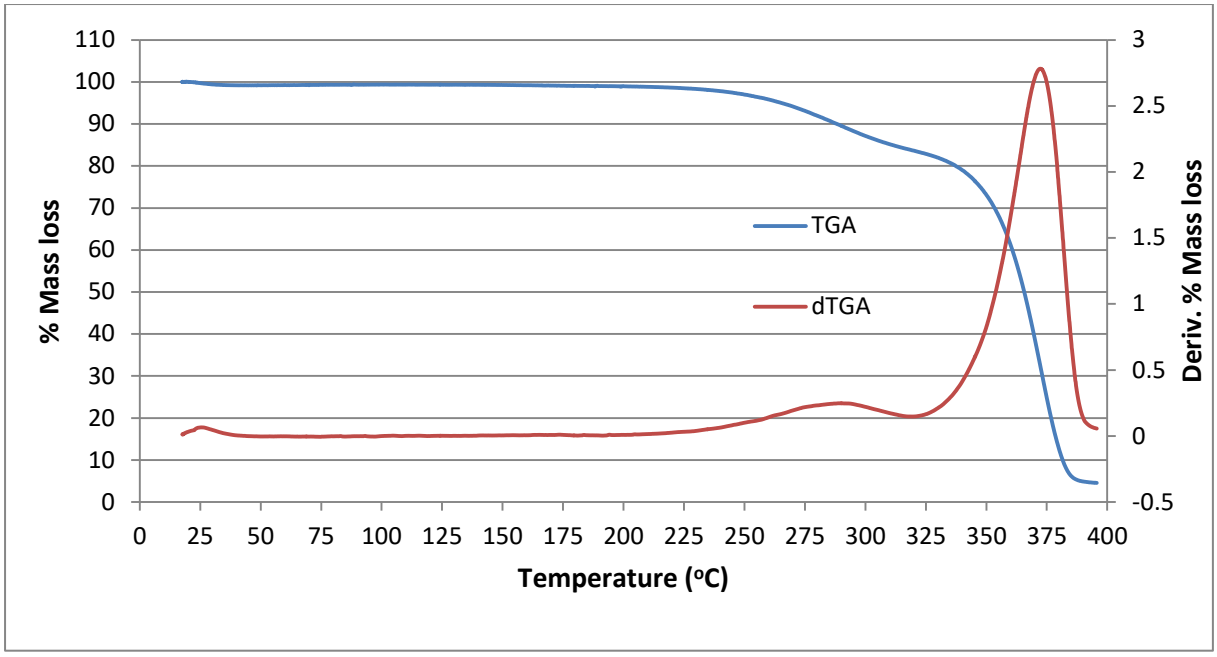


Figure 4.3.5: Representative TGA and dTGA curves for TMB·PTB.

In comparison to the HSM analysis, water loss was not observed (either in the form of bubbles or opacity) owing to the fact that the water contribution is comparatively so small that it is often not possible to observe changes caused by its loss. The sublimation of TMB was observed to occur significantly later in the HSM analysis. However, the thermal events are still reflective of one another, as the TGA mass loss was reduced to less than 5%, thus confirming full sublimation.

4.2.3.7) Differential scanning calorimetry (DSC)

The DSC curve of TMB·PTB (n=2) displayed two distinct thermal events, namely a phase transition (in the form of a pair of small consecutive endothermic peaks), and immediately thereafter a melt, as represented by the sharp endothermic peak (Figure 4.3.6). The loss of water was expectedly not observed in this experiment since the quantity of water per complex unit is very small. The onset temperature and peak temperature for the two

consecutive endothermic peaks were 92.7 ± 0.4 °C and 100.5 ± 0.4 °C respectively for the first peak, and 106.6 ± 0.5 °C and 110.9 ± 0.4 °C respectively for the second peak. Shortly after these two consecutive endothermic peaks (which possibly represent two successive phase transitions), the resultant product melted, as displayed by the large and sharp endothermic peak with an onset temperature of 128.4 ± 0.1 °C and a peak temperature of 130.6 ± 0.1 °C. These results correlated well with the HSM analysis, which indicated a melting point of 133.0 °C. The DSC experiment was stopped prior to the sublimation of the sample to prevent contamination of the cell in the instrument.

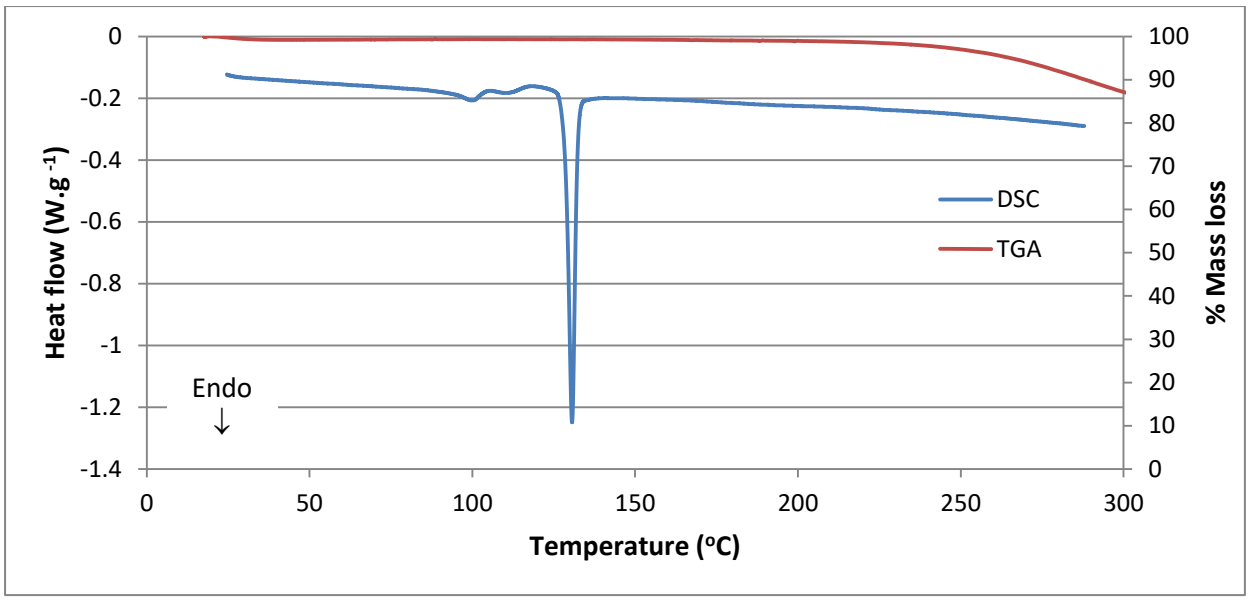


Figure 4.3.6: DSC curve of TMP·PTB, with the TGA curve as a reference.

4.2.3.8) Variable temperature PXRD

The variable temperature PXRD experiment (Figure 4.3.7) confirmed the conclusions drawn from the DSC analysis, where phase transitions occurred prior to a melt. However, the variable temperature PXRD analysis evidently only displayed one phase transition and a possible explanation is that a significantly slower rate is required as the phase transition peaks are only ~10 K apart. With reference to the variable temperature PXRD pattern, between 80 °C and 90 °C it is evident that the sample experienced a phase transition. The

peaks in the PXRD pattern that were present from 25 °C to 80 °C were nullified at 90 °C, and the emergence of a new PXRD pattern with peaks at different angular positions commenced. At 100 °C this new PXRD pattern had fully formed, and between 105 °C and 110 °C the sample melted (and remained molten even at higher temperatures), as indicated by the featureless PXRD patterns due to the liquid phase.[b] It is evident by comparing the DSC and variable temperature PXRD experiments that the thermal events appear to occur somewhat later in the DSC experiment. As explained previously, this is often expected to occur, as the two separate experiments were conducted on different pieces of equipment.

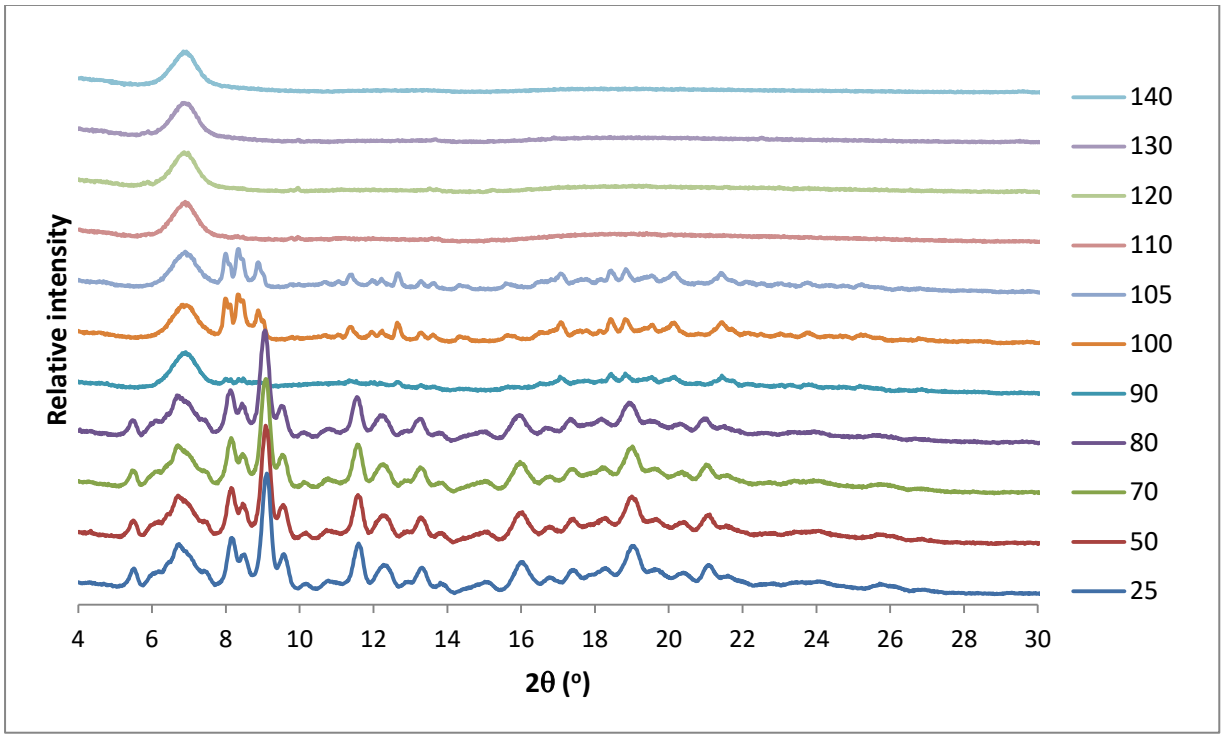


Figure 4.3.7: The variable temperature PXRD patterns of TMB·PTB over the temperature range from 25 °C to 140 °C. The numbers in the key represent the sample temperatures in °C. The peak at the angular position of 7.0° is an artefact of the variable temperature PXRD stage. No significant peaks were observed at angular positions greater than 30.0°.

In conclusion, the three CD inclusion complexes with pterostilbene as guest were successfully isolated and characterised. The single-crystal X-ray structure of β-CD·PTB unequivocally displayed the mode of inclusion of the guest molecule, as well as the packing arrangement of the dimeric units with their intramolecular and intermolecular hydrogen

[b] The peak at the angular position of 7.0° 2θ is an artefact of the variable temperature PXRD stage.

bonds. All the analytical data presented unambiguous proof that authentic inclusion complexes were formed, despite the lack of single-crystal X-ray data for γ-CD·PTB and TMB·PTB. The full molecular formulae for the three inclusion complexes, as indicated by the analytical data, are β-CD·PTB·11.6(H_2O), γ-CD·PTB·12.7(H_2O), and TMB·PTB·0.6(H_2O).

The aqueous solubilities of these three complexes were not assessed owing to the fact that a pure phase of β-CD·PTB was not easily reproducible, the insolubility of γ-CD·PTB prevents its application in the pharmaceutical industry, and the cost of TMB is too high to warrant solubility investigations with TMB·PTB. The methylated CDs (like TMB) are also less favourable in the pharmaceutical industry since they cause the most severe haemolytic effects on erythrocytes if administered parenterally.[29] However, the following section deals with a study of the assessment of pterostilbene solubility modification using amorphous CDs, whose employment displayed significant potential for pharmaceutical applications owing to the substantial solubility enhancements of PTB that resulted.

4.2.4) Phase solubility investigation with randomly methylated β-CD (RAMEB) and sulfobutyl ether β-CD (SBEBCD) sodium salt

4.2.4.1) Overview and contextualisation of the investigation

Phase solubility studies were conducted with two amorphous CDs, namely randomly methylated β-CD (RAMEB) and sulfobutyl ether β-CD (SBEBCD) sodium salt, in order to assess the potential that they might have for increasing the aqueous solubility of pterostilbene (PTB). As mentioned in the beginning of this chapter, a previous study reported phase solubility studies with hydroxypropyl β-CD (HPBCD) and hydroxypropyl γ-CD (HPGCD), which showed significant solubilisation of pterostilbene over their selected CD concentration ranges.[5] Thus, it is appropriate to assess additional CDs as potential solubilizers, especially those that are highly soluble in water, like RAMEB and SBEBCD sodium salt.

The stability of pterostilbene remains a highly problematic issue, as it is known to be unstable in acidic and alkaline media, as well as displaying instability towards light, heat, and oxidation.[30] The instability of pterostilbene towards light, and particularly UV light, can be problematic when quantitative analysis is performed on either a UV-vis or a HPLC instrument, since both instruments employ UV light sources. It is known that pterostilbene isomerises from the trans bioactive form to the inactive cis form when irradiated with UVA light, the 'trans' λ_{max} occurring between 310 and 320 nm, and the 'cis' λ_{max} around 280 nm. In view of the chemical instability of pterostilbene, López-Nicolás *et al.* reported a study of this shortcoming to develop a reliable method for its quantification.[2] An HPLC instrument was used, as the cis and trans isomers (along with other degradation products) have slightly different retention times, and thus their contributions can be separately monitored for any fluctuations during the experiment. For the purposes of the phase solubility experiments conducted by the author of this thesis, only the trans isomer was quantified, as this is the biologically active isomer and thus pharmaceutically relevant. Consequently, the analysis performed with RAMEB and SBEBCD sodium salt in this current investigation incorporated the guidelines from the paper cited above in order to quantify the solubility of the trans

isomer of pterostilbene as a function of CD concentration. The literature value for the aqueous solubility of pterostilbene is quoted as 5.023 x10^{-3} mg.cm^{-3} at 25 ^{o}C.[5]

4.2.4.2) Construction of the calibration curve

Initially, a calibration curve was prepared (Figure 4.4.1), using a similar procedure as that outlined by López-Nicolás *et al.*[2] A sample of PTB of mass 5.20 mg was dissolved in 50 cm^3 of acetonitrile:water (60:40 v/v) stock solution, from which appropriate dilutions were made. Each dilution was analysed using HPLC and the peak area of the trans isomer was recorded, as this is the isomer that is biologically active. Consequently, a calibration curve was constructed which plotted the peak area of the trans isomer against the concentration of pterostilbene. This calibration curve displayed linearity with an appropriate R^2 value of 0.998. The equation of the line was determined to be y = 10914x - 57.83.

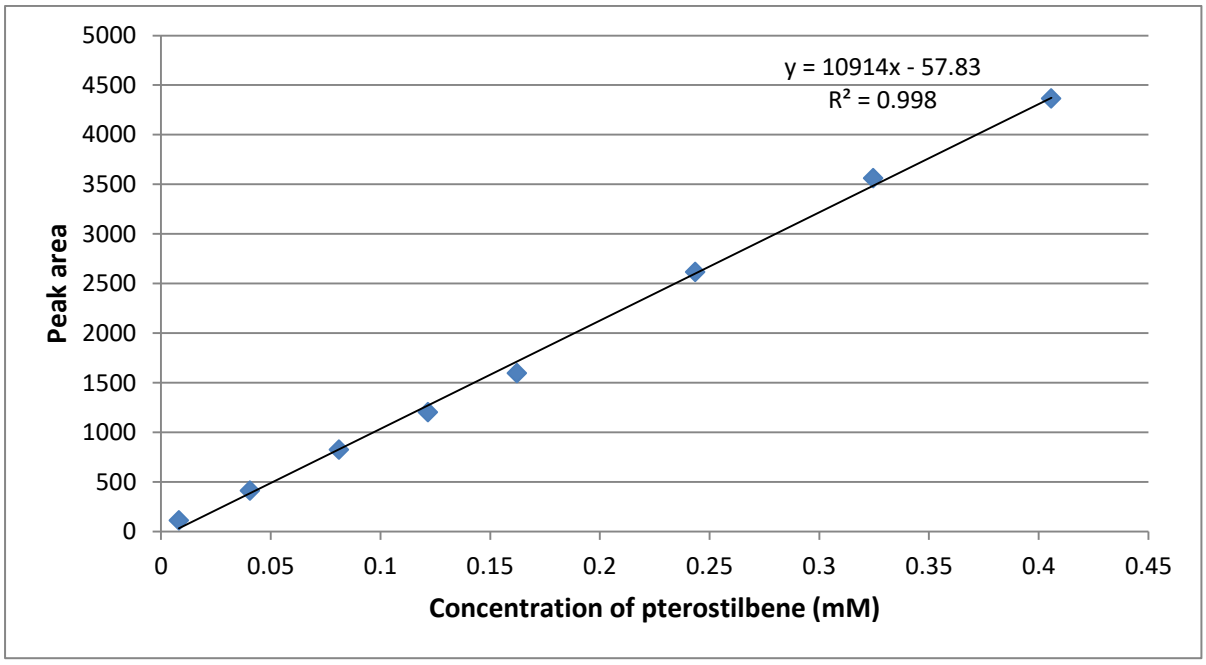


Figure 4.4.1: Calibration curve of the HPLC peak area versus the concentration of pterostilbene (mM).

4.2.4.3) Phase solubility results with RAMEB and SBEBCD sodium salt

Phase solubility profiles have been classified by Higuchi and Connors as either A-type or B-type (Figure 4.4.2).[31] Phase solubility profiles that follow an A-type behaviour display an increase in the solubility of a compound with an increase in CD concentration, while B-type profiles represent a decrease in the solubility of a compound of interest with an increase in CD concentration, and thus indicate the formation of an insoluble complex.[31] There are three sub-categories associated with the A-type behaviour. These include A_L-type curves, which represent a linear increase in the solubility of a compound with an increase in the CD concentration, and A_P-type / A_N-type curves which represent the increase in the solubility of a compound with a positive / negative deviation respectively, as the CD concentration increases (Figure 4.4.2). In addition, there are two sub-categories for B-type profiles which include the B_i-type, representing the formation of an insoluble complex, and the B_S-type representing limited solubility occurring from the formation of an insoluble complex (Figure 4.4.2).[31]

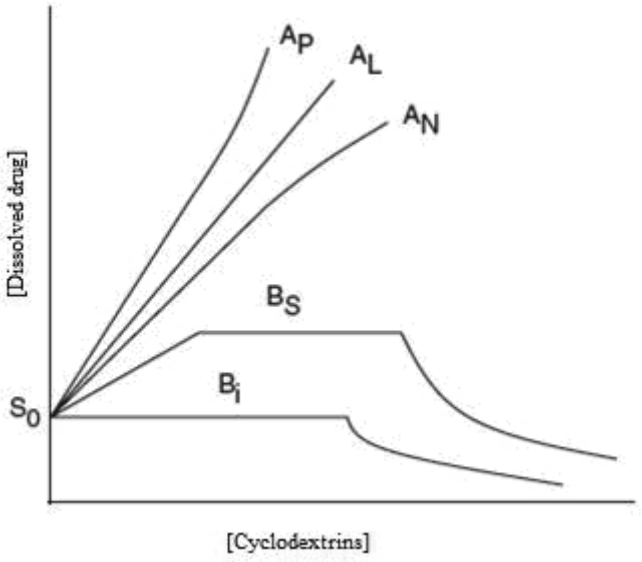


Figure 4.4.2: A- and B-type phase solubility profiles. A-type profiles comprise A_P-type, A_N-type and A_L-type, while B-type profiles comprise B_S-type and B_i-type. Taken from Neves de Lima *et al.*[32]

Five aqueous solutions containing differing concentrations of each CD (4 mM, 8 mM, 12 mM, 16 mM and 20 mM) were analysed for their solubility enhancement potential, and the

experiment was conducted according to the method described in the Experimental methods section, Chapter 2, section 2.10.2, p. 48. The results from this study are provided in Figures 4.4.3 and 4.4.4, as well as in Tables 4.4.1 and 4.4.2 and a sample calculation can be viewed in the Appendix under section 3.3.4, p. 42.

The phase solubility profiles that were assigned to RAMEB and SBEBCD sodium salt are only valid within the CD concentration range investigated, since at higher CD concentrations the profiles may take on different trends.

Consequently, an A_P-type profile can be assigned to the phase solubility profile for RAMEB owing to the overall positive exponential trend throughout the increasing concentration range of this CD (Figure 4.4.3). The solubility enhancement values for pterostilbene ranged between 63-fold and 1356-fold over the CD concentration range of 4 mM – 20 mM (Table 4.4.1).

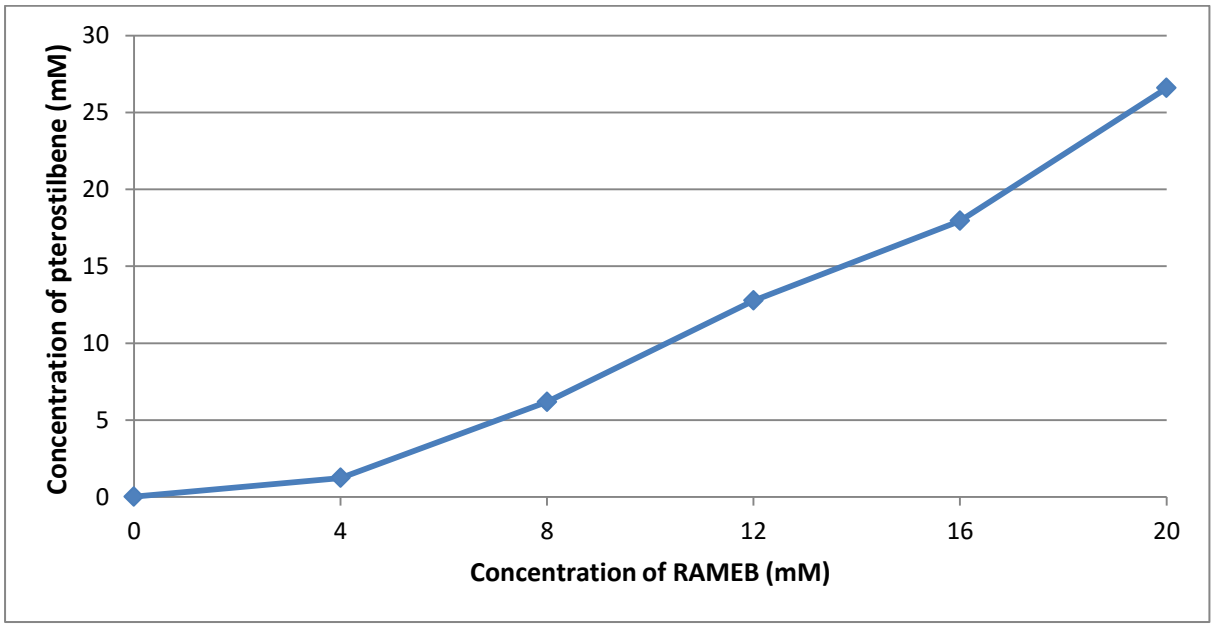


Figure 4.4.3: Solubility of PTB as a function of RAMEB concentration at 23 °C.

Table 4.4.1: PTB solubility enhancement as a function of [RAMEB] at 23 °C.

Concentration of CD (mM)	Concentration of PTB (mM)	Mass of PTB dissolved (mg.cm^{-3})	Solubility enhancement ratio
4	1.240	0.318	63
8	6.185	1.585	315
12	12.769	3.273	651
16	17.952	4.601	916
20	26.587	6.814	1356

Furthermore, the phase solubility profile of SBEBCD sodium salt displayed an overall slight positive exponential trend (as indicated by the trendline) and thus it can also be assigned an A_P-type phase solubility profile (Figure 4.4.4). However, the values at CD concentrations of 4 mM and 8 mM are underestimated and overestimated respectively. Nevertheless, the solubility enhancement values for this system over the CD concentration range of 4 mM to 20 mM ranged between 153-fold and 1431-fold (Table 4.4.2).

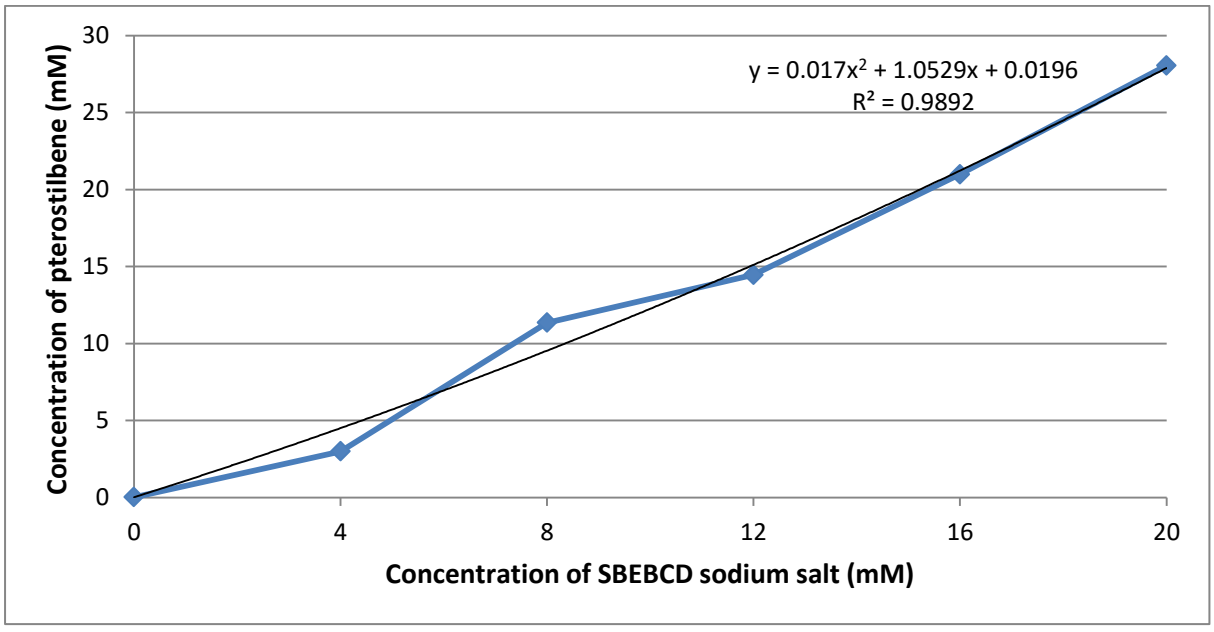


Figure 4.4.4: Solubility of PTB as a function of SBEBCD sodium salt concentration at 23 °C.

Table 4.4.2: PTB solubility enhancement as a function of [SBEBCD sodium salt] at 23 ^{o}C.

Concentration of CD (mM)	Concentration of PTB (mM)	Mass of PTB dissolved (mg.cm^{-3})	Solubility enhancement ratio
4	3.043	0.780	153
8	11.554	2.961	579
12	14.666	3.759	738
16	21.304	5.460	1071
20	28.138	7.212	1431

The association constants, K_c, for CD complex formation for both experiments were calculated using Equation (1),[31] with the "slope" in the equation representing the gradient of their phase solubility profiles at low concentration and S_0 the aqueous solubility value of PTB without the influence of the respective CD. The gradients of each phase solubility profile were calculated using the initial part of the phase solubility profiles (between 0 mM and 4 mM [CD]). This is owing to the fact that Equation (1) assumes a 1:1 stoichiometric H:G ratio and at higher CD concentrations higher-order H:G stoichiometric ratios can occur. Thus, the estimated K_c values for complex formation with RAMEB and SBEBCD sodium salt were 22 464 M^{-1} and 148 200 M^{-1} respectively. These K_c values are relatively high, thus indicating strong binding between the CD and PTB molecules and therefore this implies that competitive binding agents may be required to help promote the absorption of PTB by a biological membrane.[33]

$$K_c = \frac{slope}{S_0(1-slope)} \qquad \text{Equation (1)}$$

The results from the phase solubility investigation with RAMEB and SBEBCD sodium salt indicated significant solubility enhancement over the analysed range of CD solution concentrations.[a] Consequently, such substantial solubility increases offer the potential for pharmaceutical application, in particular for the SBEBCD sodium salt, which is considered non-toxic for all routes of administration. CD inclusion with RAMEB can however be used for administrative routes other than parenteral and oral.[29]

[a] It is important to mention that the peak areas of the cis isomer and degradation products of pterostilbene on the chromatograms were negligible even at the 20 mM concentrations of the CDs. Thus, it can be assumed that these solubility enhancement values are effectively the full contribution of pterostilbene, as only the trans isomer was predominantly present.

In summary, three crystalline CD inclusion complexes with pterostilbene were isolated and characterised, namely β-CD·PTB, γ-CD·PTB and TMB·PTB, with SCXRD data being obtained for β-CD·PTB. Solubility studies were not performed on these complexes owing to crystallization purity challenges with β-CD·PTB, γ-CD·PTB already being significantly more insoluble than pure pterostilbene, and the financial cost implications of scaling up the TMB·PTB complex for solubility studies. However, the phase solubility analysis of pterostilbene with RAMEB and SBEBCD sodium salt indicated significant solubility enhancements warranting further development in the pharmaceutical industry.

References

(1) Lim, Y. R. I.; Preshaw, P. M.; Lim, L. P.; Ong, M. M. A.; Lin, H. S.; Tan, K. S. Pterostilbene Complexed with Cyclodextrin Exerts Antimicrobial and Anti-Inflammatory Effects. *Sci. Rep.* **2020**, *10* (1), 1–10. https://doi.org/10.1038/s41598-020-66031-8.

(2) López-Nicolás, J. M.; Rodríguez-Bonilla, P.; Méndez-Cazorla, L.; García-Carmona, F. Physicochemical Study of the Complexation of Pterostilbene by Natural and Modified Cyclodextrins. *J. Agric. Food Chem.* **2009**, *57* (12), 5294–5300. https://doi.org/10.1021/jf900285e.

(3) Yu, Y. F.; Feng, W.; Zhang, Y.; Wang, C. F.; Zhao, S. C. Preparation of Hydroxypropyl Cyclodextrin Inclusion of Oxyresveratrol/Pterostilbene. *Adv. Mater. Res.* **2013**, *641–642*, 97–100. https://doi.org/10.4028/www.scientific.net/AMR.641-642.97.

(4) Silva, F.; Nerín, C.; Domingues, F. C. Stilbene Phytoallexins Inclusion Complexes: A Natural-Based Strategy to Control Foodborne Pathogen Campylobacter. *Food Control* **2015**, *54*, 66–73. https://doi.org/10.1016/j.foodcont.2015.01.039.

(5) Silva, F.; Figueiras, A.; Gallardo, E.; Nerín, C.; Domingues, F. C. Strategies to Improve the Solubility and Stability of Stilbene Antioxidants: A Comparative Study between Cyclodextrins and Bile Acids. *Food Chem.* **2014**, *145*, 115–125. https://doi.org/10.1016/j.foodchem.2013.08.034.

(6) dos Santos Lacerda, D.; Türck, P.; Gazzi de Lima-Seolin, B.; Colombo, R.; Duarte Ortiz, V.; Poletto Bonetto, J. H.; Campos-Carraro, C.; Bianchi, S. E.; Belló-Klein, A.; Linck Bassani, V.; Sander da Rosa Araujo, A. Pterostilbene Reduces Oxidative Stress, Prevents Hypertrophy and Preserves Systolic Function of Right Ventricle in Cor Pulmonale Model. *Br. J. Pharmacol.* **2017**, *174* (19), 3302–3314. https://doi.org/10.1111/bph.13948.

(7) Bureau, I. WO 2010/150271 Al (81), 2010.

(8) Couto, G. K.; Fernandes, R. O.; Lacerda, D.; Campos-Carraro, C.; Türck, P.; Bianchi, S. E.; Ferreira, G. D.; Brum, I. S.; Bassani, V. L.; Belló-Klein, A.; Araujo, A. S. R. Profile of Pterostilbene-Induced Redox Homeostasis Modulation in Cardiac Myoblasts and Heart Tissue. *J. Biosci.* **2018**, *43* (5), 931–940. https://doi.org/10.1007/s12038-018-9815-9.

(9) Lacerda, D. S.; Bianchi, S. E.; Pinós, W. L.; Campos-Carraro, C.; Türck, P.; Hickmann, A. R.; Pittol, V.; Teixeira, R. B.; Belló-Klein, A.; Bassani, V. L.; Araujo, A. S. R. Effect of Pterostilbene Complexed with Cyclodextrin on Rat Liver: Potential Reduction of Oxidative Damage and Modulation Redox-Sensitive Proteins. *Med. Chem. Res.* **2018**, *27* (10), 2265–2278. https://doi.org/10.1007/s00044-018-2233-6.

(10) Lacerda, D.; Türck, P.; Campos-Carraro, C.; Hickmann, A.; Ortiz, V.; Bianchi, S.; Belló-Klein, A.; De Castro, A. L.; Bassani, V. L.; Da Rosa Araujo, A. S. Pterostilbene Improves Cardiac Function in a Rat Model of Right Heart Failure through Modulation of Calcium Handling Proteins and Oxidative Stress. *Appl. Physiol. Nutr. Metab.* **2020**, *45* (9), 987–995. https://doi.org/10.1139/apnm-2019-0864.

(11) Lacerda, D.; Ortiz, V.; Türck, P.; Campos-Carraro, C.; Zimmer, A.; Teixeira, R.; Bianchi, S.; de Castro, A. L.; Schenkel, P. C.; Belló-Klein, A.; Bassani, V. L.; da Rosa Araujo, A. S. Stilbenoid Pterostilbene Complexed with Cyclodextrin Preserves Left Ventricular Function after Myocardial Infarction in Rats: Possible Involvement of Thiol Proteins and Modulation of Phosphorylated GSK-3β. *Free Radic. Res.* **2018**, *52* (9), 988–999. https://doi.org/10.1080/10715762.2018.1506115.

(12) Yeo, S. C. M.; Ho, P. C.; Lin, H. S. Pharmacokinetics of Pterostilbene in Sprague-Dawley Rats: The Impacts of Aqueous Solubility, Fasting, Dose Escalation, and Dosing Route on Bioavailability. *Mol. Nutr. Food Res.* **2013**, *57* (6), 1015–1025. https://doi.org/10.1002/mnfr.201200651.

(13) Catenacci, L.; Vicatos, A. I.; Sorrenti, M.; Bonferoni, M. C.; Caira, M. R. Native Cyclodextrins as Complexation Agents for Pterostilbene: Complex Preparation and Characterization in Solution and in the Solid State. *Pharmaceutics* **2021**, *14* (1), 8. https://doi.org/10.3390/pharmaceutics14010008.

(14) XPREP, Data Preparation and Reciprocal Space Exploration. Version 2008/2, Bruker Analytical X-Ray Systems. 2008.

(15) Bethanis, K.; Tzamalis, P.; Tsorteki, F.; Kokkinou, A.; Christoforides, E.; Mentzafos, D. Structural Study of the Inclusion Compounds of Thymol, Carvacrol and Eugenol in β-Cyclodextrin by X-Ray Crystallography. *J. Incl. Phenom. Macrocycl. Chem.* **2013**, *77* (1–4), 163–173. https://doi.org/10.1007/s10847-012-0230-9.

(16) Groom, C. R.; Bruno, I. J.; Lightfoot, M. P.; Ward, S. C. The Cambridge Structural Database. *Acta Crystallogr. Sect. B Struct. Sci. Cryst. Eng. Mater.* **2016**, *72* (2), 171–179. https://doi.org/10.1107/S2052520616003954.

(17) Spek, A. L. PLATON SQUEEZE: A Tool for the Calculation of the Disordered Solvent Contribution to the Calculated Structure Factors. *Acta Crystallogr. Sect. C Struct. Chem.* **2015**, *71* (1), 9–18. https://doi.org/10.1107/S2053229614024929.

(18) Spek, A. L. PLATON. *Acta Crystallogr.* **2009**, *D65*, 148–155.

(19) Caira, M. R. On the Isostructurality of Cyclodextrin Inclusion Complexes and Its Practical Utility. *Rev. Roum. Chim.* **2001**, *46* (4), 371–386.

(20) Steiner, T.; Koellner, G. Crystalline .Beta.-Cyclodextrin Hydrate at Various Humidities: Fast, Continuous, and Reversible Dehydration Studied by X-Ray Diffraction. *J. Am. Chem. Soc.* **1994**, *116* (12), 5122–5128. https://doi.org/10.1021/ja00091a014.

(21) National Center for Biotechnology Information (2020). PubChem Compound Summary for CID 5281727, Pterostilbene https://pubchem.ncbi.nlm.nih.gov/compound/Pterostilbene (accessed Aug 8, 2020).

(22) Catenacci, L.; Sorrenti, M.; Milanese, C.; Valentino, C.; Vicatos, A. I.; Caira, M. R.; Bonferoni, M. C. An Update on Solid-State Characterization of the Polyphenol Pterostilbene. *J. Drug Deliv. Sci. Technol.* **2022**, *71*, 103331. https://doi.org/10.1016/j.jddst.2022.103331.

(23) Joga, S. R.; Dorwal, H. N.; Gorantla, S. R.; Chava, S. Novel Crystalline Polymorph of Pterostilbene. IN2012CH05387 A 2015-10-30, 2013.

(24) Mahesh, M.; Subbaraju, G. V.; Ivanisevic, I.; Andres, M.; Stephens, K. Preparation of Solid Forms of Pterostilbene. WO2010141107A1, 2010.

(25) Bofill, L.; de Sande, D.; Barbas, R.; Prohens, R. Hydrogen Bond Polarization Overcomes Unfavorable Packing in the Most Stable High Z' Polymorph of Pterostilbene. *Cryst. Growth Des.* **2019**, *19* (5), 2552–2556. https://doi.org/10.1021/acs.cgd.9b00374.

(26) Kamitori, S.; Hirotsu, K.; Higuchi, T. Crystal and Molecular Structure of the γ-Cyclodextrin–12-Crown-4 1 : 1 Inclusion Complex. *J. Chem. Soc., Chem. Commun.* **1986**, No. 9, 690–691. https://doi.org/10.1039/C39860000690.

(27) Guedes, L.; Morgon, N.; Martins, M.; Pessine, F. Imiquimod/β-Cyclodextrin Inclusion Complex: Experimental and Theoretical Studies. *J. Braz. Chem. Soc.* **2020**. https://doi.org/10.21577/0103-5053.20200060.

(28) Sigma-Aldrich https://www.sigmaaldrich.com/ZA/en/product/sigma/h4645 (accessed Nov 25, 2021).

(29) Loftsson, T.; Brewster, M. E. Pharmaceutical Applications of Cyclodextrins: Basic Science and Product Development. *J. Pharm. Pharmacol.* **2010**, *62* (11), 1607–1621. https://doi.org/10.1111/j.2042-7158.2010.01030.x.

(30) Waszczuk, M.; Bianchi, S. E.; Martiny, S.; Pittol, V.; Lacerda, D. S.; Araújo, A. S. da R.; Bassani, V. L. Development and Validation of a Specific-Stability Indicating Liquid Chromatography Method for Quantitative Analysis of Pterostilbene: Application in Food and Pharmaceutical Products. *Anal. Methods* **2020**, *12* (35), 4310–4318. https://doi.org/10.1039/D0AY00989J.

(31) Higuchi Takeru; Connors Kenneth A. Phase Solubility Techniques. *Adv. Anal. Chem. Instrum.* **1965**, *4*, 117–212.

(32) Neves de Lima, Á. A.; Sobrinho, J.; Corrêa, R.; Rolim Neto, P. Alternative Technologies to Improve Solubility of Poorly Water Soluble Drugs. *Lat. Am. J. Pharm.* **2008**, *27*.

(33) Stella, V. J.; Rao, V. M.; Zannou, E. A.; Zia, V. Mechanisms of Drug Release from Cyclodextrin Complexes. *Adv. Drug Deliv. Rev.* **1999**, *36* (1), 3–16. https://doi.org/10.1016/S0169-409X(98)00052-0.

Chapter 5

Cyclodextrin inclusion complexation with β-estradiol and progesterone

5.1) Literature review

5.1.1) Literature review for CD inclusion complexes with β-estradiol

There is a significant volume of research that has been published on the CD inclusion complexation with β-estradiol over the past few decades, indicating the interest in, and importance of, this active pharmaceutical ingredient (API). This research covers a broad spectrum of topics, including publications that pertain directly to medical applications, other publications that focus on different confirmatory techniques, using CDs to enhance the fluorescence intensity of β-estradiol, as well as publications using CDs to separate oestrogens and to alter the retention time of β-estradiol.

The publications related directly to pharmaceutical applications were varied. These included a patent for eye drop formulations which stated that many CDs in general could be used in preparations,[1] and another patent for eye drop formulations where an inclusion complex was claimed to have formed between hydroxypropyl β-CD (HPBCD) and β-estradiol (stoichiometric ratio not specified).[2] Further research included a study on nasal delivery formulations that incorporated inclusion complexes of RAMEB and β-estradiol (stoichiometric ratio unknown),[3] and another study in which a RAMEB complex of β-estradiol was produced by the saturated solution method using 95% (w/w) ethanol in a 2:1 host-guest molar ratio. The EtOH was subsequently evaporated and the CD inclusion complex was dissolved in a sterile saline solution.[4]

Further pharmaceutically applicable research included descriptions of multi-component systems that incorporated CD inclusion complexes with β-estradiol into their formulations. These included two patents, the first one describing a multi-component formulation

(designed for site-specific release of the API), which contained HPBCD and β-estradiol that had been kneaded in an equimolar ratio with EtOH.[5] The second patent describes a transdermal pharmaceutical composition obtained by mixing a β-CD·β-estradiol inclusion complex with polyvidon 90 gel and propylene glycol to form a gel, which was subsequently added to a polyester sheet, and thereafter dried. The patent of this formulation indicated that the host-guest stoichiometry can be variable in the preparation, as the author stated, "The molar ratio of guest to host in an inclusion complex formed between the active substance and the CD is from about 0.1:1 to about 10:1, especially from about 0.2:1 to about 5:1, in particular from about 0.3:1 to about 4:1".[6] In addition, polymeric β-CD derivatives [which included heptakis-6-(2,3-dihydroxypropyl)thio-6-deoxy-β-CD, mono-6-deoxy-6-(3-(((2-aminoethyl)carbamoyl)oxy)-2-hydroxypropyl)thio-hexa-6-deoxy-6-(2,3-dihydroxypropyl)thio-β-CD and monoaminoethylcarbamat-hepta-thioglyceryl-β-CD-hyaluronic acid conjugate] were formulated with β-estradiol, which improved the solubility of the API during an *in vitro* evaluation. The CD:API molar ratio was unspecified.[7] Lastly, an inclusion complex formed between β-estradiol and β-cyclodextrin-poly(ethylene glycol)-folic acid conjugate was reported, the latter having been designed as a modified API carrier and demonstrating reduced haemolytic effects in comparison to unmodified β-CD.[8]

As mentioned previously, other publications also identified CD inclusion complexes with β-estradiol; however, these publications were not specifically related to pharmaceutical applications. Instead, they focused on different confirmatory techniques for characterising the inclusion complex, enhancing the fluorescence intensity of β-estradiol, and predicting the stability of α-, β-, and γ-CD inclusion complexes with β-estradiol in a computational study.

The findings from these publications included research in which chronocoulometric and differential pulse voltammetry were used to investigate the formation of CD inclusion complexes in a phosphate buffer 0.1 M/ethanol (70/30) at pH 7.4. These complexes included the host compounds β-CD, sulfobutyl ether-β-CD (SBEBCD) and hydroxypropyl-β-CD (HPBCD). The authors assumed 1:1 host-guest interaction as they claimed that this had been previously established.[9] Another publication reported the investigation of the relative affinity of estrone and β-estradiol for complexation with β-CD using voltammetric and high-

performance liquid chromatography (HPLC) techniques in mixed media aqueous solutions containing a phosphate buffer with either EtOH or acetonitrile. The authors also assumed 1:1 host-guest stoichiometries.[10]

In addition, other publications reported complexation with β-estradiol where spectrofluorimetric analysis was used to improve the fluorometric detection limits (as well as the aqueous solubility) of β-estradiol in solution using a variety of CDs [β-CD, γ-CD, 2-hydroxyethyl β-cyclodextrin (HEBCD), 2-hydroxypropyl β-cyclodextrin (HPBCD), methyl β-cyclodextrin (MBCD) and heptakis(2,6-di-*O*-methyl)-β-cyclodextrin (DMB)]. These solutions also contained organic solvents and NaOH for pH control. The authors indicated that the complexes formed with 1:1 host-guest stoichiometry.[11] On a similar theme, another publication described an investigation of the effects of differing concentrations of β-CD in aqueous solutions containing organic solvents, which were altered for pH control with ammonia. The aim was also to improve the fluorescence intensity and aqueous solubility of β-estradiol. The host-guest stoichiometry was not explicitly specified in this report.[12]

Lastly, a computational study was also conducted using a semi-empirical molecular orbital method in order to predict the stability of theoretical α-, β-, and γ-CD inclusion complexes with β-estradiol in 1:1 and 1:2 molar ratios in order to understand and interpret the NMR spectra.[13] Unfortunately, the accessibility of this article was limited and thus it was not possible to understand the methodology and results fully. The author of this doctoral thesis found that it was not possible to form inclusion complexes between α-CD and β-estradiol, and this was also indirectly confirmed in the publication by Pérez *et al.*[11] who found that the fluorometric detection limits of β-estradiol were not enhanced when α-CD was chosen for the experiment.[11]

5.1.2) Literature review for CD inclusion complexes with progesterone

As discussed above for the API β-estradiol, a substantial amount of research has also been conducted for the CD inclusion of progesterone, the use of a large variety of analytical techniques having been mentioned in different publications. The latter included many reports that focused on solubility analyses, medical applications, different confirmatory

techniques, and publications that describe the incorporation of CD complexes within nanoparticles.

The publications that pertained to phase solubility studies reported a variety of inclusion complexes with progesterone (PRO). These included a study in which the authors succeeded in increasing the aqueous solubility of the API to 50 $mg.cm^{-3}$ by using HPBCD and PRO in a 2:1 host-guest stoichiometry during a phase solubility study. Initially, the complex formed in a 1:1 molar ratio, and later a complex with 2:1 host-guest stoichiometry also formed. The authors of this study also discovered an insoluble β-CD·PRO complex.[14] Another study investigated the interaction between progesterone and the following CDs: 2-hydroxypropyl β-cyclodextrin (HPBCD), 2-hydroxypropyl γ-cyclodextrin (HPGCD), sulfobutyl ether β-cyclodextrin (SBEBCD) and randomly methylated β-cyclodextrin (RAMEB).[15] These experiments were first performed in pure aqueous solutions using HPLC to establish phase solubility profiles. Thereafter, the experiments were replicated, but with 2 $mg.cm^{-3}$ of progesterone first being dissolved in organic solvent, and the resulting solutions being added to the aqueous solutions in order to obtain phase distribution profiles. The host-guest stoichiometry was determined to be 1:1 for all experiments.[15] Another publication assessed the molecular association of β-CD and progesterone using phase solubility and spectroscopic techniques. The results suggested that a complex with 1:1 stoichiometry is thermodynamically more stable and that this 1:1 host-guest complex subsequently binds to another β-CD molecule to form a 2:1 complex in solution.[16] Lastly, another publication also reported phase solubility studies with HPGCD, SBEBCD, permethylated β-CD (TMB) and HPBCD, of which the latter two CDs showed the most efficient solubility enhancement of progesterone. Thus, these two were pursued for further experiments along with β-CD and γ-CD as references. Solid inclusion complexes were then formed using a range of preparations, where the molar ratios were taken from Lin *et al.* (1992), as the publication described.[17] In this case the host-guest stoichiometries (and the respective CDs in parentheses) were: 2:1 (β-CD), 3:2 (γ-CD); 5:2 (HPBCD), and 1:1 (TMB). Preparations included physical mixtures of the API and CD with PEG 6000, the reagents of each complex being mixed with the polymer using a spatula. Another preparation included precipitation of β-CD and γ-CD inclusion complexes with progesterone in distilled water, after which the products were ground into powders. Furthermore, freeze-drying techniques were used to

form inclusion complexes of TMB and HPBCD with progesterone in distilled water. Lastly, ternary systems of progesterone, CD and polymer (with the H:G ratios listed above) were formed using a melting method, the components being heated to 130 ^{o}C.[18]

In addition, other studies investigated producing CD inclusion complexes with progesterone *via* freeze drying methodologies, all resulting complexes displaying improved aqueous solubility of progesterone. These investigations included a study with HPBCD and progesterone prepared as a suspension in an equimolar ratio,[19] while another study with the same host and guest was prepared in a 2:1 host-guest ratio in a pure aqueous medium.[20] The authors of this publication stated that this was not necessarily the actual stoichiometry of the complex; however, the results indicated a host-guest stoichiometric ratio between 1:1 and 2:1.[20] In addition, other authors investigated inclusion complexes of β-CD, γ-CD and HPBCD with progesterone. The stoichiometric ratios were initially based on trial-and-error methods, where 2:1 (β-CD:progesterone) and 3:2 (γ-CD:progesterone) molar ratios produced the highest yields. The molar ratio for the HPBCD complex was not specified in the abstract and unfortunately, it was not possible to access the full publication.[17]

Two patents were also published, both claiming to improve the aqueous solubility of progesterone. One of these reported the formation of an inclusion complex between maltosyl-β-CD and progesterone,[21] while the other described the formation of a γ-CD inclusion complex with progesterone.[22] The molar ratios were unknown due to limited accessibility to the patent.[21,22]

Several authors also investigated pharmaceutical applications of CD complexation with progesterone. These publications included an account of the tableting properties of β-CD with progesterone (either as an inclusion complex or as a physical mixture),[23] as well as the possibility of using heptakis(2,6-di-*O*-methyl)-β-cyclodextrin (DMB) as an absorption enhancer (prepared in a 2:1 DMB-PRO ratio) for the nasal absorption of progesterone. These strategies resulted in a considerable increase in the bioavailability of PRO.[24] Furthermore, a patent was published which describes the formation of paper disks carrying a HPBCD inclusion complex with progesterone for sublingual administration. The host-guest stoichiometry was not specified as the CD solution was saturated with progesterone to form the complex.[25]

Furthermore, the authors of an assortment of publications also confirmed the presence of, or performed studies with, CD inclusion complexes with progesterone using various analytical techniques. One study investigated the interaction between progesterone and β-CD using differential pulse polarography, where a 1×10^{-4} M concentration of progesterone was kept constant in a 10/90 EtOH/0.1 M Britton-Robinson buffer, while varying β-CD concentrations between 0 and 4 mM).[26] In addition, the β-CD complex with progesterone was determined to have a 1:1 stoichiometry and further characterisation involved the determination of complex association constants as a function of temperature. The authors also used steered molecular dynamics to analyse the energetic properties of the inclusion complex.[26] Other authors used FT-IR spectroscopy to analyse a β-CD·progesterone inclusion complex that was formed *via* co-precipitation. Further details are unknown owing to limited accessibility to the publication source.[27] The authors of a different publication performed a membrane permeability study to investigate cinnarizine as a competing agent to β-CD inclusion complexes containing progesterone.[28] Inclusion complexes of progesterone with β-CD and γ-CD, investigated using PXRD and DSC techniques, have also been reported.[29] Owing to the inaccessibility of the publication, the method of preparation remains unknown. The authors claimed that they found structural changes between 60 and 80 ^{o}C using variable temperature PXRD and this was confirmed by DSC analysis.

Two NMR spectroscopic investigations were also conducted and published.[29] The authors of one paper[30] used NMR techniques to study the molecular association of progesterone with HPBCD in a D_2O solution and discovered the presence of multiple equilibria, which involved 1:1 and 2:1 host-guest stoichiometric ratios. The second publication reported the inclusion of progesterone in β-CD in a DMSO solution.[31] The results indicated that the progesterone molecule was completely immersed in the cavity of the host molecule.

Lastly, four publications involved studies incorporating CD complexes with progesterone into nanotechnological systems. The first publication reported the formation of HPBCD and DMB inclusion complexes with progesterone that were prepared in equimolar ratios using freeze drying techniques. These CD complexes were carried by bovine serum albumin nanospheres in order to measure the rate of release of progesterone *in vitro*.[30]

The second publication reported a study of CD inclusion complexes involving β-CD (formulated as nanospheres) and progesterone prepared in a 2:1 host-guest molar ratio in a water/EtOH system *via* co-lyophilisation. These progesterone-loaded β-CD nanospheres were shown to have potential application as a non-surfactant injectable delivery system.[29] A third publication included a patent describing the formation of nanoparticles with HPBCD and progesterone.[31] Lastly, inclusion complexes of β-CD and HPBCD with progesterone were formed *via* co-precipitation in a 2:1 host-guest molar ratio in a EtOH:water solution (30:70 v/v). The complexes were subsequently incorporated into two types of solid lipid nanoparticles, and the release of progesterone from these nanoparticles was compared with that from both the untreated drug and progesterone in complexed form.[32]

In summary, the CD inclusion research that has been conducted for both β-estradiol and progesterone is extensive, and the inclusion complexes that the author of this doctoral thesis intended to produce have already been produced to some extent. However, the work presented here uses different preparative methods, as well as a significantly larger variety of complementary techniques for analysis of the reported inclusion complexes, such as X-ray crystal structural analysis with CD inclusion of β-estradiol and progesterone. The material analysed by these techniques was very reproducible and therefore consistent, and consequently this work offers one of the most comprehensive accounts in terms of the analytical techniques performed on the CD inclusion complexes with β-estradiol and progesterone. Furthermore, the literature study indicated that the aqueous solubilities of both bioactive compounds were improved after forming inclusion complexes with various CDs. Thus, additional research into this field, especially to determine molecular and crystal structures hitherto unpublished and assess the potential aqueous solubility increase with different CDs (such as β-CD and γ-CD), is very relevant and warranted.

5.2) Overview of experimental results

Six CD inclusion complexes were successfully formed *via* co-precipitation and kneading with the APIs β-estradiol (BES) and progesterone (PRO), namely β-CD·BES, β-CD·PRO, γ-CD·BES, γ-CD·PRO, DMB·BES and DMB·PRO. Attempts to form inclusion complexes between α-CD and the two APIs were performed *via* co-precipitation and kneading; however, the results did not reveal evidence of a new phase. Attempts were also conducted to form TMB inclusion

complexes with β-estradiol and progesterone; however, they similarly indicated no host-guest affinity under the preparative conditions employed. For convenience, β-CD·BES and β-CD·PRO will be discussed in the next section of this chapter, followed by γ-CD·BES and γ-CD·PRO, and finally DMB·BES and DMB·PRO in the last section.

5.2.1) The inclusion complexes: β-CD·BES and β-CD·PRO

5.2.1.1) Method of preparation

The preparative methods for the inclusion complexes with native CDs, namely β-CD·BES and β-CD·PRO (as well as γ-CD·BES and γ-CD·PRO, which are discussed in the next section) were very similar, and only minor tailoring was required to successfully produce each complex.

The formation of β-CD·BES and β-CD·PRO involved preparing an aqueous solution containing 5 mg of each API (0.0184 mmol for β-estradiol and 0.0159 mmol for progesterone) in a 2:1 host-guest ratio with β-CD. Initially, respective stoichiometric amounts of β-CD were added into separate vials with specific quantities of water (41.66 mg, 0.0368 mmol β-CD dissolved in 3 cm^3 water for the β-CD·BES system, and 36.10 mg, 0.0318 mmol β-CD dissolved in 15 cm^3 water for the β-CD·PRO system). These CD solutions were stirred at 70 ^oC until dissolution was achieved. Thereafter, the APIs were added in small increments over a 10-minute period to the respective CD solutions. Almost complete dissolution was attained after 15 minutes of stirring at 70 ^oC,[a] but a very slight turbidity was observed in the β-CD·BES solution. The solutions were left to stir for an additional 3 hours (to allow for the complex equilibrium to be achieved), after which they were filtered and prepared for slow cooling. Crystals appeared after 3 days.

5.2.1.2) Crystal morphology of β-CD·BES and β-CD·PRO

Both inclusion complexes crystallized in the form of small, transparent rhombohedrons (Figures 5.1.1 and 5.1.2) and they were of adequate quality for SCXRD analysis. Furthermore, the sizes of the β-CD·BES single crystals were observed to be larger than those

[a] Both APIs in a controlled experiment using the same quantity of water displayed significant turbidity at this volume and temperature in the absence of β-CD. Thus, the onset of dissolution (or near dissolution) in these experiments indicated the occurrence of complexation.

of the β-CD·PRO complex and this is probably as a result of unaccounted miniscule differences in their slow cooling crystallization processes.

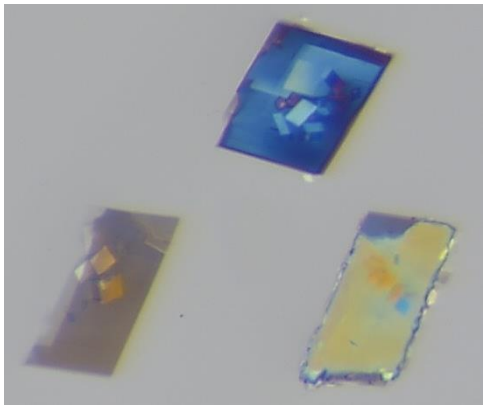


Figure 5.1.1: The crystal morphology of β-CD·BES recorded with polarised light.

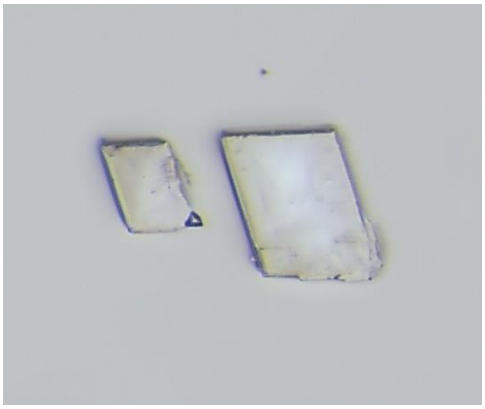


Figure 5.1.2: The crystal morphology of β-CD·PRO.

5.2.1.3) ^{1}H NMR analysis of β-CD·BES and β-CD·PRO

The ^{1}H NMR spectral analysis of the co-precipitated crystalline material confirmed 2:1 host-guest molar ratios for β-CD·BES and β-CD·PRO.[b] The assignments of the spectral results are listed in Tables 5.1.1 and 5.1.2 below with reference to Figure 5.1.3 for atomic assignments. Their respective ^{1}H NMR spectra can be viewed in the Appendix under section 4.1.1, pp. 43 - 44.

[b] It should also be noted that the sample which produced the ^{1}H NMR spectrum of β-CD·BES contained 10 mg of crystalline sample dissolved in DMSO-d_6. In a previous experiment only 3 mg was used and this was insufficient to attain a proton count consistency within the guest molecule. Therefore, for experimental reproducibility purposes, more mass was required for this particular system.

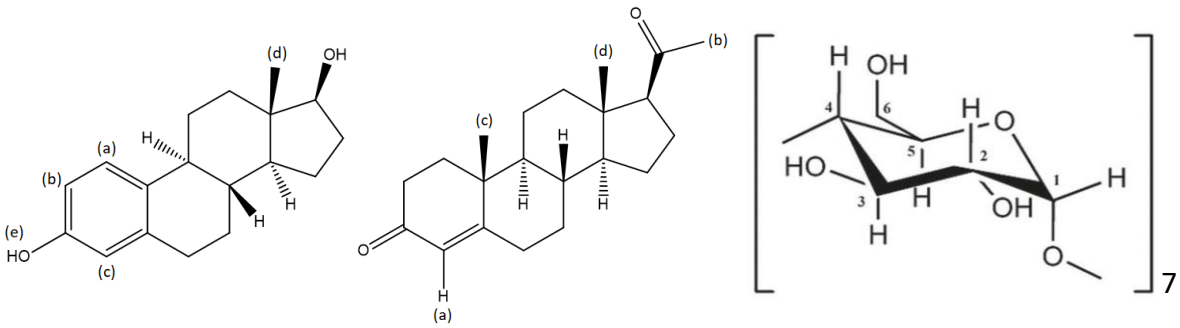


Figure 5.1.3: Molecular structures of β-estradiol (left), progesterone (centre), and β-CD (right), with specific molecular fragments labelled for the ^{1}H NMR analysis. Adapted from Guedes *et al.*[33]

Table 5.1.1: The ^{1}H NMR spectral analysis for β-CD·BES.

Assignment	δ (ppm)	Integration	Multiplicity	Proton representation (per molecule)	Stoichiometric ratio	Stoichiometric ratio (integer)
OH (e) (BES)	8.938	0.0686	singlet	1H	0.48	1
CH (a) aromatic (BES)	7.031 – 7.053	0.0716	doublet	1H	0.50	1
CH (b) aromatic (BES)	6.493 – 6.520	0.0725	doublet of doublets	1H	0.51	1
CH (c) aromatic (BES)	6.431 – 6.437	0.0697	doublet	1H	0.49	1
OH-2 and OH-3 (β-CD)	5.646 – 5.696	2.0510	two separate doublets	14H	1.03	2
CH-1 (β-CD)	4.834 – 4.843	1.0000*	doublet	7H	1.00	2
CH_3 (d) methyl (BES)	0.670	0.2180	singlet	3H	0.51	1

*reference integral

Table 5.1.2: The ^{1}H NMR spectral analysis for β-CD·PRO.

Assignment	δ (ppm)	Integration	Multiplicity	Proton representation (per molecule)	Stoichiometric ratio	Stoichiometric ratio (integer)
CH-1 (β-CD)	4.834 – 4.843	0.9914	doublet	7H	0.99	2
OH-6 (β-CD)	4.392 – 4.426	1.0000*	quartet	7H	1.00	2
CH_3 (a) methyl (PRO)	2.071	0.2043	singlet	3H	0.48	1
CH_3 (b) methyl (PRO)	1.153	0.1953	singlet	3H	0.46	1
CH_3 (c) methyl (PRO)	0.585	0.2187	singlet	3H	0.51	1

*reference integral

5.2.1.4) PXRD analysis for β-CD·BES and β-CD·PRO

PXRD analyses revealed that the β-CD·BES and β-CD·PRO inclusion complexes could be formed *via* kneading the respective reagents in a 2:1 host-guest molar ratio, and that the

angular positions of their PXRD peaks matched those of the PXRD patterns of their product counterparts obtained *via* co-precipitation (Figures 5.1.4 and 5.1.5). In addition, the PXRD patterns of the complexes prepared *via* kneading and co-precipitation matched that of an isostructural β-CD inclusion complex (CSD refcode: AJUVEG, containing the guest methylparaben) that crystallizes in the space group *C*2 (Figures 5.1.4 and 5.1.5), and thus β-CD·BES and β-CD·PRO are also isostructural. This is discussed further in the section on the single-crystal X-ray diffraction analyses of these two inclusion complexes. There are minor peak shifts in the angular positions when comparing the PXRD pattern of the isostructural β-CD inclusion complex AJUVEG with those of β-CD·BES and β-CD·PRO. This is expected owing to the different influences that the guest molecules have on the β-CD molecule when included, as well as differences in the crystal water contents, resulting primarily in small differences in the respective unit cell parameters. Furthermore, the differences in the relative peak intensities are due to structural differences in the respective guest molecules as well as experimental effects such as preferred orientation of powder samples. An example of the latter is the significant difference in the intensities of the peaks at the angular position of 12.4° 2θ in the patterns for β-CD·BES prepared by co-precipitation and kneading (Figure 5.1.4).

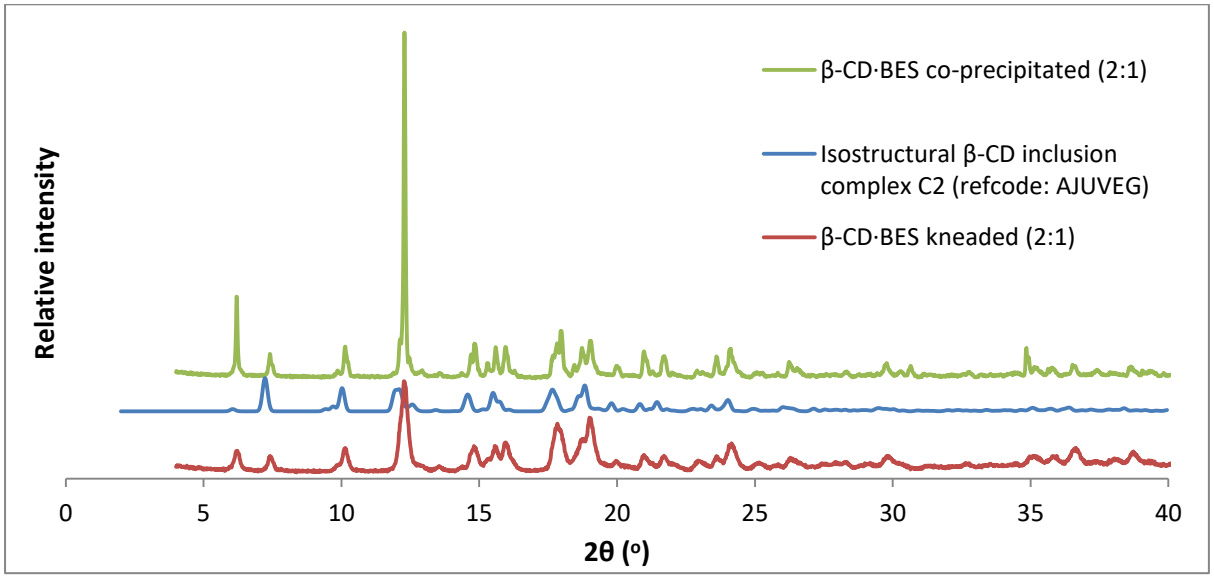


Figure 5.1.4: The PXRD patterns of the β-CD·BES complex produced *via* kneading (2:1), an isostructural β-CD complex crystallizing in the space group *C*2 (refcode: AJUVEG), and the β-CD·BES complex produced *via* co-precipitation (2:1).

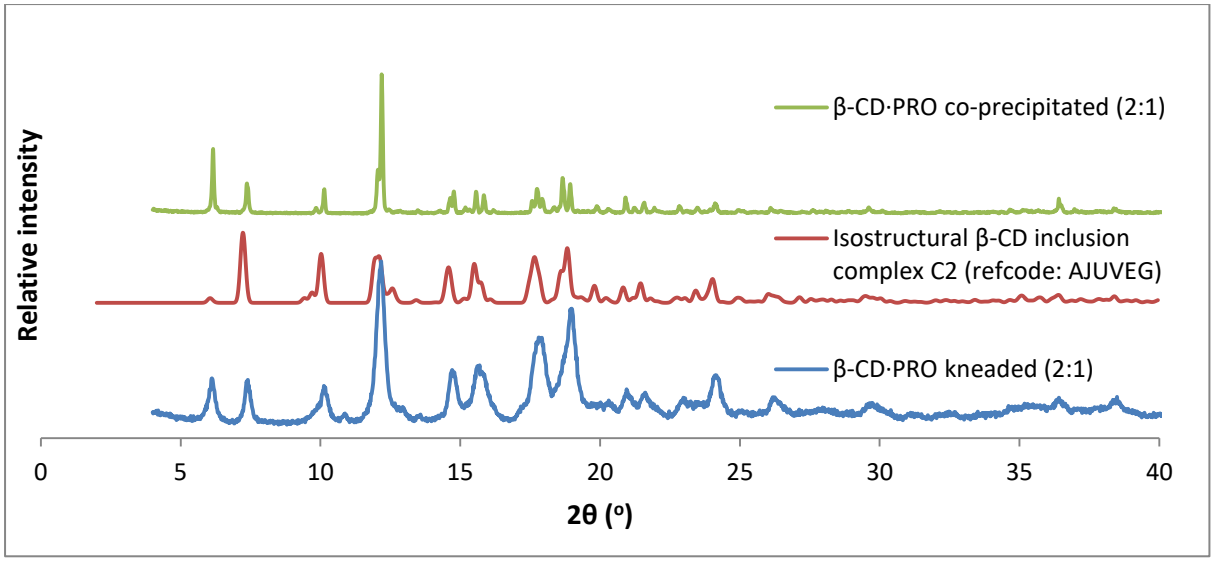


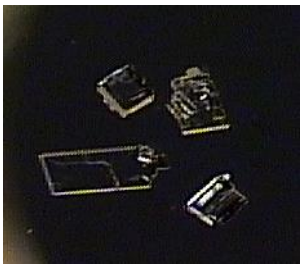
Figure 5.1.5: The PXRD patterns of the β-CD·PRO complex produced *via* kneading (2:1), an isostructural β-CD complex crystallizing in the space group *C*2 (refcode: AJUVEG), and the β-CD·PRO complex produced *via* co-precipitation (2:1).

5.2.1.5) Hot stage microscopy (HSM) of β-CD·BES and β-CD·PRO

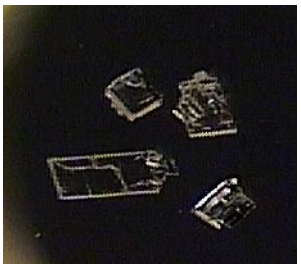
β-CD·BES:

The HSM analysis for β-CD·BES visually displays the thermal progression of the crystals that were coated in silicone oil, while heated from 25.5 ^{o}C to 255.5 ^{o}C at 10 K.min^{-1} (Figure 5.1.6). Image A displays the initial appearance of β-CD·BES at 25.5 ^{o}C. The first event occurred at 57.4 ^{o}C, where a minimal onset of opacity was observed in the form of very minor fracture planes in the crystals (image B), attributed to their dehydration. Thereafter, the crystals continued to fracture internally at a moderate rate, increasing the visual appearance of opacity spreading throughout the crystal (image C, 70.1 ^{o}C), until they began to disintegrate (image D, 80.7 ^{o}C). These events continued to represent the dehydration of the crystals. The fracturing continued at a steady rate, resulting in the crystals becoming more opaque and fragmented, this process terminating only at 209.5 ^{o}C (image E). It is presumed that the dehydration would not have continued up until 209.5 ^{o}C. Thus, it is expected that the dehydration terminated at a lower temperature, and that with further heating, the crystals continued to destabilize and disintegrate. It is evident that the water molecules play a pivotal role in maintaining the structural crystalline integrity of the complex. Finally, the onset of decomposition is displayed in image F at 255.5 ^{o}C.

Figure 5.1.6: The series of HSM micrographs for β-CD·BES.



A: Initial appearance (25.5 °C).



B: Onset of opacity (57.4 °C).



C: Increase in opacity, as a result of internal crystal fracturing (70.1 °C).



D: The crystals visually start to disintegrate (80.7 °C).



E: The crystals have ceased fracturing at 209.5 °C.



F: Onset of decomposition (255.5 °C).

β-CD·PRO:

The HSM analysis for β-CD·PRO displayed similar thermal behaviour to that of β-CD·BES, in terms of crystal fracturing being observed, at however, a significantly more rapid rate (Figure 5.1.7). Image A illustrates the crystals of β-CD·PRO at 22.5 °C prior to heating. At 55.3 °C the onset of dehydration occurred in the form of rapid crystal fracturing (image B). Fracturing continued at a fast rate as displayed in images C and D (63.3 °C and 73.9 °C respectively) and terminated by 79.7 °C, as displayed in image E, where the crystals had disintegrated and become completely opaque. This indicated that the crystals had dehydrated and that the crystalline structural integrity was predominantly dependent on the hydrogen bonding role of the water molecules. Thereafter, no observable changes occurred until the onset of decomposition at 292.7 °C (image F).

Figure 5.1.7: The series of HSM micrographs for β-CD·PRO.



A: Initial appearance (22.5 °C).



B: Onset of rapid crystal fracturing (55.3 °C).



C: Rapid continuation of crystal fracturing (63.3 °C).



D: Rapid continuation of crystal disintegration (73.9 °C).



E: No observable changes other than the fragments drifting (79.7 °C).



F: Onset of decomposition (292.7 °C).

5.2.1.6) Thermal gravimetric analysis (TGA)

The curves resulting from the thermal gravimetric analysis (TGA) experiments for β-CD·BES and β-CD·PRO had very similar profiles and the onset temperatures of their respective events correlated closely. The detailed results from each experiment are described individually below (Figures 5.1.8 and 5.1.9).

β-CD·BES:

The TGA curve of β-CD·BES (n=3) displayed the events that are associated with the dehydration and the onset of decomposition for the complex (Figure 5.1.8). With regard to the dehydration of the complex, a mass loss of 11.1 ± 0.2%, corresponding to 8.8 ± 0.2 water molecules per host molecule occurred between 18.7 ± 1.1 and 120.4 ± 1.3 °C in the form of a multi-step process as indicated by the dTGA curve. The calculation of the number of water molecules per complex unit can be viewed in the Appendix under section 4.1.2, p. 44. This multi-step dehydration process consisted of a series of differing rates at which the

water molecules were lost during this event. This is clearly evident in the dTGA curve, which indicated two distinctive peaks accompanied by a shoulder on the left-hand side of the first peak. These multi-step events were highly reproducible with respect to temperature (within a standard deviation of 1.5 °C), the only exception being that the shoulder in the dTGA curve was less pronounced in the two subsequent repetitions. The second event was the decomposition of β-CD·BES with onset at 266.4 ± 5.5 °C.

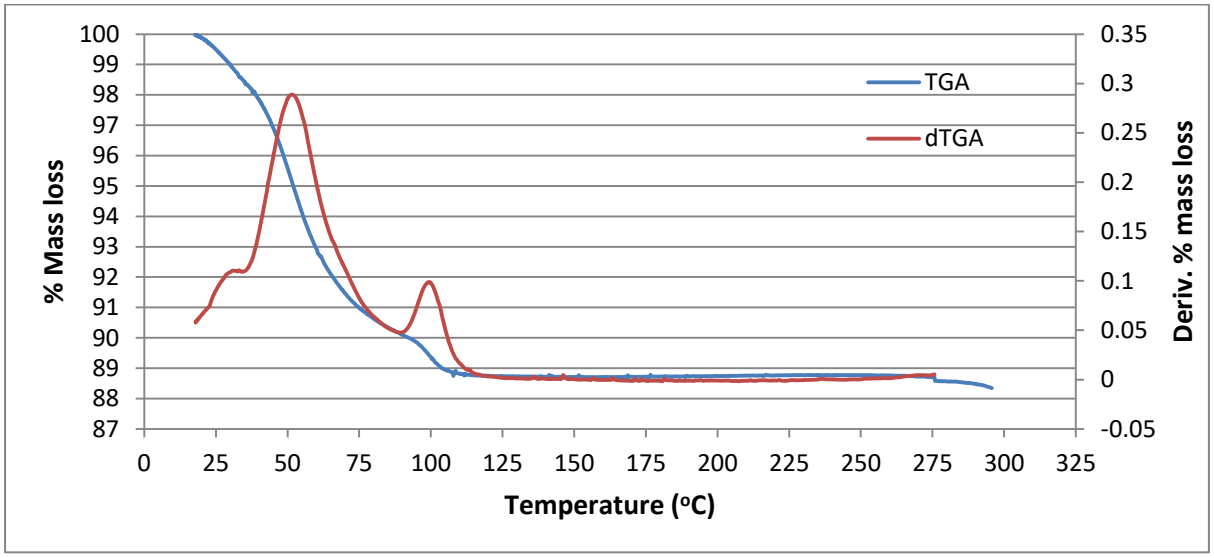


Figure 5.1.8: Representative TGA and dTGA curves for β-CD·BES.

β-CD·PRO:

The TGA curve of β-CD·PRO (n=2) also displayed the dehydration of the complex, which occurred between 20.2 ± 2.1 °C and 148.4 ± 0.9 °C and corresponded to a mass loss of 12.3 ± 0.2% (10.0 ± 0.2 water molecules per host molecule) as displayed in Figure 5.1.9. The calculation of the number of water molecules can be viewed in the Appendix under section 4.1.3, p. 45. The only way in which this multi-step dehydration differed from the dehydration profile of β-CD·BES, is that the termination of the dehydration of the β-CD·PRO complex was more gradual and thus the final temperature of the dehydration was higher. This possibly indicated that a few of the water molecules in β-CD·PRO have slightly stronger hydrogen bonding interactions in the complex and thus were removed only at higher

temperatures. Finally, the second event signified the onset of decomposition at 267.8 ± 3.1 °C.

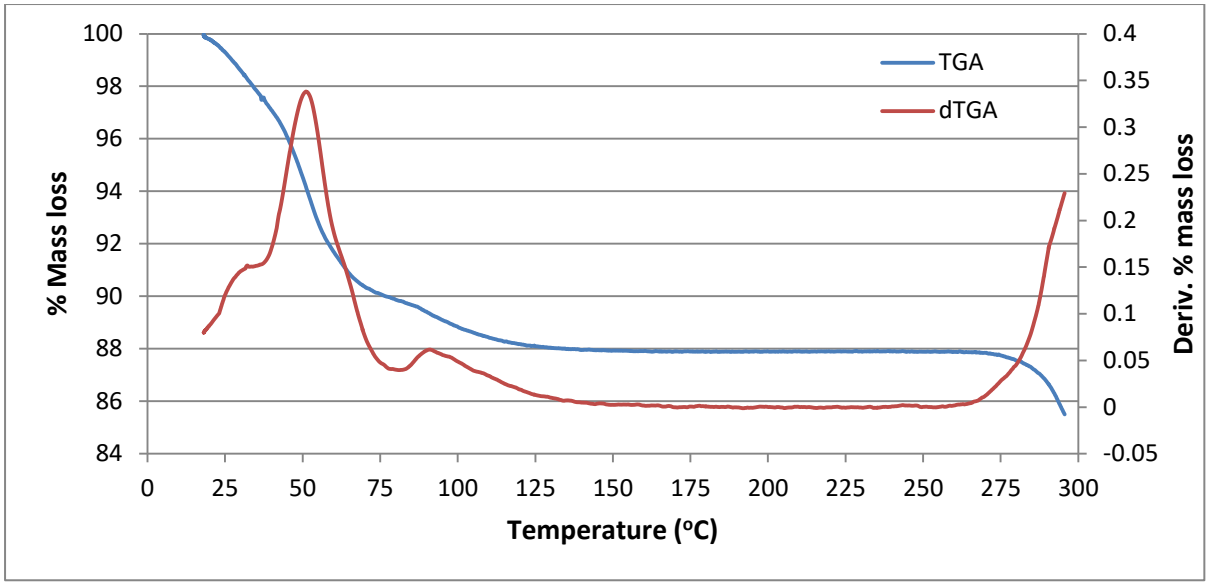


Figure 5.1.9: Representative TGA and dTGA curves for β-CD·PRO.

5.2.1.7) Differential scanning calorimetry (DSC) and variable temperature PXRD

The DSC curves and variable temperature PXRD experiments for the two complexes complemented each other and are thus discussed together below.

β-CD·BES

The DSC curve of β-CD·BES (n=2) represents the dehydration as a pseudo two-step process (Figure 5.1.10). The first broad endothermic peak, along with the shoulder, is indicative of the pseudo two-step dehydration and correlated very well with the dehydration range as observed in the overlaid TGA curve (Figure 5.1.10). The onset of this broad endothermic peak occurred at 53.2 ± 1.0 °C with a peak temperature of 83.0 ± 4.7 °C, and the onset of the shoulder for the latter part of the dehydration process was 91.8 ± 5.1 °C with the peak at 99.9 ± 5.3 °C. In addition, the variable temperature PXRD experiment reflected the

dehydration in the form of subtle changes in the crystal structure of the complex over the respective temperature range (Figure 5.1.11).

The second fairly broad endothermic peak in the DSC curve (Figure 5.1.10) had an onset temperature of 119.0 ± 3.4 °C with the peak occurring at 128.9 ± 3.5 °C. This endothermic peak was shortly followed by an exothermic peak (onset = 154.7 ± 2.5 °C, peak = 158.7 ± 2.0 °C) and thereafter by a sharp endothermic peak with an onset temperature of 213.4 ± 0.1 °C and peak temperature 216.4 ± 0.1 °C.

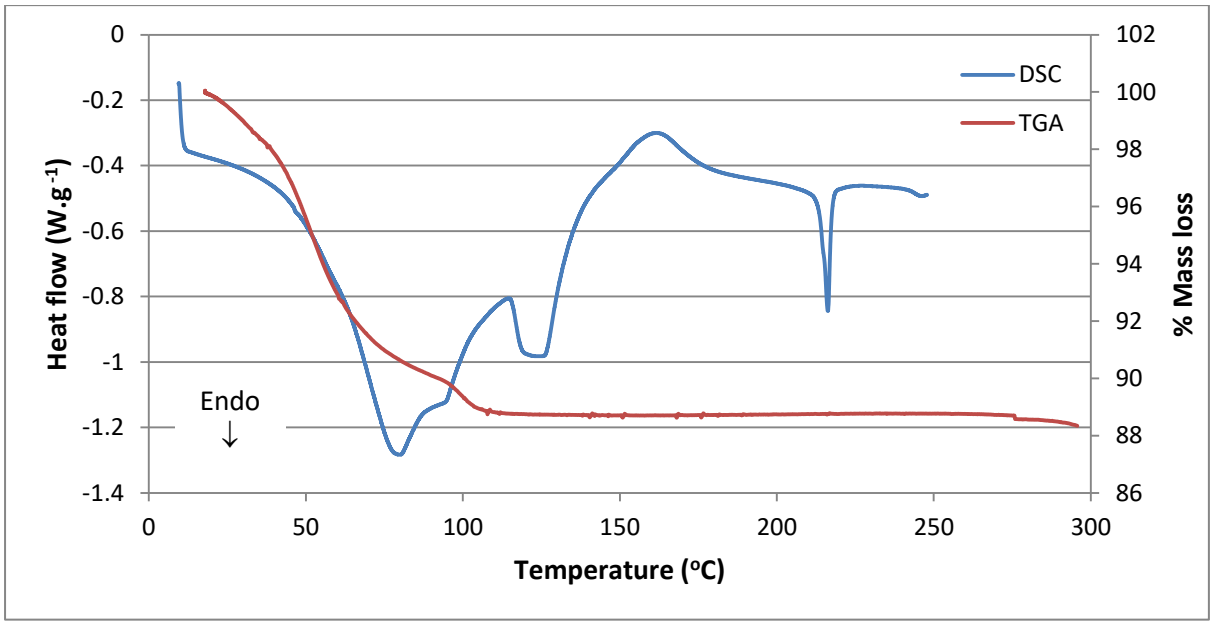


Figure 5.1.10: A representative DSC curve of β-CD·BES, with the respective TGA curve as a reference.

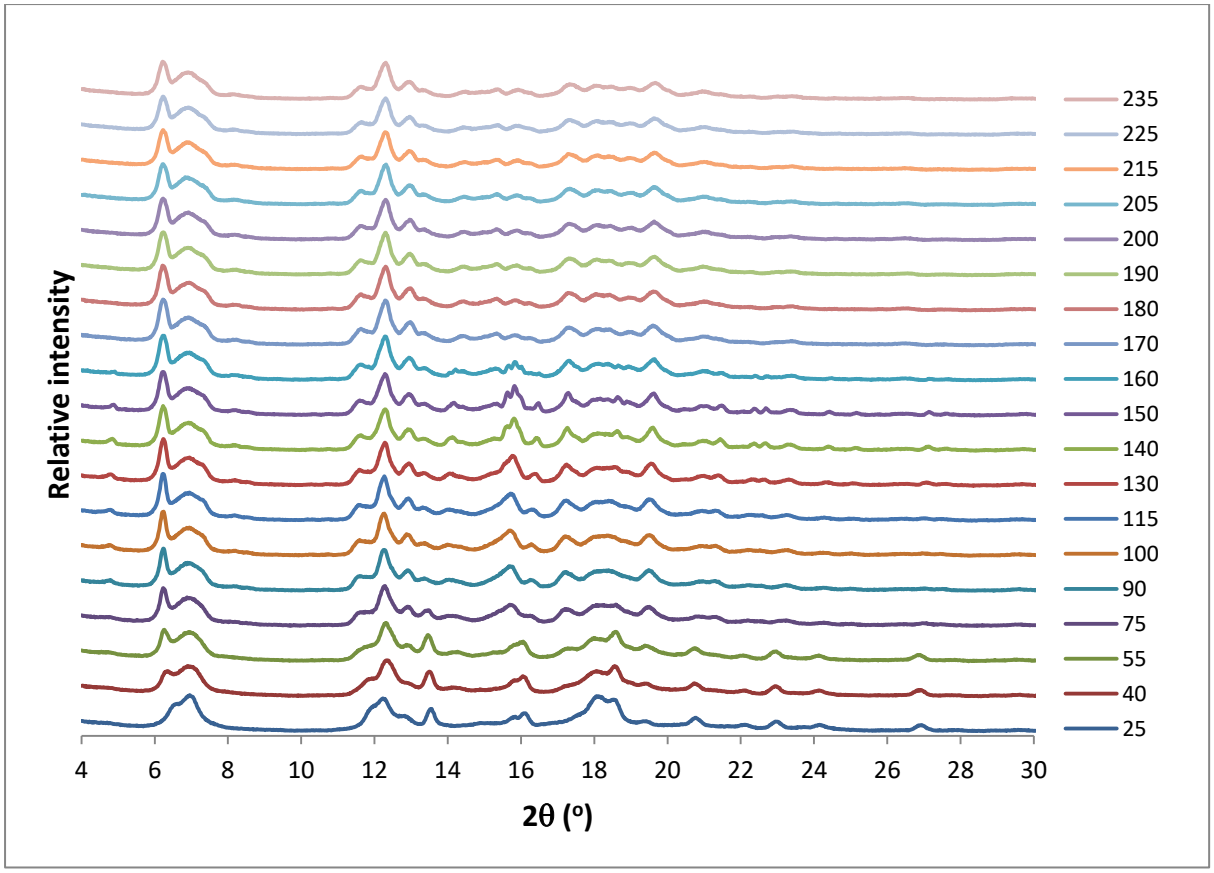


Figure 5.1.11: The variable temperature PXRD patterns of β-CD·BES over the temperature range from 25 °C to 235 °C. The numbers in the key represent the temperature in °C. The peak at the angular position of 7.0° is an artefact of the variable temperature PXRD stage. No significant peaks were observed at angular positions greater than 30.0°.

With reference to the variable temperature PXRD results illustrated in Figure 5.1.11,[c] between 25 °C and 90 °C the peaks at the angular positions 6.5°, 11.9°, 13.0°, 17.2° and 19.5° became more resolved and pronounced and thus gradually increased in intensity, while the peak at 13.5°, as well as the broad peak at 18.1°, reduced in intensity. Furthermore, between 55 °C and 75 °C, there was a sudden reduction in the relative intensities of the peaks at the angular positions 20.8°, 22.0°, 24.1°, 26.9°. These thermal changes all corresponded to the temperature range within which the first endothermic peak (excluding the shoulder) occurred in the DSC curve, and thus overlapped with the first part of the dehydration of the crystals (Figure 5.1.10). Arguably, the changes in the peak intensities in the variable temperature PXRD could be attributed to subtle structural changes occurring during the dehydration process.

[c] The peak at the angular position of 7.0° is an artefact of the variable temperature PXRD stage.

In addition, at 90 ^{o}C the peaks at the angular positions 5.0^{o} and 16.2^{o} gradually appeared, along with a broad peak at 7.5^{o}, while the peaks at 20.8^{o}, 22.0^{o}, 24.1^{o}, 26.9^{o} steadily reappeared. The temperature range of these events overlapped with that spanned by the shoulder occurring on the DSC curve, corresponding to the second part of the dehydration process (Figure 5.1.10). Furthermore, these subtle changes in the crystal structure of the complex due to the second part of the dehydration also overlapped with the endothermic event in the DSC curve where the onset was at 119.0 $\pm$ 3.4 ^{o}C with a peak temperature of 129.0 $\pm$ 3.5 ^{o}C. Lastly, between 140 ^{o}C and 160 ^{o}C in the variable temperature PXRD pattern, two peaks at 15.5^{o} and 18.5^{o} appeared, and thereafter at higher temperatures above 160 ^{o}C these peaks disappeared, along with a peak at 16.1^{o}. Thus, it is possible to correlate these short-lived peaks of the phase transition to the exothermic event in the DSC curve where the onset was at 154.7 $\pm$ 2.5 ^{o}C with a peak temperature of 158.7 $\pm$ 2.0 ^{o}C.

The variable temperature PXRD patterns did not display any evidence of a phase change between 215 ^{o}C and 225 ^{o}C (Figure 5.1.11), and the HSM experiment did not provide any insight into the characterisation of the final sharp endothermic peak in the DSC curve at an onset temperature of 213.4 $\pm$ 0.1 ^{o}C and with a peak temperature of 216.4 $\pm$ 0.1 ^{o}C (Figure 5.1.10).[d] In previous work conducted by Griffith,[34] the DSC curve of a β-CD inclusion complex containing naproxen also featured an endothermic peak at a high temperature of 261 – 273 ^{o}C which was attributed to an initial decomposition. It is not expected that the temperatures of the endothermic peaks in β-CD·BES and the naproxen complex necessarily corresponded, as they are different complexes. However, since no melting or phase transitions were observed for β-CD·BES in the HSM or variable temperature PXRD events, it is presumed that this endothermic peak in the DSC curve at an onset temperature of 213.4 $\pm$ 0.1 ^{o}C is representative of an initial decomposition.

Therefore, the comparison of thermal events occurring in the variable temperature PXRD patterns and the DSC curve of β-CD·BES is very complex owing to many subtleties in continuous and gradual peak appearances and disappearances for the multiple structural changes occurring.

[d] An additional variable temperature PXRD experiment was conducted which specifically analysed the temperature range between 205 ^{o}C and 225 ^{o}C recording PXRD patterns at 2 ^{o}C intervals. No changes were observed in these patterns either.

β-CD·PRO

The DSC curve of β-CD·PRO (n=2) displayed one very broad endothermic peak that had an onset temperature of 46.5 ± 0.4 °C and a peak temperature of 74.1 ± 0.2 °C (Figure 5.1.12). In addition, this broad peak contained a further four shoulders (occurring directly after the initial large endothermic peak) with peak temperatures of 89.6 ± 0.5 °C, 103.3 ± 0.2 °C, 121.2 ± 0.6 °C, and 138.5 ±0.9 °C. The initial broad endothermic peak was representative of the majority of the water loss and correlated very well with the first step of the dehydration process in the overlaid TGA curve (Figure 5.1.12). The subsequent four shoulders in the DSC curve indicated the remaining dehydration of the complex. It is only through the sensitivity of the DSC experiment that the complexity of the remaining dehydration process was displayed, which suggested that there were a few remaining water molecules that were tightly bound to the CD complex and released at particular intervals. Furthermore, the fact that these few remaining water molecules were removed only at relatively high temperatures, also confirms that they were tightly bound. The overlaid TGA curve (Figure 5.1.12) incorporated these four shoulders as a subsequent single-step event, but confirmed that dehydration still occurred at high temperatures (as discussed above).

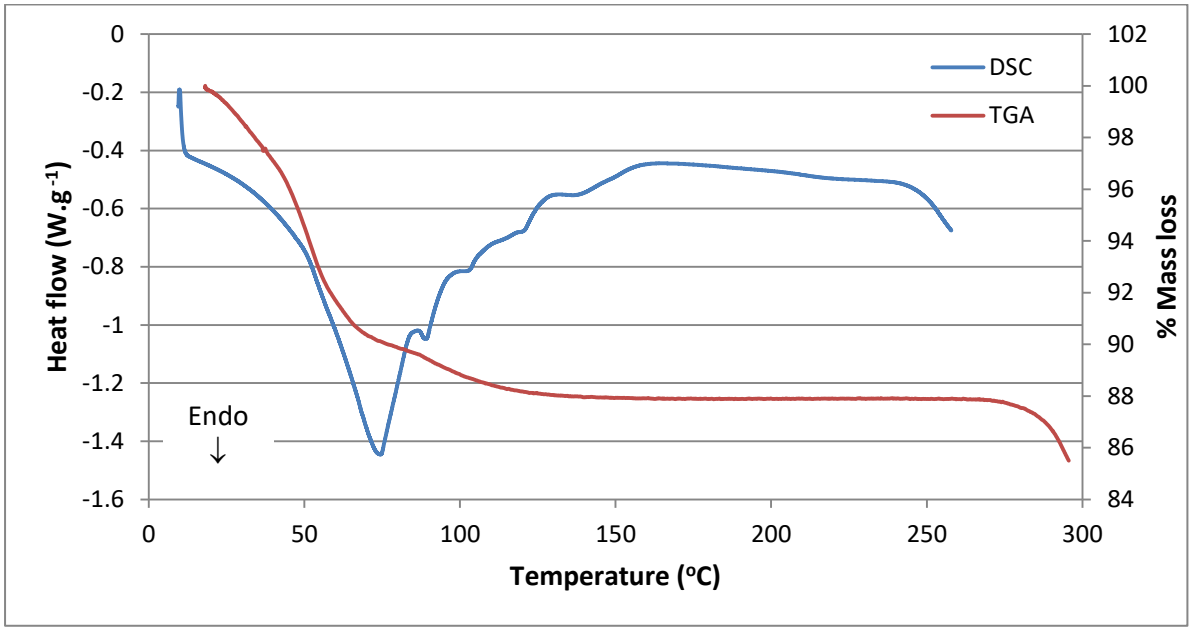


Figure 5.1.12: A representative DSC curve of β-CD·PRO, with the respective TGA curve as a reference.

In addition, the variable temperature PXRD patterns (Figure 5.1.13) confirmed that there were no phase transitions up until 155 ^{o}C, which proved that the endothermic peaks relating to the dehydration process did not simultaneously contain any phase transition contributions (Figure 5.1.11). At 155 ^{o}C in the variable temperature PXRD patterns, the peaks at the angular positions 11.0^{o}, 15.0^{o}, 15.8^{o}, 17.5°, as well as all the low intensity peaks above 20.0^{o}, began to lose their intensity, and by 170 ^{o}C most of these peaks had either disappeared or become relatively very small.[e] This phase change correlated with the small exothermic event in the DSC curve where the onset was 157.1 $\pm$ 0.1 ^{o}C with a peak temperature of 162.0 $\pm$ 0.2 ^{o}C (Figure 5.1.12). Therefore, once β-CD·PRO had been completely dehydrated, it appeared to undergo a phase transition.

[e] The peak at the angular position of 7.0^{o} is an artefact of the variable temperature PXRD stage.

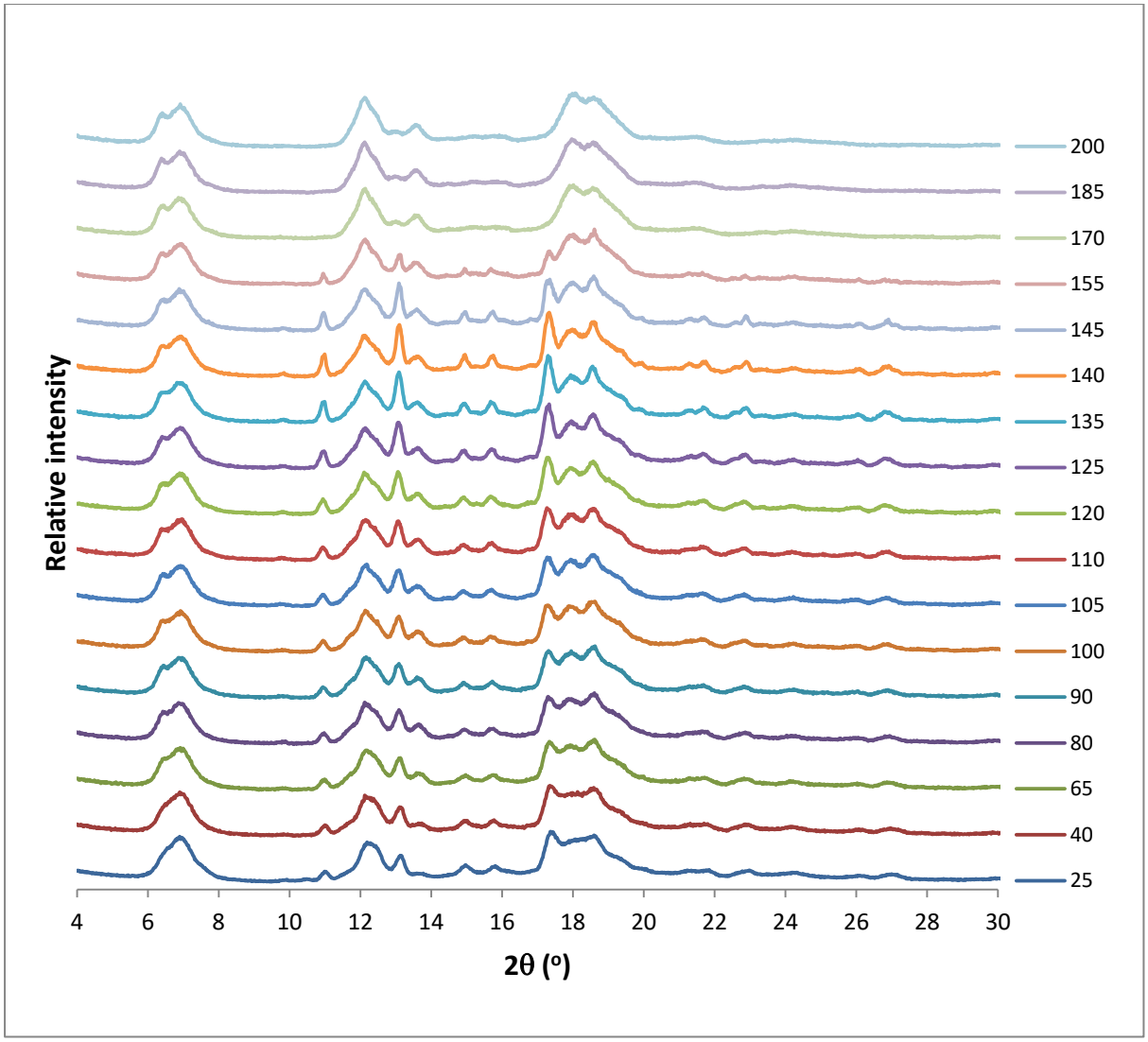


Figure 5.1.13: The variable temperature PXRD patterns of β-CD·PRO over the temperature range from 25 °C to 200 °C. The numbers in the key represent the temperature in °C. The peak at the angular position of 7.0° is an artefact of the variable temperature PXRD stage. No significant peaks were observed at angular positions greater than 30.0°.

5.2.1.8) Single-crystal X-ray diffraction (SCXRD) analysis of β-CD·BES and β-CD·PRO

Data-collection and space group determination

For both β-CD·BES and β-CD·PRO, intensity data from single, transparent, block-shaped crystals were collected at 100(2) K. The monoclinic crystal system was indicated for both of them, as the Laue group that was identified from their intensity-weighted reciprocal lattices was 2/*m*. *C*-centred lattices were determined (condition 1 in Table 5.1.3) and along with the other two conditions listed in Table 5.1.3, the following space groups were indicated as possibilities: *C*2, *Cm* and *C*2/*m*. However, the only possible space group for these inclusion complexes is *C*2, as CD molecules are chiral. This conclusion, which was also previously inferred from the isostructural comparison in the PXRD analysis above (section 5.2.1.4, pp. 211 – 213), was also confirmed by the program X-PREP, which indicated a non-centric space group ($|E^2 - 1|$ = 0.788 for β-CD·BES and 0.752 for β-CD·PRO).[35] The atomic numbering scheme for the β-CD molecule is provided in Figure 5.1.14, and additional information regarding each crystal structure will hereafter be described separately.

Table 5.1.3: The conditions limiting possible reflections for the crystals of β-CD·BES and β-CD·PRO.

Number	Conditions limiting possible reflections	Deduction
1	hkl: h+k = 2n	*C*-centred
2	[h0l: (h = 2n, redundant condition)]	-
3	[0k0: (k = 2n, redundant condition)]	-

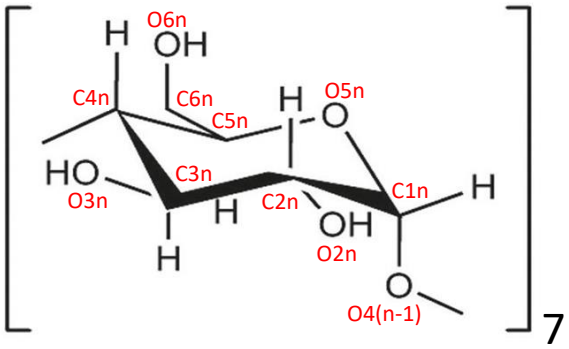


Figure 5.1.14: The numbering scheme for the β-CD molecule, with n representing one of the seven glucose units of the molecule.

Structure solution and refinement of β-CD·BES

The β-CD·BES inclusion complex was solved *via* isomorphous replacement, as outlined in the technique described in the Experimental methods (Chapter 2, section 2.6, p. 44). A template structure, with the refcode AJUVEG, was imported from the CSD,[36] and the non-hydrogen atoms of the host molecule were used as a trial model for that of β-CD·BES. This unit was refined by full-matrix least-squares using program SHELXL-97,[37] the atoms being treated isotropically initially and thereafter anisotropically. The resultant difference electron density ($\Delta\rho$) map indicated that two of the hydroxyl oxygen atoms located at C6 positions on the β-CD molecule (C6A4 and C6A7) were disordered over two positions. This disorder was modelled by assigning site-occupancy values of *x* and 1-*x* to the major and minor disorder components of each disordered hydroxyl pair, with *x* set as a free variable during the refinement. In addition, the corresponding C6 atoms for the disordered hydroxyl groups were split and each part was assigned a separate PART number, as well as the same corresponding free variable. In addition, both split C6 atoms were constrained to have the same U_{iso} value during refinement. DFIX restraints were applied only to these disordered parts of the molecule; this included restraining the C5-C6 bond lengths (at 1.51 Å, σ = 0.01 Å), the C6-O6 bond lengths (at 1.43 Å, σ = 0.01 Å) and the C5···O6 distances (at 2.45 Å, σ = 0.01 Å) in order to maintain reasonable C5-C6-O6 bond angles. In some cases, the e.s.d.s ranged between smaller values of 0.005 and 0.001 Å.

Furthermore, the thermal motion from the abnormally high temperature factor of a hydroxyl oxygen atom, O6A3, indicated that it should be split over two positions. Thus, two new partial atoms, namely O6A3 and O6B3, were placed using the suggested coordinates and treated accordingly with the same procedure as described above where required.

The site-occupancy factors (s.o.f.s) of the major components of the disordered hydroxyl oxygen atoms, namely O6A3, O6A4 and O6A7, were 0.63(1), 0.59(1) and 0.63(2) respectively after refining isotropically. The disordered atoms were not refined anisotropically.

The 'maximum electron density' model was used to place the hydrogen atoms in idealised positions on the host molecule, and an isotropic temperature factor of 1.2 times the value of the U_{iso} parameter of its parent atom was assigned to each hydrogen atom. Furthermore, it was evident from the $\Delta\rho$ map that the guest molecule was severely disordered (1.84 e.Å^{-3}

being the highest $\Delta\rho$ value within the CD cavity), thus preventing the guest molecule from being located and modelled. Consequently, a SQUEEZE routine[38] implemented in the program PLATON[39] was performed in order to calculate an electron count of the $\Delta\rho$ distribution in the unit cell. The unassigned $\Delta\rho$ is mainly attributed to the guest molecules (as well as the unassigned water hydrogen atoms), and therefore it would be possible to confirm the host-guest stoichiometry of the complex *via* this procedure. The residual electron density amounted to 399 electrons, which confirmed a 2:1 host-guest complex.[a] In addition, the SQUEEZE procedure also eliminated the majority of this unassigned electron density, which reduced the R_1 and wR_2 values significantly. The crystallographic data are summarised in Table 5.1.4.

Structure solution and refinement of β-CD·PRO

The structure solution and refinement for β-CD·PRO followed a very similar procedure to the treatment applied to β-CD·BES, as it was also solved *via* isomorphous replacement and refined with SHELXL-97,[37] initially isotropically and subsequently anisotropically. However, a different template structure from the CSD was used for the isomorphous replacement procedure, namely refcode NUFTUE (containing the guest propyl 4-hydroxy benzoate).[36,40] Following initial refinement of the host molecule, the $\Delta\rho$ map indicated that five of the hydroxyl oxygen atoms located at the C6 positions were disordered over two sites. This disorder was modelled using the same procedure as that with β-CD·BES. Similarly, the bond lengths and geometry of these disordered hydroxyl oxygen atom pairs were also treated using DFIX restraints. As with β-CD·BES, bond length restraints were employed where required, particularly for the disordered atoms. Thus, the C6-O6 bond lengths of the disordered counterparts (as well as C6A4-O6A4), were restrained to a value of 1.43 Å, σ = 0.01 Å, the C5-C6 bond lengths were restrained to 1.51 Å, σ = 0.01 Å, and the non-bonded C5···O6 distances were restrained to a value of 2.45 Å, σ = 0.01 Å. Occasionally, it was necessary to reduce the e.s.d.s to 0.001 Å to enforce the particular restraint. These

[a] The 399 electrons account for the guest molecule as well as the water hydrogen atoms that were not modelled in β-CD·BES. The theoretical electron count of the guest molecule (β-estradiol) and water hydrogen atom contributions per unit cell in a 2:1 host-guest complex are 296 and 70.8 electrons respectively. Therefore, in order to obtain the guest electron count contribution from the SQUEEZE procedure, the water hydrogen atom count was subtracted from the estimated total of 399 electrons per unit cell. This yielded 328.2 electrons which is in reasonable agreement with the theoretical value of 296, thus confirming the 2:1 host-guest stoichiometry determined accurately by ^{1}H NMR analysis.

disordered oxygen atoms were refined isotropically only and the major components of the disordered hydroxyl oxygen atom pairs included O6A2, O6A3, O6A5, O6A6 and O6A7 with s.o.f values of 0.80(1), 0.76(1), 0.70(1), 0.62(2) and 0.45(2) respectively. Finally, a SQUEEZE procedure[38] was also conducted and the residual electron density was calculated to contribute 445 electrons per unit cell. This also verified that the complex stoichiometry was a 2:1 host-guest ratio.[b] The crystallographic data and details of the refinement are summarised in Table 5.1.4.

Table 5.1.4: The crystal data and refinement parameters for the β-CD·BES and β-CD·PRO inclusion complexes.

Parameter	Value for β-CD·BES	Value for β-CD·PRO
Complex formula	$2(C_{42}H_{70}O_{35})\cdot(C_{18}H_{24}O_2)\cdot 17.7(H_2O)$	$2(C_{42}H_{70}O_{35})\cdot(C_{21}H_{30}O_2)\cdot 20(H_2O)$
Formula weight ($g.mol^{-1}$)	2859.40	2944.72
Temperature (K)	100(2)	100(2)
Wavelength (Å)	0.71073	0.71073
Crystal system	Monoclinic	Monoclinic
Space group	*C*2	*C*2
a (Å)	19.087(2)	18.9408(8)
b (Å)	24.427(2)	24.540(1)
c (Å)	15.581(1)	15.6585(8)
α (°)	90	90
β (°)	109.555(2)	109.161(1)
γ (°)	90	90
Volume ($Å^3$)	6845.4(10)	6875.1(6)
Z	2	2
Calculated density ($g.cm^{-3}$)	1.387	1.422
μ (mm^{-1})	0.123	0.126
F (000)	3056	3152
Crystal size (mm)	0.48 x 0.44 x 0.10	0.34 x 0.24 x 0.16
θ-Range scanned (°)	1.39 – 26.87	2.74 – 28.34
Index range	h: -24, 24; k: -30, 30; l: -19, 19	h: -25, 25; k: -32, 32; l: -20, 20
No. of reflections collected	75496	150313
No. of unique reflections	14663	17104
Data completeness (%)	99.5	99.6
Data/restraints/parameters	14663/19/756	17104/28/750
S (Goodness-of-fit on F^2)	1.038	1.007
Final R indices R_1, wR_2, [I > 2σ(I)]	0.0829, 0.2352	0.0888, 0.2480
R Indices, all data (R_1, wR_2)	0.1043, 0.2593	0.1010, 0.2637
Largest diff. peak and hole ($e.Å^{-3}$)	0.72, -1.30	1.34, -2.30

[b] The 445 electrons account for the guest molecule as well as the water hydrogen atoms that were not modelled in β-CD·PRO. The theoretical electron count of the guest molecule (progesterone) and water hydrogen atom contributions per unit cell in a 2:1 host-guest complex are 344 and 80 electrons respectively. Therefore, in order to obtain the guest electron density contribution from the SQUEEZE procedure, the water hydrogen atom count was subtracted from the calculated total of 445 electrons per unit cell. This yielded 365 electrons, which is in excellent agreement with the theoretical value of 344, thus confirming the 2:1 host-guest stoichiometry. The latter had been determined accurately using ^{1}H NMR spectroscopy.

Assigning the water oxygen atoms of β-CD·BES and β-CD·PRO

The oxygen atoms of the water molecules were identified as outlined in the Experimental methods (Chapter 2) under section 2.6 on pp. 44 – 45, and the details for the two β-CD inclusion complexes are described below:

With regard to β-CD·BES, the first two water oxygen atoms located, namely O1W and O2W, were initially identified as having full site-occupancies owing to their large difference electron density values, while O3W was necessarily assigned a site-occupancy of 0.5 since it was located on a two-fold rotation axis. These three oxygen atoms were refined anisotropically, and even though the oxygen atom O4W also had a fairly large electron density value of 2.61 e.Å^{-3}, its isotropic thermal parameter was abnormally high and unstable during refinement, and thus it could not be assigned a full site-occupancy. The remaining disordered water oxygen atoms (including O4W) were subsequently assigned in decreasing order of their electron density values. Their thermal parameters were initially fixed at 0.086 Å^2 (the average U_{iso} value of the first three water oxygen atoms), and their s.o.f.s were allowed to vary during refinement. In addition, two pairs of partial water oxygen atoms, namely O4W and O14W, as well as O10W and O15W, were disordered over two positions. For these disordered pairs, their U_{iso} values were constrained to be equal during refinements. Once these values converged, their U_{iso} values were allowed to vary, unless they indicated instability. The crystal structure model accounted for 9.1 water molecules per β-CD molecule, which is in agreement with the TGA results which had indicated 8.8 $\pm$ 0.2 water molecules per β-CD molecule. The refined s.o.f. values and U_{iso} parameters of β-CD·BES are displayed in Table 5.1.5.

For assignment of the water molecules for β-CD·PRO, almost the identical procedure was followed, the water oxygen atoms O1W, O3W, and O4W, being assigned full site-occupancies based on their large difference electron densities, while O2W was assigned a site-occupancy of 0.5 since it was located on a two-fold rotation axis. These water oxygen atoms were also refined anisotropically and an average of their U_{iso} values was calculated (0.059 Å^2), which was used to fix the U_{iso} parameters of the remaining partial water oxygen atoms, while allowing their s.o.f.s to vary. After further refinement, it was evident that O4W developed an additional component which was labelled O13W, and similarly O7W with

component O14W, O12W with component O17W, and lastly, O11W with components O15W and O16W. The disordered water oxygen atoms occupying multiple sites were constrained to have the same U_{iso} parameter during least-squares refinement. Their U_{iso} values were subsequently allowed to vary, unless they displayed indications of instability. The water content of the crystal structure amounted to 9.9 water molecules per complex unit, which was in perfect agreement with the TGA results indicating 10.0 $\pm$ 0.2 water molecules per complex unit. The refined values for the s.o.f. values and U_{iso} parameters are displayed in Table 5.1.6.

Due to the fact that the majority of the water oxygen atoms in these crystal structures were disordered and that the difference electron density peaks of water H atoms were generally not evident, the final models do not feature placement of water H atoms. This is a common practice when refining crystal structures of CD complexes with large complements of water molecules.

Table 5.1.5: The total number of water oxygen sites that were identified for β-CD·BES, with their respective s.o.f. and U_{iso} values.

Atom	**s.o.f.**	**U_{iso} (Å^2)**	**Atom**	**s.o.f.**	**U_{iso} (Å^2)**
O1W	1.00	0.062 (1)	O9W	0.49(2)	10.086*
O2W	1.00	0.084(2)	O10W	0.41(1)	10.086*
O3W	1.00	0.080(3)	O11W	0.36(1)	0.075(3)
O4W	0.63(1)	0.062(2)	O12W	0.24(2)	0.075(3)
O5W	0.78(3)	0.100(5)	O13W	10.50*	10.086
O6W	0.52(1)	0.075(3)	O14W	0.37(1)	0.062(2)
O7W	0.59(3)	0.075(5)	O15W	0.59(1)	10.086*
O8W	0.65(3)	0.094(6)			

*10.086 indicates a *constant* assigned value of 0.086Å^2
*10.50 indicates a *constant* assigned value of 0.50

Table 5.1.6: The total number of water oxygen sites that were identified for β-CD·PRO, with their respective s.o.f. and U_{iso} values.

Atom	s.o.f.	U_{iso} (Å^2)	Atom	s.o.f.	U_{iso} (Å^2)
O1W	1.00	0.045(1)	O10W	0.50(3)	0.081(6)
O2W	1.00	0.051(2)	O11W	0.33(1)	0.064(3)
O3W	1.00	0.064(1)	O12W	0.34(2)	0.078(6)
O4W	0.72(1)	0.049(2)	O13W	0.28(1)	0.049(2)
O5W	0.50(2)	0.051(4)	O14W	0.40(3)	0.087(5)
O6W	0.91(3)	0.104(4)	O15W	0.37(1)	0.064(3)
O7W	0.67(3)	0.087(5)	O16W	0.31(1)	0.064(3)
O8W	0.63(3)	0.077(5)	O17W	0.41(3)	0.078(6)
O9W	10.50*	10.059			

*10.059 indicates a *constant* assigned value of 0.059 Å^2
*10.50 indicates a *constant* assigned value of 0.50

Molecular Structure

The asymmetric units (ASUs) of β-CD·BES and β-CD·PRO are displayed in Figures 5.1.15 and 5.1.16 below and each comprises one β-CD molecule, one guest molecule that is not observed (either β-estradiol for β-CD·BES, or progesterone for β-CD·PRO), and water molecules distributed over 15 sites for β-CD·BES, and similarly 17 sites for β-CD·PRO. The host molecules for both complexes were only partially disordered, while their respective guest molecules were severely disordered, as evidenced by the very low Δρ peaks within the respective CD cavities, and there were no indications of their sensible molecular connectivity, despite the intensity data having been collected at 100(2) K. Lastly, the water molecules were all within adequate hydrogen bonding distance ranges of neighbouring water oxygen atoms, or the host molecules.

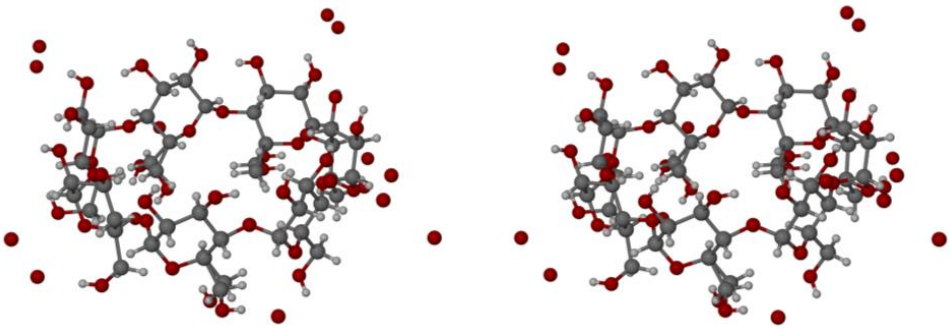


Figure 5.1.15: A stereoscopic view of the host molecule and water oxygen atoms in the ASU of β-CD·BES displaying the 'empty' host cavity.

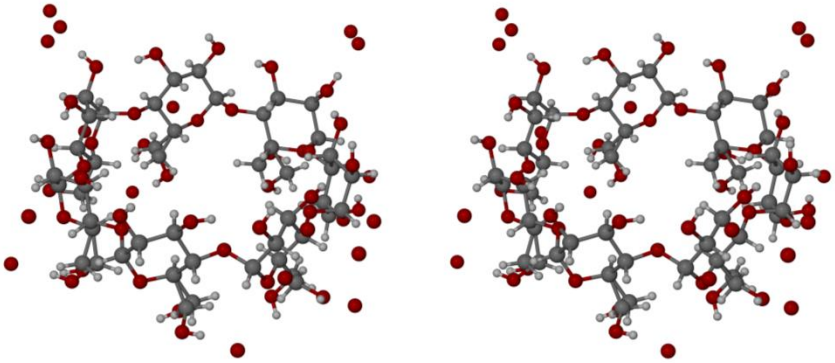


Figure 5.1.16: A stereoscopic view of the host molecule and water oxygen atoms in the ASU of β-CD·PRO displaying the 'empty' host cavity.

Comparison of the above figures shows that several of the water oxygen atom locations in β-CD·BES and β-CD·PRO are common, thus extending the level of isostructurality beyond that of just the host molecules.

Crystal Packing

Both β-CD·BES and β-CD·PRO are dimeric inclusion complexes with C_2-symmetry, and the intermolecular O-H···O hydrogen bonds formed between the secondary rims of each β-CD molecule maintain the dimeric structures. These dimeric β-CD units are stacked along the z-direction, thus forming channel-type packing arrangements (Figure 5.1.17), which are commonly observed in isostructural β-CD inclusion complexes that crystallize in the space group *C*2.[7,10] Furthermore, a small amount of lateral shifting is observed in this arrangement of the β-CD molecules, which occurs between adjacent dimers at the tail-to-tail ends of each β-CD dimeric unit. This is in contrast to the β-CD·PTB inclusion complex which also crystallized in the space group *C*2, as described in the previous chapter. With regard to β-CD·PTB, the specific mode of inclusion of the guest molecule resulted in a larger lateral shift of the dimeric units, causing the volume of the unit cell to increase significantly relative to those of β-CD·BES and β-CD·PRO. Consequently, even though β-CD·PTB crystallized in the same space group as β-CD·BES and β-CD·PRO, they represent two distinct subsets that crystallize slightly differently.

In addition, the continuous columns into which the dimeric units of β-CD·BES and β-CD·PRO self-assemble, are held together by intermolecular O-H···O hydrogen bonding between host

hydroxyl groups and the water molecules. Lastly, the host cavities of these columns form an infinitely long channel, in which the guest molecules are arranged in a disordered manner. Consequently, it is not possible to locate the guest molecule, as its electron density is diluted throughout the entire channel, which is a common occurrence for most β-CD complexes that crystallize in the space group *C*2.

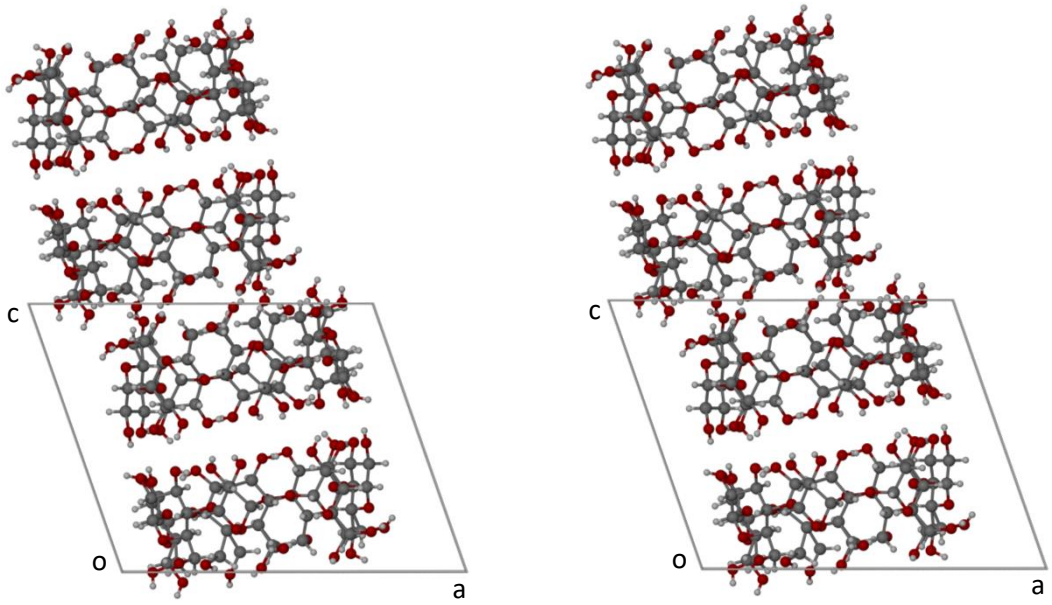


Figure 5.1.17: The channel-packing arrangement of β-CD·BES (left) and β-CD·PRO (right) viewed along [010]. The β-CD molecules form dimeric units which are stacked with a small lateral shift. The water molecules have been omitted for clarity.

Figures 5.1.18 and 5.1.19 depict stereoscopic views of the crystal structures of β-CD·BES and β-CD·PRO viewed down the c-axis, highlighting the endless channel formation. Furthermore, it is evident that the columns of complex units are held together by the water molecules which occupy the interstitial spaces between the columns. These depictions also indicate that there are a total of four β-CD molecules in the unit cell, corresponding to two dimeric complex units per cell.

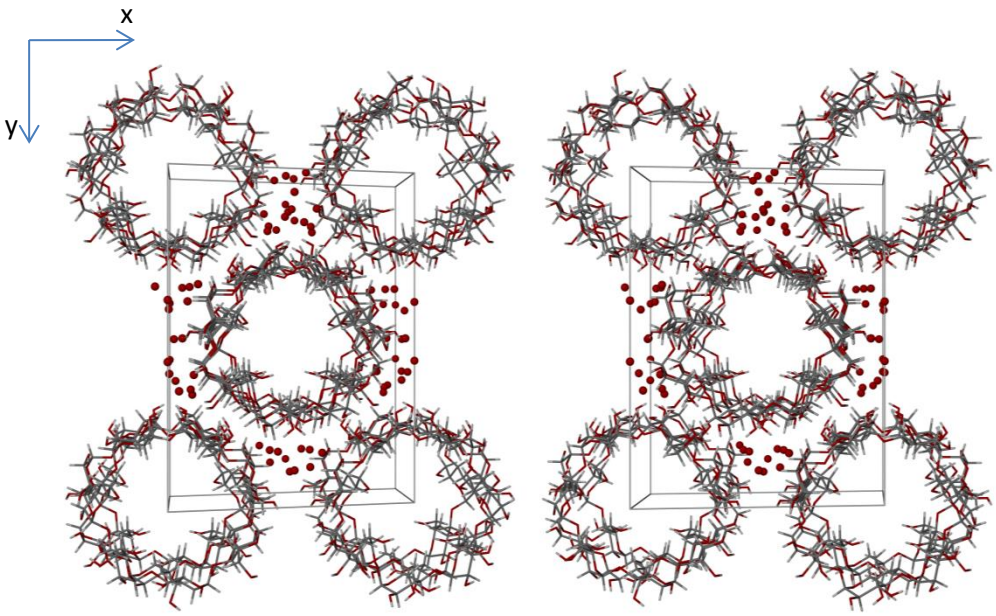


Figure 5.1.18: A stereoscopic view down the c-axis displaying the packing arrangement for β-CD·BES.

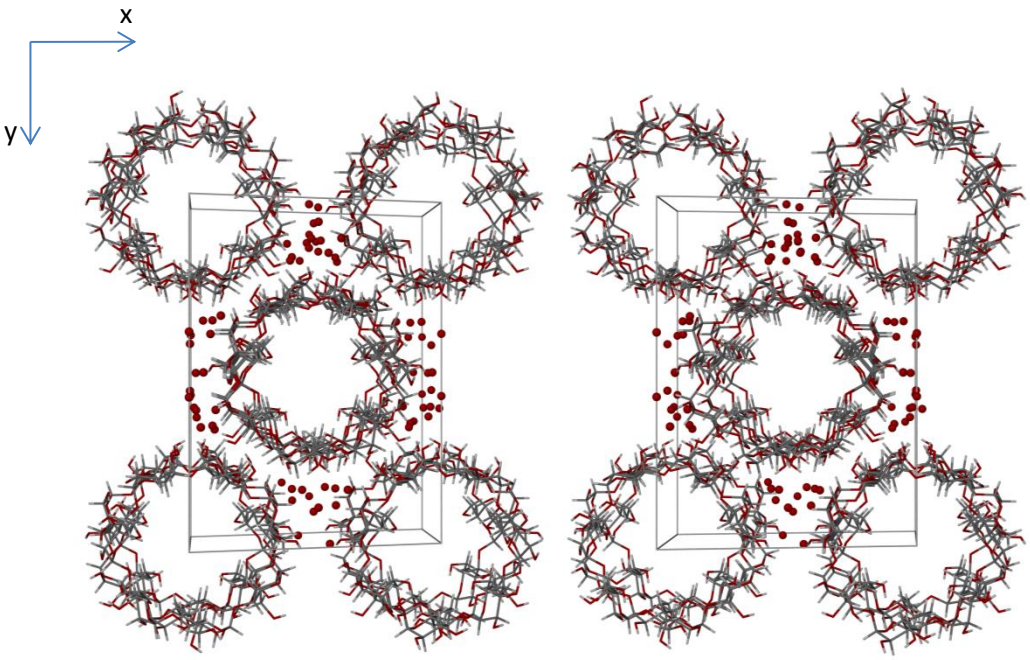


Figure 5.1.19: A stereoscopic view down the c-axis displaying the packing arrangement for β-CD·PRO.

The above figures also reveal the significant extent of 'conservation' of water molecule sites in the two isostructural complexes, a feature referred to earlier.

Host-host hydrogen bonding

The host-host hydrogen bonding observed in both CD complexes is generally very similar, both intramolecular and intermolecular hydrogen bonding being evident (Figures 5.1.20 and 5.1.21). The hydroxyl groups located on the secondary rims form intramolecular hydrogen bonds that have the ability to alternate between O2-H···O3′ and O3-H···O2′ and thus have a 'flip-flop' nature.[41] Consequently, a belt of hydrogen bonds is formed on the secondary rims with heptagonal geometry, and the overall 'round' shape of the CDs is thereby reinforced. The crystal structures of both β-CD·BES and β-CD·PRO display the directionality of this belt of intramolecular hydrogen bonds as O2-H···O3′. Furthermore, at the interface of the secondary rims, intermolecular hydrogen bonding also takes place between the O3-H hydroxyl groups from one of the CD molecules, and the O2-H or O3-H hydroxyl groups of the CD molecule related to the first by the two-fold rotation axis parallel to the crystal b-axis.

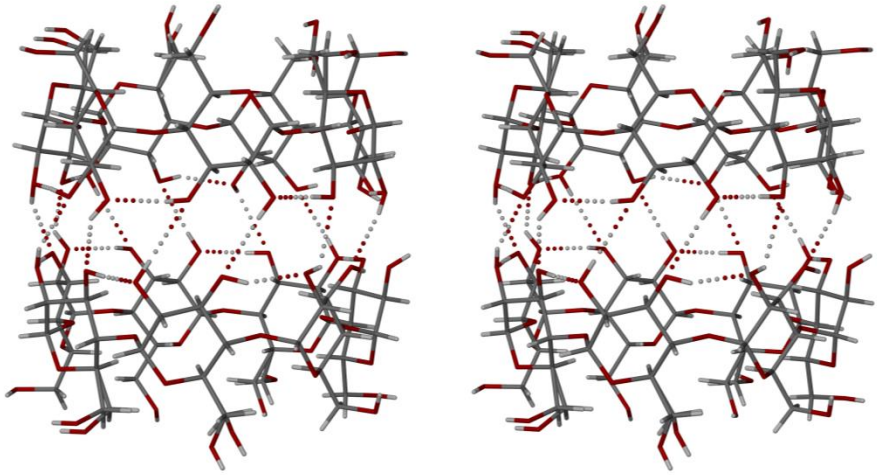


Figure 5.1.20: A stereoscopic view of the intramolecular and intermolecular host-host hydrogen bonding occurring in the dimeric unit of β-CD·BES. The water molecules have been omitted for clarity.

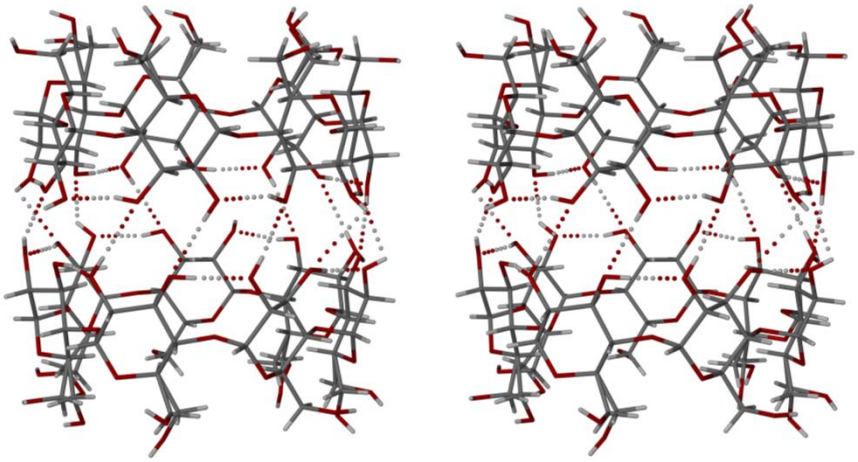


Figure 5.1.21: A stereoscopic view of the intramolecular and intermolecular host-host hydrogen bonding occurring in the dimeric unit of β-CD·PRO. The water molecules have been omitted for clarity.

The intramolecular and intermolecular hydrogen bonding parameters for the β-CD·BES and β-CD·PRO host molecules are displayed in Tables 5.1.7 and 5.1.8, which include all relevant O-H···O as well as C-H···O H-bonds. The intermolecular hydrogen bonds for both structures are evidently strong and thus confirm the stability of the complexes.

Table 5.1.7: The parameters for the hydrogen bond interactions in β-CD·BES.

Interaction type	Hydrogen bond	D-H (Å)	H···A (Å)	D···A (Å)	D-H···A (°)	Symmetry code
O2-H···O3 and O2-H···O2 Hydrogen bonds						
Intramolecular	O2A1-H2A1···O3A1	0.84	2.43	2.853(7)	112	x, y, z
Intermolecular	O2A2-H2A2···O3A3	0.84	2.36	3.024(7)	136	1-x, y, 1-z
Intermolecular	O2A2-H2A2···O2A7	0.84	2.27	2.748(7)	116	3/2-x, 1/2+y, 1-z
Intramolecular	O2A3-H2A3···O3A3	0.84	2.52	2.874(7)	107	x, y, z
Intermolecular	O2A3-H2A3···O3A2	0.84	2.29	3.073(7)	155	1-x, y, 1-z
Intermolecular	O2A7-H2A7···O3A5	0.84	2.22	3.043(6)	166	1-x, y, 1-z
Intramolecular	O2A7-H2A7···O3A7	0.84	2.47	2.868(7)	110	x, y, z
O3-H···O2′ Hydrogen bonds						
Intramolecular	O3A1-H3A1···O2A2	0.84	2.00	2.790(7)	157	x, y, z
Intramolecular	O3A2-H3A2···O2A3	0.84	2.06	2.783(8)	144	x, y, z
Intramolecular	O3A3-H3A3···O2A4	0.84	1.99	2.809(7)	165	x, y, z
Intramolecular	O3A4-H3A4···O2A5	0.84	2.10	2.865(7)	151	x, y, z
Intramolecular	O3A5-H3A5···O2A6	0.84	1.99	2.808(7)	166	x, y, z
Intramolecular	O3A6-H3A6···O2A7	0.84	1.98	2.786(8)	159	x, y, z
Intramolecular	O3A7-H3A7···O2A1	0.84	1.98	2.794(7)	163	x, y, z
O6-H···O5 and O6-H···O6 Hydrogen bonds						
Intermolecular	O6A1-H6AB···O6B4	0.84	2.26	3.03(2)	152	1-x,y,-z
Intermolecular	O6A3-H6AI···O6A5	0.84	2.02	2.78(1)	151	1/2-x, 1/2+y, -z
Intramolecular	O6A5-H6AY···O5A5	0.84	2.45	2.800(7)	106	x, y, z
Intermolecular	O6A5-H6AY···O6A2	0.84	2.05	2.825(8)	153	-1/2+x, -1/2+y, z
C-H···O Hydrogen bonds						
Intramolecular	C6A1-H6A9···O5A2	0.99	2.56	3.44(1)	148	x, y, z
Intermolecular	C1A2-H1A2···O2A6	1.00	2.50	3.293(9)	136	1/2+x, 1/2+y, z
Intermolecular	C2A2-H1···O3A5	1.00	2.37	3.347(7)	167	1/2+x, 1/2+y, z
Intramolecular	C6A4-H6AF···O5A5	0.99	2.57	3.35(1)	136	x, y, z
Intermolecular	C6A5-H6A5···O6A7	0.99	2.51	3.12(2)	120	1-x, y, -z
Intramolecular	C6A5-H6A6···O5A6	0.99	2.55	3.38(1)	141	x, y, z
Intermolecular	C6A6-H6A7···O6B7	0.99	2.53	3.278(2)	132	1-x, y, -z
Intermolecular	C2A7-H10···O3A3	1.00	2.40	3.324(9)	154	1/2+x, -1/2+y, z

Table 5.1.8: The parameters for the hydrogen bond interactions in β-CD·PRO.

Interaction type	Hydrogen bond	D-H (Å)	H···A (Å)	D···A (Å)	D-H···A (°)	Symmetry code
O2-H···O3 and O2-H···O2 Hydrogen bonds						
Intramolecular	O2A1-H2A1···O3A1	0.84	2.42	2.833(7)	111	x, y, z
Intermolecular	O2A1-H2A1···O3A2	0.84	2.19	3.028(6)	173	1-x, y, 1-z
Intramolecular	O2A3-H3···O3A3	0.84	2.47	2.895(6)	112	x, y, z
Intermolecular	O2A3-H3···O3A7	0.84	2.44	3.277(6)	177	1-x, y, 1-z
Intramolecular	O2A6-H8···O3A6	0.84	2.46	2.824(6)	107	x, y, z
Intermolecular	O2A6-H8···O3A4	0.84	2.23	3.017(6)	156	1-x, y, 1-z
Intramolecular	O2A7-H10···O3A7	0.84	2.45	2.848(6)	110	x, y, z
Intermolecular	O2A7-H10···O3A3	0.84	2.35	3.185(6)	170	1-x, y, 1-z
Intermolecular	O2A7-H10···O2A4	0.84	2.56	2.883(6)	104	1-x, y, 1-z
O3-H···O2′ Hydrogen bonds						
Intramolecular	O3A1-H3A1···O2A2	0.84	1.93	2.764(7)	171	x, y, z
Intramolecular	O3A2-H2···O2A3	0.84	2.04	2.814(7)	154	x, y, z
Intramolecular	O3A3-H4···O2A4	0.84	2.03	2.853(6)	168	x, y, z
Intramolecular	O3A4-H12···O2A5	0.84	1.95	2.781(6)	168	x, y, z
Intramolecular	O3A5-H7···O2A6	0.84	1.99	2.787(6)	158	x, y, z
Intramolecular	O3A6-H9···O2A7	0.84	1.97	2.757(6)	157	x, y, z
Intramolecular	O3A7-H11···O2A1	0.84	1.95	2.781(6)	168	x, y, z
O6-H···O5 and O6-H···O6 Hydrogen bonds						
Intermolecular	O6A2-H6AF···O6A4	0.84	1.92	2.761(9)	174	1/2-x, 1/2+y, -z
Intramolecular	O6A5-H6A5···O5A5	0.84	2.55	2.885(9)	105	x, y, z
Intermolecular	O6A7-H6AZ···O6B3	0.84	2.25	3.03(3)	155	1-x, y, -z
C-H···O Hydrogen bonds						
Intermolecular	C2A4-H2A5···O15W	1.00	2.60	3.09(2)	110	x, y, z
Intermolecular	C6A5-H13···O6B6	0.99	2.55	3.38(1)	141	1-x, y, -z
Intermolecular	C2A6-H2A7···O3A2	1.00	2.39	3.299(7)	151	1/2+x, -1/2+y, z
Intramolecular	C6A7-H20···O5A1	0.99	2.59	3.38(1)	138	x, y, z

Hydrogen bonds that involve water molecules

Water-host and water-water hydrogen bonding was observed for both β-CD·BES and β-CD·PRO. The water-host interactions are summarized in Tables 5.1.9 and 5.1.10, the water molecules acting as either hydrogen bond acceptors or donors. For interactions between host O5 atoms and water oxygen atoms, relevant H-bonds were inferred from O···O distances.

Table 5.1.9: The parameters for the intermolecular interactions in β-CD·BES.

Hydrogen bond interaction	D-H (Å)	H···A (Å)	D···A (Å)	D-H···A (°)	Symmetry code
O6A2-H6AZ···O1W	0.84	1.92	2.725(8)	160	x, y, z
O3A2-H3A2···O14W	0.84	2.28	2.69(2)	111	1-x, y, 1-z
O2A3-H2A3···O4W	0.84	2.26	2.66(1)	110	x, y, z
O2A3-H2A3···O14W	0.84	2.25	2.86(2)	130	x, y, z
O2A4-H2A4···O6W	0.84	2.44	2.80(2)	106	-1+x, y, z
O6A4-H6AH···O5W	0.84	1.98	2.75(2)	152	x, y, z
O2A5-H2A5···O15W	0.84	1.73	2.54(2)	161	x, y, z
O2A5-H2A5···O10W	0.84	2.23	3.04(2)	164	x, y, z
O2A6-H2A6···O11W	0.84	1.97	2.78(2)	164	-1/2+x, -1/2+y, z
O6A6-H6AC···O7W	0.84	1.94	2.78(2)	171	x, y, z
O6A7-H6AG···O2W	0.84	1.92	2.73(2)	162	x, y, z
O5A4···O13W*	-	-	2.944(6)	-	x, y, z
O5A4···O13W*	-	-	2.944(6)	-	-x, y, -z
O5A4···O7W*	-	-	2.96(1)	-	1/2-x, 1/2+y, -z
O5A5···O3W*	-	-	2.955(6)	-	x, y, z
O5A5···O3W*	-	-	2.955(6)	-	-x, y, -z
O5A6···O7W*	-	-	3.03(1)	-	x, y, z

*The water oxygen atom is the hydrogen bond donor

Table 5.1.10: The parameters for the intermolecular interactions in β-CD·PRO.

Hydrogen bond interaction	D-H (Å)	H···A (Å)	D···A (Å)	D-H···A (°)	Symmetry code
O6A1-H6A1···O1W	0.84	1.89	2.704(7)	162	x, y, z
O2A2-H1···O4W	0.84	1.81	2.646(9)	176	x, y, z
O2A2-H1···O13W	0.84	2.07	2.87(2)	159	x, y, z
O6A3-H17···O6W	0.84	1.98	2.77(1)	155	x, y, z
O6A4-H6A4···O1W	0.84	1.93	2.765(6)	170	1/2-x, -1/2+y, -z
O2A4-H5···O11W	0.84	1.87	2.68(2)	162	x, y, z
O2A4-H5···O15W	0.84	1.80	2.61(2)	159	x, y, z
O6A5-H6A5···O5W	0.84	1.91	2.75(1)	174	x, y, z
O2A5-H6···O12W	0.84	1.99	2.81(2)	166	-1/2+x, -1/2+y, z
O6A6-H6AC···O3W	0.84	1.90	2.73(1)	169	x, y, z
O2A7-H10···O7W	0.84	2.38	2.76(1)	108	x, y, z
O5A3···O9W*	-	-	2.985(6)	-	-x, y, -z
O5A3···O5W*	-	-	2.933(11)	-	1/2-x, 1/2+y, -z
O5A4···O2W*	-	-	2.982(4)	-	x, y, z
O5A4···O2W*	-	-	2.982(4)	-	-x, y, -z

*The water oxygen atom is the hydrogen bond donor

Host molecular geometry

The conformations of the O4-heptagons of the host molecules of β-CD·BES and β-CD·PRO are defined by the geometrical parameters provided in Tables 5.1.11 and 5.1.12 with reference to Figures 5.1.22a and 5.1.22b. Detailed descriptions of the geometrical parameters were mentioned in Chapter 1 (section 1.2.9, pp. 13 – 15) and for convenience abbreviated descriptions are shown below in Table 5.1.11.

In a regular heptagon the angles are all equal, as are the lengths of the sides; however, since variations in the values of *l*, D and Φ occur in the O4-heptagon of CD molecules on complexation, it becomes distorted. The variation in the torsion angles (d) and the deviations (α) for both complexes under discussion are small, indicating that the extent of planarity of the O4-heptagon is relatively high. The ranges of the D_3 values are 2.783(8) – 2.865(7) Å for β-CD·BES and 2.757(6) – 2.853(6) Å for β-CD·PRO, which are typical for O···O distances in O-H···O hydrogen bonds. Furthermore, the ranges of the tilt angles are 4.1° – 13.1° for β-CD·BES and 4.7° – 12.5° for β-CD·PRO and thus evidently very similar. These ranges are smaller than that of uncomplexed hydrated β-CD, which has a tilt angle range of 4.5° – 27.0°.[42] Consequently, it is apparent that additional distortion occurred with host-guest complexation, owing to a mutual-induced fit taking place between the host and guest molecules during complexation.

5.1.11: The geometrical parameters of the host molecule in the complex β-CD·BES.

Residue	*l* (Å)	D (Å)	Φ (°)	d (°)	α[a] (Å)	D_3 (Å)	τ_2 (°)[b]
A1	5.165	4.286	125.3	2.9	0.065	2.794(7)	10.5
A2	4.893	4.489	131.9	-4.0	0.006	2.790(7)	4.1
A3	4.966	4.333	129.8	0.6	-0.079	2.783(8)	11.6
A4	5.211	4.311	124.4	2.1	0.045	2.809(7)	13.1
A5	5.003	4.439	129.8	-0.2	0.041	2.865(7)	7.7
A6	4.901	4.358	130.8	-2.6	-0.0461	2.808(7)	12.6
A7	5.078	4.355	127.9	1.4	-0.032	2.786(8)	11.9

[a] mean esd: 0.003 Å; [b] mean esd: 0.1°

Key to symbols
l: the distance between each O4 atom and the centroid of the O4-polygon;
D: the consecutive glycosidic O4···O4′ distances;
Φ: the O4···O4′···O4″ angle;
d: the O4···O4′···O4″···O4‴ torsion angle;
α, the deviation of each O4 atom from the mean O4-plane;
D_3: the O2···O3′ intra-ring distance;
τ_2: the tilt angle: the angle between the mean O4-plane and the plane containing O4, C4, C1 and O4′ of a given glucose ring.

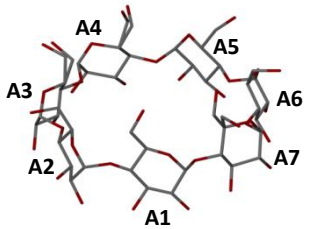


Figure 5.1.22a: The numbering scheme of the β-CD·BES glucose units.

Table 5.1.12: The geometrical parameters of the host molecule in the complex β-CD·PRO.

Residue	*l* (Å)	D (Å)	Φ (°)	d (°)	α[a] (Å)	D_3 (Å)	τ_2 (°)[b]
A1	4.989	4.450	130.1	-4.2	-0.005	2.781(6)	4.7
A2	4.994	4.350	129.1	1.8	-0.071	2.764(7)	9.8
A3	5.094	4.347	127.1	0.7	0.055	2.814(7)	12.5
A4	5.029	4.378	129.1	0.5	0.020	2.853(6)	7.7
A5	4.998	4.351	128.8	-3.0	-0.035	2.781(6)	10.4
A6	5.004	4.411	129.6	1.9	-0.028	2.787(6)	9.1
A7	5.116	4.285	126.2	2.3	0.064	2.757(6)	9.4

[a] mean esd: 0.003 Å; [b] mean esd: 0.1°

Key to symbols
l: the distance between each O4 atom and the centroid of the O4-polygon;
D: the consecutive glycosidic O4···O4′ distances;
Φ: the O4···O4′···O4″ angle;
d: the O4···O4′···O4″···O4‴ torsion angle;
α, the deviation of each O4 atom from the mean O4-plane;
D_3: the O2···O3′ intra-ring distance;
τ_2: the tilt angle: the angle between the mean O4-plane and the plane containing O4, C4, C1 and O4′ of a given glucose ring.

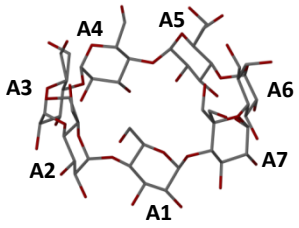


Figure 5.1.22b: The numbering scheme of the β-CD·PRO glucose units.

PXRD analysis

The PXRD patterns for β-CD·BES and β-CD·PRO produced *via* co-precipitation both display very good correspondence with their respective PXRD patterns calculated from their single-crystal X-ray structures (Figure 5.1.23). This proves that both models are reasonable representations of their respective bulk crystallized materials. Furthermore, the isostructurality between the two complexes is again evident and confirmed with their respective experimental and calculated PXRD patterns. Even though discrepancies do occur in the relative intensities of the corresponding peaks, these inconsistencies are a result of preferred orientation in the experimental samples, which is often unavoidable. The large difference between the temperature at which the experimental PXRD patterns were collected (21 °C) and the single-crystal X-ray analyses were recorded (-173 °C) also contributes to small peak angular shifts and minor peak intensity differences.

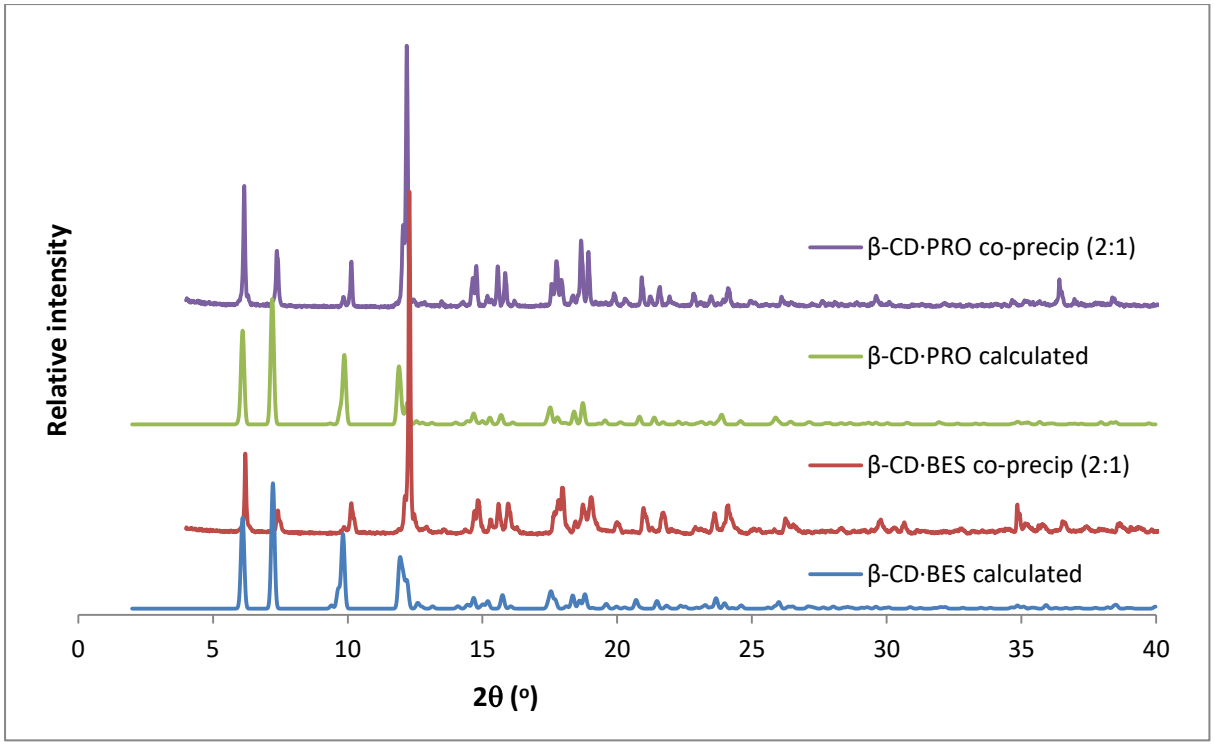


Figure 5.1.23: The calculated PXRD patterns of β-CD·BES and β-CD·PRO, as well as the PXRD patterns of β-CD·BES and β-CD·PRO prepared *via* co-precipitation. The results confirm that the structures share a high level of isostructurality.

5.2.2) The inclusion complexes γ-CD·BES and γ-CD·PRO

5.2.2.1) Method of preparation

The co-precipitation preparation for both γ-CD·BES and γ-CD·PRO utilized a large excess of γ-CD in order to obtain crystalline inclusion complexes with 1:1 and 3:2 stoichiometric ratios respectively. Approximately 100 mg (0.0771 mmol) of γ-CD was used for both systems, and the masses of the APIs were both 5 mg each (0.0184 mmol β-estradiol and 0.0159 mmol progesterone). The two weighed samples of γ-CD were dissolved in water in separate vials (3 cm^3 for the γ-CD·PRO system and 2.5 cm^3 for the γ-CD·BES system) and stirred vigorously at 70 ^oC. The APIs were added fairly slowly to their respective vials over a period of about 5 minutes. The times for full dissolution of the BES and PRO samples were 15 and 20 minutes respectively. This indicated that complexation had occurred. The solutions were left to stir for a further 3 hours and were subsequently filtered and prepared for slow cooling. Crystals appeared after 3 days and it is imperative to state that it was necessary to avoid complete evaporation of the mother liquors of these solutions in order to prevent the excess γ-CD subsequently precipitating.

5.2.2.2) Crystal morphologies of γ-CD·BES and γ-CD·PRO

The crystal morphologies of γ-CD·BES and γ-CD·PRO were similar in terms of their transparent tetragonal rods, as generally observed for γ-CD inclusion complexes (Figures 5.2.1 and 5.2.2). Even though the average crystal size of γ-CD·PRO was larger than that of γ-CD·BES, neither of the crystals selected diffracted well. Consequently, it was only possible to collect SCXRD data for γ-CD·PRO.

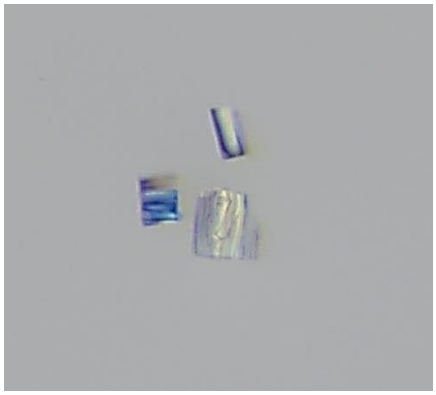


Figure 5.2.1: The crystal morphology of γ-CD·BES.

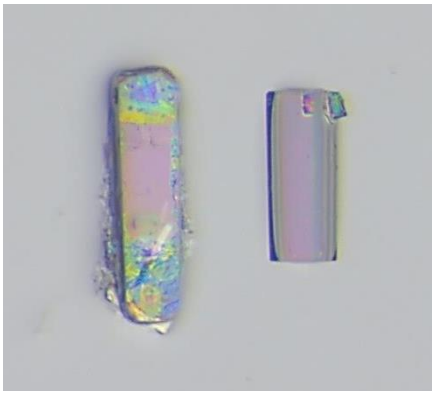


Figure 5.2.2: The crystal morphology of γ-CD·PRO.

5.2.2.3) ^{1}H NMR analysis of γ-CD·BES and γ-CD·PRO

The stoichiometric host-guest ratios were different for γ-CD·BES and γ-CD·PRO as the ^{1}H NMR analysis indicated 1:1 and 3:2 stoichiometric ratios respectively (Tables 5.2.1 and 5.2.2, and Figure 5.2.3). This suggests that although β-estradiol and progesterone have similar steroidal scaffolds, their small structural differences cause significant variations in terms of their host-guest interactions. The integrated ^{1}H NMR spectra of these inclusion complexes are provided in the Appendix under section 4.2.1, pp. 46 – 47.

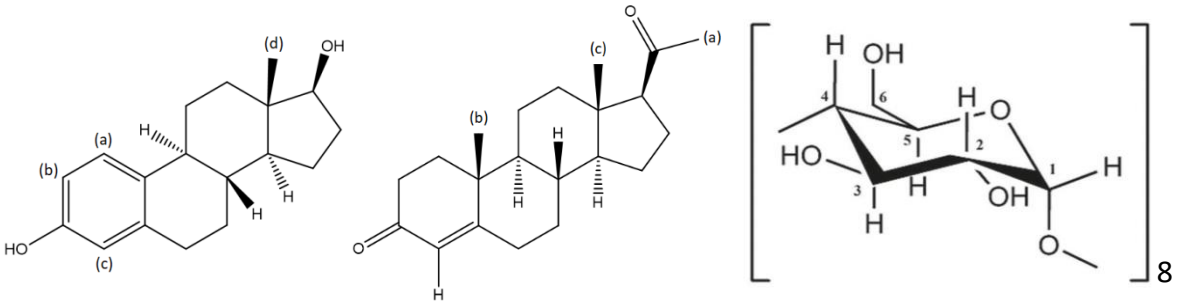


Figure 5.2.3: Molecular structures of β-estradiol (left), progesterone (centre) and γ-CD (right). Specific atoms have been labelled for the ^{1}H NMR analyses. Adapted from Guedes *et al.*[33]

Table 5.2.1: The ^{1}H NMR spectral analysis of γ-CD·BES.

Assignment	δ (ppm)	Integration	Multiplicity	Proton representation (per molecule)	Stoichiometric ratio	Stoichiometric ratio (integer)
CH (a) aromatic (BES)	7.033 – 7.054	0.1147	doublet	1H	0.92	1
CH (b) aromatic (BES)	6.494 – 6.522	0.1217	doublet of doublets	1H	0.97	1
CH (c) aromatic (BES)	6.432 – 6.439	0.1141	doublet	1H	0.91	1
OH-2 and OH-3 (γ-CD)	5.689 – 5.735	1.9683	Two separate doublets[a]	16H	0.98	1
CH-1 (γ-CD)	4.893 – 4.902	1.0000*	doublet	8H	1.00	1
CH_3 (d) methyl (BES)	0.672	0.3522	singlet	3H	0.94	1

*reference integral

Table 5.2.2: The ^{1}H NMR spectral analysis of γ-CD·PRO.

Assignment	δ (ppm)	Integration	Multiplicity	Proton representation (per molecule)	Stoichiometric ratio	Stoichiometric ratio (integer)
CH-1 (γ-CD)	4.889 – 4.899	0.9964	doublet	8H	1.00	3
OH-6 (γ-CD)	4.469 -4.497	1.0000*	triplet	8H	1.00	3
CH_3 (a) methyl (PRO)	2.072	0.2444	singlet	3H	0.65	2
CH_3 (b) methyl (PRO)	1.150	0.2583	singlet	3H	0.69	2
CH_3 (c) methyl (PRO)	0.579	0.2408	singlet	3H	0.64	2

*reference integral

5.2.2.4) PXRD analyses for γ-CD·BES and γ-CD·PRO

The PXRD patterns of γ-CD·BES and γ-CD·PRO were in good correlation. This close resemblance was evident regardless of whether they were prepared *via* co-precipitation or kneading, and regardless of the guest compound (Figures 5.2.4 and 5.2.5). The PXRD patterns of these complexes correlated well with the PXRD pattern of an isostructural γ-CD

[a] The ^{1}H NMR spectrum displays one doublet and a singlet with a shoulder. This shoulder would resolve into the second peak to become the other doublet at a higher resolution, or if more mass was available at the time of the experiment (which was the case with β-CD·BES).

inclusion complex (refcode DOCYID, containing the guest compound 12-crown-4), that crystallizes in the tetragonal space group $P42_12$ (Figures 5.2.4 and 5.2.5).

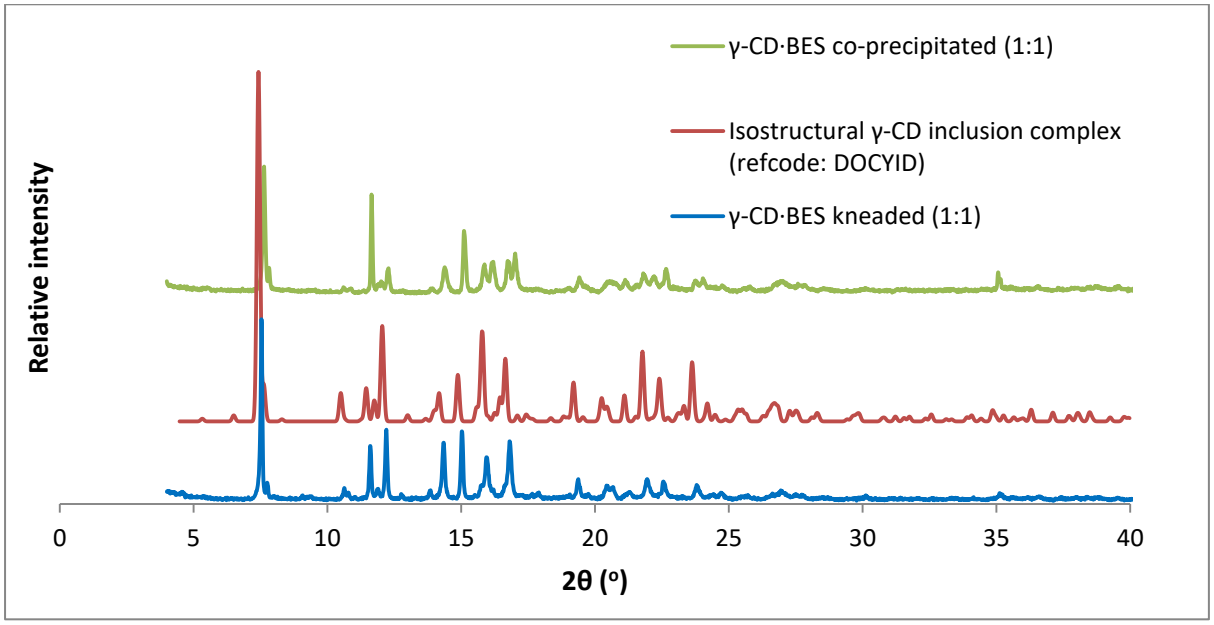


Figure 5.2.4: The PXRD patterns of the γ-CD·BES complex produced *via* kneading (1:1), an isostructural γ-CD complex crystallizing in the space group $P42_12$ (refcode: DOCYID), and the γ-CD·BES complex produced *via* co-precipitation (1:1).

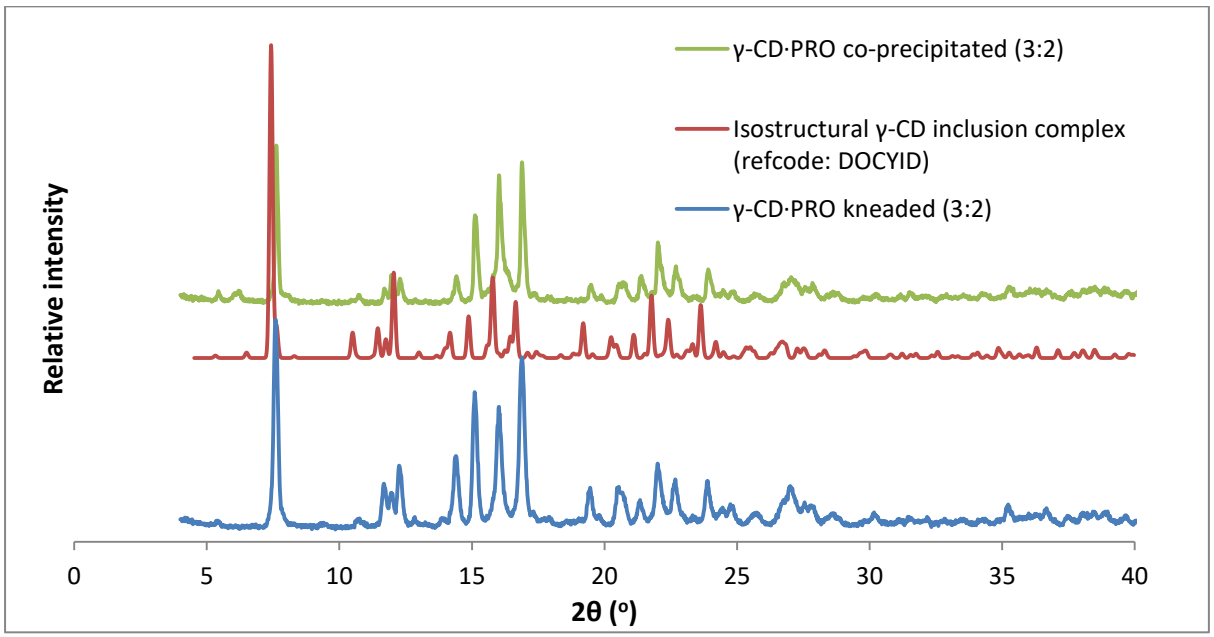


Figure 5.2.5: The PXRD patterns of the γ-CD·PRO complex produced *via* kneading (3:2), an isostructural γ-CD complex crystallizing in the space group $P42_12$ (refcode: DOCYID), and the γ-CD·PRO complex produced *via* co-precipitation (3:2).

5.2.2.5) Hot stage microscopy (HSM) analysis of γ-CD·BES and γ-CD·PRO

Comparative overview

The HSM analyses for the two inclusion complexes were similar overall in that they displayed dehydration and the expected subsequent decomposition. The dehydration for γ-CD·BES was represented by an onset of opacity (without the presence of bubbling), while for γ-CD·PRO, the dehydration was indicated by the onset of opacity and bubbling. The experimental details for each complex are provided below.

γ-CD·BES:

The HSM analysis indicated the dehydration and decomposition of the crystals over the temperature range 22.4 – 281.9 ^{o}C (Figure 5.2.6). Image A indicated the initial appearance of the complex prior to heating at a rate of 10 K.min^{-1}. The onset of dehydration occurred almost immediately after the heating commenced, as this is evident by the hardly discernible onset of opacity at 29.4 ^{o}C (image B), which indicated a loss of crystallinity due to water loss. The dehydration of the complex continued (image C at 50.4 ^{o}C) until an initial level of opacity was achieved, as displayed in image D at 88.2 ^{o}C. Thereafter, the extent of the opacity gradually increased (as the crystals continued to lose their crystallinity) until 257.7 ^{o}C (image E) where the maximum level of opacity was achieved. This could be attributed to residual amounts of water loss (at lower temperatures) and subsequent further loss of crystallinity from heating. This interpretation emulated the stepwise dehydration trend in the TGA experiment (which is discussed later in this section), where water molecules are initially lost more rapidly and thereafter the dehydration rate decreases significantly.[b] Lastly, the onset of decomposition occurred at 262.5 ^{o}C (image F) and continued with noticeable discolouring of the crystals, as represented in image G at 281.9 ^{o}C.

[b] The dehydration of the crystals is usually accompanied with the formation of bubbles in the silicone oil medium; however, these were not present during this experiment, the reason being the small crystal size and small number of crystals present. In a previous experiment, the formation of bubbles was observed where a significantly larger sample of crystals was present. However, other finer details, such as the onsets and different levels of opacity, were not observed in that experiment.

Figure 5.2.6: The series of HSM micrographs for γ-CD·BES



A: Initial appearance of γ-CD·BES (22.4 °C).



B: Hardly discernible onset of opacity (29.4 °C).



C: Continuation of opacity (50.4 °C).



D: Initial level of opacity achieved (88.2 °C).



E: Maximum opacity achieved (257.7 °C).



F: Onset of decomposition (262.5 °C).



G: Continuation of decomposition (281.9 °C).

γ-CD·PRO:

The HSM analysis indicated two events, which included the dehydration and decomposition of the complex (Figure 5.2.7). The initial appearance of γ-CD·PRO is displayed in image A at 23.1 °C. The subsequent five images (B – F) represent the dehydration of the crystal. The start of dehydration is represented in image B at 70.1 °C by an onset of opacity at the bottom left area of the crystal. The onset of opacity is associated with the loss of water molecules (which caused the degradation of the crystallinity in the individual crystal). The dehydration was then further characterised by bubbling (accompanied by an increase in opacity), where the onset of bubbling occurred at 88.4 °C (image C). The rate of the formation of bubbles was constant throughout the dehydration; however, additional dehydration sites began to feature (as represented in image D at 103.6 °C), thus indicating a faster rate of dehydration. The bubbling from these additional sites lessened (image E) and eventually ceased at 193.4 °C (image F). Thereafter, the onset of decomposition occurred at 263.4 °C (image G), and image H (at 286.6 °C) displays the continuation of this event with further discolouration.

Figure 5.2.7: The series of HSM micrographs for γ-CD·PRO



A: Initial appearance of γ-CD·PRO (23.7 °C).



B: The onset of opacity (70.1 °C).



C: The onset of bubbling (88.4 °C).



D: The maximum bubbling occurred (103.6 °C).



E: The bubbling lessened (145.5 °C).



F: The bubbling terminated (193.4 °C).



G: The onset of decomposition (263.4 °C).



H: The continuation of decomposition (286.6 °C).

5.2.2.6) Thermal gravimetric analysis (TGA)

The TGA curves of γ-CD·BES and γ-CD·PRO are very similar (even more so than the TGA curves of β-CD·BES and β-CD·PRO), and the temperatures of the dehydration events for both samples are in close agreement. The only significant difference between the two curves is that the onset of decomposition for γ-CD·PRO occurred at a temperature 27.3 °C higher than that for γ-CD·BES, indicating slightly more thermal stability. The two

experiments were performed under the same conditions and are described separately in detail below.

γ-CD·BES

The TGA curve of γ-CD·BES (n=2) displayed two events (namely the dehydration and onset of decomposition of the anhydrous complex) over the heating range 18 – 300 °C (Figure 5.2.8). With regard to the dehydration, it was accompanied by a mass loss of 12.7 ± 0.4% (corresponding to 12.7 ± 0.4 water molecules per complex unit) over the temperature range 17.8 ± 0.3 to 144.9 ± 0.1 °C. The dehydration took place in a single-step, as confirmed by the single peak in the dTGA curve over this temperature range (Figure 5.2.8). However, there was a significant decrease in the rate of mass loss for the remaining water molecules, which continued over a significantly long temperature interval from 64.5 ± 0.6 °C to 144.9 ± 0.1 °C. This was verified by the shallow shoulder that occurred in the dTGA curve within this temperature range. Consequently, this could signify different binding strengths of the water molecules in the complex. The calculation of the number of water molecules can be viewed in the Appendix under section 4.2.2, p. 47. The second event in the TGA is the onset of decomposition of the anhydrous complex, which occurred at 219.5 ± 2.4 °C.

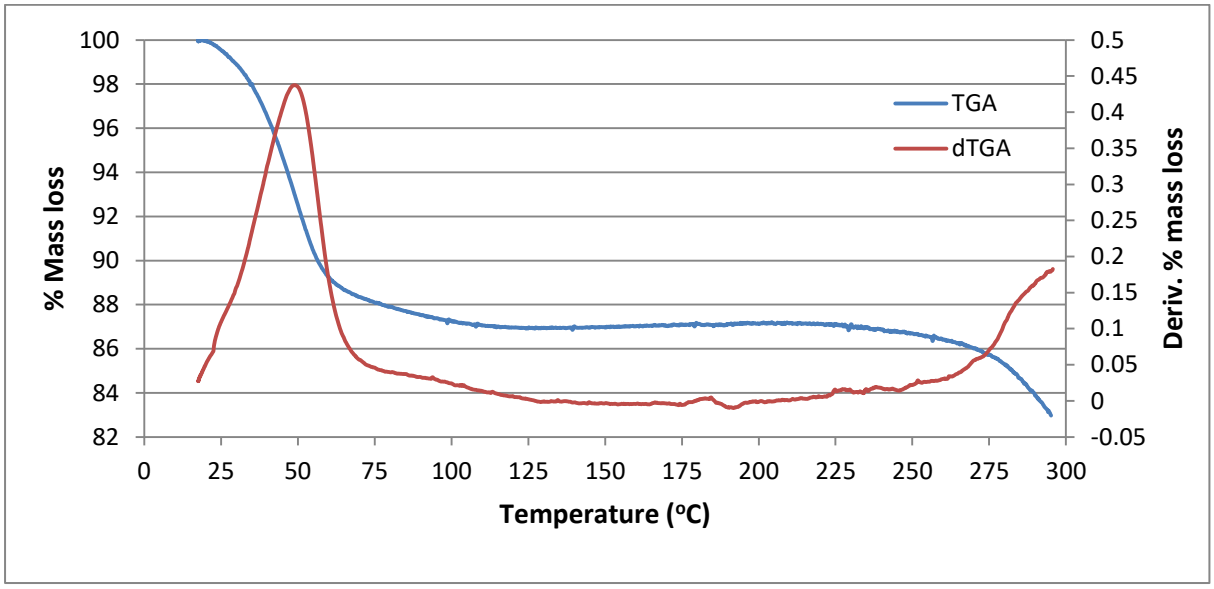


Figure 5.2.8: Representative TGA and dTGA curves of γ-CD·BES.

γ-CD·PRO

The TGA curve of γ-CD·PRO (n=3) also displayed two events over the heating range, which included the dehydration and onset of decomposition of the anhydrous complex (Figure 5.2.9). The first event (which occurred between 20.6 ± 1.8 °C and 119.6 ± 5.0 °C), is a pseudo single-step process, as the dTGA curve displayed one major peak with a subsequent shoulder. The mass loss of the dehydration amounted to 14.7 ± 0.3% (14.4 ± 0.3 water molecules per γ-CD molecule) between 20.6 ± 1.8 °C and 119.6 ± 5.0 °C. The onset of the shoulder occurred at 77.5 ± 4.5 °C (with reference to the dTGA curve) and signified that there was a significant change in the initial rate of water loss. However, this was not enough to be a distinctive two-step process but enough to indicate that some of the water molecules do engage in somewhat stronger hydrogen bonding interactions and they are thus removed more slowly and at higher temperatures. The calculation of the number of water molecules can be viewed in the Appendix under section 4.2.3, p. 48. The second event denotes the onset of decomposition of the anhydrous complex at 246.8 ± 2.5 °C.

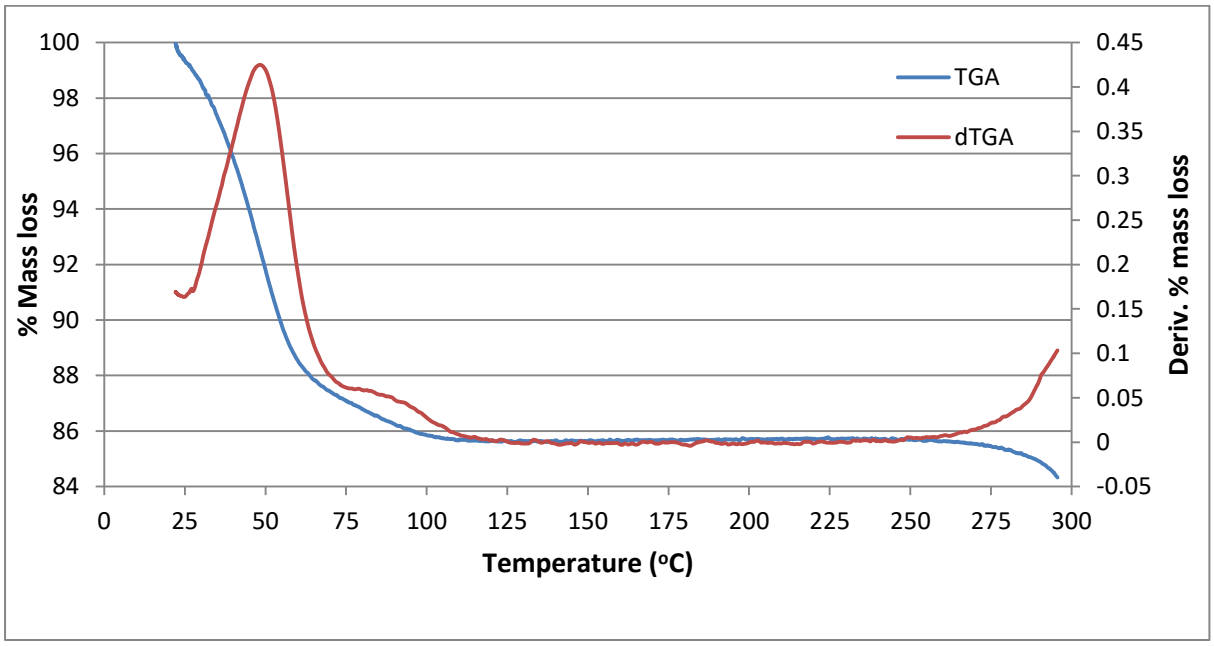


Figure 5.2.9: Representative TGA and dTGA curves of γ-CD·PRO.

5.2.2.7) Differential scanning calorimetry (DSC)

The DSC curves of γ-CD·BES and γ-CD·PRO were also very similar with a hardly discernible difference occurring during the pseudo second step of the dehydration of γ-CD·PRO. This pseudo second step in γ-CD·PRO was minimally more pronounced than in the DSC curve of γ-CD·BES and these details are described below.

γ-CD·BES

The DSC curve of γ-CD·BES (n=2) displayed a large endothermic event (onset = 46.7 ± 2.5 °C, peak = 83.5 ± 2.9 °C) representing the major part of the dehydration, with a change in the gradient of the heat flow as the temperature increased after 105 °C (Figure 5.2.10). This change in gradient represented a slower rate of water loss, which could result from a few water molecules being more tightly bound in the crystal structure. This was well reiterated by the trends in the overlaid TGA curve, where (as was described previously), there was a predominant 'single-step' mass loss which was accompanied thereafter by a hardly discernible mass loss up until 144.9 ± 0.1 °C.

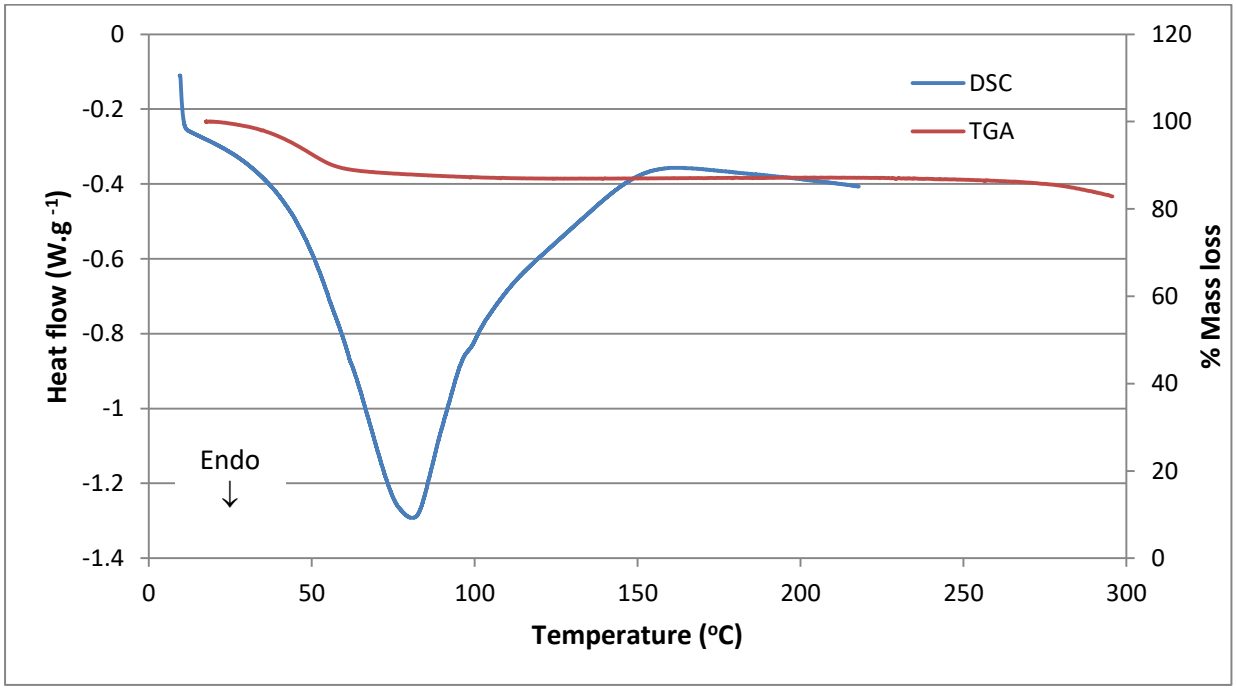


Figure 5.2.10: A representative DSC curve of γ-CD·BES, with the respective TGA curve as a reference.

γ-CD·PRO

The DSC curve of γ-CD·PRO (n=3) followed very similar behaviour to that of γ-CD·BES. The main difference was the more pronounced formation of a shoulder towards the end of the broad endothermic peak, rather than just a change in the gradient of the heat flow (Figure 5.2.11). This indicated that more water molecules were still bound in the crystal structure at higher temperatures in comparison to γ-CD·BES. The broad endothermic peak (onset = 49.3 ± 0.5 °C, peak = 87.9 ± 0.1 °C) signified the majority of the dehydration, while the shoulder (peak temperature of 131.1 ± 0.6 °C) represented the loss of the remaining water molecules. Similarly, even though the temperatures of the events did not match, the overall trend of the DSC results correlated with the overlaid TGA curve. This trend also reflected the increased water loss at higher temperatures causing the shoulder to be more pronounced in comparison to that of γ-CD·BES.

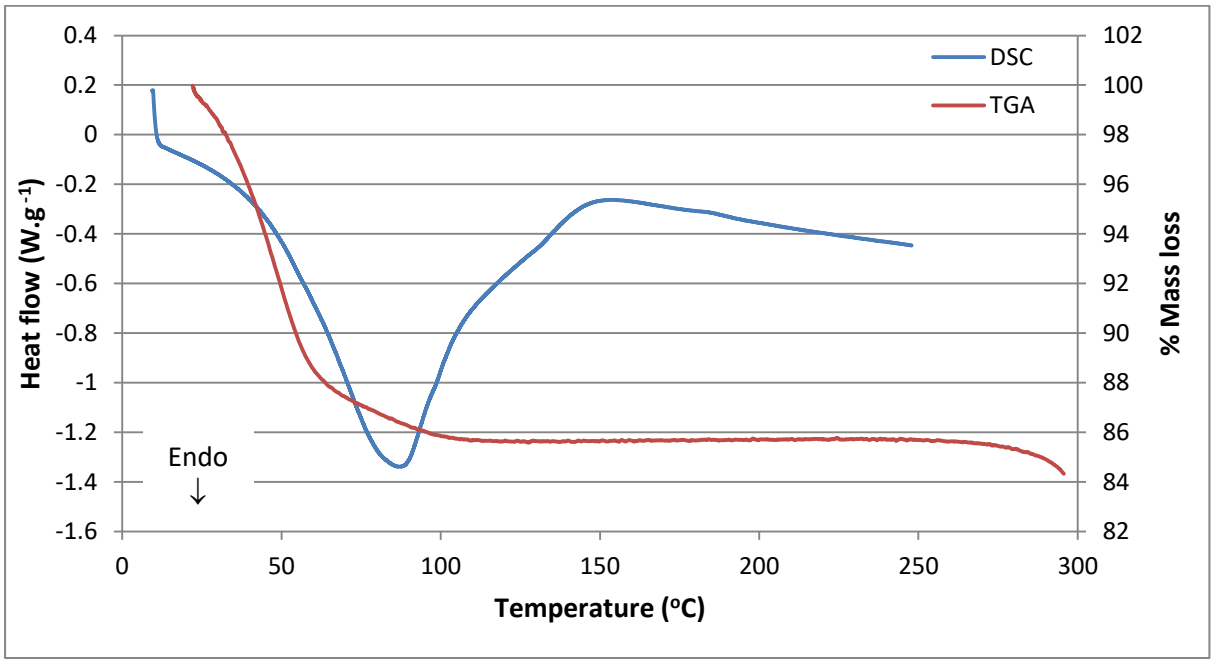


Figure 5.2.11: A representative DSC curve of γ-CD·PRO, with the respective TGA curve as a reference.

5.2.2.8) Single-crystal X-ray diffraction (SCXRD) analysis of γ-CD·PRO

Data-collection and space group determination

The intensity data for γ-CD·PRO were determined from a very small, transparent crystal at 100(2) K, which diffracted rather weakly. γ-CD inclusion complexes generally crystallize in the tetragonal space group $P42_12$, and this was confirmed for γ-CD·PRO by the PXRD analysis described earlier, which indicated a high level of isostructurality with a known complex crystal belonging to this tetragonal space group. The program XPREP[35] failed to determine this space group and instead suggested *P*4, which was incorrect. The reason the program failed to identify the correct space group was that the intensities of several reflections violating the systematic absences (h00, l = 2n + 1) for $P42_12$ were marginally greater than the 3σ(I) threshold. Consequently, the space group was confirmed manually by analysing the intensity weighted reciprocal lattice, which displayed 4/*mmm* as the Laue group, indicating the tetragonal crystal system. Similarly, the space group $P42_12$, was also confirmed from the conditions limiting possible reflections as listed in Table 5.2.3. The numbering scheme for the γ-CD molecule is displayed in Figure 5.2.12 below.

Table 5.2.3: The conditions limiting possible reflections for the crystal of γ-CD·PRO.

Number	Conditions limiting possible reflections	Deduction
1	hkl: none	Primitive lattice
2	h00: h = 2n, (0k0: k = 2n)	Two-fold screw axis parallel to the a-axis (and to the b-axis, which is identical to the a-axis by symmetry)
3	00l: none	-

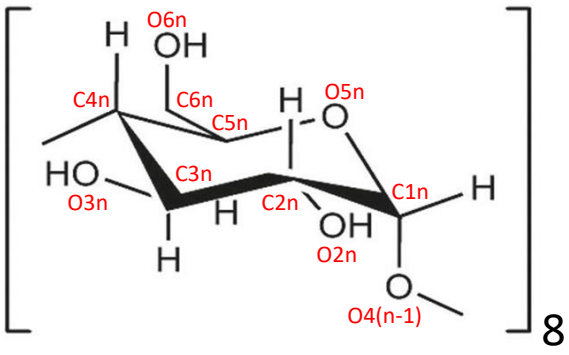


Figure 5.2.12: The numbering scheme for the γ-CD molecule, with n representing the nth glucose residue in the molecule.

Structure solution and refinement

The crystal structure of γ-CD·PRO was solved by isomorphous replacement (using the rigid host atoms of the complex with CSD refcode MUXBIT, containing trans-resveratrol as guest, as the trial structure), as SHELXS-97, SHELXD-97 and SHELXT-97 all failed to provide a sensible solution.[37] Once all the non-hydrogen host atoms were placed and refined isotropically, all the ordered host atoms and ordered water oxygen atoms were refined anisotropically.

Two of the hydroxyl oxygen atoms, namely O6C2 and O6A1 displayed evidence of disorder in the difference Fourier map, and thus the disorder was treated as previously described for β-CD·BES and β-CD·PRO. This entailed assigning free variable values of *x* and 1-*x*, as well as PART numbers to the major and minor components of each of the disordered hydroxyl groups in question. In addition, the C6 atom was split in order to allow the methylene hydrogen atoms to be added with the correct electron density assignment. Similarly, DFIX restraints were used to maintain reasonable bond lengths and the geometry of the disordered fragments. This included restraining the C5-C6 bond lengths (to 1.51 Å, σ = 0.005 Å), C6-O6 bond lengths (to 1.43 Å, σ = 0.01 Å / 0.005 Å) and the C5-O6 distances (to 2.45 Å, σ = 0.005 Å) in order to maintain the C5-C6-O6 angular geometry. The site-occupancy factors (s.o.f.s) of the major components of the disordered host atoms were 0.69(2) for C6C2 and O6C2, and 0.81(2) for C6A1 and O6A1 after their isotropic refinement.

The hydrogen atoms were placed in idealised positions using a 'maximum electron density' model, each hydrogen atom being assigned an isotropic temperature factor of 1.2 times the value of the U_{iso} parameter of its parent atom. As often expected for tetragonal γ-CD host-guest complexes, the guest molecule was completely disordered, as was evident from the $\Delta\rho$ map, in which the highest peak density in the cavity was only 1.24 e.Å^{-3}. This resulted in the guest molecule being unlocatable and hence not modelled. This shortcoming for structural analysis of γ-CD inclusion complexes is due to the four-fold rotation axis of the γ-CD molecules, a symmetry element which most guest molecules do not possess. The SQUEEZE procedure[38] in the program PLATON[39] was performed and the residual electron count was calculated to be 966 electrons per unit cell, which did not convincingly indicate

that the complex host-guest stoichiometry was 3:2,[c] the ratio determined accurately by ^{1}H NMR spectroscopy. The SQUEEZE procedure was also used to optimise the R_1 and wR_2 parameters by eliminating the residual electron density.

In addition, 20 sites for water molecules were observed in the ASU, three of which were fully occupied with water oxygen atoms, and the remaining 17 sites were only partially occupied. This amounted to 10.6 water molecules in the ASU, which equated to 14.1 water molecules per γ-CD molecule. This value also correlated with the results presented in the TGA analysis above, which indicated 14.4 ± 0.3 water molecules per CD molecule. The crystallographic data and details for the post-SQUEEZE refinement of this structure are summarised in Table 5.2.4.

[c] The 966 electrons account for the guest molecules as well as the water hydrogen atoms that were not modelled in γ-CD·PRO. The theoretical electron count for the guest (progesterone) molecules and water hydrogen atom contributions per unit cell in a 3:2 host-guest complex are 688 and 172.8 electrons respectively. Therefore, in order to obtain the guest electron density contribution from the SQUEEZE procedure, the water hydrogen atom count must be subtracted from the calculated total of 966 electrons per unit cell. This yields 793.2 electrons (equivalent to ~4.6 molecules of PRO per unit cell) as opposed to a theoretical value of 688 electrons (corresponding to 4.0 molecules of PRO per unit cell). Thus, the level of agreement is not reliable. However, since the stoichiometry of the complex had been determined accurately as 3:2 by ^{1}H NMR spectroscopy, reliance on the SQUEEZE estimate was not a requirement.

Table 5.2.4: The crystal data and refinement parameters for the γ-CD·PRO inclusion complex.

Parameter	Value
Complex formula	$C_{48}H_{80}O_{40}\cdot(C_{21}H_{30}O_2)_{0.67}\cdot 14.4(H_2O)$
Formula weight ($g.mol^{-1}$)	1765.64
Temperature (K)	100(2)
Wavelength (Å)	0.71073
Crystal system	Tetragonal
Space group	$P42_12$
a (Å)	23.6991(9)
c (Å)	22.896(1)
Volume ($Å^3$)	12860(1)
Z	6
Calculated density ($g.cm^{-3}$)	1.368
μ (mm^{-1})	0.121
F (000)	5678
Crystal size (mm)	0.20 x 0.21 x 0.36
θ-Range scanned (^{o})	1.24 – 26.41
Index range	h: -29, 29; k: -29, 29; l: -27, 28
No. of reflections collected	118399
No. of unique reflections	13196
Data completeness (%)	99.7
Data/restraints/parameters	13196/12/365
S (Goodness-of-fit on F^2)	1.099
Final R indices R_1, wR_2, [I > 2σ(I)]	0.0969, 0.2319
R Indices, all data (R_1, wR_2)	0.0996, 0.2337
Largest diff. peak and hole ($e.Å^{-3}$)	0.85, -0.46

Molecular structure

The asymmetric unit (ASU) as displayed in Figure 5.2.13, consists of three pairs of glucose rings that generate three complete γ-CD molecules when the four-fold rotational axis parallel to the c-axis is applied. The host molecules display relatively minor disorder, as only two of the hydroxymethyl groups were disordered over two positions. This is in contrast to the guest molecules which are severely disordered and consequently not observed. Lastly, water oxygen atoms were identified over 20 sites (as previously mentioned) and it is evident that these sites are all external to the γ-CD molecule (Figure 5.2.14). Hydrogen atoms were not placed on the water oxygen atoms, as there was no evidence for them in the difference Fourier map.

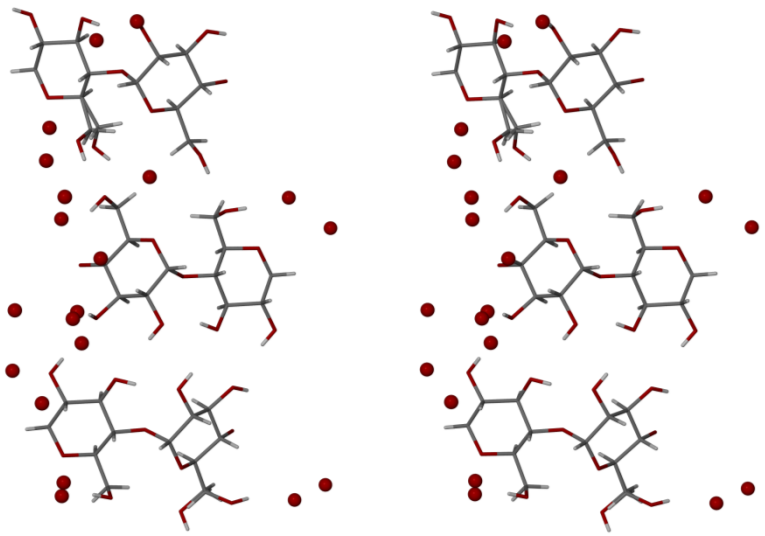


Figure 5.2.13: A stereoscopic view of the host atoms and water oxygen atoms in the ASU of γ-CD·PRO.

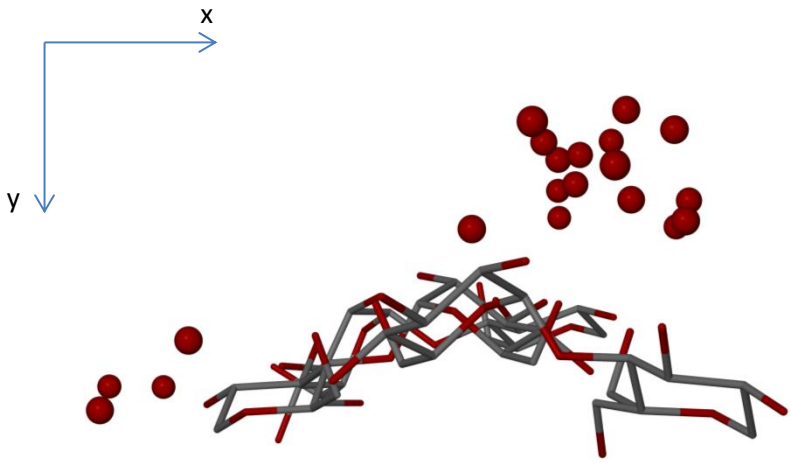


Figure 5.2.14: The host atoms and water oxygen atoms of the ASU viewed down the c-axis, showing that the water molecule sites are all external to the cavity of the γ-CD molecule.

Crystal Packing

The major structural motif in the γ-CD·PRO crystal thus consists of three independent γ-CD molecules (Figure 5.2.15), referred to as A, B, C, which stack in infinite columns and arrange themselves in a head-to-tail motif between molecules C and A, a tail-to-tail motif between molecules B and C, and lastly, a head-to-head motif between molecules A and B.[43] Extensive O-H···O hydrogen bonding occurs at each of the C-A, B-C and A-B interfaces. This is a

characteristic structural arrangement that has been observed in all γ-CD inclusion complexes crystallizing in the space group $P42_12$.[44]

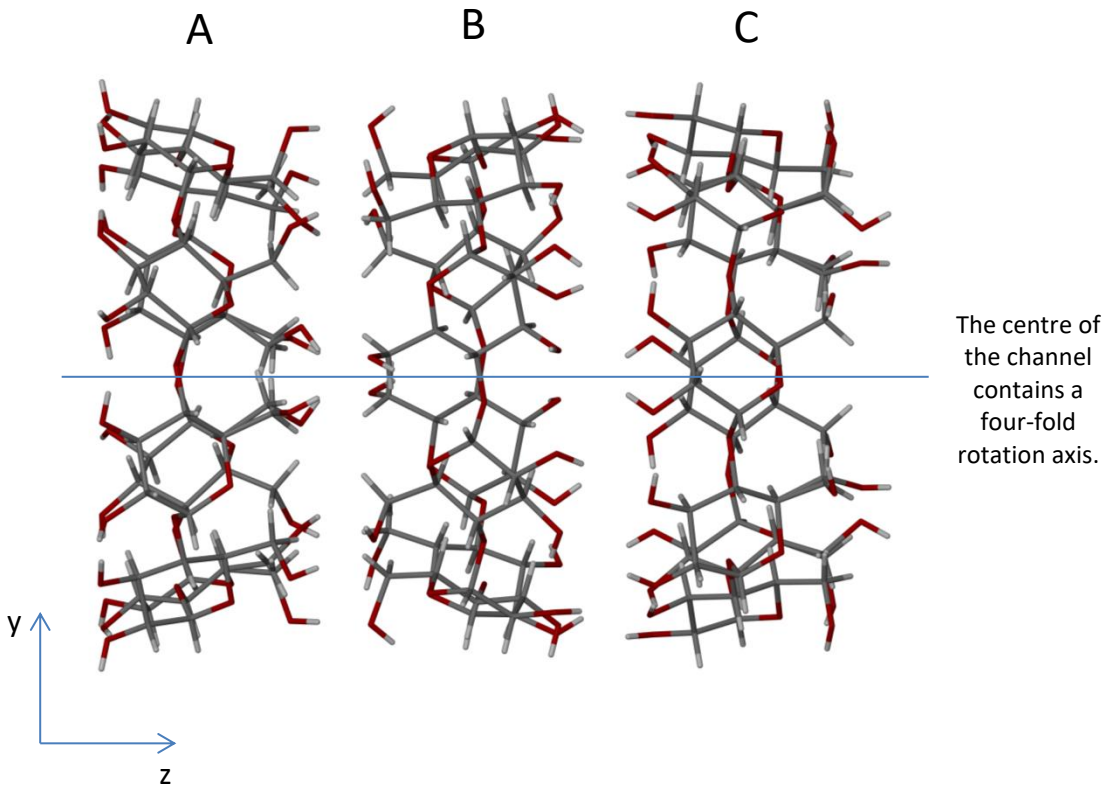


Figure 5.2.15: The distinct packing arrangement of the repeat unit of the host molecules in γ-CD·PRO. The four-fold axis runs through the centre of the channel, parallel to the c-axis. The water molecules are omitted for clarity.

The γ-CD columns are held together by the water molecules that form water-water and water-host hydrogen bonds. These water molecules occupy the interstitial spaces between the columns, as displayed in Figure 5.2.16 viewed down the c-axis.

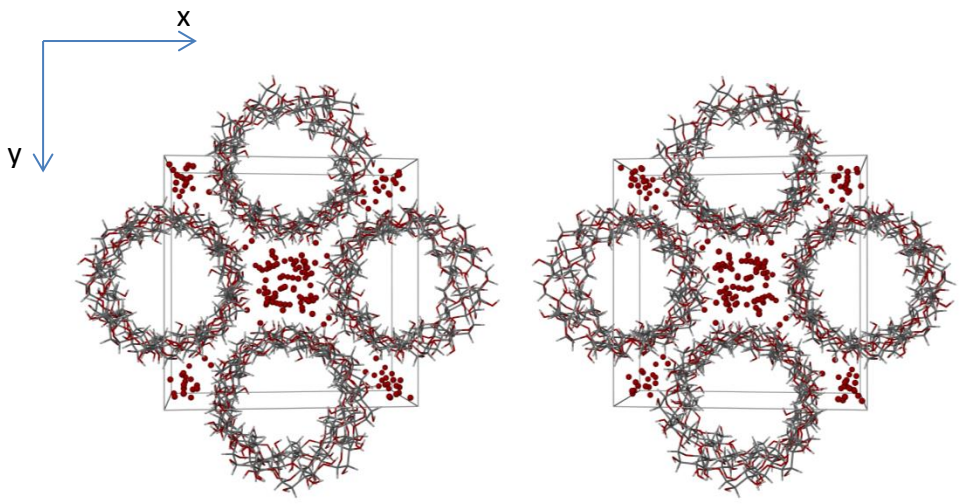


Figure 5.2.16: A stereoscopic view of γ-CD·PRO viewed down the c-axis, which displays the infinite channel packing arrangement. The water molecules (red spheres) occupy the interstitial spaces between the columns of stacked complex units.

PXRD analysis

The PXRD pattern of the co-precipitated complex and that based on the refined crystal structure (Figure 5.2.17) are in good agreement with respect to the peak angular values (disregarding small temperature-induced shifts). However, corresponding peak intensities are different, which is an effect caused by preferred orientation of crystallites comprising the sample. This phenomenon is further enhanced by the columnar morphology of the tetragonal complex crystals, which would result in the finely ground sample containing some proportion of crystallites with such morphology. Nonetheless, it is still evident that the single crystal selected for the analysis was representative of the bulk material.

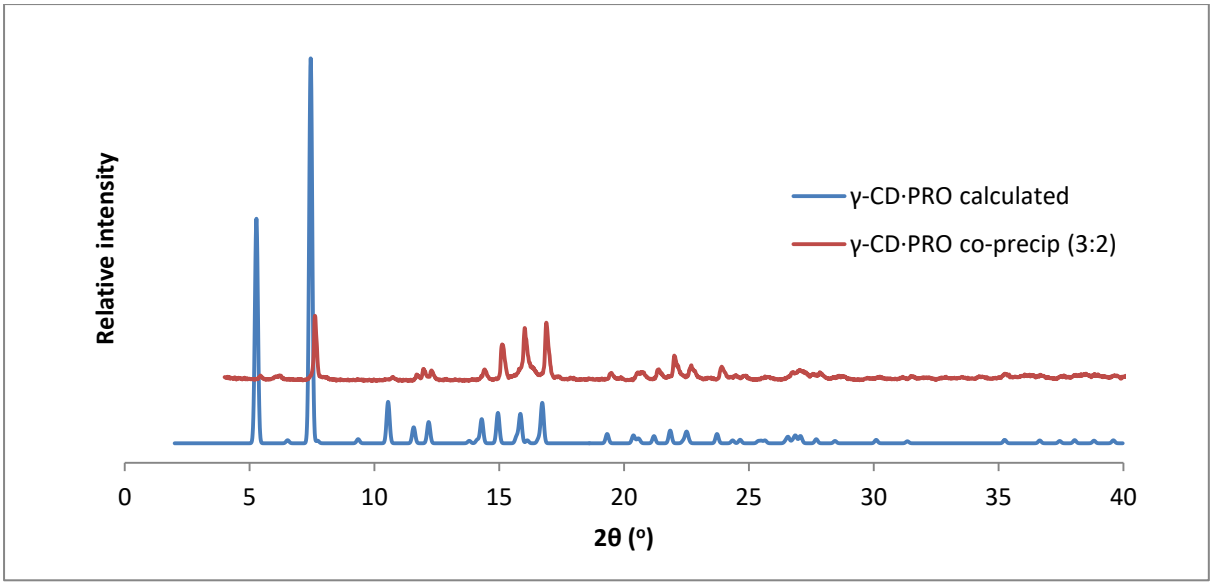


Figure 5.2.17: The calculated PXRD pattern of γ-CD·PRO and the PXRD pattern of γ-CD·PRO prepared *via* co-precipitation. The small shift in the angular peak positions is due to the custom-made sample holder used for the experimental PXRD pattern, as explained in the Experimental methods under section 2.4, p. 43.

In summary, the four native CD inclusion complexes (β-CD·BES, β-CD·PRO, γ-CD·BES and γ-CD·PRO) were successfully characterised and the analytical data verified that genuine inclusion complexes had formed. Despite the fact that the guest molecules were not observed in the three crystal structures presented above, they nevertheless provided valuable information regarding their respective crystal packing arrangements and both intramolecular and intermolecular hydrogen bonding between the host molecules. ^{1}H NMR spectroscopy of solutions of these crystalline complexes was essential for establishing their host-guest stoichiometries and thermal gravimetric analysis provided accurate values of their water contents. The complete molecular formulae of these hydrated complexes are as follows: 2(β-CD)·BES·17.7(H_2O), 2(β-CD)·PRO·20(H_2O), γ-CD·BES·12.7(H_2O) and 3(γ-CD)·2(PRO)·43.2(H_2O). The following section describes the measurement of the aqueous solubility enhancement of the APIs contained in these four native CD inclusion complexes and assesses the potential of the complexes for pharmaceutical application.

5.2.3) Solubility analysis *via* gravimetric mass increments

Duplicate solubility experiments *via* gravimetric mass increments were conducted simultaneously for the native CD inclusion complexes, which included β-CD·BES, β-CD·PRO, γ-CD·BES and γ-CD·PRO. The procedure used for these experiments is described in the Experimental methods (Chapter 2, section 2.10.3, p. 49), and the calculations can be viewed in the Appendix under section 4.3, pp. 49 – 52. The aqueous solubilities of β-estradiol and progesterone are 3.6 x 10^{-3} mg.cm^{-3} (at 27 ^{o}C) and 8.81 x 10^{-3} mg.cm^{-3} (at 25 ^{o}C) respectively,[45,46] and the results obtained indicated that the CD inclusion of β-estradiol and progesterone enhanced the aqueous solubility of both APIs (Table 5.3.1). With regard to β-estradiol, the β-CD and γ-CD complexation resulted in approximate solubility enhancement ratios ($S_{API(CD)}/S_{API}$) of 21.3 ± 0.1 and 6.1 ± 0.3 respectively (at 27 ^{o}C), where $S_{API(CD)}$ is the aqueous solubility of the API in the form of a CD inclusion complex, and S_{API} is the aqueous solubility of the API. For progesterone, the β-CD and γ-CD complexation resulted in $S_{API(CD)}/S_{API}$ ratios of 5.5 ± 0.1 and 19.9 ± 0.1 respectively (at 27 ^{o}C).

Table 5.3.1: Aqueous solubility data for the β-CD·BES, β-CD·PRO, γ-CD·BES, γ-CD·PRO inclusion complexes at 27 ^{o}C.

Number	CD complex	Solubility range of API (mg.cm^{-3})	Approximate solubility enhancement ratio ($S_{API(CD}/S_{API}$)	Average $S_{API(CD}/S_{API}$ ratio
1	β-CD·BES produced *via* kneading (experiment 1)	0.0710 – 0.0768	21.3	21.3 ± 0.1
2	β-CD·BES produced *via* kneading (experiment 2)	0.0694 – 0.0762	21.2	
3	β-CD·PRO produced *via* kneading (experiment 1)	0.0363 – 0.0488	5.5	5.5 ± 0.1
4	β-CD·PRO produced *via* kneading (experiment 2)	0.0370 – 0.0481	5.5	
5	γ-CD·BES produced *via* kneading (experiment 1)	0.0147 - 0.0232	6.4	6.1 ± 0.3
6	γ-CD·BES produced *via* kneading (experiment 2)	0.0139 - 0.0210	5.8	
7	γ-CD·PRO produced *via* kneading (experiment 1)	0.158 - 0.174	19.9	19.9 ± 0.1
8	γ-CD·PRO produced *via* kneading (experiment 2)	0.158 - 0.175	19.9	

The aqueous solubility enhancement factors for the APIs derived from these inclusion complexes indicated their potential to be utilised by the pharmaceutical industry. This is with particular reference to β-CD·BES and γ-CD·PRO, which displayed the largest solubility increases, and to γ-CD·BES, since γ-CD has a very favourable toxicological profile and is preferred for parenteral administration.[47,48] Since these steroids are commercially available, an enhanced solubility has the potential to improve the efficacy of the therapeutic treatment, and it may also potentially lower the cost of the medication, since a lesser quantity of the API may be sufficient in each dosage.

5.2.4) The inclusion complexes DMB·BES and DMB·PRO

5.2.4.1) Method of preparation

The formation of the two methylated CD inclusion complexes, DMB·BES and DMB·PRO, required slightly different co-precipitation preparative methods. With regard to DMB·BES, the preparation for a crystalline phase involved successfully dissolving DMB (48.88 mg, 0.0368 mmol)[a] in 2 cm^3 of water at 23 ^oC. Thereafter, β-estradiol (5 mg, 0.0184 mmol) was added in small increments very slowly while the solution was stirred over a period of 2 hours. Temperature cycling was used in order to promote solution complexation between each successive addition of β-estradiol. The solution was then left to stir for one day in the cold room at 4 ^oC so that it would be fully transparent, indicating that complexation had occurred.

A similar preparation was conducted for DMB·PRO (42.34 mg, 0.0318 mmol DMB, and 5 mg, 0.0159 mmol progesterone were used), except that no temperature cycling was required during the preparation. The first couple of incremental additions of the API dissolved after about two minutes with vigorous stirring; subsequent additions took a little longer to dissolve in the solution. The last incremental addition caused the solution to remain slightly turbid, and thus it was left in the cold room at 4 ^oC to stir overnight.

Both solutions were then filtered at 4 ^oC into clean, pre-cooled vials, which were thereafter sealed and placed in the oven at 60 ^oC to encourage crystal growth. Crystals appeared after three days when the volume of the water was slowly reduced to a minimum.

5.2.4.2) Crystal morphologies of DMB·BES and DMB·PRO

The general morphology of DMB·BES is that of fractured, irregular plates (Figure 5.4.1). Despite this, it was possible to cut a small fragment to yield an unflawed single crystal for SCXRD analysis. In contrast, DMB·PRO consisted of well-defined plates with chamfered corners (Figure 5.4.1).

[a] Previous experimentation indicated that anything less than this quantity of DMB could not attain dissolution with the API, despite extensive stirring periods, temperature cycling, and increased volume.

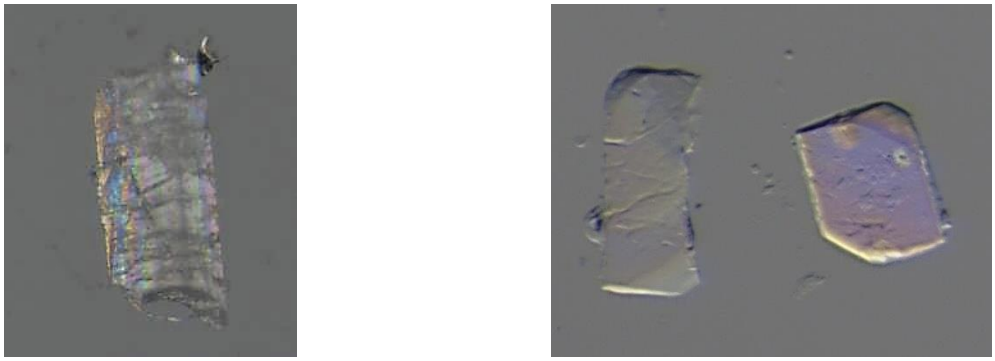


Figure 5.4.1: The crystal morphology of DMB·BES (left) and DMB·PRO (right).

5.2.4.3) ^{1}H NMR analysis of DMB·BES and DMB·PRO

The results from the ^{1}H NMR analyses (Figure 5.4.2 and Tables 5.4.1 and 5.4.2) indicated that both DMB·BES and DMB·PRO formed in 1:1 host-guest stoichiometric ratios. The integrated spectra can be viewed in the Appendix under section 4.4.1, pp. 53 – 54.

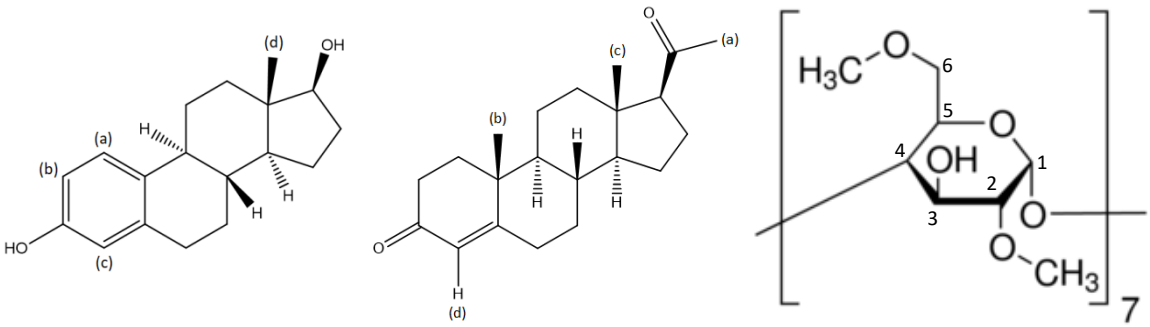


Figure 5.4.2: Molecular structures of β-estradiol (left), progesterone (centre), and DMB (right) with particular molecular moieties labelled for ^{1}H NMR characterisation and complex stoichiometric determination. Adapted from Sigma-Aldrich.[49]

Table 5.4.1: The ^{1}H NMR spectral analysis of DMB·BES.

Assignment	δ (ppm)	Integration	Multiplicity	Proton representation (per molecule)	Stoichiometric ratio	Stoichiometric ratio (integer)
CH (a) aromatic (BES)	7.033 – 7.055	0.0454	doublet	1H	0.64	~1†
CH (b) aromatic (BES)	6.493 – 6.521	0.0464	doublet of doublets	1H	0.65	~1†
CH (c) aromatic (BES)	6.431 – 6.438	0.0505	doublet	1H	0.71	~1†
CH (1) (DMB)	4.949 – 4.984	1.0000*	doublet	14H	1.00	1
OH (3) (DMB)			singlet		1.00	1
CH_2 (6) (DMB)	3.569 – 3.576	1.0863	doublet	14H	1.08	1
OCH_3 (6) methoxy (DMB)	3.263	1.9671	singlet	21H	1.31	1
CH (5) (DMB)	3.187 – 3.220	0.6678	doublet of doublets	7H	1.34	1
CH_3 (d) methyl (BES)	0.672	0.2222	singlet	3H	1.03	1

*reference integral

†Due to the paucity of the supply of DMB which is a costly commodity, the sample mass used in the analysis was small (~3 mg) and thus the proton integration of the guest molecule was not consistent. For this particular complex a larger mass (~10 mg) would be required to record consistent signal integrals.

Table 5.4.2: The ^{1}H NMR spectral analysis of DMB·PRO.

Assignment	δ (ppm)	Integration	Multiplicity	Proton representation (per molecule)	Stoichiometric ratio	Stoichiometric ratio (integer)
CH (d) (PRO)	5.640	0.0481	singlet	1H	1.01	1
CH (1) (DMB)	4.949 – 4.983	0.6350	doublet	7H	0.95	1
OH (3) (DMB)			singlet	7H	0.95	1
CH_2 (6) (DMB)	3.569 – 3.576	0.6604	doublet	14H	0.99	1
OCH_3 (2) methoxy (DMB)	3.512	1.0000*	singlet	21H	1.00	1
OCH_3 (6) methoxy (DMB)	3.263	1.0067	singlet	21H	1.01	1
CH (5) (DMB)	3.187 – 3.219	0.3634	doublet of doublets	7H	1.09	1
CH_3 (a) methyl (PRO)	2.070	0.1326	singlet	3H	0.93	1
CH_3 (b) methyl (PRO)	1.144	0.1553	singlet	3H	1.09	1
CH_3 (c) methyl (PRO)	0.585	0.1331	singlet	3H	0.93	1

*reference integral

5.2.4.4) PXRD analyses of DMB·BES and DMB·PRO

Kneading experiments were performed for DMB with β-estradiol, as well as DMB with progesterone (1:1 mixtures in both cases); however, the results revealed that after kneading, the products were predominantly amorphous (Figures 5.4.3 and 5.4.4). These patterns display the peaks corresponding to the respective APIs superimposed on a broad halo, which is due to the amorphous host compound. The kneading experiments were attempted under varying conditions in order to obtain the best results. With regard to the product from kneading DMB with β-estradiol, kneading times of 5 minutes and 30 minutes were attempted, and the 5-minute experiment displayed improved results (Figure 5.4.3), as the intensities of the peaks at 13.5^{o} and 18.5^{o} were not reduced to the noise level. Upon further kneading it appeared that the product became more amorphous.

With regard to the product from kneading DMB with progesterone, kneading times of 5, 15 and 45 minutes were attempted, as well as an additional kneading experiment for 45 minutes, when the sample was placed as a dry powder (instead of the conventional moist sample) on the zero-background sample holder in the PXRD instrument. All the resulting PXRD patterns displayed the same level of signal-to-noise ratio despite the varying conditions, and consequently a representative experiment, where the sample was kneaded for 5 minutes, was selected (Figure 5.4.4).

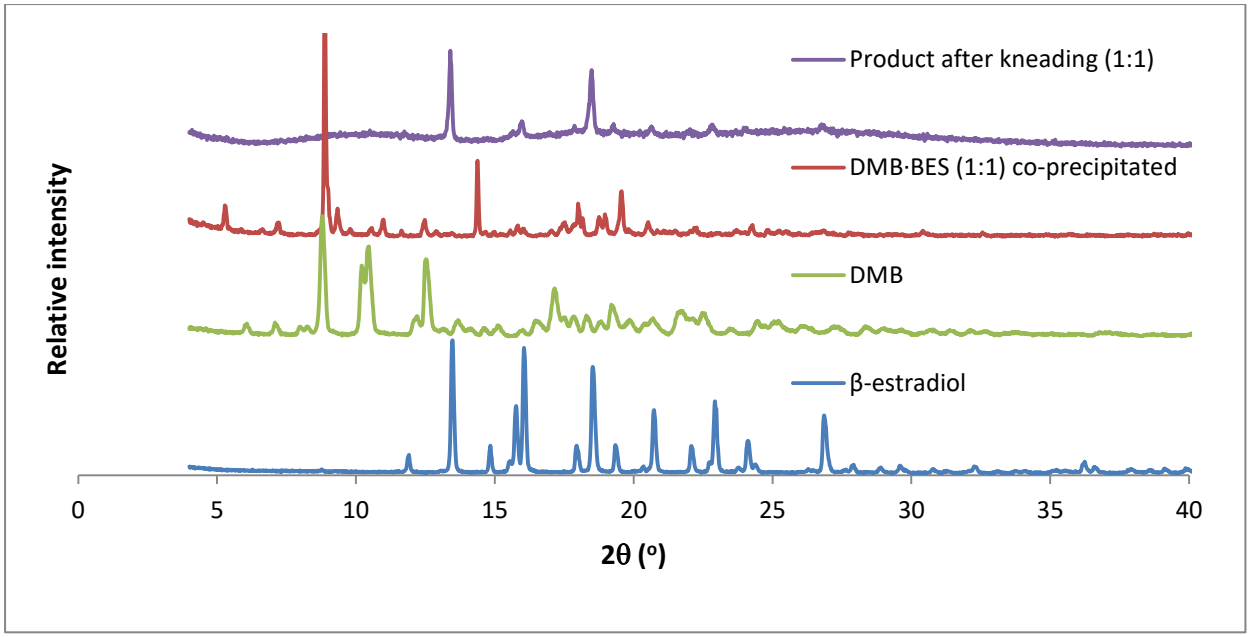


Figure 5.4.3: The PXRD patterns of β-estradiol, DMB, DMB·BES formed *via* co-precipitation (1:1), and a product formed from kneading DMB and β-estradiol (1:1) for five minutes.

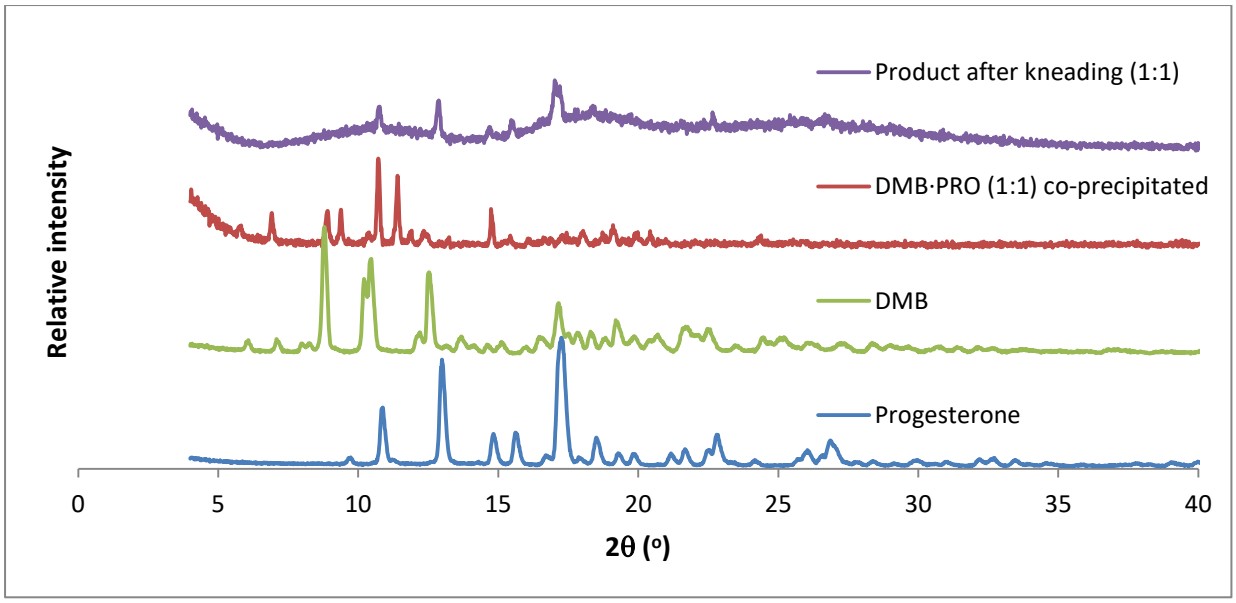


Figure 5.4.4: The PXRD patterns of progesterone, DMB, DMB·PRO formed *via* co-precipitation (1:1) and a product formed from kneading DMB and progesterone (1:1) for five minutes.

In addition, the products represented by the PXRD patterns of DMB·BES and DMB·PRO formed *via* co-precipitation are not isostructural with any other known DMB inclusion

complex, nor are they isostructural between themselves, as a fair number of their respective peak positions differ (Figure 5.4.5). This point will be discussed in more detail in the SCXRD section, where it is shown that even though DMB·BES and DMB·PRO crystallize in the same space group, namely $P2_1$, they have significantly different packing arrangements.

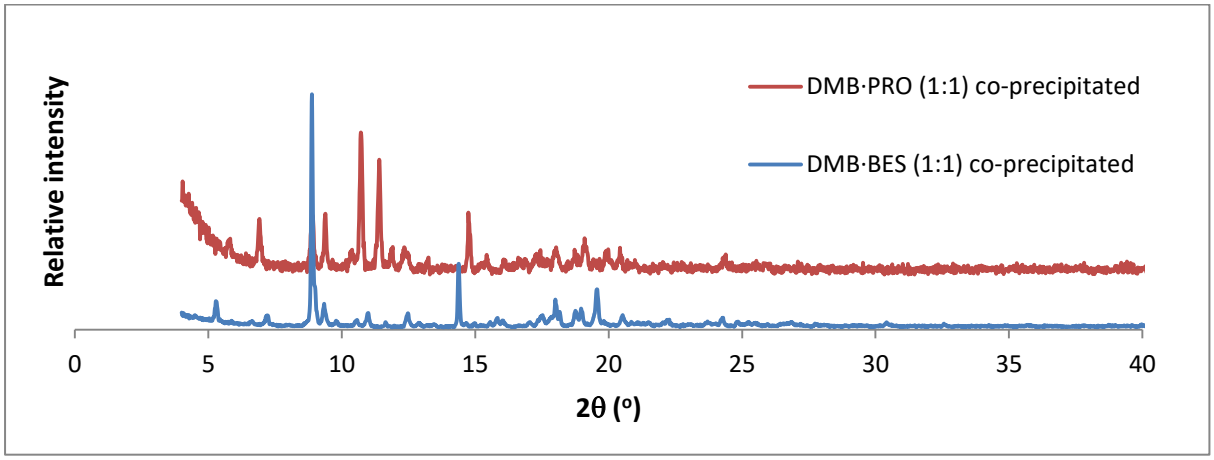


Figure 5.4.5: The PXRD patterns of DMB·BES formed *via* co-precipitation (1:1) and DMB·PRO formed *via* co-precipitation (1:1).

5.2.4.5) Hot stage microscopy (HSM) of DMB·BES and DMB·PRO

DMB·BES

The HSM results for DMB·BES indicated three events, which included the loss of crystallinity, sublimation and decomposition over the temperature range 21.7 – 285.3 °C (Figure 5.4.6). Image A displays the initial appearance at 21.7 °C. Thereafter, the crystal fractured down the middle and this event was accompanied by the onset of opacity, owing to a loss of crystallinity (image B at 40.4 °C). Image C displayed the continuation of the onset of opacity at 58.7 °C. At 65.9 °C the perimeter of the crystal began to fragment and form a periphery of opaque satellite crystallites (image D). The onset of bubbling occurred at 81.0 °C (image E), which eventually reached a maximum at 124.2 °C (image F). All the events that have thus far been discussed are associated with the dehydration of the crystal. At 145.3 °C the bubbling ceased and at this temperature the onset of guest sublimation was observed (image G),

which reached its peak at 250.0 °C (image H). The onset of decomposition commenced at 285.3 °C (image I).

Figure 5.4.6: A series of HSM micrographs for DMB·BES.



A: Initial appearance of DMB·BES (21.7 °C).



B: Hardly discernible crystal fracturing and the simultaneous onset of opacity (40.4 °C).



C: Continuation of opacity (58.7 °C).



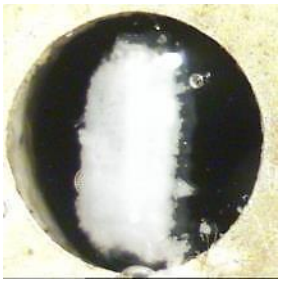
D: Onset of peripheral crystal fragmentation (65.9 °C).



E: Onset of bubbling (81.0 °C).



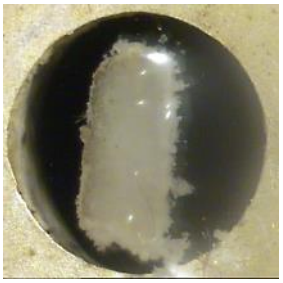
F: Maximum bubbling (124.2 °C).



G: Bubbling ceased, maximum opacity, and onset of guest sublimation (145.3 °C).



H: Maximum sublimation (250.0 °C).



I: Onset of decomposition (285.3 °C).

DMB·PRO

The HSM results for DMB·PRO possibly indicated three different events through different types of opacity changes (Figure 5.4.7). Image A displayed the initial appearance at 21.5 ^{o}C. The onset of opacity occurred almost immediately upon heating (image B) at 31.1 ^{o}C and this was possibly due to the small loss of water (as confirmed in the TGA analysis which is described below). However, the opacity continued until it reached a maximum at 106.9 ^{o}C (image C) and this possibly indicated that the onset of opacity from the small amount of water loss merged into the onset of opacity that could be associated with a possible polymorphic transition. This is reiterated in the DSC analysis below. This level of opacity remained the same until 172.1 ^{o}C (image D) where a second onset of opacity commenced until it reached its maximum at 202.3 ^{o}C (image E). This event possibly indicated a second polymorphic transition. The onset of decomposition occurred at 251.1 ^{o}C (image F) and continued through to 332.9 ^{o}C (image G).

Figure 5.4.7: A series of HSM micrographs for DMB·PRO.



A: Initial appearance of DMB·PRO (21.5 °C).



B: The onset of opacity (31.1 °C).



C: The maximum opacity achieved initially (106.9 °C).



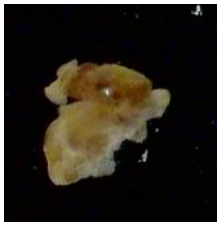
D: The onset of the second stage of opacity (172.1 °C).



E: The maximum second stage of opacity achieved (202.3 °C).



F: Hardly discernible onset of decomposition (251.1 °C).



G: Continuation of decomposition (332.9 °C).

5.2.4.6) Thermal gravimetric analyses (TGA) of DMB·BES and DMB·PRO

In summary, the TGA curves for DMB·BES and DMB·PRO displayed different events. DMB·BES displayed dehydration, guest loss and decomposition, while DMB·PRO displayed only dehydration and decomposition (Figures 5.4.8 and 5.4.9). The TGA results for each complex will be discussed individually.

DMB·BES

The TGA curve of DMB·BES (n=2) indicated three events between 19 °C and 400 °C, which included dehydration, loss of the guest molecules and decomposition, and all of these occurred as single-step processes, as represented by the respective single peaks in the dTGA curve (Figure 5.4.8). With regard to the dehydration, this event took place between 20.1 ± 1.3 °C and 50.4 ± 0.1 °C and was associated with a mass loss of 3.1 ± 0.1% (which corresponded to 2.9 ± 0.1 water molecules per DMB molecule).

In addition, the loss of the guest molecules occurred between 180.5 ± 4.6 °C and 324.8 ± 1.3 °C; however, the 'end' temperature coincided with the onset of decomposition. The mass loss that was associated with the loss of the guest molecules amounted to 13.8 ± 0.5%, which was slightly less than what is expected theoretically for the 1:1 host-guest complex (determined by ^{1}H NMR spectroscopy). The expected value is 17.0%, and a possible explanation for the estimate of 13.8 ± 0.5% (as displayed in the TGA curve) is that the onset of decomposition occurred before all the guest molecules had been fully removed. The calculations for the dehydration and loss of the guest molecules can be viewed in the Appendix under sections 4.4.2 and 4.4.3, pp. 54 – 55.

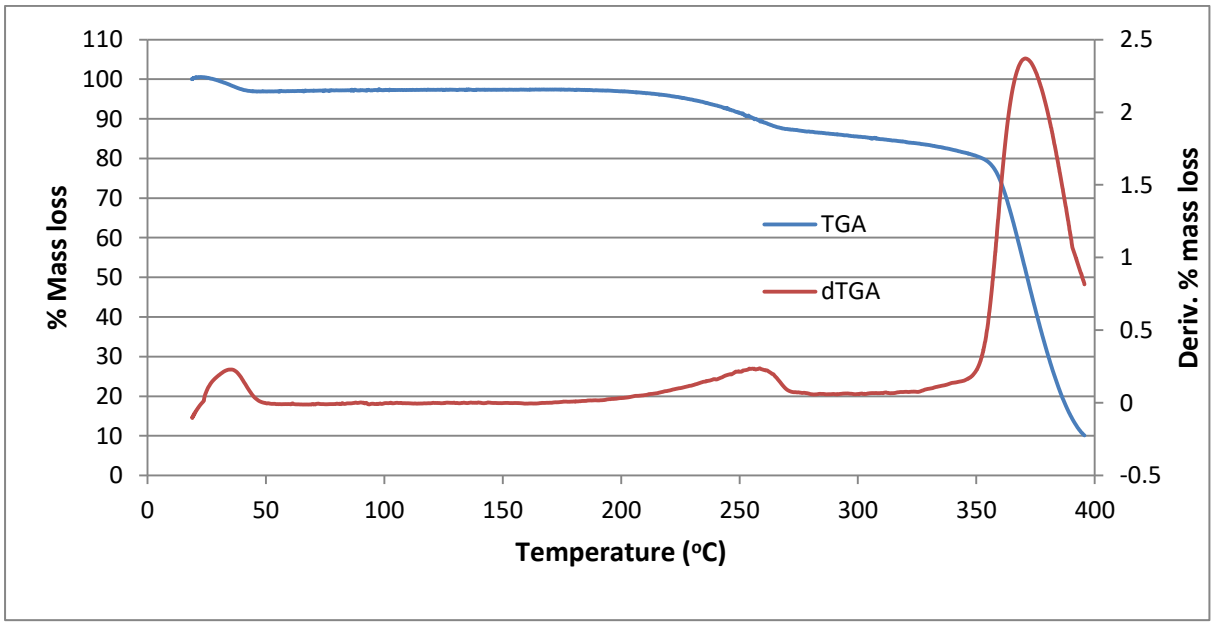


Figure 5.4.8: Representative TGA and dTGA curves of DMB·BES.

DMB·PRO

The TGA curve of DMB·PRO (n=3) displayed two single-step events (dehydration and decomposition) over a temperature range between 20.0 ± 3.4 °C and 177.3 ± 6.5 °C (Figure 5.4.9). The dehydration indicated a mass loss of 1.2 ± 0.3% (which corresponded to 1.1 ± 0.2 water molecules per complex unit) over a temperature range between 20.0 ± 3.4 °C and 62.0 ± 2.4 °C. Unlike DMB·BES, this inclusion complex does not display any evidence for the

loss of guest molecules on heating and thus the subsequent event is the decomposition of the dehydrated complex at 177.3 ± 6.5 °C. The calculation for the dehydration can be viewed in the Appendix under section 4.4.4, p. 55.

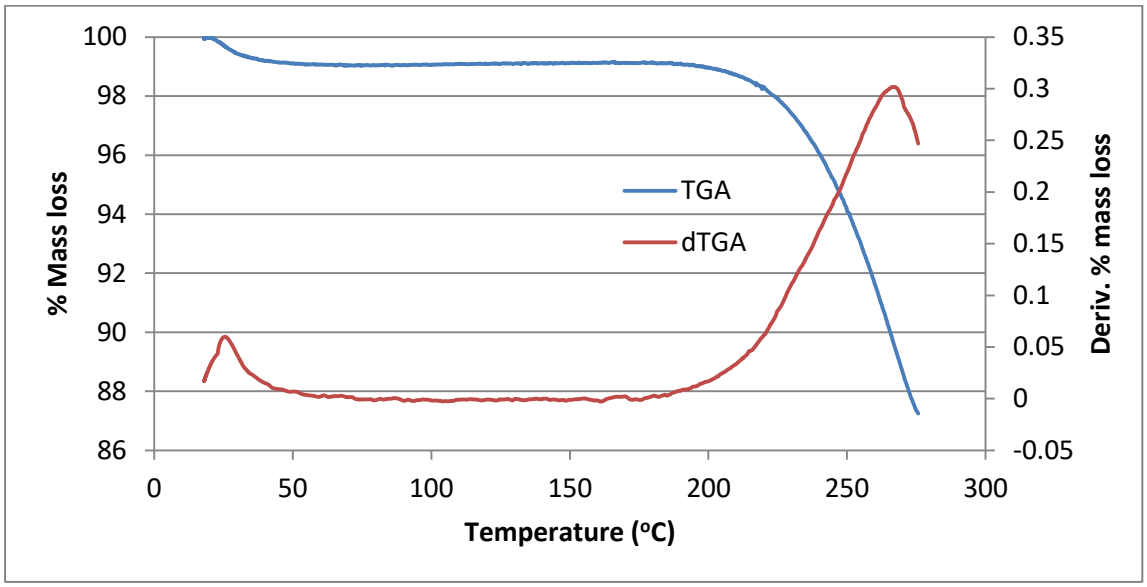


Figure 5.4.9: Representative TGA and dTGA curves of DMB·PRO.

5.2.4.7) Differential scanning calorimetry (DSC) of DMB·BES and DMB·PRO

DMB·BES

The DSC curve (n=2) displayed events over the heating range which corresponded to the loss of water, an exothermic phase transition (recrystallization), and the endothermic loss of the guest molecules (Figure 5.4.10). The first three endothermic peaks were effectively a composite set representing the dehydration of the complex. The onset and peak temperatures of the first endothermic peak were 38.6 ± 0.5 °C and 54.7 ± 0.2 °C respectively, and for the second endothermic peak they were 57.8 ± 0.4 °C and 59.4 ± 0.6 °C respectively. It could be argued that the third endothermic peak (which had an onset temperature of 76.9 ± 0.8 °C and a peak temperature of 81.5 ± 0.1 °C), represented a phase transition, as it was slightly high and too far removed to be water loss in comparison to the overlaid TGA curve (Figure 5.4.10). However, with reference to the HSM experiment that

was described previously, the dehydration continued up until 145.3 °C, which suggested that this endothermic peak could be attributed to the dehydration of the complex.

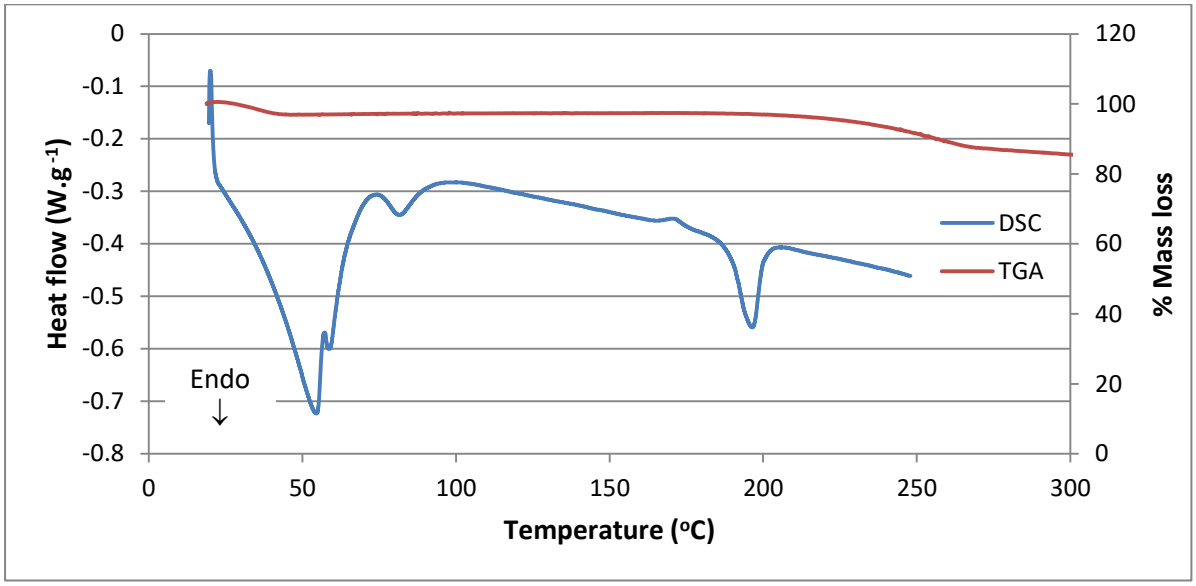


Figure 5.4.10: A representative DSC curve of DMB·BES, with the respective TGA curve as a reference.

Furthermore, a small exothermic peak occurred at an onset temperature of 164.8 ± 1.4 °C and with a peak temperature of 170.8 ± 0.3 °C (Figure 5.4.10). This possibly represented a recrystallization prior to a final endothermic peak that represented the loss of the guest molecules from the complex (onset temperature = 189.39 ± 0.2 °C, peak temperature = 196.4 ± 0.1 °C).

As expected, the thermal trends of the DSC and TGA results correlated; however, the precise temperatures of these trends did not correlate. Ultimately, a variable temperature PXRD experiment would be required to fully determine the presence or absence of phase transitions. However, since the complex could not be prepared *via* kneading, it was not possible to obtain a sufficiently large sample *via* co-precipitation to perform an experiment on the variable temperature PXRD instrument.

DMB·PRO

The DSC curve of DMB·PRO (n=2) displayed two events, the first being an endothermic and exothermic pair, with peaks occurring at 56.5 ± 0.4 °C and 79.4 ± 0.1 °C respectively (Figure 5.4.11). The second event contained a double exothermic peak, with peak temperatures at 162.9 ± 0.1 °C and 173.8 ± 0.1 °C respectively. This curve did not indicate any water loss, possibly due to the fact that there was very little water in the complex (as indicated by the TGA results), and thus the DSC instrument was not sensitive enough to record it. All the events represented in the DSC curve were most likely attributable to phase transitions, as there was no mass loss indicated in the overlaid TGA curve at the temperatures at which they occurred. Furthermore, the HSM experiment displayed the possibility of two phase transitions occurring when the crystals experienced separate developments in opacity. Naturally, variable temperature PXRD would be required to verify this. However, as with DMB·BES, it was not possible to perform this experiment, since the complex could not be replicated *via* kneading and not enough sample could be obtained from co-precipitation experiments in a cost-effective manner.

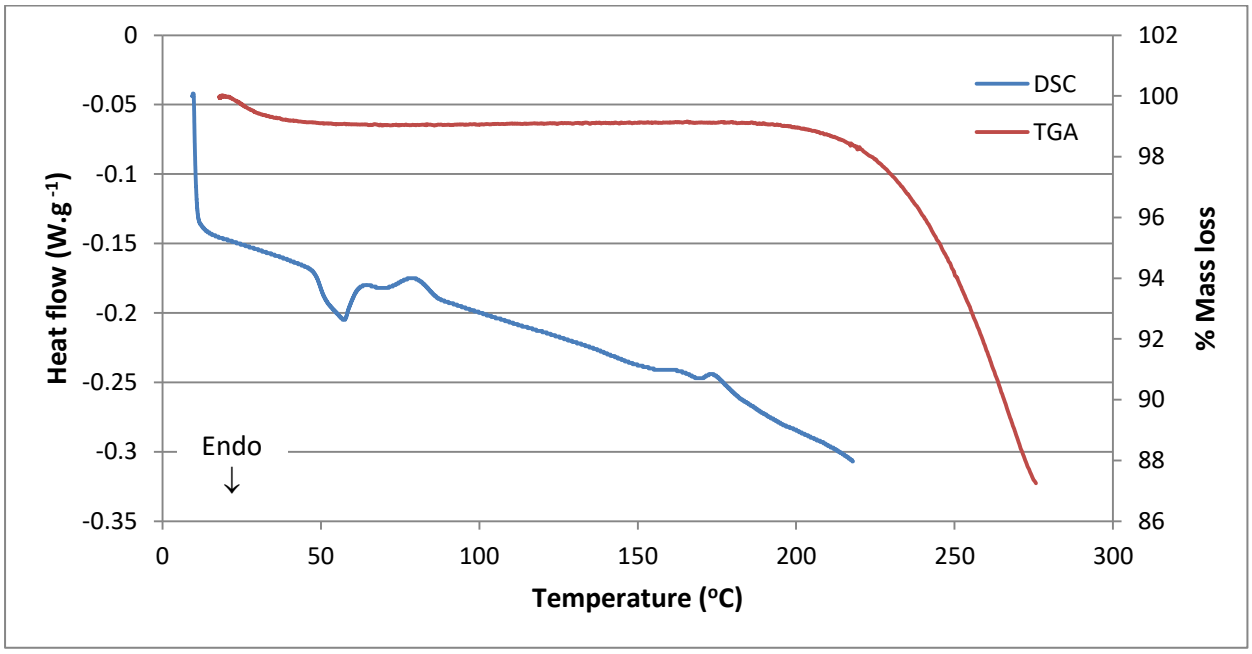


Figure 5.4.11: A representative DSC curve of DMB·PRO, along with the respective TGA curve as a reference.

5.2.4.8) Single-crystal X-ray diffraction (SCXRD) analysis

Data-collection and space group determination: DMB·BES and DMB·PRO

The intensity data for both DMB·BES and DMB·PRO were collected at 100(2) K from single, transparent crystals. The Laue groups were determined to be 2/*m* for both CD complexes from the two intensity-weighted reciprocal lattices and thus the monoclinic crystal system was assigned to them. Primitive lattice types were determined and the common space group $P2_1$ was assigned from the conditions limiting possible reflections listed in Table 5.4.3 for both CD complexes. The SCXRD structural results were different for the two complexes, and consequently it is appropriate to describe each CD complex separately hereafter. The atomic numbering scheme for the molecular structures of β-estradiol, progesterone and DMB are provided in Figure 5.4.12 below.

Table 5.4.3: The conditions limiting possible reflections for DMB·BES and DMB·PRO.

Number	Conditions limiting possible reflections	Deduction
1	hkl: none	Primitive lattice
2	h0l: none	No glide plane ⊥ b
3	0k0: k = 2n	2_1-axis parallel to the b-axis

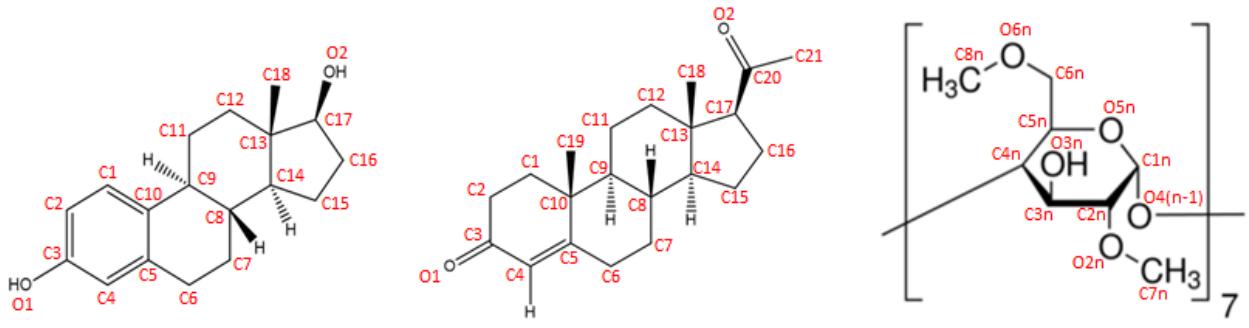


Figure 5.4.12: The numbering scheme for the molecular structures of β-estradiol (left), progesterone (centre) and DMB (right), with n representing one of the seven glucose units of the molecule.

Structure solution and refinement of DMB·BES

The structure was solved using SHELXS-97,[37] with the number of phase sets in the TREF command set to 5000 and the structure solution by direct methods revealed that the ASU

comprised two independent complex units designated A and B. The atoms of the host molecules were initially assigned and refined isotropically, and subsequently anisotropically. The disorder of a methoxy and hydroxyl group was treated by assigning s.o.f.s of *x* and 1 - *x* (where *x* is a free variable), as well as separate PART numbers to the disordered counterparts. The electron density map indicated that the methoxy oxygen atom O6B2 on the primary ring of the host molecule B, and the hydroxyl oxygen atom O3A5, on the secondary ring of the host molecule A, were disordered over two positions. The disorder of O6B2 (along with its methoxy carbon atom, C8B2) and O3A5 were modelled as described above.

In addition, the atom at the C6 position (C6B2) was artificially split (with a minimal distance apart) in order to allow the methylene hydrogen atoms to be correctly placed in idealised positions on the relevant components. Consequently, the resulting atoms, C6B2 and C6D2, were also treated as disordered counterparts and assigned the respective free variable and PART numbers, along with a restraint that enforced their U_{iso} parameters to be equal.

Furthermore, there were multiple carbon and oxygen atoms from hydroxyl and methoxy groups of both CD molecules that displayed very large thermal ellipsoids after anisotropic refinement, indicating that they should be split into two disordered counterparts. These atoms (C7B1, O3B6, C7B6, C7B7, C7A2 and C7A6) were all refined isotropically.

The C-O and C5-C6 bonds of the disordered pairs were maintained at reasonable lengths with DFIX restraints to values of 1.40 Å (σ = 0.01 Å), and 1.51 Å (σ = 0.01 Å) respectively, and for some disordered pairs, it was necessary to reduce the standard deviation to 0.002 Å in order to enforce the restraints. In addition, the disordered pair O6B2 and O6D2 was also constrained geometrically to retain a reasonable geometry around the C6 atom by applying a DFIX restraint of 2.45 Å (σ = 0.002 Å) to the O6B2-O6D2 bond length. The major components of these disordered atoms were C6B2, O6B2, C8B2 [refined s.o.f. = 0.76(1)] and O3A5 [refined s.o.f. = 0.65(1)].

Once the host molecules were refined to a suitable standard, the electron density peaks in the difference Fourier map corresponding to the respective guest molecules were assigned based on their geometrical arrangement. These atoms were also initially refined isotropically, and thereafter anisotropically.

Finally, the hydrogen atoms were placed on both the host and guest molecules in idealised positions using a riding model with an isotropic temperature factor of either 1.2 or 1.5 times the U_{iso} value of their parent atoms.

Lastly, the difference Fourier map displayed evidence of partial methylation on an O3 oxygen atom (O3B5), a feature which is occasionally encountered in crystals of DMB complexes. It was not possible to assign this methyl group full site-occupancy and disorder was modelled between a hydrogen atom and methyl group, forming a partial hydroxyl and methoxy functionality respectively. For this particular partial carbon atom, hydrogen atoms were placed on it in a staggered conformation. The major component was the hydrogen atom, H3B5, with a refined s.o.f. of 0.68(3). Table 5.4.4 displays the summarized crystallographic data and details of the refinement. The complex formula indicates that the host complement comprises both a chemically intact DMB molecule ($C_{56}H_{98}O_{35}$) and one with the formula $C_{56.4}H_{98.8}O_{35.2}$ which features the partial methylation described above.

Table 5.4.4: The crystal data and refinement parameters for DMB·BES.

Parameter	Value
Complex formula	$C_{56}H_{98}O_{35}\cdot C_{56.4}H_{98.8}O_{35.2}\cdot(C_{18}H_{24}O_2)_2\cdot 11.6(H_2O)$
Formula weight ($g.mol^{-1}$)	3317.52
Temperature (K)	100(2)
Wavelength (Å)	0.71073
Crystal system	Monoclinic
Space group	$P2_1$
a (Å)	14.1388(17)
b (Å)	30.448(4)
c (Å)	21.052(3)
α (°)	90
β (°)	107.687(2)
γ (°)	90
Volume ($Å^3$)	8634.5(18)
Z	2
Calculated density ($g.cm^{-3}$)	1.276
μ (mm^{-1})	0.103
F (000)	3570
Crystal size (mm)	0.20 x 0.32 x 0.59
θ-Range scanned (°)	2.52 – 24.80
Index range	h:-18, 18; k:-40, 40; l:-28, 28
No. of reflections collected	160787
No. of unique reflections	43105
Data completeness (%)	99.6
Data/restraints/parameters	43105/21/2092
S (Goodness-of-fit on F^2)	1.023
Final R indices R_1, wR_2, [I > 2σ(I)]	0.0745, 0.1905
R Indices, all data (R_1, wR_2)	0.1040, 0.2110
Largest diff. peak and hole ($e.Å^{-3}$)	1.17, -0.65

The remaining electron density peaks that displayed adequate heights (as well as appropriate hydrogen bonding distances from other atoms), were assigned as water oxygen atoms. This accounted for 11.6 water molecules being assigned over 15 sites. Their refined s.o.f. values and U_{iso} parameters are listed in Table 5.4.5. Initially, the first eight electron density peaks, which had peak heights ranging from 2.83 to 4.40 e.Å^{-3}, were assigned as oxygen atoms with s.o.f.s equal to 1.0 and refined initially isotropically and thereafter anisotropically. The remaining electron density peaks at the potential water molecule sites were assigned as partial disordered oxygen atoms, their s.o.f. values being allowed to vary and their common U_{iso} parameter being initially fixed at a pre-calculated value, namely the average of the U_{iso} values of the first eight fully occupied water oxygen atoms.

A further seven partial water oxygen atoms were identified and were refined isotropically only. In addition, it was apparent that the atom pairs, O12W and O13W, as well as O9W and O14W, were disordered over two positions and each disordered atom pair was constrained to have the same U_{iso} value during refinement. As mentioned previously, the crystallographic model indicated that there were 11.6 water molecules in the ASU. This value was also verified using the SQUEEZE routine[38] implemented in program PLATON,[39] where the water molecules were temporarily deleted from the model and the resulting difference electron density yielded an electron count amounting to 221 electrons per unit cell (compared with a theoretical value of 232 electrons for 11.6 water molecules). However, these estimates were not in agreement with the TGA results. The latter had indicated a water loss of 5.8 $\pm$ 0.2 water molecules for two CD molecules, and a probable reason that the value is significantly lower than the crystallographic estimate, is owing to unavoidable premature water loss during sample preparation for TGA. The HSM experiment (as previously described under section 5.2.4.5, pp. 268 – 269) showed that dehydration commenced at 40.4 ^{o}C. Furthermore, the low standard deviation in the TGA estimate of water content quantity reflected good experimental repeatability, which confirmed that an unavoidable constant amount of water loss was occurring prior to the start of the TGA experiment. As a result, the TGA water content value was not used to establish the molecular formula of the complex, and thus the number of water molecules determined for the crystal structure model was used instead.

Table 5.4.5: The total number of water oxygen sites that were identified, with their respective s.o.f.s and U_{iso} values.

Atom	s.o.f.	U_{iso} (Å^2)	Atom	s.o.f.	U_{iso} (Å^2)
O1W	1	0.052(1)	O9W	0.557 (9)	0.058(2)
O2W	1	0.056(1)	O10W	0.75(1)	0.066
O3W	1	0.060(1)	O11W	0.65(2)	0.058(3)
O4W	1	0.071(2)	O12W	0.52(1)	0.064(2)
O5W	1	0.077(2)	O13W	0.48(1)	0.063(2)
O6W	1	0.060(1)	O14W	0.443(9)	0.058(2)
O7W	1	0.068(2)	O15W	0.22(2)	0.06(1)
O8W	1	0.097(2)			

Molecular structure

The asymmetric unit (ASU) consists of two crystallographically independent DMB molecules (A and B, the latter displaying partial methylation at one O3 atom), that are pseudo inverted relative to one another, and which display bimodal inclusion of the guest molecules in the CD cavities (Figures 5.4.13 and 5.4.14).

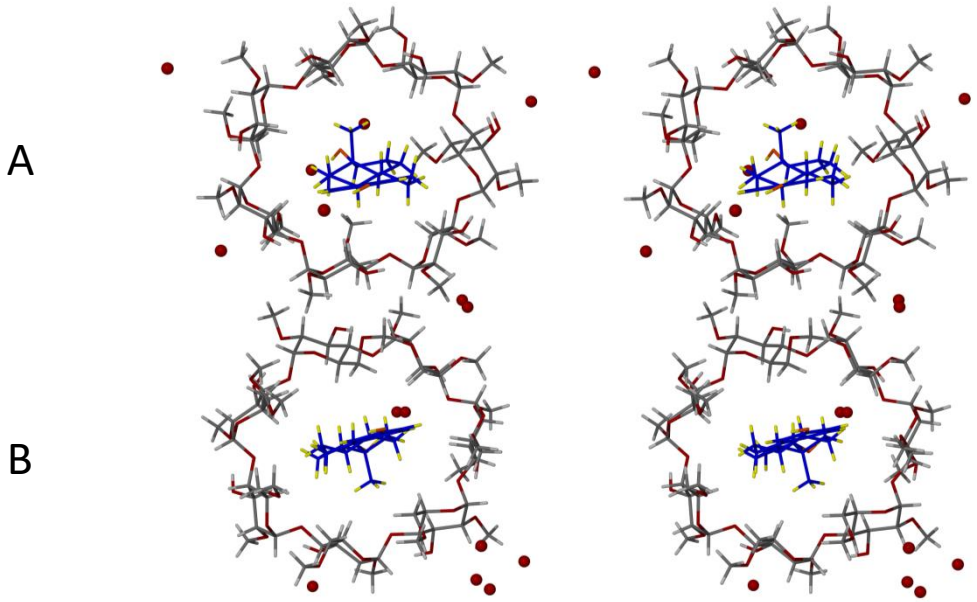


Figure 5.4.13: A stereoscopic representation of the ASU of DMB·BES; the individual monomeric units are labelled A and B. An alternative colour scheme was used to differentiate the guest atoms: carbon atoms (blue), hydrogen atoms (yellow) and oxygen atoms (orange). Monomeric unit A is viewed from the secondary (wider) side of the DMB molecule, while monomeric unit B is viewed from the primary (narrower) side of the DMB molecule.

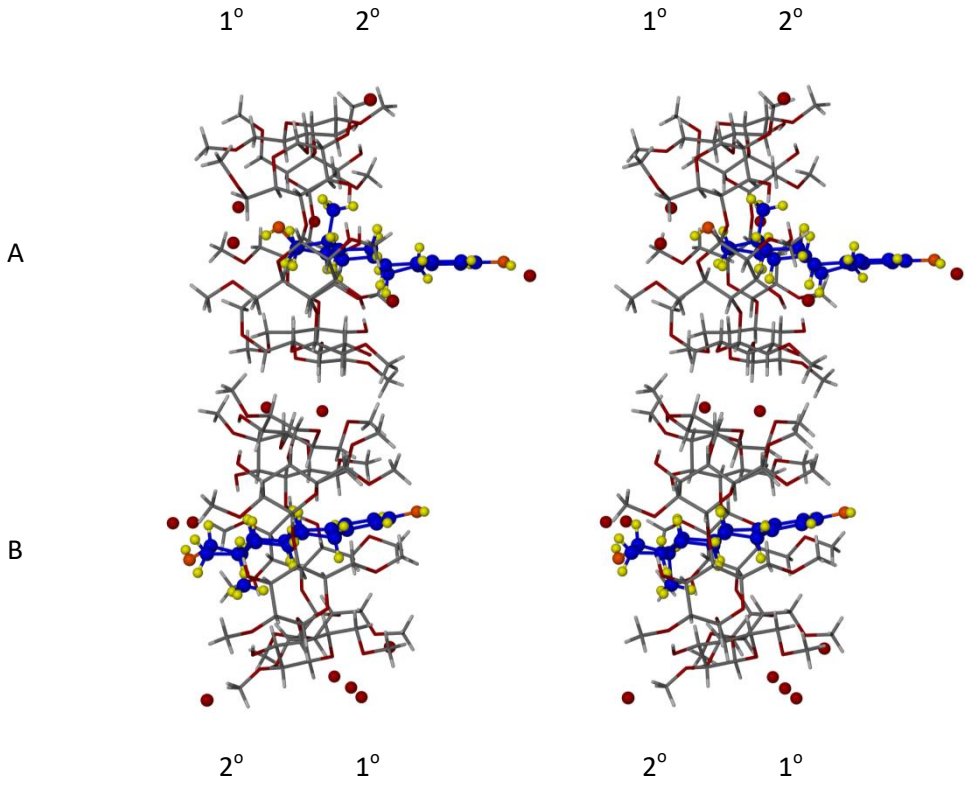


Figure 5.4.14: A stereoscopic view of the ASU of DMB·BES displaying the pseudo inverted relationship between the two CD molecules, A and B respectively. The primary and secondary rims of the two CD molecules are represented by the symbols 1^{o} and 2^{o} in the figure.

The term 'bimodal guest inclusion' in this unusual case refers to the major structural difference in the two distinct modes of BES inclusion, most evident in Figure 5.4.14: in complex unit A, the aromatic ring of BES is located near the secondary rim of the DMB host molecule, while in complex unit B, the aromatic ring of BES is located at the primary rim of the DMB host molecule.

It is also evident from these figures, that the depths of guest molecule inclusion in the host molecules of A and B differ. Only rings C and D of the steroidal scaffold (with reference to Figure 5.4.15) are included inside the cavity of host molecule A, while rings A, B, C and D of the second steroidal molecule are encapsulated in host molecule B. Figure 5.4.16 displays a cross-section through the CD molecules to illustrate these features. Finally, 11.6 water molecules (of which seven had s.o.f.s < 1.0) were identified over fifteen sites, and they were within hydrogen bonding range of either

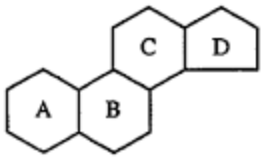


Figure 5.4.15: Steroid scaffold with labelled rings.

the host molecule, the guest molecule, or symmetry-related water molecules. Hydrogen atoms were not placed on the water molecules since there was no evidence for them in the difference Fourier map.

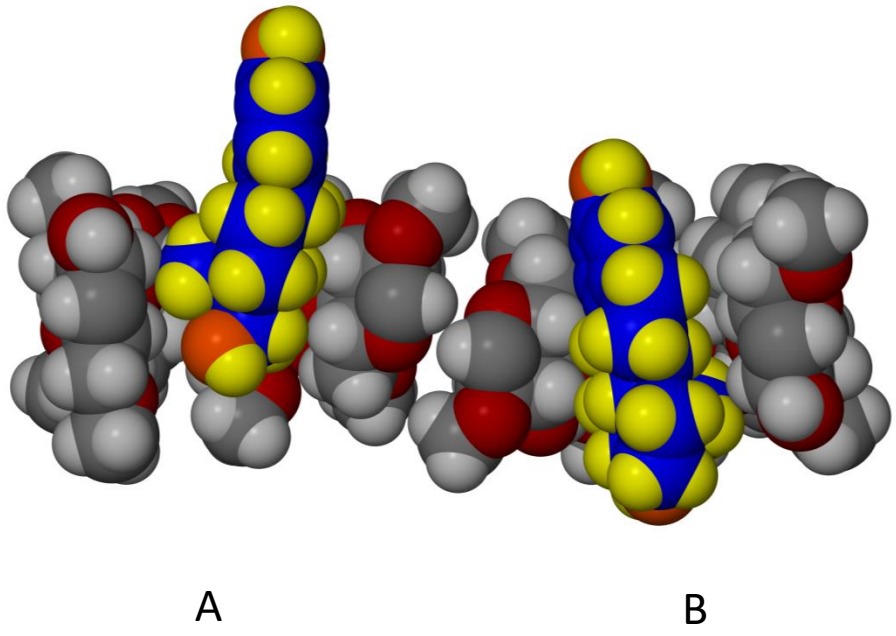


Figure 5.4.16: A space-filling representation of a cross-section of the ASU of DMB·BES, which illustrates the bimodal inclusion of the guest molecules. The water molecules have been omitted for clarity.

Hydrogen bonding interactions involving the host, guest and water molecules

The hydrogen bonds involved in inclusion for each guest molecule are displayed in the stereoscopic view in Figure 5.4.17. With regard to complex unit A, the guest hydroxyl oxygen atom on the D-ring, O2A, hydrogen bonds to the water molecule, O1W, which in turn hydrogen bonds to the host atom O6A2. Similarly, the guest hydroxyl oxygen atom on the aromatic ring, O1A, hydrogen bonds to a water oxygen atom, O2W (which in turn is hydrogen bonded to O10W′ and O3W′ (related by x, y, -1+z and -1+x, y, z respectively), but not shown in Figure 5.4.17).

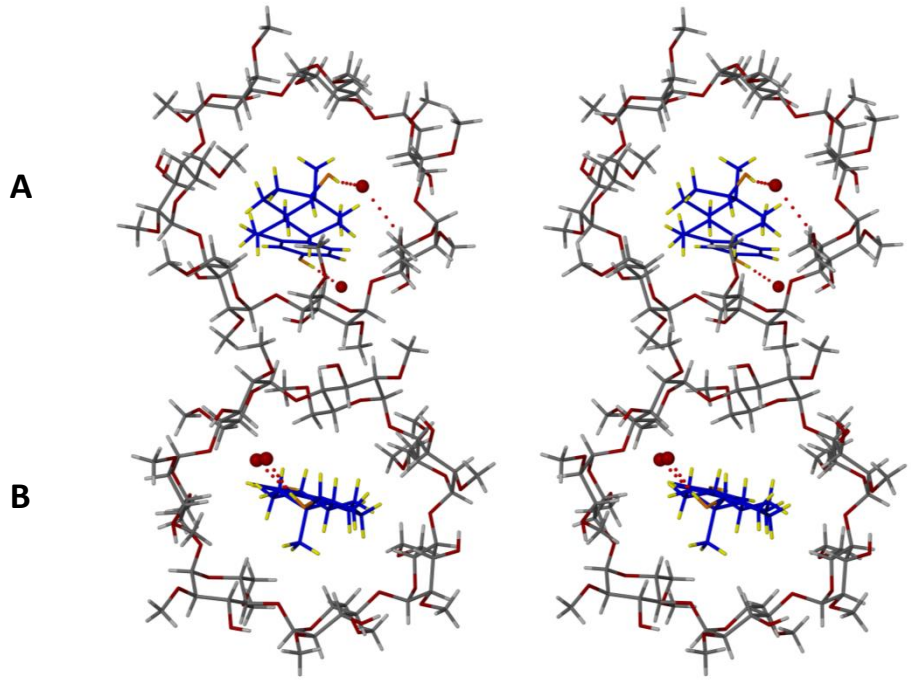


Figure 5.4.17: A stereoscopic view of the ASU of DMB·BES displaying the hydrogen bonding interactions (depicted as red spheres) between the guest molecules and the water oxygen atoms inside the cavities of the DMB molecules. The water oxygen atoms not involved in this hydrogen bonding have been omitted for clarity.

With regard to complex B, a similar trend occurs where the guest hydroxyl oxygen atom, O2B on the D-ring, hydrogen bonds to a disordered water oxygen atom split over two positions (O9W and O14W); however, this disordered water oxygen atom pair hydrogen bonds to atom O3A1 of a symmetry-related guest molecule (related by x, y, -1+z) but for clarity this is not shown in Figure 5.4.17. In addition, the other hydroxyl oxygen atom on the aromatic ring of the guest molecule B, O1B, hydrogen bonds to a symmetry-related host oxygen atom O3A6 (related by -x, -1/2+y, 1-z), again not shown in the figure. Table 5.4.6 displays the hydrogen bonding data for all these interactions, and for other water-host interactions involving the remaining water oxygen atoms. Lastly, geometrical data for weaker C-H···O host-guest hydrogen bonding, as well as water-water hydrogen bonding observed in these structures are listed in Table 5.4.6.

Table 5.4.6: H-bonding parameters for host-guest, host-water and guest-water interactions in DMB·BES.

Hydrogen bond	D-H (Å)	H···A (Å)	D···A (Å)	D-H···A (°)	Symmetry code
O1A-H1A···O2W	0.84	1.88	2.717(6)	175	x, y, z
O1B-H1B···O3A6	0.84	1.87	2.712(6)	178	-x, -1/2+y, 1-z
O2A-H2A···O1W	0.84	1.88	2.692(7)	164	x, y, z
O2B-H2B···O9W	0.84	1.93	2.77(1)	170	x, y, z
O2B-H2B···O14W	0.84	2.10	2.89(1)	157	x, y, z
C1B6-H14···O2W	1.00	2.45	3.43(1)	166	x, y, 1+z
C1B2-H1B2···O1A	1.00	2.53	3.499(6)	162	-x, -1/2+y, 1-z
C2B4-H2B4···O5W	1.00	2.43	3.425(8)	173	x, y, z
C6A-H6AX···O6B2	0.99	2.59	3.546(7)	162	-x, 1/2+y, 1-z
C2A4-H2A4···O11W	1.00	2.25	3.13(1)	146	x, y, z
C8A2-H8A4···O1B	0.98	2.42	3.39(1)	172	1+x, y, z
C2B7-H2B7···O11W	1.00	2.48	3.38(1)	148	-x, -1/2+y, 2-z
C4A5-H4A5···O7W	1.00	2.54	3.421(9)	146	x, y, z
C7B7-H7BC···O4W	0.98	2.52	3.38(1)	147	x, y, z
C7A2-H7AI···O15W	0.98	1.79	2.72(3)	158	x, y, z
O6A2···O1W*	-	-	2.805(6)	-	x, y, z
O2W···O3W*	-	-	2.867(8)	-	-1+x, y, z
O2W···O10W*	-	-	2.79(1)	-	x, y, -1+z
O3A1···O9W*	-	-	2.71(1)	-	x, y, -1+z
O3A1···O14W*	-	-	2.70(1)	-	x, y, -1+z
O2B4···O3W*	-	-	2.938(7)	-	x, y, 1+z
O6B7···O5W*	-	-	2.869(8)	-	-x, -1/2+y, 2-z
O3B7···O4W*	-	-	2.979(7)	-	x, y, z
O6B4···O11W*	-	-	2.70(1)	-	x, y, z
O5B6···O8W*	-	-	3.07(1)	-	x, y, z
O6B6···O8W*	-	-	2.86(1)	-	x, y, z

*The water oxygen atom is the hydrogen bond donor

Host intramolecular and intermolecular hydrogen bonding

The heptagonal geometry of each host molecule is reinforced by intramolecular hydrogen bonds on the secondary rim linking contiguous glucose residues to form an O2-H···O3' hydrogen bonding belt (Figure 5.4.18).

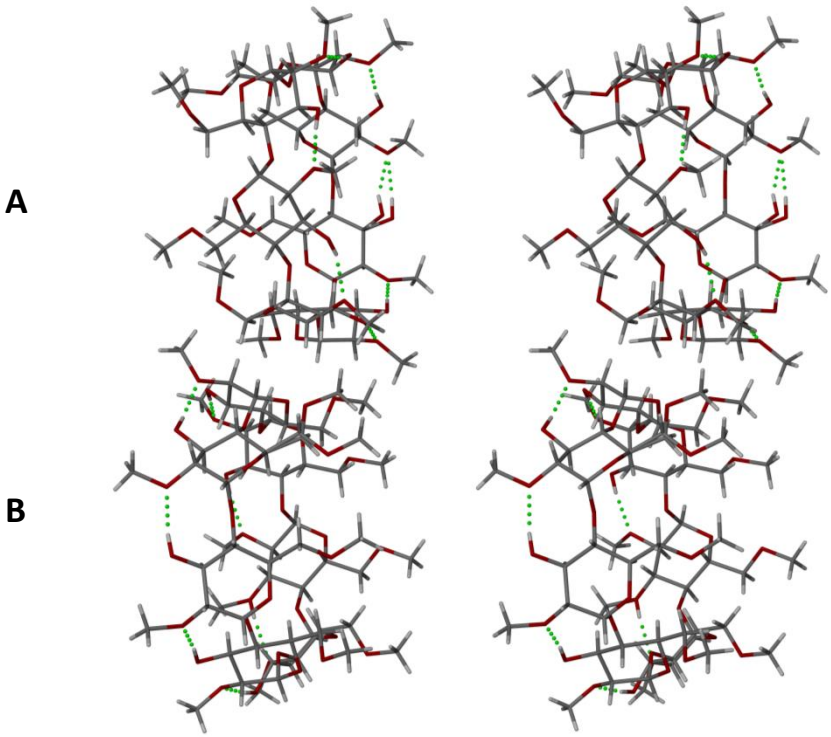


Figure 5.4.18: A stereoscopic view of the host intramolecular hydrogen bonding 'belt' (H-bonds depicted as green dotted lines). The water molecules and guest molecules have been omitted for clarity.

The most significant hydrogen bonds that involve the DMB molecules were mostly observed to be O-H···O intramolecular interactions, and no hydrogen bond interactions were observed to occur between the host molecules A and B in the ASU (Tables 5.4.19A and 5.4.19B). However, there were many intramolecular C-H···O hydrogen bonds and only a few weak intermolecular interactions of this type between molecules A-A′, B-B′, A-B′ and B-A′ (the prime symbol referring to symmetry-generated atoms). The maximum listed C···O distance is 3.554(7) Å (Table 5.4.19B). These interactions are weak, as the sum of the van der Waals radii of carbon and oxygen is 3.22 Å, and many of these interactions also have unfavourable (e.g., < 140°) bond angles. However, these interactions have been listed for completeness. Nonetheless, the intermolecular C-H···O hydrogen bonds contribute towards cohesion between the DMB molecules in the crystal structure.

Table 5.4.19A: The parameters for the hydrogen bond interactions in DMB·BES for molecule A.

Interaction type	Hydrogen bond	D-H (Å)	H···A (Å)	D···A (Å)	D-H···A (°)	Symmetry code
O3-H···O2′ Hydrogen bonds						
Intramolecular	O3A7-H3A7···O2A1	0.84	1.97	2.798(5)	169	x, y, z
Intramolecular	O3A1-H3A1···O2A2	0.84	1.90	2.737(6)	173	x, y, z
Intramolecular	O3A2-H3A2···O2A3	0.84	2.06	2.863(6)	160	x, y, z
Intramolecular	O3A3-H3A3···O2A4	0.84	1.95	2.775(7)	167	x, y, z
Intramolecular	O3A4-H3A5···O2A5	0.84	2.01	2.840(8)	169	x, y, z
Intramolecular	O3A5-H3A9···O2A6	0.84	1.99	2.754(8)	150	x, y, z
Intramolecular	O3A6-H3A6···O2A7	0.84	1.91	2.745(6)	172	x, y, z
C-H···O Hydrogen bonds						
Intramolecular	C8A1-H8A2···O5A1	0.98	2.39	3.031(8)	123	x, y, z
Intermolecular	C2A2-H2A2···O5A6	1.00	2.40	3.310(7)	151	1-x, -1/2+y, 1-z
Intramolecular	C6A2-H6A3···O5A3	0.99	2.54	3.433(7)	150	x, y, z
Intramolecular	C7A2-H7AI···O3A2	0.98	2.46	3.10(2)	122	x, y, z
Intramolecular	C6A3-H6A7···O5A4	0.99	2.57	3.477(7)	151	x, y, z
Intramolecular	C7A3-H7A7···O3A3	0.98	2.50	3.107(8)	120	x, y, z
Intramolecular	C4A4-H4A4···O6A4	1.00	2.42	2.820(7)	103	x, y, z
Intramolecular	C5A5-H5A5···O4A4	1.00	2.35	2.76(1)	103	x, y, z
Intramolecular	C7A5-H7AX···O3A5	0.98	2.59	3.14(1)	115	x, y, z
Intramolecular	C7A5-H7AX···O3C5	0.98	2.16	2.80(2)	121	x, y, z
Intermolecular	C7A5-H7AY···O3B6	0.98	2.47	3.17(1)	128	-x, 1/2+y, 2-z
Intramolecular	C4A6-H4A6···O6A6	1.00	2.41	2.795(8)	102	x, y, z
Intramolecular	C6A7-H6A5···O5A1	0.99	2.58	3.481(6)	151	x, y, z
Intermolecular	C8A7-H8AC···O3A4	0.98	2.39	2.86(1)	109	1+x, y, z
Intramolecular	C7A7-H5···O3A7	0.98	2.59	3.030(7)	107	x, y, z
Intermolecular	C2A7-H2A7···O3B2	1.00	2.55	3.514(7)	162	1-x, 1/2+y, 1-z

Table 5.4.19B: The parameters for the hydrogen bond interactions in DMB·BES for molecule B.

Interaction type	Hydrogen bond	D-H (Å)	H···A (Å)	D···A (Å)	D-H···A (°)	Symmetry code
O3-H···O2′ Hydrogen bonds						
Intramolecular	O3B7-H3B7···O2B1	0.84	1.98	2.810(7)	172	x, y, z
Intramolecular	O3B1-H3B1···O2B2	0.84	1.91	2.738(7)	170	x, y, z
Intramolecular	O3B2-H3B2···O2B3	0.84	2.03	2.848(6)	166	x, y, z
Intramolecular	O3B3-H3B3···O2B4	0.84	2.17	3.011(6)	176	x, y, z
Intramolecular	O3B4-H3B4···O2B5	0.84	2.09	2.916(6)	168	x, y, z
Intramolecular	O3B5-H3B5···O2B6	0.84	2.13	2.96(1)	172	x, y, z
Intramolecular	O3B6-H3B8···O2B7	0.84	2.08	2.914(1)	173	x, y, z
C-H···O Hydrogen bonds						
Intramolecular	C7B1-H7BF···O3B1	0.98	2.26	2.97(1)	128	x, y, z
Intermolecular	C1B2-H1B2···O1A	1.00	2.53	3.499(6)	162	-x, -1/2+y, 1-z
Intramolecular	C5B2-H5B2···O4B1	1.00	2.41	2.781(6)	101	x, y, z
Intramolecular	C6B2-H6B9···O5B3	0.99	2.56	3.49(1)	156	x, y, z
Intramolecular	C7B2-H7B4···O3B2	0.98	2.53	3.019(7)	111	x, y, z
Intermolecular	C7B2-H7B5···O3A7	0.98	2.54	3.502(7)	168	1-x, -1/2+y, 1-z
Intermolecular	C2B3-H2B3···O5A3	1.00	2.57	3.541(6)	162	x, y, z
Intramolecular	C5B3-H5B3···O4B2	1.00	2.46	2.810(6)	100	x, y, z
Intermolecular	C8B3-H8B3···O3A3	0.98	2.43	3.276(7)	144	x, y, z
Intermolecular	C2B4-H2B4···O5W	1.00	2.43	3.425(8)	173	x, y, z
Intramolecular	C6B5-H10···O5B6	0.99	2.46	3.361(9)	152	x, y, z
Intramolecular	C7B5-H12···O3B5	0.98	2.43	3.060(8)	122	x, y, z
Intermolecular	C1B6-H14···O2W	1.00	2.45	3.43(1)	166	x, y, 1+z
Intramolecular	C5B6-H5B6···O4B5	1.00	2.41	2.77(1)	100	x, y, z
Intermolecular	C2B7-H2B7···O11W	1.00	2.48	3.38(1)	148	-x, -1/2+y, 2-z
Intramolecular	C5B7-H5B7···O4B6	1.00	2.48	2.841(7)	101	x, y, z
Intermolecular	C7B7-H7BA···O3A4	0.98	2.55	3.48(1)	158	-x, -1/2+y, 2-z
Intermolecular	C7B7-H7BC···O4W	0.98	2.52	3.39(1)	147	x, y, z
Intermolecular	C8B7-H8B6···O3B4	0.98	2.58	3.554(7)	175	-x, -1/2+y, 2-z

Host molecular geometry

Tables 5.4.20A and 5.4.20B list the geometrical parameters for the O4-heptagon conformations of host molecules A and B in the complex DMB·BES, as well as the tilt angles of the individual glucose units, and Figures 5.4.19a and 5.4.19b are the keys for labelling the glucose residues. Detailed descriptions of the geometrical parameters were mentioned in Chapter 1 (section 1.2.9, pp. 13 – 15) and abbreviated descriptions are provided below in Table 5.4.20 for convenience.

With reference to both host molecules, it is evident that small levels of distortion have occurred from regular heptagonal shapes as a result of complexation, since the individual values of *l*, D and Φ of the O4-heptagon display small deviations. In addition, the degrees of

planarity of the O4-heptagons are modified, as small variations occur in the torsion angles and the deviations of the O4 atoms from the O4-heptagons (α). Furthermore, the D_3 values (ranging between 2.739(7) Å and 3.012(6) Å for molecule A, and 2.739(7) Å and 3.012(6) Å for molecule B), suggest that the steric hindrance from the methyl groups was not significant enough to hinder the formation of hydrogen bonds. This is a well-documented characteristic of DMB.[50]

Table 5.4.20A: The geometrical parameters for the host molecule A in the complex DMB·BES.

Residue	*l* (Å)	D (Å)	Φ (°)	d (°)	α[a] (Å)	D_3 (Å)	τ_2 (°)[b]
A1	5.207	4.323	125.8	0.4	0.161	2.737(6)	15.4
A2	5.095	4.460	127.1	2.6	-0.076	2.863(6)	11.8
A3	4.848	4.449	133.6	5.0	-0.102	2.775(7)	7.0
A4	5.171	4.329	125.4	-13.4	0.065	2.840(8)	8.5
A5	5.186	4.363	125.8	9.4	0.151	2.754(8)	17.0
A6	4.892	4.459	131.7	2.8	-0.219	2.745(6)	8.9
A7	4.984	4.358	129.5	-6.5	0.019	2.798(5)	4.5

[a] mean esd: 0.003 Å; [b] mean esd: 0.3°

Key to symbols
l: the distance between each O4 atom and the centroid of the O4-polygon;
D: the consecutive glycosidic O4···O4′ distances;
Φ: the O4···O4′···O4′′ angle;
d: the O4···O4′···O4′′···O4′′′ torsion angle;
α, the deviation of each O4 atom from the mean O4-plane;
D_3: the O2···O3′ intra-ring distance;
τ_2: the tilt angle: the angle between the mean O4-plane and the plane containing O4, C4, C1 and O4′ of a given glucose ring.

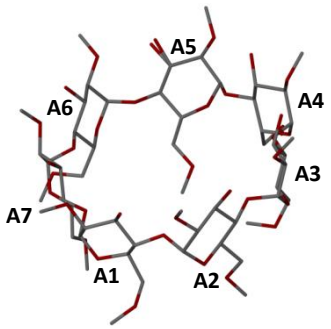


Figure 5.4.19a: The numbering scheme of the glucose residues in the DMB·BES complex unit A.

Table 5.4.20B: The geometrical parameters for the host molecule B in the complex DMB·BES.

Residue	*l* (Å)	D(Å)	Φ (°)	d(°)	α[a](Å)	D_3(Å)	τ_2 (°)[b]
B1	5.375	4.350	121.8	-9.3	-0.010	2.738(7)	8.7
B2	5.011	4.461	129.2	-1.2	-0.197	2.848(6)	4.7
B3	4.742	4.489	134.5	8.8	0.104	3.011(6)	24.5
B4	5.211	4.221	125.4	-3.8	0.154	2.916(6)	9.2
B5	5.306	4.359	122.3	-6.6	-0.180	2.96(1)	9.9
B6	4.706	4.570	136.4	4.8	-0.554	2.914(1)	27.4
B7	4.975	4.266	129.4	5.5	0.185	2.810(7)	6.8

[a] mean esd: 0.003 Å; [b] mean esd: 0.3°

Key to symbols
l: the distance between each O4 atom and the centroid of the O4-polygon;
D: the consecutive glycosidic O4···O4′ distances;
Φ: the O4···O4′···O4′′ angle;
d: the O4···O4′···O4′′···O4′′′ torsion angle;
α, the deviation of each O4 atom from the mean O4-plane;
D_3: the O2···O3′ intra-ring distance;
τ_2: the tilt angle: the angle between the mean O4-plane and the plane containing O4, C4, C1 and O4′ of a given glucose ring.

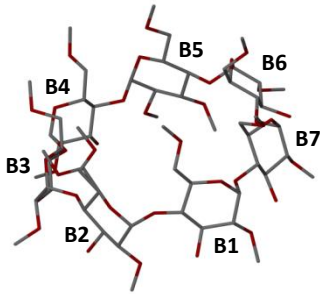


Figure 5.4.19b: The numbering scheme of the glucose residues in the DMB·BES complex unit B.

The tilt angles (τ_2) of the two DMB molecules (A and B) in the ASU further display the influence that the bimodal inclusion of the respective guest molecules has on the geometry of the CD molecules. The ranges of the tilt angles for host molecules A and B differ significantly, as the ranges are 4.5° – 17.0° and 4.7° – 27.4° respectively. This reflects significant differences in the distortion of the host molecules in the A and B complex units during complexation.

In addition, the range of the tilt angles for uncomplexed DMB is 2.8° – 27.6°,[51] which is different to what is observed for the DMB·BES complex monomeric units, A and B. This implies that the complexation of β-estradiol caused further distortion to different extents in both DMB complex monomeric units, A and B, in order to optimally accommodate the guest molecules individually through a mutual-induced fit in each monomeric unit.

Furthermore, it is apparent that the primary rims of the glucose units A1, A2, and A5, and similarly B3 and B6, are tilted significantly more towards the centre of the cavity of the DMB molecules, in comparison to the other glucose units in the host macrocycles. Lastly, the overall sizes of the tilt angles and level of distortion on molecule B are generally larger and

more pronounced in comparison to those on molecule A. This is most likely as a consequence of the different modes of inclusion of the guest molecules.

Guest molecule conformations

Close inspection of the ring conformations in the β-estradiol molecule A revealed the following: ring-A is aromatic and hence planar, ring-B adopts a half-chair conformation, ring-C is a chair-form, and ring-D is an envelope on atom C13A. The β-estradiol molecule in the complex unit B adopts the same conformations as in guest molecule A.

Small differences in the conformations of the guest molecules A and B were observed, as depicted in Figure 5.4.20, which displays an overlay of these two molecules. Overall, there is generally a good fit between the rigid scaffolds of the independent steroid molecules; however, the substituents attached to the scaffolds deviate more significantly. This is verified by the RMSD value of 0.223 Å and a maximum deviation value of 0.4983 Å (which naturally reflects the largest deviation for the substituents).

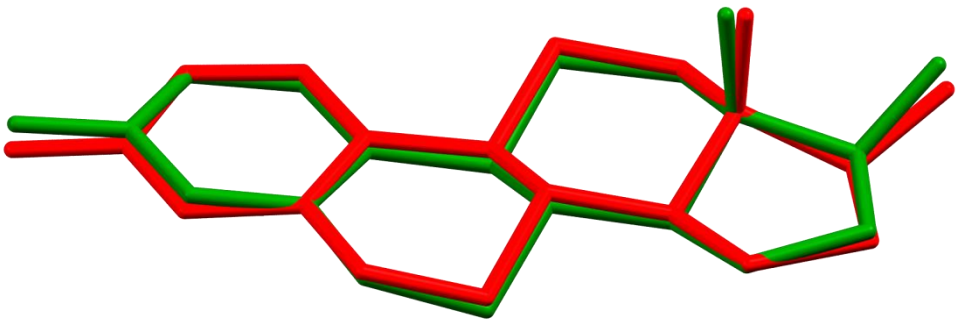


Figure 5.4.20: An overlay of the guest molecules, A (green) and B (red), which highlights the small conformational differences.

These small conformational differences of the independent guest molecules (A and B) are expected, as each has adopted a different orientation within its respective host cavity and penetrates the host cavity to a different depth. As described previously, the DMB host molecules also display different extents of distortion. Consequently, the bimodal inclusion is a result of a "mutual-induced fit" between the host and guest molecules of each complex

unit. This phenomenon of a “mutual-induced fit” is known to occur in many biological systems, yet is rarely observed in synthetic, small molecular host-guest structures.[50,52]

Crystal packing

The crystal packing arrangement incorporates a brickwork-type layered arrangement (Figures 5.4.21 and 5.4.22). This arrangement allows the guest molecule residues (from complex A) that protrude from the cavity of the CD molecule to fit into voids in between the CD molecules in the subsequent layer.

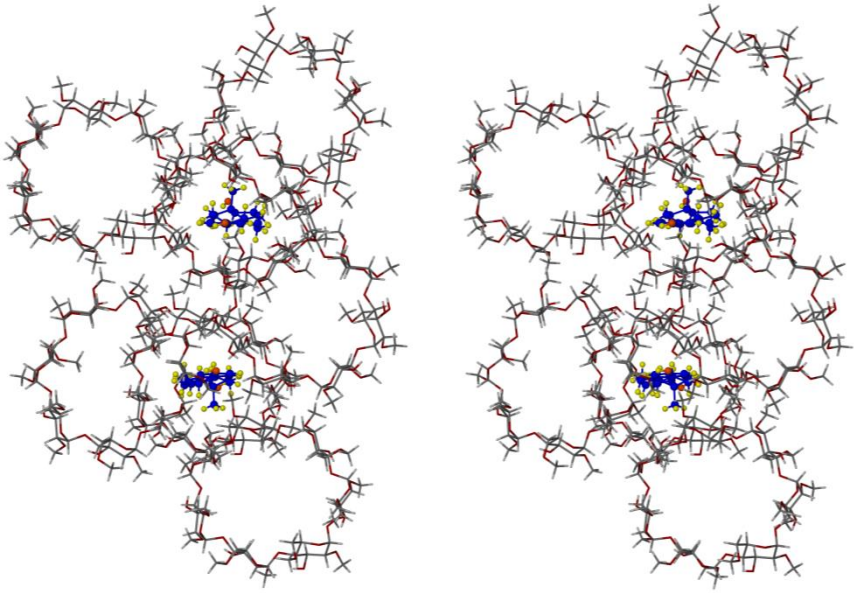


Figure 5.4.21: A topographical stereoscopic view of the brickwork-type packing displaying the guest molecule (of complex A) in the ASU in the lower layer penetrating the void space created by the host molecules in the layer above. The included guest molecules in the host cavities in the layer above are not shown, and the water molecules have also been omitted for clarity.

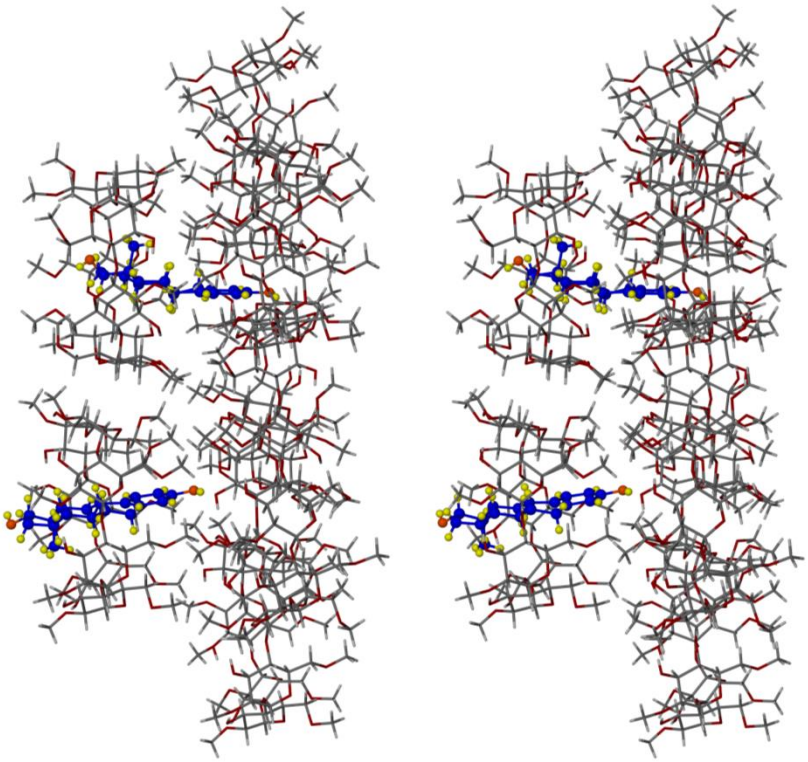
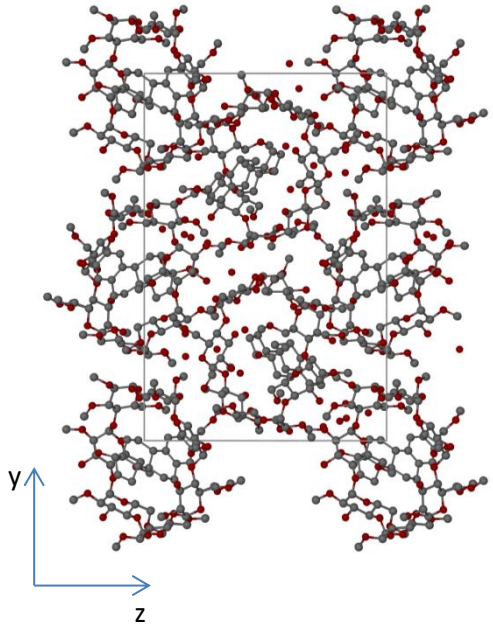


Figure 5.4.22: A side view of the brickwork-type layered packing arrangement, showing how the protruding guest residue of the included BES molecule (of complex A) in the left-hand side layer penetrates the void space in between the host molecules in the right-hand layer. The included guest molecules are not shown in the host cavities in the right-hand layer, and the water molecules have also been omitted for clarity.

Lastly, Figures 5.4.23 and 5.4.24 display the packing arrangements of DMB·BES viewed down the a- and b-axes respectively.



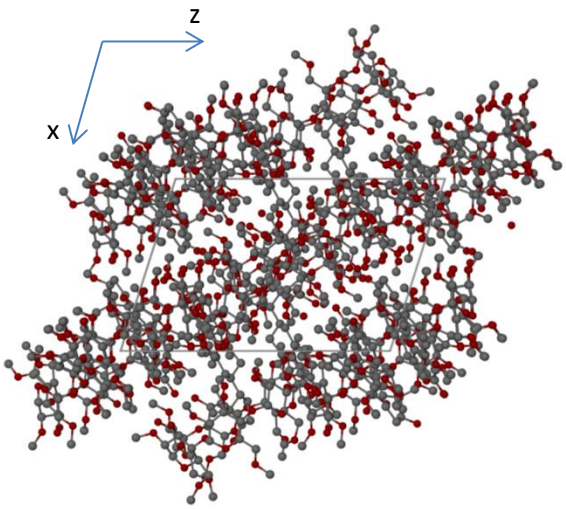


Figure 5.4.23 (left) and Figure 5.4.24 (right) displaying the packing arrangement viewed down the a-axis and the b-axis respectively. The layered arrangement of the complex units is evident in Figure 5.4.24.

PXRD analysis

The PXRD analysis indicated a good correlation between the PXRD pattern of the DMB·BES complex produced from co-precipitation experiments, and the PXRD pattern calculated from the single-crystal X-ray structure (Figure 5.4.25). As often expected, there are differences between the relative intensities of some of the peaks (particularly in the vicinity of the angular positions ~9, 15 and 20° 2θ); however, this is attributed to preferred orientation of the crystallites in the experimental sample and is thus accounted for. Therefore, it is evident that the crystal selected for the SCXRD analysis is representative of the bulk sample.

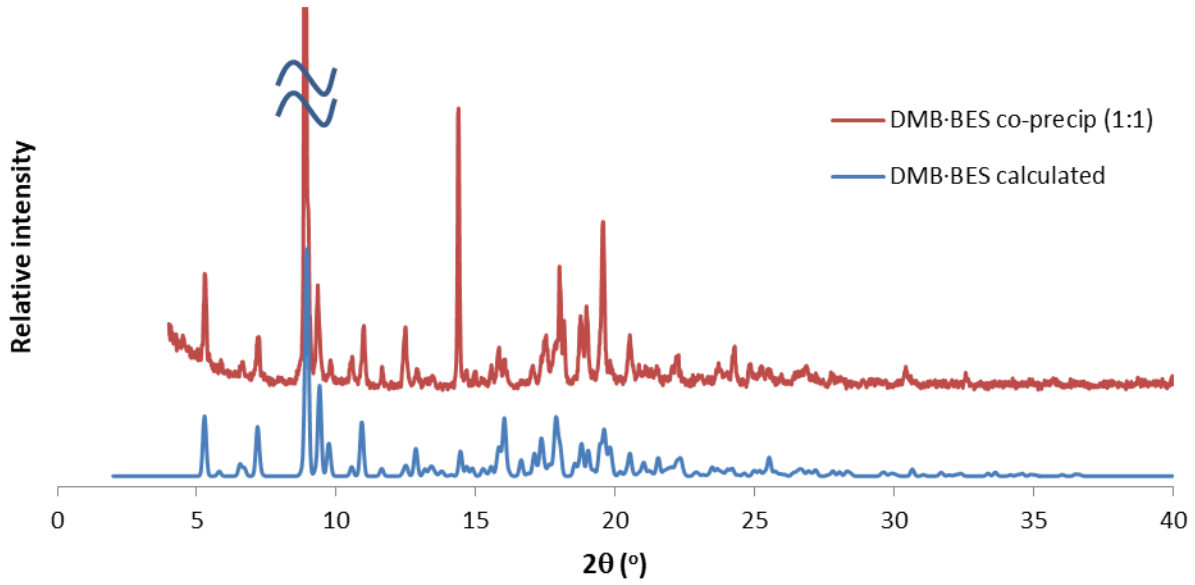


Figure 5.4.25: The PXRD pattern of DMB·BES prepared *via* co-precipitation, and the PXRD pattern calculated from the single-crystal X-ray structure of DMB·BES.

Structure solution and refinement of DMB·PRO

The crystal structure of DMB·PRO was also solved with SHELXS-97, which revealed one DMB host molecule and one PRO guest molecule in the ASU. The host atoms were initially assigned and refined isotropically with SHELXL-97,[37] and thereafter anisotropically. The thermal ellipsoids of four atoms on the host molecule were abnormally large and they were thus modelled as disordered atoms, where both components of a disordered atom were constrained to have the same U_{iso} values. These included two carbon atoms from two methoxy groups, as well as the oxygen and carbon atoms from another methoxy group (and the disorder was treated as previously described for DMB·BES). Similarly, DFIX constraints were applied to the C-O bond lengths (1.43 Å, σ = 0.01 Å), as well as the C5-C6 bond lengths (1.51 Å, σ = 0.01 Å) of the disordered pairs, and in some cases, it was necessary to reduce the standard deviation to 0.002 Å in order to enforce the restraint. The major components of these disordered atoms were C7B2 [s.o.f. = 0.55(2)], C8A2 [s.o.f. = 0.76(5)], C6B1, O6B1 and C8B1 with s.o.f.s. of 0.55(1).

The atoms of the progesterone molecule were thereafter assigned by analysing the geometry of the electron density peaks in the difference Fourier map. After the guest molecule was refined anisotropically, the carbonyl oxygen atom, O2A, displayed a large thermal ellipsoid and thus was modelled as a disordered atom. A bond length restraint of 1.20 Å (σ = 0.01 Å) was applied to both C=O lengths (C20=O2A, C20=O2B) and the components O2A and O2B were assigned a common U_{iso} value as a constraint.

The difference Fourier map displayed a very low electron density peak of 0.58 e.Å^{-3} indicating that there was partial methylation on the oxygen atom O3A5; however, after assigning this electron density peak and allowing the s.o.f. to vary, refinement of the partial atom led to a singularity (indicated by a 'non-positive definite' warning) and the partial atom was omitted from the model.

Lastly, the hydrogen atoms were thereafter assigned to both the host and guest molecules using a riding model with isotropic thermal parameters between 1.2 to 1.5 times the U_{iso} values of their parent atoms. In addition, with regard to the disordered methoxyl groups, hydrogen atoms were placed in a staggered conformation. The crystallographic data and details of the refinement are summarized in Table 5.4.21.

Table 5.4.21: The crystal data and refinement parameters for DMB·PRO.

Parameter	Value
Complex formula	$C_{56}H_{98}O_{35}\cdot C_{21}H_{30}O_2\cdot 1.1(H_2O)$
Formula weight ($g.mol^{-1}$)	1665.60
Temperature (K)	100(2)
Wavelength (Å)	0.71073
Crystal system	Monoclinic
Space group	$P2_1$
a (Å)	15.469(2)
b (Å)	17.297(2)
c (Å)	16.518(2)
α (°)	90
β (°)	101.616(2)
γ (°)	90
Volume ($Å^3$)	4329(1)
Z	2
Calculated density ($g.cm^{-3}$)	1.278
μ (mm^{-1})	0.102
F (000)	1794
Crystal size (mm)	0.08 x 0.10 x 0.22
θ-Range scanned (°)	1.34 – 25.35
Index range	h:-18, 18; k:-20, 20; l:-19, 19
No. of reflections collected	41489
No. of unique reflections	15752
Data completeness (%)	99.4
Data/restraints/parameters	15752/17/1043
S (Goodness-of-fit on F^2)	1.024
Final R indices R_1, wR_2, [I > 2σ(I)]	0.0624, 0.1578
R Indices, all data (R_1, wR_2)	0.0950, 0.1771
Largest diff. peak and hole (e. $Å^{-3}$)	0.64, -0.38

Once the model of the guest molecule was complete, the oxygen atoms of the water molecules were assigned by examining the remaining difference electron density (Δρ) peaks in the difference Fourier map that were located in positions within hydrogen bonding distance of appropriate donor or acceptor atoms. Two (Δρ) peaks, with heights 2.28 and 1.98 e.$Å^{-3}$ respectively, were identified within the cavity of the host molecule and each was initially assigned as an oxygen atom with full site-occupancy. However, after isotropic refinement, both displayed U_{iso} values exceeding 0.15 $Å^2$ and thus were rather treated as partial oxygen atoms and refined isotropically. Following further refinement, acceptable U_{iso} values for the two partial oxygen atoms resulted, the sum of their s.o.f.s totalling 1.17 water oxygen atoms per CD unit. This value correlated with the TGA results that had indicated 1.1 ± 0.2 water molecules per CD molecule. No further partial oxygen atoms were identified in the difference Fourier map, as the remaining Δρ peak heights were less than 0.64 e.$Å^{-3}$ and

not chemically reasonable, and they were thus considered negligible. Table 5.4.22 provides the s.o.f. values and U_{iso} parameters of the partial water molecules after the final refinement.

Table 5.4.22: The water oxygen sites that were identified for DMB·PRO, with their respective s.o.f.s and U_{iso} values.

Atom	s.o.f.	U_{iso} (Å^2)
O1W	0.64(2)	0.072(4)
O2W	0.53(2)	0.058(4)

Molecular structure of DMB·PRO

Figure 5.4.26 is a schematic diagram of the steroid scaffold with the ring designations and reference to these will follow in the discussion below. The ASU of DMB·PRO (Figure 5.4.27) consists of one DMB molecule, one progesterone molecule and ~1.2 water molecules (disordered over two sites). The disorder on the host molecule is evident at the bottom right of Figure 5.4.27, where a C6-O6-C8 chain is disordered over two positions, together with two additional methoxy carbon atoms that are also disordered over two positions. In addition, the carbonyl oxygen atom that is included in the cavity is disordered over two positions.

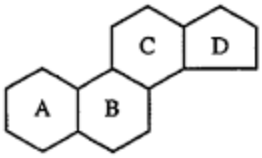


Figure 5.4.26: Steroid scaffold with labelled rings.

The conformations of the individual rings in the progesterone molecule are as follows: ring-A adopts an envelope conformation (^{2}E, on atom C1), both rings B and C are chair-forms, and ring-D is an envelope on atom C13.

With reference to Figure 5.4.26, the rings C and D of the progesterone molecule (which amount to approximately half of the progesterone molecule) are included in the host cavity, as illustrated in the cut-away space-filling model of the ASU (Figure 5.4.28).

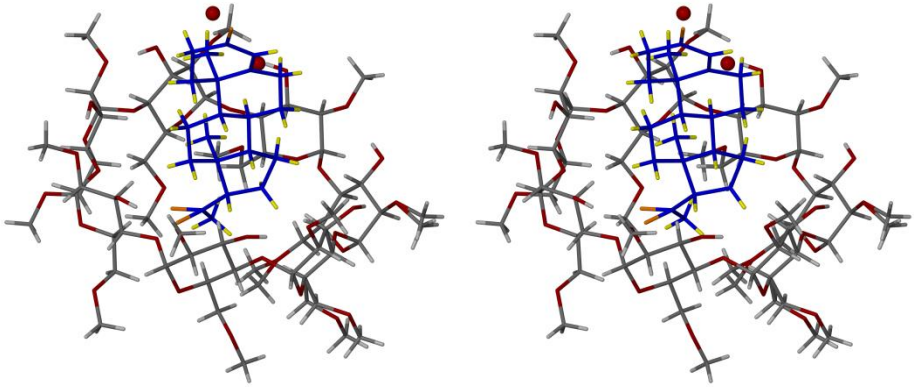


Figure 5.4.27: A stereoscopic view of the ASU of DMB·PRO. An alternative colour scheme was used to differentiate the guest atoms: carbon atoms (blue), hydrogen atoms (yellow) and oxygen atoms (orange).

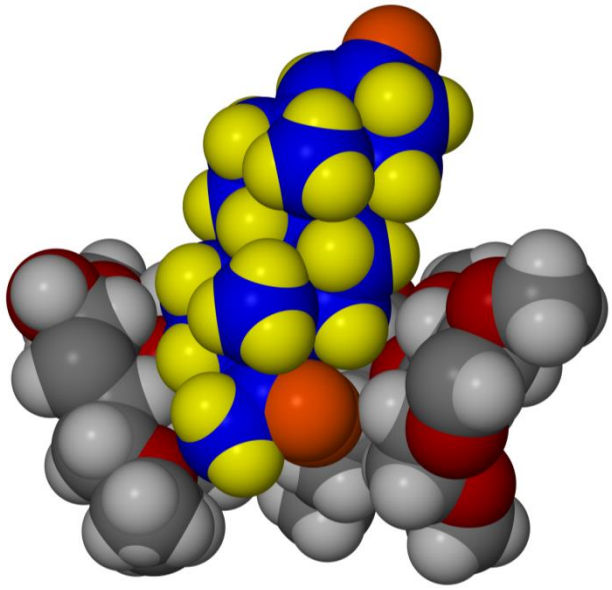


Figure 5.4.28: A cut-away view of the ASU displaying the extent and mode of inclusion of the progesterone molecule.

Hydrogen bonding interactions involving the host, guest and water molecules

The only significant intermolecular interaction between the host and the guest molecules is of the type C-H···O, namely C5A6-H5A6···O2B, occurring between a host methine group on the A6 glucose unit of the DMB molecule and one component of the disordered guest carbonyl oxygen atom (Figure 5.4.29).

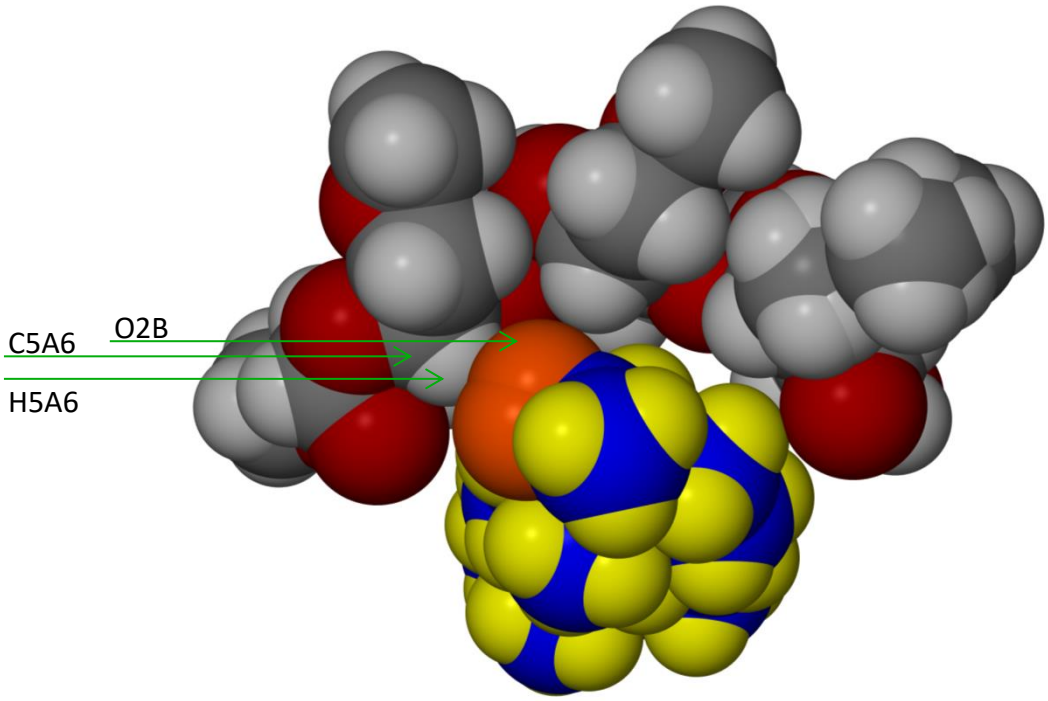


Figure 5.4.29: Host-guest intermolecular hydrogen bonding.

Figure 5.4.30 displays the water-host and water-water hydrogen bonding interactions taking place, and it was evident that no water-guest hydrogen bonding interactions occurred. It was inferred that hydrogen bonding involving the water oxygen atoms occurred only with the water molecules acting as hydrogen bond donors. Table 5.4.23 provides the parameters for the above-mentioned interactions.

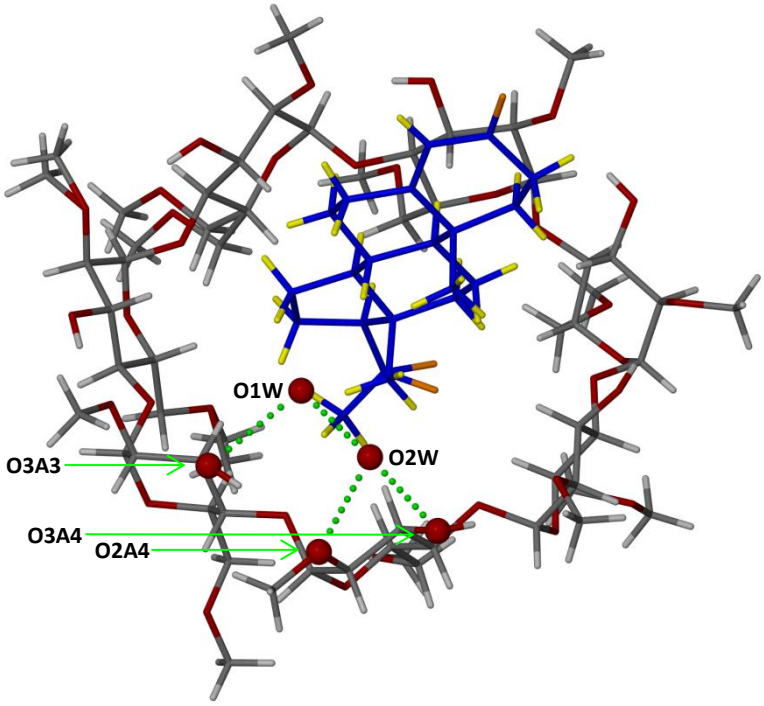


Figure 5.4.30: The water-host and water-water hydrogen bonding in the ASU. The atoms involved in the bonding have been labelled and represented as red spheres and the hydrogen bonds are represented by green dotted lines.

Table 5.4.23: The host-guest, host-water and water-water hydrogen bond interactions.

Hydrogen bond	D-H (Å)	H···A (Å)	D···A (Å)	D-H···A (°)	Symmetry code
C5A6-H5A6···O2B	1.00	2.52	3.40(1)	147	x, y, z
O3A4···O2W*	-	-	2.93(1)	-	x, y, z
O2A4···O2W*	-	-	2.92(1)	-	x, y, z
O5A3···O1W*	-	-	3.10(1)	-	2-x, -1/2+y, 2-z
O6A3···O1W*	-	-	3.07(1)	-	2-x, -1/2+y, 2-z
O3A3···O1W*	-	-	2.80(1)	-	x, y, z
O1W···O2W*	-	-	2.79(1)	-	x, y, z

*The water oxygen atom is the hydrogen bond donor

Host intramolecular and intermolecular hydrogen bonding

As with DMB·BES, a series of intramolecular hydrogen bonds O2-H···O3' that form a 'belt' on the secondary rim of the CD molecule is also observed in DMB·PRO, as displayed in Figure 5.4.31. This is a characteristic feature of the DMB molecule which reinforces its heptagonal geometry, and these were the only hydrogen bonds of the type O-H···O to occur.

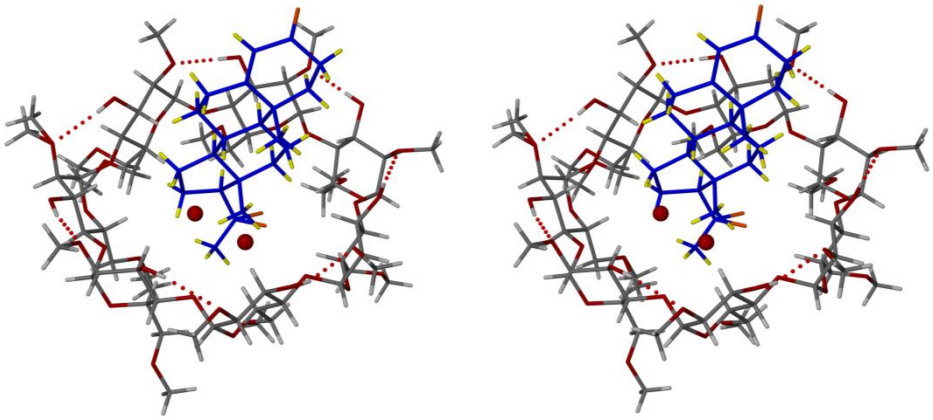


Figure 5.4.31: A stereoscopic view of the host intramolecular hydrogen bonding.

In addition, there were numerous C-H···O hydrogen bonds which were also observed to occur between symmetry-generated molecules and assist in maintaining the cohesion of the DMB molecules in the crystal structure. The C···O distances of these intermolecular hydrogen bonds ranged between 3.255(7) Å and 3.486(8) Å. The C···O intramolecular hydrogen bond interactions were also listed for completeness, despite many of them being geometrically unfavourable and hence very weakly attractive. Table 5.4.24 summarises all the hydrogen bond parameters in DMB·PRO.

Table 5.4.24: The parameters for the hydrogen bond interactions in DMB·PRO.

Interaction type	Hydrogen bond	D-H (Å)	H···A (Å)	D···A (Å)	D-H···A (°)	Symmetry code
O3-H···O2′ Hydrogen bonds						
Intramolecular	O3A7-H3A7···O2A1	0.84	1.97	2.799(7)	168	x, y, z
Intramolecular	O3A1-H3A8···O2A2	0.84	2.23	3.067(8)	175	x, y, z
Intramolecular	O3A2-H3A2···O2A3	0.84	2.00	2.821(7)	165	x, y, z
Intramolecular	O3A3-H3A3···O2A4	0.84	2.46	3.298(7)	173	x, y, z
Intramolecular	O3A4-H3A4···O2A5	0.84	2.21	3.013(7)	159	x, y, z
Intramolecular	O3A5-H3A5···O2A6	0.84	2.18	3.015(7)	175	x, y, z
Intramolecular	O3A6-H3A6···O2A7	0.84	2.00	2.836(7)	179	x, y, z
C-H···O Hydrogen bonds						
Intermolecular	C1A1-H1A1···O3A4	1.00	2.53	3.342(8)	138	-1+x, y, z
Intramolecular	C4A1-H4A1···O6A1	1.00	2.25	2.73(1)	108	x, y, z
Intramolecular	C7A1-H7AI···O3A1	0.98	2.55	3.14(1)	119	x, y, z
Intramolecular	C1A2-H1A2···O6A1	1.00	2.59	3.28(2)	126	x, y, z
Intramolecular	C5A2-H5A2···O4A1	1.00	2.39	2.77(1)	102	x, y, z
Intramolecular	C5A3-H5A3···O4A2	1.00	2.45	2.804(8)	100	x, y, z
Intramolecular	C6A3-H6AX···O5A4	0.99	2.42	3.180(8)	133	x, y, z
Intramolecular	C6A3-H6AX···O6A4	0.99	2.58	3.524(8)	159	x, y, z
Intermolecular	C8A3-H8A7···O2A3	0.98	2.57	3.382(9)	140	2-x, -1/2+y, 2-z
Intermolecular	C2A4-H2A4···O5A1	1.00	2.54	3.486(8)	158	1+x, y, z
Intramolecular	C5A4-H5A4···O4A3	1.00	2.42	2.799(6)	102	x, y, z
Intermolecular	C7A4-H7AC···O6A1	0.98	2.41	3.39(2)	175	1+x, y, z
Intermolecular	C8A4-H8A6···O3A5	0.98	2.42	3.383(9)	168	2-x, -1/2+y, 1-z
Intramolecular	C4A5-H4A5···O6A5	1.00	2.50	2.846(6)	100	x, y, z
Intramolecular	C5A5-H5A5···O4A4	1.00	2.48	2.821(7)	100	x, y, z
Intramolecular	C6A5-H6A2···O5A6	0.99	2.58	3.267(7)	127	x, y, z
Intermolecular	C1A6-H1A6···O3A2	1.00	2.48	3.255(7)	134	x, y, -1+z
Intramolecular	C4A6-H4A6···O6A6	1.00	2.44	2.852(7)	104	x, y, z
Intermolecular	C5A6-H5A6···O2B	1.00	2.52	3.40(1)	147	x, y, z
Intramolecular	C6B1-H6B2···O5A2	0.99	2.49	3.27(2)	135	x, y, z
Intramolecular	C4A7-H4A7···O6A7	1.00	2.40	2.807(6)	103	x, y, z

Host molecular geometry

The conformation of the O4-heptagon of the host molecule in the complex DMB·PRO is defined by the geometrical parameters listed in Table 5.4.25, with reference to Figure 5.4.32 which shows the numbering of the glucose residues. As mentioned in previous sections, detailed descriptions of the geometrical parameters were described in Chapter 1 (section 1.2.9, pp. 13 – 15) and for convenience abbreviated descriptions are shown below in Table 5.4.25.

The variations in the values of *l*, D and Φ occurring in the O4-heptagon of CD molecules on complexation indicate distortion. In addition, the degree of planarity of the O4-heptagon in

DMB·PRO is also modified (as was the case for DMB·BES), since small variations occur in the torsion angles and the deviations of the O4 atoms from the O4-heptagon (α). Furthermore, the D_3 values, which ranged between 2.799(7) Å and 3.298(7) Å, signified that there was not sufficient steric hindrance from the methyl groups to inhibit intramolecular hydrogen bonding from occurring. As mentioned previously, this is a typical characteristic of DMB complex structures.

Table 5.4.25: The geometrical parameters for the host molecule in the complex DMB·PRO.

Residue	l (Å)	D (Å)	Φ (°)	d (°)	α[a] (Å)	D_3 (Å)	τ_2 (°)[b]
A1	5.137	4.243	125.6	-7.7	-0.020	2.799(7)	3.7
A2	5.197	4.416	126.0	0.4	-0.177	3.067(8)	24.5
A3	4.935	4.447	130.4	4.0	0.088	2.821(7)	9.5
A4	4.933	4.420	130.8	3.2	0.113	3.298(7)	21.1
A5	4.200	4.269	125.2	-13.1	-0.096	3.013(7)	11.2
A6	5.115	4.417	126.2	9.3	-0.134	3.015(7)	21.3
A7	4.769	4.466	134.7	3.5	0.225	2.836(7)	13.3

[a] mean esd: 0.003 Å; [b] mean esd: 0.2°

Key to symbols
l: the distance between each O4 atom and the centroid of the O4-polygon;
D: the consecutive glycosidic O4···O4′ distances;
Φ: the O4···O4′···O4′′ angle;
d: the O4···O4′···O4′′···O4′′′ torsion angle;
α, the deviation of each O4 atom from the mean O4-plane;
D_3: the O2···O3′ intra-ring distance;
τ_2: the tilt angle: the angle between the mean O4-plane and the plane containing O4, C4, C1 and O4′of a given glucose ring.

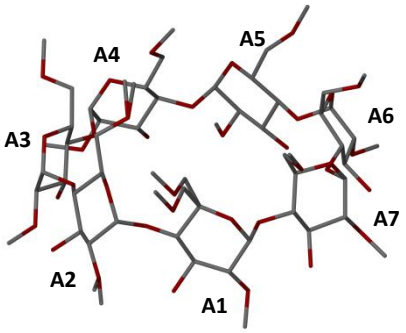


Figure 5.4.32: The numbering scheme of the DMB glucose units in DMB·PRO.

The tilt angles (τ_2) for the individual glucose units span a broad range of values. However, this range is similar to the tilt angle range for uncomplexed DMB (2.8° – 27.6°),[51] indicating that the inclusion of progesterone did not significantly alter the geometry of the glucose tilt angles, but rather merely caused small shifts to accommodate the guest molecule. Lastly, the results indicated that the glucose units A2, A4 and A6 were those that were most tilted towards the centre of the cavity of the host DMB molecule.

Crystal packing

The packing arrangement is based on a layered brickwork pattern, where one of the monomeric units positions itself below the centre of the void space created by the arrangement of four monomeric units in the layer above. As previously mentioned, a significant portion of the steroid guest molecule protrudes from the cavity of its CD host molecule and consequently occupies the void space between the four monomeric CD complex units in the layer above. Figures 5.4.33 and 5.4.34 display stereoscopic views of this packing arrangement.

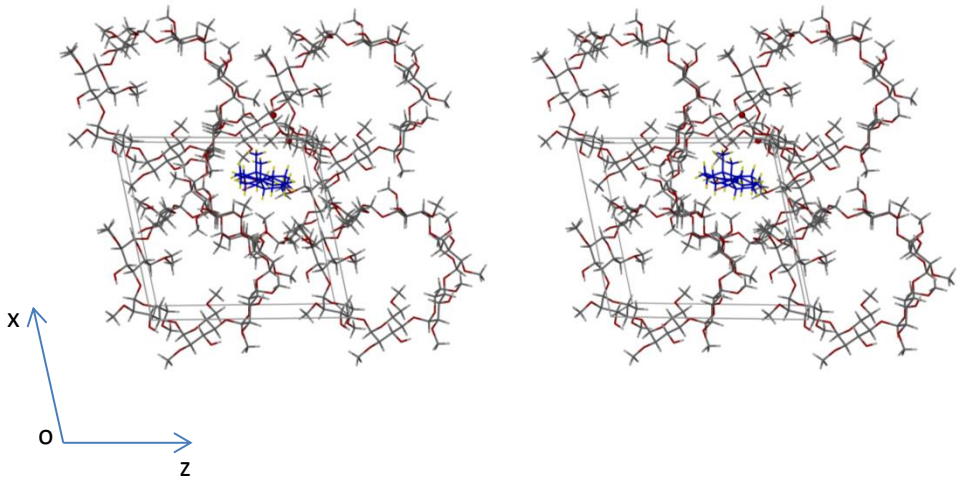


Figure 5.4.33: A stereoscopic view of the packing arrangement of DMB·PRO viewed down the b-axis towards the origin, displaying the penetration of the guest molecule residue into the void space between the host molecules positioned in the layer above. The included guest molecules in the top layer were omitted for clarity.

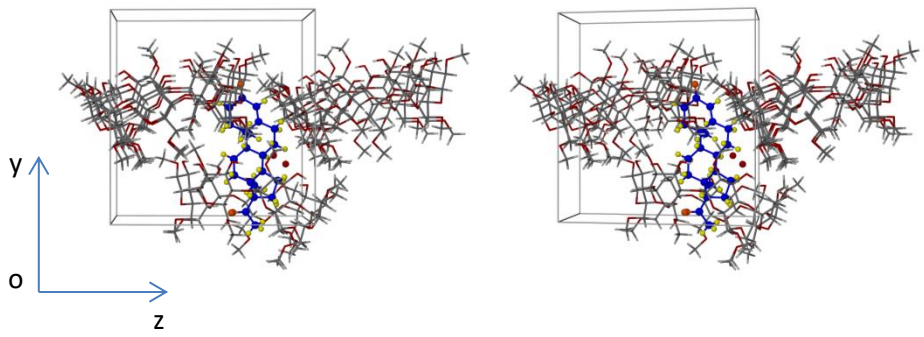


Figure 5.4.34: A stereoscopic view of the packing arrangement of DMB·PRO viewed down the a-axis displaying the penetration of the guest molecule residue (represented as a ball and stick model) into the void space between the CD molecules in the layer above. The included guest molecules in the top layer were omitted for clarity.

PXRD analysis

The PXRD pattern calculated from a single crystal of DMB·PRO did not correlate with the PXRD pattern from a crystalline sample prepared *via* co-precipitation (Figure 5.4.35). A plausible explanation for this is that DMB·PRO is not very stable at ambient temperatures. The HSM analysis (section 5.2.4.5 pp. 270 – 271) displayed an early dehydration and the loss of crystallinity at 31.1 ^{o}C, and the DSC curve (section 5.2.4.7 p. 275) indicated the occurrence of a phase transition with the first peak occurring at 56.5 $\pm$ 0.4 ^{o}C. Consequently, it is evident that DMB·PRO is heat-sensitive and thus when the crystals were exposed to the X-rays in a Bruker D2 Phaser desktop powder diffractometer for an extended period of time, structural changes could have occurred, given also that the temperature inside the instrument is slightly above ambient temperature when it is recording the sample.

The experimental PXRD pattern produced *via* co-precipitation has fewer peaks than the calculated PXRD pattern, which signified that contamination of the starting materials and resultant formation of a physical mixture is not the case for the experimental PXRD pattern. Therefore, it is very possible that the low thermal stability of DMB·PRO prevented recording of an accurate representation of its experimental PXRD pattern.

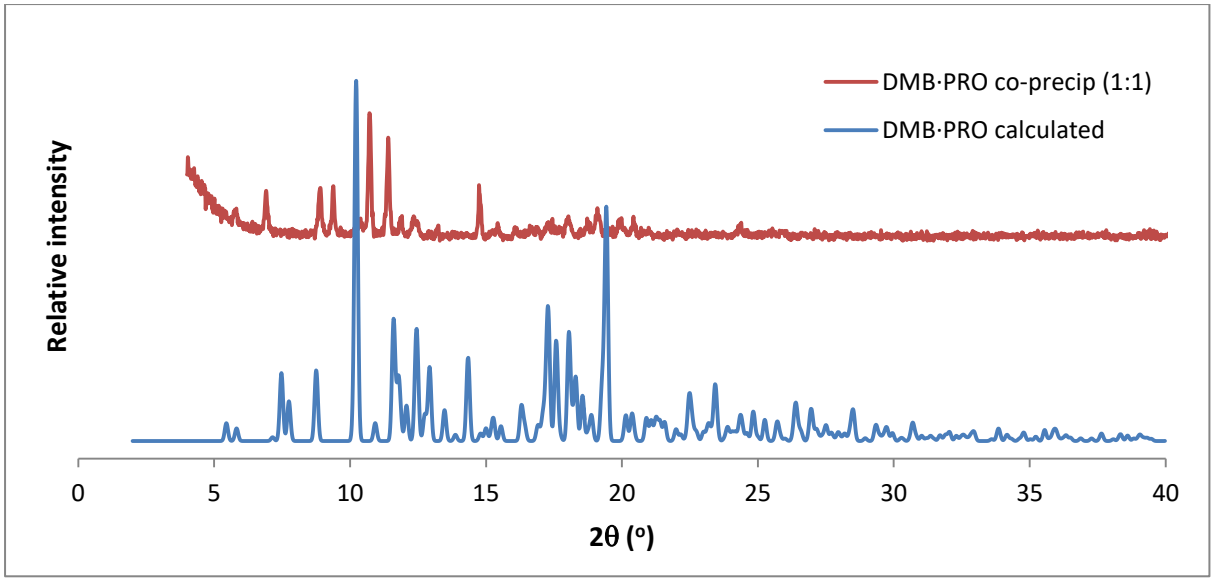


Figure 5.4.35: The PXRD pattern of DMB·PRO prepared *via* co-precipitation, and the PXRD pattern calculated from the single-crystal X-ray structure of DMB·PRO.

In summary, the DMB·BES and DMB·PRO complexes were successfully characterised, with the analytical data definitively confirming the formation of these inclusion complexes. However, solubility experiments were not conducted owing to the expense of scaling up co-precipitation experiments to produce a sufficient quantity of samples for solubility analysis. The full molecular formulae of these hydrated complexes are DMB·BES·5.8(H_2O) and DMB·PRO·1.1(H_2O). Furthermore, the single-crystal X-ray structures of these complexes are the first for CD inclusion complexes of the biologically highly relevant steroidal APIs, β-estradiol and progesterone, revealing their modes of inclusion.

References

(1) Okamoto, S. Eye Drops and Kits for Treatment of Eye Disease. WO2006040839 A1 2006-04-20, 2006.

(2) Okamoto, S. Ophthalmic Preparations Containing Steroids. WO2004093882 A1 2004-11-04, 2004.

(3) Pharmatech GmbH. Water-Soluble Inclusion Complexes of Drugs with Methyl-β-Cyclodextrin. DE4207922 A1 1993-09-23, 1993.

(4) Wang, X.; He, H.; Leng, W.; Tang, X. Evaluation of Brain-Targeting for the Nasal Delivery of Estradiol by the Microdialysis Method. *Int. J. Pharm.* **2006**, *317* (1), 40–46. https://doi.org/10.1016/j.ijpharm.2006.02.055.

(5) Lee, B. J. Site-Specific Release Preparation Containing Inclusion Complex. KR211222 B1 1999-07-15, 1999.

(6) Hansen, J.; Mollgaard, B. Transdermal Pharmaceutical Composition Containing Cyclodextrin Inclusion Compounds, 1991.

(7) Hesler, M.; Schwarz, D. H.; Dähnhardt-Pfeiffer, S.; Wagner, S.; von Briesen, H.; Wenz, G.; Kohl, Y. Synthesis and in Vitro Evaluation of Cyclodextrin Hyaluronic Acid Conjugates as a New Candidate for Intestinal Drug Carrier for Steroid Hormones. *Eur. J. Pharm. Sci.* **2020**, *143*, 105181. https://doi.org/10.1016/j.ejps.2019.105181.

(8) Caliceti, P.; Salmaso, S.; Semenzato, A.; Carofiglio, T.; Fornasier, R.; Fermeglia, M.; Ferrone, M.; Pricl, S. Synthesis and Physicochemical Characterization of Folate−Cyclodextrin Bioconjugate for Active Drug Delivery. *Bioconjug. Chem.* **2003**, *14* (5), 899–908. https://doi.org/10.1021/bc034080i.

(9) Yañez, C.; Basquinzay, R. Chronocoulometry Diffusion Coefficients as a Measure of Cyclodextrin–Estradiol Complex Association. *J. Electroanal. Chem.* **2008**, *622* (2), 242–245. https://doi.org/10.1016/j.jelechem.2008.06.005.

(10) Yañez, C.; Basualdo, J.; Jara-Ulloa, P.; Squella, J. A. Inclusion Complexes of Estrone and Estradiol Withβ-Cyclodextrin: Voltammetric and HPLC Studies. *J. Phys. Org. Chem.* **2007**, *20* (7), 499–505. https://doi.org/10.1002/poc.1186.

(11) Pérez, R. L.; Escandar, G. M. Spectrofluorimetric Study of Estrogen–Cyclodextrin Inclusion Complexes in Aqueous Systems. *Analyst* **2013**, *138* (4), 1239. https://doi.org/10.1039/c2an36395j.

(12) Arafa, R. M.; Yehia, A. M.; Abbas, S. S.; Amer, S. M. Exploiting Steroid–Cyclodextrin Complexes for Selective Determination of Estradiol Valerate and Norethisterone Acetate by Synchronous Fluorescence Spectrofluorimetry. *Spectrochim. Acta Part A Mol. Biomol. Spectrosc.* **2019**, *222*, 117237. https://doi.org/10.1016/j.saa.2019.117237.

(13) Takahashi, K.; Kaburagi, W.; Narusawa, T. Molecular Structure of Estradiol-Cyclodextrin Inclusion Complexes: Strategy for Estimation of Multi Inclusion Complexes. *Tokyo Kogei Daigaku Kogakubu Kiyo* **2012**, *35* (1), 87–94.

(14) Zoppetti, G.; Puppini, N.; Pizzutti, M.; Fini, A.; Giovani, T.; Comini, S. Water Soluble Progesterone–Hydroxypropyl-β-Cyclodextrin Complex for Injectable Formulations. *J. Incl. Phenom. Macrocycl. Chem.* **2007**, *57* (1–4), 283–288. https://doi.org/10.1007/s10847-006-9174-2.

(15) Másson, M.; Karlsson, F. J.; Valdimarsdóttir, M.; Magnúsdóttir, K.; Loftsson, T. Cyclodextrins and the Liquid-Liquid Phase Distribution of Progesterone, Estrone and Prednicarbate. *J. Incl. Phenom. Macrocycl. Chem.* **2007**, *57* (1–4), 481–487. https://doi.org/10.1007/s10847-006-9238-3.

(16) Liu, F.; Kildsig, D. O.; Mitra, A. K. Beta-Cyclodextrin/Steroid Complexation: Effect of Steroid Structure on Association Equilibria. *Pharm. Res.* **1990**, *7*, 869–873. https://doi.org/10.1023/A:1015973218303.

(17) Lin, S.-Z.; Skiba, M.; Wouessidjewe, D.; Agnus, B.; Duchene, D. Inclusion Complexes of Progesterone and Its Analog X with Cyclodextrins. In *Minutes of the International Symposium on Cyclodextrins*; 1992; pp 460–465.

(18) Lahiani-Skiba, M.; Barbot, C.; Bounoure, F.; Joudieh, S.; Skiba, M. Solubility and Dissolution Rate of Progesterone-Cyclodextrin-Polymer Systems. *Drug Dev. Ind. Pharm.* **2006**, *32* (9), 1043–1058. https://doi.org/10.1080/03639040600897093.

(19) Cerchiara, T. Effect of Chitosan on Progesterone Release from Hydroxypropyl-β-Cyclodextrin Complexes. *Int. J. Pharm.* **2003**, *258* (1–2), 209–215. https://doi.org/10.1016/S0378-5173(03)00202-3.

(20) Zoppetti, G.; Puppini, N.; Ospitali, F.; Fini, A. Solid State Characterization of Progesterone in a Freeze Dried 1:2 Progesterone/HPBCD Mixture. *J. Pharm. Sci.* **2007**, *96* (7), 1729–1736. https://doi.org/10.1002/jps.20671.

(21) Kanehito, K.; Kazuo, Y. Solubilization of Pharmaceuticals by Maltosyl-β-Cyclodextrin. JP63135402 A 1988-06-07, 1988.

(22) Gedeon, R.; Hung, V. G. R. Inclusion Complexes of Steroids with γ-Cyclodextrin and Pharmaceutical Compositions Containing Them. BE894825 A1 1983-02-14, 1983.

(23) Shangraw, R. F.; Pande, G. S.; Gala, P. Characterization of the Tableting Properties of β-Cyclodextrin and the Effects of Processing Variables on Inclusion Complex Formation, Compactibility and Dissolution. *Drug Dev. Ind. Pharm.* **1992**, *18* (17), 1831–1851. https://doi.org/10.3109/03639049209046334.

(24) Schipper, N. G. M.; Hermens, W. A. J. J.; Romeyn, S. G.; Verhoef, J.; Merkus, F. W. H. M. Nasal Absorption of 17-Beta-Estradiol and Progesterone from a Dimethyl-Cyclodextrin Inclusion Formulation in Rats. *Int. J. Pharm.* **1990**, *64* (1), 61–66. https://doi.org/10.1016/0378-5173(90)90179-8.

(25) Pitha, J. Verifiable Absorption Drug Delivery Form Based on Cyclodextrins. US20040048831 A1 2004-03-11, 2004.

(26) Caballero, J.; Zamora, C.; Aguayo, D.; Yañez, C.; González-Nilo, F. D. Study of the Interaction between Progesterone and β-Cyclodextrin by Electrochemical Techniques and Steered Molecular Dynamics. *J. Phys. Chem. B* **2008**, *112* (33), 10194–10201. https://doi.org/10.1021/jp8006766.

(27) Wang, X.; Xuan, Z. Preparation of Progesterone-β-Cyclodextrin Inclusion Compound. *Zhongguo Yiyuan Yaoxue Zazhi* **2003**, *23* (12), 719–721.

(28) Muraoka, A.; Tokumura, T.; Machida, Y. In Vitro Evaluation of Cinnarizine as a Competing Agent to β-Cyclodextrin Inclusion Complexes: Effect of Cinnarizine on the Membrane Permeation Rate of Progesterone from Its β-Cyclodextrin Inclusion Complex. *Yakugaku Zasshi* **2008**, *128* (1), 89–95. https://doi.org/10.1248/yakushi.128.89.

(29) Memişoğlu, E.; Bochot, A.; Şen, M.; Duchêne, D.; Hıncal, A. A. Non-Surfactant Nanospheres of Progesterone Inclusion Complexes with Amphiphilic β-Cyclodextrins. *Int. J. Pharm.* **2003**, *251* (1–2), 143–153. https://doi.org/10.1016/S0378-5173(02)00593-8.

(30) Luppi, B.; Cerchiara, T.; Bigucci, F.; Caponio, D.; Zecchi, V. Bovine Serum Albumin Nanospheres Carrying Progesterone Inclusion Complexes. *Drug Deliv.* **2005**, *12* (5), 281–287. https://doi.org/10.1080/10717540500176704.

(31) Da Silveira, M.; Ponchel, G.; Duchene, D.; Couvreur, P.; Puisieux, F. Nanoparticles Comprising Polyisobutylcyanoacrylate and Cyclodextrins. WO9943359 A1 1999-09-02, 1999.

(32) Cavalli, R. Solid Lipid Nanoparticles as Carriers of Hydrocortisone and Progesterone Complexes with β-Cyclodextrins. *Int. J. Pharm.* **1999**, *182* (1), 59–69. https://doi.org/10.1016/S0378-5173(99)00066-6.

(33) Guedes, L.; Morgon, N.; Martins, M.; Pessine, F. Imiquimod/β-Cyclodextrin Inclusion Complex: Experimental and Theoretical Studies. *J. Braz. Chem. Soc.* **2020**. https://doi.org/10.21577/0103-5053.20200060.

(34) Griffith, V. J. Physicochemical Characterisation of Cyclodextrin-Drug Complexes, University of Cape Town, 1996.

(35) XPREP, Data Preparation and Reciprocal Space Exploration. Version 2008/2, Bruker Analytical X-Ray Systems. 2008.

(36) Groom, C. R.; Bruno, I. J.; Lightfoot, M. P.; Ward, S. C. The Cambridge Structural Database. *Acta Crystallogr. Sect. B Struct. Sci. Cryst. Eng. Mater.* **2016**, *72* (2), 171–179. https://doi.org/10.1107/S2052520616003954.

(37) Sheldrick, G. M. A Short History of SHELX. *Acta Crystallogr. Sect. A Found. Crystallogr.* **2008**, *64* (1), 112–122.

(38) Spek, A. L. PLATON SQUEEZE: A Tool for the Calculation of the Disordered Solvent Contribution to the Calculated Structure Factors. *Acta Crystallogr. Sect. C Struct. Chem.* **2015**, *71* (1), 9–18. https://doi.org/10.1107/S2053229614024929.

(39) Spek, A. L. PLATON. *Acta Crystallogr.* **2009**, *D65*, 148–155.

(40) de Vries, E. J. C.; Caira, M. R.; Bogdan, M.; Farcas, S. I.; Bogdan, D. Inclusion of Parabens in β-Cyclodextrin: A Solution NMR and X-Ray Structural Investigation. *Supramol. Chem.* **2009**, *21* (5), 358–366. https://doi.org/10.1080/10610270801956202.

(41) Betzel, C.; Saenger, W.; Hingerty, B. E.; Brown, G. M. Topography of Cyclodextrin Inclusion Complexes, Part 20. Circular and Flip-Flop Hydrogen Bonding in .Beta.-Cyclodextrin Undecahydrate: A Neutron Diffraction Study. *J. Am. Chem. Soc.* **1984**, *106* (24), 7545–7557. https://doi.org/10.1021/ja00336a039.

(42) Steiner, T.; Koellner, G. Crystalline .Beta.-Cyclodextrin Hydrate at Various Humidities: Fast, Continuous, and Reversible Dehydration Studied by X-Ray Diffraction. *J. Am. Chem. Soc.* **1994**, *116* (12), 5122–5128. https://doi.org/10.1021/ja00091a014.

(43) Steiner, T.; Saenger, W. Channel-Type Crystal Packing in the Very Rare Space Group P 42 1 2 with Z ' = 3/4: Crystal Structure of the Complex γ-Cyclodextrin–Methanol– n -Hydrate. *Acta Crystallogr. Sect. B Struct. Sci.* **1998**, *54* (4), 450–455. https://doi.org/10.1107/S0108768197014547.

(44) Caira, M. R. On the Isostructurality of Cyclodextrin Inclusion Complexes and Its Practical Utility. *Rev. Roum. Chim.* **2001**, *46* (4), 371–386.

(45) Yalkowsky, S.H., He, Y. *Handbook of Aqueous Solubility Data: An Extensive Compilation of Aqueous Solubility Data for Organic Compounds Extracted from the AQUASOL DATAbASE*; CRC Press LLC, Boca Raton, FL., 2003.

(46) National Center for Biotechnology Information (2020). PubChem Compound Summary for CID 5757, Estradiol. https://pubchem.ncbi.nlm.nih.gov/compound/Estradiol (accessed Jan 3, 2022).

(47) Loftsson, T.; Brewster, M. E. Pharmaceutical Applications of Cyclodextrins: Basic Science and Product Development. *J. Pharm. Pharmacol.* **2010**, *62* (11), 1607–1621. https://doi.org/10.1111/j.2042-7158.2010.01030.x.

(48) Saokham, P.; Loftsson, T. γ-Cyclodextrin. *Int. J. Pharm.* **2017**, *516* (1–2), 278–292. https://doi.org/10.1016/j.ijpharm.2016.10.062.

(49) Merck, Sigma-Aldrich https://www.sigmaaldrich.com/ZA/en/product/sigma/h0513 (accessed Aug 6, 2020).

(50) Trollope, L.; Cruickshank, D. L.; Noonan, T.; Bourne, S. A.; Sorrenti, M.; Catenacci, L.; Caira, M. R. Inclusion of Trans -Resveratrol in Methylated Cyclodextrins: Synthesis and Solid-State Structures. *Beilstein J. Org. Chem.* **2014**, *10*, 3136–3151. https://doi.org/10.3762/bjoc.10.331.

(51) Aree, T.; Hoier, H.; Schulz, B.; Reck, G.; Saenger, W. Novel Type of Thermostable Channel Clathrate Hydrate Formed by Heptakis(2,6-Di-O-Methyl)-β-Cyclodextrin·15 H2O—A Paradigm of the Hydrophobic Effect. *Angew. Chemie Int. Ed.* **2000**, *39* (5), 897–899. https://doi.org/10.1002/(SICI)1521-3773(20000303)39:5<897::AID-ANIE897>3.0.CO;2-R.

(52) Caira, M. R.; Bourne, S. A.; Samsodien, H.; Smith, V. J. Inclusion Complexes of 2-Methoxyestradiol with Dimethylated and Permethylated β-Cyclodextrins: Models for Cyclodextrin–Steroid Interaction. *Beilstein J. Org. Chem.* **2015**, *11*, 2616–2630. https://doi.org/10.3762/bjoc.11.281.

Chapter 6

Conclusions and future work

6.1) General conclusions

In summary, the author of this doctoral thesis successfully isolated and characterised supramolecular derivatives of selected pharmaceutically relevant compounds, many of which displayed superior aqueous solubility enhancements. The conclusions and future work relating to these results are described in detail below. These results include the initial characterisation of the three pyrido[1,2-a]benzimidazole derivatives (GMP-23, GMP-31 and GMP-58), the identification of a new polymorph or tautomeric form of GMP-23, and six GMP-coformer products that formed dispersions, which are more specifically classed as two-phase solid systems containing the crystalline GMP compounds in amorphous coformer matrices.[1] In addition, three solid-state cyclodextrin (CD) inclusion complexes were formed with the potent antioxidant pterostilbene (PTB), and phase solubility studies were performed with two amorphous CDs, yielding remarkable PTB solubility enhancements. Lastly, three CD inclusion complexes were formed with β-estradiol and a further three CD inclusion complexes were formed with progesterone and they were comprehensively characterised.

6.1.1) Pyrido[1,2-a]benzimidazole derivatives (GMP-23, GMP-31 and GMP-58)

The three pyrido[1,2-a]benzimidazole derivatives (GMP-23, GMP-31 and GMP-58) were successfully characterised using PXRD, HSM, TGA and DSC analytical techniques. The thermal analyses indicated that GMP-23 and GMP-58 were overall thermally stable until their main decomposition temperatures, despite the negligible decomposition that occurred throughout the heating range prior to the main decomposition. However, GMP-31 was not as thermally stable, since it displayed a more significant initial decomposition throughout

the heating range until the main decomposition occurred. In addition, a different polymorph or tautomeric form of GMP-23 was identified and could be successfully formed through recrystallization of the synthesised sample from EtOH, chloroform, chlorobenzene, 1,4 dioxane and THF. The single-crystal X-ray structures of GMP23·DMF, GMP31·DMF and GMP58·DMSO provided valuable insight into the type of crystal packing arrangement and hydrogen bonding synthons that are possible when combining various entities with the three GMP compounds. In addition, the single-crystal X-ray structure of unsolvated GMP-58 is the first reported for this compound and it provided evidence for the specific tautomeric form of GMP-58 being utilized in this study. It also suggested that this could be the predominant tautomeric form for crystal structures containing GMP-58, since it was the same tautomeric form observed in GMP58·DMSO.

No co-crystals of the GMP compounds were obtained despite the predictions from the Co-crystal Design and Motif searching tools available in the program Mercury.[2] However, six GMP-coformer combinations produced six corresponding molecular dispersions that were characterised. These included GMP-23-MAL (1:1), GMP-23-NIC (1:1), GMP-31-MAL (1:1), GMP-31-NIC (1:1), GMP-58-MAL(1:1) and GMP-58-NIC (1:1). Although program Mercury did not predict co-crystal formation between L-malic acid and the two potential drug leads GMP-31 and GMP-58, L-malic acid formed hydrogen bonding interactions with these drug leads and produced dispersions.

The aqueous solubility enhancements of the GMP compounds in the form of these six GMP-coformer products ranged between 2-fold and 20-fold, and they thus warrant further investigation for their potential utility in the treatment of schistosomiasis. Future work could also involve utilizing alternative coformers to generate other new GMP-coformer products and assessing them for potential solubility enhancements of the GMP compounds. It is particularly important to discover alternative therapeutic drugs and their supramolecular derivatives for the treatment of schistosomiasis, since the overuse and reliance by patients on praziquantel (the main therapeutic drug in use to treat the disease), has caused concern for drug resistance.[3]

6.1.2) Pterostilbene

Three CD inclusion complexes with the potent antioxidant pterostilbene as guest, namely β-CD·PTB (1:1), γ-CD·PTB (1:1) and TMB·PTB (1:1) were isolated and characterised. In addition, the crystal structure of β-CD·PTB displayed a rare and seldom observed packing arrangement of β-CD complexes that crystallize in the space group *C*2, highlighting the existence of two distinct isostructural series of β-CD complexes crystallizing in the common space group *C*2.

The phase solubility studies of pterostilbene with randomly methylated β-CD (RAMEB) and sulfobutyl ether β-cyclodextrin (SBEBCD) sodium salt, displayed very significant aqueous solubility enhancement values of 1356-fold and 1431-fold in 20 mM CD solutions of the RAMEB and SBEBCD sodium salt respectively. These results indicate the potential for pharmaceutical applicability, particularly as pterostilbene is currently undergoing clinical trials on healthy, human subjects as a potent anti-cancer agent for many malignancies including resistant haematological malignancies, as well as for the treatment of cardiovascular disease, liver diseases and type 2 diabetes.[4–7]

It is imperative to extend the research reported here on the phase solubility experiments of pterostilbene with RAMEB and SBEBCD sodium salt. The results obtained from these experiments thus far warrant further *in vivo* studies in order to assess the application of these solubilizing media and their potential in pharmaceutical formulations. In addition, the phase solubility studies described in the present study could be repeated, with the intention of assessing the potential of the CDs to prevent the isomerisation of pterostilbene when exposed to light for extended periods of time.

6.1.3) β-estradiol and progesterone

The six CD inclusion complexes, namely β-CD·BES (2:1), β-CD·PRO (2:1), γ-CD·BES (1:1), γ-CD·PRO (3:2), DMB·BES (1:1) and DMB·PRO (1:1) were successfully isolated and fully characterised, with the crystal structure of DMB·BES displaying a rare bimodal inclusion of β-estradiol. This phenomenon resulted in small differences in the conformation of the β-estradiol molecule when included in the separate cavities of the two CD host molecules, and

significantly different concomitant host conformational changes, thus providing evidence for complexation involving 'mutual-induced fit' of host and guest molecules.[8,9] Given that the first crystal structures of CD inclusion complexes of steroidal APIs were reported only very recently,[9] the structural results reported here for the new β-CD and DMB inclusion complexes of BES and PRO contribute significantly to the knowledge base on CD-drug inclusion chemistry.

The aqueous solubility measurements involving the four inclusion complexes with native CDs yielded notable API solubility enhancement factors in the range 5.5-fold - 21.3-fold, thus indicating potential pharmaceutical application of these inclusion complexes. Both β-estradiol and progesterone are available commercially and thus alternative formulations of these steroids that display improved solubility and bioavailability could result in lowered retail costs, since less of the active ingredient would be required in the formulation.

We noted that a derivative of β-estradiol is already available commercially, namely ethinyl estradiol, which displays a 3-fold aqueous solubility increase relative to the solubility of pure β-estradiol;[10–12] however, in the present study it was discovered that γ-CD·BES displayed a 6.1-fold increase in the aqueous solubility of β-estradiol and β-CD·BES displayed an even greater increase, namely 21.3-fold. Thus, these two CD complexes already display superior solubility enhancement properties in comparison with ethinyl estradiol, therefore indicating their potential as alternative solid forms for pharmaceutical formulations. In addition, micronized progesterone is the only formulation of progesterone widely used as an alternative to facilitate absorption.[13] In the present study, the API solubility enhancement ratios derived from the dissolution of β-CD·PRO and γ-CD·PRO were 5.5-fold and 19.9-fold respectively, and thus these inclusion complexes also display significant potential as new solid forms for alternative pharmaceutical formulations. Consequently, future *in vivo* research should be conducted with β-CD·BES, γ-CD·BES, β-CD·PRO and γ-CD·PRO in order to assess their applicability as alternative, improved candidates for formulations of β-estradiol and progesterone.

References

(1) Allawadi, D.; Singh, N.; Singh, S.; Arora, S. Solid Dispersions: A Review on Drug Delivery System and Solubility Enhancement. *Int. J. Pharm. Sci. Res.* **2013**, *4* (6), 2094–2105. https://doi.org/10.13040/IJPSR.0975-8232.4(6).2094-05.

(2) Macrae, C. F.; Sovago, I.; Cottrell, S. J.; Galek, P. T. A.; McCabe, P.; Pidcock, E.; Platings, M.; Shields, G. P.; Stevens, J. S.; Towler, M.; Wood, P. A. Mercury 4.0 : From Visualization to Analysis, Design and Prediction. *J. Appl. Crystallogr.* **2020**, *53* (1), 226–235. https://doi.org/10.1107/S1600576719014092.

(3) Okombo, J.; Singh, K.; Mayoka, G.; Ndubi, F.; Barnard, L.; Njogu, P. M.; Njoroge, M.; Gibhard, L.; Brunschwig, C.; Vargas, M.; Keiser, J.; Egan, T. J.; Chibale, K. Antischistosomal Activity of Pyrido[1,2- a]Benzimidazole Derivatives and Correlation with Inhibition of β-Hematin Formation. *ACS Infect. Dis.* **2017**, *3* (6), 411–420. https://doi.org/10.1021/acsinfecdis.6b00205.

(4) Estrela, J. M.; Ortega, A.; Mena, S.; Rodriguez, M. L.; Asensi, M. Pterostilbene: Biomedical Applications. *Crit. Rev. Clin. Lab. Sci.* **2013**, *50* (3), 65–78. https://doi.org/10.3109/10408363.2013.805182.

(5) McCormack, D.; McFadden, D. A Review of Pterostilbene Antioxidant Activity and Disease Modification. *Oxid. Med. Cell. Longev.* **2013**, *2013*, 1–15. https://doi.org/10.1155/2013/575482.

(6) McCormack, D.; McFadden, D. Pterostilbene and Cancer: Current Review. *J. Surg. Res.* **2012**, *173* (2), e53–e61. https://doi.org/10.1016/j.jss.2011.09.054.

(7) Chan, E. W. C.; Wong, C. W.; Tan, Y. H.; Foo, J. P. Y.; Wong, S. K.; Chan, H. T. Resveratrol and Pterostilbene: A Comparative Overview of Their Chemistry, Biosynthesis, Plant Sources and Pharmacological Properties. *J. Appl. Pharm. Sci.* **2019**, *9* (7), 124–129. https://doi.org/10.7324/JAPS.2019.90717.

(8) Trollope, L.; Cruickshank, D. L.; Noonan, T.; Bourne, S. A.; Sorrenti, M.; Catenacci, L.; Caira, M. R. Inclusion of Trans -Resveratrol in Methylated Cyclodextrins: Synthesis and Solid-State Structures. *Beilstein J. Org. Chem.* **2014**, *10*, 3136–3151. https://doi.org/10.3762/bjoc.10.331.

(9) Caira, M. R.; Bourne, S. A.; Samsodien, H.; Smith, V. J. Inclusion Complexes of 2-Methoxyestradiol with Dimethylated and Permethylated β-Cyclodextrins: Models for Cyclodextrin–Steroid Interaction. *Beilstein J. Org. Chem.* **2015**, *11*, 2616–2630. https://doi.org/10.3762/bjoc.11.281.

(10) Drugbank, Estradiol https://www.drugbank.ca/drugs/DB00783 (accessed Aug 9, 2020).

(11) National Center for Biotechnology Information (2020). PubChem Compound Summary for CID 5757, Estradiol. https://pubchem.ncbi.nlm.nih.gov/compound/Estradiol (accessed Jan 3, 2022).

(12) National Center for Biotechnology Information (2020). PubChem Compound Summary for CID 5991, Ethinyl estradiol. https://pubchem.ncbi.nlm.nih.gov/compound/Ethinyl-estradiol (accessed Aug 9, 2020).

(13) Goletiani, N. V.; Keith, D. R.; Gorsky, S. J. Progesterone: Review of Safety for Clinical Studies. *Exp. Clin. Psychopharmacol.* **2007**, *15* (5), 427–444. https://doi.org/10.1037/1064-1297.15.5.427.

Appendix

Section 1: General

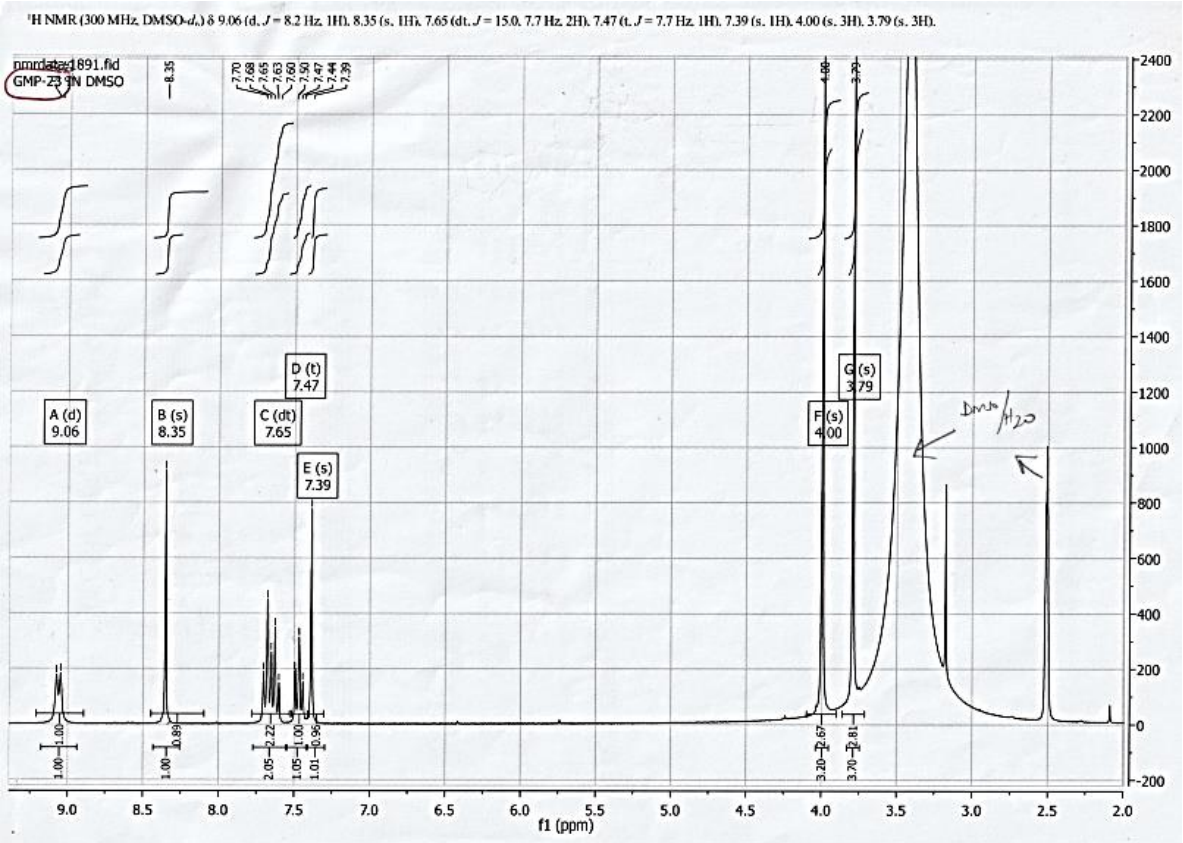
Table 1.1: List of available coformers in the supramolecular laboratory at the University of Cape Town.

Number	Coformer	Number	Coformer
1	Adipic acid	20	L-Valine
2	Aspartic acid	21	Maleic acid
3	Benzamide	22	Malonic acid
4	Caffeine	23	Nicotinic acid
5	Cinnamamide	24	Nicotinamide
6	Citric acid	25	Orotic acid
7	d-Lactose	26	Oxalic acid
8	D-Tartaric acid	27	Piperazine
9	Fumaric acid	28	Propionamide
10	Glutaric acid	29	Pyrazinecarboxamide
11	Glycine	30	L-Pyroglutamic acid
12	Isonicotinamide	31	Riboflavin
13	Lactic acid	32	Saccharin
14	L-Arginine	33	Salicylic acid
15	L-Ascorbic acid	34	Sorbic acid
16	L-Glutamic acid	35	Suberic acid
17	L-Malic acid	36	Succinic acid
18	L-Proline	37	Uracil
19	L-Tartaric acid	38	Urea

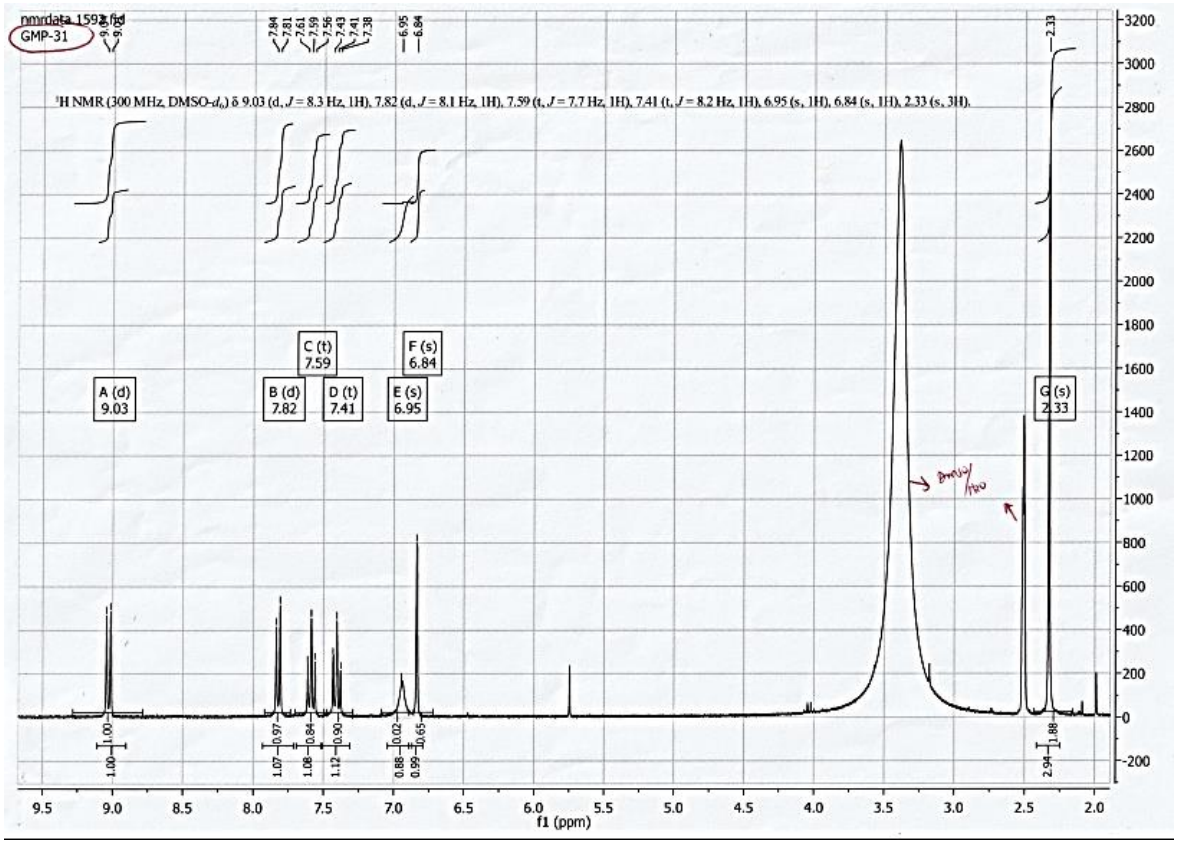
Section 2: The pyrido[1,2-a]benzimidazole derivatives (GMP-23, GMP-31 and GMP-58)

2.1) General

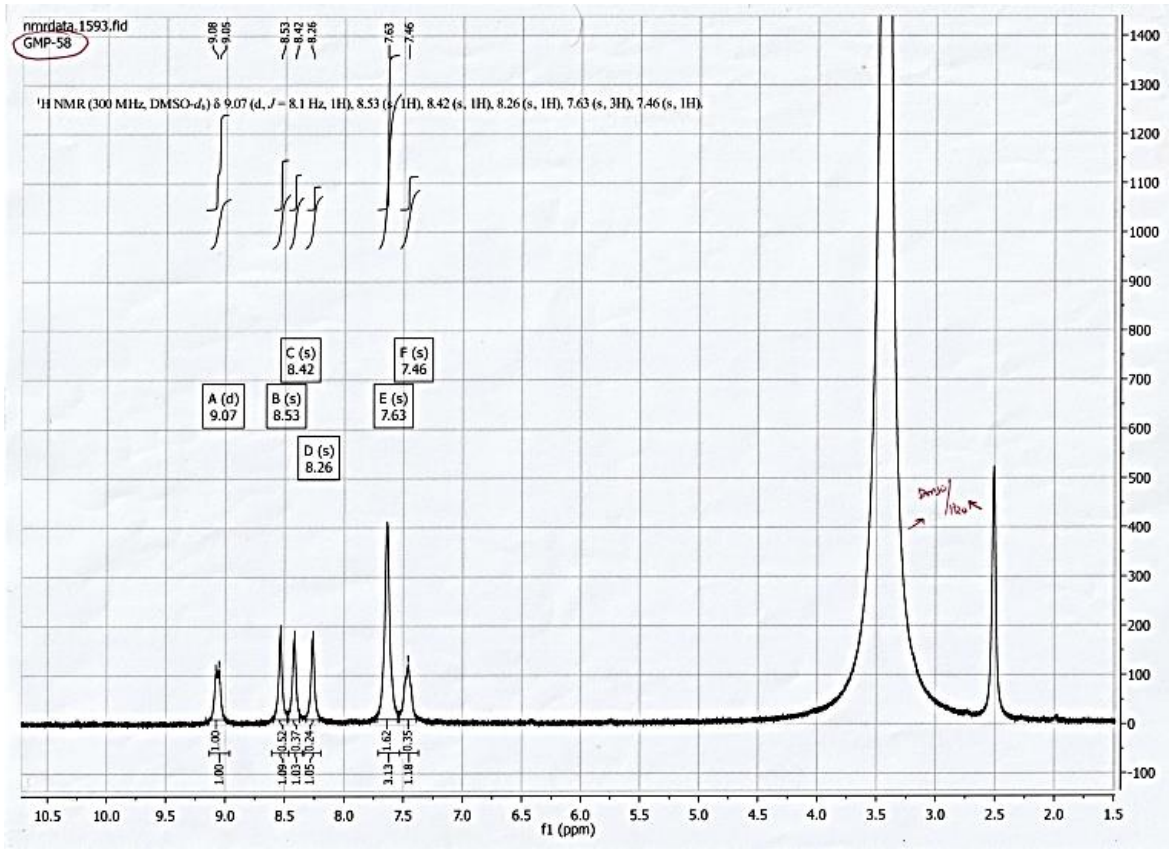
2.1.1) A scanned copy of the ^{1}H NMR spectrum of GMP-23 for reference purposes.



2.1.2) A scanned copy of the ^{1}H NMR spectrum of GMP-31 for reference purposes.



2.1.3) A scanned copy of the ^{1}H NMR spectrum of GMP-58 for reference purposes.



2.2) Stoichiometric determinations of the GMP solvates

2.2.1) GMP23·DMF ^{1}H NMR spectrum and stoichiometric determination

The ^{1}H NMR spectral analysis of the co-precipitated crystalline material of GMP23·DMF indicated a 1:1 stoichiometric ratio (Figures 2.2.1a and 2.2.1b, and Table 2.2.1).

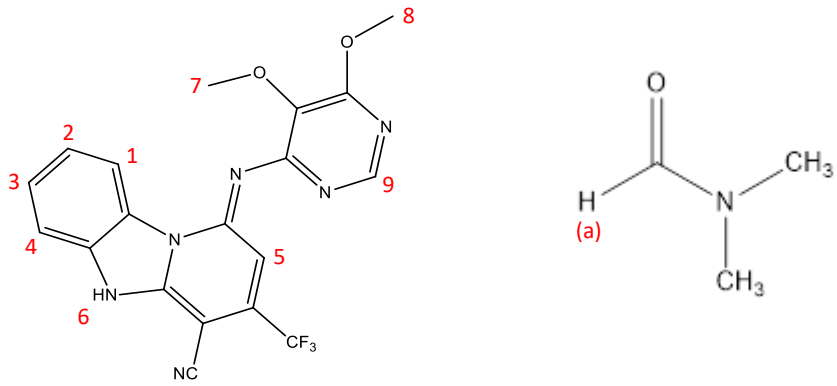


Figure 2.2.1a: Molecular structures of GMP-23 (left) and DMF (right), with specific molecular fragments labelled for the ^{1}H NMR analysis.

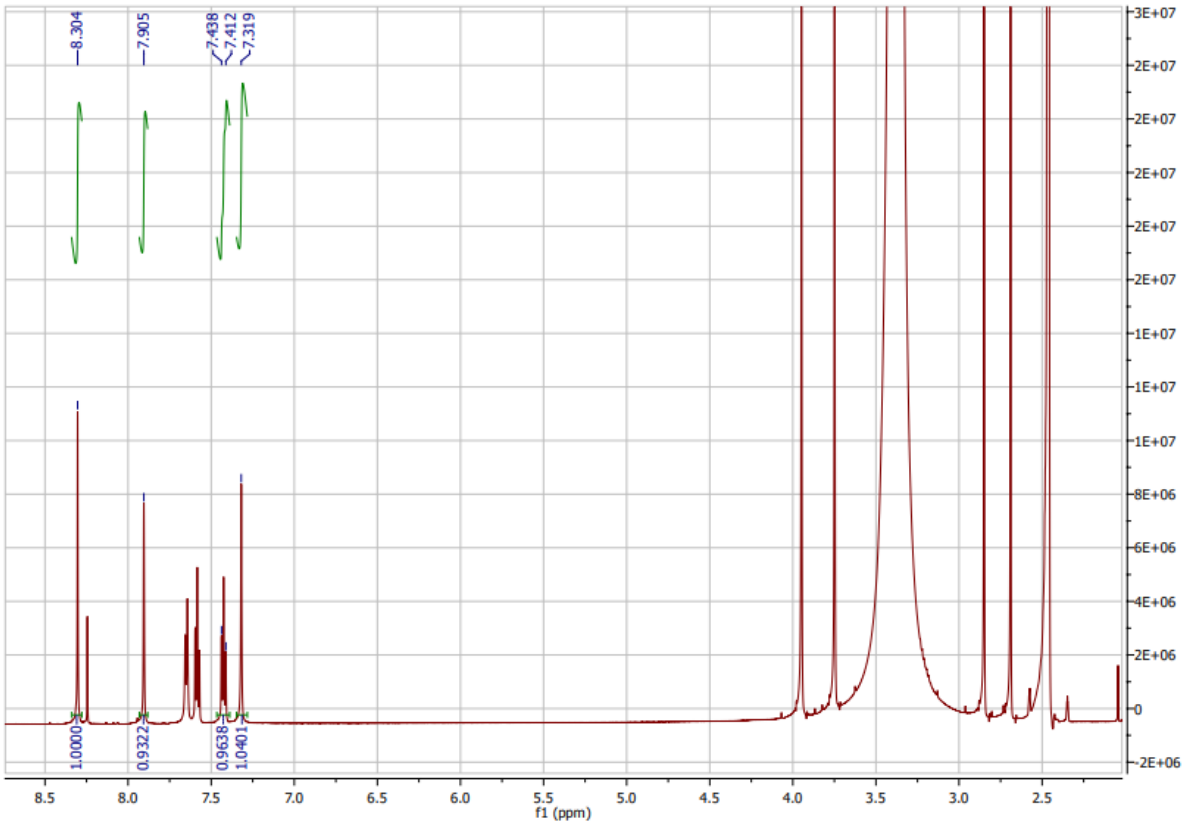


Figure 2.2.1b: The ^{1}H NMR spectrum of GMP23·DMF.

Table 2.2.1: The ^{1}H NMR spectral analysis of GMP23·DMF.

Assignment	δ (ppm)	Integration	Multiplicity	Proton representation (per molecule)	Stoichiometric ratio	Stoichiometric ratio (integer)
H9 (GMP-23)	8.304	1.0000*	singlet	1H	1.00	1
H(a) (DMF)	7.905	0.9322	singlet	1H	0.93	1
H2 (GMP-23)	7.412 – 7.438	0.9638	triplet	1H	0.96	1
H5 (GMP-23)	7.319	1.0401	singlet	1H	1.04	1

2.2.2) GMP31·DMF TGA curve and stoichiometric determination

The percentage mass loss due to desolvation at the onset temperature of 101.2 ± 0.4 °C was 15.2 ± 0.1%, which corresponded to a theoretical percentage mass loss of 16.4% for a 1:1 stoichiometric ratio (Figure 2.2.2).

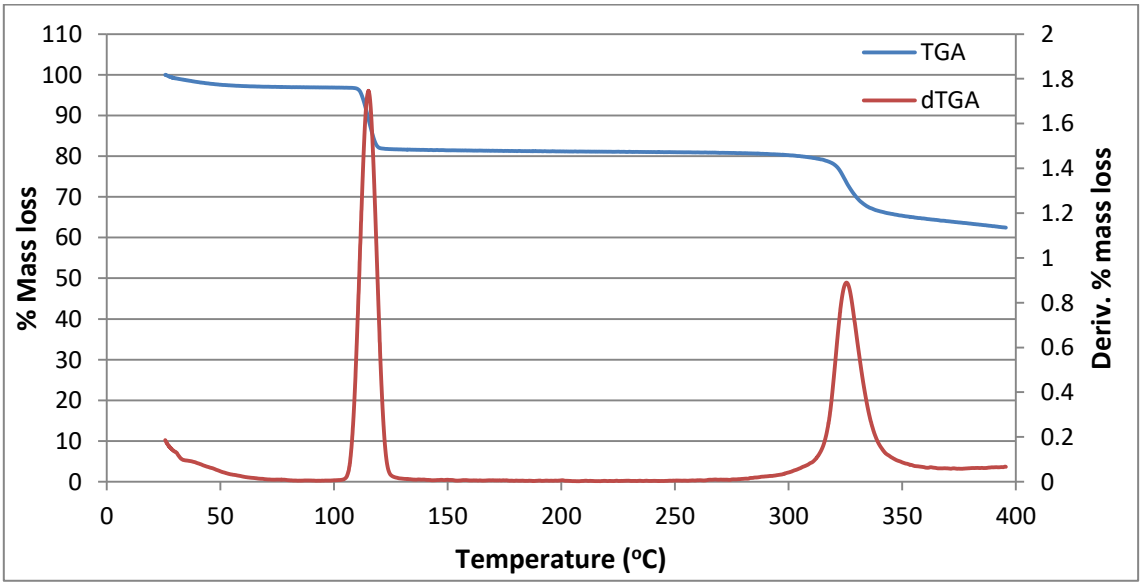


Figure 2.2.2: Representative TGA and dTGA curves of GMP31·DMF.

2.2.3) GMP58·DMSO TGA curve and stoichiometric determination

The percentage mass loss due to desolvation at the onset temperature of 75.8 ± 0.4 °C was 17.5 ± 0.1%, which corresponded to a theoretical percentage mass loss of 18.1% for a 1:1 stoichiometric ratio (Figure 2.2.3).

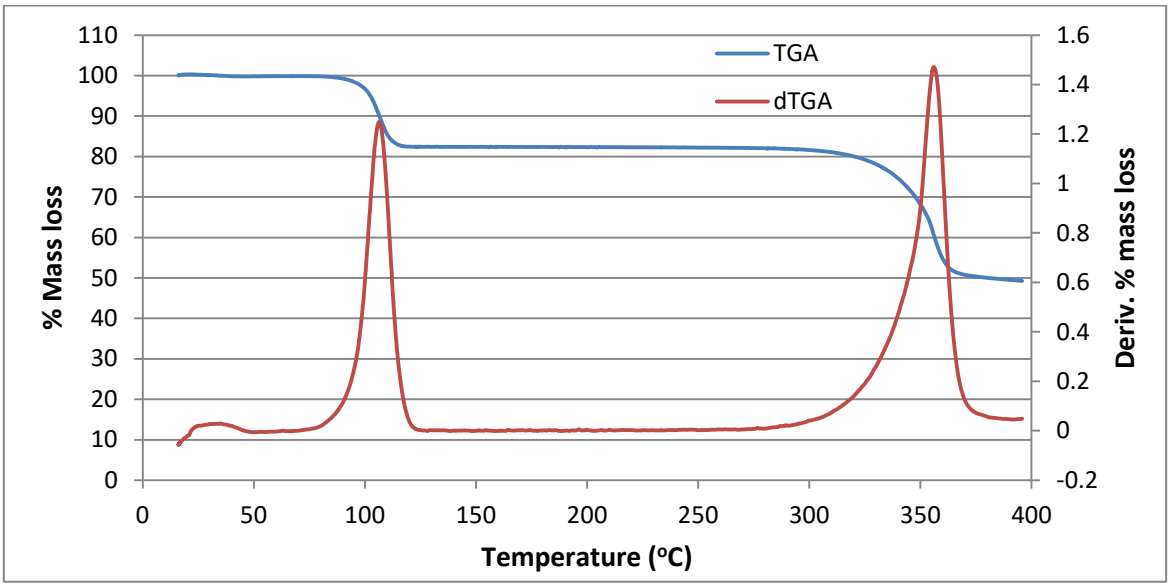


Figure 2.2.3: Representative TGA and dTGA curves of GMP58·DMSO.

2.3) Virtual co-crystal screening

Table 2.3.1: The resulting coformers from the screening by molecular complementarity investigation for the GMP-23 tautomeric forms: GMP-23a and GMP-23b.

Number	Coformer
1	2-Amino-5-methylbenzoic acid
2	3-Methylpyridine
3	4-Acetamidobenzoic acid
4	4-Aminobenzoic acid
5	4-Hydroxybenzoic acid
6	D-Pantothenol
7	EDTA
8	L-Arginine
9	L-Glutamic acid
10	L-Glutathione
11	L-Mandelic acid
12	L-Methionine
13	L-Phenylalanine
14	L-Tryptophan
15	L-Tyrosine
16	N-Ethylacetamide
17	Acetophenone oxime
18	Acetylenedicarboxylic acid
19	Alitame
20	Apigenin
21	Benzoic acid
22	Biotin
23	Ethylparaben
24	Fumaric acid
25	Gentisic acid
26	Glutaric acid
27	Hesperetin
28	Hippuric acid
29	Imidazole
30	Isonicotinamide
31	Ketoglutaric acid
32	Lactose
33	Maleic acid
34	Malic acid
35	Methylparaben
36	Monobutyrin
37	Nicotinamide
38	Pamoic_acid
39	Phthalamide
40	Propylparaben
41	Pyrazine
42	Riboflavin
43	Sorbic acid
44	Succinic acid
45	t-Butylhydroxyanisole
46	Theophylline
47	Xanthine

Table 2.3.2: The resulting coformers from the screening by molecular complementarity investigation for the GMP-31 tautomeric forms: GMP-31a, GMP-31b and GMP-31c.

Number	Coformer
1	2-Amino-5-methylbenzoic acid
2	3-Methylpyridine
3	4-Aminobenzoic acid
4	4-Hydroxybenzoic acid
5	D-Pantothenol
6	L-Glutathione
7	L-Leucine
8	L-Mandelic acid
9	L-Methionine
10	L-Phenylalanine
11	L-Tryptophan
12	L-Tyrosine
13	N-Ethylacetamide
14	Acetophenone oxime
15	Alitame
16	Apigenin
17	Benzoic acid
18	Biotin
19	Ethylparaben
20	Gentisic acid
21	Hesperetin
22	Hippuric acid
23	Imidazole
24	Isonicotinamide
25	Lactose
26	Methylparaben
27	Monobutyrin
28	Nicotinamide
29	Pamoic acid
30	Phthalamide
31	Pyrazine
32	Riboflavin
33	Saccharin
34	t-Butylhydroxyanisole
35	Theophylline
36	Thymidine
37	Valerolactam

Table 2.3.3: The resulting coformers from the screening by molecular complementarity investigation for the GMP-58 tautomeric forms: GMP-58a, GMP-58b and GMP-58c.

Number	Coformer
1	2-Amino-5-methylbenzoic acid
2	3-Methylpyridine
3	4-Aminobenzoic acid
4	4-Hydroxybenzoic acid
5	EDTA
6	L-Glutamic acid
7	L-Glutathione
8	L-Mandelic acid
9	L-Methionine
10	L-Tryptophan
11	L-Tyrosine
12	N-Ethylacetamide
13	Acesulfame
14	Acetophenone oxime
15	Acetylenedicarboxylic acid
16	Alitame
17	Apigenin
18	Benzoic acid
19	Biotin
20	Ethylparaben
21	Fumaric acid
22	Gentisic acid
23	Hesperetin
24	Imidazole
25	Isonicotinamide
26	Lactose
27	Maleic acid
28	Methylparaben
29	Monobutyrin
30	Nicotinamide
31	Pamoic acid
32	Phthalamide
33	Pyrazine
34	Riboflavin
35	Saccharin
36	t-Butylhydroxyanisole
37	Theophylline
38	Thymidine
39	Valerolactam

2.4) Co-crystal screening

Initially, dry grinding and liquid-assisted grinding (LAG) experiments were conducted. 3 mg of the GMP active compound was added to the mortar with an equivalent 1:1 stoichiometric amount of coformer and ground for 15 minutes. In addition, several solvents (which included EtOH, THF, DMSO, and 1,4 dioxane) were used for LAG experiments. Furthermore, co-precipitation experiments were also performed which reused the material from the LAG experiments. Solvents in which the GMP compound and the coformer displayed comparable solubility were selected. These solvents were either THF, DMSO or 1,4 dioxane and for a few experiments EtOH was also used. Unfortunately, none of the co-crystal screening experiments produced a new phase that could be further analysed (Tables 2.4.1 – 2.4.3). However, instead, a serendipitous polymorph or tautomeric form of GMP-23 (referred to hereafter as GMP-23 form 2) was discovered. This is discussed in more detail in the main section of this thesis in Chapter 3, section 3.2.5.3, p. 110.

Table 2.4.1: The dry grinding experiments conducted with GMP-23, GMP-31 and GMP-58.

Number	Active compound	Coformer	Result (determined by PXRD)
1	GMP-23	L-Malic acid	Physical mixture displaying a semi-amorphous phase.
2	GMP-23	Nicotinamide	Physical mixture displaying a semi-amorphous phase.
3	GMP-31	Nicotinamide	Amorphous.
4	GMP-31	L-Malic acid	Physical mixture (GMP-31 was significantly amorphous).
5	GMP-58	Nicotinamide	Amorphous.
6	GMP-58	L-Malic acid	Physical mixture (GMP-58 was significantly amorphous).

Table 2.4.2: The LAG experiments conducted with GMP-23, GMP-31 and GMP-58, and a corresponding coformer and solvent.

Number	Active compound	Coformer	Solvent	Result (determined by PXRD)
1	GMP-23	Benzoic acid	THF	GMP-23 form 2 (possibly starting a transition).
2	GMP-23	L-Glutamic acid	DMSO	New phase. Not possible to isolate.
3	GMP-23	L-Malic acid	THF	GMP-23 form 2.
4	GMP-23	Nicotinamide	THF	GMP-23 form 2 (possibly starting a transition into another phase).
5	GMP-23	Riboflavin	DMF	New phase. Not possible to isolate.
6	GMP-23	Riboflavin	DMSO	New phase. Not possible to isolate.
7	GMP-23	Succinic acid	THF	Physical mixture of GMP-23 form 2 and succinic acid.
8	GMP-31	Benzoic acid	THF	PXRD pattern depicting the crystalline presence of the coformer only.
9	GMP-31	Nicotinamide	THF	Physical mixture.
10	GMP-31	Riboflavin	DMF	New phase. Not possible to isolate.
11	GMP-31	Riboflavin	DMSO	New phase. Not possible to isolate
12	GMP-31	Isonicotinamide	EtOH	PXRD pattern depicting the crystalline presence of the coformer only.
13	GMP-31	Fumaric acid	EtOH	Physical mixture.
14	GMP-31	Saccharin	EtOH	Physical mixture.
15	GMP-31	d-Lactose monohydrate	EtOH	Physical mixture.
16	GMP-31	D-Tartaric acid	EtOH	Physical mixture.
17	GMP-58	Benzoic acid	THF	Physical mixture.
18	GMP-58	L-Glutamic acid	DMSO	PXRD pattern depicting the crystalline presence of the coformer only.
19	GMP-58	Nicotinamide	THF	PXRD pattern depicting the crystalline presence of the coformer only.
20	GMP-58	Nicotinamide	EtOH	PXRD pattern depicting the crystalline presence of the coformer only.
21	GMP-58	Riboflavin	DMF	New phase. Not possible to isolate.
22	GMP-58	Riboflavin	DMSO	New phase. Not possible to isolate
23	GMP-58	Saccharin	EtOH	Physical mixture.
24	GMP-58	Isonicotinamide	EtOH	Physical mixture.
25	GMP-58	d-Lactose monohydrate	EtOH	Physical mixture.
26	GMP-58	Fumaric acid	EtOH	Physical mixture.

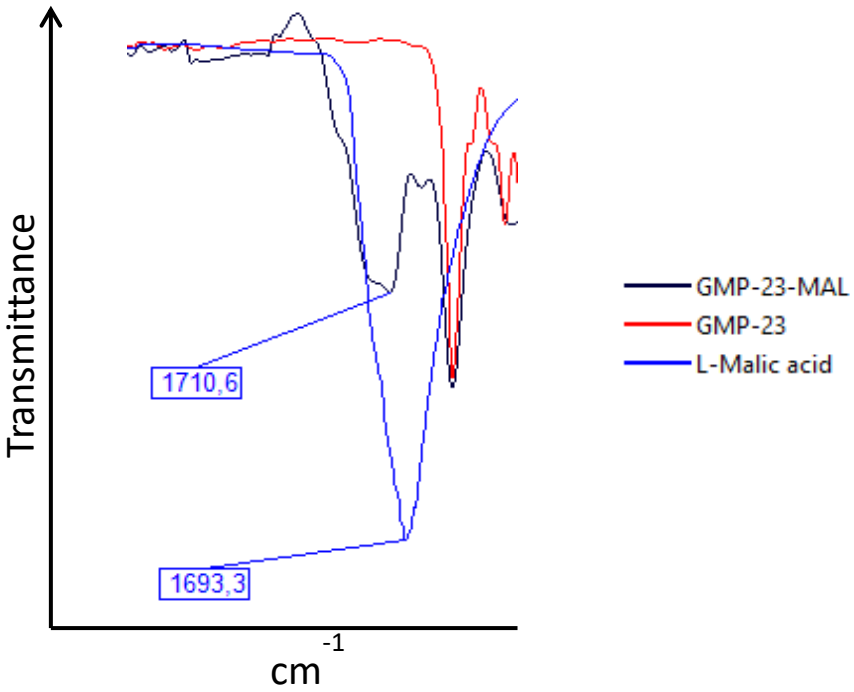
Table 2.4.3: The co-precipitation experiments conducted with GMP-23, GMP-31 and GMP-58, and a corresponding coformer and solvent.

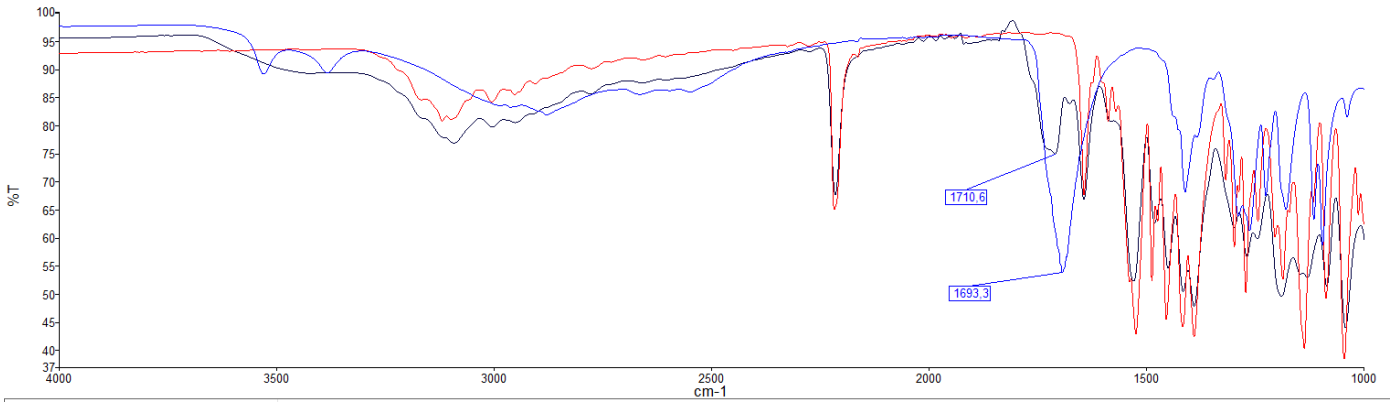
Number	Active compound	Coformer	Solvent	Result (determined by PXRD)
1	GMP-23	Benzoic acid	1,4 dioxane	GMP-23 form 2.
2	GMP-23	Benzoic acid	EtOH	GMP-23 form 2.
3	GMP-23	L-Glutamic acid	DMSO	New phase. Not possible to isolate.
4	GMP-23	L-Malic acid	1,4 dioxane	GMP-23 form 2.
5	GMP-23	L-Malic acid	EtOH	GMP-23 form 2.
6	GMP-23	Nicotinamide	1,4 dioxane	PXRD pattern depicting the crystalline presence of the coformer only.
7	GMP-23	Riboflavin	DMSO	New phase. Not possible to isolate.
8	GMP-23	Succinic acid	1,4 dioxane	Physical mixture of GMP-23 form 2 and succinic acid.
9	GMP-31	Benzoic acid	THF	PXRD pattern depicting the crystalline presence of the coformer only.
10	GMP-31	Nicotinamide	1,4 dioxane	Physical mixture.
11	GMP-31	Riboflavin	DMSO	New phase. Not possible to isolate
12	GMP-31	Isonicotinamide	THF	Semi-amorphous new phase. Not possible to isolate.
13	GMP-31	Fumaric acid	THF	New phase. Not possible to isolate.
14	GMP-31	Saccharin	THF	Physical mixture.
15	GMP-31	d-Lactose monohydrate	EtOH	No dissolution.
16	GMP-31	D-Tartaric acid	THF	Physical mixture.
17	GMP-58	Benzoic acid	1,4 Dioxane	Physical mixture.
18	GMP-58	L-Glutamic acid	DMSO	PXRD pattern depicting the crystalline presence of GMP-58 only.
19	GMP-58	Nicotinamide	1,4 Dioxane	PXRD pattern depicting the crystalline presence of GMP-58 only.
20	GMP-58	Riboflavin	DMSO	No precipitate.
21	GMP-58	Saccharin	THF	Physical mixture.
22	GMP-58	Isonicotinamide	1,4 Dioxane	PXRD pattern depicting the crystalline presence of GMP-58 only.
23	GMP-58	d-Lactose monohydrate	EtOH	No dissolution.
24	GMP-58	Fumaric acid	THF	Physical mixture.

2.5) The FT-IR spectra of the GMP-coformer products

The FT-IR spectra of each GMP-coformer product and the individual components are provided below. The first figure for each sample displays a close-up of the region relevant for observing differences in the C=O stretching frequencies of the pure coformers and their corresponding products of interaction with the respective GMP compounds, while the second figure displays the corresponding full FT-IR spectra pertaining to the specific sample.

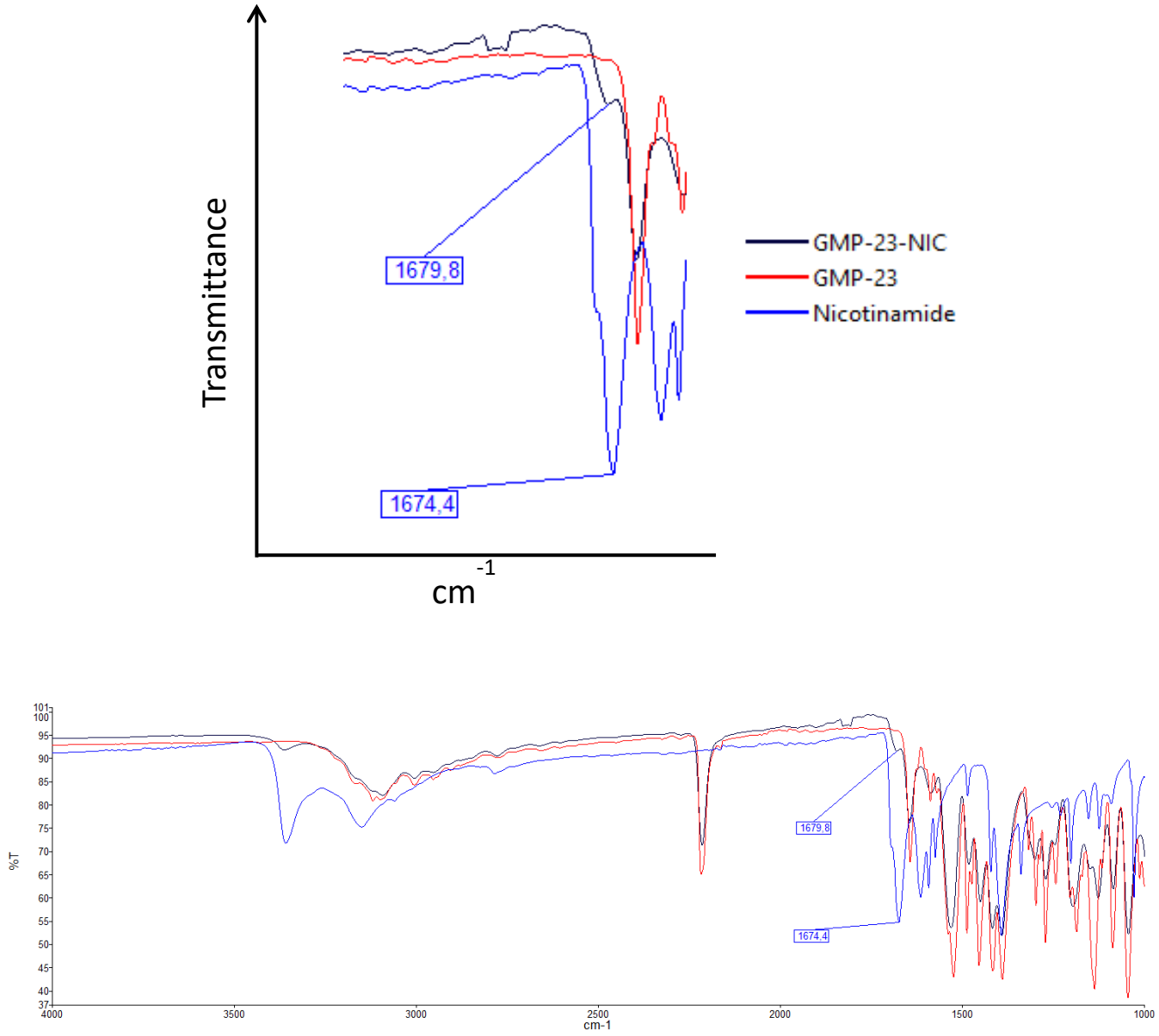
Sample GMP-23-MAL





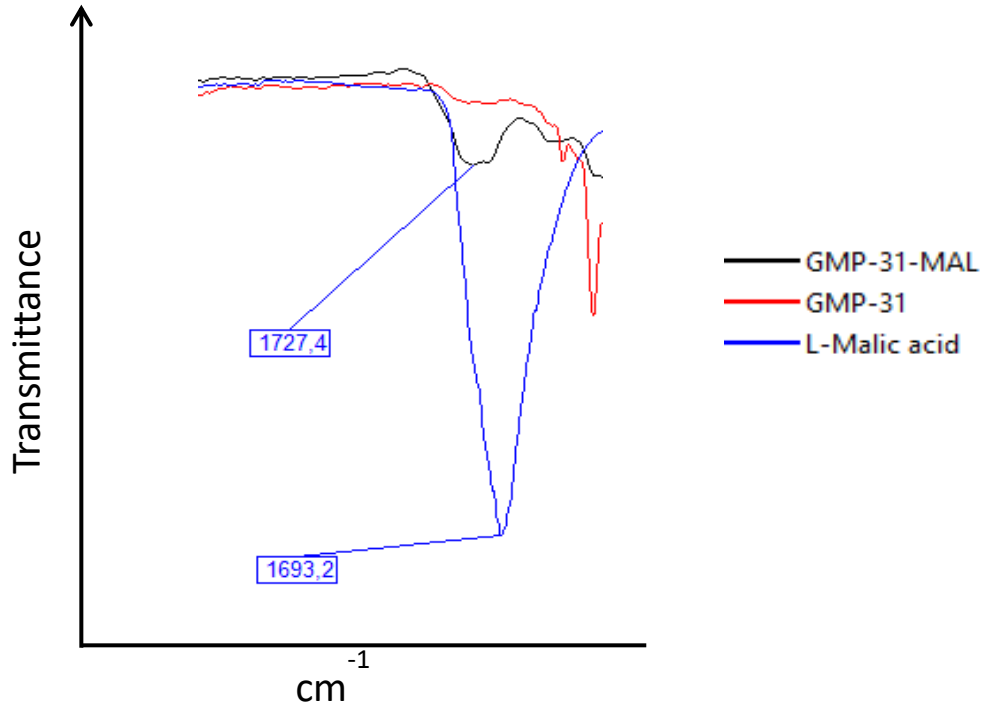
The full range of the FT-IR spectra of GMP-23-MAL (black), GMP-23 (red) and L-malic acid (blue).

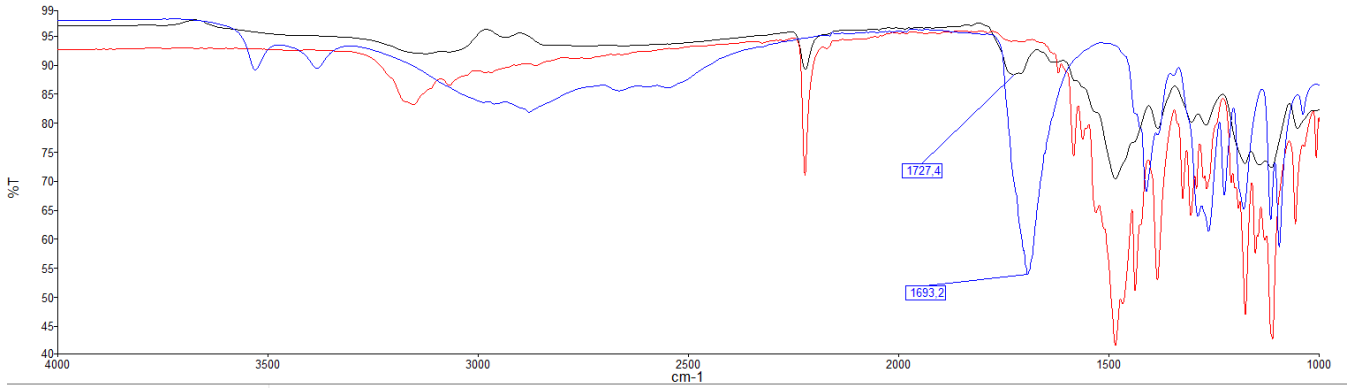
Sample GMP-23-NIC



The full range of the FT-IR spectra of GMP-23-NIC (black), GMP-23 (red) and nicotinamide (blue).

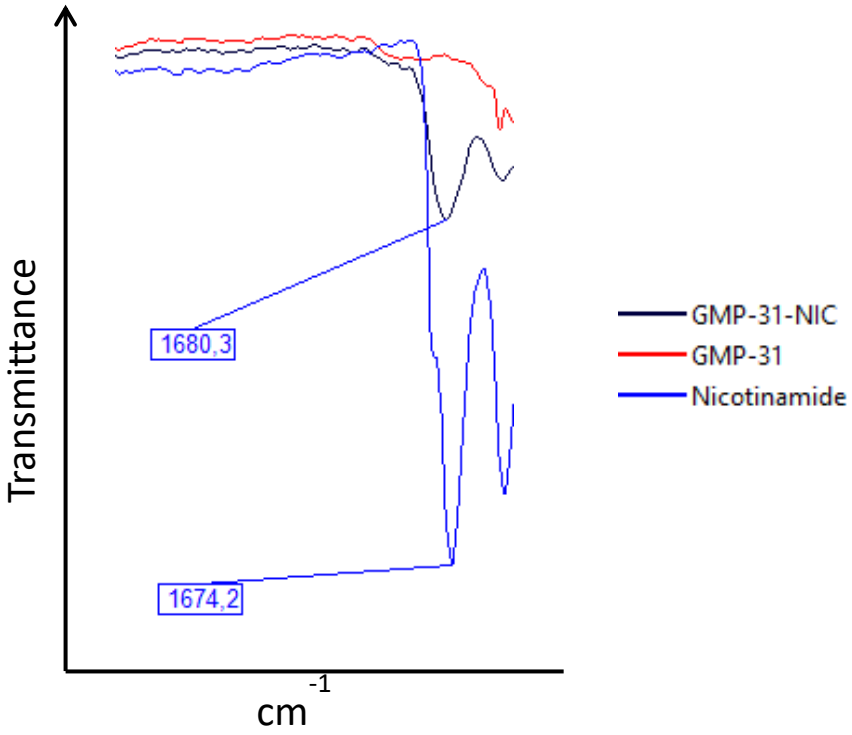
Sample GMP-31-MAL

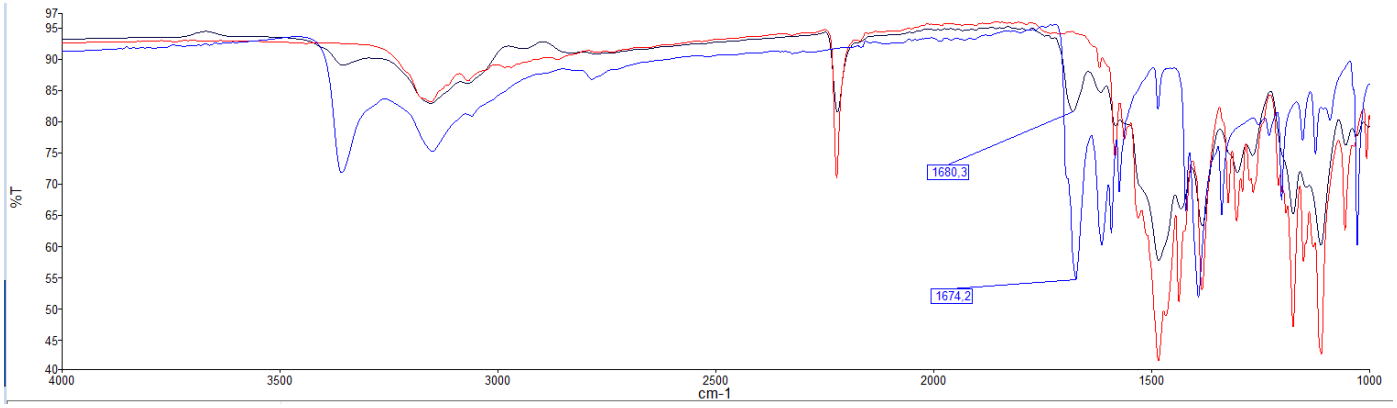




The full range of the FT-IR spectra of GMP-31-MAL (black), GMP-31 (red) and L-malic acid (blue).

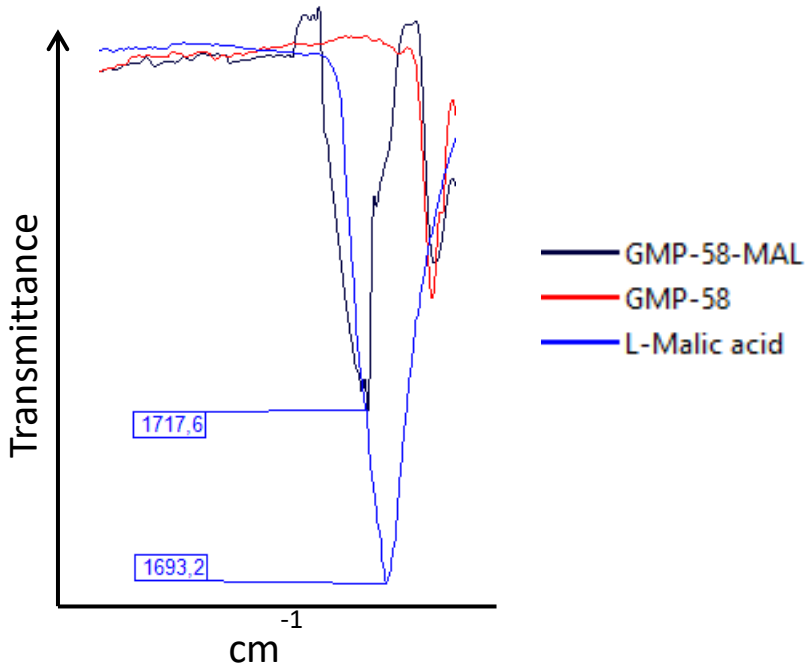
Sample GMP-31-NIC

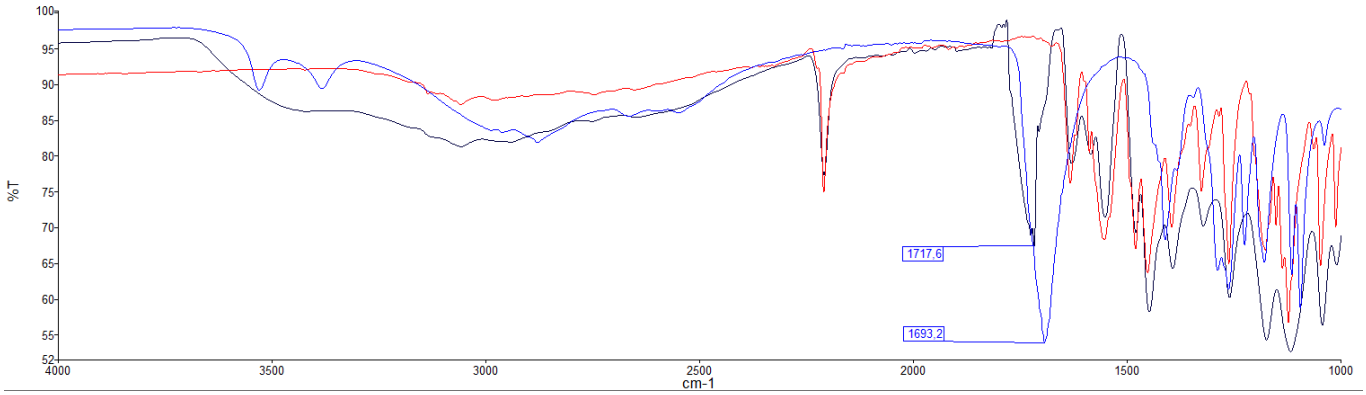




The full range of the FT-IR spectra of GMP-31-NIC (black), GMP-31 (red) and nicotinamide (blue).

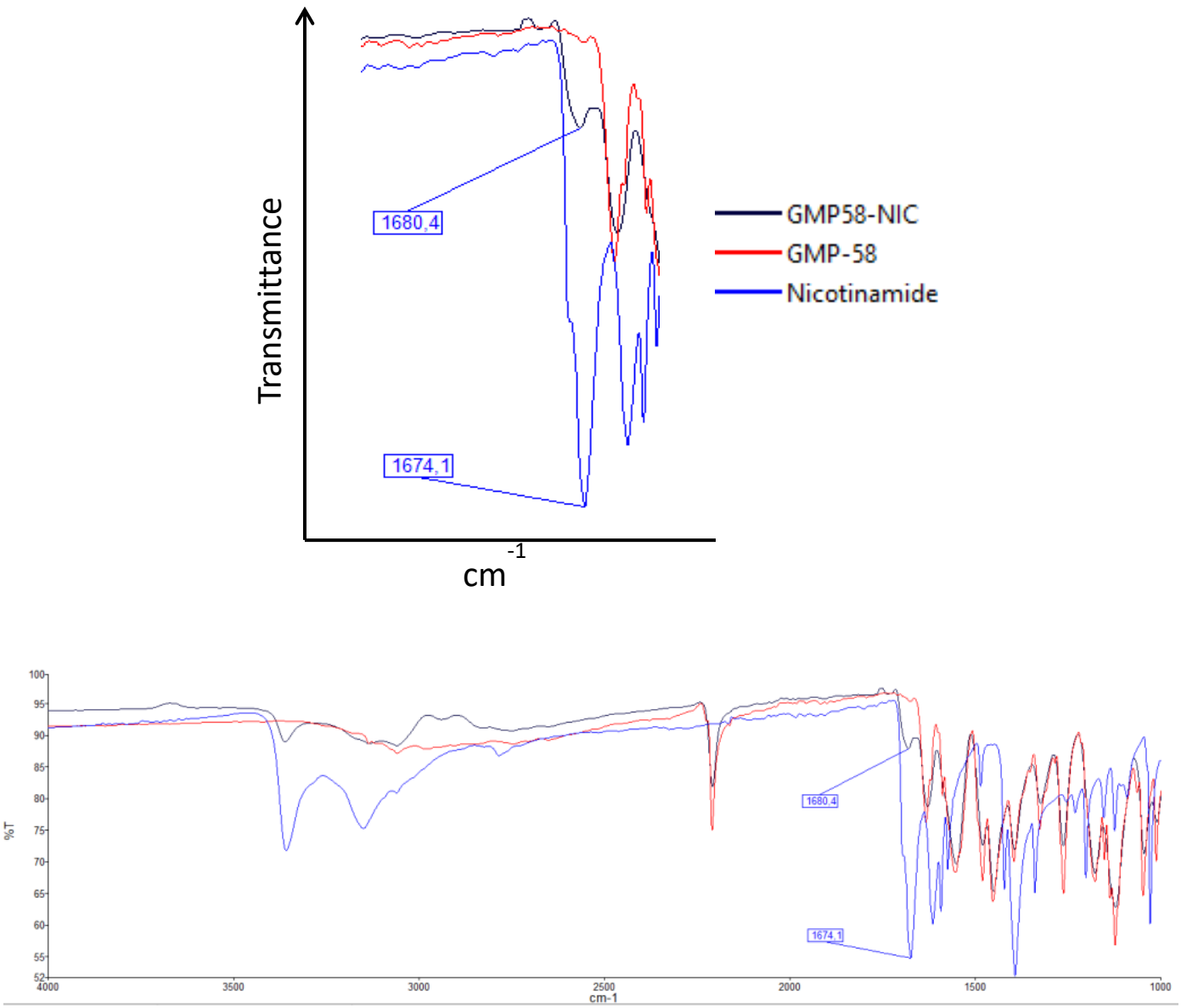
Sample GMP-58-MAL





The full range of the FT-IR spectra of GMP-58-MAL (black), GMP-58 (red) and L-malic acid (blue).

Sample GMP-58-NIC



The full range of the FT-IR spectra of GMP-58-NIC (black), GMP-58 (red) and nicotinamide (blue).

2.6) ^{1}H NMR spectra of the GMP-coformer products

2.6.1) GMP-23-MAL and GMP-23-NIC

Figure 2.6.1 displays the specific atoms of GMP-23, L-malic acid, and nicotinamide that have been labelled for the ^{1}H NMR assignments that follow below. Figures 2.6.1.1 – 2.6.1.2 and Tables 2.6.1.1 and 2.6.1.2 display the results from the ^{1}H NMR analyses.

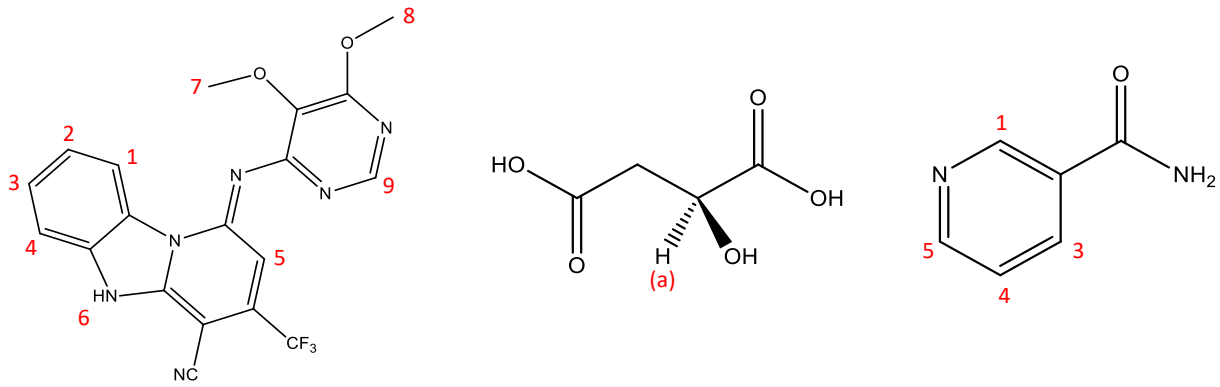


Figure 2.6.1: Molecular structures of GMP-23 (left), L-malic acid (centre), and nicotinamide (right), with specific molecular fragments labelled for the ^{1}H NMR analysis.

2.6.1.1) GMP-23-MAL

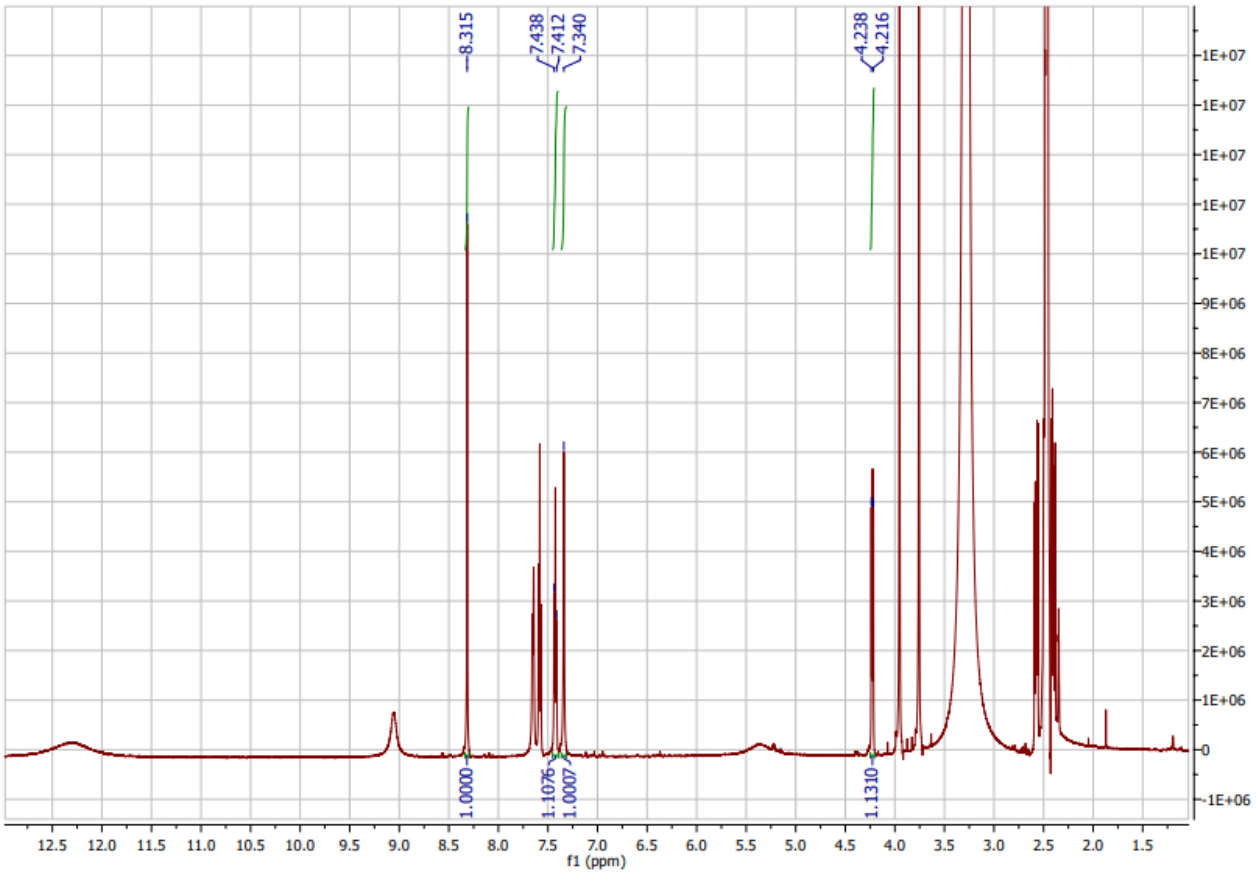


Figure 2.6.1.1: ^{1}H NMR spectrum of GMP-23-MAL.

Table 2.6.1.1: The ^{1}H NMR spectral analysis of GMP-23-MAL.

Assignment	δ (ppm)	Integration	Multiplicity	Proton representation (per molecule)	Stoichiometric ratio	Stoichiometric ratio (integer)
H9 (GMP-23)	8.315	1.0000*	singlet	1H	1.00	1
H2 (GMP-23)	7.412 – 7.438	1.1076	triplet	1H	1.11	1
H5 (GMP-23)	7.340	1.0007	singlet	1H	1.00	1
H(a) (MAL)	4.216 – 4.238	1.1310	quartet	1H	1.13	1

*reference integral

2.6.1.2) GMP-23-NIC

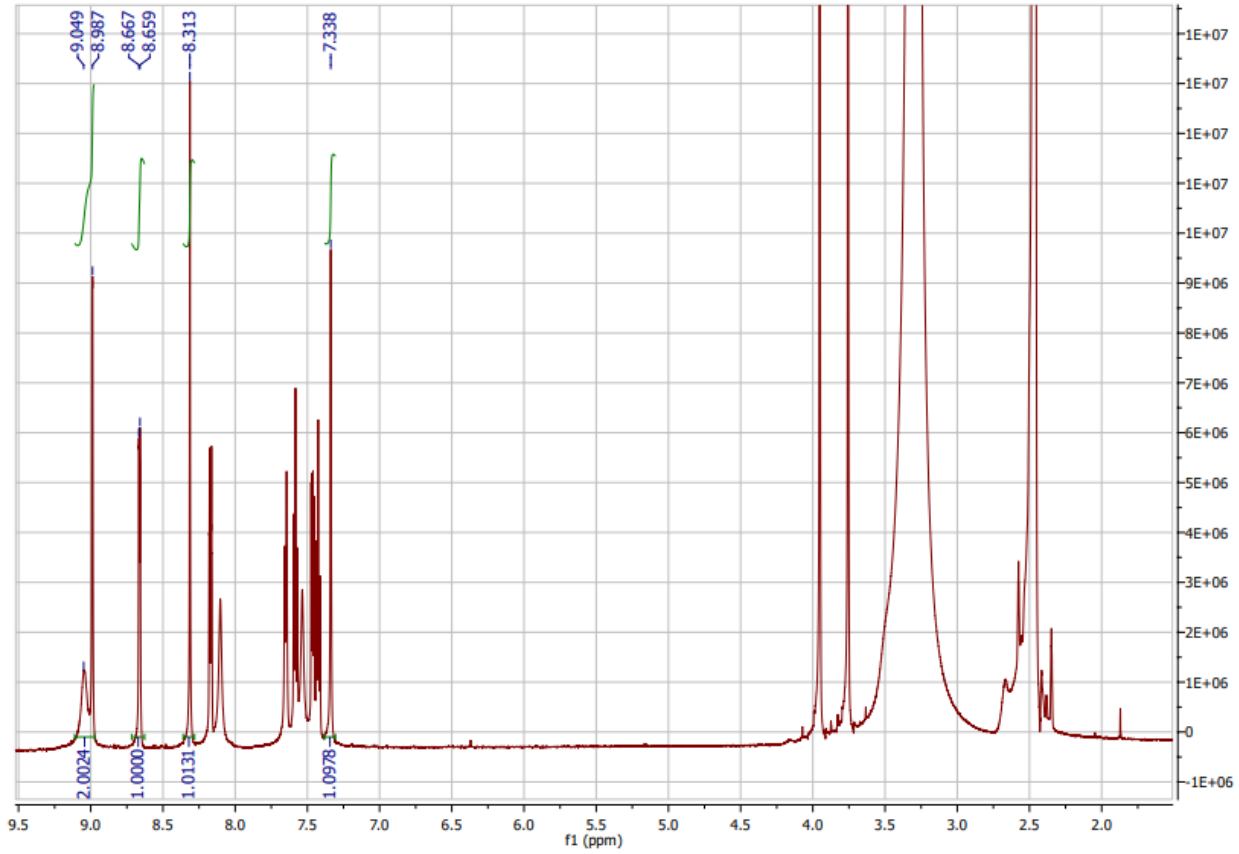


Figure 2.6.1.2: ^{1}H NMR spectrum of GMP-23-NIC.

Table 2.6.1.2: The ^{1}H NMR spectral analysis of GMP-23-NIC.

Assignment	δ (ppm)	Integration	Multiplicity	Proton representation (per molecule)	Stoichiometric ratio	Stoichiometric ratio (integer)
H1 (GMP-23) and H1 (NIC)	8.987 – 9.049	2.0024	singlet and doublet	1H & 1H	1.00	1
H5 (NIC)	8.659 – 8.667	1.0000*	doublet	1H	1.00	1
H9 (GMP-23)	8.313	1.0131	singlet	1H	1.01	1
H5 (GMP-23)	7.338	1.0978	singlet	1H	1.10	1

*reference integral

2.6.2) GMP-31-MAL and GMP-31-NIC

Figure 2.6.2 displays the specific atoms of GMP-31, L-malic acid, and nicotinamide that have been labelled for the ^{1}H NMR assignments that follow below. Figures 2.6.2.1 – 2.6.2.2 and Tables 2.6.2.1 and 2.6.2.2 display the results from the ^{1}H NMR analyses.

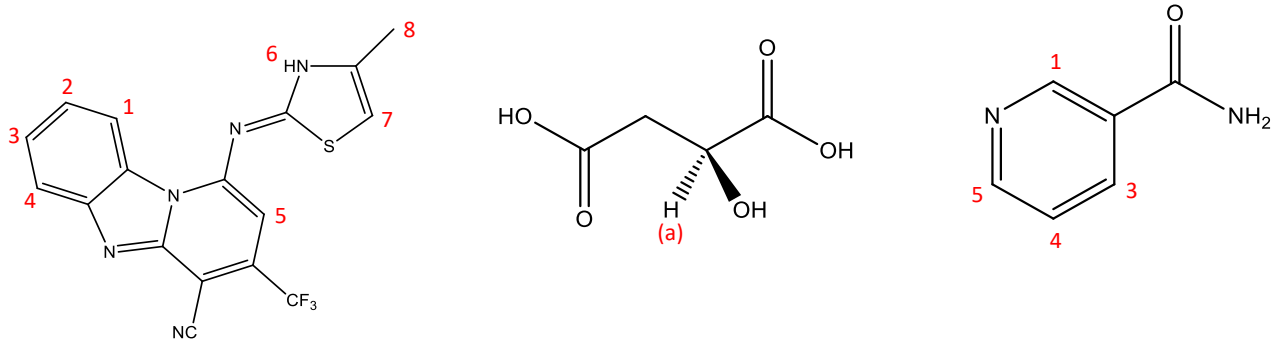


Figure 2.6.2: Molecular structures of GMP-31 (left), L-malic acid (centre), and nicotinamide (right), with specific molecular fragments labelled for the ^{1}H NMR analysis.

2.6.2.1) GMP-31-MAL

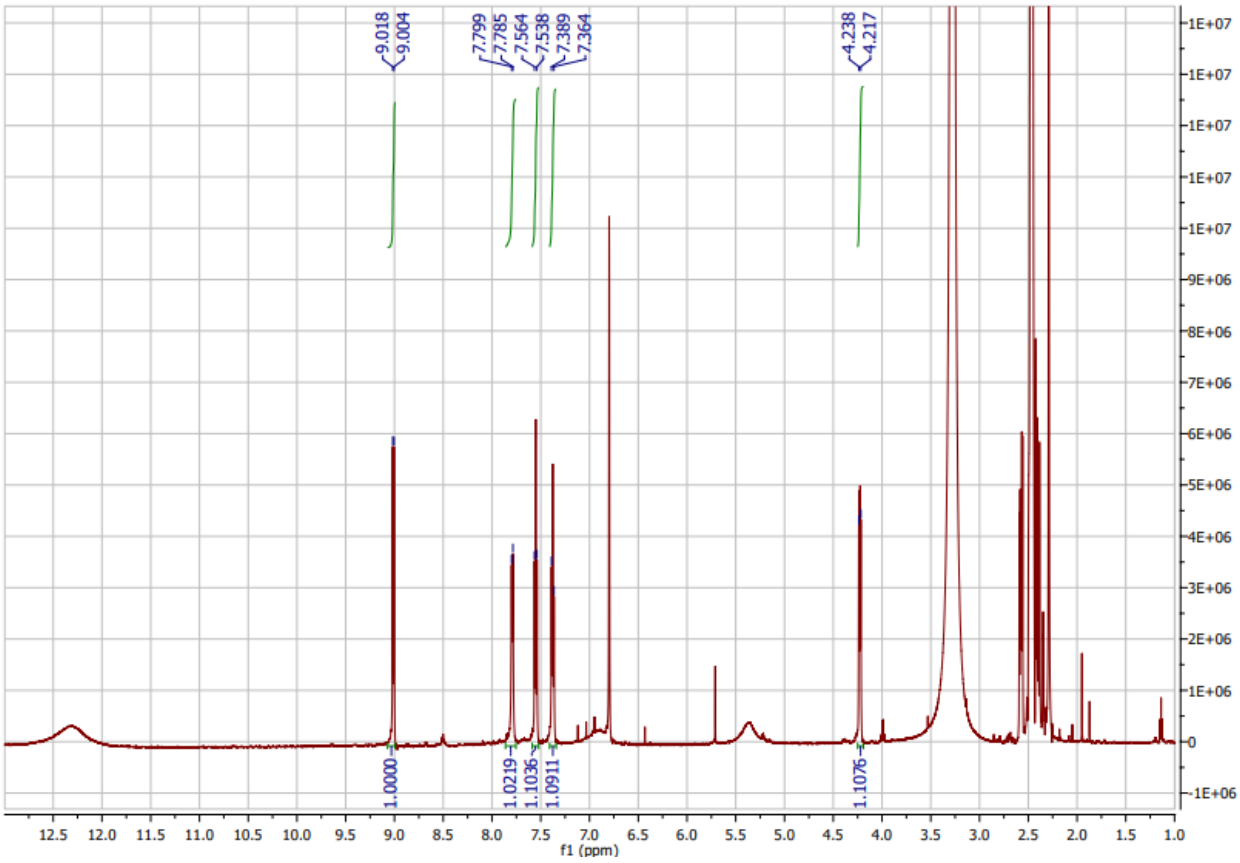


Figure 2.6.2.1: ^{1}H NMR spectrum of GMP-31-MAL.

Table 2.6.2.1: The ^{1}H NMR spectral analysis of GMP-31-MAL.

Assignment	δ (ppm)	Integration	Multiplicity	Proton representation (per molecule)	Stoichiometric ratio	Stoichiometric ratio (integer)
H1 (GMP-31)	9.004 – 9.018	1.0000*	doublet	1H	1.00	1
H4 (GMP-23)	7.785 – 7.799	1.0219	doublet	1H	1.02	1
H3 (GMP-23)	7.538 – 7.564	1.1036	triplet	1H	1.10	1
H2 (GMP-23)	7.364 – 7.389	1.0911	triplet	1H	1.09	1
H(a) (MAL)	4.217 – 4.238	1.1076	quartet	1H	1.11	1

2.6.2.2) GMP-31-NIC

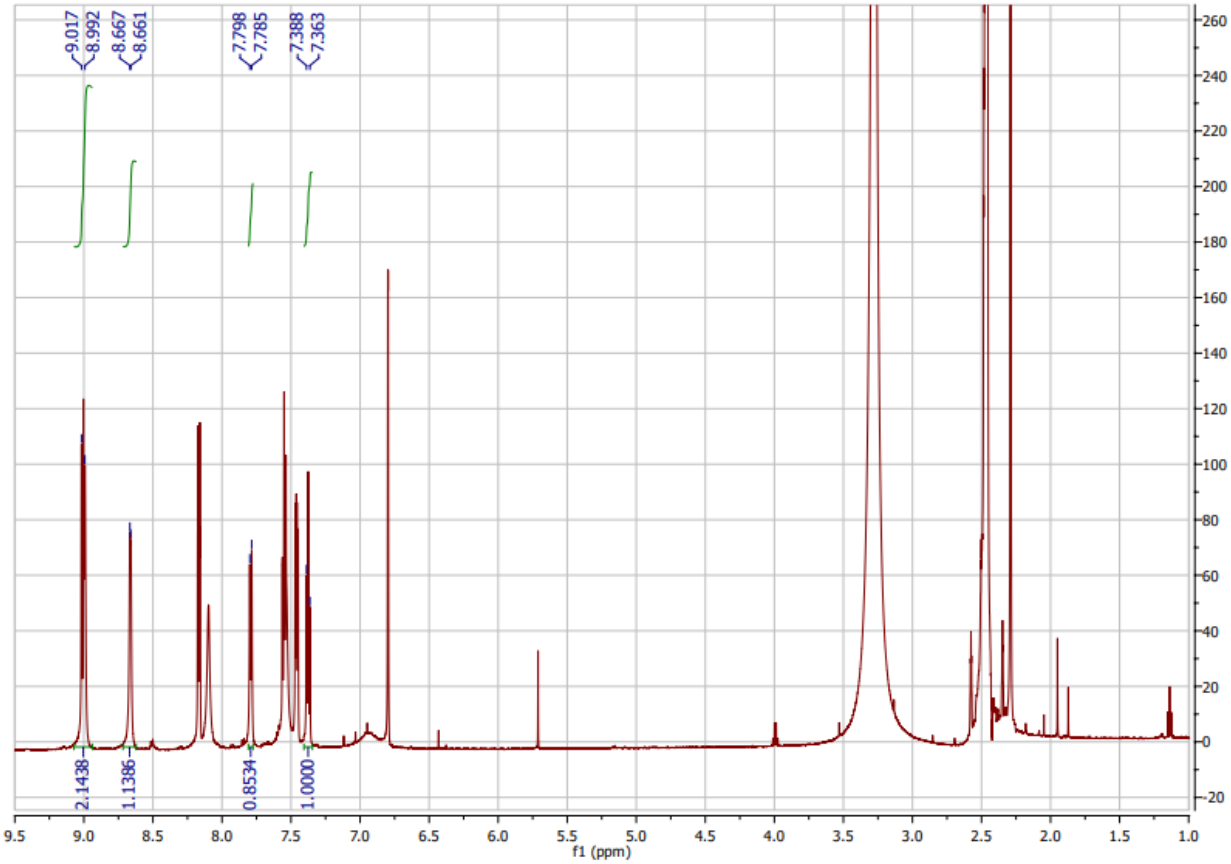


Figure 2.6.2.2: ^{1}H NMR spectrum of GMP-31-NIC.

Table 2.6.2.2: The ^{1}H NMR spectral analysis of GMP-31-NIC.

Assignment	δ (ppm)	Integration	Multiplicity	Proton representation (per molecule)	Stoichiometric ratio	Stoichiometric ratio (integer)
H1 (GMP-31) and H1 (NIC)	8.992 – 9.017	2.1438	singlet and doublet	1H & 1H	1.10	1
H5 (NIC)	8.661 – 8.667	1.1386	doublet	1H	1.14	1
H4 (GMP-23)	7.785 – 7.798	0.8534	doublet	1H	0.85	1
H2 (GMP-23)	7.363 – 7.388	1.0000*	triplet	1H	1.00	1

*reference integral

2.6.3) GMP-58-MAL and GMP-58-NIC

Figure 2.6.3 displays the specific atoms of GMP-58, L-malic acid, and nicotinamide that have been labelled for the ^{1}H NMR assignments that follow below. Figures 2.6.3.1 – 2.6.3.2 and Tables 2.6.3.1 and 2.6.3.2 display the results from the ^{1}H NMR analyses.

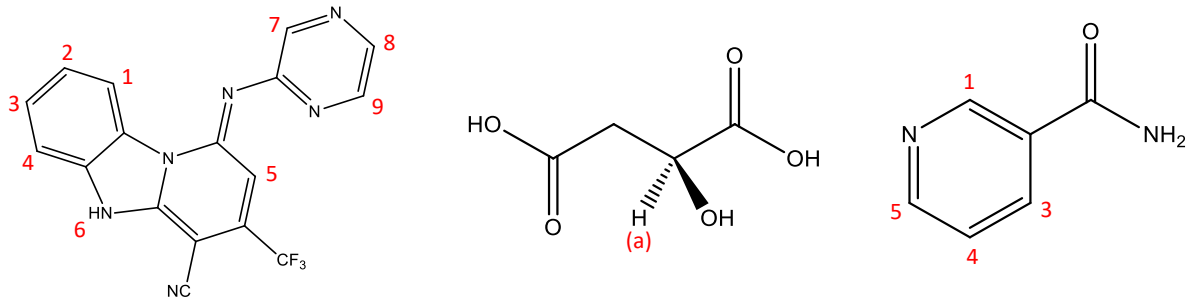


Figure 2.6.3: Molecular structures of GMP-58 (left), L-malic acid (centre), and nicotinamide (right), with specific molecular fragments labelled for the ^{1}H NMR analysis.

2.6.3.1) GMP-58-MAL

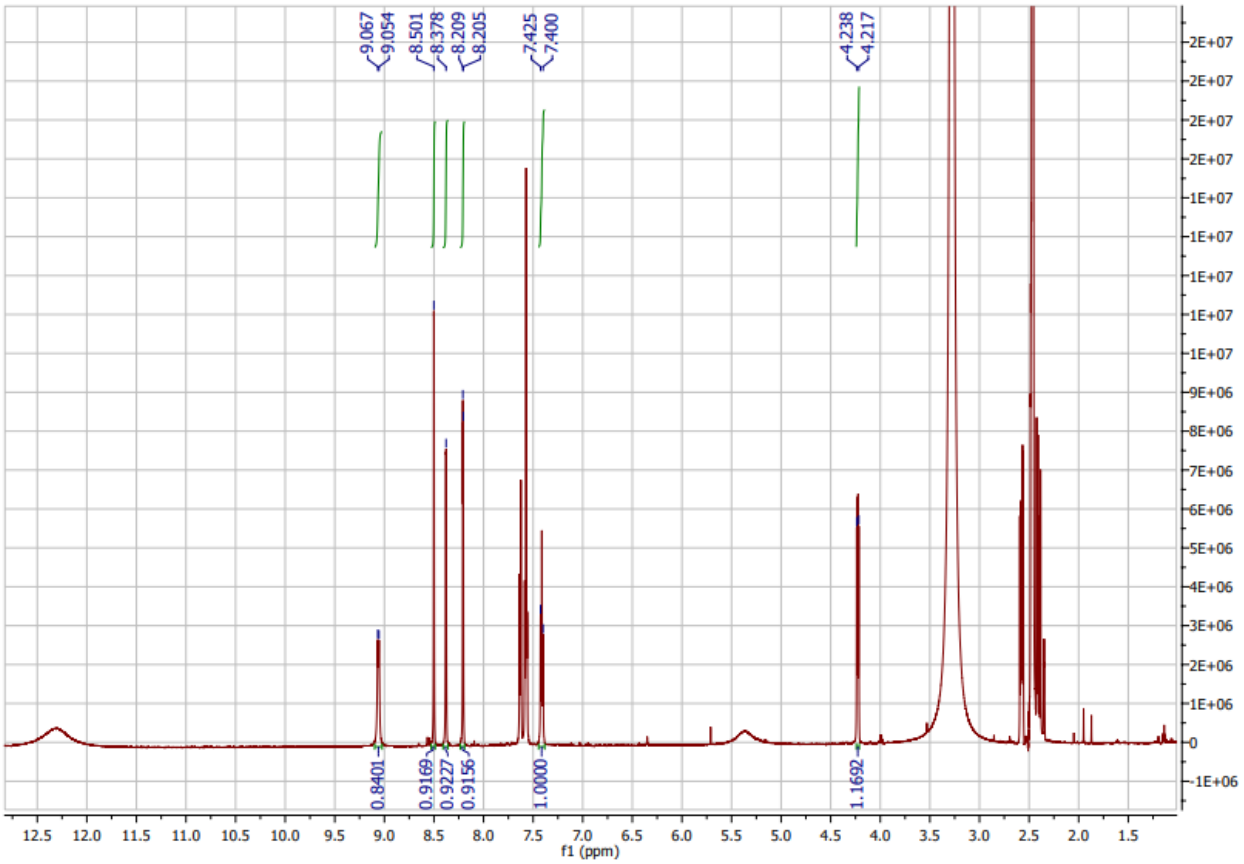


Figure 2.6.3.1: ^{1}H NMR spectrum of GMP-58-MAL.

Table 2.6.3.1: The ^{1}H NMR spectral analysis of GMP-58-MAL.

Assignment	δ (ppm)	Integration	Multiplicity	Proton representation (per molecule)	Stoichiometric ratio	Stoichiometric ratio (integer)
H1 (GMP-58)	9.054 – 9.067	0.8401	doublet	1H	0.84	1
H7 (GMP-58)	8.501	0.9169	singlet	1H	0.92	1
H8 (GMP-58)	8.378	0.9227	singlet	1H	0.92	1
H9 (GMP-58)	8.205 – 8.209	0.9156	doublet	1H	0.92	1
H2 (GMP-58)	7.400 – 7.425	1.0000*	triplet	1H	1.00	1
H(a) (MAL)	4.217 – 4.238	1.1692	quartet	1H	1.17	1

*reference integral

2.6.3.2) GMP-58-NIC

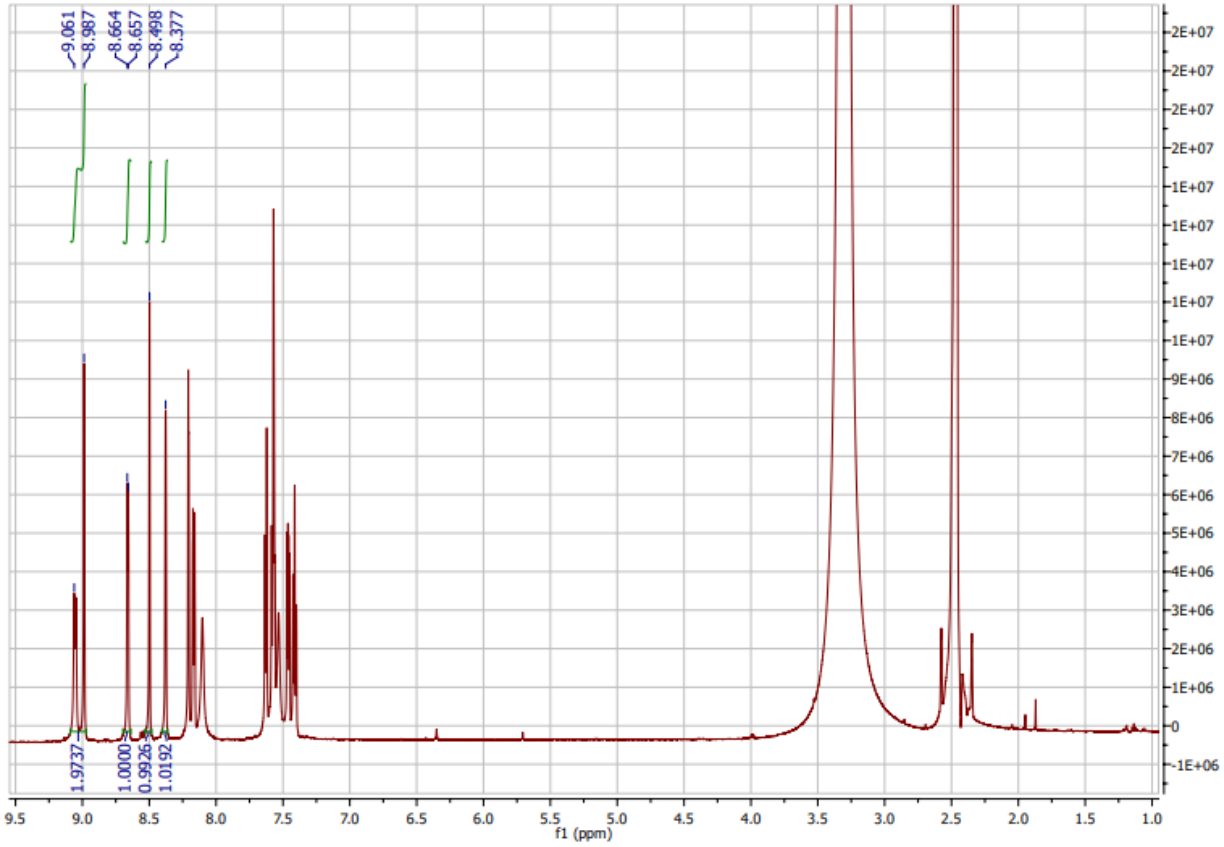


Figure 2.6.3.2: ^{1}H NMR spectrum of GMP-58-NIC.

Table 2.6.3.2: The ^{1}H NMR spectral analysis of GMP-58-NIC.

Assignment	δ (ppm)	Integration	Multiplicity	Proton representation (per molecule)	Stoichiometric ratio	Stoichiometric ratio (integer)
H1 (GMP-58) and H1 (NIC)	8.987 – 9.061	1.9737	singlet and doublet	1H & 1H	0.99	1
H5 (NIC)	8.657 – 8.664	1.0000*	doublet	1H	1.00	1
H7 (GMP-58)	8.498	0.9926	singlet	1H	0.99	1
H8 (GMP-58)	8.377	1.0192	singlet	1H	1.02	1

*reference integral

2.7) The solubility enhancement results for the six GMP-coformer products and for the amorphous forms of GMP-23, GMP-31 and GMP-58

Figures 2.7.1 – 2.7.15 and Table 2.7.1 display the results for the solubility analysis of the GMP-coformer products, and for the amorphous forms of GMP-23, GMP-31 and GMP-58.

Solubility results for products formed with GMP-23:

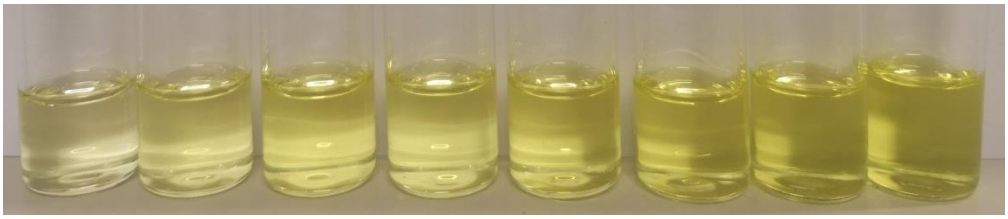


Figure 2.7.1: A series of reference concentrations of GMP-23, indicating how much more concentrated a particular vial is in comparison to the initial vial on the far left (labelled 1×).

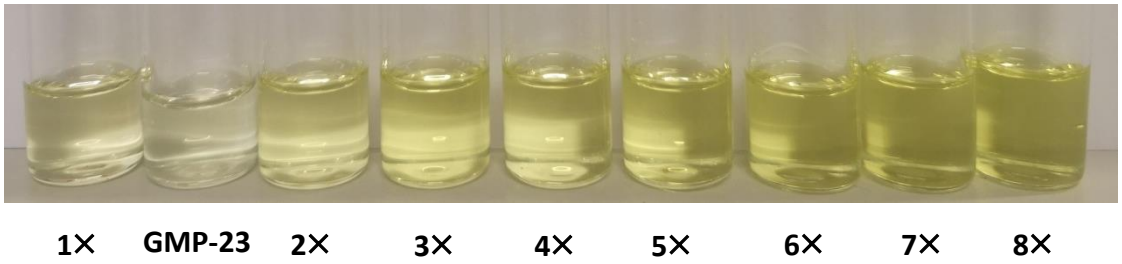


Figure 2.7.2: The solution containing the dissolved quantity of GMP-23 at 37 ^{o}C (labelled GMP-23). It is evident that the closest concentration is the reference solution labelled 1×.

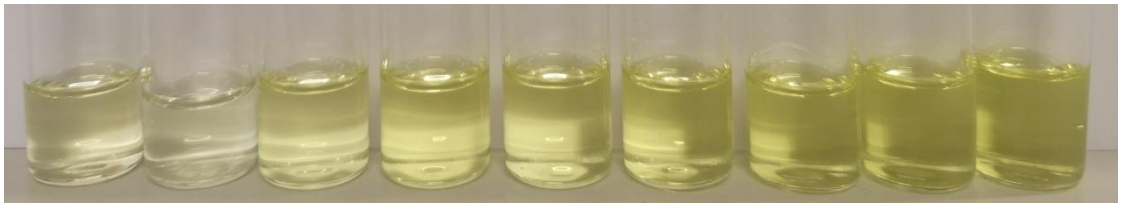


Figure 2.7.3: The solution containing the dissolved quantity of amorphous GMP-23 (GMP-23 ground for 15 minutes) at 37 °C. It is also evident that the closest concentration is the reference solution labelled 1× and thus no solubility increase was observed for the amorphous GMP-23 sample.

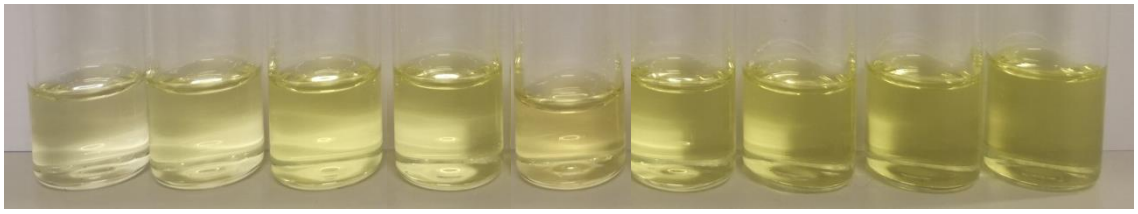


Figure 2.7.4: The solution containing the dissolved quantity of GMP-23-MAL at 37 °C. It is apparent that the closest concentration is the solution labelled 4× and thus an approximate 4-fold solubility increase was observed for GMP-23-MAL.

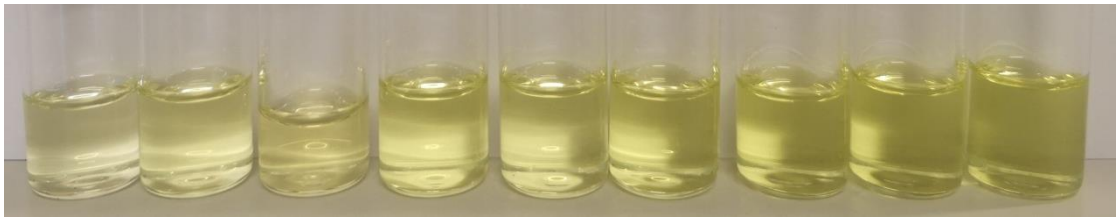


Figure 2.7.5: The solution containing the dissolved quantity of GMP-23-NIC at 37 °C. It is evident that the closest concentration is the solution labelled 2× and thus an approximate 2-fold solubility increase was observed for GMP-23-NIC.

Solubility results for products formed with GMP-31:

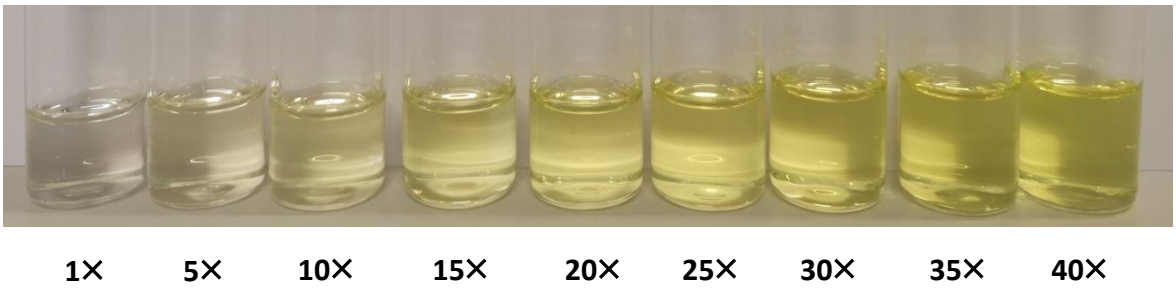


Figure 2.7.6: A series of reference concentrations of GMP-31, indicating how much more concentrated a particular vial is in comparison to the initial vial on the far left (labelled 1×).

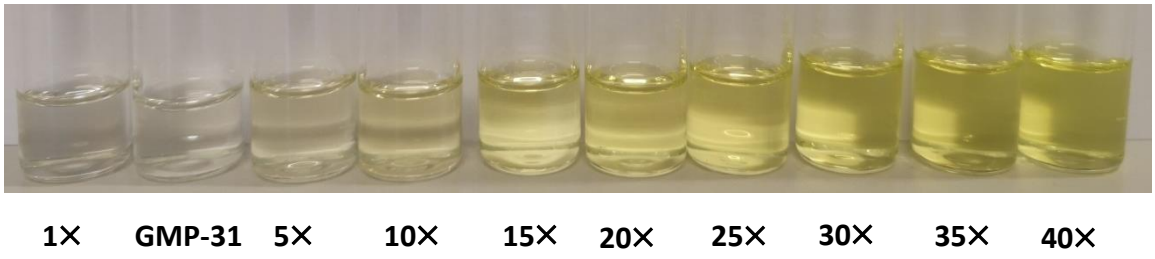


Figure 2.7.7: The solution containing the dissolved quantity of GMP-31 at 37 °C (labelled GMP-31). It is evident that the closest concentration is the reference solution labelled 1×.

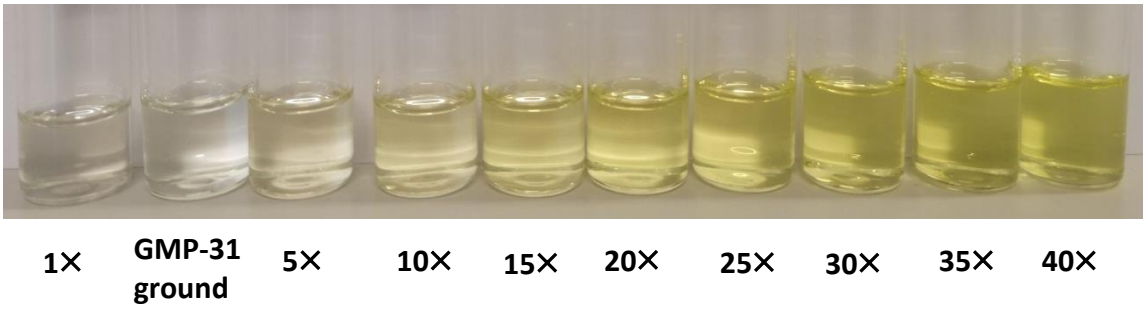


Figure 2.7.8: The solution containing the dissolved quantity of amorphous GMP-31 (GMP-31 ground for 15 minutes) at 37 °C. It is also evident that the closest concentration is the reference solution labelled 1× and thus no solubility increase was observed for the amorphous GMP-31 sample.

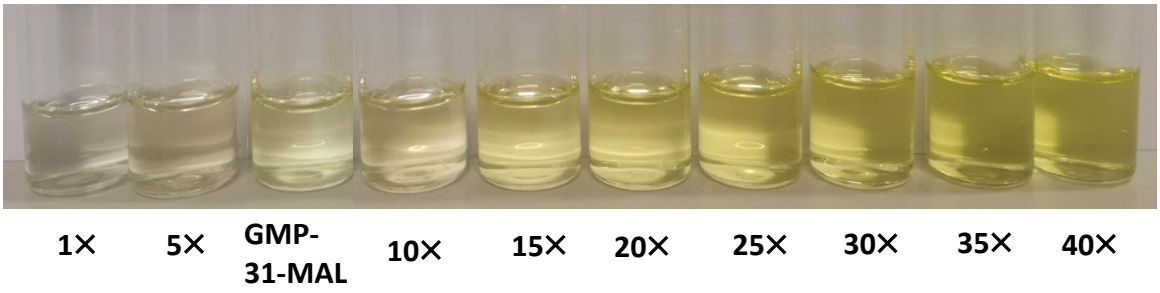


Figure 2.7.9: The solution containing the dissolved quantity of GMP-31-MAL at 37 °C. It is apparent that the closest concentration is the solution labelled 10× and thus an approximate 10-fold solubility increase was observed for GMP-31-MAL.

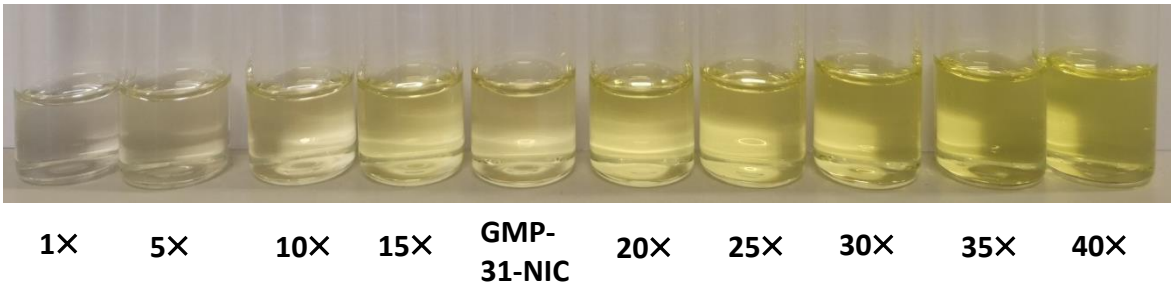


Figure 2.7.10: The solution containing the dissolved quantity of GMP-31-NIC at 37 °C. It is apparent that the closest concentration is between 15× and 20×, thus indicating an approximate solubility increase between 15-fold and 20-fold for GMP-31-NIC.

Solubility results for products formed with GMP-58:



Figure 2.7.11: A series of reference concentrations of GMP-58, indicating how much more concentrated a particular vial is in comparison to the initial vial on the far left (labelled 1×).

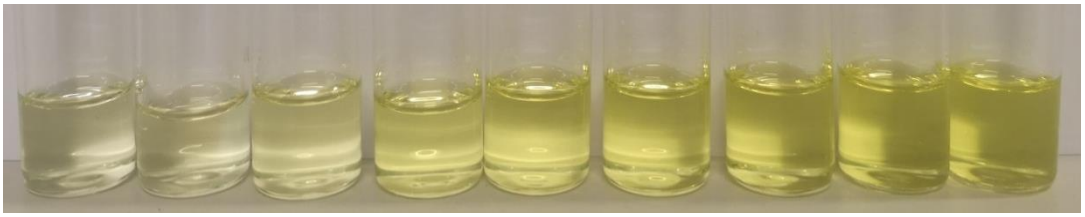


Figure 2.7.12: The solution containing the dissolved quantity of GMP-58 at 37 °C (labelled GMP-58). It is evident that the closest concentration is the reference solution labelled 1×.

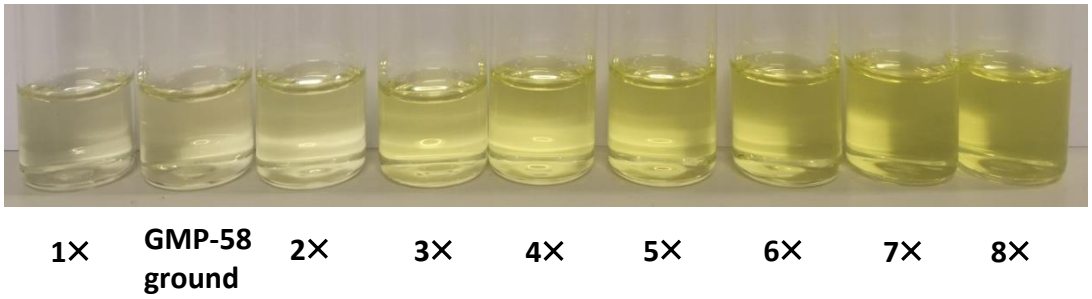


Figure 2.7.13: The solution containing the dissolved quantity of amorphous GMP-58 (GMP-58 ground for 15 minutes) at 37 °C. It is evident that the closest concentration is the reference solution labelled 2× and thus an approximate 2-fold solubility increase has occurred for GMP-58 in an amorphous state.



Figure 2.7.14: The solution containing the dissolved quantity of GMP-58-MAL at 37 °C. It is apparent that the closest concentration is the reference solution labelled 1× and thus no solubility increase was observed for GMP-58-MAL.

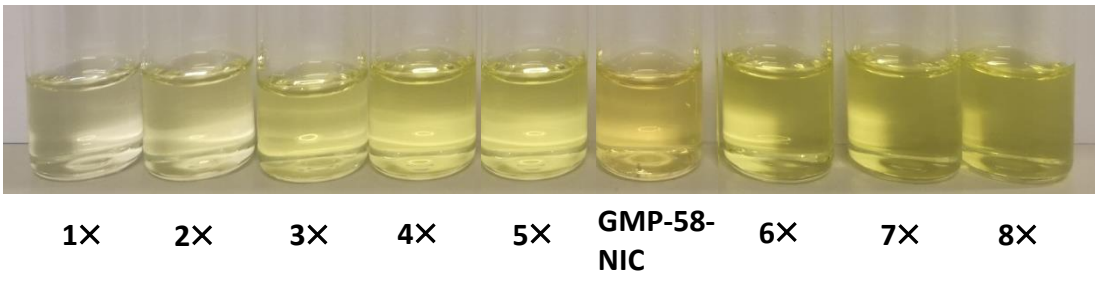


Figure 2.7.15: The solution containing the dissolved quantity of GMP-58-NIC at 37 °C. It is apparent that the closest concentration is the solution labelled 6× and thus an approximate 6-fold solubility increase was observed for GMP-58-NIC.

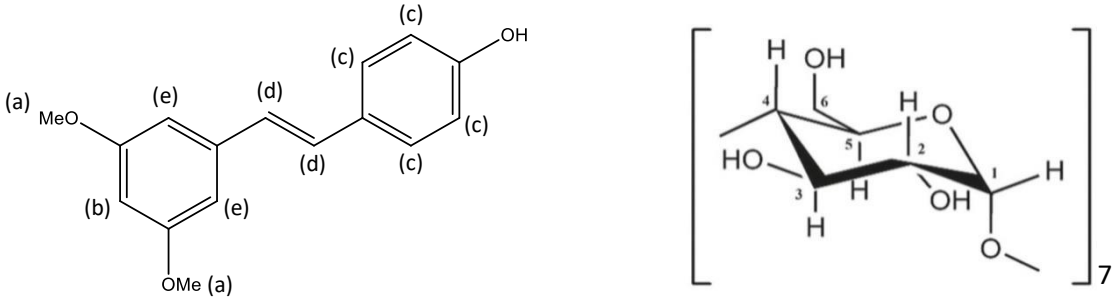
Table 2.7.1: The solubility enhancement factors for the products of interest.

Product	Solubility enhancement		Product	Solubility enhancement		Product	Solubility enhancement
GMP-23 ground	None		GP-31 ground	None		GMP-58 ground	2-fold
GMP-23-MAL	4-fold		GMP-31-MAL	10-fold		GMP-58-MAL	None
GMP-23-NIC	2-fold		GMP-31-NIC	(15 – 20)-fold		GMP-58-NIC	6-fold

Section 3: Cyclodextrin inclusion with pterostilbene

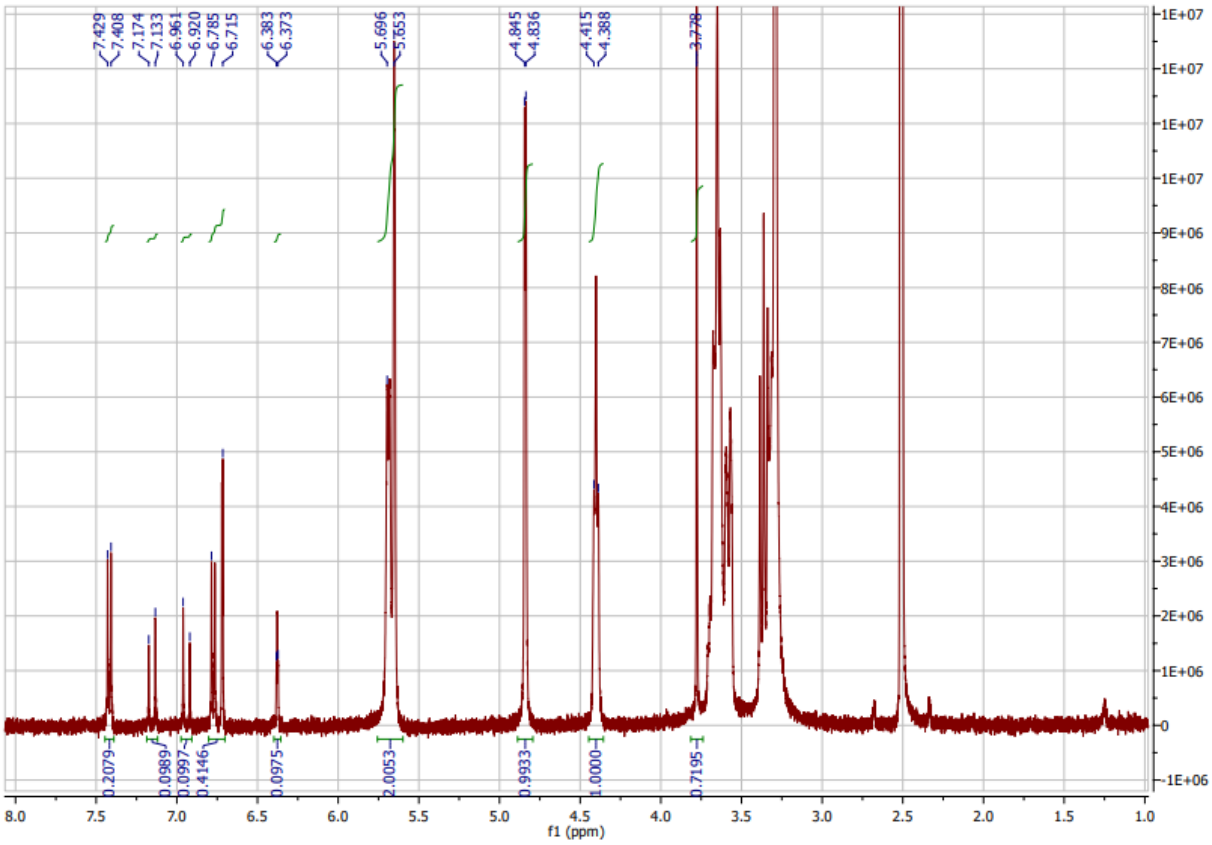
3.1) Supplementary data for β-CD·PTB

3.1.1) The ^{1}H NMR analysis of β-CD·PTB.

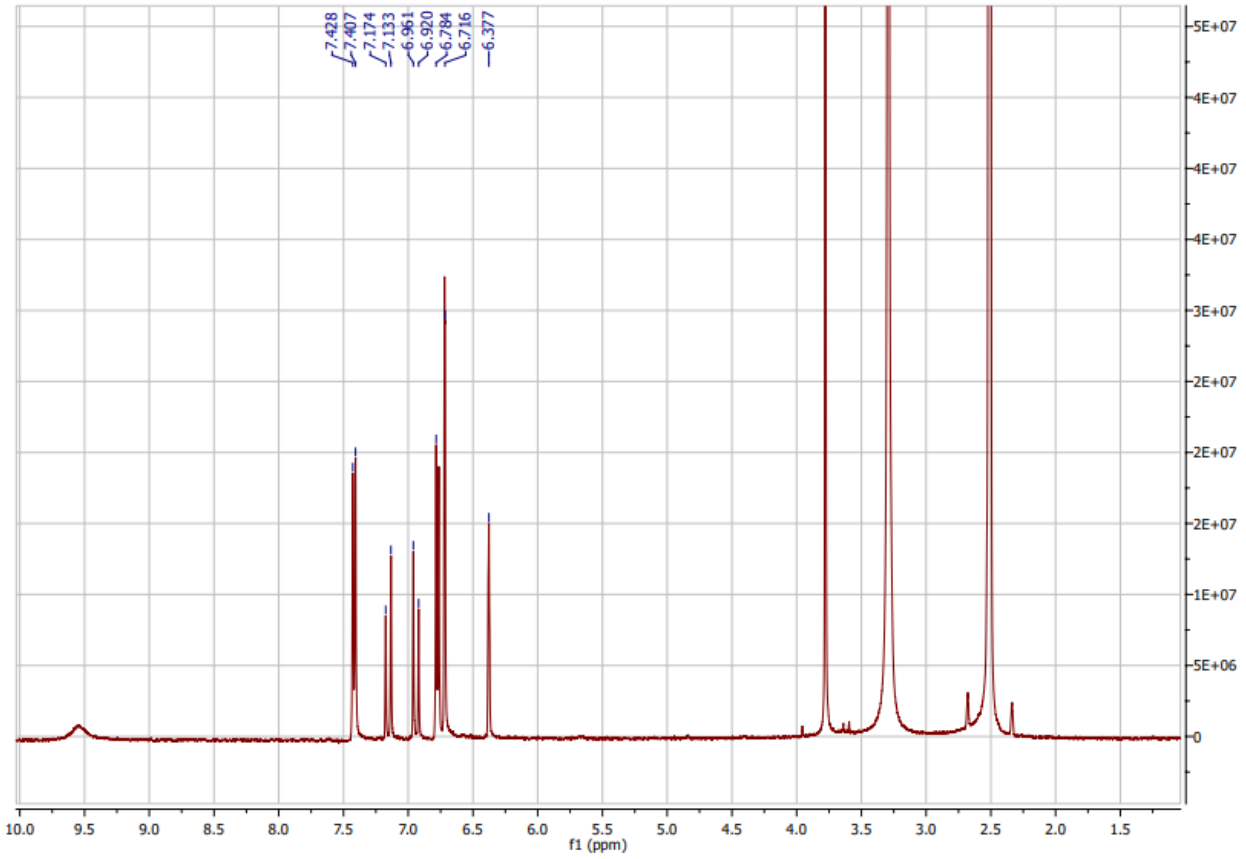


Molecular structures of pterostilbene (left) and β-CD (right). Specific atoms have been labelled for reference in the ^{1}H NMR analysis. Adapted from Guedes *et al.*[1]

The ^{1}H NMR spectrum of β-CD·PTB.



3.1.2) The ^{1}H NMR spectrum of the polymorph of pterostilbene for reference purposes.



3.1.3) Calculation of the number of water molecules in β-CD·PTB·nH_2O, and the number of water molecules per β-CD molecule (from the TGA analysis).

$$13.1 \pm 0.4\% = \frac{MW(Water)n}{(MW(\beta - CD)) + MW(Pterostilbene) + MW(Water)n}$$

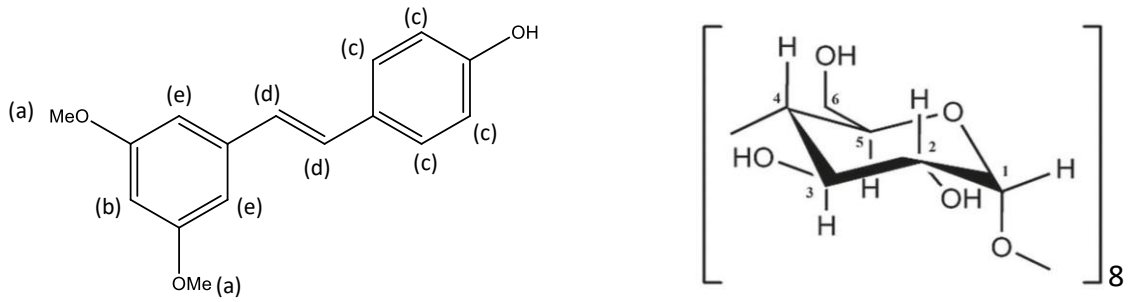
$$0.131 = \frac{18.016n}{1134.987 + 256.296 + 18.016n}$$

n = 11.6 water molecules

Therefore there are 11.6 ± 0.4 water molecules per β-CD molecule.

3.2) Supplementary data for γ-CD·PTB

3.2.1) The ^{1}H NMR analysis of γ-CD·PTB (experiment 1).



Molecular structures of pterostilbene (left) and γ-CD (right). Specific atoms have been labelled for reference in the ^{1}H NMR analysis. Adapted from Guedes *et al.*[1]

The ^{1}H NMR spectrum of γ-CD·PTB (experiment 1).

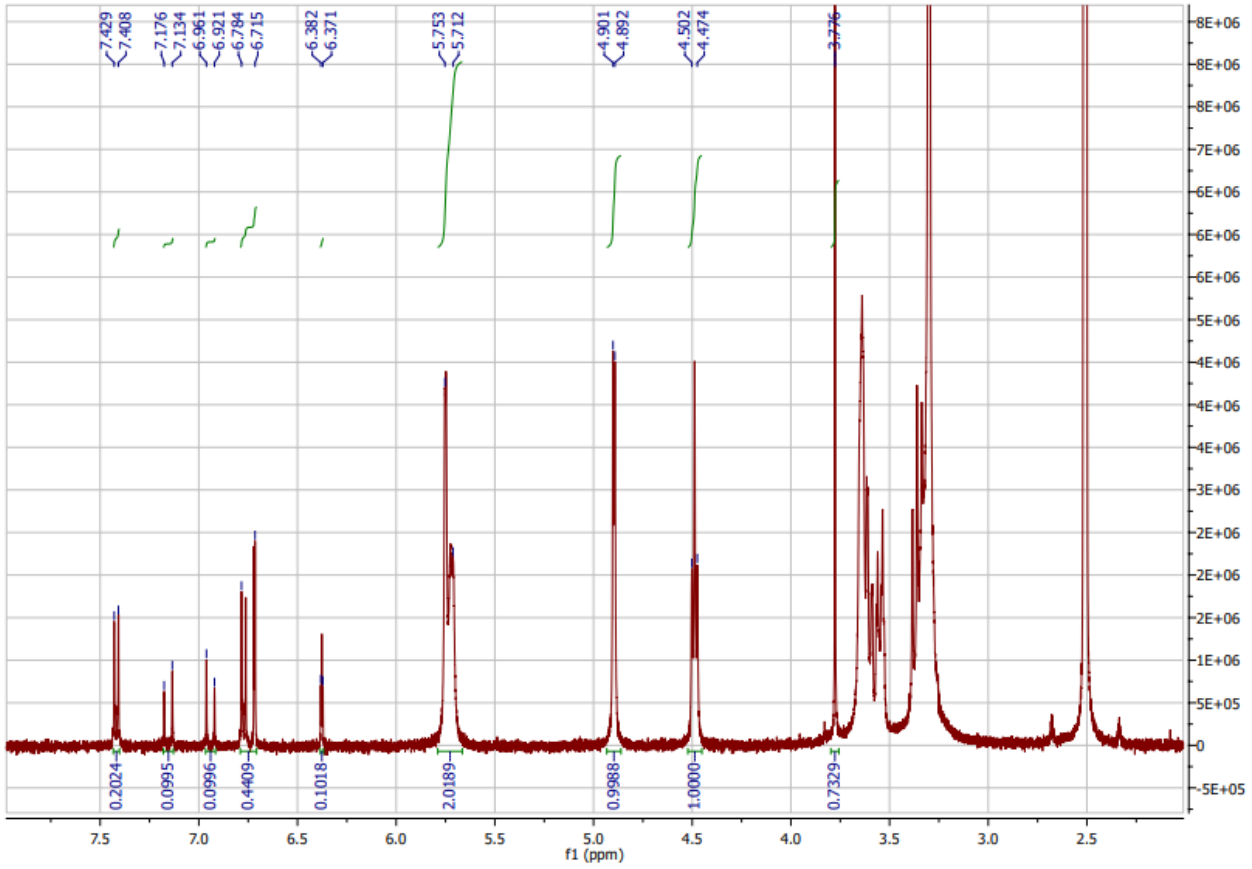


Table 3.2.1: The ^{1}H NMR spectral analysis of γ-CD·PTB, with reference to Figure 3.2.1 (experiment 1).

Assignment	δ (ppm)	Integration	Multiplicity	Proton representation (per molecule)	Stoichiometric ratio	Stoichiometric ratio (integer)
2X OC<u>H</u>$_3$ (a) (PTB)	3.776	0.7329	singlet	6H	0.98	1
O<u>H</u>-6 (γ-CD)	4.474 – 4.502	1.0000*	triplet	8H	1.00	1
C<u>H</u>-1 (γ-CD)	4.892 – 4.901	0.9988	doublet	8H	1.00	1
O<u>H</u>-3 and O<u>H</u>-2 (γ-CD)	5.712 – 5.753	2.0189	two separate doublets	16H	1.01	1
C<u>H</u> (b) aromatic (PTB)	6.371 – 6.382	0.1018	triplet (long range coupling)	1H	0.81	1
4X C<u>H</u> (c) aromatic (PTB)	6.715 – 6.784	0.4409	doublet of doublets	4H	0.88	1
C<u>H</u> (d) vinylic (PTB)	6.921 – 6.961	0.0996	doublet	1H	0.80	1
C<u>H</u> (d) vinylic (PTB)	7.134 – 7.176	0.0995	doublet	1H	0.80	1
2X C<u>H</u> (e) aromatic (PTB)	7.408 – 7.429	0.2024	doublet of triplets	2H	0.81	1

*reference integral

3.2.2) The ^{1}H NMR spectrum of γ-CD·PTB (experiment 2).

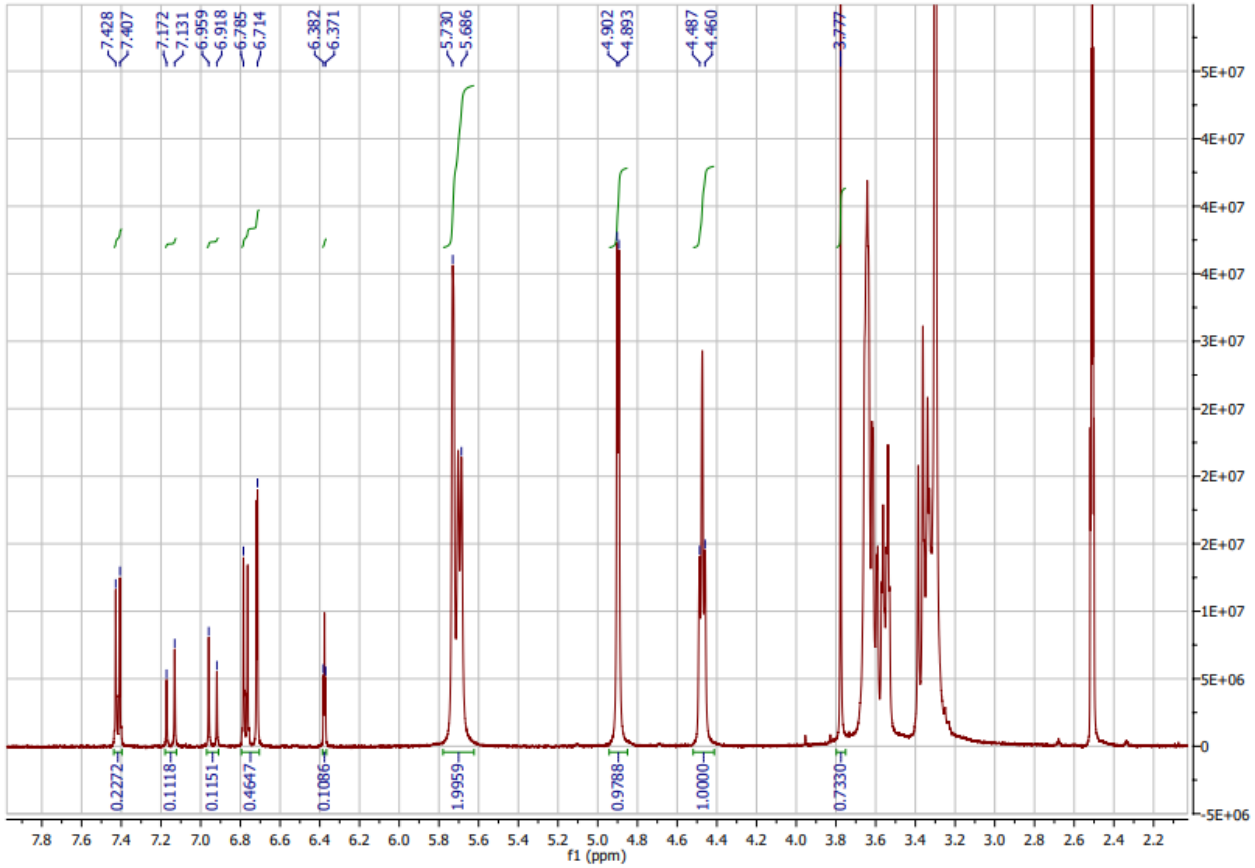


Table 3.2.2: The ^{1}H NMR spectral analysis of γ-CD·PTB, with reference to Figure 3.2.1 (experiment 2).

Assignment	δ (ppm)	Integration	Multiplicity	Proton representation (per molecule)	Stoichiometric ratio	Stoichiometric ratio (integer)
2X OC<u>H</u>$_3$ (a) (PTB)	3.777	0.7330	singlet	6H	0.98	1
O<u>H</u>-6 (γ-CD)	4.460 – 4.487	1.0000*	triplet	8H	1.00	1
C<u>H</u>-1 (γ-CD)	4.893 – 4.902	0.9788	doublet	8H	0.98	1
O<u>H</u>-3 and O<u>H</u>-2 (γ-CD)	5.686 – 5.730	1.9959	two separate doublets	16H	1.00	1
C<u>H</u> (b) aromatic (PTB)	6.371 – 6.382	0.1086	triplet (long range coupling)	1H	0.87	1
4X C<u>H</u> (c) aromatic (PTB)	6.714 – 6.785	0.4647	doublet of doublets	4H	0.93	1
C<u>H</u> (d) vinylic (PTB)	6.918 – 6.959	0.1151	doublet	1H	0.92	1
C<u>H</u> (d) vinylic (PTB)	7.131 – 7.172	0.1118	doublet	1H	0.89	1
2X C<u>H</u> (e) aromatic (PTB)	7.407 – 7.428	0.2272	doublet of triplets	2H	0.91	1

*reference integral

3.2.3) Calculation of the number of water molecules in γ-CD·PTB·nH_2O, and the number of water molecules per γ-CD molecule (from the TGA analysis).

$$12.8 \pm 0.4\% = \frac{\mathrm{MW(Water)n}}{(\mathrm{MW}(\gamma - \mathrm{CD})) + \mathrm{MW(Pterostilbene)} + \mathrm{MW(Water)n}}$$

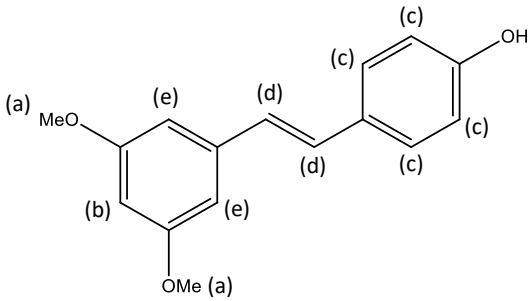
$$0.128 = \frac{18.016n}{1297.12 + 256.296 + 18.016n}$$

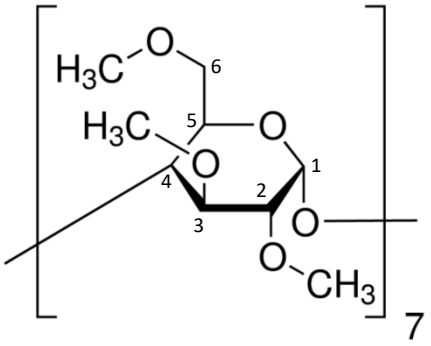
$\mathrm{n} = 12.7$ water molecules

Therefore there are 12.7 ± 0.4 water molecules per γ-CD molecule.

3.3) Supplementary data for TMB·PTB

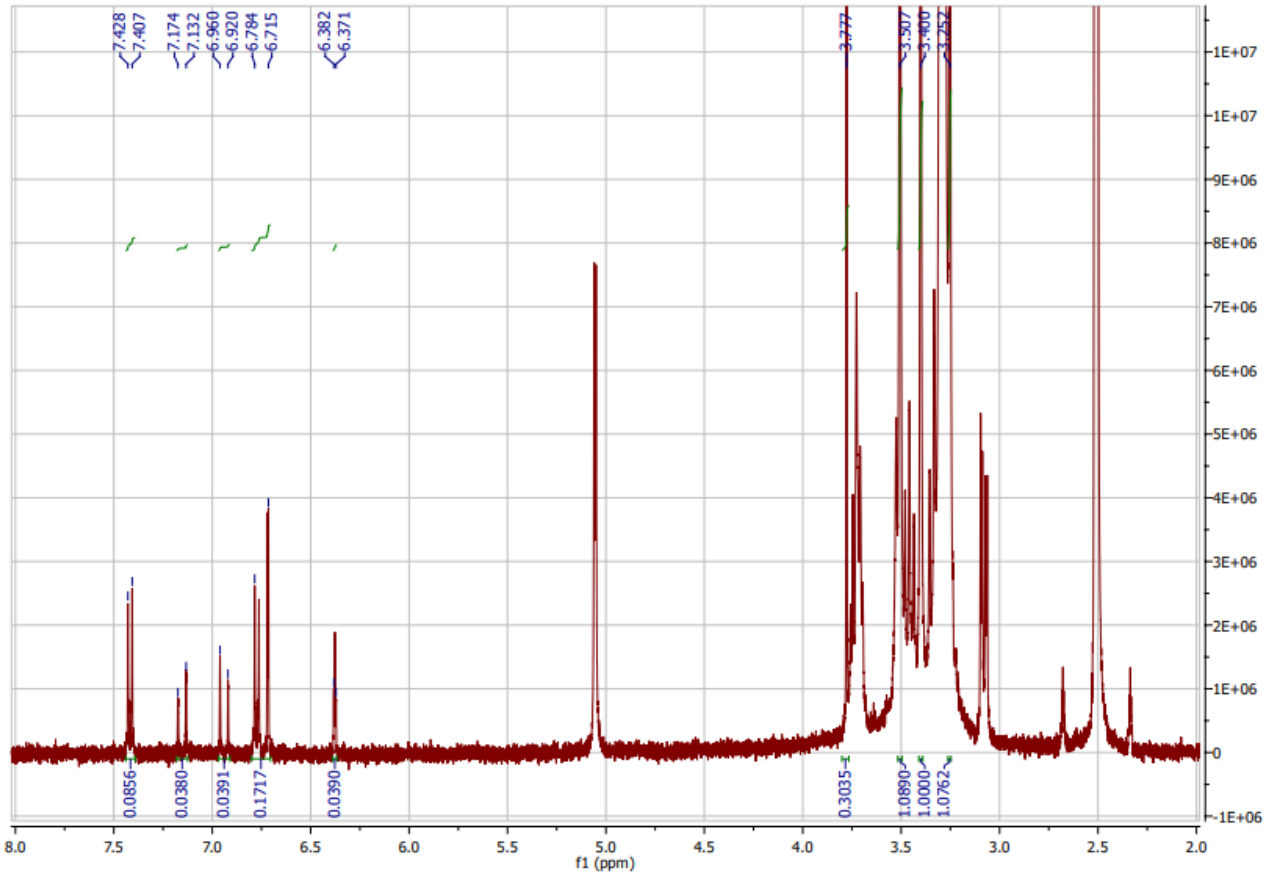
3.3.1) The ^{1}H NMR analysis of TMB·PTB.





Molecular structures of pterostilbene (left) and TMB (right). Specific atoms have been labelled for the ^{1}H NMR analysis. Adapted from Sigma-Aldrich.[2]

The ^{1}H NMR spectrum of TMB·PTB.



3.3.2) Calculation of the number of water molecules in TMB·PTB·nH_2O, and the number of water molecules per TMB molecule (from the TGA analysis).

$$0.6 \pm 0.2\% = \frac{\mathrm{MW(Water)n}}{\mathrm{MW(TMB) + MW(Pterostilbene) + MW(Water)n}}$$

$$0.006 = \frac{18.016n}{1429.54 + 256.296 + 18.016n}$$

$\mathrm{n} = 0.6$ water molecules

Therefore there are 0.6 ± 0.1 water molecules per TMB molecule.

3.3.3) Calculation for determining the stoichiometry of the anhydrous TMB·PTB inclusion complex (from the TGA analysis).

Percentage mass loss of pterostilbene (from TGA): $14.9 \pm 1.4\%$

Ratio of pterostilbene to a 1:1 stoichiometric host-guest anhydrous inclusion complex:

$$\frac{\mathrm{M(Pterostilbene)}}{\mathrm{M(Pterostilbene) + M(TMB)}}$$

$$\frac{256.296}{256.296 + 1429.54} \times 100 = 15.2\%$$

3.3.4) Phase solubility sample calculation

Determining the concentration of pterostilbene dissolved in 4 cm^3 of the 4 mM concentration solution of RAMEB

Initially, the 4 mM CD solution was diluted 1:100 in order to be within the readable range of the high-performance liquid chromatography (HPLC) instrument.

The peak area of the pterostilbene contribution for the 1:100 dilution of the 4 mM CD solution was 77.65.

Therefore, using the equation of the line from the calibration curve, y = 10914x - 57.83, the concentration of pterostilbene in the 1:100 dilution of the 4 mM CD solution was 0.01240 mM.

Consequently, the concentration of pterostilbene in the 4 mM CD solution (undiluted) was 1.240 mM (volume was 4 cm^3).

Determining the mass of pterostilbene dissolved in 4 cm^3 of the 4 mM CD solution

Following on from the previous calculation with the concentration of pterostilbene in the 4 mM CD solution (undiluted) being determined to be 1.240 mM (volume was 4 cm^3).

$C = n / v$

$1.240 \times 10^{-3}\ M = n / 4 \times 10^{-3}\ dm^3$

$n = 4.961 \times 10^{-6}\ mol$

Therefore: $n = m / M$

$4.961 \times 10^{-6}\ mol = m / 256.296\ g.mol^{-1}$

$m = 1.271 \times 10^{-3}\ g$

m = 1.271 mg of pterostilbene dissolved in 4 cm^3 of the 4 mM CD solution.

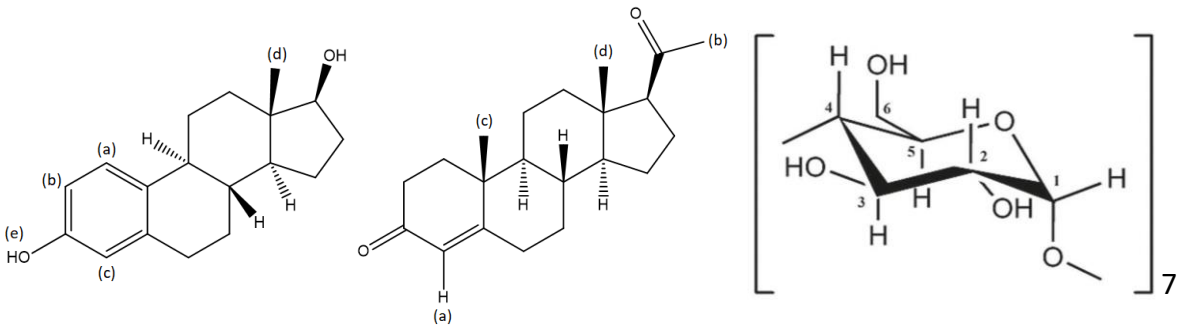
Therefore, 0.318 mg of pterostilbene was dissolved per cm^3 in the 4 mM CD solution.

Thus, the solubility enhancement is: $0.318\ mg.cm^{-3} / 5.023 \times 10^{-3}\ mg.cm^{-3}$ = 63-fold.

Section 4: Cyclodextrin inclusion with β-estradiol and progesterone

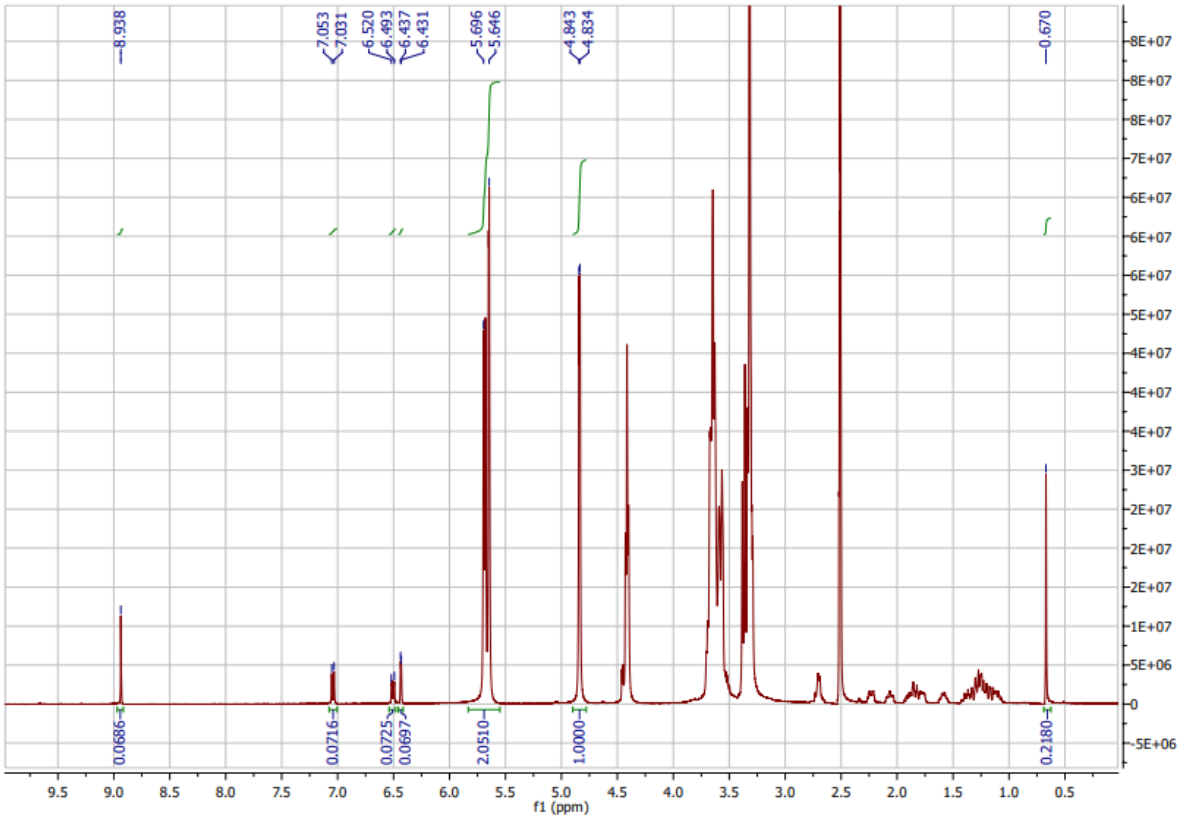
4.1) Supplementary data for β-CD·BES and β-CD·PRO

4.1.1) The ^{1}H NMR analyses of β-CD·BES and β-CD·PRO.

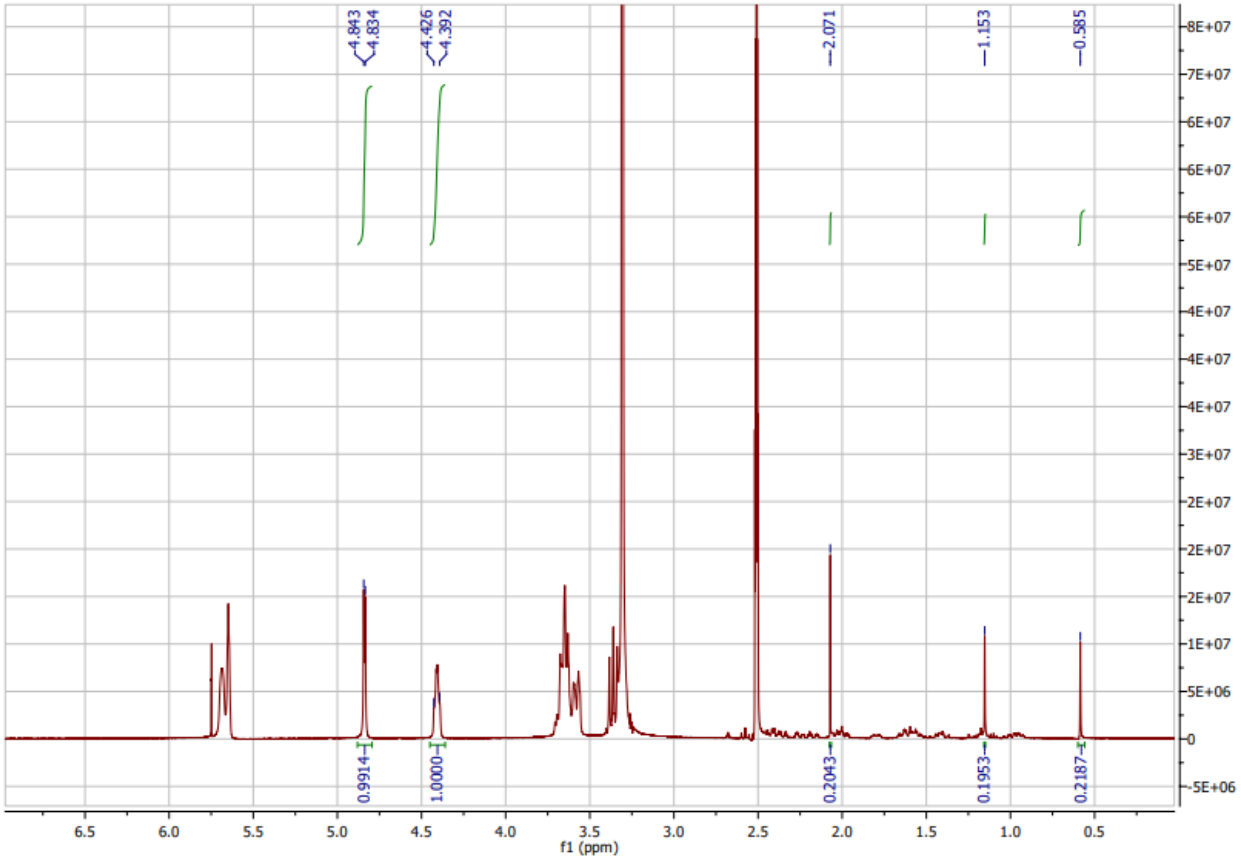


Molecular structures of β-estradiol (left), progesterone (centre), and β-CD (right), with specific molecular fragments labelled for the ^{1}H NMR analysis. Adapted from Guedes *et al.*[1]

The ^{1}H NMR spectrum of β-CD·BES.



The ^{1}H NMR spectrum of β-CD·PRO.



4.1.2) Calculation of the number of water molecules in $(\beta\text{-CD})_2\cdot BES\cdot nH_2O$, and the number of water molecules per β-CD molecule (from the TGA analysis).

$$11.1 \pm 0.2\% = \frac{\mathrm{MW(Water)n}}{2(\mathrm{MW}(\beta - \mathrm{CD})) + \mathrm{MW}(\beta - \mathrm{Estradiol}) + \mathrm{MW(Water)n}}$$

$$0.111 = \frac{18.016n}{2(1134.987) + 272.382 + 18.016n}$$

$n = 17.7$ water molecules

Therefore there are 8.8 ± 0.2 water molecules per β-CD molecule in the complex.

4.1.3) Calculation of the number of water molecules in (β-CD)$_2$·PRO·nH_2O, and the number of water molecules per β-CD molecule (from the TGA analysis).

$$12.3 \pm 0.2\% = \frac{\mathrm{MW(Water)n}}{2(\mathrm{MW}(\beta - \mathrm{CD})) + \mathrm{MW(Progesterone)} + \mathrm{MW(Water)n}}$$

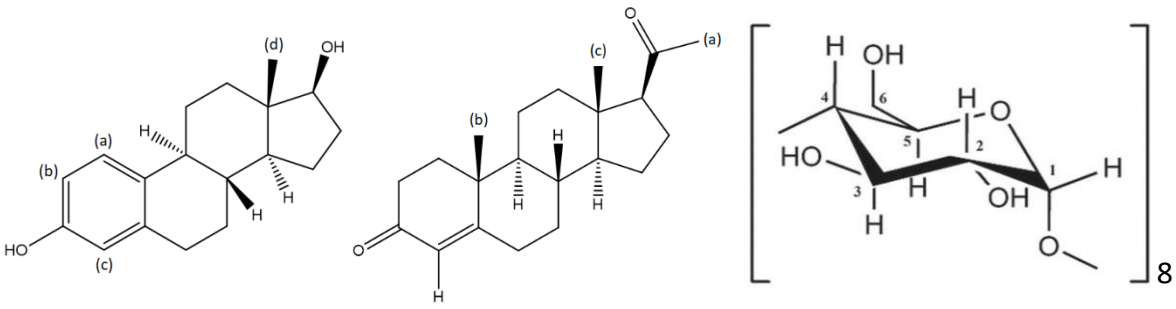
$$0.123 = \frac{18.016n}{2(1134.987) + 314.469 + 18.016n}$$

$\mathrm{n} = 20.0$ water molecules

Therefore there are 10.0 ± 0.2 water molecules per β-CD molecule.

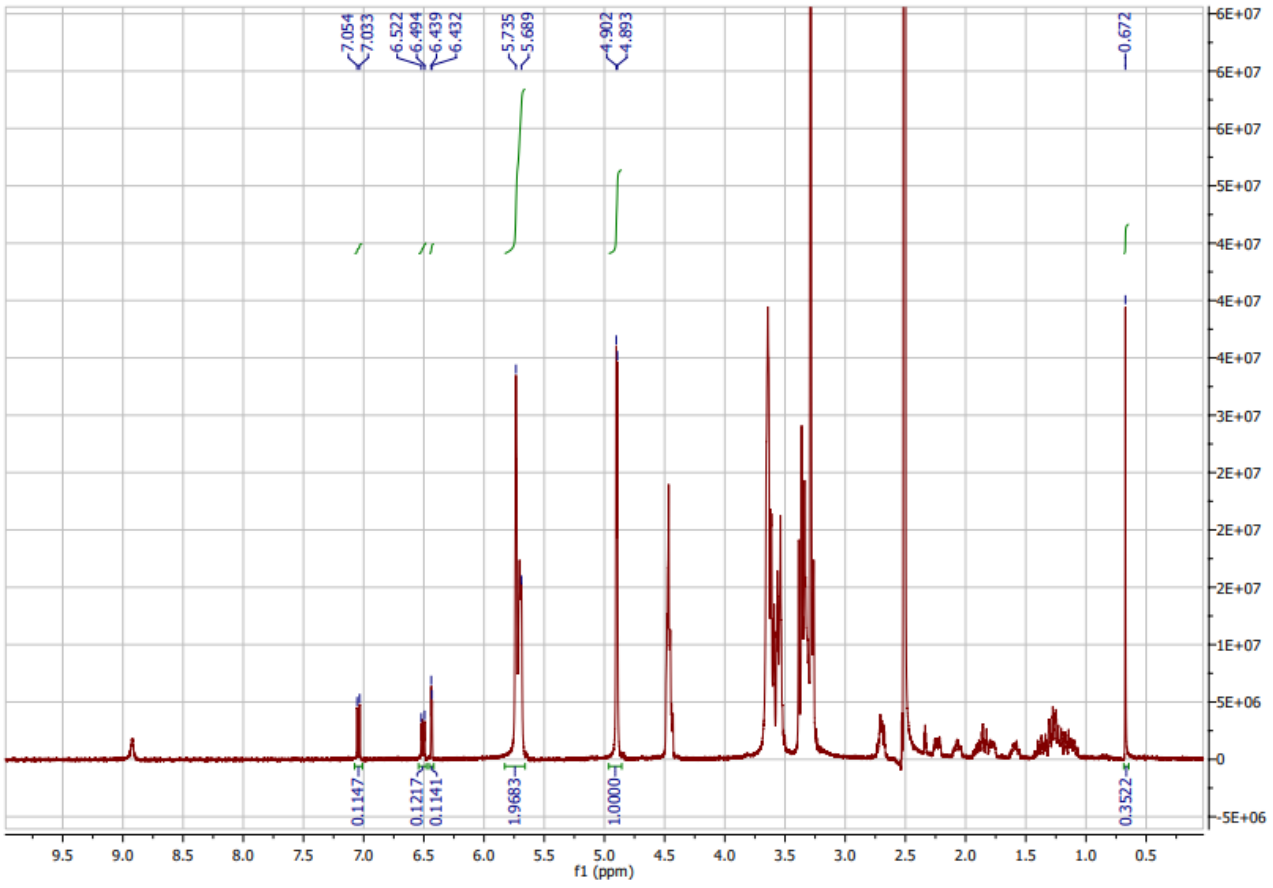
4.2) Supplementary data for γ-CD·BES and γ-CD·PRO

4.2.1) The ^{1}H NMR analyses of γ-CD·BES and γ-CD·PRO.

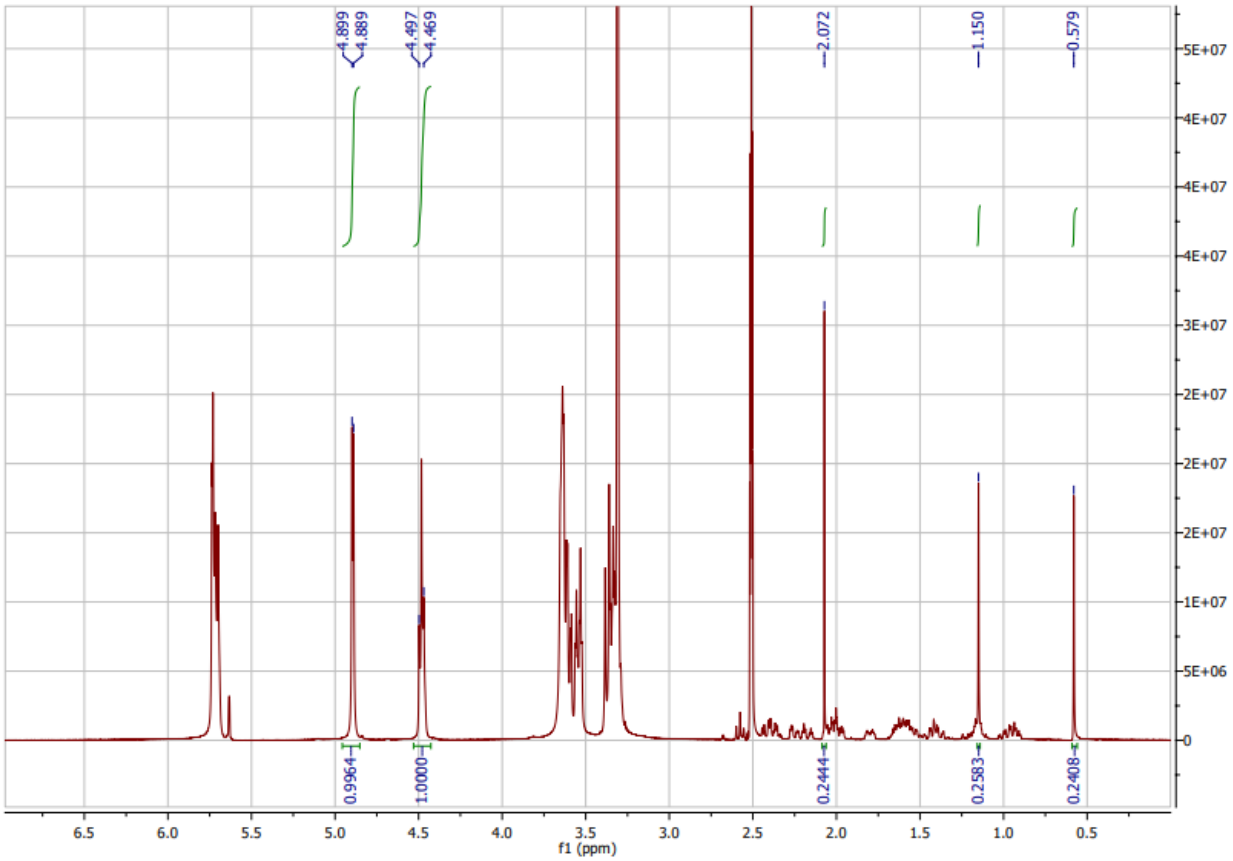


Molecular structures of β-estradiol (left), progesterone (centre) and γ-CD (right). Specific atoms have been labelled for the ^{1}H NMR analyses. Adapted from Guedes *et al.*[1]

The ^{1}H NMR spectrum of γ-CD·BES.



The ^{1}H NMR spectrum of γ-CD·PRO.



4.2.2) Calculation of the number of water molecules in γ-CD·BES·nH_2O, and the number of water molecules per γ-CD molecule (from the TGA analysis).

$$12.7 \pm 0.4\% = \frac{\mathrm{MW(Water)n}}{(\mathrm{MW}(\gamma - \mathrm{CD})) + \mathrm{MW}(\beta - \mathrm{Estradiol}) + \mathrm{MW(Water)n}}$$

$$0.127 = \frac{18.016n}{1297.125 + 272.382 + 18.016n}$$

$\mathrm{n} = 12.7$ water molecules

Therefore there are 12.7 ± 0.4 water molecules per γ-CD molecule in the complex.

4.2.3) Calculation of the number of water molecules in (γ-CD)$_{3/2}$·PRO·nH_2O, and the number of water molecules per γ-CD molecule (from the TGA analysis).

$$14.7 \pm 0.3\% = \frac{\mathrm{MW(Water)n}}{\frac{3}{2}(\mathrm{MW}(\gamma - \mathrm{CD})) + \mathrm{MW(Progesterone)} + \mathrm{MW(Water)n}}$$

$$0.147 = \frac{18.016n}{\frac{3}{2}(1297.125) + 314.469 + 18.016n}$$

$n = 21.6$ water molecules

Therefore there are 14.4 ± 0.3 water molecules per γ-CD molecule.

4.3) Supplementary data for the gravimetric solubility analysis calculations of β-CD·BES, β-CD·PRO, γ-CD·BES and γ-CD·PRO.

- **4.3.1) β-CD·BES:**

These replicated experiments were conducted in a solution containing 3 cm^3 of water.

Experiment 1: Mass of penultimate and final increment of inclusion complex: 2.24 – 2.42 mg

Experiment 2: Mass of penultimate and final increment of inclusion complex: 2.19 – 2.40 mg

Fraction of β-estradiol in $(\beta\text{-CD})_2\cdot BES\cdot 17.7(H_2O)$:

$$\frac{272.382\ \mathrm{g/mol}}{272.382\ \mathrm{g/mol} + 2(1134.987) + 17.7(18.016)\ \mathrm{g/mol}} = 0.095197$$

Therefore, the mass range of β-estradiol solubilized in 1 cm^3 H_2O is:

Experiment 1:

Lower limit: (0.095197 x 2.24 mg) / 3 cm^3 = **0.0710 $mg.cm^{-3}$**

Upper limit: (0.095197 x 2.42 mg) / 3 cm^3 = **0.0768 $mg.cm^{-3}$**

Experiment 2:

Lower limit: (0.095197 x 2.19 mg) / 3 cm^3 = **0.0694 $mg.cm^{-3}$**

Upper limit: (0.095197 x 2.40 mg) / 3 cm^3 = **0.0762 $mg.cm^{-3}$**

- **4.3.2) β-CD·PRO:**

These replicated experiments were conducted in a solution containing 3 cm^3 of water.

Experiment 1: Mass of penultimate and final increment of inclusion complex: 1.02 – 1.37 mg

Experiment 2: Mass of penultimate and final increment of inclusion complex: 1.04 – 1.35 mg

Fraction of progesterone in $(\beta\text{-CD})_2\cdot PRO\cdot 20.0(H_2O)$:

$$\frac{314.469\ g/mol}{314.469\ g/mol + 2(1134.987) + 20.0(18.016)\ g/mol} = 0.106789$$

Therefore, the mass range of progesterone solubilized in 1 cm^3 H_2O is:

Experiment 1:

Lower limit: (0.106789 x 1.02 mg) / 3 cm^3 = **0.0363 $mg.cm^{-3}$**

Upper limit: (0.106789 x 1.37 mg) / 3 cm^3 = **0.0488 $mg.cm^{-3}$**

Experiment 2:

Lower limit: (0.106789 x 1.04 mg) / 3 cm^3 = **0.0370 $mg.cm^{-3}$**

Upper limit: (0.106789 x 1.35 mg) / 3 cm^3 = **0.0481 $mg.cm^{-3}$**

- **4.3.3) γ-CD·BES:**

These replicated experiments were conducted in a solution containing 6 cm^3 of water.

Experiment 1: Mass of penultimate and final increment of inclusion complex: 0.58 – 0.92 mg

Experiment 2: Mass of penultimate and final increment of inclusion complex: 0.55 – 0.83 mg

Fraction of β-estradiol in γ-CD·BES·12.6(H_2O):

$$\frac{272.382\ \text{g/mol}}{272.382\ \text{g/mol} + 1297.128\ \text{g/mol} + 12.6(18.016)\ \text{g/mol}} = 0.15162$$

Therefore, the mass range of β-estradiol solubilized in 1 cm^3 H_2O is:

Experiment 1:

Lower limit: (0.15162 x 0.58 mg) / 6 cm^3 = **0.0147 $mg.cm^{-3}$**

Upper limit: (0.15162 x 0.92 mg) / 6 cm^3 = **0.0232 $mg.cm^{-3}$**

Experiment 2:

Lower limit: (0.15132 x 0.55 mg) / 6 cm^3 = **0.0139 $mg.cm^{-3}$**

Upper limit: (0.15132 x 0.83 mg) / 6 cm^3 = **0.0210 $mg.cm^{-3}$**

- **4.3.4) γ-CD·PRO:**

These replicated experiments were conducted in a solution containing 3 cm^3 of water.

Experiment 1: Mass of penultimate and final increment of inclusion complex: 4.00 – 4.40 mg

Experiment 2: Mass of penultimate and final increment of inclusion complex: 4.00 – 4.42 mg

Fraction of progesterone in $(\gamma\text{-CD})_{3/2}\cdot PRO\cdot 21.6(H_2O)$:

$$\frac{314.469\ \mathrm{g/mol}}{314.469\ \mathrm{g/mol} + \frac{3}{2}(1297.128)\ \mathrm{g/mol}\ + 21.6(18.016)\ \mathrm{g/mol}} = 0.11870$$

Therefore, the mass range of progesterone solubilized in 1 cm^3 H_2O is:

Experiment 1:

Lower limit: (0.11870 x 4.00 mg) / 3 cm^3 = **0.158 $mg.cm^{-3}$**

Upper limit: (0.11870 x 4.40 mg) / 3 cm^3 = **0.174 $mg.cm^{-3}$**

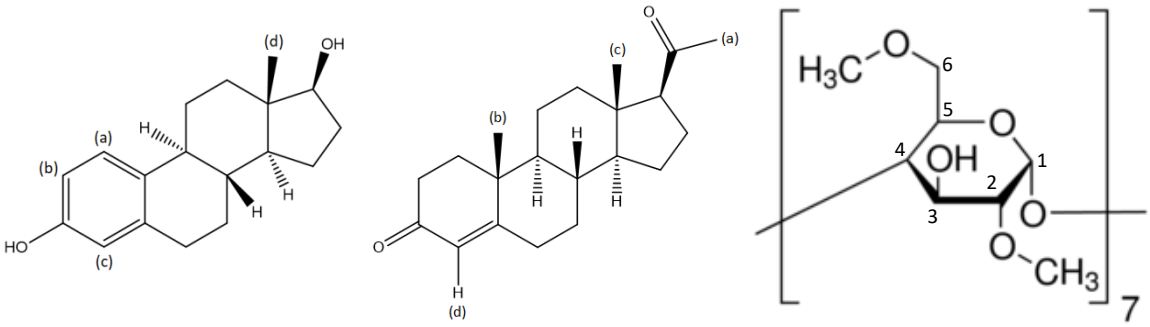
Experiment 2:

Lower limit: (0.11870 x 4.00 mg) / 3 cm^3 = **0.158 $mg.cm^{-3}$**

Upper limit: (0.11870 x 4.42 mg) / 3 cm^3 = **0.175 $mg.cm^{-3}$**

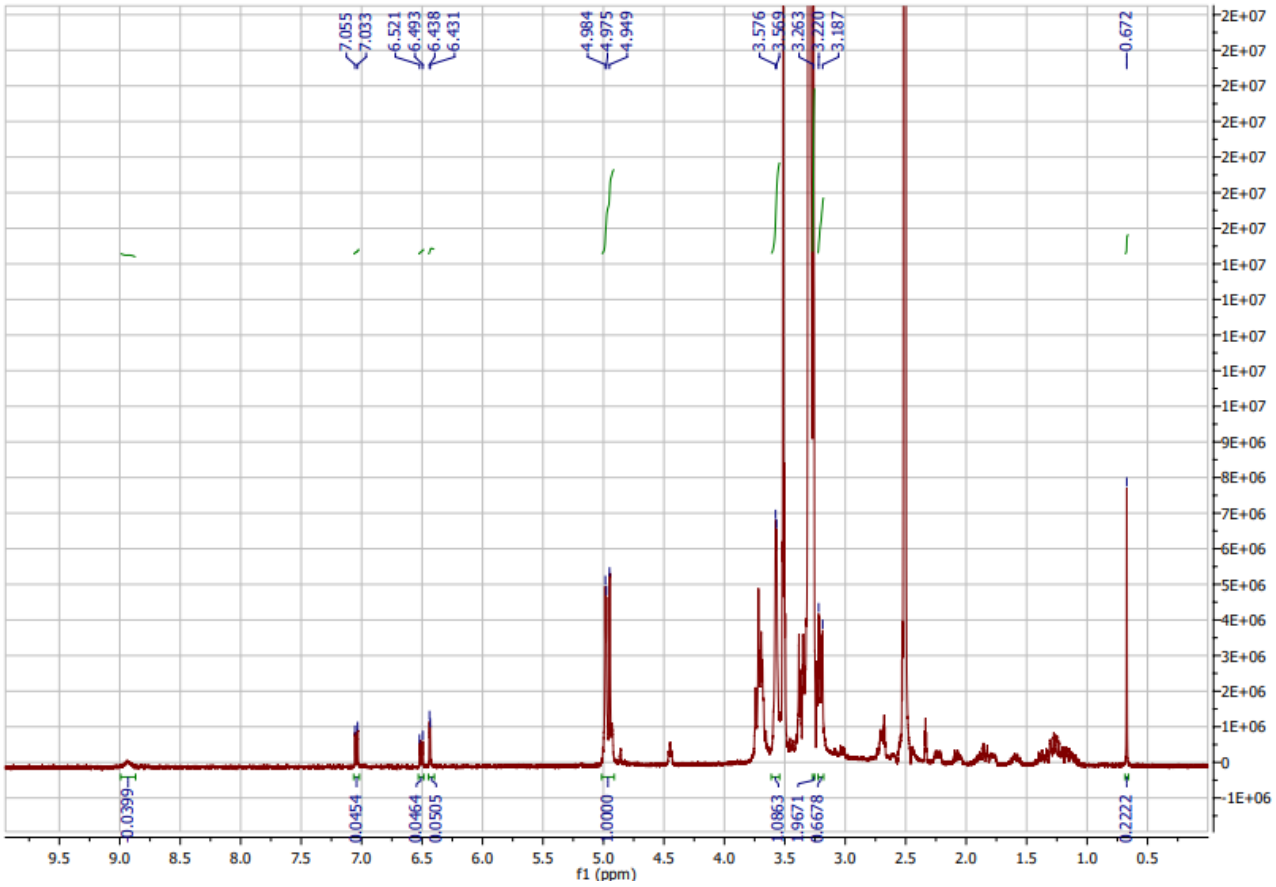
4.4) Supplementary data for DMB·BES and DMB·PRO

4.4.1) The ^{1}H NMR analyses of DMB·BES.

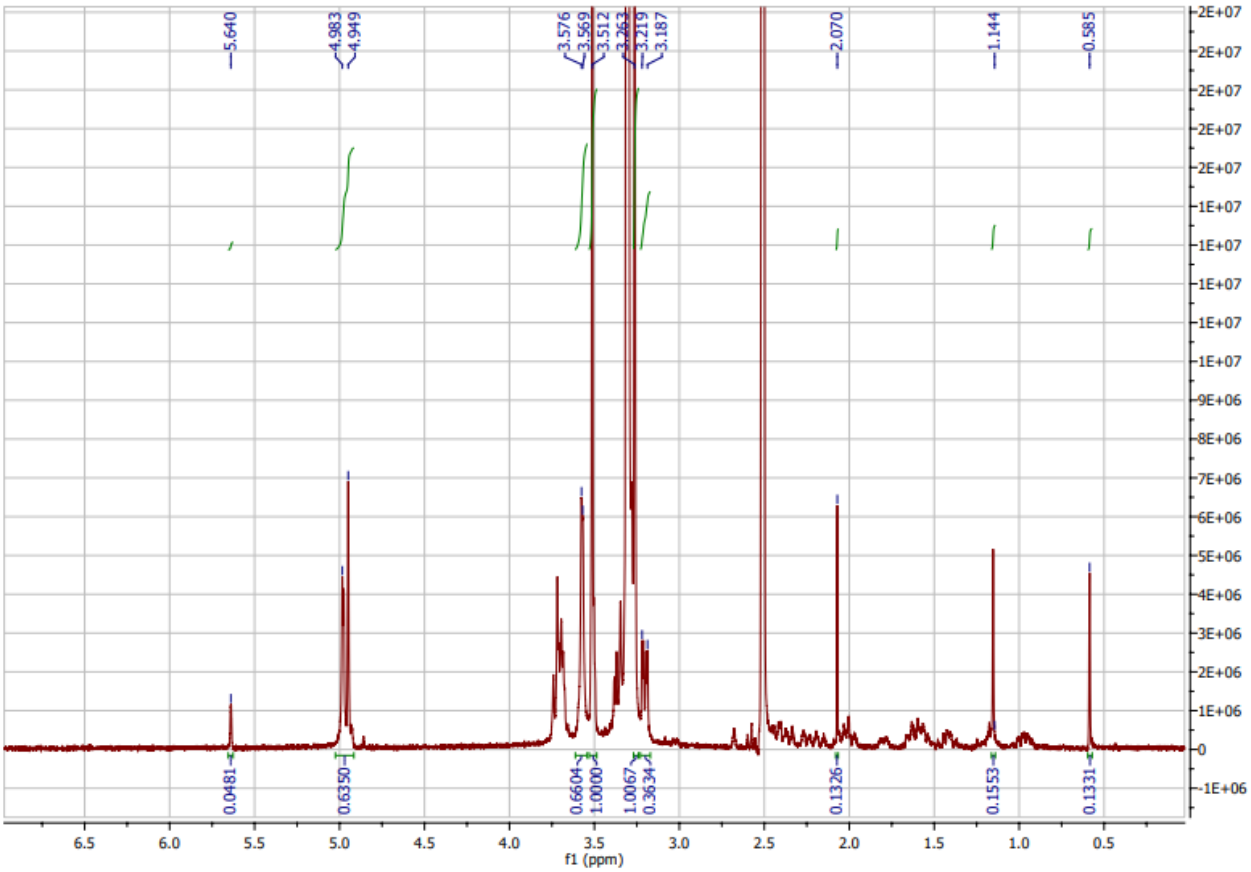


Molecular structures of β-estradiol (left), progesterone (centre), and DMB (right) with particular molecular moieties labelled for ^{1}H NMR characterisation and stoichiometric determination. Adapted from Sigma-Aldrich.[3]

The ^{1}H NMR spectrum of DMB·BES.



The ^{1}H NMR spectrum of DMB·PRO.



4.4.2) Calculation of the number of water molecules in DMB·BES·nH_2O, and the number of water molecules per DMB molecule (from the TGA analysis).

$$3.12 \pm 0.1\% = \frac{\mathrm{MW(Water)n}}{(\mathrm{MW(DMB)}) + \mathrm{MW}(\beta - \mathrm{Estradiol}) + \mathrm{MW(Water)n}}$$

$$0.0312 = \frac{18.016\mathrm{n}}{1331.365 + 272.382 + 18.016\mathrm{n}}$$

$\mathrm{n} = 2.89$ water molecules

Therefore there are 2.9 ± 0.1 water molecules per DMB molecule in the complex.

4.4.3) Calculation for determining the stoichiometry of the anhydrous DMB·BES inclusion complex (from the TGA analysis).

Percentage mass loss of β-estradiol: $13.8 \pm 0.5\%$ (from TGA experiment)

Ratio of β-estradiol to an equimolar anhydrous inclusion complex:

$$\frac{MW(\beta - \text{estradiol})}{MW(\beta - \text{estradiol}) + MW(DMB)}$$

$$\frac{272.382}{272.382 + 1331.365} \times 100 = 17.0\%$$

4.4.4) Calculation of the number of water molecules in DMB·PRO·nH_2O, and the number of water molecules per DMB molecule (from the TGA analysis).

$$1.17 \pm 0.3\% = \frac{MW(Water)n}{(MW(DMB)) + MW(Progesterone) + MW(Water)n}$$

$$0.0117 = \frac{18.016n}{1331.365 + 314.469 + 18.016n}$$

$n = 1.1$ water molecules

Therefore there are 1.1 ± 0.2 water molecules per DMB molecule in the complex.

References

(1) Guedes, L.; Morgon, N.; Martins, M.; Pessine, F. Imiquimod/β-Cyclodextrin Inclusion Complex: Experimental and Theoretical Studies. *J. Braz. Chem. Soc.* **2020**. https://doi.org/10.21577/0103-5053.20200060.

(2) Sigma-Aldrich https://www.sigmaaldrich.com/ZA/en/product/sigma/h4645 (accessed Nov 25, 2021).

(3) Merck, Sigma-Aldrich https://www.sigmaaldrich.com/ZA/en/product/sigma/h0513 (accessed Aug 6, 2020).